



**GEOMETRIC AND RADIOMETRIC CALIBRATION OF
VIDEO INFRARED IMAGERS
FOR
PHOTOGRAMMETRIC APPLICATIONS**

BY

GURCAN BUYUKSALIH

VOLUME I

A Thesis Submitted for the Degree of Doctor of Philosophy (Ph.D.)
in Photogrammetry and Remote Sensing
in the Faculty of Science at the University of Glasgow

Topographic Science, November 1997

ProQuest Number: 13815380

All rights reserved

INFORMATION TO ALL USERS

The quality of this reproduction is dependent upon the quality of the copy submitted.

In the unlikely event that the author did not send a complete manuscript and there are missing pages, these will be noted. Also, if material had to be removed, a note will indicate the deletion.



ProQuest 13815380

Published by ProQuest LLC (2018). Copyright of the Dissertation is held by the Author.

All rights reserved.

This work is protected against unauthorized copying under Title 17, United States Code
Microform Edition © ProQuest LLC.

ProQuest LLC.
789 East Eisenhower Parkway
P.O. Box 1346
Ann Arbor, MI 48106 – 1346

GLASGOW
UNIVERSITY
LIBRARY

Thesis 11043 (copy 1)

GLASGOW UNIVERSITY
LIBRARY

IN THE NAME OF ALLAH

TO MY DECEASED GRANDMOTHER KEBIRE BUYUKSALIH

SUMMARY

This thesis is concerned with the geometric and radiometric calibration of infrared imagers with a view to their use in close-range and airborne photogrammetric applications. From the geometric point of view, three quite different types of infrared imager can be distinguished - these comprise (i) the pyroelectric vidicon camera; (ii) the CCD camera based on the use of an areal array of solid-state detectors; and (iii) the thermal video frame scanner (TVFS). The special optics and the detector technologies that are used in these imagers to generate images in the middle and thermal bands of the infrared spectrum, together with the underlying video technology, are first reviewed and discussed in some detail with an emphasis on their fundamental geometric and radiometric characteristics and properties. On this basis, the design and construction of a special target plate has been undertaken that allows all these different types of imager to be calibrated both geometrically and radiometrically. After describing this target plate, the actual experiment set-up and procedures and the subsequent data processing and analysis are outlined, including the method devised and used for the automatic measurement of the positions of all the target crosses on the calibration plate employing image matching techniques.

The results obtained from the successful calibration of a representative sample of CCD cameras and thermal video frame scanners are presented and discussed in detail. They provide much new and accurate information on the geometric characteristics of these types of infrared imager that will be invaluable to those undertaking photogrammetric measurements on the infrared images that are being acquired and used in military, medical, industrial and environmental applications. For the radiometric calibration of each imager, measurements of the grey level values were made over the whole of the image covering the target radiation source for a range of temperatures. Thus much original and valuable information on the radiometric characteristics of the imagers has been obtained from the work undertaken during this research project, more especially at lower operational temperatures. However the techniques used gave less good results at higher temperatures and these need to be modified if more useful results are to be obtained. Suggestions are made for the further development of the calibration technique, in particular for its use with low-resolution imagers such as the pyroelectric vidicon camera which have not been calibrated in this research project due to time and financial limitations.

ACKNOWLEDGEMENTS

The author wishes to express his sincere gratitude to his supervisor, Professor G. Petrie, for suggesting this topic, for his continuous advice and supervision and for supplying the materials relevant to this research. Without all this help, this research would never come to its present form.

The author's sincere thanks also go to Mr. J. Shearer, his second supervisor from September 1995, for his help, advice and encouragement. Special thanks also go to Mr. D.A. Tait for his advice in specific matters and his general encouragement. The assistance received from the other Topographic Science staff members, who are always ready to help, is also gratefully acknowledged, in particular, that given by Dr. J. Drummond and Mr. T. Ibbs.

Thanks are also due to the Department's Chief Technician, Mr. I. Gerrard and his assistant, Mr. L. Hill, for preparing the photographs included in this dissertation. Mr Gerrard was also very helpful in setting up the author's experimental work. Sincere thanks must also be given to the Department's senior Cartographer, Mr. M. Shand, both for his technical support and for the immediate assistance which he gave for the scanning of some of the graphs included in this thesis.

The author also wishes to extend his gratitude to Professor J. Briggs (Head of the Department) for granting the freedom to use the facilities available in the Department.

The author wishes to thank Mr. K. Ellis, Mr. M. Bosworth and Mr. I. Dibley from Agema Company for providing the Agema imagers used for most of the calibration tests and their help and technical support.

The author also wishes to thank Mr. P. McCartney from the Amber company, for providing the Radiance PM1 camera and for his help and assistance while carrying out the calibration of this camera.

Thanks and gratitude are due to the relevant members of staff at Strathclyde and Glasgow Caledonian Universities through the use of their imagers for this project and their help and technical support.

Thanks and gratitude are also due to Mr. G. Ross from Barr & Stroud, for providing his experience and his ideas about the design and construction of the new target plate.

It is a pleasure to acknowledge the willing help and advice of the technical staff of the Departments of Mechanical and Electrical & Electronics Engineering at this University in the construction of the target plate.

Sincere thanks are also due to his research colleagues in Topographic Science, in particular, Mr. A.R. Alias, Mr. N. Al-Rousan, Mr. M. Duckham, Dr. Y.J. Kuo, Mr. H. Rammali, Mr. J.H. Yom, Mr. Z. Zamlupe, and Dr. M.J.Valadan Zoej for their support and friendship throughout the period of this study in the Department of Geography and Topographic Science.

The author wishes to express thanks to his sponsor, Zonguldak Karaelmas University in Turkey, for providing the Scholarship which supported him during the period of his study.

I wish to express my gratitude to my family and relatives in Turkey - my father and mother, Omer and Betul, my brothers and sisters - Ayse, Emel, Erhan and Ismail; my late grandfathers, Ismail and Sukru; my grandmothers, Kebire (now deceased) and Fethiye; my uncles, Mehmet, Hakki and Hasan; my aunts, Alev, Gulseren, Tulay and Hamiyet; my cousins, Fethi, Feyza, Seda, Betul Sema, Aslan, Fatih, Ali, Murat and Osman; my father and mother-in-law, Mehmet and Ayse; my brother-in-law, Ercan and my grandmother-in-law, Elmas for all their support and encouragement in completing my studies. They have borne a long separation and the author owes his every achievement to them.

Finally, the author is extremely pleased to acknowledge the marvellous support provided by his wife, Mrs. Nagihan Buyuksalih, and his daughter Fatma Irem who share life's joys and sorrows with him and who have been a constant source of inspiration even in moments of utter despondency. His wife's patience and continuous encouragement and support, which had a great impact on the progress of the work, never stopped.

TABLE OF CONTENTS
VOLUME I

ABSTRACT	i
ACKNOWLEDGEMENTS	ii
TABLE OF CONTENTS	v
 CHAPTER 1 : INTRODUCTION	
1.1 The Importance of the Infrared Imaging Systems for Photogrammetric Applications	1
1.1.1 The Unique Characteristics of Infrared Imaging Systems	2
1.1.2 The Photogrammetric Processes Required on Infrared Imagery Acquired for Mensuration and Mapping Purposes	5
1.2 The Geometric and Radiometric Characteristics of Different Infrared Imaging Systems	6
1.2.1 Pyroelectric Vidicon Cameras	7
1.2.2 CCD-based Cameras	8
1.2.3 Thermal Video Frame Scanners	10
1.2.4 Radiometric Aspects of Infrared Imagers	12
1.3 Research Objectives	13
1.4 Outline of the Thesis	14

CHAPTER 2 : FUNDAMENTAL THEORY UNDERLYING THE INFRARED IMAGING SYSTEMS

2.1 Introduction	18
2.2 Nature of Electromagnetic Radiation	18
2.3 Characteristics of Electromagnetic Radiation	23
2.4 Electromagnetic Wavebands	25
2.4.1 The Infrared Spectrum	26
2.5 Basic Laws of Infrared Radiation	27
2.5.1 Planck's Blackbody Law	27
2.5.2 Wien's Displacement Law	28
2.5.3 Stefan-Boltzmann Law	29
2.6 Atmospheric Transmission	30
2.7 Total Scene Radiation and Contrast	31
2.8 Conclusions	33

CHAPTER 3: INFRARED OPTICAL MATERIALS AND COMPONENTS

3.1 Introduction	34
3.2 Infrared Optical Materials	35
3.3 Optical Arrangements	37
3.3.1 Refracting Optics	38
3.3.2 Reflecting Optics	42
3.3.3 Catadioptric Optics	45
3.3.4 Relay Lens (Auxiliary Optics)	45
3.4 Anti-Reflection (AR) Coatings	46
3.5 Infrared Telescopes and Lens Systems	47
3.5.1 Examples of Infrared Imager Optical Systems	48
3.6 Infrared Lens Quality	50
3.7 Resolution	54
3.7.1 Aperture and Resolution	55
3.7.2 Wavelength and Resolution	56

3.7.3 Depth of Field and Aperture	57
3.7.4 Depth of Focus	58
3.8 Conclusion	59

CHAPTER 4: INFRARED DETECTORS

4.1 Introduction	60
4.1.1 Detectors	60
4.2 Definition of Relevant Terms	61
4.3 Thermal Detectors	65
4.3.1 Bolometers	65
4.3.1.1 Metal and Semi-conductor (Thermistor)	
Bolometers	66
4.3.2 Pyroelectric Detectors	67
4.4 Physics of Semi-conductors	68
4.4.1 The Periodic Lattice	68
4.4.2 Energy Bands in a Perfect Crystal	69
4.4.3 Imperfections in the Lattice	71
4.5 Photon (Quantum) Detectors	71
4.5.1 Photoconductive Detectors	72
4.5.2 Photovoltaic Detectors	73
4.5.3 Materials Used for Photon Detectors	74
4.5.4 The SPRITE Detector	76
4.6 Noise In Detectors	77
4.7 Detector Cooling	78
4.8 Detector Arrays	79
4.8.1 Read Out Mechanisms of Detector Arrays	80
4.8.2 Organization of Different Detector Types in Areal	
Array CCDs	82
4.8.3 Geometric Properties of Arrays of CCD Detectors	85
4.8.3.1 Geometry of Detector Elements	85
4.8.3.2 Surface Flatness	86

4.8.4 Spurious Signals	87
4.8.5 Infrared CCD (IR-CCD) Areal Arrays	90
4.8.5.1 Monolithic IR-CCDs	90
4.8.5.2 Hybrid IR-CCDs	91
4.8.5.3 Practical Limitations with IR-CCDs	92
4.9 Conclusions	93

CHAPTER 5 : VIDEO TECHNOLOGY

5.1 Introduction	94
5.2 Video System	96
5.2.1 Video Tube Camera	96
5.2.1.1 Electron Beam Scanning	99
5.2.1.2 Colour Video Cameras	100
5.3 Video Imaging Devices in the Infrared Band	102
5.4 Video Image Resolution	102
5.5 Video Image Geometry	106
5.6 Video Recording	106
5.6.1 U-matic VTR	108
5.6.2 VHS, Betamax and Video 2000 VTR systems	108
5.7 Video Displays	109
5.7.1 Monochrome Displays	109
5.7.2 Colour Displays	110
5.7.3 Computer Graphics Display	112
5.8 Distortions in the Video System	113
5.8.1 Distortions in the Video Camera	113
5.8.1.1 Distortions in the Vidicon Tube	113
5.8.1.2 Lens Distortions	115
5.8.1.2.1 Radial Distortion	115
5.8.1.2.2 Decentering (Tangential) Distortion	118
5.8.2 Distortions Stemming From the VTR	119
5.8.3 Distortions in a CRT-based Display Monitor	120

5.9 Conclusion	122
----------------------	-----

CHAPTER 6 : VIDEO STANDARDS

6.1 Introduction	124
6.2 Data Capture and Signal Transmission	125
6.3 Video Inputs	127
6.3.1 Standard Video Formats	128
6.3.2 High Definition Television (HDTV)	131
6.3.3 S-Video	133
6.3.4 PC Video Standards	134
6.3.5 Workstation Video Standards	135
6.4 Synchronisation and Transmission of Video Signals	136
6.4.1 The Composite Video Signal	136
6.4.2 Other Synchronisation Signals	139
6.5 Conclusions	140

CHAPTER 7 : ANALOGUE VIDEO TO DIGITAL CONVERSION

7.1 Introduction	141
7.2 Monochromatic Frame Grabber	142
7.2.1 Analogue Front End	143
7.2.2 Synchronisation	145
7.2.2.1 PLL Line Synchronization	145
7.2.2.2 Pixel Synchronous Sampling	147
7.2.3 Analogue-to-Digital (A/D) Conversion	148
7.2.3.1 Quantization Error	150
7.2.3.2 Signal-to-Noise Ratio (SNR)	150
7.2.3.3 Integral Linearity Error	151
7.2.3.4 Differential Linearity Error	151
7.2.3.5 Missing Code	151
7.2.3.6 Offset Error	152

7.2.3.7 Gain Error	152
7.2.3.8 Resolution	152
7.2.4 Data Buffering	152
7.3 Frame Grabbers Used in the Project	153
7.4 Image Display	155
7.5 Processing Hardware	156
7.6 Conclusions	157

CHAPTER 8: INFRARED FRAME TYPE (PLANAR) IMAGERS

8.1 Introduction	158
8.1.1 Classification of Infrared Imagers	160
8.2 Thermal Infrared Pyroelectric Vidicon Cameras	162
8.2.1 Image Modulation - Chopping versus Panning Mode	163
8.2.1.1 Lag	164
8.2.1.2 Observer Fatigue	164
8.2.1.3 Compensating Positive Current	165
8.2.2 Geometric Aspects of the Pyroelectric Vidicon	166
8.2.3 Commercially Available Pyroelectric Vidicon Cameras	166
8.3 Infrared CCD Camera	167
8.4 Commercially Available Infrared CCD Cameras	170
8.5 Conclusions	171

CHAPTER 9 : INFRARED SCANNER IMAGERS

9.1 Introduction	172
9.2 Optical-Mechanical Line Scanners	173
9.2.1 Airborne Infrared Line Scanner	173
9.2.2 Geometry of Optical-Mechanical Line Scanner Imagery	174
9.2.3 Multispectral Line Scanners	175
9.2.3.1 Satellite Systems	176
9.2.3.1.1 HCMM (Heat Capacity Mapping	

Mission)	177
9.2.3.1.2 Landsat MSS and TM Series	178
9.3 Thermal Video Frame Scanners (TVFS)	178
9.3.1 Scanning Configuration	179
9.3.1.1 Serial Scanning	179
9.3.1.2 Parallel Scanning	180
9.3.1.3 Serial/Parallel Scanning	181
9.3.2 Scanning Mechanism of TVFS	181
9.3.2.1 The Oscillating Plane Mirror	182
9.3.2.2 The Rotating Reflective Polygon	182
9.3.2.3 The Rotating Refractive Polygon	183
9.3.3 Geometric Effects of the Scanning Mechanism	183
9.3.4 Geometric Potential of TVFS	185
9.3.5 Commercially Available Thermal Video Frame Scanners	186
9.3.6 Optical Arrangement of the TVFSs	190
9.3.6.1 Optical Design of the HDTI	190
9.3.6.2 Scanning Arrangement of the Agema Thermovision 1000	192
9.4 Conclusions	193

CHAPTER 10: GEOMETRIC AND RADIOMETRIC CHARACTERISTICS OF INFRARED IMAGING SYSTEMS

10.1 Introduction	194
10.2 Geometric Characteristics	194
10.2.1 Instantaneous Field of View of the Infrared Imaging System	194
10.2.1.1 IFOV and FOV of Infrared Scanners	194
10.2.1.2 Trade-off Between the Geometric and Radiometric Resolution of Scanners	197
10.2.1.3 IFOV and FOV of Infrared Cameras	198
10.3 Radiometric Characteristics	201

10.3.1 Dynamic Range	202
10.3.2. Noise	203
10.3.3 Signal Non-Uniformities and Radiometric Correction	204
10.3.3.1 Photo Response Non-Uniformity (PRNU)	204
10.3.3.1.1 Non-Uniformity Correction Algorithm ..	205
10.3.3.1.2 Pre-processing and Conditions for Radiometric Correction	205
10.3.3.2 Dark Signal Non-Uniformity (DSNU)	206
10.3.4 Modulation Transfer Function (MTF)	207
10.3.5 Noise Equivalent Temperature Difference (NETD)	208
10.3.6 Minimum Resolvable Temperature Difference (MRTD)	209
10.4 Conclusions	211

VOLUME II

CHAPTER 11: SUB-PIXEL MEASUREMENTS OF CROSS TARGETS IN THE DIGITAL INFRARED IMAGES

11.1 Introduction	212
11.2 Image Segmentation	213
11.2.1 Thresholding	213
11.2.2 Edge Detection	215
11.2.2.1 Edge Operators	216
11.2.2.2 Edge Locators	217
11.2.3 Image Correlation	219
11.2.3.1 Image Correlation Classification	220
11.2.3.2 Image Matching Fundamentals	221
11.2.3.3 Image Matching Problems	222
11.2.3.4 Least Squares Image Matching Method	222
11.2.3.4.1 Image Pyramids	225
11.3 The Measurement of the Positions of Cross Targets	226
11.3.1 Automatic Detection, Recognition and Location	

of Cross Targets	226
11.3.1.1 Detection of Cross Targets	226
11.3.1.2 Recognition of Cross Targets	227
11.3.1.3 Location of Cross Targets	228
11.3.2 Cross Target Measurement	229
11.3.2.1 Measurement of the Cross Position Using the Gradient Method	230
11.3.2.2 Image Modelling and Least Squares Matching Method for Cross Target Measurement	234
11.3.2.2.1 The General Adjustment Model	235
11.3.2.2.2 Measuring a One-dimensional Edge	238
11.3.2.2.3 Point Spread Function	240
11.3.2.2.4 Edge Pointing With Gaussian Spread Function	241
11.3.2.2.5 Cross-type Targets	241
11.4 Conclusion	243

CHAPTER 12: COMPUTER PROGRAMMING OF THE IMAGE MATCHING PROCEDURE

12.1 Introduction	244
12.2 Development of Program SUBPIX	244
12.2.1 Structure of Program SUBPIX	245
12.2.2 Sub-Program GRAD	249
12.2.3 Sub-Program PTSUB	251
12.2.4 Routines	253
12.3 Test Results	254
12.3.1 Test Results With Thermal Images	255
12.3.2 Test Results With CCD Images	258
12.3.3 Tests with Alternative Method	258
12.3.4 Comments on the Use of the Program and the Accuracy Results	259

12.4 Conclusions	260
------------------------	-----

CHAPTER 13: EXPERIMENTAL PROCEDURES AND SUBSEQUENT DATA PROCESSING

13.1 Introduction	261
13.2 Actual Experimental Procedures	261
13.2.1 Geometric Calibration Procedures	263
13.2.1.1 Difficulties with the Target Plates	265
13.2.1.2 Characteristics of Dr. Amin's Plate	267
13.2.1.3 Design of the New Calibration Target Plate	269
13.2.2 Radiometric Calibration Procedures	272
13.2.3 Problems Experienced During the Experimental Work	274
13.3 Processing of the Data	275
13.3.1 Digital Image Processing by Photoshop	276
13.3.1.1 Grey Level Value Adjustment and Contrast Enhancement	276
13.3.1.2 Photoshop's Filters	281
13.3.1.2.1 Median Noise Filter	281
13.3.1.2.2 Sharpen Filters	282
13.3.2 Data Processing for Geometric Calibration Purposes	283
13.3.3 Data Processing for Radiometric Calibration Purposes	284
13.4 Analysis of the Data Obtained During the Geometric Calibration	285
13.4.1 Linear Conformal Transformation	286
13.4.2 Affine Transformation	287
13.4.3 Polynomial Transformation	288
13.4.4 Plotting of Residual Errors	290
13.4.5 Systematic and Random Components of Geometric Distortion	291
13.5 Analysis of the Data Obtained During the Radiometric Calibration ...	292
13.5.1 Computation of the Mean and Standard Deviation of the Grey Level Values	293

13.5.2 Temporal Average of the Quadrants	293
13.5.3 Spatial Average and Noise	294
13.5.4 Statistical Processing of the Grey Level Values of the Quadrant	295
13.5.5 Graphical Representation of the Grey Level Values of the Pixels by SURFER	297
13.6 Conclusion	298

CHAPTER 14: RESULTS AND ANALYSIS OF THE GEOMETRIC CALIBRATION OF INFRARED CCD CAMERAS

14.1 Introduction	299
14.2 Agema 550 CCD Camera	299
14.2.1 Experimental Procedure with Agema 550	300
14.2.2 Results and Analysis of the Geometric Calibration of the Agema 550	301
14.2.2.1 Results and Analysis with the 20° Lens	301
14.2.2.2 Results and Analysis with the 10° lens	308
14.2.2.3. Results and Analysis with the 40° Lens (Second Occasion)	313
14.3 Amber Radiance PM1 CCD Camera	318
14.3.1 Result and Analysis of the Geometric Calibration of the Radiance PM1	318
14.4 Overall Analysis	322
14.4.1 Analysis of the Effective Terms for Each of the Lenses	323
14.4.2 Analysis of the Residual Errors	325
14.4.3 Systematic and Random Components of Geometric Distortion	328
14.5. Conclusion	329

CHAPTER 15: RESULTS AND ANALYSIS OF THE RADIOMETRIC CALIBRATION OF INFRARED CCD CAMERAS

15.1 Introduction	330
15.2 Radiometric Calibration of the Agema 550 CCD Camera	330
15.2.1 Radiometric Calibration with the 20° lens	330
15.2.1.1 Radiometric Calibration of Whole Frames	331
15.2.1.2 Radiometric Calibration of Quadrants and Patches	337
15.2.1.2.1 Computation of the Means and Standard Deviations of the Grey Level Values	337
15.2.1.2.2 Non-Uniformity Correction	337
15.2.1.2.3 Statistical Processing of the Grey Level Values of Pixels	341
15.2.1.2.4 Graphical Representation of the Grey Level Values of the Pixels	344
15.2.1.2.5 Different Fixed Patterns Present at Different Temperatures	346
15.2.2 Radiometric Calibration with the 10° Lens	347
15.3 Radiometric Calibration of the Amber Radiance PM1 Camera	352
15.3.1 Discussion of the Results from the Radiance PM1 Camera	356
15.4 Overall Analysis	363
15.5 Conclusion	366

CHAPTER 16: RESULTS AND ANALYSIS OF THE CALIBRATION OF THERMAL VIDEO FRAME SCANNERS

16.1 Introduction	367
16.2 Agema 1000	368
16.2.1 Geometric Calibration of the Agema 1000	368
16.3 Agema 900 LW	373

16.3.1 Geometric Calibration of the Agema 900	374
16.4 Agema 880	378
16.4.1 Geometric Calibration of the Agema 880 TVFS	378
16.5 Agema 470	381
16.5.1 Geometric Calibration of the Agema 470	383
16.6 Systematic and Random Components of the Distortion	385
16.7 Radiometric Calibration of the Agema 1000	385
16.8 Radiometric Calibration of the Agema 900	391
16.9 Radiometric Calibration of the Whole Frames	396
16.10 Conclusion	397

CHAPTER 17: CONCLUSIONS AND RECOMMENDATIONS

17.1 Introduction	399
17.2 Conclusions	399
17.2.1 General Conclusions	400
17.2.2 Specific Conclusions	404
17.3 Recommendations for Future Work	410
17.4 Potential Applications	413
17.5 A Final Note	414

REFERENCES	416
-------------------------	------------

APPENDICES

APPENDIX A: PROGRAM SUBPIX	427
APPENDIX B: REFERENCE COORDINATES OF THE CROSS TARGETS	448
APPENDIX C: PROGRAM LINCON	452
APPENDIX D: PROGRAM POLY25	470
APPENDIX E: PROGRAM STMN	489
APPENDIX F: PROGRAM PRNU	493
APPENDIX G: PROGRAM STAT	498

CHAPTER 1: INTRODUCTION

1.1 The Importance of the Infrared Imaging Systems for Photogrammetric Applications

For topographic mapping applications, aerial photogrammetric cameras have been commonly used for over sixty years. These cameras utilize photographic film and are designed, constructed and calibrated specifically to produce an image with a precisely known geometry. Their geometric characteristics, i.e. their inner orientation parameters - the principal distance, the location of the principal point and the lens distortion model - and their radiometric characteristics, which determine how a specific film responds to scene radiation of varying intensity, are very well known and have been determined with very high accuracy. The extensive use of these aerial photogrammetric cameras in combination with the classical analogue and analytical photogrammetric instrumentation has shown that together they form a very powerful and versatile tool for mapping applications. Their high image resolution, their geometric and radiometric fidelity and the possibility of generating 3-D information from the stereoscopic capabilities of these cameras cannot be matched at this time by any other imaging systems that are currently in use.

In parallel with the development of photogrammetric methods and technology for aerial mapping purposes has been that of close-range photogrammetry for industrial and scientific purposes. While much of the methodology is in principle either identical or similar to that employed in aerial photogrammetry, it has also developed its own distinctive technology in the form of highly portable small format photographic cameras and even specialized photogrammetric instruments (e.g. the Zeiss Stereoautograph and Wild A40 Autograph). In recent years, the close-range photogrammetric community has pioneered the development and use of all-digital cameras based on CCD technology in the photogrammetric field, primarily for industrial applications. It must be said that these CCD cameras fall far short of aerial photographic cameras in terms of their format size and geometric resolution, but nevertheless they have been the subject of intensive research and development for use

in industrial, medical and architectural applications. In particular, they have lent themselves to the creation of an all-digital photogrammetric environment and to the implementation of highly automated photogrammetric operations based on extensive use of image matching techniques. In turn, this has led to close contacts and cooperation with the image processing community (mainly made up of computer scientists and electronic engineers) as evidenced by the Videometrics meetings organised by the SPIE and held in the United States on an annual basis.

By contrast, in the first instance, infrared imaging systems have been developed primarily for military reconnaissance, surveillance and targeting purposes. But, now, they are just beginning to be utilised by a number of users working in the field of photogrammetry and remote sensing. These systems offer several advantages in terms of ease of use, speed of operation, portability and cost as compared with alternative imaging systems. Mostly they operate in the near infrared part of the electro-magnetic spectrum but of increasing interest are those imaging systems that operate in the middle and thermal infrared part of the electromagnetic (EM) spectrum. However, their geometric and radiometric characteristics, which are essential for photogrammetric applications, have had limited attention up until now and often they are not known or have not been determined.

1.1.1 The Unique Characteristics of Infrared Imaging Systems

Infrared imaging is a technique for converting a scene's infrared radiation pattern - which is invisible to the human eye - into a visible image that can be seen and used by human beings. It is therefore concerned with the measurement of the radiant energy emanating from an area of the Earth's surface in the infrared part of the spectrum. This mostly consists of two components - the reflected solar radiation and the emitted object radiation - that are present within the spectral wavelength (λ) regions lying between 3 to 5.6 μm and 5.6 to 15 μm respectively. The first of these two bands is usually termed the middle infrared band in which reflected solar radiation represents about 80% of the total radiation from the object. In the second case, the energy band coincides with the wavelengths normally associated with the heat being emitted from

object, hence it is termed the thermal infrared band. Infrared imaging in these two bands is a real-time and totally passive remote sensing technique, requiring no external source of illumination. Therefore, it allows day and night operation, and covert sensing of the object or area requiring imaging. In an industrial context, it is ideal for the detection of hot or cold spots or of areas of different emissivities within a scene. Moreover, infrared imagers can penetrate smoke and mist more readily than imagers operating in the visible part of the spectrum allowing visually obscured objects to be detected, e.g. in military or firefighting operations.

The long operating wavelengths of these infrared imaging systems make them optically and electronically very different to those that are operated in the visible and near infrared regions of the EM spectrum. In particular, the resolution, aberrations and diffraction effects are functions of the much longer wavelengths of the radiation that are being used. This limits the imaging characteristics of infrared optical systems and could affect the accuracy of the measurements that can be made on the images which are obtained by these systems. In addition, many materials that are transparent in the visible band and can be used as **optical components** in imagers operating in this region are not transparent throughout the infrared part of the spectrum. Since ordinary silicate-based glass does not transmit radiation beyond the wavelength of $2.5\mu\text{m}$, in the infrared regions, the designers of optics of infrared imagers have had to rely on much less commonly available materials that are often very expensive to produce and are difficult to fabricate into optical components such as lenses and prisms. Germanium and special silicon glasses have been used extensively as lens materials in infrared imaging systems. While the silicon-based materials are mostly used in devices operating in the middle infrared band, germanium is used as a transmissive material in the thermal region.

The detection of electromagnetic energy can be performed either photographically or electronically. Photography uses chemical reactions on the surface of a light-sensitive film to detect the radiation variations occurring in a scene within the sensitivity range of its emulsion. By developing out the resulting image chemically, a record of the detected signals is obtained. Thus, the film acts both as the detecting and the

recording medium. By contrast, in infrared imaging systems, the corresponding detection and recording stages have to be implemented separately and by quite different means - since photographic emulsions are not sensitive to radiation in the middle and far infrared bands. Instead of the silver halide based emulsions used in photography, **electronic detectors** are used to detect and measure the radiation being emitted or reflected from the object (and which has been collected by the optical components of the imaging systems) and to convert this radiation into form of an electrical signal. Those detectors that are commonly used in infrared imaging systems can be divided into two groups - thermal detectors and photon detectors - based on the type of the responsive element actually employed. As with the optical components, the materials that are used in the detector systems of infrared cameras and scanners are quite different to those deployed in the corresponding types of imagers (CCD cameras and line scanners) that have been developed for use in the visible part of the spectrum. Again this stems from the quite different physical characteristics of the components that can be employed at the operating wavelength of these systems.

At the present time, since the direct visual display of infrared radiation in a form that can be seen by human beings is not possible, all the acquisition, display and recording of images that is carried out by infrared imaging systems is **video-based**. Indeed it is impossible to envisage present day infrared cameras and scanners as operational systems without the supporting video technology. Moreover, the transmission of images from the infrared imager to the user's display or processing system is governed by the characteristics of the **analogue video signals** used in television broadcasting which have been adopted almost universally as the standard used in infrared imaging. As the name implies, analogue video is transmitted as a continuous signal at a radio frequency through the atmosphere or along a coaxial cable. The timing and the structure of these signals are determined by the specifications and standards defined and established for broadcast television systems. From these initial definitions, the monochrome and colour video standards that are in current use have been developed. To carry out the computer processing of those infrared images that have been generated and recorded using analogue (continuous) video signals, they

have to be converted to digital (discrete) form. This conversion is normally carried out by a **frame grabber** that is installed in a PC or some other type of computer.

From the above discussion, it can be seen that the use of infrared imagery involves many considerations and number of technologies that are unfamiliar to almost all photogrammetrists. Nevertheless it is obvious that, since these images contain information that is valuable to a wide variety of users, then as the technology is further developed, the use of infrared images will become still more widespread. Quite certainly, some users will want to make photogrammetric measurements on these images. Thus, it is timely to investigate the basic geometric and radiometric characteristics of infrared imagery from the photogrammetric point of view and this forms part of the justification for undertaking the research project reported in this dissertation.

1.1.2 The Photogrammetric Processes Required on Infrared Imagery Acquired for Mensuration and Mapping Purposes

Arising from the various factors mentioned above, currently an increasing number of users have been considering the potential of these systems (i) in the context of remote sensing applications; (ii) in the field of mapping; and (iii) for close-range industrial and medical applications of photogrammetry. However, in order to implement such applications, the various photogrammetric procedures that are well known and commonly used for the analysis and measurement of photographic camera images must be investigated in the context of using them with the very different imagery that is produced by infrared imagers. The result of such an investigation will almost certainly mean that the procedures that are familiar to photogrammetrists may need to be modified or indeed completely new equipment and procedures may need to be developed for the purpose. Specific aspects that need to be investigated include the following:-

- (i) an analysis of the geometric and radiometric characteristics of the devices and systems used for image generation;

- (ii) the development of a geometric calibration methodology to determine the interior orientation parameters which are not precisely known or established and the parallel development of radiometric calibration procedures to calibrate the accurate grey level value information that is contained in the infrared image data; and
- (iii) devising and implementing suitable digital or analytical photogrammetric techniques for mapping purposes.

As can be seen from the discussion conducted above, to obtain photogrammetric information from infrared images, the geometric and radiometric characteristics of the various types of infrared imagers and the procedures that are employed to obtain images using these devices should be known. However this is simply not the case at the present time. So, in the first instance, the geometric and radiometric calibration procedures that will establish all of these characteristics accurately should be developed and tested and applied to the infrared imaging systems. Obviously this needs to be done with a view to assessing their suitability for the measurement of dimensions, volumes, locations, etc. both in the field of surveying and mapping and in the various domains of close-range photogrammetry. Thus the development of these procedures and the actual geometric and radiometric calibration of a representative group of infrared imagers constitutes a major part of the research work that is reported in this dissertation.

1.2 The Geometric and Radiometric Characteristics of Different Infrared Imaging Systems

As will be discussed in detail later in this dissertation, imagers operating in the middle and thermal infrared bands may be classified into three main groups:

- (i) Pyroelectric vidicon cameras;
- (ii) CCD cameras; and
- (iii) Video frame scanners.

1.2.1 Pyroelectric Vidicon Cameras

Pyroelectric vidicon cameras have been used extensively in certain industrial, medical and fire-fighting applications since they cost much less than the other types of infrared imager. However, in recent years, they have also been used widely for the condition monitoring of electrical switch gear and other predictive / preventative maintenance applications in an industrial context. They have similar geometric characteristics to those of the vidicon cameras operating in the visible part of the spectrum. However, it should be recognized at the outset that the major disadvantage of this type of imager as compared with that of other infrared cameras and scanners is its low resolution. The commonly used pyroelectric vidicon imagers typically have the resolution of 200 x 200 pixels. Like an aerial photograph, an image acquired by this type of camera can be regarded as having the geometry of a central projection whose main geometric characteristics are determined by the combination of the format size and the focal length of the camera lens and the position of its principal point. The image that is produced by these devices has a fixed size and therefore a fixed scale in the imaging plane like that of an air photo. Thus, at least in principle, the geometry of the imagery produced by a vidicon tube camera corresponds to the geometry of the photographs produced by a photogrammetric frame camera.

However, in video-based imagers, geometric distortions are present that have no counterpart in classical photogrammetry based on the use of hard copy photographic images. In particular, electronic distortions arise from the deflection of the scanning beam by the magnetic fields that exist between the coils inside the vidicon tube. The resulting distortion pattern will often be pincushion or barrel-shaped. The fundamental nature of these distortions were investigated by Wong (1969, 1970, 1973, 1975) on the vidicon cameras used from space vehicles. It was found then that the electronic distortions of these cameras were largely systematic and caused scale differences between the x and y axes of the video image. Lens distortion is another important distortion that is likely to be present in a vidicon tube-based video camera. Thus radial and decentering lens distortions are likely to be encountered in the images produced by an video-based infrared imaging system. Of course, the presence of these

electronic and lens distortions is of great importance to the photogrammetrist and their occurrence and magnitude must be determined by the geometric calibration procedure with a view to their elimination or correction.

1.2.2 CCD-based Cameras

CCD-based imagers have come into quite common use for certain photogrammetric applications over the last two decades. They use solid-state detectors that are arranged in a two-dimensional array to provide a complete record of the radiation falling onto its surface at a particular instant. There is a considerable limitation in the size of these arrays that are available at the present time and therefore the resulting CCD cameras have mostly been employed in certain close-range photogrammetric applications, e.g. in the industrial field, that can tolerate small format imagers. Also they have come into use in certain airborne monitoring applications where again geometric resolution is not a major concern.

These imagers use solid-state detector technology in which the vidicon tube is replaced by a large number of discrete radiation-sensitive elements that are mounted on an integrated circuit board. The image of the object field that is defined by the field of view of the CCD camera is formed on the imaging surface of the solid-state detector array whose size is limited by the technology that is currently available. At the present time, the commonly used CCD cameras operating in the visible part of the spectrum use arrays containing between 500 x 500 and 1,000 x 1,000 discrete elements. Some less common CCD cameras use arrays of 2,000 x 2,000 elements, while currently the very best (and highly expensive) CCD cameras operating in the visible part of the spectrum - which are very rare - employ an array of 5,120 x 5,120 detector elements. In this particular context, an individual element as small as 1 μ m can be fabricated (Seitz, et al, 1995). By contrast, the size of the detector arrays used in infrared CCD cameras is currently limited to 320 x 240 pixels with a pixel size of 50 μ m. Although no vidicon tube is used in this type of camera, the rest of its design and construction uses video technology with video circuits and signals; recording on a VTR; and final image display on a video display monitor. Again this results in a

technology that is very different to that of the familiar photographic camera and requires investigation.

Real-time photogrammetric systems employing CCD cameras in the visible part of the EM spectrum were first developed in the first half of the eighties (Haggren, 1984 and 1986; El-Hakim, 1986; Wong and Ho, 1986; Murai et al, 1986; Gruen, 1986). At the same time, and in parallel with this development, a number of investigators have analysed different aspects of the calibration of CCD cameras (Gulch, 1984 and 1985, Curry et al, 1986). Accuracies of up to 0.1 pixel could be verified with these systems. The increasing interest in the characterization and calibration of CCD cameras is evidenced by the comparatively large number of research publications that have come more recently from quite diverse scientific areas (Lenz, 1987; Luchmann, 1987; Tsai, 1987; Burner et al, 1990; Beyer, 1992; Fan and Yuan, 1993; Melen and Balchen, 1993). It will be seen from these investigations that self-calibration with bundle-adjustment and direct linear transformation (DLT) methods are the methods that have been frequently used with CCD cameras, rather than a pre-operational calibration of the type familiar to photogrammetrists.

However, in Beyer (1992), the geometric calibration of a conventional CCD camera operating in the visible part of the spectrum was carried out using a 3-D test field consisting of targets placed on a wall and on an aluminium structure placed in front of the wall. This was carried out with close-range photogrammetric applications in mind. The targets used were black circles on a white background with a small dot in the centre. However, at the analysis stage, self-calibration utilizing the bundle adjustment method based on the use of collinearity equations was again employed. The additional parameters that were utilised in the analysis of the calibration data were grouped into those additional parameters modelling the interior orientation; those parameters which model the inadequencies of the camera's solid state detector array and its synchronization; a set of parameters modelling the camera's lens distortion; a group of parameters used to model other effects such as the arrays deviation from a flat surface; and finally additional (fudge) parameters to absorb arbitrary deformations. Somewhat surprisingly, it was found that radial lens distortion was the largest and dominant

systematic error present when calibrating this particular solid-state CCD camera. Of course, it should be noted that the camera that was calibrated by Beyer had not been built with photogrammetric applications in mind.

Thus as stated above, a small number of studies have been carried out to calibrate and model the geometric characteristics of certain CCD cameras that operate in the visible part of the spectrum. However, as yet, no research or development into the geometric calibration of the recently developed CCD cameras operating in the middle infrared spectrum has been carried out. So, this deficiency has been addressed specifically in the present project through the calibration of a number of these cameras.

1.2.3 Thermal Video Frame Scanners

Thermal video frame scanners (TVFS) use photon detectors in which the object space is scanned using optical elements such as oscillating mirrors and rotating polygons, in combination with a complex optical telescope. These scan the scene from top to bottom and left to right in swaths depending on the available number of detector elements. The relay lens or detector optics - which may comprise several lens elements - takes the radiation emerging from the scanner optical system and focuses it onto the sensitive area of a SPRITE detector.

As mentioned before, these frame scanners have a quite different geometry to that of the optical-mechanical line scanners that are familiar from airborne and spaceborne applications of remote sensing. These line scanners produce a continuous strip image which, from a geometrical viewpoint, will have either a single cylindrical surface (in the case of an optical-mechanical scanner) or a planar imaging surface (in the case of a pushbroom scanner). In each case, the scanner images the object field in one direction only, while the forward motion of the platform advances the scan pattern to build up the final single continuous strip image. By contrast, a TVFS generates a frame-type image that has the basic geometry of a **spherical surface**. By contrast with line scanners, a TVFS scans the object in two dimensions in the object space using two scanning mirrors or prism to produce video images which are not dependent on

the motion of the platform. Thus, entire frames of image data are captured from a single exposure station with the TVFS rather than a single line as in the case of the line scanner.

However, it is quite difficult to calibrate a TVFS geometrically since it has a complex optical system and there is no target plate or focal plane present in a video frame scanner of the type present in vidicon or CCD cameras. Thus there is no possibility of using a method such as an etched reseau grid as has been done with vidicon cameras. As yet, the study of the geometric characteristics and the calibration of TVFS has only been carried out by Amin (1986) at the University of Glasgow and published by Amin and Petrie (1993 and 1994).

In that work, a special calibration plate which had a good thermal emissivity to ensure a high contrast between the images of this plate and its background was designed and built and this was then calibrated using a Ferranti monocomparator equipped with high resolution ($1\mu\text{m}$) linear encoders. The four commercially available video frame scanners which have been used in Dr. Amin's work were the Barr & Stroud IR-18 Mk-II, the GEC Avionics / Rank Taylor Hobson TICM II, the Rank Pullin Controls RPC and the Agema Thermovision. The first three of these were designed mainly for military surveillance and targeting applications; only the Thermovision was designed for industrial and medical applications. The images of the target plate which were taken by these TVFS imagers for calibration purposes were measured on a video-based monocomparator first devised and described by Petrie (1983).

The set of coordinate values derived from the calibration of the plate using the Ferranti Monocomparator were regarded as being error free. The second set of coordinates from each of the scanner images that had been measured using the video monocomparator contained the various distortions generated by the operation of the frame scanner including lens distortion and those displacements generated both by its basic system geometry (i.e. its spherical image plane) and any deviation from its nominal operation, e.g. by its scanning elements. These two sets of coordinate values were analysed using a polynomial transformation which was implemented as a

flexible computer program. As a result, specific correction polynomials were identified and used to compensate for the effects of geometric distortion when measuring video frame scanner images.

As can be seen from the above account, the only overall study of a TVFS from the photogrammetric point of view has been carried out by Amin (1986). No similar work with the new generation of TVFS developed over the last decade has been carried out. Therefore, the geometric calibration of these recently developed devices will also be carried out within the present project.

1.2.4 Radiometric Aspects of Infrared Imagers

The general lack of geometric integrity of infrared imagery when compared to the images produced in the visible part of the spectrum often precludes its use as a source of metric information, e.g. for precise mapping. It is then often used solely for its radiometric information content. In order to obtain accurate radiometric information from the image data produced by the infrared imager, it must be calibrated radiometrically. In practice, the radiometric characteristics of infrared video cameras and scanners have a major impact on the performance and accuracy achievable by an imager. Noise and signal non-uniformities are important parameters of all imagers. Indeed the overall performance of an infrared imager is, to a considerable extent, governed by those parameters. Although not all of these parameters can be corrected for, if at all possible, the amount and significance of each parameter has to be determined to verify the capability of specific imaging systems to carry out photogrammetric measurements.

In this context, Kosonocky et al (1985) and Hou et al (1995) have investigated the non-uniformity of the radiometric characteristics of infrared CCD cameras. They have developed and used a two point non-uniformity correction algorithm in their work. The authors reported that the resulting correction realised at least a six-fold improvement in the value of the standard deviation of grey values of the pixels and the image quality increased through the use of an increasing number of averaging

frames. It will be very interesting to investigate whether such a startling improvement can be realised with other infrared imagers, besides those used by these researchers.

1.3 Research Objectives

Having set out the context within which the author's research project has been conducted, it is then possible to set out the objectives that it was hoped could be achieved by the project. The aim of this research is, first of all, to carry out the geometric calibration of (i) vidicon cameras, (ii) the new generation of video frame scanners and (iii) those CCD cameras which operate in the middle and thermal infrared parts of the EM spectrum. As discussed above, some investigations have been carried out into the calibration of vidicon cameras used from space. However, so far, no work has been carried out to determine the geometric distortions of thermal pyroelectric vidicon cameras. Similarly investigations have been made which have determined the geometric calibration of CCD cameras, but the goal here is to carry out work on imagers operating in the middle region of the infrared spectrum. Furthermore, the geometric calibration of the new generation of video frame scanners that operate in the thermal part of the infrared spectrum also forms part of the research project.

After this, the radiometric calibration of these devices will be carried out. As can be seen from the above account, some limited studies have been conducted into the radiometric calibration of infrared CCD cameras. However, to the author's knowledge no work has been published on the radiometric calibration of the pyroelectric vidicon cameras and thermal video frame scanners.

Thus, the main objectives of the research project that will be described in this dissertation concerned three main aspects:-

- (i) **The geometric and radiometric calibration of thermal pyroelectric vidicon cameras;**
- (ii) **The geometric and radiometric calibration of infrared CCD cameras; and**

- (iii) **The geometric and radiometric calibration of thermal video frame scanners.**

1.4 Outline of the Thesis

The overall structure of this dissertation is that it should first review the different fundamental aspects of infrared imaging from a photogrammetric standpoint. These have been covered in the first part of the dissertation (in Chapters 2 to 7) including the optical materials and components, electronic detectors and video technology employed in infrared imagers. This is followed in Chapters 8, 9 and 10 by a detailed description and analysis of the geometric and radiometric characteristics of each of the various types of infrared imager that are currently available. These ten chapters comprise Volume 1 of this dissertation and provide the solid background needed to understand the fundamental basis and operation of infrared imagers.

In Volume 2, the automatic image measuring techniques that have been developed for use in this project are first covered in Chapters 11 and 12 and this is followed in Chapter 13 by a description of the experimental procedures actually used in the geometric and radiometric calibration work undertaken within the project. Finally (in Chapters 14, 15, 16 and 17) the results of all this calibration work on a wide selection of imagers are given, followed by recommendations for future work in this area.

Thus, in total, there are 16 chapters contained in the dissertation in addition to this introduction. More specific descriptions of the content of these individual chapters are as follows:

- **Chapter 2** deals with the fundamental physical theory on which infrared imaging systems are based. It also reviews the physical properties of the middle and thermal infrared bands of the electro-magnetic spectrum in which commercially available infrared imaging systems operate.

- **Chapter 3** outlines the main characteristics of the optical materials and components that are used in the design and construction of infrared imaging systems. It also discusses the main impacts of these components on the images produced by such systems and their potential effects on the geometric and radiometric calibration of these imagers.

- **Chapter 4** describes the different methods of detecting and measuring the infrared radiation that is used to create an image in the middle and thermal infrared regions. It also presents the main design characteristics of the two-dimensional detector arrays that are now being employed widely in CCD-based infrared imagers.

- **Chapter 5** explains the main concepts of the video technology that underlies infrared imaging systems and has been used throughout this research work - in that the imaging systems, the recording and display devices are all video-based. It also gives information about the resolution and geometry of video images and the distortions that stem from the individual parts of the video system.

- **Chapter 6** describes the commonly used standards for the analogue video signals utilised for monochrome or colour signal transmission and displays. It also covers the synchronisation and transmission characteristics of the monochrome video signals that are output from infrared video imagers. The main radiometric and geometric properties of video signal transmission and synchronisation and their main influences on the infrared images that will be used for calibration purposes have also been discussed in this chapter.

- **Chapter 7** deals with the pre-processing and synchronization of video signals and their analogue-to-digital (A/D) conversion using the frame grabber. It also reviews the frame grabbers with their characteristics that have been used in this project. The digital-to-analogue (D/A) conversion of digital images to display them on a video monitor and the processing hardware required for this operation have also been examined and analyzed in this chapter.

- In **Chapter 8**, those video tube based and CCD areal array imaging systems that operate in the infrared region of the EM spectrum and produce planar images are described. The chapter also presents a summary of recently produced and commercially available imaging systems for each type of imager in conjunction with tables that review the main characteristics of these devices.

- **Chapter 9** explains firstly the design and construction of infrared optical-mechanical line scanners with an emphasis on their geometric characteristics. It also gives the main features of the line scanners that are operated in the airborne and spaceborne applications in outline only - since they fall outwith the scope of this research project. This chapter describes secondly the thermal video frame scanners (TVFSs) that are used extensively in thermal imaging applications, together with the main factors concerning their operation in more detail - since they fall very fully within the scope of the author's research project. It also compares and discusses the different scanning actions of line and frame scanners, and their implications for the geometry of the resulting images, in particular, the spherical surface geometry of the TVFS.

- **Chapter 10** discusses the geometric and radiometric characteristics of the various infrared imaging systems that are the main concern of this thesis and which should be established and corrected by the geometric and radiometric calibration procedures.

- **Chapter 11** explains the automatic image matching method which has been used in this project to measure to sub-pixel level the centres of the cross targets used to calibrate the infrared imagers. It also summarizes and discusses other matching techniques which have been developed up to till now.

- **Chapter 12** presents the algorithms and procedures used in the computer programming of the automatic image matching procedure. It also gives the results of testing this program with the thermal images obtained using a TVFS during a previous research project carried out in this Department. Furthermore it reports on the results obtained in actual accuracy tests using these images and comments on the

experience gained in the development and use of this computer program. The measurement of the same images using a manual mensuration method is also given in this chapter which finishes with a discussion on the advantages of using the automatic method over the manual method.

- **Chapter 13** describes the actual experimental procedures used in the geometric and radiometric calibration of the infrared imaging systems in association with the design of a new target plate. It also gives an overview of the various stages involved in the computer processing of the image data and reviews the enhancement of the digital infrared images using Adobe Photoshop 3 processing package. The analyses of the image data collected during the geometric and radiometric calibration have also been outlined and examined in this chapter.

- **Chapters 14, 15, 16 and 17** present the results from the geometric and radiometric calibration of a representative selection of infrared CCD cameras and thermal video frame scanners. A much wider analysis of these results has also carried out for each of the imagers involved in this calibration activity. Each chapter also attempts to explain the reasons for the occurrence of the geometric and radiometric distortions which are present in the infrared images and discusses the elimination of these distortions using suitable methods.

- Finally, **Chapter 18** forms the conclusion to this dissertation. It summarizes the overall results of this research project and gives recommendations for future work.

CHAPTER 2: FUNDAMENTAL THEORY UNDERLYING INFRARED IMAGING SYSTEMS

2.1 Introduction

Infrared imaging is a technique for converting a scene's infrared radiation pattern - which is invisible to the human eye - into a visible image. Its usefulness is due to four main factors:-

- (i) It is a totally passive technique, requiring no external source of illumination. This allows day and night operation, and covert sensing without need for an external illumination source.
- (ii) It is ideal for the detection of hot or cold spots or of areas and objects of different infrared emissivities, within a scene.
- (iii) Infrared radiation can penetrate smoke and mist more readily than visible radiation, allowing visually obscured objects to be detected.
- (iv) It is a real-time, remote sensing technique.

The potential uses of infrared imaging are wide ranging, and currently include civil, industrial, medical, scientific and military applications. In this chapter, the fundamental theory on which infrared imaging is based will be dealt with in some detail.

2.2 Nature of Electromagnetic Radiation

One important point of controversy in physics over the last 250 years has concerned the nature of electromagnetic radiation. Newton, while not explicitly rejecting the idea that light was a wave-like form of energy (the wave theory) inclined to view that it comprised a stream of particles (the corpuscular theory). Newton's early studies culminated in 1704 in his comprehensive mathematical treatment of the major properties of refraction, diffraction, interference, polarization and dispersion in his book "Opticks". In this seminal work, Newton did much to establish and advance the field of optics. Nevertheless, his book did inhibit further progress to some extent

because of his bias toward the corpuscular theory of light. Newton's reputation, gained deservedly through his triumphs in formulating calculus and mechanics, helped to prevent more accurate or alternative theories of optics from being taken seriously for some time. Indeed his elegantly constructed but fundamentally inaccurate picture of the nature of light dominated the serious study of optics for an entire century.

In 1678, Christian Huygens had already postulated the wave theory of light mathematically. He proposed that "if a point of the ether is illuminated by a ray of light, it produces a disturbance, or 'wavelet,' that fans out in all directions, forming a spherical wave. The 'envelope' created by the common convolute of all these wavelets becomes a new 'wave front' of the light ray." From the geometric construction of this principle, Huygens derived the laws of reflection and refraction. He concluded that the index of refraction of any medium is the ratio of the speed of light in a vacuum to its speed in that medium.

Newton's particle theory and Huygen's wave theory remained in strong competition for scientific acceptance until the mid-nineteenth century when James Maxwell combined light with other types of electromagnetic waves and devised his electromagnetic equations.

A decisive experiment performed in 1803 by Thomas Young, a London physician, demonstrated that a monochromatic beam of light passed through two pinholes would set-up an interference pattern resembling the wave patterns of water when disturbed by an object falling into it (Fig. 2.1).

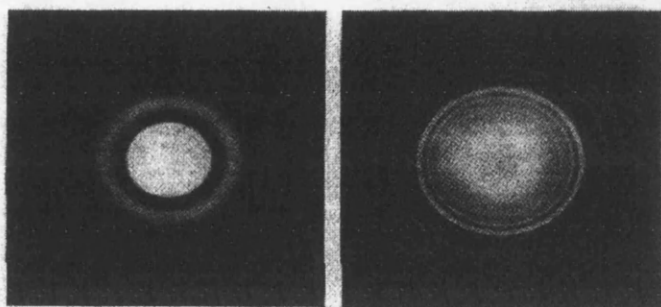


Fig 2.1. Wave nature of light (Feinberg, 1968).

At about this time, Fresnel and Arago also came forward with the correct interpretation of an experiment previously performed by Huygens. They showed that the light transmitted by Huygen's blocks of calcite crystal is polarized and therefore the light waves could not be longitudinal compression waves as Huygens had thought but must be transverse waves oscillating at right angles to their direction of propagation (Fig. 2.2). All of this activity gave additional credence to Huygens' ideas.

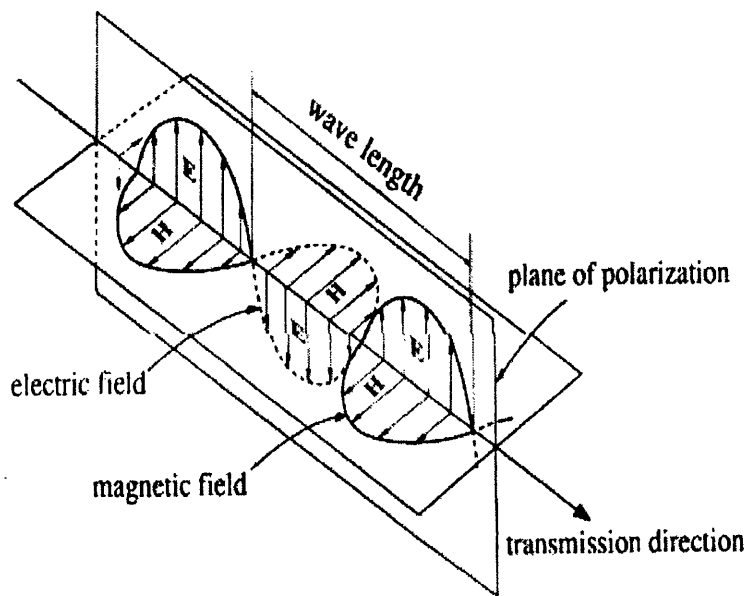


Fig. 2.2. Electro-magnetic radiation (Murai, 1993)

Indeed this elucidation of the wave nature of light fitted nicely into the electromagnetic theory propounded later in the 19th Century by James Maxwell. In his theoretical studies, light is described as a rapid variation in the electromagnetic field surrounding a charged particle, the variations in the field being generated by the oscillation of the particle. As such a varying field, light took its place beside a number of other forms of radiant energy that had been described earlier in the 19th Century. These different kinds of electromagnetic radiation - radio waves and infrared radiation on one side of the spectrum of visible light and ultra-violet radiation and X- and gamma rays on the other - correspond to the different rates of variation of the field.

Thus in Maxwell's theory, light appears not as an independent element in nature but rather as an aspect of electromagnetism.

The momentous developments in physics in this century have first re-opened and then resolved the wave-particle controversy. Whereas the association of light with electromagnetism remains valid, the interpretation of this connection has changed. It has been shown that certain of the wave properties of light such as interference and polarization are also exhibited under suitable circumstances by the sub-atomic constituents of matter such as electrons. Conversely, it has been shown that light, in its interaction with matter, behaves as though it is composed of many individual bodies called photons, which carry such particle-like properties as energy and momentum.

In 1900, Max Planck was concerned to explain the relation between wavelength and the intensity of the radiant energy emanating from a hot body. According to classical electromagnetic theory, the intensity was supposed to increase as the square of the frequency; by this reckoning, an almost infinite amount of energy should be radiated at the higher frequencies or shorter wavelengths. However, actual measurements had shown a quite different distribution of intensity with respect to wavelength for any given temperature. Planck devised an empirical formula that described this distribution (Eq. 2.1). It contained a constant, the value of which Planck chose in order to produce the best agreement with the observations. To explain why this formula should work, he had to assert that light must change its energy with the matter of the hot body in terms of quanta. His equation showed that the amount of energy (E) in each quantum would be equal to the frequency (f) multiplied by the constant $h = 6.63 \times 10^{-34}$ Joule-second.

$$E = hf \text{ (joules)} \tag{2.1}$$

In 1905, Albert Einstein extended Planck's quantum concept further. He asserted that not only is the energy of the light exchanged in quanta; the energy of the light beam is itself always divided into discrete quanta. His argument was based on his analysis of

the photoelectric effect. This effect is the best known example of the quantum nature of electromagnetic radiation. When electromagnetic radiation falls on a solid, electrons may be ejected from the surface. These electrons constitute a measurable electric current called a photocurrent. The photocurrent has three properties:-

Characteristic 1. The current is proportional to the intensity of the radiation.

Characteristic 2. The kinetic energy of the electrons depends only on the frequency of the radiation and not on its intensity.

Characteristic 3. There is no current below a certain threshold radiation frequency.

Einstein was able to explain these effects, for which he won a Nobel Prize in 1921. His theory begins by stating that electrons require a certain minimum energy to escape from a solid and that this energy is $e\phi$, where e is the electronic charge and ϕ is the so-called work function of the material. As in Planck's radiation theory, in Einstein's description, when a quantum of radiation, or photon, is absorbed by an electron, it gives the electron energy equal to hf , where h is the Planck's constant and f is the frequency. The intensity of the radiation (i.e., the energy per second per unit area) is proportional to the number of photons per unit time falling on a unit area of the surface. The photocurrent is proportional to the number of electrons ejected by absorbed photons per unit time per unit area. Thus the photocurrent is proportional to the intensity (Characteristic 1).

The energy given to a photoelectron is equal to the photon energy, which is in turn proportional to the energy. Thus the kinetic energy of the ejected electrons, KE, is

$$KE = hf - e\phi \quad (\text{joules}) \quad (2.2)$$

(Characteristic 2).

When $KE = 0$ in Eq. 2.2, $f = e\phi / h$, and an electron is emitted with no kinetic energy. If f is less than $e\phi/h$, the electrons will not be given sufficient energy to do the work to escape, and there will be no photocurrent (Characteristic 3).

This is the principle upon which the photon detectors used in semi-conductor solid-state imaging devices are based. The photons simply raise the energy of the electron from the valence band, where they are immobile, to the conduction band of the semi-conductor, where the electrons are free to move under externally applied voltages. Electrons may also be given energy thermally, and this contributes noise to the detection system. Hence most solid-state detectors must be operated at the extremely low temperatures produced by cooling devices to achieve maximum sensitivity.

According to the above account, from the point of view of quantum mechanics, electro-magnetic radiation is both a wave and a stream of particles. The wave-like characteristics of electromagnetic radiation allow the distinction to be made between different manifestations of such radiation (for example, between microwave and infrared radiation). However, the particle-like properties of the radiation allow us to understand the interactions between electromagnetic energy and the Earth's atmosphere and surface at an atomic and molecular scale (Mather, 1987; Lintz and Simonett, 1976).

2.3 Characteristics of Electromagnetic Radiation

In the context of imaging and remote sensing, the important parameters characterizing the electromagnetic radiation being sensed and measured by an imaging device are the frequency (or wavelength), the amplitude, the direction of propagation and the polarization (Cracknell and Hayes, 1991).

Waves can be described in terms of their frequency, which is the number of cycles or waveforms per second or Hertz (Hz). Frequency corresponds to the colour of an object in the visible region which is given by a unique characteristic curve relating to the wavelength and the radiant energy. In the microwave region, information about objects can be obtained by a passive microwave radiometer operating between the wavelengths $\lambda = 0.1\text{cm}$ and $\lambda = 1.0\text{m}$ using an antenna to pick up the radiation instead of an optical system.

Alternatively, the concept of wavelength can be used (Fig. 2.3). The wavelength is the distance between successive peaks (or successive troughs) of a waveform, and is normally measured in metres or fractions of a metre. Basically both measures - frequency and wavelength - convey the same information and are often used interchangeably. The symbol used for wavelength is the Greek letter lambda (λ). The number of wavelengths per second is the frequency (f) of the waveform. Frequency (f) and wavelength (λ) are related by the speed of electromagnetic radiation (c) which is constant at 2.998×10^8 metres per second (Eq. 2.3).

$$c = \lambda f \text{ (metre /second)} \quad (2.3)$$

Another useful measure is the period (P) of the waveform; this is the time, in seconds or fractions of a second, needed for one full wave to pass a fixed point. The relationship between wavelength, frequency and period is given by:

$$P = \lambda / f \text{ (second)} \quad (2.4)$$

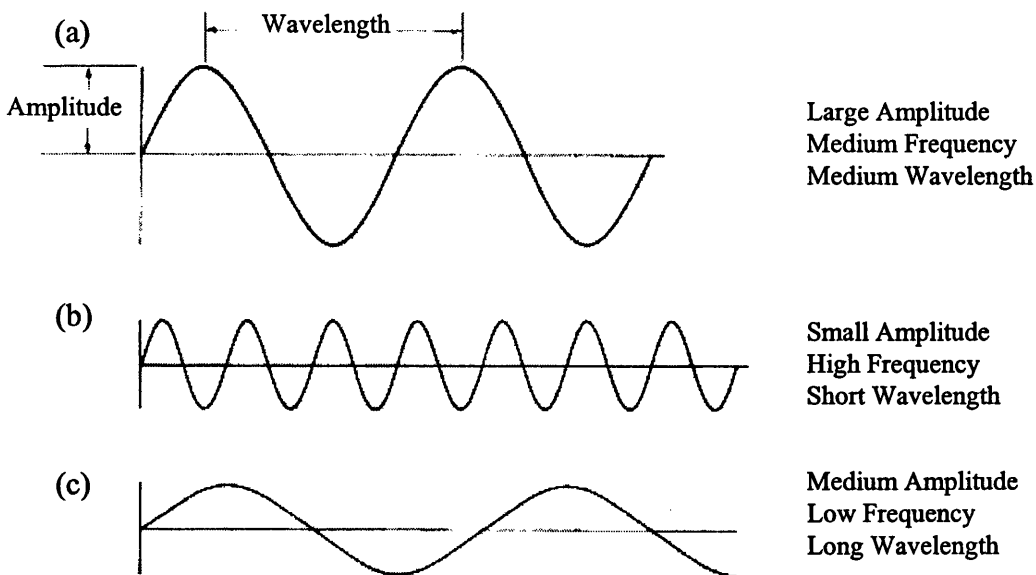


Fig. 2.3. Amplitude, frequency, and wavelength (Campbell, 1996).

The amplitude (A) of a wave is the maximum distance on the vertical axis attained by the wave from its mean position (Fig. 2.3). The amount of energy, or intensity, of the waveform is proportional to the square of the amplitude. The amount of energy carried by the waveform, or the squared amplitude of the wave, is defined for a single photon by Planck's equation given in Eq. 2.1. The amplitude and the linearity of the transmission direction give the information about the spatial location and shape of the object.

The plane of the polarization is influenced by the geometrical shape of object in the case of reflection or scattering in the microwave region. In the case of radar, the use of horizontal polarization and vertical polarization produce different responses in a radar image.

2.4 Electromagnetic Wavebands

The Sun's light is the form of electromagnetic radiation that is most familiar to human beings. In most situations, the light that is reflected by physical objects travels in a straight line to the observer's eye. On passing through the lens and reaching the retina, it generates electrical signals that are transmitted to the brain by the optic nerve. These signals are used by the brain to construct an image of the observer's surroundings. This is the process of vision which is closely analogous to the process of imaging performed by an imager or remote sensing system. Visible light is so called because it can be detected by the eye, whereas other forms of electromagnetic radiation cannot. Newton investigated the nature of light, and came to the conclusion that it was formed by the sum of separate colours. Later, the astronomer Herschel demonstrated the existence of electromagnetic radiation beyond the visible spectrum of red, orange, yellow, green, blue, indigo and violet. He called the non-visible radiation "infrared" (IR), meaning "beyond the red". It was subsequently found that electromagnetic radiation also existed beyond the violet end of the visible (V) spectrum; this form of radiation became known as ultra-violet (UV). Then other forms of electromagnetic radiation, such as X-rays and radio waves were soon discovered and eventually it was realized that all were different manifestations of the same kind of radiation which

travelled at the speed of light in a wave-like form. The set of all electromagnetic waves is called the electromagnetic spectrum, which includes the range from the long radio waves, through the microwave and infrared wavelengths to visible light waves and beyond to the ultraviolet and to the short-wave X- and gamma rays (Fig. 2.4).

2.4.1 The Infrared Spectrum

The wavelength (λ) limits of the infrared spectrum are generally considered to lie between the red limit of the visible region at $\lambda=0.7\mu\text{m}$ to approximately $\lambda=1,000\mu\text{m}$ (1mm). It is usually divided into four distinct regions, called respectively:-

- (i) the near infrared region (NIR), from $\lambda=0.7$ to $1.5\mu\text{m}$;
- (ii) the middle infrared region (MIR) covering wavelengths (λ) from 1.5 to $5.6\mu\text{m}$;
- (iii) the far infrared (thermal) region (FIR), with wavelengths (λ) from 5.6 to $15\mu\text{m}$; and
- (iv) the extreme infrared region (EIR), stretching from $\lambda=15$ to $1,000\mu\text{m}$.

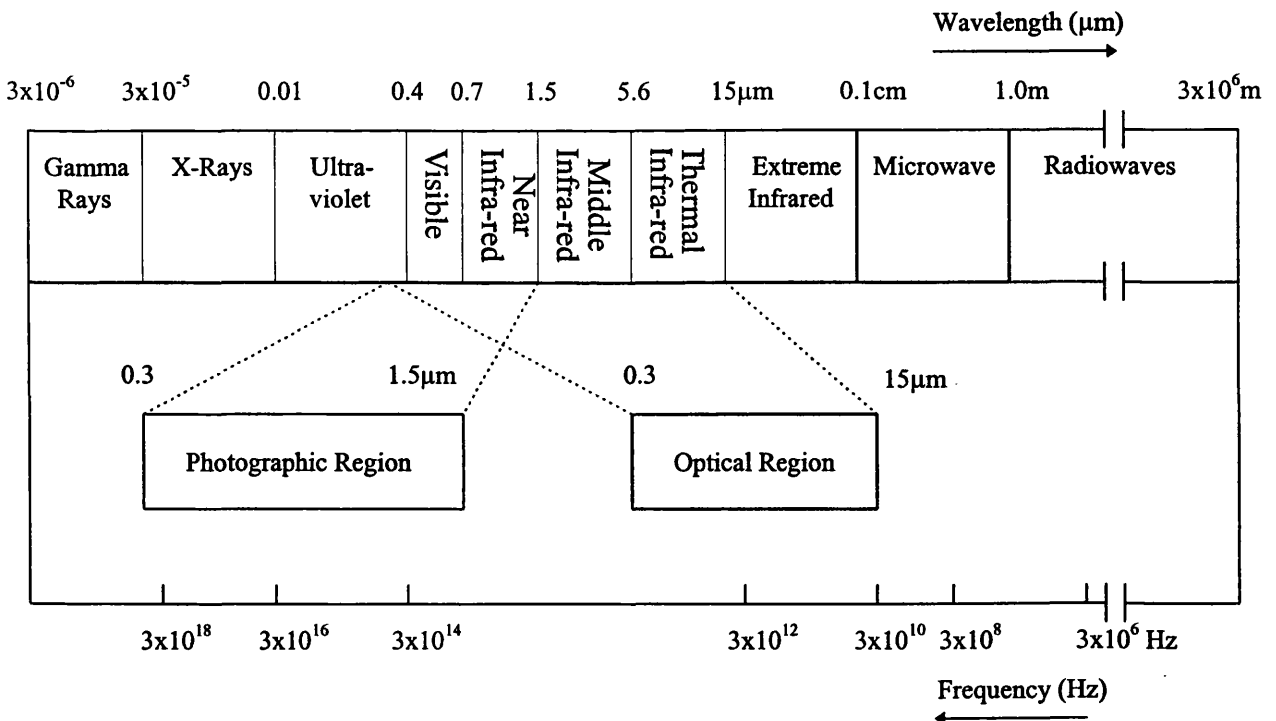


Fig. 2.4. Electromagnetic spectrum (Amin, 1986)

2.5 Basic Laws of Infrared Radiation

The amount of radiation emitted from an object at a certain wavelength is related to its temperature and to its emissivity. The higher the temperature of the object, the more infrared radiation that will be emitted from it.

Material that absorbs all incident energy, converts it to heat energy, transforms the heat back into radiant energy and emits it at the maximum possible rate allowed by the thermodynamic laws is known as a blackbody or a perfect thermal emitter. Kirchhoff demonstrated in 1860 that a perfect emitter is also a perfect radiator. The total radiant emissivity ϵ of a particular surface is defined as

$$\epsilon = I / I_b \quad (2.5)$$

where I is the total radiant power per unit area emitted from the surface of an object and I_b is the radiant power generated by a blackbody at the same temperature.

All the laws of physics applying to the infrared part of the electromagnetic spectrum which will be given below have been derived for and apply to a blackbody with an emissivity of unity, that is equal to 1.0. However, most bodies encountered in practice are not perfect blackbodies. They are greybodies that radiate or absorb less radiation than a blackbody would at the same temperature. Thus, their emissivity is always less than unity. Therefore, the emissivity is an indication of the greyness of the radiating body. The lower the emissivity, the greyer the body; the higher the emissivity, the blacker the body. Because of these emissivity variations, it is possible for objects to be at the same temperature and yet have completely different emissivity values.

2.5.1 Planck's Blackbody Law

Since the radiant emittance of any substance can be expressed as the product of its emissivity and the radiant emittance of a blackbody, an accurate theoretical representation of the latter quantity is of great importance. Nineteenth Century

physicists were unable to derive an equation that represented the emission from a blackbody. The problem was solved in 1901 by Planck. According to his blackbody law, the relationship between the radiation intensity, spectral distribution and temperature of a blackbody is

$$W_{\lambda}d\lambda = \{2\pi hc / [\lambda^5(\exp(hc/\lambda kT) - 1)]\} d\lambda \quad \text{Watt.cm}^{-2}.\mu\text{m}^{-1} \quad (2.6)$$

where:-

- W_{λ} is the amount of radiation emitted by the blackbody in the wavelength range λ to $\lambda+d\lambda$;
- T is the absolute temperature (K) of the blackbody;
- λ is the wavelength (μm) of the emitted radiation;
- h is Planck's constant ($= 6.63 \times 10^{-34}$ Joule.s);
- c is the velocity (m/s) of light; and
- k is Boltzmann's constant ($= 1.38 \times 10^{-23}$ Joule.K⁻¹).

The spectral radiant emittance for a blackbody at various temperatures is shown in Fig. 2.5. It can be seen that, as the temperature of the blackbody increases, the intensity of the emitted radiant energy increases rapidly.

2.5.2 Wien's Displacement Law

Another result from Fig. 2.5 is that, as the temperature increases, the wavelength of the peak emission decreases. This given by Wien's displacement law:

$$\lambda_m T = A \quad \mu\text{m.K} \quad (2.7)$$

where:-

- λ_m is the wavelength at which $W_{(\lambda,T)}$ is a maximum;
- A is the constant ($A = 2898 \mu\text{m.K}$); and
- T is the absolute temperature (K) of the blackbody.

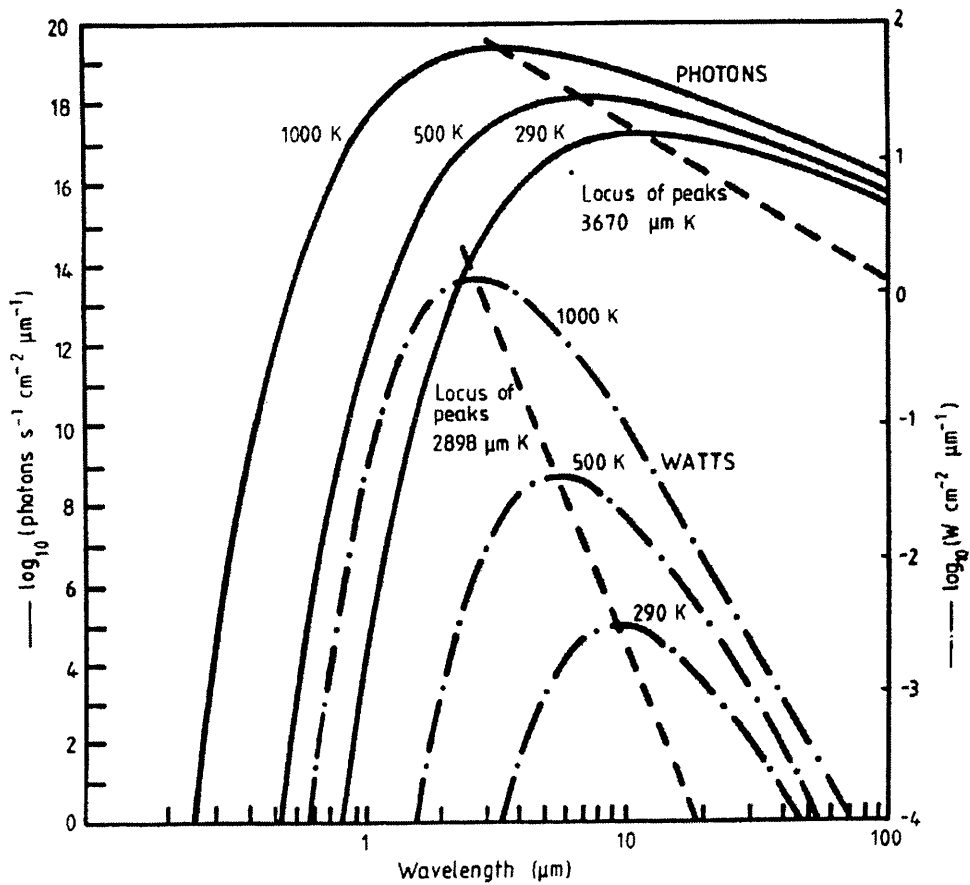


Fig. 2.5. Planck's law for the spectral radiant emittance of a blackbody at infrared wavelengths (Burnay, et. al., 1988).

For an object at an ambient temperature of 290K, λ_m occurs at $10\mu\text{m}$, while for a high temperature such as 1,000K, λ_m is about $3\mu\text{m}$. Thus the waveband 1.5 to $15\mu\text{m}$, in the middle or far infrared region of the electro-magnetic spectrum, contains the maximum radiative emission that can be used for infrared imaging purposes.

2.5.3 Stefan-Boltzmann Law

The total radiant emittance from a blackbody at the absolute temperature T is obtained by integrating $W_\lambda d\lambda$ in Eq. 2.6 with respect to λ between the limits $\lambda=0$ and $\lambda=\infty$.

$$W = \int_{\lambda=0}^{\lambda=\infty} W_\lambda d\lambda = \sigma T^4 \quad (2.8)$$

where:-

- W is the total blackbody radiant emittance, measured in watts.cm^{-2} of the radiating surface;
- σ is the Stefan-Boltzmann constant, equal to $5,673 \times 10^{-12} \text{ watt.cm}^{-2} \cdot \text{K}^{-4}$; and
- T is the absolute temperature (K) of the blackbody.

It can be seen from Eq. 2.8 that the total radiant emittance of a blackbody increases as the fourth power of the temperature of the blackbody.

2.6 Atmospheric Transmission

The atmosphere influences the EM radiation in two main respects - firstly by scattering and secondly by absorption. Scattering of the incoming radiation generated by the Sun and passing to the Earth and of the reflected radiation from the Earth's surface is caused primarily by tiny particles of dust, smoke, pollen and water suspended in the atmosphere. On the other hand, absorption occurs primarily as a consequence of the attenuating nature of molecules of ozone (O_3), carbon dioxide (CO_2) and water vapour (H_2O) in the atmosphere. Since these gases absorb EM radiation in specific wavelength bands, they govern the particular region of the spectrum that can be sensed by an airborne, spaceborne or terrestrial imaging device.

Regions of the spectrum that are highly transmittive are referred to as atmospheric windows. It can be seen from Fig. 2.6 that the atmosphere is highly transmittive in the visible part of the spectrum ($\lambda = 0.4$ to $0.7\mu\text{m}$). Other atmospheric windows present in the infrared part of the spectrum cover the wavelength ranges 0.7 to $1.3\mu\text{m}$ in the near-infrared; 1.5 to $1.8\mu\text{m}$; 2.0 to $2.6\mu\text{m}$; and 3.0 to $5.6\mu\text{m}$ in the middle infrared and 8.0 to $14.0\mu\text{m}$ in the thermal infrared region.

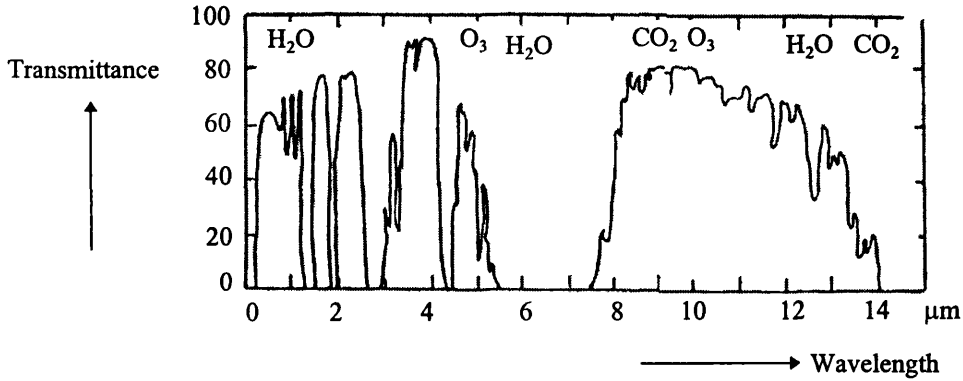


Fig. 2.6. Atmospheric windows (Amin, 1986)

2.7 Total Scene Radiation and Contrast

When radiation is incident upon a body that is not a blackbody, some of it is transmitted, some is absorbed, and some is reflected. Thus, the ratios of each of these relative to the strength of the incident radiation must add up to unity:

$$\alpha + \beta + \tau = 1$$

or

$$\Phi_{\text{absorbed}} + \Phi_{\text{reflected}} + \Phi_{\text{transmitted}} = \Phi_{\text{incident}} \quad (2.9)$$

where:-

$$\alpha = \Phi_{\text{absorbed}} / \Phi_{\text{incident}} = \text{absorption};$$

$$\beta = \Phi_{\text{reflected}} / \Phi_{\text{incident}} = \text{reflection}; \text{ and}$$

$$\tau = \Phi_{\text{transmitted}} / \Phi_{\text{incident}} = \text{transmission}.$$

During daylight, the radiant energy from the Earth consists of two components - reflected solar radiation and emitted object radiation. Within the infrared region, it is apparent that, as the wavelength increases, the emitted infrared component becomes progressively more significant. As can be seen from Table 2.1 and Fig. 2.7 below, the main source of radiation in the near infrared region is the reflection of energy from the Sun incident upon the object. In the middle infrared region, the reflected solar radiation still represents about 80% of the total radiation from the object. In the far

infrared, the emitted energy represents nearly 100% of the total energy from the object. Reflected sunlight will have negligible effect on this region.

Wavelength band (μm)	Solar radiation (watt.m^{-2})	Emitted radiation (watt m^{-2})
0.3 - 3.0 (UV, V, NIR)	750.0	0
3.0 - 5.6 (MIR)	24.0	6
5.6 - 15.0 (TIR)	1.5	150

Table 2.1. Radiation from the Earth in the ultra-violet; visible; near, middle and thermal infrared bands of the spectrum (Amin, 1986).

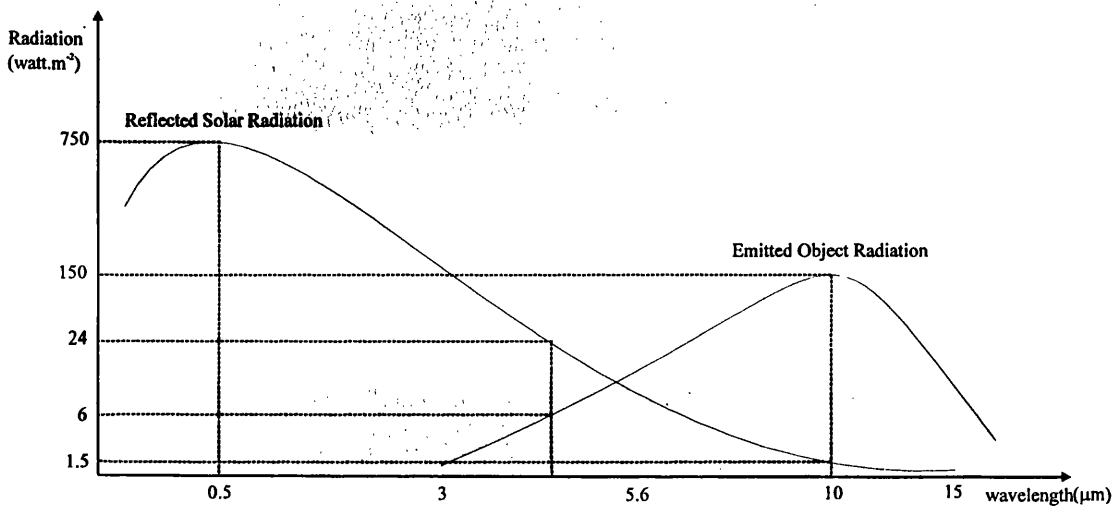


Fig. 2.7. Reflected and emitted component of the Earth radiation

A infrared image arises from the measurement of the temperature variations or differences in emissivity that occur within a scene. The equivalent temperature differences may be fractions of 1°C at the mean temperature existing in the scene. Therefore the contrast in a infrared image will be small when compared with the visible image contrast, which is due to differences in reflectivity. As can be seen from Table 2.2 below, the middle infrared region ($\lambda = 3$ to $5.6\mu\text{m}$) has the greatest contrast since it also contain reflected solar radiation as well as emitted object radiation. This region also has the advantages that the diameter of the optics required to obtain a certain optical resolution is smaller, and that the detectors may be operated at a higher temperature than is usual in the far infrared region ($\lambda = 5.6$ to $14\mu\text{m}$). However, the

far infrared region has the advantage of higher sensitivity to ambient-temperature objects and better transmission through mist and smoke due to its longer wavelength.

Wavelength band (μm)	Contrast ($\Delta E / E$)
3 to 5	0.039
8 to 14	0.017

Table 2.2. Contrast in the middle and thermal infrared bands (Burnay et. al., 1988)

2.8 Conclusions

In this chapter, the basic physical theory, on which infrared imaging systems are based, has been discussed in some detail. In addition, the physical properties of the middle and thermal infrared bands of the electro-magnetic spectrum in which commercially available infrared imaging systems operate have been fully described. In the next chapter, the optical components and materials that are used in the infrared cameras and scanners will be discussed in some detail.

CHAPTER 3: INFRARED OPTICAL MATERIALS AND COMPONENTS

3.1 Introduction

In the previous chapter, the basic physical theory that applies to the middle and thermal infrared bands of the EM spectrum and is relevant to the author's project has been explained in some detail. Following on from this discussion, this chapter will discuss the main optical materials and components that are used in the design and construction of infrared imaging systems along with their main influences on the images produced by such systems and their potential effects on the geometric and radiometric calibration of these imagers.

It is clear that the characteristics of those optical materials and components that are employed in infrared imagers are critical when assessing the performance of these imagers. Since they have properties that are very different to those used in optical imaging systems operating in the visible part of the spectrum, these need to be discussed in some detail.

Essentially the chief differences between infrared optical and visible optical designs and elements lie in two areas. First, many materials that are transparent in the visible part of the EM spectrum and can be used as optical components in imagers operating in this band are not transparent throughout the infrared part of the spectrum. By the same token, there are other materials that exhibit useful transmission in the infrared regions which are not transparent in the visible. As a result, a quite different collection of transmittive materials has had to be assembled, developed and tested for use the infrared part of the spectrum. A second set of factors that are different for infrared optical systems are those resulting from the magnitude of the wavelength of the radiation that is being utilised for the generation of the images. Certain limitations in the imaging characteristics of infrared optical systems due to aberrations and diffraction effects are functions of the much longer wavelengths of the radiation used in the imaging process. In this chapter, these two matters will also be discussed in more detail.

3.2 Infrared Optical Materials

It is unfortunate that ordinary silicate-based glass does not transmit radiation beyond a wavelength (λ) of $2.5\mu\text{m}$ in the infrared region; thus the designers of the optics of infrared imagers have had to rely instead on much less commonly available materials that are often difficult to fabricate into optical components such as lenses and prisms. The range of infrared transmitting materials that are potentially available for use as windows, lenses and prisms is shown in Table 3.1.

Type of material	$\lambda = 3$ to $5 \mu\text{m}$	$\lambda = 8$ to $14 \mu\text{m}$
Alkali halides	----	KCL, NaCL, CsI
Other halides	BaF ₂ , LiF, MgF ₂	KRS ₅ , PbF ₂ , ThF ₄
Glasses	Si	Ge, GaAs, InP, GaP
Chalcogenide glass	----	ZnS, ZnSe, CdS, CaLaS
Oxides, Nitrides and other refractory materials	Al ₂ O ₃ , SiN, SiC, ZrO, Y ₂ O ₃	----

Table 3.1. Potentially useful infrared transmitting materials (Burnay et al., 1988).

(a) Although the alkali halides have excellent infrared transmission, they find little use outside the laboratory environment because of their softness and their solubility in water. Their most important application is to act as a prism material in infrared spectrometers.

(b) Among the other halides, PbF₂ and ThF₄ find applications in coatings rather than in optical components. This is because PbF₂ is soft and ThF₄ is radioactive, and neither would be suitable in bulk form for use as optical components. Magnesium fluoride (MgF₂) is used for the windows of infrared imaging systems operating under severe environmental conditions, where high surface temperatures are encountered.

(c) Germanium and silicon glasses have been used extensively as lens materials in infrared imaging systems. Silicon is usually used in devices operating in the $\lambda = 3$ to $5 \mu\text{m}$ middle infrared band. It is cheaper than germanium and easier to obtain. However,

it is not as highly transmittive as germanium in the $\lambda = 8$ to $14 \mu\text{m}$ thermal band. On the other hand, germanium possesses most of the characteristics required for thermal imaging. It can be used either in the middle infrared or in the far infrared band. However, its refractive index has a high temperature dependence and so the telescopes or lenses in practical imaging systems using germanium optics may need to be athermalised.

Germanium is of little use above 100°C . The reason for this is that the transmission of infrared radiation in this material at these higher temperatures is reduced through the increase in the number of free carriers generated in the germanium crystalline material. In this context, gallium arsenide may be used in the $\lambda = 8$ to $14\mu\text{m}$ region at temperatures up to 200°C , although at present, the supply of gallium arsenide in adequate sizes is severely limited and is very expensive mainly due to the high cost of gallium. It is however, rare in most industrial applications for the front window of an infrared imager to become as hot as 100 to 200°C . So germanium optics are widely used in infrared imagers.

(d) Of the chalcogenides, only three have been developed to any extent. These are zinc sulphide, zinc selenide and chalcogenide glass. Germanium becomes too absorbing above about 70°C so that the most favoured candidate materials are gallium arsenide (GaAs) and zinc sulphide (ZnS). As discussed above, GaAs is useful at temperatures of up to 200°C but it is very expensive and is only likely to find limited use in certain special applications. Zinc sulphide is therefore the most likely material in this group to be used in an infrared optical system, but it does suffer from transmittance limitations in the range $\lambda = 8$ to $10\mu\text{m}$, particularly when hot (Savage, 1985). Zinc selenide has far better transmission in the range $\lambda = 8$ to $12\mu\text{m}$ and is the preferred material for many low-loss infrared applications. However it is softer than zinc sulphide and is far more expensive, both of which are factors that tend to limit its general application. Chalcogenide glass has poor thermal shock properties and it is difficult to make it optically homogenous. For this reason, it has not been exploited to the extent originally anticipated. The other compound in the list of chalcogenides, namely calcium lanthanum sulphide, is still under development. It is harder than zinc

sulphide and has better optical transmission, and could, in the future, become a replacement for zinc sulphide, although there is some doubt about its thermal shock properties.

(e) The refractory materials listed in Table 3.1 have been developed mainly for special purpose high-temperature military applications and, apart from sapphire (aluminium oxide), they are unlikely to be used in civilian or industrial applications of thermal imaging. Sapphire is one of the hardest of the oxide crystals and maintains a good strength at high temperatures. It possesses good thermal properties and excellent chemical durability. Therefore it would appear to be an ideal candidate for the windows of infrared imaging systems. But there are two main problems associated with Al_2O_3 . One is that the material is difficult to shape into components because of its high strength and hardness, and the other is that its properties are anisotropic because it has a hexagonal crystal structure.

3.3 Optical Arrangements

The optical arrangements that are used in infrared imaging systems are, in some ways, similar to the optical arrangements used in visual systems such as a camera or telescope. In these devices, the optical configuration of the lenses or mirrors that initially focus the radiation from the object to form an image on the photosensitive surface is termed the objective. This may need to be supplemented by internal focussing lenses to achieve a sharp focus of the image in the image plane - especially if the objects that have to be imaged lie at different distances from the imager as in close-range photogrammetry. Alternatively - and more commonly - the objective itself may be used as the focussing element of the imager - in which case, it will affect the geometric calibration when it is reset. Thus a complete calibration should give a range of image distance values corresponding to the range of focus settings of the objective lens. A potential problem that can arise comes when the objective lens is shifted during focussing. If the movement of the lens is not true, due to shortcomings in the manufacture of its housing and // or of the rack and pinion or helical screw thread

mechanism used to control its motion, then the optical centre of the lens may drift off the optical axis.

If the telescope is to be used by a human observer, an additional optical arrangement called the ocular, or eyepiece, is needed to allow the image plane to be seen by the eye. Such an eyepiece usually contains two components - the field lens and the eye lens. The field lens serves to divert radiation from the outermost parts of the field of view to the eye lens. The eye lens, in conjunction with the lens of the human eye, refocuses the image of the object onto the retina. However the requirements of an optical system used in an infrared imager are very different to those of a purely optical telescope such as an astronomical telescope or surveyor's theodolite where provision has to be made for direct observation of the image plane by a human observer. Instead, in an infrared imager, the optical image plane is replaced by a plane of detectors or a vidicon tube and the visual image generated by an eyepiece is replaced by a video system that allows both the display of the image and its recording on magnetic media.

As noted above, the optics of an infrared imaging systems will contain an objective lens or mirror. Also, a relay lens is often used to enhance the performance of the system. The objective optics can be grouped into three categories:-

- (i) dioptric, or refracting optics;
- (ii) reflecting optics; and
- (iii) catadioptric, or reflecting-refracting optics.

3.3.1 Refracting Optics

Either a single lens or, more commonly, a lens system will be used as a refracting optical element in many infrared imaging systems. Those which are commonly used in optical systems are: the simple lens (or singlet); achromatic doublet; triplet; multi-element (Petzval); and Fresnel. Amongst them, the simple lens and the achromatic doublet are those that have found most application in infrared imagers.

A simple lens (or singlet) with two convex surfaces is a positive, or converging optical element that may be used to focus the radiation from the object field into a plane to form an image. This simple type of lens was used as an objective lens in the first telescope built by Galileo and later was used in the Keplerian telescope. Other simple lens elements having double concave, concavo-convex, plano-convex or other surfaces (see Fig. 3.1) may also be used as required in an infrared imaging system. However these various simple lenses exhibit all the commonly encountered aberration phenomena, especially chromatic and spherical aberration, that result in a deterioration in the quality of the final image. Thus a simple lens will only be used in an infrared imaging system when high image quality is not required. Combinations of these individual lens elements will almost certainly be employed in higher performance infrared imagers.

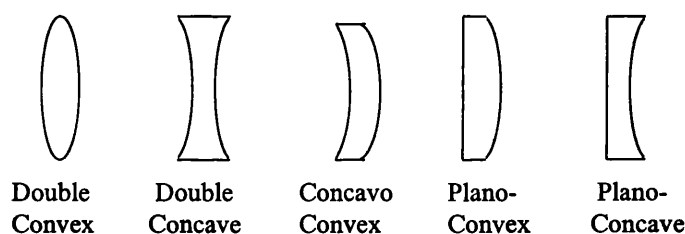


Fig. 3.1. Simple lens types.

In 1733, Hall discovered that the chromatic aberration commonly encountered with simple lenses could be reduced by the use of an achromatic doublet which is the combination of two lenses having different indices of refraction. Thus, depending on the spectral region and the availability of suitable materials, chromatic aberration can be greatly reduced or eliminated. In the visible region of the EM spectrum, combinations of suitable crown or flint optical glasses are used; in the near infrared, calcium fluoride and silicon glasses can be combined. Silicon and germanium form a suitable pair for use in the middle and thermal infrared bands. Small achromatic doublets are often designed with their inner surfaces having identical radii so that the two elements can be cemented together. This eliminates surface reflections and allows a convenient compact construction. It is also possible to use more than two lenses to achieve the desired characteristics in the optical system. Thus a triplet is sometimes formed also.

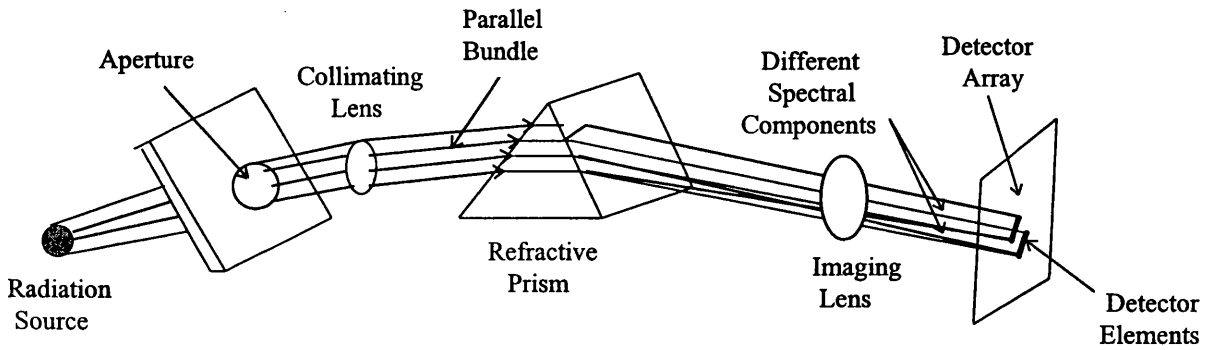


Fig. 3.2. Separation of the components of incoming radiation by refractive prism.

Turning next to refractive prisms, a simple type triangular prism of glass (see Fig. 3.2) will produce a deviation of the incident radiation depending upon the angle of the prism, the angle of incidence of the radiation and the refractive index of the material. Because the index of refraction of the glass material varies with wavelength, a separation of the incoming radiation into different wavelengths results from passing the radiation through a prism of this type. Transmittive prisms of this type have been used to separate out the different wavelengths used in multi-spectral scanners, which may include one or more channels devoted to the infrared part of the EM spectrum. For example, both the Landsat MSS (Multi-Spectral Scanner) and TM (Thematic Mapper) use the refractive / transmittive triangular prism to split the incoming radiation into a series of spectral channels or bands before reaching the arrays of detectors, placed in positions behind the prism. The Landsat MSS and TM scanners produce four and seven spectral channels respectively. They are shown in Table 3.2.

Landsat MSS		Landsat TM		
Channels	Wavelengths (nm)	Channels	Wavelengths (nm)	
Green	500 to 600	Blue	450 to 520	Visible
Red	600 to 700	Green	520 to 600	
		Red	630 to 690	
Near Infrared	700 to 800	Near Infrared	760 to 900	Infrared
Near Infrared	800 to 1,100	Middle Infrared	1,550 to 1,750	
		Middle Infrared	2,100 to 2,350	
		Thermal Infrared	10,400 to 12,500	

Table 3.2. Spectral channels of Landsat MSS and TM.

The incoming radiation is essentially split into multiple bands, or channels, each of which is measured independently by a separate detector. Each detector is designed to have its peak spectral sensitivity in a specific wavelength band. As can be seen from Table 3.2, by means of a refractive prism, the incoming radiation has been separated into two visible and two near infrared channels in the Landsat MSS, and into three visible, one near infrared, two middle infrared and one thermal infrared components in Landsat TM.

Alternatively, some multispectral scanners use a diffraction grating instead of a refractive prism. It is used instead of a prism to separate out different radiation bands whenever more accurate measurements of wavelength need to be made. A diffraction grating consists of many parallel wires spaced at equal distances apart. A grating with four wires is shown in cross section in Fig. 3.3. Part of incoming radiation travels straight through. For each wavelength, some of the radiation will be deflected in each of several other directions. The angle through which it is deflected is determined by the requirement that the radiation through each opening should travel an integer number of wavelengths farther than radiation through the adjacent opening. In Fig. 3.3, the deflected first-order and second-order beams of radiation are shown along with the undeflected beam. Since the angle deflection depends on the wavelength, the radiation can be split into the required spectral channels.

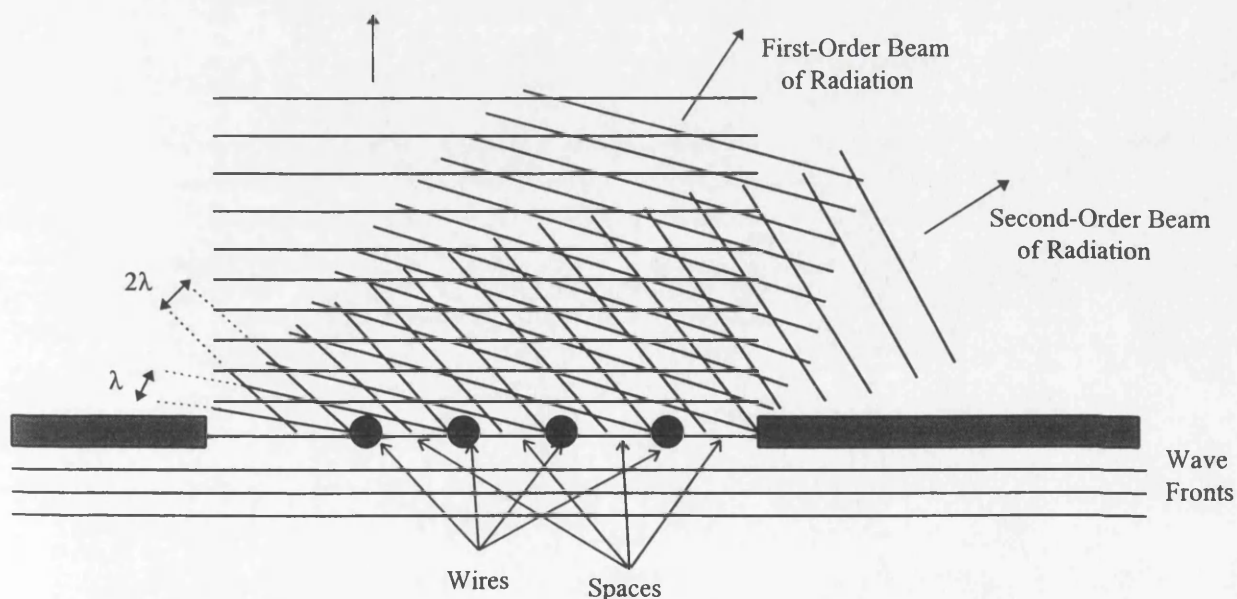


Fig. 3.3. Diffraction gratings.

3.3.2 Reflecting Optics

The advantages of a reflective system, that is, a system using spherical mirrors instead of lenses to focus and generate an image of the object, are compact construction and chromatic independence. This latter property not only means freedom from chromatic aberration but it is particularly advantageous in infrared systems for other reasons. At long wavelengths, the infrared optical designer has a limited choice of suitable refractive materials. This restriction is circumvented by choosing reflective optics, which will work at all wavelengths. It is also worth noting that the image produced by a refractive system operating in the infrared will be focussed at a significantly different image distance from the objective as compared with the visible image produced by the same system. This consideration must be borne in mind by the designer of the optical system and may lead him to adopt a reflective mirror system to form the image.

Both single mirror and folded mirror systems are commonly used in infrared imagers. A simple concave spherical mirror will cause the incoming parallel rays of radiation to converge and be focussed in the image plane. This configuration is the analogue to the simple lens and performs the same functions; however its advantage is the absence of chromatic aberration. Thus it is often used in infrared imaging systems with small fields of view. Spherical mirrors are used as the objectives of the afocal telescope often employed in thermal video frame scanners (TVFS) and sometimes for the front optics of pyroelectric vidicons.

In folded optical systems, the rays are often folded using mirror optics, either to shorten the overall size of the imager or to place the focal plane in a more convenient position. The arrangement of concentric folding is often used in infrared imaging systems. In this arrangement, the focal plane is placed in an accessible position along the axis of the primary mirror. The concentrically folded systems are broadly named Gregorian and Cassegrain depending on whether the folding occurs before or after the

prime focus. The Gregorian utilizes a concave secondary mirror; the Cassegrain usually has a convex folding, or secondary, mirror (see Fig. 3.4(a) and (b)).

The disadvantage of these systems is the blocking of radiation by the secondary mirror, resulting in lowered overall transmission efficiency of the system. The blocking of radiation in these systems is generally about 25%, but can be compensated for by increasing the size (diameter) of the primary mirror.

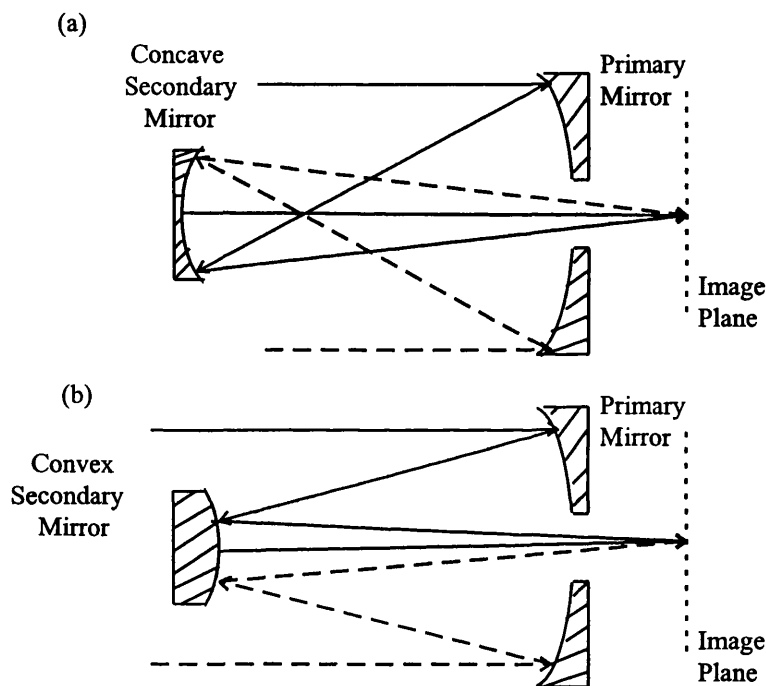


Fig. 3.4(a) Gregorian and (b) Cassegrain systems.

Plane mirrors are used in thermal video frame scanners to redirect the incident radiation without introduction of aberrations. Indeed, a plane mirror can be thought of as the only aberration-free optical surface (Slama et al, 1980). However, in practice, mirrors may not actually be mathematically or optically plane. Furthermore, quite apart from the need to ensure that errors do not arise during manufacture, a plane mirror needs to be sufficiently rigid and well mounted for its application within the imager to be effective. Plane mirrors are used to fold the optical path (see Fig. 3.5). As can be seen from this figure, the changes in the direction of the optical path provided by these mirrors provides compact construction.

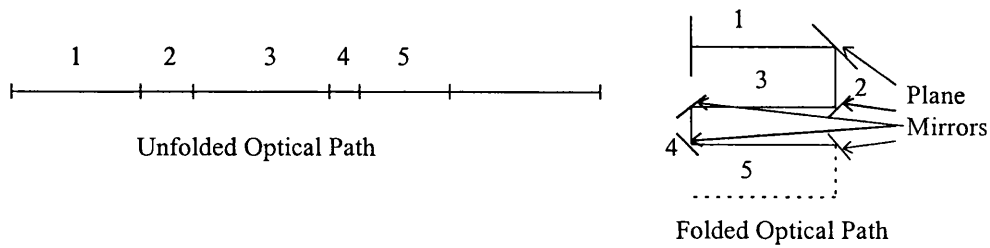


Fig. 3.5. Reduction in the overall size of an imager through folding of the optical path using plane mirrors.

Mirrors are used extensively inside infrared scanners where normally there is a clean and dry environment. Elsewhere they need a protective coating to prevent them from tarnishing. So the choice of coating material is an important matter. For the highest reflectivity in the infrared part of the spectrum, mirror surfaces are coated with thin films of gold or dielectric multilayers. Mirrors were originally fabricated in glass and were front silvered or aluminised, but now, for ease of manufacture and reliability, it is usual to machine reflecting surfaces directly as aluminium components using single-point diamond machining. The reason for this is that aluminum is yielding greater than 90% reflectivity. Other components that are manufactured in this way include the rotating polygons and flapping mirrors used in scanners as well as their relay optics and fold mirrors.

Reflecting prisms can be used as an alternative to plane mirrors to re-direct the radiation or may invert, revert or rotate an image in its own plane. The simplest form of reflecting prism is the right-angle prism as shown in Fig. 3.6. In this case, the entering ray is normal to one of the sides. A total internal reflection occurs at the hypotenuse face without loss of energy and without aberrations. The deflected ray is turned 90 degrees with respect to the initial direction. For use in wide angle systems, one often requires that the hypotenuse face be silvered to include reflections within the critical angle and for the minimum loss of reflection. Absorption of some of the radiation by the glass is of course a disadvantage of the prism as compared with the plane mirror. Transmission of middle and thermal infrared radiation will of course require the use of more esoteric and expensive materials such as germanium.

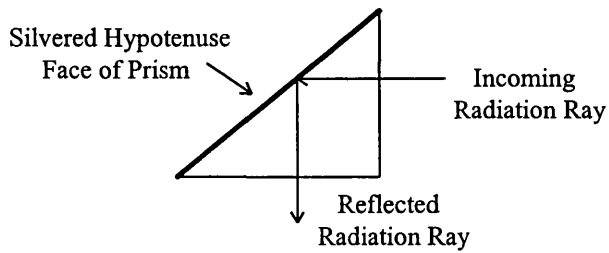


Fig. 3.6. Reflective prism.

3.3.3 Catadioptric Optics

These well-known systems combine both lenses and mirrors; typical of these are the Mangin mirror; Schmidt system; and Bouwers-Maksutov system. However the use of such systems appears to be restricted to astronomical telescopes and satellite tracking cameras. No example of their use in infrared imagers is known to the author, so they will not be dealt with here. However as will be seen later, quite other combinations of lenses and mirrors are used, more especially in those infrared imagers using a scanning mechanism.

3.3.4 Relay Lens (Auxiliary Optics)

After the infrared radiation has been focussed by the objective lens, it must then be detected and measured by a detector. It is known that the system sensitivity improves as the detector is made smaller. The dimensions of the detectors have to be related to the instantaneous field of view of the imagers. With the use of a relay lens, the detector size is reduced approximately in the ratio of the f-number of the relay lens to the f-number of the objective lens.

The second advantage of using relay lens with a detector arises from the fact that many detectors have non-uniformities of detectability over their surface. The response of a detector to radiation at one point in the scene will not be the same at another. A relay lens distributes the radiation more uniformly over the detector surface (Jamieson et al, 1963). This matter of non-uniformity will be explained in Chapter 10.

3.4 Anti-Reflection (AR) Coatings

These coatings are applied to the surfaces of lenses, prisms and mirrors to cut down the loss of radiation through unwanted reflections from these surfaces. The reflectivity R of an optical glass surface is given by

$$R = (n - 1)^2 / (n + 1)^2 \quad (3.1)$$

where n is the refractive index of the reflecting surface. Germanium has a refractive index of 4, so that 36% of all incident radiation is reflected at each uncoated surface of a germanium lens. It is therefore essential to put an anti-reflection (AR) coating on all germanium lenses and windows. The same is true of all the other optical materials used in infrared imagers, but the lower the refractive index of a material, the lower are the demands on the coating.

With the AR coatings that have been developed at Royal Signals and Radar Establishment (RSRE), Malvern it is possible to coat an anti-reflection layer on an infrared lens at a specific wavelength by using a single layer provided that

$$n_1^2 = n_2 \quad \text{and} \quad n_1 d = \lambda / 4 \quad (3.2)$$

where n_1 is the refractive index of the coating and d its thickness, n_2 is the refractive index of the substrate and λ is the design wavelength (Burnay et al, 1988). From Eq. 3.2, a coating of refractive index 2 and a thickness of $1.25\mu\text{m}$ is needed for a single layer anti-reflection coating for germanium optics. Diamond, with its refractive index of 2, would make a perfect AR coating. Since this coating also improves the scratch resistance and chemical durability of germanium optics, it is generally used on the outside surfaces of the germanium lenses used in infrared systems.

For the other surfaces of the optical elements used in an infrared telescope or lens that need to have higher transmissions, multilayer anti-reflection coatings are often used (Burnay et al, 1988). The highest efficiencies are obtained by using multilayer combinations of germanium, zinc sulphide and thorium fluoride. For these, the average transmission is 98% and the reflection loss is less than 0.3% per surface.

There could be more than ten such coated internal surfaces in an infrared optical system and so a few per cent loss per surface could become significant. It is also essential to reduce the reflection losses on these elements, particularly for systems using detectors cooled by liquid nitrogen, since there is a tendency for the cold detector surround to be reflected back on to the detecting element, creating a cold region in the centre of the field of view of the infrared imaging system. This is usually called the narcissus effect and is reduced by careful optical design and the use of the highest-efficiency coatings. These high efficiency coatings are delicate and difficult to handle. For those internal surfaces that might possibly be exposed during maintenance, a special coating has been defined which has the low reflection loss of the high-efficiency coating but not necessarily the same transmission (Burnay et al, 1988; Savage, 1985).

3.5 Infrared Telescopes and Lens Systems

Many thermal infrared frame scanners use an afocal telescope to collect and focus the emitted radiation from the object and to collimate this radiation into a narrow beam which can then be focussed onto the focal plane of the detector. The basic afocal telescope consists of two lenses separated by a distance equal to the algebraic sum of their two focal lengths. Such a system forms its image of an infinitely distant object at infinity. There are two types of afocal telescopes - the astronomical and Galilean types. In the astronomical type, there is a real focal plane between two lenses, while in the Galilean type there is a virtual focal plane and the second lens is negative in power. Fig. 3.7 shows the reflecting and the refracting versions of both types of telescope, the former employing mirrors, the latter based on the use of lenses.

Galilean telescopes are much shorter in length than the astronomical ones. However, their objective lenses are larger in diameter than those of the corresponding astronomical type and they are not in such common use in thermal infrared frame scanners as the astronomical type. From the diagrams (Fig. 3.7(a) and (b)), it is obvious that, since the radiation emerging from an afocal telescope is a parallel

bundle, there is a need for a further internal focussing lens or lens system to focus the radiation on to the detectors located in the image plane.

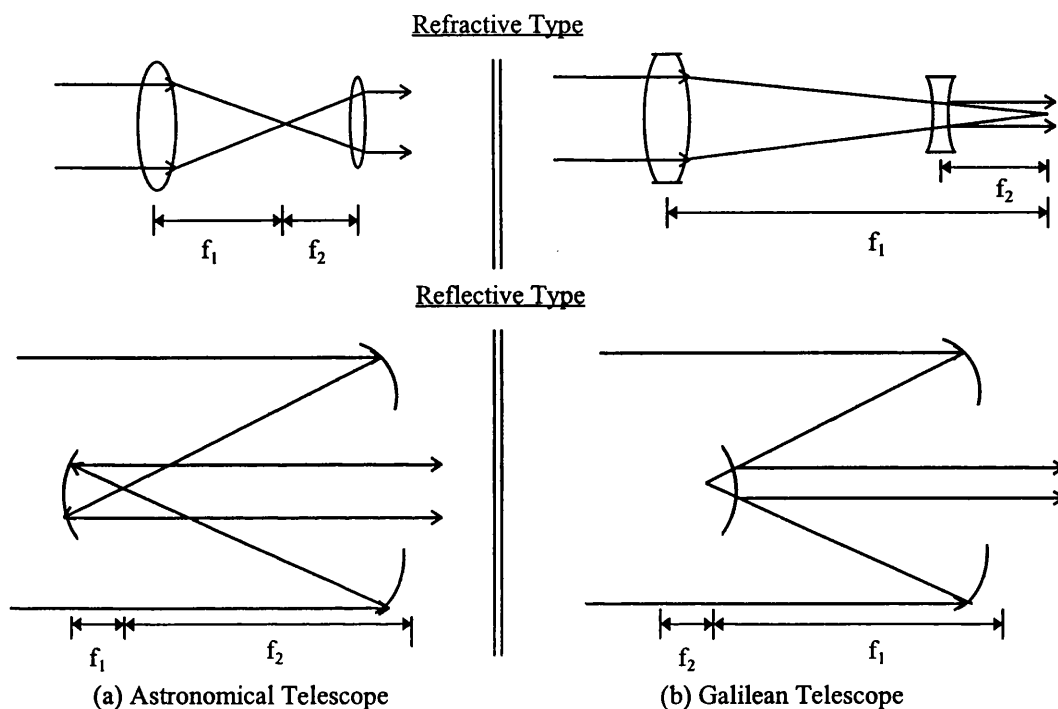


Fig. 3.7. Astronomical and Galilean types of afocal telescope (Amin, 1986).

3.5.1 Examples of Infrared Imager Optical Systems

The Agema 1000 TVFS uses a telescope consisting of an objective lens system and a collimator. The objective lens collects radiation from the scene and delivers it to a collimator which supplies a collimated bundle to the scanning system. As can be seen from Fig. 3.8, the objective lens system uses a number of double concave, double convex, concavo-convex, plano-convex, plano-concave singlet and doublet lenses. The collimator typically comprises two or more refractive optical elements. This is used for both the narrow (5°) and wide field of view (20°) (see Fig. 3.8). The interchange between these fields of view is provided by a turret that can tumble the optical elements in the objective lens system. In the narrow field of view, the successive optical elements are numbered 1 to 5 (see Fig. 3.8), i.e. there are 5 optical elements present in the objective in this field of view. For the wide field of view,

these elements are tumbled by the turret and the positions of the previously unused elements I, II and III will be changed into the optical path while optical elements 3 and 4 will be rotated out of the optical path. There will now 6 lens elements used in the wide angle configuration.

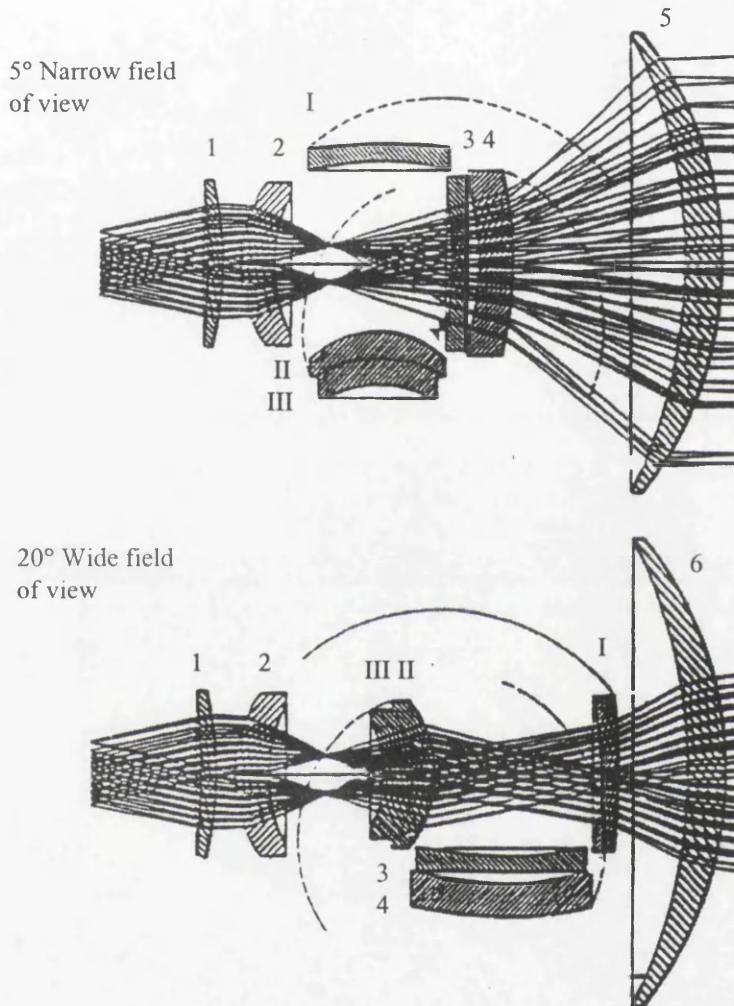


Fig. 3.8. Dual field of view of the optical design of Agema 1000.

The Barr & Stroud HDTI imager also uses a telescope that gives a dual field of view (4° and 12.5°) (see Fig. 3.9). In this system, all the optical components are athermalized and are made of germanium, apart from a zinc selenide colour correcting component used in the objective. The field of view change is carried out through the insertion of extra elements into the internal focussing lens system using a turret with the additional lenses positioned as shown in the Fig. 3.9.

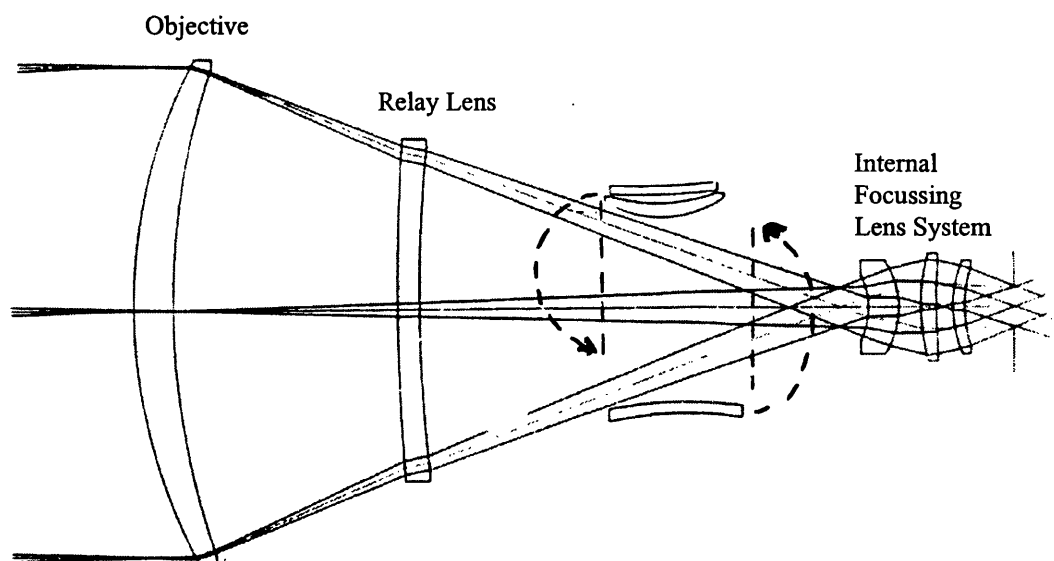


Fig. 3.9. Schematic diagram of the telescope of the HDTI imager when utilizing the narrow field of view; a turret with additional optical elements is used to change the field of view and magnification.

3.6 Infrared Lens Quality

It is impossible for a single lens to produce a perfect image; in practice, it will always be somewhat blurred. Those imperfections which degrade the sharpness of the image are termed aberrations. Their presence gives rise to the use of combinations of lenses (comprising a lens system). Through the use of these additional lens elements, lens designers are able to correct for aberrations and either eliminate them or bring them within tolerable limits.

The primary lens aberrations are: (i) spherical aberration; (ii) coma; (iii) astigmatism and curvature of field; and (iv) chromatic aberration (Jamieson et al, 1963; Wolfe, 1965; Wolfe and Zissis, 1978; Slama et al, 1980; Wolf, 1983;).

Spherical aberration, as illustrated in Fig. 3.10, is the degradation of the axial image. It is caused by faulty grinding of the spherical surfaces of the lens elements and results in light rays entering near the outer edge of the lens being brought to focus nearer lens than the rays which enter near the centre of the lens. The image of point

thus formed is a circle called the circle of confusion. If spherical aberration exists for a lens, the size of the circle of confusion may be reduced by adjusting the position of the image plane until the smallest possible circle is obtained. The image plane position that produces the circle of least confusion is illustrated in Fig. 3.10.

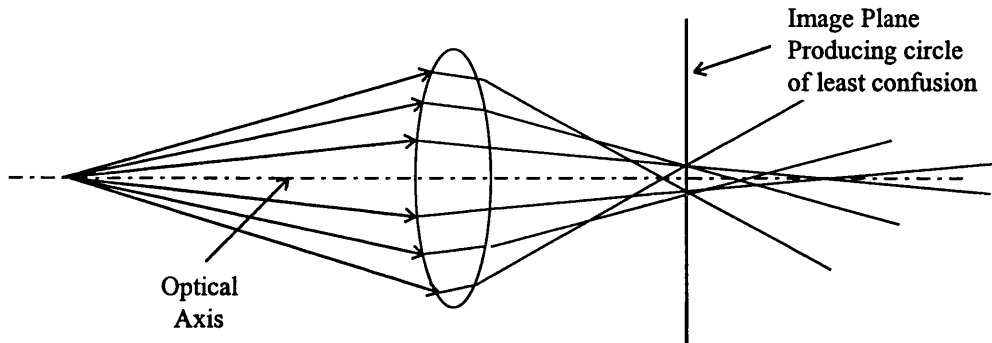


Fig. 3.10 Spherical aberration.

Coma is similar to spherical aberration, except that it applies to the failure of oblique rays, instead of axial rays, to come to focus at a point. Instead of the point being a circle, it is in the shape of a comet.

Astigmatism is a condition in which lines in the object space that are perpendicular to each other do not come to focus at the same image distance. As shown in Fig. 3.11, rays 1 and 2 from a vertical object line are focussed at a, while rays 3 and 4, which are from a perpendicular line in the object, are focused at b. Astigmatism is caused by imperfect grinding of the lens surfaces. It is common in the human eye. With an astigmatic lens, images from points of equal object distances; but whose rays make varying angles with the optical axis, will not come to focus in the same image plane. Rather, they will form a curved surface. This condition is called curvature of field. Astigmatism and curvature of field can be minimized by using a combination of lenses comprising converging and diverging elements.

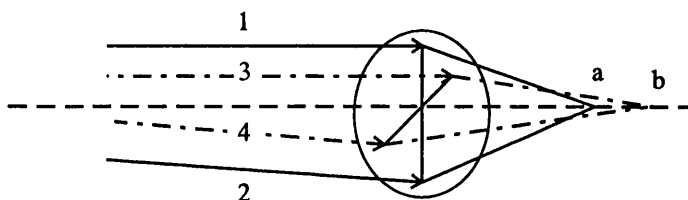


Fig. 3.11. Astigmatism.

Chromatic aberration is caused by the quite different refractive indexes of the visible light and infrared radiation that reach the lens. As shown in Fig. 3.12, visible light is refracted by a glass lens more than infrared radiation, and therefore these two fail to come to focus at common point or in a common imaging plane. The reason for this is that infrared radiation has a longer wavelength than visible light. So the plane of sharp focus of the image has to be altered in position in the case of infrared radiation. For the near infrared, one might expect to extend the image plane of sharp focus within the range of from 1/200 to 1/400 of the focal length (Maruyasu and Nishio, 1960). Camera companies, therefore, have to design and build special lenses for use with infrared sensitive photographic emulsions. For example, Wild produced the special series of lenses called the Infragon, Super Infragon and Infratar for use with infrared photographic emulsions in their aerial cameras as variants of the Aviogon, Super Aviogon and Aviotar lenses used in the visible part of the spectrum.

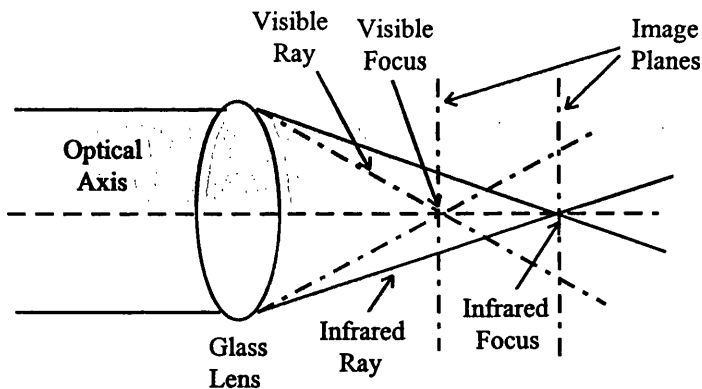


Fig. 3.12. Chromatic aberration of a lens which due to the visible rays undergoing a greater refraction than the infrared rays.

The aberrations of an infrared optical system can be given in a general equation as follows (Jamieson et al, 1963):

$$x_0 = Am + Bw + Cm^3 + Dm^2w + Emw^2 + Fw^3 + \dots \tag{3.3}$$

$$y_0 = 0$$

where:-

- x_0, y_0 are the positions of the image plane;
- A,B,C,D,E and F are the coefficients of the terms used in the equation;

m is the f-number of the optical system; and
 w is the size of the field of view.

Chromatic aberration is a first order term ($A_m + B_w$), increasing linearly with both the field of view and the f-number of optical system. Since chromatic aberration is a function of the variation of the refractive index of the material with wavelength, the effective bandpass of the imaging system should be restricted, especially in those wavelength regions where the refractive index changes rapidly. Otherwise, this term can easily become the dominant one for many of the materials with high refractive indices used in infrared lenses.

Spherical aberration is the only term (C_m^3) independent of the field coverage. It is, however, very sensitive to the f-number. Both chromatic and spherical aberration can be reduced by making a doublet lens that is a combination of two lenses having materials of different indices.

The introduction of coma ($D_m^2 w$) will be observed in an off-axis position, increasing in extent in direct proportion to an increase in field angle and as the square of the f-number.

At large angles from the axis of the optical system, the image is often dominated by the astigmatism and field curvature (see Fig. 3.13) that degrade the image sharpness as the square of the field angle ($E_m w^2$).

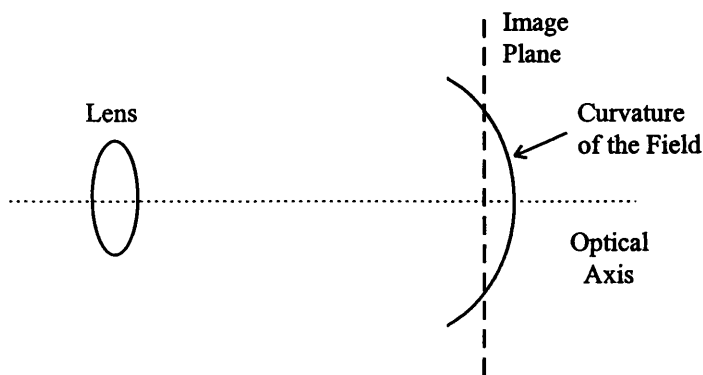


Fig. 3.13. Field curvature produced by a single lens.

Barrel and pincushion lens distortions alter the position of the point along the optical axis by an amount varying as the cube of the field angle.

The aberrations discussed above degrade the quality or sharpness of the image. On the other hand, lens distortions do not degrade image quality but deteriorate the geometric quality (or positional accuracy) of the image. So, they have their main impacts on the geometric fidelity of the infrared imaging systems and have to be corrected and taken into account in the geometric calibration of the imagers. This important matter will be discussed in more detail in Chapter 5 together with other distortions that are encountered with these imagers.

3.7 Resolution

When the optical designs are relatively free of aberration, a ray trace indicates geometric convergence to a point. However, it is found that the energy does not converge to a point but is spread over an area, forming a diffraction pattern. This diffraction phenomenon is explained by the wave nature of light which has been discussed in the previous chapter. It is only when aberrations have been reduced sufficiently by suitable design that diffraction is of importance and it then imposes a fundamental limit on the resolution and therefore on the ultimate accuracy of the imaging systems.

It was established by the astronomer Airy in 1834 that the image of a point source produced by an ideal optical system cannot be a mathematical point, but instead it will consist of a small central disc surrounded by diffraction rings (see Fig. 2.1 in Chapter 2). This central disc of greatest intensity is known as the spurious disc, or more often as the Airy disc. If the total energy in the image of a point is taken as being of unit value, the Airy disc contains 84% of the energy, the first bright ring about 6%, and so on. Airy also found that the diameter of the spurious disc depends on the wavelength of the radiation and on the aperture-ratio or f-number of the lens.

The diffraction theory developed by Rayleigh shows that the least separation (d) between the Airy discs (see Fig. 3.14) is given by

$$d = 0.61\lambda / \sin U' \quad (3.4)$$

where λ is the wavelength of the radiation, and U' is the absolute value of the slope angle of the marginal ray passing through the aperture under consideration.

For an object located at infinity,

$$\sin U' = h / f \quad (3.5)$$

where h is the radius of the effective free aperture of the lens and f is the focal length.

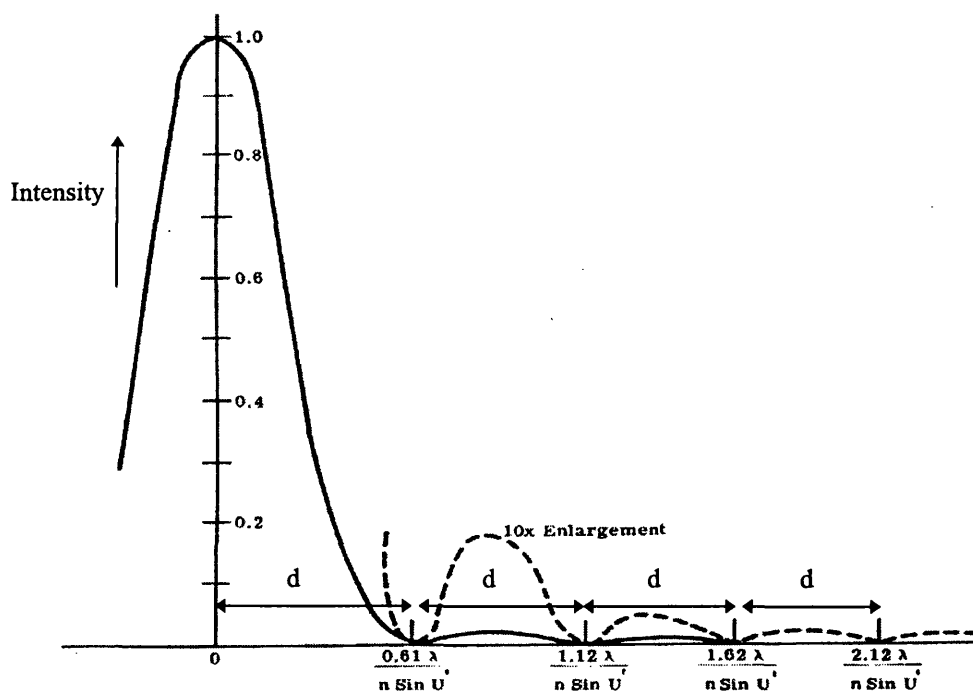


Fig. 3.14. Distribution of energy in the diffraction pattern (Wolfe and Zissis, 1978)

3.7.1 Aperture and Resolution

This led many years ago to the concepts of relative aperture and of f-number. The relative aperture is defined as the ratio of the focal length of the lens to the diameter ($2h$) of its effective aperture. The symbol for relative aperture is $f/$ followed by the

numerical value of the ratio just defined. For example, $f/2$ signifies that the diameter of the effective aperture is one-half the focal length. From these definitions and Eq. 3.5, it is obvious that the following relationship exists when the object is at infinity:

$$\text{f-number} = 1 / (2 \sin U') \quad (3.6)$$

So Eq. 3.4 can be written in terms of the f-number as

$$d = 1.22 \lambda (\text{f-number}) \quad (3.7)$$

Thus, the total diameter of the central diffraction disc can be written as

$$D = 2d = 2.44 \lambda (\text{f-number}) \quad (3.8)$$

Eq. 3.8 also describes the width of the point spread function of the diffraction-limited lens, which has a Gaussian shaped curve (see Fig. 3.14).

However, lenses with the same aperture or f-number could have different resolutions. For instance, the older and newer versions of the Wild Aviogon lens have the same f-number of $f/3.5$, but the former has a resolution of 40lp/mm while the latter has 70lp/mm. The reason for this is the improvement in the quality of lens brought about by the more compact design of lenses, their higher light transmission due to the use of rare earths and the use of very good anti-reflection coatings.

3.7.2 Wavelength and Resolution

Eq. 3.8 shows that resolution also depends on the wavelength (λ) of the incident radiation which is incoming to the imaging system. If one assumes that the f-number is constant, then the use of the radiation occurring in the middle and thermal infrared bands of the EM spectrum would suggest that imagers operating in this part of the spectrum would have an order of magnitude lower resolution than imaging systems that operate in the visible region. This relationship between the wavelength and

resolution could affect the accuracy of measurement (measurability) that can take place on the images which are obtained by infrared imaging systems.

3.7.3 Depth of Field and Aperture

The depth of field of a lens is the range in object distance that can be accommodated by a lens without introducing significant image deterioration. In Fig. 3.15, light rays from object point B are perfectly focused as a point B' in the image plane. Light rays from A and C, on the other hand, are imaged as circles of confusion of diameter D. The larger the circles of confusion become, the more deteriorated is the image.

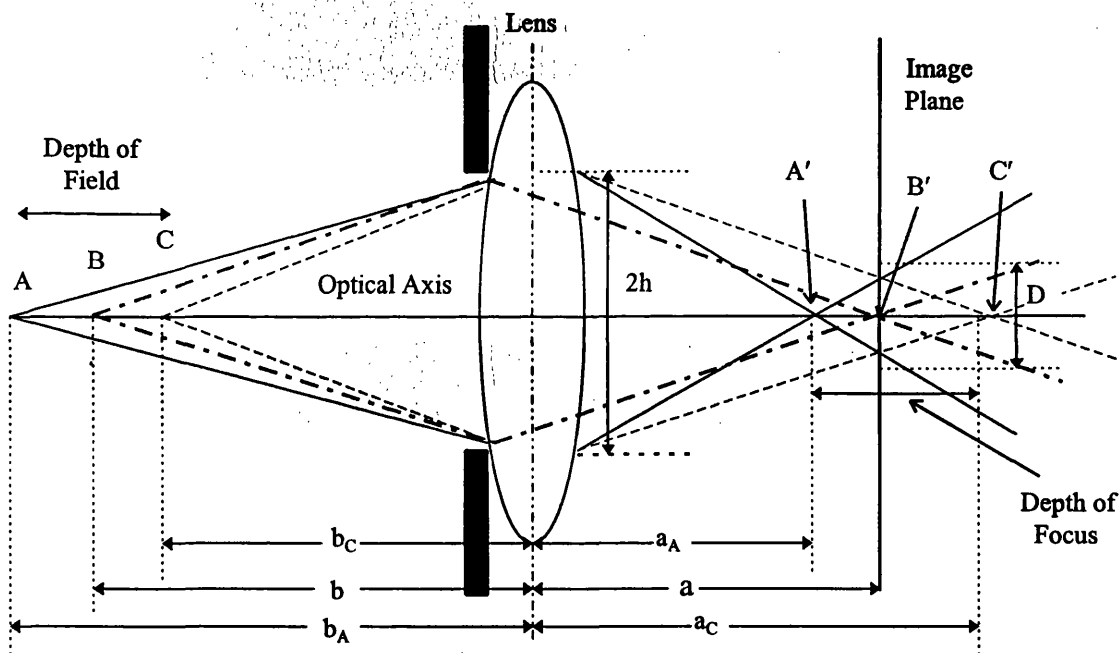


Fig. 3.15. Depth of field and depth of focus

The basic Newton lens equation of optics for sharp imagery is:

$$1/a + 1/b = 1/f \quad (3.10)$$

where:-

- a is the image distance;
- b is the object distance; and
- f is the focal length.

From Eq. 3.10

$$a = (bf) / (b - f) \quad a_A = (b_A f) / (b_A - f) \quad a_C = (b_C f) / (b_C - f) \quad (3.11a)$$

where:-

- b_A is the object distance for the point A;
- b_C is the object distance for the point C;
- a_A is the image distance for the point A; and
- a_C is the image distance for the point C.

and from the similar triangles,

$$2h / a_A = D / a_A - a \quad 2h / a_C = D / a_C - a \quad (3.11b)$$

can be written.

Introducing Eq. 3.11(a) into 3.11(b) and rewriting, one obtains:

$$b_C = 2hbf / (2hf + D(b - f)) \quad b_A = 2hbf / (2hf - D(b - f)) \quad (3.12)$$

If the numerator and denominator are multiplied by $f / 2h$, so that the f -number or relative aperture appear in one position with a clear effect:

$$b_C = bf^2 / (f^2 + (f / 2h)D(b - f)) \quad b_A = bf^2 / (f^2 - (f / 2h)D(b - f)) \quad (3.13)$$

As can be seen Eq. 3.13, the depth of field can be increased by reducing the size of the lens aperture.

3.7.4 Depth of Focus

The depth of focus (see Fig. 3.13), which is akin to depth of field is the range in the image distance that can be tolerated without introducing a significant or discernable deterioration of the image in terms of its sharpness.

Real optical systems usually produce blur spot images which are larger than the diffraction limit described above. Larger blur spots may results from aberrations, that is, from a failure of the optical system to produce a perfect focus. It can be said that

the diameter of the Airy discs increases with the aberrations when they are present. However, in a perfect system (that is, one which has no aberrations or defects of manufacture), the wavelength of the radiation that reaches and is being focussed by the optical system will determine the size of the Airy disc, of course, taking into account the aperture size.

3.8 Conclusion

In this chapter, the main aspects of the optical materials and components that are used in infrared imaging systems have been fairly fully covered. In addition, their impacts on the infrared image have been described. Thus, the optical side of the infrared imagers that are the main concern of this thesis has been dealt with. In the next chapter, the infrared detectors that have been designed to sense the infrared radiation being collected by the optical system will be described and discussed in some detail.

CHAPTER 4: INFRARED DETECTORS

4.1 Introduction

Two of the main elements common to all infrared imaging systems are their optical components which collect the radiation being emitted or reflected from the object scene and their detector mechanisms which convert this radiation into the form of an electrical signal. Basically, these two main parts of the system form the infrared image that will be used for other stages in the process and, as such, they largely define the geometric and radiometric characteristics of the infrared imagers which are main concern of this project. The optical components of these imagers have been fully discussed in the previous chapter. In this chapter, the various detectors that have been designed and built to collect and detect radiation in the middle and thermal infrared bands will be dealt with in some detail on the basis of the account of the fundamental physics underlying these systems that has already been given in Chapter 2. In addition, the two-dimensional areal arrays of these detectors that can be used to image the object scene will be described together with their design structures. This chapter will conclude with the characteristics of the detectors that can be employed in infrared imaging systems.

4.1.1 Detectors

A detector may be defined as a device that provides an electrical output that is a useful measure of the radiation incident on the device. The actual responsive element is called a radiation transducer. It changes the incoming radiation into an electrical signal which is amplified by the accompanying electronics. Detectors can be separated into two groups:- thermal detectors and photon detectors - based on the type of transducer used. The responsive element of thermal detectors is sensitive to changes in temperature brought about by changes in the incident radiation. The responsive element of photon detectors is sensitive to changes in the number or the mobility of the free charge carriers, i.e. the electrons and/or holes, that are brought about by changes in the number of incident photons.

Thermal detectors employ various types of transducers - including those based on the measurement of bolometric, thermovoltaic, thermopneumatic and pyroelectric effects. Similarly, photon detectors employ different types of transducers - including those based on the measurement of photoconductive, photovoltaic, photoelectromagnetic and photoemissive effects.

4.2 Definition of Relevant Terms

An infrared imaging system is designed around the characteristics of the infrared detector. These are defined by certain terms describing the performance of the detector under specified operating conditions. Although a large number of terms exist, the most important ones can be defined or described as follows (Burnay et al, 1988; Jamieson et al, 1963; Kruse et al, 1962; Wiebelt, 1966):

(i) Response: In general, the response of an infrared detector can be defined as the ratio of the output electrical signal to the incident radiation power. However, usually it is defined rigorously only for periodically modulated radiation. For this case, the response is defined as the ratio of the root-mean-square (rms) value of the fundamental component of the electrical output signal of the detector to the rms value of the fundamental component of the input radiation power. The units of response are given in volts per watt or amperes per watt. However, the response tells the user nothing about the detection ability (detectability) of the transducer, i.e. it tells him nothing about how small a radiation input is detectable.

(ii) Noise Level: Under conditions where no radiation from the source of interest is incident upon the detector, the output of the detector is generally classified as noise. The noise level of a detector is then defined as the output level observed under the particular conditions of its operation where no source radiation is incident on the detector. A detailed discussion of the origin and nature of the many types of noise encountered in infrared detectors will be given in the later part of this chapter.

(iii) Signal-to-Noise Ratio (SNR): It is the ratio between the signal generated by the detector as a result of the incident radiation and the combined noise produced by the detector. Using this figure, the relative importance of noise in terms of the observed response can be indicated.

(iv) Noise-Equivalent Power (NEP): To evaluate the detection ability (or detectability), the characteristics of the electrical noise in the output of the detector must be known. If one divides the rms voltage of the noise by the response, one obtains the NEP of the detector. Thus

$$\text{NEP} = N/R \quad \text{Watt} \quad (4.1)$$

where N is the noise level, and R is the response. The relationship between the response and the NEP is an important factor in assessing the performance of detectors. A detector that produces a greater output from a given radiation signal has a greater response. But a detector that has a greater detection ability (detectability) has a smaller NEP. Thus the NEP value can be considered to be an inverse measure of the detectability of the detector.

(v) Detectability: The reciprocal of the NEP is called the detectability. The detectability D is defined, in general, as the response divided by the rms value of the noise voltage. Thus,

$$D = R/N \quad \text{Watt}^{-1} \quad (4.2)$$

If P is used to denote the radiation input power, and S the voltage output, the following relationships hold:-

$$S = RP; \text{ and}$$

$$S/N = DP \quad (4.3)$$

Thus, to determine the electrical signal output, the radiation signal P is multiplied by R , and to obtain the SNR, P is multiplied by D .

In general terms, the detectability of photon detectors is twice greater than that of thermal detectors.

(vi) Specific Detectability: In many instances, it has been found that the detectability varies inversely with the square root of both the detector's sensitive area and the electrical bandwidth. In order to simplify the comparison of different detectors, the term specific detectability, D^* , has been introduced. This is referred to a bandwidth of 1Hz and a detector area of 1cm^2 . Hence,

$$D^* = D (A \Delta f)^{1/2} \quad (4.4)$$

where A is the sensitive area of the detector in cm^2 and Δf is the bandwidth in Hz. The units of D^* are $\text{cm.Hz}^{1/2}.\text{Watt}^{-1}$.

(vii) Spectral Response: In general, infrared detectors do not respond with equal effectiveness to incident radiation at all wavelengths. It is therefore necessary to describe the variation in the response of the detector with respect to the wavelength of the incident radiation. This variation, known generally as the spectral response of the detector, may be expressed in any one of several different forms. One commonly used method is to plot the response (R) against wavelength (λ).

(viii) Responsive Time Constants: Many infrared detectors have a response versus frequency curve that is an approximation to the form (Hackforth, 1960),

$$R(f) = R_0 / [1+(2\pi f\tau)^2]^{1/2} \quad (4.5)$$

where $R(f)$ is the response at frequency f ; R_0 is the response at zero frequency; and τ is the response time constant. When this is true, the shape of the response versus frequency curve is compactly described by giving the value of the time constant τ . But

when the shape of the curve departs widely from the above equation, there is no generally accepted way to define a time constant. However, most materials used in infrared detectors obey this equation, and so Eq. 4.5 is generally applicable. Eq. 4.5 is plotted in Fig. 4.1.

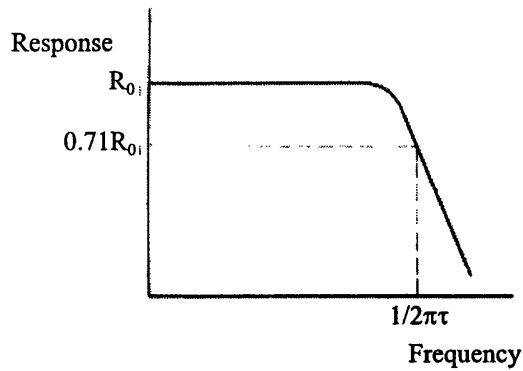


Fig. 4.1. Frequency dependence of response (Kruse et al., 1962).

At low frequencies such that $f < 1/2\pi\tau$, the response is frequency independent. However, at higher frequencies, it begins to drop, attaining a value $R = 0.71R_0$ at $f = 1/2\pi\tau$. At higher frequencies, at which $f > 1/2\pi\tau$, the response is inversely proportional to the frequency.

Although the majority of infrared detectors have a single time constant, some detectors are characterized by two such constants, one much longer than the other. In this case, the graphical representation of the response has the form shown in Fig. 4.2.

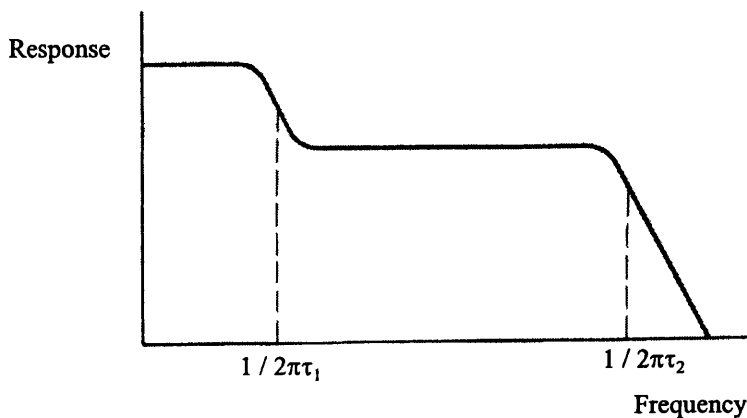


Fig. 4.2. Response of a double time constant detector (Kruse et al., 1962).

τ is expressed in seconds, or fraction of seconds, depending upon the particular detector being considered. The frequency-response curve of a detector is dependent upon its time constant characteristics and this determines the chopping speed or modulation frequency of the incident radiation required to produce optimum signal response.

4.3 Thermal Detectors

Thermal detectors utilise materials with a temperature-dependent property. When incident radiation is absorbed, the temperature of the device increases or decreases and this produces a measurable physical change. Thermal detectors therefore respond to the absorbed radiant power, irrespective of its spectral distribution. They usually suffer from a low thermal sensitivity and a fairly slow response time, but they have the advantage of operation at ambient temperatures.

As noted in Section 4.1.1, thermal detectors may employ one of four different types of transducers. These are: (i) bolometers; (ii) thermocouples and thermopiles; (iii) golay cells; and (iv) pyroelectric detectors. However, amongst these transducers, bolometers and pyroelectric detectors are those which are actually used in infrared imaging systems. So the remaining sections of this account on thermal detectors will be devoted to these.

4.3.1 Bolometers

The bolometer is a sensitive radiation detector which indicates the presence of radiation by the process of its changing electrical resistance arising from the change in temperature of the element caused by the absorption of the radiant energy. The simplest form of bolometer is a short length of fine wire. At the temperature at which it is operated, it has a given resistance. If radiation is allowed to fall upon it, this is absorbed, causing the temperature of the wire to rise. The resistance change due to the change in temperature is a measure of the radiant power absorbed. The detector is

operated using an appropriate electrical circuit which can provide information about the resistance changes proportional to the temperature changes.

A typical bolometer structure is shown in Fig. 4.3. Since the physical change occurring in the bolometer is a resistance change, a supplementary bridge circuit is required to produce a signal voltage that can be measured. As indicated in the figure, both an active element and a compensating element are used in the bridge circuit. The infrared radiation incident on the active element results in a small temperature change, which in turn causes a corresponding resistance change. In order to convert the resistance change into a form of a voltage or current variation, it is necessary to pass a current (called the bias current) through the compensating element. This voltage variation can be obtained via the lead wires.

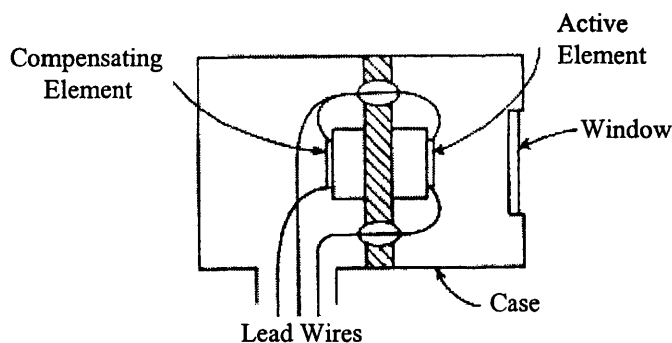


Fig. 4.3. Bolometer (Wiebelt, 1966).

Bolometers may be of two types - metal and semi-conductor bolometers - both of which are operated at ambient temperatures.

4.3.1.1 Metal and Semi-conductor (Thermistor) Bolometers

A bolometer has a sensitive element composed of a material that has an appreciable coefficient of resistance with respect to temperature. This condition in bolometers is satisfied by the use of metals such as platinum or nickel which can be formed into thin but strong foil strips and by semi-conductor materials that can be made into flakes.

Whereas metal bolometers exhibit a linear dependence upon the change in temperature, semi-conductors show an exponential dependence on the temperature change which is more pronounced. Therefore, semi-conductors are more widely used than metals for bolometers.

Semi-conductor bolometers are also known as “thermistor” bolometers, the word thermistor denoting a thermally sensitive resistor. This type of detector has recently begun to be used in infrared imaging systems. For example, the Sentinel infrared CCD areal array camera from the Amber company uses an integrated circuit that is made up of 76,800 small microresistors set out in a 320 x 240 pixel array. Each detector (microresistor) is essentially a small thermistor integrated onto a micro-bridge structure that is less than 50 μm across, providing thermal isolation and mechanical support for each individual detector element. The thermistors change their temperature due to the incident radiation from the scene, and the changes in their temperature create the corresponding changes in the resistances which can be measured and used to generate a video image.

4.3.2 Pyroelectric Detectors

This is the other type of thermal detector employed in current infrared imaging systems along with the semi-conductor bolometer which has been discussed above. This detector is made of a single crystal of pyroelectric material which has a very high impedance. It has the property that a change in the material temperature produces a change in its electrical polarization. The materials generally used are either triglycine sulphate (TGS) or one of its derivatives, or a ceramic called lead zirconate titanate (PZT). Fig. 4.4 illustrates the principles of a pyroelectric detector. The pyroelectric crystal in the detector is spontaneously polarized. If the crystal is heated to a temperature just below the Curie temperature in an electrical field, dipoles line up in the direction of the impressed electrical field. If opposing electrodes are brought into contact with the polarized crystal, the crystal surface is electrically charged. This charge is neutralized by the ions in the air. When infrared radiation enters the crystal and is absorbed, the temperature of the crystal changes, altering the spontaneous

polarization, so that the charge on the crystal surface becomes unbalanced. This effect known as the pyroelectric effect. This unbalanced charge is output as a voltage change, and in this way, the amount of infrared radiation falling on the crystal can be detected.

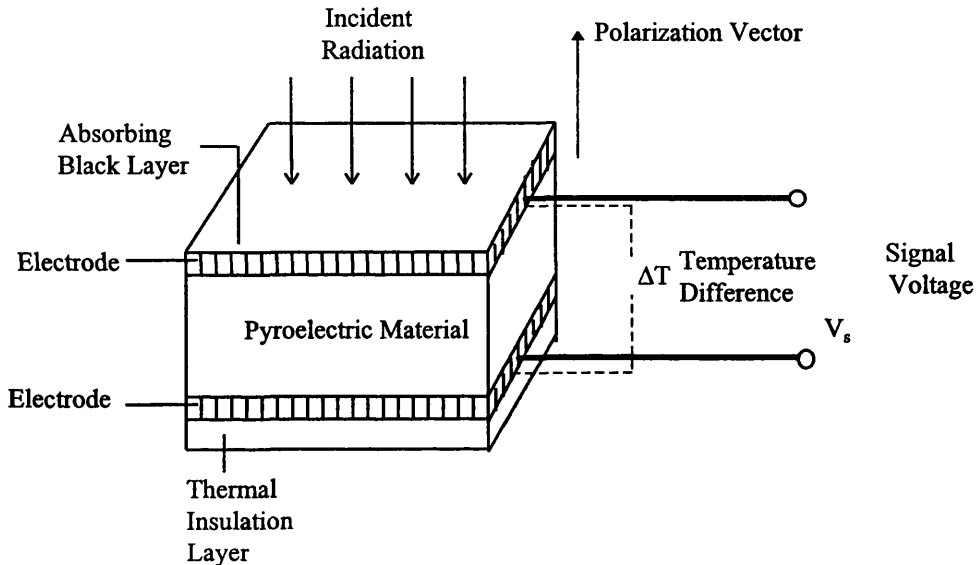


Fig. 4.4. Operating principles of the pyroelectric detector (Burnay et al, 1988).

4.4 Physics of Semi-conductors

Semi-conductors have a special prominence in infrared detector systems. Their most important application in infrared imaging technology is found in photon detectors, where semi-conductors are more widely used than any other material. In order to understand their detection mechanisms, this part of the chapter will be devoted to a brief account of the physics of semi-conductors .

4.4.1 The Periodic Lattice

Solids can be divided according to their electrical properties into three classes: metals, insulators (dielectrics), and semi-conductors. In terms of their electrical resistivities, it is generally considered that metals have resistivities less than 10^{-3} ohm/cm and dielectrics more than 10^{12} ohm/cm, while semi-conductors occupy a range intermediate between metals and dielectrics. Another criterion by which solids can be

classified depends on whether their atoms are arranged in a regular array, termed a periodic lattice, or in a disorganized manner. The former are termed crystalline solids; the latter, amorphous solids.

Semi-conductors, metals, and some dielectrics have a periodic lattice; thus they are crystalline solids. The existence of the periodic lattice is basic to their electrical properties. This periodicity - which refers to the repetitive nature of the structure found in a crystalline material - can exist in microscopic localized regions, or it can exist in large, macroscopic regions. The former, comprising an array of crystallines, is referred to as a “ polycrystalline solid “; the latter comprises a “ single crystal “. Obviously, the polycrystalline solid is composed of an aggregate of small single crystalline regions. The electrical and physical properties of semi-conductors are influenced by their crystallinity - the degree to which they approach being a single crystal. The widespread use of semi-conductor materials in solid-state devices today has been largely due to the development by scientists of an ability to produce large single crystals of high purity.

4.4.2 Energy Bands in a Perfect Crystal

Electrons in an atom are forced to have only certain discrete energies; so also electrons in a crystal are allowed only discrete energies. The discrete levels of shell electrons in an atom are broadened into energy bands by the proximity of the other atoms in the periodic lattice. The allowed energy bands of interest in electronic conduction phenomena are two: the valance band and the conduction band. They are separated by a region of forbidden energies referred to as the forbidden band. This band structure is represented schematically in Fig. 4.5.

To give an approximate order of magnitude to the energies involved; the width of the forbidden band in semi-conductors ranges from about 1/1,000 of an electron volt to a few electron volts. The distance between levels is of the order of 10^{-14} ev (electron volts). Thus the levels form practically a continuum.

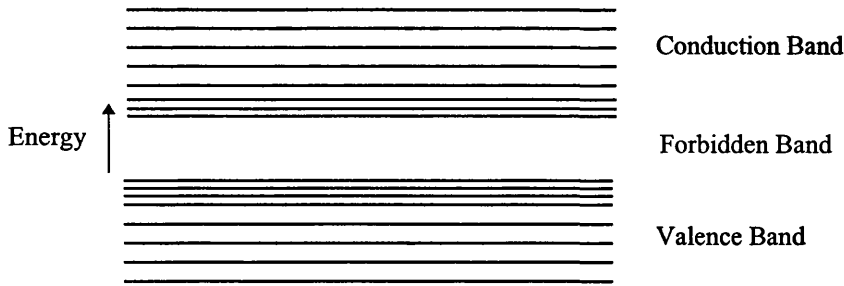


Fig. 4.5. Band structures in a semi-conductor (Kruse et al, 1962).

Electrons having energies in the conduction band are referred to in various ways - either as electrons in the conduction band, conduction band electrons or free electrons. Their energies are sufficiently great such that they are not attached to any atom. Since the uniform character of the lattice does not obstruct their movement, they wander freely through the crystal. The number of free electrons and their ease of movement account for the magnitude of the electrical conductivity.

The absence of an electron in a lattice is termed a hole. It is possible for an electron in a bond on an adjacent atom to move into the bond from which the electron is missing. Thus, the original bond is complete, but the hole appears in the adjacent bond. This bond in turn can be filled by an electron from a bond on a neighbouring atom. This motion of electrons in one direction can be represented by the motion of holes in the opposite direction. Holes not in motion are termed "bound holes". Holes in motion are "free holes" and have energies in the valance band. Free electrons and holes, contributing to the conductivity of the semi-conductor are called "current carriers" or simply "carriers". In the presence of an electric field, holes flow in the direction of the field, whereas electrons flow against the field. Since the flow of holes is opposite in direction to the electron flow, the hole has a positive charge, in contrast to the negative charge of the electron. Thus holes also contribute to the conductivity.

At any temperature above absolute zero, the atoms comprising the lattice, which are bound to each other by the electron bonds, are undergoing rapid vibrational motion about their lattice sites. The energy of these vibrations is sufficient to free some electrons and holes, the number of which is dependent upon the forbidden energy gap

and upon the temperature. In pure semi-conductors, this process, known as thermal excitation, produces simultaneously a free electron and a free hole, termed an electron-hole pair. The number of free electrons and holes determine to a large extent the electrical conductivity of the material. It can be seen that materials with wide forbidden bands that require large energies for excitation, have fewer free carriers (electrons and holes), thus lower conductivity, than materials having a smaller band gap. In accordance with this, dielectric materials with very low conductivity must have wide forbidden gaps. Metals having very high conductivity must have small gaps. As a matter of fact, most metals have no forbidden band, their conduction bands touching the valence bands.

4.4.3 Imperfections in the Lattice

Semi-conductors can be divided into two general categories called intrinsic and extrinsic (impurity) semi-conductors. The intrinsic form is characterized by the presence of only the valence band and the conduction band, with no additional energy between. Electron excitations may take place only with sufficient energy to traverse the forbidden energy gap. In cases where the semi-conductor is not a pure, perfect crystal but contains imperfections such as impurities, lattice defects, or dislocations, additional energy levels may occur within the forbidden gap. This type of semi-conductor material is called an extrinsic detector. Where the impurity levels occur nearer the conduction band than the valence band, they are called n-type (negative type) semi-conductors. Those with impurity levels occurring nearer the valence band are known as p-type (positive type) semi-conductors.

4.5 Photon (Quantum) Detectors

Infrared radiation may be detected by means other than the effects arising from thermal heating. These other phenomena result from the direct reaction of the energy condition of matter to the incidence of radiation photons. In general, the photon detector, as distinct from the thermal detector, does not respond equally well to all the wavelengths of the incident radiation. They respond only to photons with an energy

equal to or greater than the energy gap between the carriers, and consequently have a long wavelength (λ_c) or short frequency cut-off, according to Eq. 2.1. The spectral response of a photon detector is compared with that of a thermal detector in Fig.4.6.

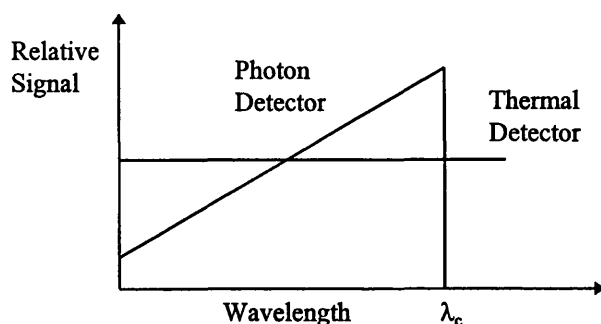


Fig 4.6. Spectral responses of photon and thermal detectors (Burnay et al., 1988).

In providing an indication of the relative effectiveness of the photons incident on the detector element in producing a response, it is convenient to define the so-called quantum efficiency. This is defined as the ratio of the number of incident photons per time interval to the number of output events occurring over the same time interval.

As discussed in Section 4.1.1, there are four different types of photon detectors available. They are: (i) photoconductive detectors; (ii) photovoltaic detectors; (iii) photoelectromagnetic detectors; and (iv) photoemissive detectors. However, amongst them, the photoconductive and photovoltaic types are those used in infrared imaging systems. Therefore, they will be described in the next sections.

4.5.1 Photoconductive Detectors

In a photoconductive detector, the photo-generated carriers produce an increase in the conductivity of the device. If a constant bias current is passed through the detector, there will be a corresponding decrease in the output voltage. Alternatively, a constant voltage applied to the device will produce a change in the current. Fig. 4.7 illustrates the basic operating principle of a photoconductor. Both intrinsic and extrinsic photoconductors are in use.

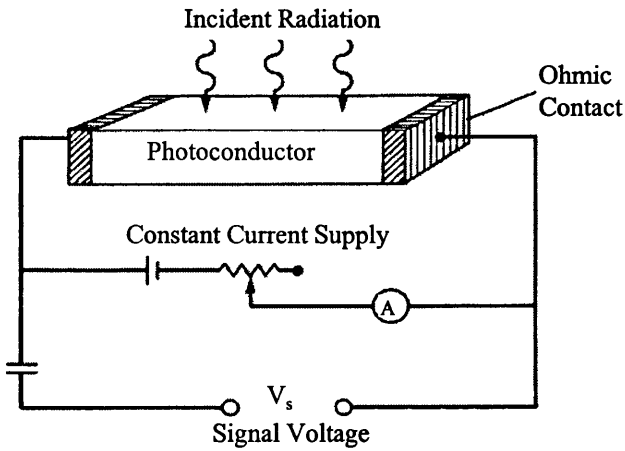


Fig. 4.7. Operational principle of photoconductive detector (Burnay et al., 1988).

4.5.2 Photovoltaic Detectors

Photovoltaic detectors are also known as photodiodes and junction detectors, and are almost always intrinsic devices. Electrical contact is established between two semi-conductors of the same material, but of different impurity content such that one is p-type and the other, n-type. This will produce an energy configuration as indicated schematically in Fig. 4.8.

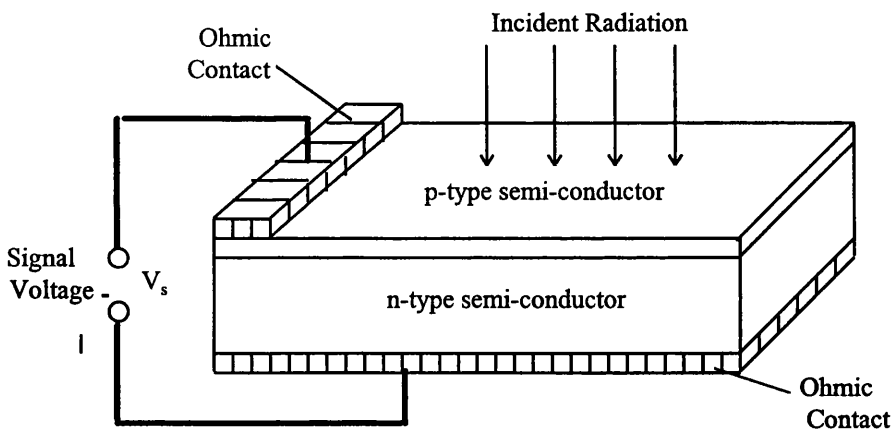


Fig. 4.8. Operational principle of photovoltaic detector (Burnay et al., 1988).

The energy bands in the p-type region are displaced upward in relation to those in the n-type region, because of the space charge established at the boundary. As a result, when electron-hole pairs are produced by photon absorption in the boundary region, the current carriers are separated by the local electric field at the junction. This

produces a voltage across a junction, which can cause a current to flow in a closed circuit containing the junction.

4.5.3 Materials Used for Photon Detectors

Table 4.1 gives the principal photon detector materials currently used in infrared imagers, together with their mode of operation, operating temperature and cut-off wavelengths.

Material	Mode of Operation Photoconductive (PC) or Photovoltaic (PV)	Operating Temp. (K)	Cut-off Wavelength (μm)	
InSb	PC	196	6.0	Middle Infrared
InSb	PC, PV	77	5.2	
PbSe	PC	196	5.1	
PbSe	PC	77	6.6	
PbTe	PC	77	5.4	
$\text{Pb}_{1-x}\text{Sn}_x\text{Te}$				Thermal Infrared
$x=0.85$	PV	77	10.0	
$x=0.83$	PV	77	11.0	
$x=0.81$	PV	77	12.0	
$x=0.80$	PV	77	13.0	
$\text{Hg}_{1-x}\text{Cd}_x\text{Te}$				Thermal Infrared
$x=0.219$	PC, PV	77	10.0	
$x=0.212$	PC, PV	77	11.0	
$x=0.206$	PC, PV	77	12.0	
$x=0.201$	PC, PV	77	13.0	
$x=0.314$	PC, PV	196	4.2	
$x=0.297$	PC, PV	196	4.6	
$x=0.282$	PC, PV	196	5.0	
PtSi	Schottky	77	5.1	Middle Infrared

Table 4.1 Principal photon detector materials (Burnay et al., 1988).

Among them, InSb (indium antimonide), PbSe (lead selenium), PbTe (lead telluride) and PtSi (platinum silicide) Schottky barrier detectors have narrow bandgaps.

Therefore, they cannot respond to incident radiation with a wavelength greater than about $7\mu\text{m}$ and generally operate in the middle infrared region of EM. However, to cover the thermal infrared band, the wavelength range has been extended considerably through the development of ternary alloy systems. The two most important systems are compounds of mercury telluride (HgTe) and cadmium telluride (CdTe) (cadmium mercury telluride or CMT), and of lead telluride (PbTe) and tin telluride (SnTe) (lead tin telluride or LTT). The compositions of these alloys $\text{Hg}_{1-x}\text{Cd}_x\text{Te}$ and $\text{Pb}_{1-x}\text{Sn}_x\text{Te}$, may be varied to give a wide range of cut-off wavelengths, as illustrated in Table 4.1.

As can be seen from Table 4.1, various types of Cadmium Mercury Telluride (HgCdTe) detector are available for operation either in the middle or in the thermal infrared region. The reason for this unusual phenomenon is that the crystal of HgCdTe alters its bandgap depending upon the compositional ratio of HgTe to CdTe. This means that altering the compositional ratio of the two compounds allows for the production of this detector having a maximum response at various wavelengths. Fig. 4.9 illustrates the spectral response of the Hamamatsu HgCdTe infrared detectors that have different bandgaps.

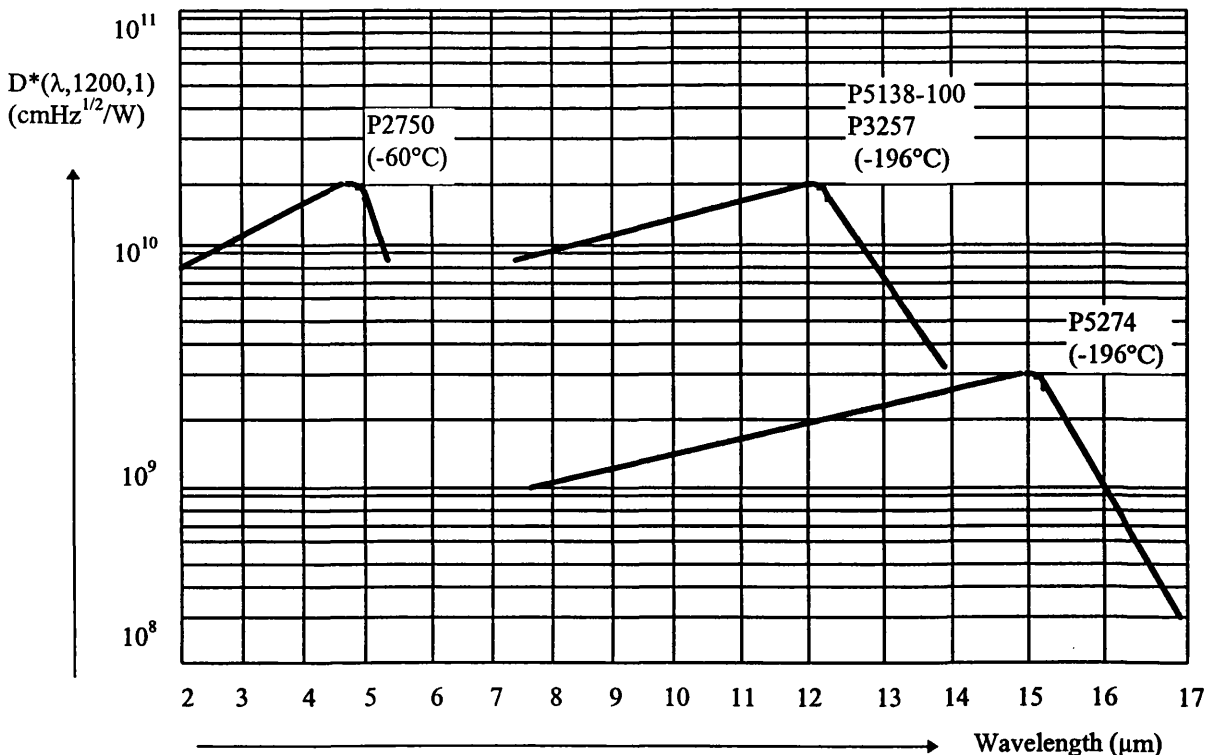


Fig. 4.9. Spectral responses of CMT detectors (Hamamatsu, 1993).

4.5.4 The SPRITE Detector

This is a special type of photoconductive detector devised specifically for use in a scanned thermal imaging system. The name of this detector is an acronym derived from the words Signal PRocessing In The Element (SPRITE). It performs the same function as a row of serial detectors, with the time delay and integration operation taking place within the detector element. Thus it operates using the serial scanning technique that will be described later in Chapter 9. It consists of a strip or filament of n-type CMT, typically 700mm long, 60mm wide and 10mm thick, with three ohmic contacts. The operating principle is illustrated in Fig. 4.10.

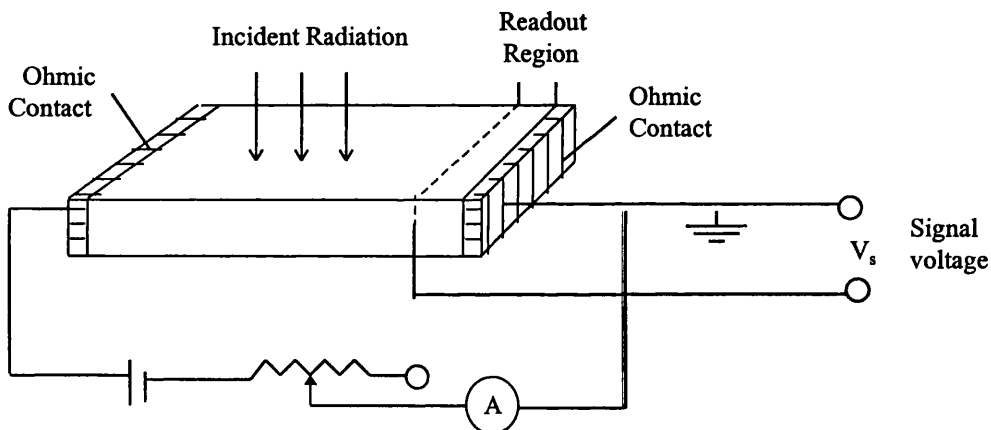


Fig. 4.11. Operating principle of the SPRITE detector (Burnay et al., 1988)

A constant current bias is applied across the filament, and this causes the photogenerated carriers to drift along the filament to the readout region. The drift velocity is equal to the product of the electric field and the ambipolar mobility, and if it is made equal to the image scan velocity, then the signal will be integrated along the filament. Integration continues until the photocarrier recombination rate equals the generation rate. When the photogenerated carriers enter the readout zone, the conductivity is decreased and this modulates the voltage on the readout contact. If a number of these SPRITE detectors are used in parallel, then a small areal array is formed and the serial/parallel scan that will be explained in Chapter 9 can be implemented. Thus the advent of the SPRITE detector made the serial/parallel scanning technique the preferred one in many thermal imaging systems. The

complexity of the required electronic circuitry was drastically reduced, since the TDI circuits were eliminated altogether and the number of amplifying channels was reduced. With this came a reduction in the cost, weight, size and complexity of the thermal imager.

4.6 Noise In Detectors

Noise may arise in the detector itself, in its associated circuitry, or as statistical fluctuations in the incident radiation. There are three main types of noise that may be encountered in a photon detector.

- (i) The first type results from the random thermal motion of the carriers. In a photoconductor, this is known as Johnson noise, Nyquist noise, or thermal noise, analogous to that observed in a resistor.
- (ii) The second noise source arises from fluctuations in the rates of the thermal generation and recombination of carriers. In photoconductors, it is known as generation-recombination (g-r) noise. In junction (photovoltaic) devices, thermal and g-r noise taken together are known as shot noise.
- (iii) The third type of noise occurs at low frequencies and is less well understood. It is associated with surface and contact effects, and is known as 1/f noise because its power spectrum has approximately an inverse dependence on frequency. It is also called current, modulation, or excess noise.

Johnson noise and possibly 1/f noise will be present in thermal detectors employing electrical readout mechanisms. Thermal detectors will also exhibit temperature noise, due to random temperature changes that arise from fluctuations in the rate of heat transfer from the detector to its surroundings.

Statistical fluctuations in the incident background radiation will set the fundamental limit to any detector's performance, and are known as photon noise or radiation noise.

These fluctuations will produce variations in the generation and recombination rates of a photoconductor. In junction detectors, the carriers are swept across junctions, and there are no fluctuations in the recombination rate. Junction detectors therefore have an ultimate noise level having a factor of 1.4 lower than that of photoconductors. In thermal detectors, the fluctuations in the incident flux will produce additional temperature noise.

A detector whose performance is limited solely by radiation noise is known as a Background Limited Infrared Photoconductor (BLIP) detector. Its D^* value will depend on the background temperature and on the area of background viewed by the detector. This latter should be minimised by limiting it to the field of view required for imaging. With a cooled detector, this is achieved by surrounding the detector by a cold-shield, with an aperture just large enough to admit the required cone of radiation. The cold shield may be either a cold surface or a reflective spherical surface centred on the detector. The radiation noise that is produced is proportional to the f-number of the aperture.

4.7 Detector Cooling

In order to reduce the thermal generation of carriers and minimise noise, photon detectors must be cooled and must therefore be encapsulated in a Dewar flask or other similar type of cooling device. In thermal infrared applications, the method of cooling varies according to the operating temperature and the system's logistic requirements. These cooling methods can be divided into four:-

- (i) Cryogenic Dewar cooling using liquid nitrogen;
- (ii) Joule-Thompson cooling;
- (iii) Mechanical-refrigerator cooling systems based on the Stirling-cycle or Gifford-McMahon/Solvay-cycle; and
- (iv) Thermoelectric cooling based on the Peltier effect.

Of the four, the first three are basically mechanical in operation; the last one is purely electrical in terms of its function.

As was set out in Table 4.1, most detectors operating in the thermal infrared band ($\lambda=8$ to $13\mu\text{m}$) operate at about 77K (-196°C), and can be cooled by liquid nitrogen. As the author can testify, this is a messy and inconvenient procedure to implement, needing frequent refilling of the liquid as it boils off. Thus, in practice, its use is limited to laboratory operations where reasonable access to stored liquid nitrogen is possible. In field conditions, however, it is more convenient to use compressed air and a Joule-Thompson mini-cooler. Nowadays the use of small refrigerators, in particular those employing the Stirling cycle, is becoming a practical possibility. Alternatively, refrigerators based on the Gifford-McMahon/Solvay cycle, which consist of a compressor to maintain the cooling system at the necessary temperature, are also becoming more readily available.

As shown in Table 4.1, in the middle infrared ($\lambda=3$ to $5\mu\text{m}$) waveband, most of the detectors operate at 196K (-77°C), and this temperature is conveniently achieved by the use of thermoelectric coolers based on the Peltier effect. However, in this region, there are some detectors such as InSb, PbSe and PbTe that operate at 77K (-196°C), hence they are cooled by one of the mechanical cooling systems, especially by liquid nitrogen when operated in a laboratory situation.

4.8 Detector Arrays

Ideally, to achieve maximum thermal sensitivity, a two-dimensional array of detectors should be used, with a sufficient number of detectors to give a one-to-one correspondence with desired number of picture points in the scene. Such an array is called a staring array (see Fig. 4.11). These arrays have recently become available for the middle infrared part of the spectrum. Due to the complexity involved in their manufacture and the high cost incurred in fabricating these arrays so that they can operate in the middle infrared region, current technology does not allow sufficiently large arrays to be produced to give the fields of view demanded in many imaging applications. Thus the detectors are often made as linear arrays or as small areal arrays, which are scanned over the object scene to generate the complete field of view.

However there are now quite a large number of infrared imagers on the market which use small areal arrays with comparatively low resolution (e.g. 256 x 256 or 240 x 320 pixels) that can carry out useful work. As the technology and fabrication of areal arrays develops further to produce larger arrays, these may be expected to take over more of the infrared imager market, since they dispense with the need for the optical and mechanical scanning elements required in frame scanners.

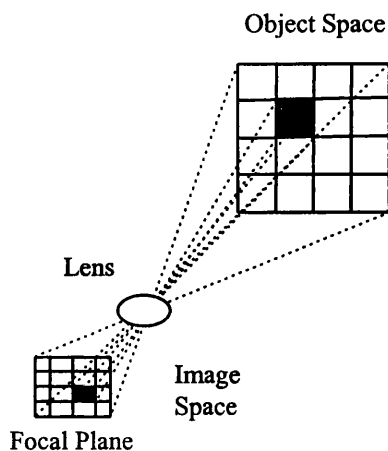


Fig. 4.11. Mapping of the object space onto a staring array (Mooney et al, 1989)

4.8.1 Read Out Mechanisms of Detector Arrays

Detector arrays are categorized by the readout mechanisms that are used to transfer the charge at each detector out of the array. Three schemes of detector arrays with different readout mechanisms are in use. They are:

- (i) the MOS capacitor;
- (ii) Charge Injection Devices (CID); and
- (iii) Charge Coupled Devices (CCD).

For instance, CID and CCD detector arrays both use photoconductive and photovoltaic detectors, however they employ different readout mechanisms. In this section, only detector arrays with a CCD readout mechanism will be discussed since they are the type mainly used in infrared imaging applications. Charge coupling, which is used in CCD detector arrays, refers to the process by which pairs of electrodes are used to transfer the charge between adjacent potential wells. Voltages

of these electrodes are manipulated in a sequence that passes the accumulated charge from one well to the next. At the end of the line of detectors, the charge is transferred to output registers and scanned by an amplifier which has the same capacitance as a detector element, thereby reducing noise.

In Fig. 4.12, the operation of a three-phase CCD (consisting of three electrodes (gates)) is shown. At time $t = t_0$, the charge is stored in the potential well underneath the ϕ_1 electrode because of the higher positive values of the voltage on ϕ_1 than on ϕ_2 and ϕ_3 . At time $t = t_1$, the same voltage is present on ϕ_1 and ϕ_2 . However, the potential well is initially deeper under ϕ_2 than under ϕ_1 since the latter is partially collapsed as a result of its stored charge. This initiates the charge transfer process from the ϕ_1 to the ϕ_2 electrode. As the voltage on the ϕ_1 electrode decreases, $t_1 < t < t_3$, the charge continues to spill into the region under the ϕ_2 electrode. At time $t = t_3$, the charge is isolated under the ϕ_2 electrode, and thus a shift of one-third of a cell has been effected. As the phase drive pulses continue to change periodically with time, the charge will be shifted from ϕ_2 to ϕ_3 and so on through the device.

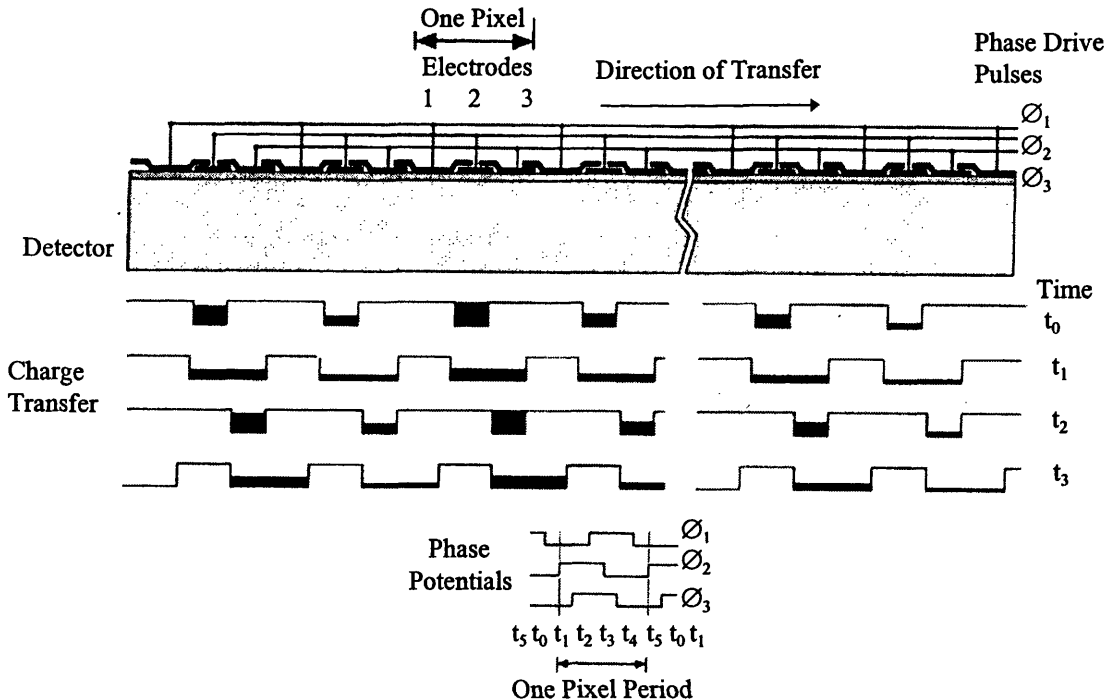


Fig. 4.12. Longitudinal section showing charge transfer using charge coupling principles (Shortis and Beyer, 1996).

4.8.2 Organization of Different Detector Types in Areal Array CCDs

CCD detector arrays have different types of logical organization for imaging and read out. Frame transfer (FT) CCD detector arrays have imaging areas that are composed only of detector elements. They can be differentiated into those arrays with an imaging zone and a storage area, called field FT CCDs and arrays containing only sensitive elements, called full frame FT CCDs. A third type called interline transfer detector arrays are more complex, since this type employs additional columns of non-imaging detectors to read out the image (Shortis and Beyer, 1996).

(a) Field Frame Transfer CCDs

The field FT CCD consists of an imaging area, a field storage area and a horizontal read out register (Fig. 4.13). The imaging and storage areas are composed of columns of detector elements which are defined by a gate structure (Fig. 4.14). The columns are separated by channel stops which laterally confine the charge. After a charge integration period defining a single field, the charges representing the image are transferred from the imaging to the storage area. The charges are transferred in the column direction using the gates. From the storage area, the charges are then transferred row by row to the serial read out register and then counted at the output amplifier.

The method of ensuring the interlacing of full frame images is unique for the field FT CCD. The imaging and storage areas each contain only as many rows of detector elements as is required to hold one field. Interlacing is achieved by integrating the different gate electrodes with specific arrangements dependent on the number of phases in the charge coupling. The logical detector elements of the two fields overlap due to the effective shift of half the element spacing in the column direction (Fig. 4.14).

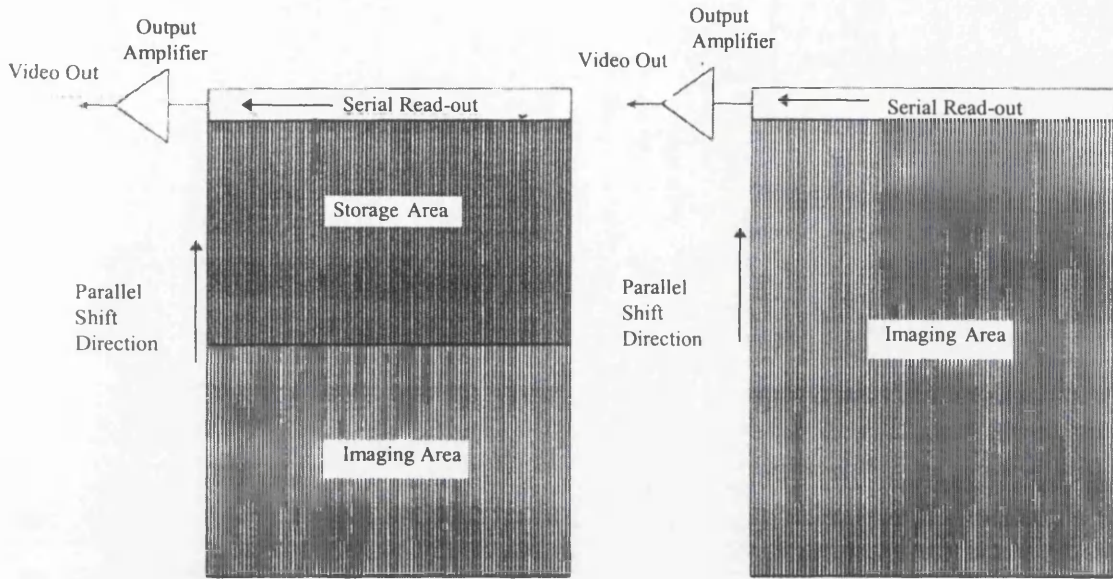


Fig. 4.13. Field (left) and full (right) frame transfer CCD (Shortis and Beyer, 1996)

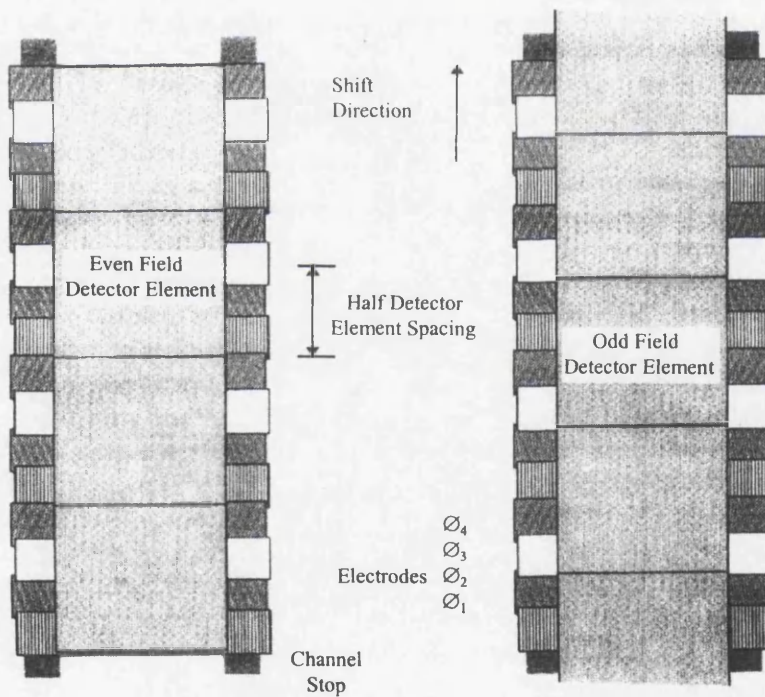


Fig. 4.14. Detector element layout for a four phase field frame transfer CCD (Shortis and Beyer, 1996).

(b) Full-Frame Frame Transfer CCDs

Full frame FT CCDs have the simplest structure of any CCD areal array. The detector comprises only an imaging area and a serial read out register (Fig. 4.13). The charges

transfer gate to shift the charge horizontally from the detector element to the transfer elements, and a two phase transfer to shift the charge vertically within the transfer elements.

Interlacing cannot be performed by shifting the sensitive area because of the structure of the interline transfer and the discrete nature of the individual detector elements. Each detector element is defined by channel stops on three sides and the transfer gate on the fourth side. The detector elements in each row are also separated by the transfer elements, leading to an area utilization factor as low as 35%. This results in problems with aliasing, which is the phenomenon where patterns of high spatial frequency are imaged at lower frequencies.

IL CCDs currently dominate the broadcast and domestic markets for video imaging systems. Despite problems with aliasing and the greater complexity of fabrication, IL CCDs are favoured because of their relatively better vertical resolution and their elimination of smear, and because high volume production of this type of detector array has reduced manufacturing costs.

4.8.3 Geometric Properties of Arrays of CCD Detectors

The geometric performance that can be expected from CCD detector arrays is of major interest. The uniformity of the detector element spacing and the flatness of the detector surface can be used to help assess the geometric accuracy that can be achieved. However manufacturers do not provide specifications regarding the regularity of the spacing or the surface flatness of the detector elements.

4.8.3.1 Geometry of Detector Elements

CCD detector arrays are fabricated by the deposition of a series of layers on the silicon substrate. Each layer serves a particular purpose, such as acting as insulation or as a series of gates. The geometry of the deposited layers is controlled by a photolithography process which is common to the manufacture of all integrated

circuits based on silicon wafers. Photolithography uses masks (as is done with colour separations in cartographic work). These are prepared at a much larger size than that of the finished product and they are then brought to the correct size using an optical and photographic reduction process. The unmasked area is sensitized to deposition using doping material, and the vaporized material which is introduced is then deposited only onto those sensitized areas. Alternatively, the surface is exposed to vapour etching and material is removed only from the unmasked areas.

One of the common photolithographic tools for production of high performance circuits is the step-and-repeat system, or wafer stepper. The most obvious measure of this system is the minimum feature size that can be printed, also called the design rules. In the early 1970s, typical design rules of 6-8 μm were employed, while today's commercial optical steppers meet the requirements for sub-micrometre design rules which approach 0.2 μm . However, especially for large CCD detector arrays, design rules of 1.2 to 2 μm are typical (Seitz et al, 1995). The overall capability of a wafer stepper depends on the column errors, the precision of the alignment system, and the wafer stage stepping precision. It has been reported in Pol et al (1987), that to reach 0.5 μm design rules, allowing for column errors and stage stepping errors, it is necessary that the alignment precision be well within $\pm 0.1\mu\text{m}$.

The spacing of the detector elements has been verified by measurements. For example, Curry et al (1986) measured the detector spacing and found that it was within $\pm 0.2\mu\text{m}$ of the manufacturer's specification for a 45.54 μm detector spacing.

4.8.3.2 Surface Flatness

The flatness of the CCD detector array is a matter of concern both in terms of the overall shape of the silicon substrate and the microtopography of its surface. Early CCD arrays were of low resolution and, more importantly, had small formats. Therefore overall surface flatness was a matter of little concern. With increases in array resolution have come increases in the format size, so the maximum angles of incidence near the edge of the format have risen to values as great as 45°. With one or

two exceptions, very few CCD manufacturers actually specify the flatness of the array surface, largely because most detector arrays are prepared for broadcast or domestic markets that are not concerned overly with geometric quality.

Thompson CSF specify an flatness tolerance of $\pm 10\mu\text{m}$, corner to corner, for their 1,024 x 1,024 detector array. With an element spacing of $19\mu\text{m}$, the diagonal of this array is equal to 27.5mm. Using a lens with 14mm focal length, an angle of incidence approaching 45° would be expected. Flatness errors of this order of magnitude are certainly significant and require correction for very precise applications of CCD detector arrays (Shortis and Beyer, 1996).

Microtopography is caused by the lack of flatness in the detector array surface and the structure of the gates used for the charge coupling. The surface roughness of the array material can be measured using an electron microscope. Lee et al (1985) showed that it is of the order of $\pm 0.5\mu\text{m}$. The deposition of several layers of electrodes and insulators leads to additional local surface variations of the order of $\pm 1\mu\text{m}$. The effects of microtopography, especially when combined with low fill factors and large angles of incidence, have yet to be theoretically quantified or experimentally investigated.

4.8.4 Spurious Signals

Spurious signals from CCDs are systematic or transient effects that are caused by faults in the fabrication of the CCD detector arrays or deficiencies in the technology of the CCDs. The most important effects are dark current, blooming, smear, traps and blemishes. All of these effects result in the degradation of the image quality and can be minimized by radiometric calibration of the CCD array (Shortis and Beyer, 1996).

(a) Dark Current

The thermal generation of electrons produced in any semi-conductor is known as dark current. In CCDs, dark current cannot be distinguished from the charges generated by the incident radiation falling on the detector array. It is produced at different rates

depending on the depth within the detector and the absolute temperature of the detector material.

Dark current is strongly correlated with operating temperature, and a reduction of 5 to 10°C can decrease the generation of noise by a factor of 2. Middle infrared CCDs operating in the 3 to 5µm wavelength region incorporate cooling systems to reduce the operating temperature to around -77°C in order to improve dynamic range and therefore the radiometric sensitivity of the detector array. The cooling methods that are used by imaging systems operating in the middle (3 to 5µm) and thermal (8 to 14µm) infrared parts of the spectrum have already been discussed in detail in Section 4.7.

(b) Blooming

When too much radiation falls onto a detector element or group of detector elements, the charge capacity of the wells can be exceeded. The excess charge then spills over into neighbouring elements. This effect is known as blooming.

Although blooming cannot be totally eliminated from CCD detector arrays, the inclusion of so called anti-blooming drains has dramatically reduced the problem in the current generation of CCDs, as compared to the first CCDs. There are two types of anti-blooming structure that can be incorporated in CCDs to reduce the blooming. Vertical anti-blooming structures use a special deep diffusion to produce a potential profile which draws the extra charge into the substrate. Horizontal anti-blooming methods use additional gate electrodes and channel stops to drain off excess charge above a set threshold potential. Horizontal anti-blooming drains are placed adjacent to the transfer gates in IL CCDs and parallel to the channel stops in FT CCDs.

(c) Smear

Smear describes the phenomenon that an intense radiation source influences the brightness in the column direction. The apparent effect of smear in the acquired image

is very similar for all detector types, but the physical source of the smearing may be different in different types. Smear is usually defined as the ratio between the change in image brightness above or below a bright area in the column direction.

Smear in FT CCDs originates from the accumulation of charge during the transfer from the imaging to the storage zones. Therefore smear can be reduced dramatically in FT CCDs by reducing the transfer time. However, the smear for IL CCD detector arrays is a result of radiation penetration during the charge transfer period.

(d) Traps

Traps are defect sites caused by a local degradation in the efficiency of the charge transfer process. Traps capture charges from charge packets being transferred and release the trapped charge slowly once there is an equilibrium of charge in the trap. Traps originate from design flaws, material deficiencies and defects induced by the fabrication process. Trap defects can be reduced by improving the quality of materials and the fabrication process. An alternative method is to always keep the traps filled with charge. This technique has the disadvantage of reducing the dynamic range of the detector array.

(e) Blemishes

Blemishes on images acquired from CCD detector arrays are often caused by material deficiencies, such as crystallographic defects in the silicon, or defects induced by the fabrication process. Such defects introduce dark current or other effects which exceed the specification for the CCD detector array and are manifest as a spurious signal in the image.

Blemishes are characterized by type as single point, area or column and row defects; these affect a single detector element, a group of adjacent elements or a column and a row respectively. Single point and area blemishes are most often caused by small sources of dark current or shorts between gates or between gates and the substrate.

Detector elements with exceptionally high dark current give rise to dark current spikes and produce white spots or areas. Area blemishes can take different shapes, such as “swirl patterns”, “white clouds” or “swiss cheese”. Column defects in IL CCDs are usually due to fabrication deficiencies in the channel stops. Detectors with row defects are generally culled by the manufacturer. A blemish compensation circuit is included in some CCD cameras to remove defects in the images that are output by the detector arrays. The addresses of these defects are stored in read only memory (ROM) as a table of locations. The detector elements ahead of each blemish are read twice by the scanning circuits and then output as sequential elements to disguise the defect.

4.8.5 Infrared CCD (IR-CCD) Areal Arrays

Generally IR-CCDs can be classified into two main categories: monolithic and hybrid devices (Wolfe and Zissis, 1978).

4.8.5.1 Monolithic IR-CCDs

The monolithic IR-CCD category comprises those devices in which both the photon detection and charge generation, as well as the charge transfer, are achieved in a structure built around semi-conductor detector material. Monolithic devices generally use the basic CCD concept and structure, in conjunction with an IR sensitive substrate consisting of either a narrow bandgap semi-conductor or an extrinsic semi-conductor having an appropriate impurity energy level.

(a) Extrinsic IR-CCDs

By monolithically integrating extrinsic-silicon IR detectors with silicon circuits, one can use integrated circuit technology in the development of sophisticated IR detectors. The main drawback of extrinsic silicon IR-CCD is the low temperature required for its operation. For operation in the 8 to 14 μm wavelength region, a temperature between 15 and 30°K is generally required, while for the 3 to 5 μm wavelength region, the temperature range is typically between 40 and 65°K. This represents a serious

problem in certain applications and results in a higher cooling system cost in most applications. The extrinsic silicon also inherits the relatively low quantum efficiency (5 to 30%) associated with the long impurity absorption length that is characteristic of extrinsic detectors. In turn, this effect can result in increased crosstalk due to the repeated reflection of radiation within a detector array.

(b) Intrinsic IR-CCDs

The intrinsic IR-CCD is the infrared equivalent of the original silicon IR-CCD where the detector now consists of a narrow-bandgap semi-conductors which include compounds such as InSb, $\text{Hg}_{1-x}\text{Cd}_x\text{Te}$ and $\text{Pb}_{1-x}\text{Sn}_x\text{Te}$.

(c) Platinum Silicide (PtSi) Schottky-Barrier IR-CCD

Another monolithic IR-CCD approach is based on internal photoemission from a metal-semiconductor Schottky-barrier array mounted on a silicon substrate. In this approach, photons are absorbed in the metal resulting in the excitation of hot carriers. Carriers with energy larger than the contact barrier, and with sufficient momentum in that direction, are emitted into the semi-conductor. With radiation incident on the Schottky barrier through the semi-conductor, the photogeneration process depends only on the absorption in the metal and emission over the barrier, resulting in a uniform response. The quantum efficiency of a Schottky barrier detector decreases with decreasing photon energy and is quite small at IR wavelengths. However, potentially the combined characteristics of high-uniformity and low-response can be useful in large staring arrays where the long integration time increases the detectivity.

4.8.5.2 Hybrid IR-CCDs

Since the hybrid IR-CCD involves basically the coupling of two fairly well developed technologies, initially it received more attention than monolithic IR-CCDs. The detector materials investigated and used in various IR-CCD configurations have included InSb for 3 to 5 μm operation and $\text{Pb}_{1-x}\text{Sn}_x\text{Te}$ and $\text{Hg}_{1-x}\text{Cd}_x\text{Te}$ for 8 to 14 μm

operation. The two basic methods for introducing IR signals from the detector array into the tapped CCD shift register are the direct coupled input and the buffer interface input. In the direct coupled input, the detector is connected either to the input diffusion (direct injection) or to the input gate (gate modulation) of the CCD tap (in the direct injection IR-CCD, the photogenerated charge is directly introduced into the CCD shift-register). In the second method - the buffer interface input - the IR signal is first processed through a buffer stage before being introduced into the CCD. The use of this buffer stage takes place between the IR detector array and the CCD shift-register. The buffer stage generally performs signal conditioning; amplification, ac coupling, etc. and so offers the advantage given by the versatility inherent in the type of pre-processing that it can provide. There are serious drawbacks however: increased electrical power requirements, increased thermal power dissipation, increased device complexity, and, inevitably, increased cost.

4.8.5.3 Practical Limitations with IR-CCDs

A major difference between the operation of CCDs in the visible and in the infrared parts of the EM spectrum is the large background flux rate that is present in the infrared. This results in increasingly shorter background chargeup or saturation time with increasing wavelength of operation (from about 1 sec for the 2.0 to 2.5 μm window to about 10 μsec for the 8 to 14 μm region). In addition, the internally generated charge is simultaneously integrated, further reducing the saturation time. Thus, one limitation of practical IR-CCD devices is the length of exposure time that is needed to produce a satisfactory image. This is especially important in airborne systems.

Another important consideration for IR-CCDs is the lower contrast that is present when compared to that encountered in the visible region of electro-magnetic spectrum. This matter has been explained fully in Chapter II. In addition, non-uniformity in the response of infrared detectors can seriously degrade the minimum resolvable temperature and results in severe fixed pattern noise (Wolfe and Zissis, 1978). These matters will be one of the main radiometric characteristics of CCD

detector arrays that has to be corrected by radiometric calibration stage, and will be discussed in some detail in Chapter 10.

4.9 Conclusions

In this chapter, the different methods of detecting and measuring the infrared radiation that is used to create an image in the middle and thermal infrared regions have been presented and discussed. In addition, the main design characteristics of the two-dimensional detector arrays that are employed widely in infrared imaging systems have also been outlined. The next chapter will cover the video technology on which all the image acquisition, display and recording carried out using infrared imagers is based. In this context, the main elements of the video systems that have been used throughout this project will be described. More importantly, those distortions stemming from the operation of individual parts of these video systems and which have to be determined and corrected by geometric and radiometric calibration, will be discussed in some detail.

CHAPTER 5: VIDEO TECHNOLOGY

5.1 Introduction

Video is a latin word meaning “I see” and is often associated with the word “television (TV)” in general conversation. However, originally the term video had a narrower meaning in that it was used in connection with the circuits and signals that deal with the picture information generated within a television system. It is still used in this sense in the specialist technical literature dealing with such circuits and signals even today. However, nowadays, while the term television tends to be used in the specific context of the transmission and reception of picture signals that have been broadcast using radiowaves, “video” is often used to cover the broader uses of television techniques. Thus one reads of “video cameras” being used in security surveillance systems and industrial monitoring, and “video recording” when referring to the recording of images by broadcast or closed circuit television (CCTV) systems.

Video technology has many attributes that are attractive for photogrammetry and remote sensing. Among the most prominent are:-

- (i) the near real-time availability of the imagery acquired by video cameras and imagers;
- (ii) the use of recording and playback of video images;
- (iii) video cameras have a higher light sensitivity than film cameras and this permits imaging in narrow spectral bands and gives sensitivity further into the infrared spectrum than can be achieved by film cameras; and
- (iv) the potential for immediate or rapid digital processing of the electronic signal for subsequent computer analysis.

At least three of these attributes - (i), (ii) and (iv) - if not all four, have particular relevance to the infrared imagers that are the main concern of this thesis. Indeed it is impossible to envisage present day infrared cameras and scanners as operational systems without the supporting video technology.

The near real-time availability of video imagery makes it particularly useful in applications such as disaster assessment (i.e. flooding, rangeland fires), military operations, etc. requiring a rapid response or turnaround time. The near real-time imagery also makes video technology useful when operating in remote locations allowing field work to be carried out immediately with the imagery to hand.

In addition to the above advantages, video equipment is portable, versatile, easy to use, widely available and can tolerate variable light conditions. Moreover, video recording systems have a lower operating cost than photographic systems (standard video tapes cost less than £5.00, provide two hours of coverage, and are reusable) and they do not require the extensive and time-consuming processing required with the films generated by photographic systems. Another advantage of using video technology is that it confers on the operator the ability to view “live” imagery on a monitor during an experiment or mission, making video images less subject to error than photography. Furthermore the image display allows the user to set the camera and the other test equipment in the required position and orientation. The audio track associated with video tapes is yet another attribute, permitting commentary during the experiment or operation. The high picture rate (25 or 30 frames per second) offers data redundancy that can be useful in some forms of analyses.

However it must be recognised that the major disadvantage of all video-based imagery is its low resolution which is much less than that of photographic film. For example, the resolutions of a U-matic tape recorder used to record colour and black-and-white video images are 250 and 300 pixels respectively, in the horizontal direction. By contrast, the resolution of 35mm slide film (which has a small 24 x 36 mm format), when digitized with a scanner using different pixel sizes is much greater, as shown in Table 5.1. Larger film formats will give still larger numbers of pixels in each coordinate direction.

As can be seen from Table 5.1, even when scanned with a bigger pixel size, the resolution of a digitized 35mm slide film is 4 or 5 times greater than that of standard

video images. The primary reasons for the low resolution of video imagery are the limitations of the basic technology, i.e. the camera, recorder and display. The typical video tube used in a camera has about 500 pixels of resolution in the horizontal direction, though there are tubes available with at least 1,400 pixels of resolution (Everitt, 1988). Thermal infrared vidicon tubes have a still lower resolution, e.g. 200 x 200 pixels is typical. Another disadvantage of video imagery is the difficulty in obtaining hardcopy images from the recorded data. At present, users have to either take photographs of the screen or use a special type of video monochrome or colour printer.

Pixel Size	No. of pixels in the vertical direction	No. of pixels in the horizontal direction
10 μ m	2,400	3,600
20 μ m	1,200	1,800
25 μ m	960	1,440

Table 5.1. Resolution of 35mm slide film digitized with a scanner using different pixel sizes.

5.2 Video System

A video system comprises three main parts: a video imager, which can either be a video tube camera; a CCD camera or a video frame scanner; a video tape recorder (VTR) and a video monitor, which function in the following way:-

- (i) the video imager acquires an image of the scene;
- (ii) the image is recorded on magnetic tape on the video tape recorder (VTR); and
- (iii) the video monitor can display on its screen the recorded image when it is played back from the VTR.

5.2.1 Video Tube Camera

Whether it is imaging in the visible or the infrared parts of the electromagnetic spectrum, electronically, a video camera works like a television receiver, but in

reverse. It breaks down the picture or image acquired or framed by its lens into a coded video signal; which the television receiver or video monitor then reassembles it into a complete picture or image. Optically, a video camera is similar to a film camera except that a light sensitive target takes the place of the photographic film.

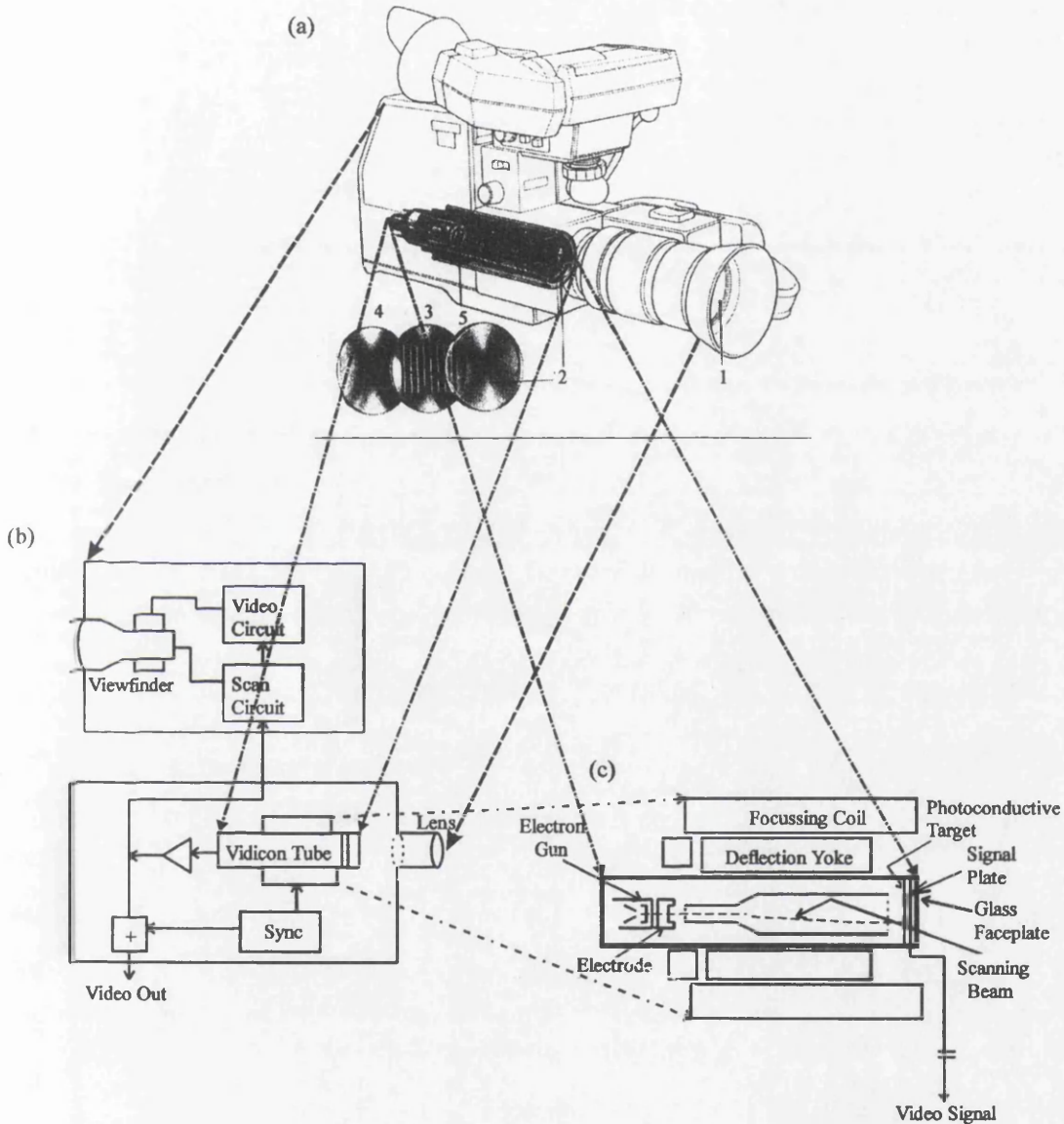


Fig. 5.1 (a) and (b) Schematic diagram of the video camera and its main parts;
(c) Cross section of its vidicon tube.

Fig. 5.1(a) and (b) shows a schematic diagram of the construction of a video camera and its main parts. The principal components in a video camera are the camera tube together with its associated optical system and viewfinder. There are many different

types of video camera tube in use - the iconoscope, the orthicon, the isocon, the vidicon, the return beam vidicon, the permachom, the plumbicon, the silicon charge storage and the solid state vidicon. However, amongst them, the vidicon tube is that most widely used. Its cross-section is shown in Fig. 5.1(c).

According to Fig. 5.1(a), the light that enters the camera is focussed by the lens (1) and passes through the glass faceplate (2) at the end of the vidicon tube, thereafter passing through an electrode (3) and travelling on to the target plate (4), which is coated with photoconductive material and gives off electrons (which are negatively charged particles) when the light is falling on it. In the visible part of the EM spectrum, a thin non-crystalline layer of this photoconductive material, antimony trisulphide (Sb_2S_3), is coated on to the target plate and acts both as a detector and the charge storage element. The more intensely illuminated parts of the target emit more electrons than the poorly illuminated parts. These electrons travel backwards toward the electrode (see Fig. 5.1(c)). Each electron emitted by the target leaves behind an equal, but positive charge. At any moment, therefore, the target is an accurate electrical map of the scene framed by the lens; areas of high positive charge correspond to the brighter parts of the image; areas with the lower charge values correspond to its darker parts. The electron gun, (5), converts the electrical charge values into an electric signal. It focuses a fine beam of electrons on the target, and scans across it in a systematic manner progressing from top to bottom. The focussing and deflection coils and yoke are mounted around the vidicon tube to control the movement of the electron beam (scanning beam) across the target plate as shown in Fig. 5.1(c). When the target has been scanned, the varying stream of electrons fall on a signal plate, which is used to generate a video signal whose intensity varies directly with the intensity of light in the scene (see Fig. 5.1(b) and (c)). The changing flow of electrons produces an analogue video signal in the form of a fluctuating DC voltage which is passed down the cable to the video monitor for direct display (on a small CRT or an LCD display) or to a VTR on which the signals are recorded on magnetic tape.

As can be seen from Fig. 5.1(c), the electronic circuits associated with the video camera add a synchronising (synch) signal to the analogue video signal. This is used to control the electron beam of the displaying monitor so that it moves in the same pattern as the scanning beam of the camera tube. These signals are added to the row analogue video signal to form what is called a composite video signal which will be discussed in some detail later in Chapter 6.

5.2.1.1 Electron Beam Scanning

There are two alternative patterns by which the electron beam scans the image on the target plate of the video camera tube are:-

- (i) non-interlaced scanning; and
- (ii) interlaced scanning

These are illustrated in Fig. 5.2.

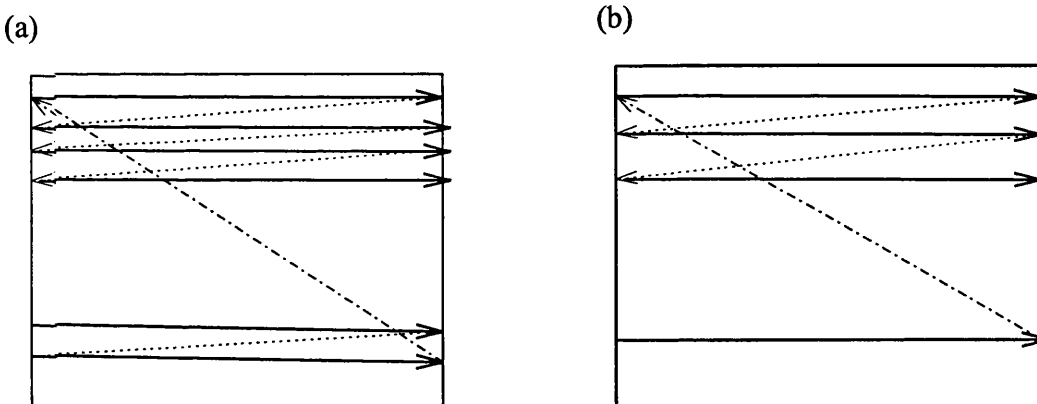


Fig. 5.2 (a) and (b). Non-interlaced and interlaced scanning patterns in video tube cameras (Amin, 1986).

- (i) Non-interlaced Scanning:-

In this method, (Fig. 5.2(a)), the electron beam of the camera tube moves with a constant velocity along a straight line from left to right. As it reaches the right edge of the frame, it is stopped and blacked out while it re-traces its path from right to left to the starting position of the next line (i.e. at the left hand

edge) which is contiguous to the starting point of the line just scanned. This process is repeated line after line until the beam has scanned the whole target plate. When it reaches the end of the frame, it is again blacked out while it re-traces its path back to the start of the next frame.

(ii) Interlaced Scanning:-

In this type of scanning, (Fig. 5.2(b)), basically the beam moves in the same manner as in non-interlaced scanning. However it scans first of all the odd numbered lines sequentially and then flies back to scan all the even numbered lines. Thus, every frame is divided into two interlaced fields. The first contains all the odd numbered lines and the second, all the even numbered lines. This process is called interlaced scanning.

There are two types of interlaced scanning. The first is called random interlaced in which the exact position of each line may vary with each frame scanned. For example, line 5 will lie between lines 4 and 6, but it may not be exactly centered between the two lines and its position may vary a little with each frame. This is the system used with home video cameras.

The other type of interlaced scanning is called positive interlaced. In this method, each line has a specific position where it will be located in every frame. So line 1 is in the same position in every frame, as are line 2, line 3, and so on. In positive interlaced scanning, each line will always be centered exactly between the lines that precede and follow it. All professional broadcast equipment uses positive interlaced scanning.

5.2.1.2 Colour Video Cameras

The basic colour video camera used by professional broadcasting organisations utilises three separate vidicon tubes with colour filters in front of each, so that each one responds only to radiation in either the Red, Green, or Blue (R,G, or B) windows

of the visible spectrum. A diagram of such a three tube camera is shown in Fig. 5.3. While some video cameras may record the separate R, G and B signals directly, others will record the image in terms of its luminance (Y) and chrominance (C). The RGB, YC and other colour formats will be described in some detail later in Chapter 6.

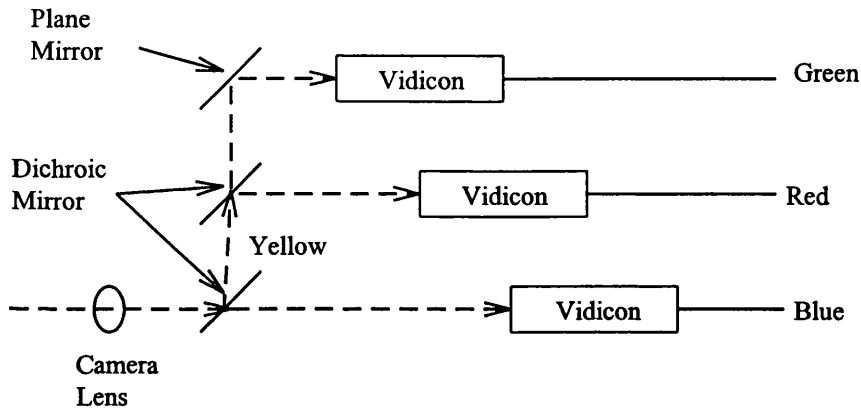


Fig. 5.3. A three tube colour video camera (Amin, 1986).

Most home video cameras use a simpler system having either one or two tubes. In the two-tube type of camera, the light gathered by the lens is split equally between the two tubes. One tube is used to provide the luminance signal (Y), while the other is a special tube that has a striped colour filter bonded to the front of its target and consists of a series of narrow vertical stripes which pass red or blue light alternately. As the scanning beam passes over the target, the video output switches alternately between the red (R) and blue (B) signals and these are separated out by the camera electronics to produce the R and B output signals. The G video signal is generated by combining the R, B and Y signals.

In a single tube camera, the filter of the tube has alternating R, G and B filter stripes. The target is divided into vertical stripes grouped into three sets corresponding to these filter stripes. In effect, the tube has three interlaced targets, each with its own colour filter. Three separate connections are brought out from the tube to give the three colour output signals from which the luminance and chrominance signals are generated.

5.3 Video Imaging Devices in the Infrared Band

Vidicon tube based cameras are used in thermal infrared imaging. The electron gun, the focussing and deflection coils, and the tube envelope are like those of a visible vidicon. However, they use the infrared transmitting faceplate which is usually a germanium glass with antireflection coatings for maximum transmission in the 8 to 14 μ m band, whereas silica-based glass is used in the visible spectrum. In addition, the radiation sensing target plate is formed from a single crystal of a pyroelectric material such as tryglycine sulphate (TGS) - as was explained in Chapter 4 - is used in the thermal infrared bands.

There are other video imaging devices operating in the infrared region of the EM spectrum that do not use vidicon tubes. Among them are those imagers employing solid-state technology in which the vidicon tube is replaced by a large number of light-sensitive discrete electronic cells (diodes) mounted on an integrated circuit board. The image of the object that is defined by the field of view of the resulting CCD areal array camera is formed on the imaging surface of this solid state array and is scanned by the photovoltaic seats of the detector array. Thus, although there is no vidicon tube used in this device, the rest of its design uses video technology - with video circuits and signals; recording on a VTR; and final image display on a video display monitor. Another type of video imaging device is the video frame scanner in which the object within the field of view of the imager is scanned in two directions using two optical mechanical scanning elements. Again there is no vidicon tube, but the output side uses video technology. These imagers will be discussed in more detail in Chapters 8 and 9.

5.4 Video Image Resolution

Resolution is defined as the ability to resolve fine detail in the image. In the case of tube cameras, it is equal to the number of lines generated in the vertical direction and number of pixels contained in a single line in the horizontal direction. It is usually determined by and adheres to broadcast television standards, which will be explained

in Chapter 6. As an example, if camera produces a PAL TV output, the resulting video image will have the format size of 575 (lines per frame) x 768 (pixels per line) that provides an aspect ratio of 4:3.

In the television industry, resolution is usually stated in terms of TV lines and thus it is specified in an entirely different manner to that of the photographic resolution that is familiar to and extensively used by photogrammetrists. Both methods employ a target with a series of black and white lines of equal width for the measurement of the resolution. In the former case, each line, white or black, is counted. However, when the photographic resolution is being specified, only line pairs (each pair consisting of a black and a white line) are counted. Thus, photographic resolution is described by a statement of the resolving power which can be expressed in terms of a minimum resolvable object size or the closeness of the spacing of these discernable lines. It is usually quoted as the number of line pairs per millimetre (lp/mm) that can be resolved in the image plane. The ability to state the resolving power capabilities of a camera system and consequently the approximate minimum sizes of objects likely to be usefully recorded on the photograph is an important matter in photography. However, up till 1970s, the techniques available to most engineers, photogrammetrists, earth scientists and others obtaining these estimates were largely of an empirical nature without consideration for target types, contrast, lens and film characteristics or the human observer. However, attempts have been made to develop formulas from which the resolving power of a complete photographic system comprising both its lens and film components can be determined. The following empirical expressions (Welch, 1972) has been used for computing the resolving power of a system:

$$1/R_{\text{system}} = 1/R_{\text{lens}} + 1/R_{\text{film}} \quad (5.1)$$

where:-

R_{system} is the imaging system's resolving power;

R_{lens} is the lens resolving power; and

R_{film} is the film resolving power.

Although this equation is used to compute a system's resolving power, the method is not flexible and reliability decreases as variables such as lens aberrations, different target contrasts and image motion are introduced (Welch, 1972). In addition, the determination of resolving power requires many tests to provide a comprehensive set of information about an optical system's spatial frequency response via calibration using test (bar) targets. This difficulty is overcome by the Modulation Transfer Function (MTF) which will be explained later in some more detail in Chapter 10. MTF can be measured in cycles per millimetre (cycles/mm). Potentially MTFs represent a powerful tool for image-quality evaluation that can be employed by photogrammetrist to optimize or compare photographic systems (Welch, 1971). However, although the MTF is increasingly employed by photographic system engineers and by lens and film manufacturers, it has received only limited attention from photogrammetrists. The reasons for this include the largely undemonstrated value of the MTF to the photogrammetrist; the complexity of analyzing and producing them; and the lack of standards against which results can be compared. Thus, most photogrammetrists continue to use the lp/mm yardstick both for camera resolution and system (camera + film) resolution.

However design engineers have quite other concerns and have developed resolution prediction techniques that take into account numerous variables. The most useful of these has been to employ a lens or system (excluding film) MTF in combination with a film threshold modulation (TM) curve for a three-bar target. When the MTF and TM curves are plotted on log-log paper, the MTF normally intersects the TM curve and this intersection point is taken as representative of the system resolving power for a high contrast target. In order to predict the resolving power for targets of lower contrast, the system MTF must be shifted vertically downward to the corresponding target modulations where:

$$M = (I_{\max} - I_{\min}) / (I_{\max} + I_{\min})$$

For example, for a 2:1 target contrast:

$$M = (2-1)/(2+1) = 1/3 = 0.33$$

Consequently, provided the system MTF and film TM curves are known, it would appear that the system resolving power can be predicted for any target contrast. Under normal circumstances, because of variations in scene radiations, errors in photographic exposure and the aberrations available in aerial camera lens, something less than the optimum resolving power will be obtained. A high quality aerial camera used in combination with modern high resolution films will produce 80% of the maximum lens-film resolving power. Using the 80% criterion, a modified TM curve can be obtained by converting the linear contrast ratios of 1.6:1 and 1,000:1 to modulations 0.23 and 1.0, computing 80% of the manufacturer's listed resolving power and plotting points on log-log paper. A straight line connecting these points provides a reasonable approximation for a TM curve representing 80% of maximum film resolving power (Welch, 1972).

Once the TM function has been plotted on log-log graph paper, the lens MTF is drawn on a tracing paper overlay. If the system MTF is shifted downward through a number of target modulations, the system resolving power for each target contrast can be obtained from the corresponding intersection points of the MTF and modified TM curves.

In video imaging, the resolution is often measured or stated in terms of pixels per inch or mm. The relationship between lp/mm and pixel resolution is provided through the Kell-factor of $2\sqrt{2}$ ($\cong 2.8$) as follows (Vlcek, 1988):-

$$1 \text{ lp/mm} = 2.8 \text{ TV lines} = 2.8 \text{ pixels} \quad (5.2)$$

For example, video cameras that can resolve 2,000 TV lines/inch ($\cong 78$ TV lines/mm) can be thought of as resolving $78 / 2.8 \cong 28$ lp/mm. Video cameras operating to the PAL standard (575 lines) can be thought of as having a resolution of $\cong 8$ lp/mm.

5.5 Video Image Geometry

Like an aerial photograph, a video image acquired by a vidicon camera or a camera utilizing a staring array of detectors, can be regarded as having a central projection whose geometry is determined by (i) the combination of the format size and the focal length of the camera lens (which in turn define its angular coverage) and (ii) the position of its principal point (defined as the position where the perpendicular dropped from the rear nodal point of the lens meets the image plane). The image from a video imager has a fixed size and therefore a fixed scale like that of an airphoto. However, it can be displayed using different display format sizes to give enlarged or reduced size images in the same way as an airphoto can be represented by different enlargements and reductions in size. The scale of the video image is normally determined by comparing distances between objects on the displayed image and the corresponding ground distances as in an airphoto. This subject will also be reviewed in more detail in Chapter 8 when the geometry of pyroelectric vidicon thermal cameras is dealt with.

5.6 Video Recording

The video signal generated by a video camera may be stored on a video tape using a Video Tape Recorder (VTR). The principle of operation of the video tape recorder is similar to that of the audio tape recorder where an audio tape is passed over a recording head which changes the pattern of the magnetism on the tape. There are two main helical scan techniques which are commonly used to write the video information on the video tape - quadruplex helical scan and duplex helical scan.

The quadruplex helical scan technique uses a two-inch wide tape running over a head wheel carrying four recording heads mounted at 90° intervals around the wheel, as shown in Fig. 5.4(a). As the head wheel rotates, each recording head writes a transverse track across the width of the tape. As the tape moves past the wheel, the successive head tracks are laid down side-by-side as shown in Fig. 5.4(b). This method is used only in professional broadcasting.

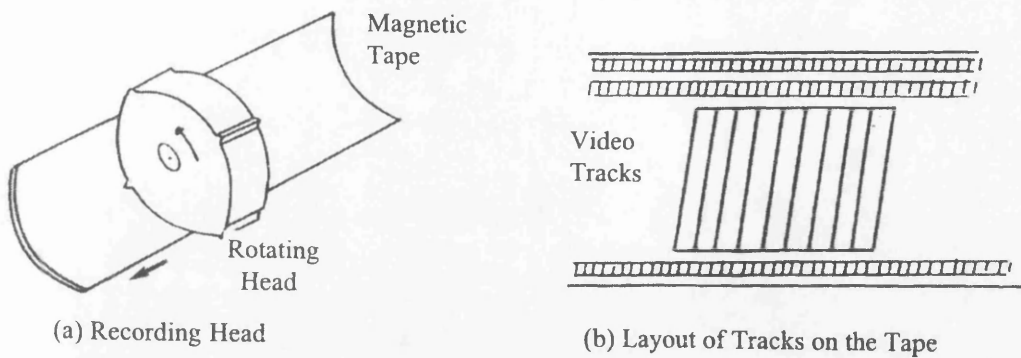


Fig. 5.4 (a) and (b). The quadruplex helical scan format (Amin, 1986)

On the other hand, duplex helical scanning is used in almost all other video systems. In this method, two heads are mounted 180° apart on a rotating drum assembly as shown in Fig. 5.5(a). The tape is wrapped around the drum in a spiral path so that each head contacts the tape in turn for half a revolution of the drum. As a result, each head traces out a diagonal track across the tape as shown in Fig. 5.5(b).

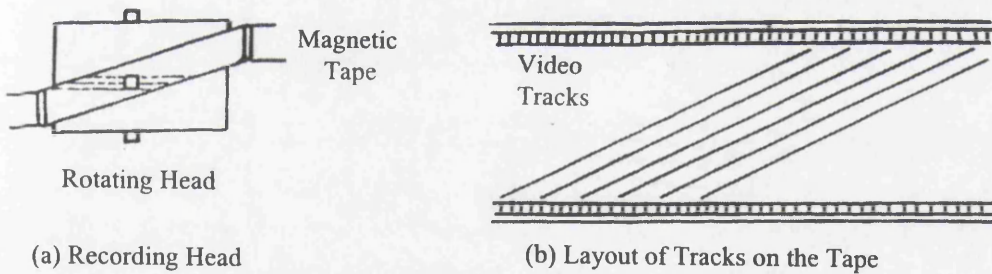


Fig. 5.5 (a) and (b). The duplex helical scan format (Amin, 1986)

Currently there are four main VTR systems using the duplex helical scan technique. These are:-

- (i) U-matic, which is the main professional system with the highest quality;
- (ii) Video Home System (VHS);
- (iii) Betamax; and
- (iv) Video 2000.

5.6.1 U-matic VTR

The U-matic VTR machines are designed for industrial and professional use. They use 3/4 inch (19mm) wide magnetic tape and run at a writing speed of 8.54m/sec which is faster than that of the other (domestic) systems. The dimensions of the U-matic cassettes are 219 x 138 x 31mm. The dimensions of the specific machine used in this project are 646 x 425 x 226mm, which is about twice the size of the biggest domestic system. Nevertheless, in terms of professional usage, U-matic recorders are regarded as being small, mobile, cheap and easy to use and give good picture quality. Throughout this project, this type of VTR has been used for recording and playback. A Sony model VO-2030 U-matic VTR was used in earlier part of the project. However, because of electronic disturbances, it was replaced by a Sony model VO-5630 U-matic VTR in the later part of the project.

5.6.2 VHS, Betamax and Video 2000 VTR systems

These three systems, designed for home and commercial use, all use 1/2 inch (12.5mm) wide tape, but the cassettes used with such systems are each different in size. The Betamax cassette is the smallest, while the other two have the same size. In a VHS machine, the writing speed is 4.85m/sec; in Betamax, it is 6.6m/sec; and in Video 2000, the speed is 5m/sec. The three systems give similar picture quality but the formats are quite different. Thus the tape recorded on one system will not playback on machines of the other systems, since the layout of the video tracks across the tape is different. In recent years, the Japan Victor Company (JVC) has released a much improved VTR system called Super VHS (S-VHS). It also uses the 1/2 inch wide tape format, but it has a very high horizontal resolution compared with the other three previous formats. While the VHS format provides a maximum resolution of about 240 pixels, the S-VHS format provides more than 400 pixels of resolution in the horizontal direction of the recorded video image (Lee and Faig, 1996).

5.7 Video Displays

The video signal generated by the video camera or played back from a VTR or video disk player is fed through a cable to the display unit which is usually a video monitor or a domestic television receiver. Unlike broadcast television receivers, most video monitors are designed to run from a direct video input, e.g. from a video camera, a VTR or a home computer. Video monitors cannot tune into different broadcast TV channels nor can they playback sound like television receivers. On the other hand, the picture tube of the video display monitor is designed to give a smaller spot size and more accurate focussing over the whole screen, hence giving better resolution and a steadier picture. Also video monitors are not limited to the format and resolution of broadcast television systems. However, it should be observed that some of the newer designs of television receiver have a particular channel allocated specifically to receive video signals from a direct input, e.g. from a video camera, VTR or home computer, so that they can also act as video monitors.

5.7.1 Monochrome Displays

The main component of a monochromatic video display monitor is a monochrome Cathode Ray Tube (CRT) shown in Fig. 5.6. The body of the glass tube consists of a narrow cylindrical neck which flares out into a cone to end in a slightly curved glass face plate on which the video image or picture is displayed. The air in the tube is evacuated and the tube itself is sealed to leave a vacuum inside. In the neck of the tube is an electron gun assembly similar to that of the camera tube explained in Section 5.2.2 above. A grid electrode which is mounted in front of the cathode is used to control the intensity of the electron beam generated by the heated cathode and hence the brightness of the spot on the screen. Two anodes are used to focus the electron beam on the back of the glass screen. In addition, four deflection coils or plates are mounted around the neck of the tube to provide deflection fields. Two of these deflect the beam in the up and down directions, while the other two deflect the beam left and right. The electrons are focussed and impact on a phosphor material that covers the inside of the faceplate and forms the actual screen on which the picture is produced.

When struck by the beam of electrons, the phosphor glows to produce a spot of light, the brightness of which depends on the intensity of the beam. To build up a complete image or picture, the electron beam must be scanned over the screen in a series of horizontal lines in the same way as the image of the original scene was scanned by the camera tube.

The monochromatic image produced on the monitor screen usually consists of different shades or intensities of white on a black background giving a range of grey levels, but black lines and text on a white background can also be produced on a certain high-quality monitors and an amber or green phosphor is also used in some other types of monochrome monitors, though the latter are less suitable for the images produced by infrared imagers.

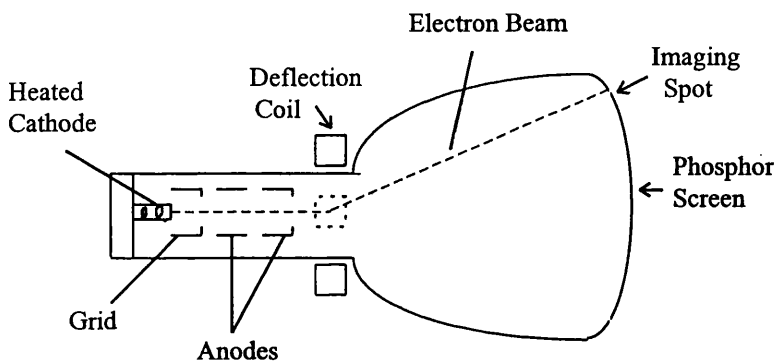


Fig. 5.6. Cathode Ray Tube (Amin, 1986)

A 14 inch Panasonic model WV-5410 monochrome video monitor has mostly been used for image display and monitoring in this project. It is a very high resolution monitor (850 lines at the centre) with standard BNC type input and output connectors.

5.7.2 Colour Displays

Colour monitors must have a composite colour video input or separate Red, Green, and Blue (RGB) inputs. The most commonly employed display technology utilises a single tube with three electron guns, one for each of the three basic colours. These are mounted in the neck of the tube in a triangular lay-out in such a manner that their

beams converge at a single position on the phosphor-coated screen. The composite video signal received by the monitor is decoded into its three colour components and the corresponding sync (synchronisation) pulses are produced by the video monitor electronics and each of the three component colour signals is used to drive the Red, Green or Blue gun as appropriate.

Instead of the normal monochrome phosphor coating, the whole screen is covered by an array of tiny Red, Green, and Blue phosphor dots which are arranged in groups of three, each group arranged in a triad or triangular pattern to match the layout of the electron guns. Between the screen and the guns is a steel shadow mask, which contains a pattern of tiny holes, one for each group of dots on the screen. The holes on the mask are aligned relative to the dots on the screen and to the layout of the electron guns so that the beam from the red gun passing through a hole in the mask will fall on a red dot on the screen, while the green and blue beams passing through the same hole will hit only the appropriate green and blue dots respectively as shown in Fig. 5.7. When the video signal is applied for a specific position on the screen, the electrons from the red gun will produce a red spot image on the screen, while the green and blue guns will produce green and blue images respectively, which are adjacent to the red one. Since the three dots are very tiny and close to one another, a person observing them is unable to resolve the individual dots and his eye will merge the three dot images together to form a composite colour image at that position.

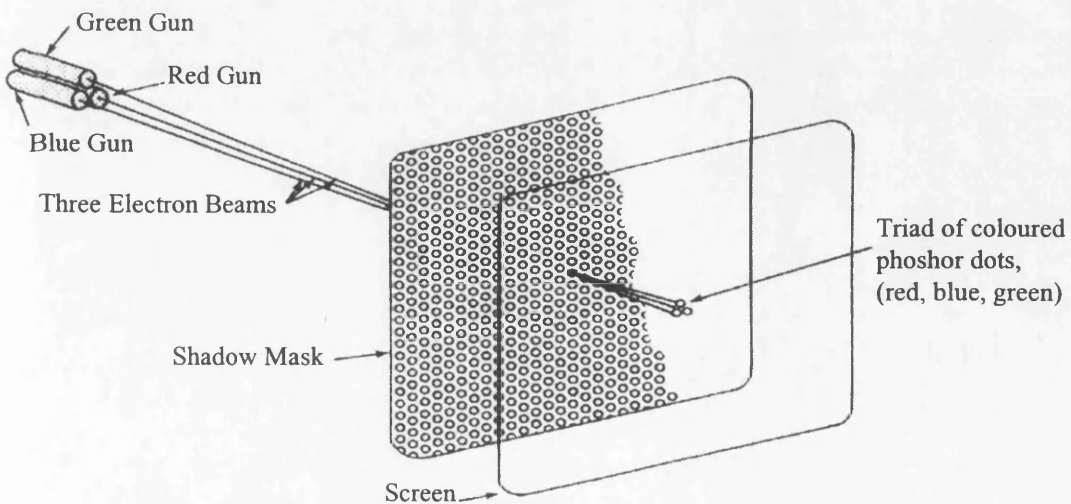


Fig. 5.7. The shadow mask of the colour video monitor (Petrie, 1990)

5.7.3 Computer Graphics Display

Up to till now, the discussion in this chapter has been concerned only with the video images generated by video cameras and displayed on a video monitor. However, there are other cases where the images are generated by other means and are then represented digitally in a computer memory. These may also be displayed on a video display monitor or computer terminal. An example of these is the computer simulation of pictures which create images of objects entirely mathematically. Another example is the scanner image data from spacecraft and satellites which is recorded directly on high-density video tapes. For distribution to users, the image data is then transformed and written on to Computer Compatible Tapes (CCTs) which are read by a computer and then displayed on a video monitor. In the context of the present research project, a comparable situation occurs when the image data is produced using an thermal infrared frame scanner.

In practice, there are two types of video-based computer graphics displays - raster-driven and vector-driven. The difference between them is mainly in how the image data is arranged and written on the video display. A display file in a vector driven device - few of which are still in use - contains only information about the specific points, lines and characters to be drawn on the screen. The void areas of the screen are ignored and the display of the variations in the density of the displayed vector information is usually not possible. On the other hand, the raster driven display involves the scanning every dot or pixel on a rectangular matrix which covers the entire screen. In principle, such a display is similar to that of a broadcast television set.

It should be noted that colour video monitors have only been used to a very minor extent in the present project, since the infrared images themselves are invariably monochrome and colour displays have only been used to display isotherms or colour-coded processed images.

5.8 Distortions in the Video System

Distortions stemming from the video system can be divided into three parts, since, the system itself consists of three main parts. These are:-

- (i) distortions in the video tube camera;
- (ii) distortions stemming from the VTR; and
- (iii) distortions in a CRT-based display monitor.

All of these need to be considered when the calibration of infrared imagers is being carried out. Thus the distortions present in the vidicon tube camera will also occur with the pyro-electric vidicon camera. If a VTR is being used for the intermediate storage of images (as is the case in the present work) even when they are acquired by a non-vidicon based imager, then the distortions generated by the VTR have to be taken into account. Then finally, if measurements are to be made visually on a display monitor, the distortions inherent in this device will also have to be considered.

5.8.1 Distortions in the Video Camera

However, distortions in the video tube camera can be divided into two main parts:-

- (i) the distortions present in the vidicon tube; and
- (ii) the distortion stemming from the camera lens.

5.8.1.1 Distortions in the Vidicon Tube

As stated in the earlier part of this chapter, in order to scan a target, the electron beam of the camera tube must be focused on it and must, in addition, be deflected so as to traverse the target in the desired manner. In general, the electron beams will be deflected by electric or magnetic deflection fields: electric deflection was used in early television receivers, but magnetic deflection is now almost universal both in television camera tubes and television monitors. This magnetic deflection is the main source of the distortions experienced with vidicon tube cameras.

The field between the deflection coils, while uniform at the centre, may become curved at the edges, and the scanning beam reaching the edge of the field can be influenced by both a vertical component and a horizontal component. This has the two-fold effect of distorting the shape of the scanning beam and the trace on the target of the vidicon tube.

Assuming a circular spot or beam initially, at the edge of the field, the vertical component will produce the required deflection, while the horizontal component will stretch the circle into an ellipse with its major axis perpendicular to the direction of the deflection. If two magnetic fields are used for scanning; the combined curvatures will act on the beam at the corners of the target and may deflect it outwards to form an elongated corner or “pincushion” pattern (Fig. 5.8(a)). If, on the other hand, the field shape is concave, the pattern on the target will be “barrel-shaped” with retracted corners (Fig. 5.8(b)). A combination of these defects to a greater or less degree is often found with asymmetric (non-uniform) deflecting fields (Parr, 1941). Thus, in the manufacturing phase, the greatest care is necessary in mounting and centring the camera’s deflection coils.

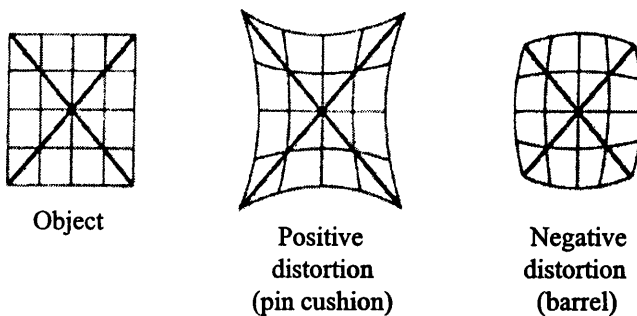


Fig. 5.8 (a) and (b). Pincushion and barrel-shaped distortions (Sherr, 1979).

Arising from the use of magnetic deflection, problems such as the formation of a non-uniform field or a fringe field and oscillations in the windings, which are often present in the CRT, can also occur in camera tubes. These problems will be described in more detail in Section 5.8.3.

These electronic distortions occurring in vidicon tube cameras have been investigated and calibrated by Wong (1969, 1970, 1973,1975). For this purpose, he has used a grid of calibrated reseau crosses which was located on the photoconductive surface of the video tube. Detailed discussion on his results and approaches that he developed for correcting these distortions will be described in Chapter 8.

5.8.1.2 Lens Distortions

The various lens aberrations such as spherical aberrations, coma, chromatic aberrations and astigmatism are important factors for the radiometric quality of the image. The combined effects of such aberrations disturb photogrammetrists only when the deterioration of the image decreases the radiometric quality of image so preventing him from identifying details of interest or increasing the uncertainties of measurement. However lens distortion has to do with the change in position of the image point in the image plane but not with the radiometric quality. The presence of any substantial distortion is therefore of great importance to the photogrammetrist and must be taken into account when measuring the coordinates of the cross targets of a calibration plate and, if possible, it will be removed by the geometric calibration.

Two main types of lens distortions are likely to be encountered in an infrared imaging system. They are:-

- (i) radial distortion; and
- (ii) decentering (tangential) distortion.

5.8.1.2.1 Radial Distortion

If the image of an off-axis target is displaced radially either closer to or farther from the principal point then it has radially distorted. The barrel or pincushion distortions, which have been discussed above, are used to describe the image shape of a rectangle which has radially distorted closer to or farther from principal point respectively. The point of symmetry for radial distortion may not be exactly at the principal point, but is usually so close that the principal point is adopted as the origin.

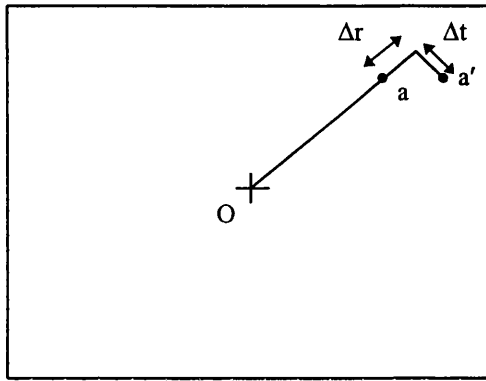


Fig. 5.9. Radial and tangential distortion

In Fig. 5.9, instead of the incident light ray being imaged at its correct position a , it is imaged a' . The magnitude of the radial distortion is Δr , and the magnitude of the tangential distortion is Δt .

A radial distortion curve of a lens may be drawn by plotting radial distortion on the ordinate versus radial distance as the abscissa. An example of such a curve is shown in Fig. 5.10.

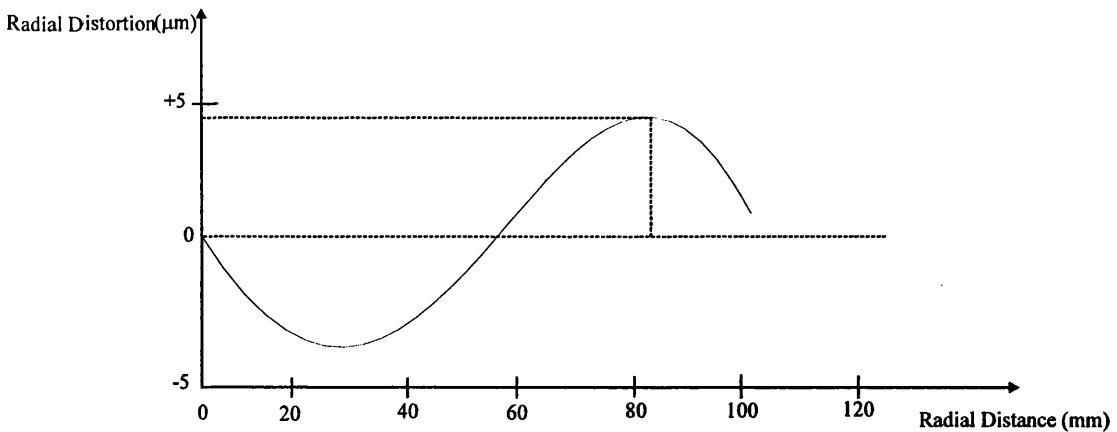


Fig. 5.10. Radial distortion curve

There are two different methods of correcting for radial distortion are (Wolf, 1983):-

- (i) reading required corrections from a radial distortion curve; and
- (ii) numerical methods in which the radial distortion curve is approximated by a polynomial.

In the first case, the radial distance r from the principal point can be computed as

$$r = ((x - x_p)^2 + (y - y_p)^2)^{1/2} \quad (5.3)$$

where:-

- r is the radial distance;
- x, y are the coordinates of the image point; and
- x_p, y_p are the coordinates of the principal point.

Entering the abscissa of Fig. 5.10 with r value, moving vertically to intersect the distortion curve, and then moving leftward horizontally to the ordinate scale (see dashed line of Fig. 5.10), radial distortion Δr is read. The corrected radial distance to image point is obtained by subtracting the distortion from radial distance and

$$r' = r - \Delta r \quad (5.4)$$

where:-

- r' is the corrected radial distance;
- r is the radial distance; and
- Δr is the radial distortion.

Now corrected x' and y' coordinates of the image point are calculated in proportion to the ratio of r' / r ; and

$$\begin{aligned} x' &= (r' / r)x \\ y' &= (r' / r)y \end{aligned} \quad (5.5)$$

where:-

- x' is the corrected x coordinate of the image point; and
- y' is the corrected y coordinate of the image point.

The method of approximating radial distortion with a polynomial is more complex; however, it is often regarded as convenient when being used on a computer. The

method consists of approximating the radial distortion curve with a polynomial of the form

$$\Delta r = K_0 r + K_1 r^3 + K_2 r^5 + K_3 r^7 + \dots \quad (5.6)$$

where:-

K_0, K_1, K_2, K_3 are the coefficients of radial distortion; and

r is the radial distance and can be calculated from Eq. 5.3.

In Eq. 5.6, the K coefficients define the shape of the curve. They are obtained through a least squares curve fitting computation which matches a curve to the known values of the radial distortions at varying radial distances as determined through camera calibration.

5.8.1.2.2 Decentering (Tangential) Distortion

All the individual elements in a lens system should be aligned, ideally at the time of manufacture, to be collinear to the optical axis of the entire lens system. Any displacement or rotation of a lens element from the perfect alignment of the system will cause the geometric displacement of images known as decentering distortion. Literally, this title refers to the “off-centering” of the lens elements (see Fig. 5.11)

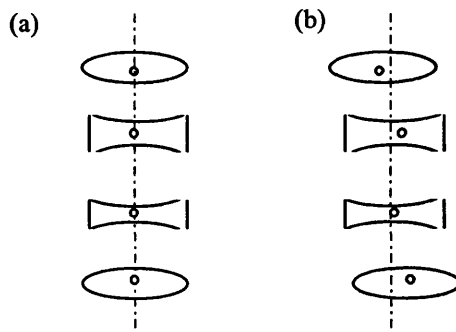


Fig. 5.11. Misalignment of lens element: (a) perfectly centred lens system; (b) decentered lens system.

Where this distortion present, it is manifests itself as an asymmetry in radial distortion. In Kalao and Petrie, (1975), a number of Russar 29b super wide angle lenses, which had been fitted to the Russian AFA topographic camera, have been

tested and a highly asymmetrical distortion pattern was encountered which was thought to have been caused by lack of alignment of the lens elements. This was only overcome by manufacturing special asymmetrical lens distortion correction plates. More recently (Jacobsen, 1993) has also commented on the non-regular lens distortion patterns encountered in Russian space cameras.

The effect of the decentering distortion to image coordinates of point can be given as follows (Fryer, 1996):

$$\Delta x_s = (1 - (c / S)) [P_1(r^2 + 2(x - x_p)^2) + 2P_2(x - x_p)(y - y_p)]$$

$$\Delta y_s = (1 - (c / S)) [P_2(r^2 + 2(y - y_p)^2) + 2P_1(x - x_p)(y - y_p)]$$

where

$\Delta x_s, \Delta y_s$ are the components of the decentering distortion at an image point x, y ;

P_1, P_2 are the coefficients of the decentering distortion;

r is the radial distance from principal point;

c is the principal distance for lens; and

S is the object distance from the lens.

It is not known how much attention is given to the exact centering of the optical elements in an infrared imaging system by the manufacturers.

5.8.2 Distortions Stemming From the VTR

The sources of the distortion present in a VTR derive from the playback process of the video tape. Since the VTR cannot playback the tape at exactly the same speed at which it was recorded, the information derived from the playback operation will not be precisely the same as that existing when the image was recorded. This inability of a VTR to playback at exactly the same speed is called the time base error. It takes the electron gun in the vidicon tube 63.5 μ sec to scan a video line. So if the playback signal is only 63.5 μ sec off from where it should be, then there will be an error of one line. Dealing with a time base error can thus be an integral part of utilizing a video tape recording. If the amount of error is small and can be corrected, the resulting image problems will be minimal. However, large errors can produce effects such as

jitters, jumps and rolls in the image. Time base errors can also result from any change in the actual composition of the tape, generally due to variations in air temperature, humidity, recorder position, and recorder movement. All of these factors play a part in determining how much time base error can be expected on tape playback. It could be less than a line in a studio machine, or add up to 20 or 30 lines on a field recorder (Hartwig, 1995). This error can be corrected with a time base corrector, a device which can cost as much as a VTR. Time base correctors will take the unstable signal coming out of the VTR and stabilize it.

5.8.3 Distortions in a CRT-based Display Monitor

As with a video tube camera, the most serious source of distortion in a display monitor based on the use of a CRT is the electron beam's scanning process. Proper deflection of the electron beam in the CRT is implemented by two mutually perpendicular magnetic fields. As explained in Section 5.7.1, two pairs of magnetic coils are mounted on the neck of the CRT. The top and bottom coils produce a field which deflects the beam in a vertical direction, whereas the side coils produce a field which causes horizontal deflection. The amount of deflection in both the horizontal and vertical directions (which is controlled by the display controller) depends on the amount of current flowing through the corresponding pair of coils.

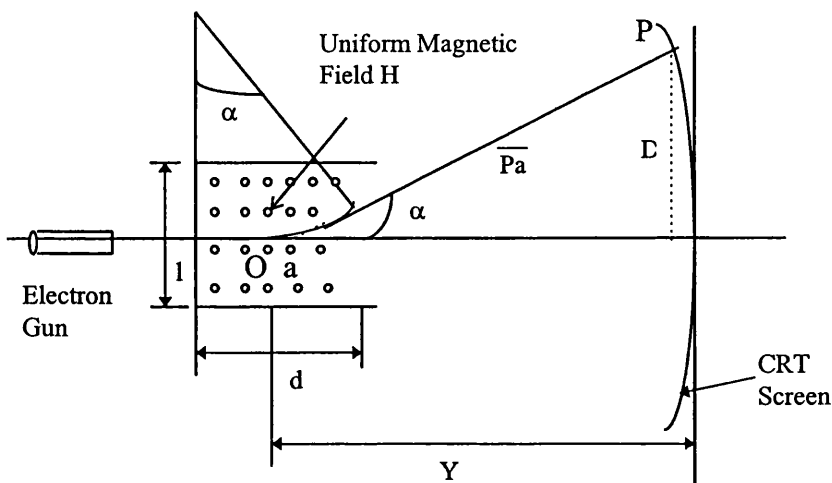


Fig. 5.12. Magnetic deflection in a CRT (Wong, 1969)

Fig. 5.12 is a vertical cross section of a CRT showing the principle of magnetic deflection. H is a horizontal magnetic field produced by the side coils. In ideal conditions, the magnitude of deflection is directly proportional to the current present in the deflection coil and can be expressed by the following linear equation:

$$D = aI \quad (5.7)$$

where D is the deflection distance, a is the system constant, and I is the current in the deflection coil. The exact implementation of this simple linear equation is the main objective of all deflection coil design. However, in practice, it is not easy to create a perfectly uniform magnetic field. The sum of the deflections produced by the two magnetic fluxes may form a pincushion or barrel-shaped field as already explained in Section 5.8.1.

Indeed, as in Section 5.8.1, a non-uniform field generated between the coils can also cause a distortion in the shape of the electron beam. The deflection of the electron beam is also affected by external magnetic or electromagnetic fields that may be present in the area between the deflection field and the display screen. One magnetic field is always present in the atmosphere; namely, that of the Earth's magnetic field. The effect of the Earth's magnetic field can be eliminated by providing a compensating field at the deflection coils. However, because the strength and direction of the Earth's magnetic field differs from one location to another on the Earth's surface, and because other external fields may also be present, the best solution for eliminating external interference is to provide adequate magnetic shielding around the cathode ray tube used in the display monitor.

It is also not possible to produce a field which drops abruptly to zero outside of the deflection region. Thus the small fringe field, which does exist both in front of and behind the deflection region, forms a circular magnetic lens and causes an aberration in the electron beam, so producing distortions in the scanning pattern. The behaviour and shape of the distortions is similar to that caused by a non-uniform field.

The small fringe field located behind the deflection region may also interact with the focusing field that is normally placed in front of the electron gun to focus the scanning beam. The effects of this interaction are complicated and seem not to be too well understood. At least two effects due to focusing-deflection interaction have been recognized. They are: (1) a rotation of the image about the axis; and (2) line-splitting which results in bowed scan lines. The rotational effect can be corrected by rotating the deflection coils by the same amount but in the opposite direction. The line-splitting effect must be minimized by proper isolation of the focusing and deflection fields.

A distortion called hook is caused by insufficient flyback time being available at the end of each line sweep. Under such conditions, the deflected beam does not have sufficient time to return to its zero position, and a residual deflection remains at the beginning of the next line sweep resulting in displacement of the beginning of that line.

Line jitters are caused by a non-uniform scanning rate, and line wiggles can be caused by oscillations in the individual windings of the deflection coil or cross-talk between the windings. Oscillations in the deflection coil become more serious in high-frequency scanning and must be adequately insulated by proper tube design.

It should be said that, while the geometric distortions present in a display monitor have to be considered carefully when carrying out measurements on video images visually on the monitor, most of these potential difficulties have been circumvented in the present project through the use of automatic image matching for the measurement of the target images during the geometric calibration operations carried out during the project.

5.9 Conclusion

This chapter has explained the main concepts of the video technology which underlies infrared imaging systems and has been used throughout this research project in that

the imaging systems, the recording and display devices are all video-based. In addition to this knowledge, this chapter has also given information about the resolution and geometry of video images and the distortions that stem from the individual parts of the video system. However, the transmission of images from the infrared video imager to the user's display or processing system is also governed by the analogue video signals used in television broadcasting. As the name implies, analogue video is a continuous signal which is transmitted at a radio frequency through the atmosphere or along a coaxial cable. The timing and structure of these signals are determined by the specifications and standards established for broadcast television systems. The next chapter will examine the basic concepts of these systems in more detail and consider their effects and implications in infrared video imagers.

CHAPTER 6: VIDEO STANDARDS

6.1 Introduction

The transmission of video signals from the imaging system for them to be recorded on a storage medium can be made in either a digital or an analogue mode. Digital signal transmission is a very new method for transferring video image data and its compatibility with standard video systems is still in its infancy. However, analogue signal transmission is a fairly well known technique to output the image data that has been acquired or used during photogrammetric applications. Furthermore the transmission of images from thermal video frame scanners, CCD cameras and pyroelectric vidicon cameras has largely been carried out utilising the analogue video signals employed in television broadcasting. These signals are used to generate the analogue video image which is output from infrared imagers. The timing and structure of these broadcast signals was defined in the early days of television, in order to standardize both on the format of the image and on the characteristics of the broadcast transmission. From these initial definitions, the monochrome and colour video standards that are in current use have been developed.

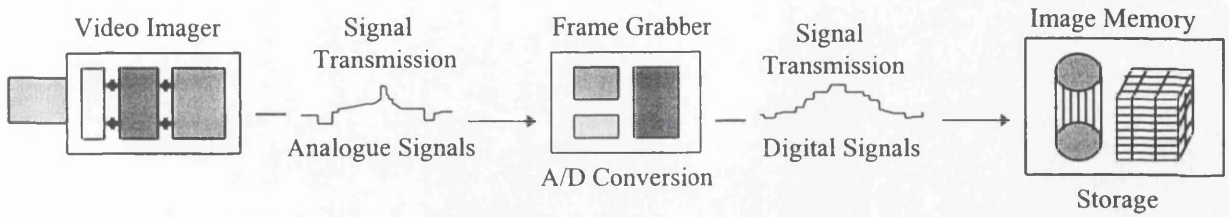
In this chapter, the commonly used standards for analogue video signals utilised for monochrome or colour signal transmission and display will be described. In particular, the synchronisation and transmission characteristics of monochrome video signals will be discussed in detail. In addition, their effects on the geometric and radiometric characteristics of infrared images will be explained. It is essential that these matters are fully understood if the geometric and radiometric calibration of infrared imagers - which is the main concern of the author's research project - is to be conducted in a proper manner and with a full understanding of the imaging, recording and display processes.

6.2 Data Capture and Signal Transmission

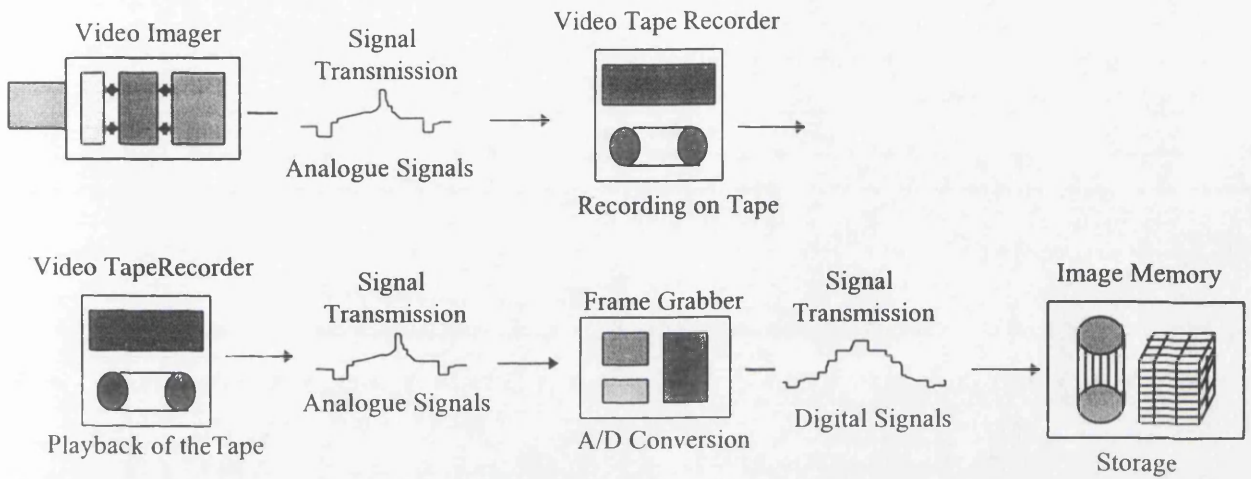
In the specific context of photogrammetric applications, there are four main (different) methods that are used to perform the capture and transmission of the image information (see Fig. 6.1).

- (i) An analogue video imager with real time operation (Fig. 6.1(a)) transmits the image data contained in an analogue video signal and the analogue-to-digital (A/D) conversion is performed in the frame grabber mounted in the computer so that the image can be processed in the computer.
- (ii) An analogue video imager with non-real time operation (Fig. 6.1(b)) sends the image data to the VTR where the image is recorded on magnetic tape. After that, the analogue image data recorded on the tape is played back and converted to digital form using the frame grabber. This digital image can be saved either in the computer memory or on a floppy disk or hard disk. This type of procedure has been used throughout the present project.
- (iii) A digital video imager with real time operation (Fig. 6.1(c)) performs the analogue-to-digital (A/D) conversion in the imager itself and the resulting digital signals are then transmitted or transferred to the frame grabber's image memory. The latter is buffered to allow the input from the A/D converter of the imager to take place at one rate and to allow the read out to write and store the image data on the host computer to take place at a different rate.
- (iv) A digital video imager with non-real time operation (Fig. 6.1(d)) performs the analogue-to-digital (A/D) conversion in the imager itself and stores the digital image data on the on-board local storage rather than transmit the data to the computer. Nowadays, many still video cameras and low resolution areal array CCD cameras use PCMCIA cards or other similar storage devices for image storage in the imager. Later these can be removed and downloaded into a personal computer.

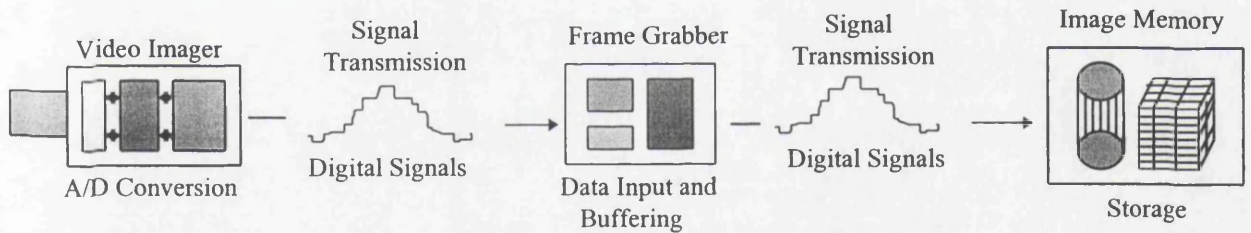
(a) Analogue Video Imager with Real Time Operation



(b) Analogue Video Imager with Intermediate Recording



(c) Digital Video Imager with Real Time Operation



(d) Digital Video Imager with Non-Real Time Operation

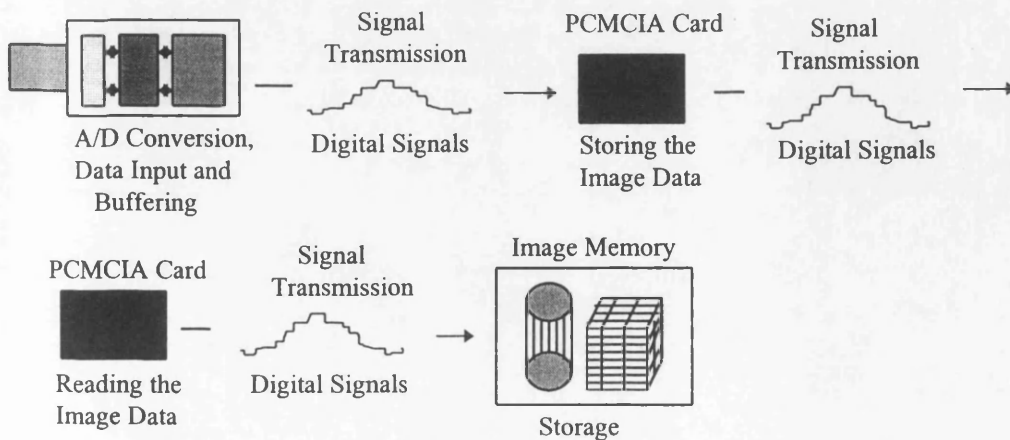


Fig. 6.1. Signal transmission and frame grabbing with analogue and digital video cameras in photogrammetric applications.

According to the above account, the basic functions involved in transferring the analogue image data from the infrared video imagers to the digital memory of the computer used in this project are:-

- (i) Analogue video signal processing in the infrared imager;
- (ii) The analogue video image data coming from the imager is recorded on a U-matic magnetic tape mounted in the video tape recorder (VTR);
- (iii) The analogue image data stored on U-matic tape is played back using the VTR and is sent to the frame grabber;
- (iv) Analogue-to-digital (A/D) conversion and data buffering of the data takes place in the frame grabber; and
- (v) Data storage and processing takes place in the computer.

6.3 Video Inputs

As noted above, a distinction is made between digital and analogue inputs to a processing system. Digital input is typically delivered by satellite remote sensors, Computerised Tomography (CT) Scanners, Scanning Electron Microscopes (SEM), and digital cameras in which the solid-state sensor is integrated with the A/D converter which is incorporated in the imager. Analogue input comes in three different forms - Slow Scan, Standard Video and High Definition Television (HDTV) - essentially distinguished by the corresponding 8-bit pixel conversion rate. Table 6.1 gives a comparison between these three different norms.

	Slow Scan	Standard Video	HDTV
Pixel Data Rate(MHz)	<5 MHz	7.5 to 15 MHz	>15 MHz
Frame Size (pixels)	1k x 1k to 4k x 4k	256 x 256 512 x 512 780 x 540	1,920 x 1,080
Grey Value Resolution	6 to 16 bit	6 to 10 bit	6 to 8 bit

Table 6.1. Analogue inputs (Gruen, 1988)

Real-time video systems with a 512 x 512 pixel format and a 30Hz frame acquisition rate require approximately a 10 MHz A/D conversion rate. According to Table 6.1,

slow scan devices cannot meet this requirement. Typically these devices are used together with the high resolution CCD cameras deployed in scientific and medical work which often do not output standard video signals. Consequently their read out rates are much lower than those from standard video, often using pixel output frequencies as low as 50kHz in order to minimize circuit noise. For example, at a 50kHz read out rate, a 1k x 1k image requires approximately 21 seconds to be output and displayed. This slow read out is usually carried out by a Slow Scan Controller (SSC) which is usually a separate module attached to the camera. As a consequence of using this type of controller, there is no necessity for additional electronic circuitry to generate synchronisation signals that may introduce additional noise.

At the other end of the scale, for the digitisation of high bandwidth signals, i.e. those with rates beyond 15MHz, there is, as yet, no standard. At the moment, one has to deal with data rates between 15MHz and 100MHz. Typical bandwidths employed with High Definition TV (HDTV) cameras are 30MHz and 45MHz for standard applications; for TV studio applications, one can find standards such as 27MHz, 54MHz and 104MHz (Kern, 1987). For all of these applications, currently only tube type cameras are available. Because of the current shortcomings inherent in their technology, CCD cameras are too slow to fulfill these requirements. Therefore, direct digital, slow scan and HDTV devices give rise to so-called "non-standard inputs". In this context, "standard input" refers to one of the various television video norms and is, by definition, of an analogue type and form.

6.3.1 Standard Video Formats

The first standard for broadcast monochrome television, known as RS-170, was defined by the National Television Systems Committee (NTSC) and the Electronic Industry Association (EIA) and was adopted by the Federal Communications Commission (FCC) of the USA in 1941. In 1953, an enhancement to the RS-170 standard was adopted by the same bodies in order to define a colour television standard. However, the NTSC tag has persisted ever since. The NTSC standard is

used in 32 countries such as the USA, Canada and other countries in North and South America and in Japan and the Philippines.

In the 1950s, the Committee Consultatif International des Radiocommunications (CCIR) also defined video standards for both monochrome and colour television broadcasts. Various versions of the CCIR standard are used for monochrome television in a number of countries. The colour video standards associated with it are the Phase Alternate Line (PAL) and Sequential Colour and Memory (SECAM) standards. Whereas the PAL standard is used with broadcast TV in most of Europe and in Australia, the SECAM standard is used with broadcast TV in France, Russia, Iraq and Iran.

The two major monochrome video signal standards - RS-170 and CCIR - give interlaced signals. The essential differences between these two standards lie in the number of horizontal lines in the image and the transmission rate that is used (Table 6.2), which make them quite incompatible at a basic level. Another monochrome video standard is RS-330 which is based on the RS-170 standard, but has additional signal characteristics by way of modified timing waveforms and tighter tolerances. It produces fast non-interlaced signals.

Standard	RS-170	CCIR	HDTV
Frame rate (Hz)	30	35	30
Interlace	2:1	2:1	2:1
Field rate (Hz)	60	50	60
Number of horizontal lines	525	625	1,125
Number of active horizontal lines	480	576	1,080
Line frequency (Hz)	15,750	15,625	33,750
Active line time (μ s)	52.5	52	25.85
Pixels per line	752	744	1,920
Aspect ratio	4:3	4:3	16:9
Single band image size (pixels)	360,960	428,544	2,160,000

Table 6.2. Selected characteristics of the RS-170, CCIR and HDTV video standards
(Shortis and Beyer, 1996).

Although NTSC, PAL and SECAM are the colour video standards used in broadcast television, they can give monochrome output as well as colour. The PAL monochrome system has been used throughout this project as the video input and output standard for the infrared video signals. This the reason why all the items of video equipment used in the project; including infrared video imagers, the VTR and the video monitor all have PAL type video input and output.

These three colour video standards are employed to produce interlaced signals in broadcast television. Their characteristics are given in Table 6.3.

Standards	PAL	SECAM	NTSC
Frame frequency (Hz)	25	25	30
Field frequency (Hz)	50	50	60
No. of lines per frame	625	819	525
No. of active lines per frame	575	737	497
Line frequency (Hz)	15,625	20,475	15,750
No. of pixels per line	767	982	663
Line scan time (μ s)	64.0	48.8	63.5

Table 6.3. Specifications of the main broadcast video colour standard formats (Amin, 1986).

In addition, the RGB colour standard is used in the colour monitors of the computers that are often used to display the video images and to allow measurements to be carried out when they are used in a photogrammetric context. This system is used in both interlaced and non-interlaced forms in these colour monitors. Although colour frame grabbers normally acquire and output images in the form of 8 bits of data for each of the Red, Green and Blue components of each pixel, this is not necessarily the most useful format when it comes to image processing. Indeed the RGB format is only one of three commonly used colour formats; the others are YUV and HSI (Transtech, 1995). The use of these alternative colour formats saves processing time because, in most cases with RGB data, all three components must be processed to achieve the desired results. By contrast, YUV is a quite different way of representing

the same image and does so in terms of its luminance or brightness (Y) and its colour difference values (U and V are obtained from B-Y and R-Y). The third standard, HSI, describes the image in terms of the hue, saturation and intensity of each pixel. Hue is the colour itself (green or yellow), saturation the strength of colour (pink or red) and intensity, the lightness of the pixel. The use of HSI saves processing time since only one component has to be examined and processed, whereas with RGB almost always all three components need to be examined and processed.

6.3.2 High Definition Television (HDTV)

Several efforts are under way to improve the existing video standards and/or to introduce a new standard (or standards) that provide for significantly improved performance. They are generally referred to as HDTV.

The development of HDTV was pioneered by NHK (Nippon Hoso Kyokai), the Japan Broadcasting Corporation. NHK has been broadcasting its Hi-Vision service via a home-direct satellite experimentally since 1990 and officially since November 25, 1995. Hi-Vision is a HDTV system composed of 1,125 scan lines; 1,920 pixels per line; 2:1 interlacing; a field-rate of 60Hz; and an aspect ratio of 9 by 16. This specification would give a spatial resolution close to that of 35mm film and an aspect ratio that recognised the subjective improvement achieved by the wider screens now used in the cinema (Sandbank, 1990). By the end of 1997, Hi-Vision programmes will be produced in an entirely digital format. Currently over 10 hours of Hi-Vision programs are being broadcasted each day in Japan.

However, in addition to Hi-Vision, several alternative proposals for HDTV have been put forward and many research and various development initiatives are currently under way in America and Europe. In the USA, the Advanced Television Systems Committee (ATSC) has proposed a sampling rate of 74.25Mhz which would result in 1,920 pixels being available during the active line time. The system developed within the European project Euroka 95 called D2-MAC uses 1,152 lines; 1,920 pixels per

line; and a 50Hz field rate instead. Table 6.2 contains the NHK specifications for HDTV.

Very recently, HDTV has begun to find an application in photogrammetry. For example, the new Intergraph Image Station Z digital photogrammetric workstation (DPW) uses an 28 inch panoramic multi-sync HDTV monitor which gives a 2.5 megapixel (2,112 x 1,188 pixels) maximum screen resolution.

Standard video formats are often specified by the diagonal size (in inches) of the video tube camera. The diagonal size of the CCD detector arrays were equivalent to a 2/3 inch (16.9mm), which corresponds to a detector array size of 8.8 x 6.6mm $[(8.8^2 + 6.6^2)^{1/2} = 11\text{mm in diagonal}]$. Due to improvements in the manufacturing technology, the format size has decreased and the current generation of CCD detector arrays are available in 1/2 inch (12.7mm) and 1/3 inch (8.5mm) diagonal size which correspond to 6.4 x 4.8mm (8mm in diagonal) and 4.9 x 3.7mm (6.1 in diagonal) format sizes respectively. As can be seen this account, the diagonal sizes given by video tube technology are not equal to those encountered using the CCD array format size. The reason for this is that the actual sensitive area which is scanned by the electron gun inside the tube to derive the video image is somewhat smaller than the total sensitive area of the tube (Information from Dr. M. Shortis via e-mail).

Only during recent years have CCD cameras been specifically developed for HTDV. For example, Sony has released a 1,024 x 1,920 pixel CCD camera that outputs an HDTV video signal. The CCD detector size is 1 inch (25.4mm) which corresponds to 14 x 8 mm (16.1mm in diagonal) and the image has an aspect ratio of 16:9 (Shortis and Beyer, 1996).

The main drawback of HDTV with respect to its use in photogrammetry is that its requirements are to a large extent determined by consideration of the broadcasting aspects of the standard. But, undoubtedly, the higher resolution of HDTV will be welcomed by photogrammetrists; however, unfortunately the current CCD technology used in infrared imagers falls quite a long way below these new video standards.

6.3.3 S-Video

High quality VTRs (Video Tape Recorders) and camcorders now use a video standard called S-Video or Y/C. Whereas the NTSC and PAL standards give rise to signals that are referred to as composite colour signals; S-Video (Y/C) is sometimes referred to as component video, because the luminance (Y) and chrominance (C) signals are transmitted separately (Transtech, 1995).

Conventional video recording methods take the video signal derived from a camera, VTR or a non-broadcast video source which is then presented to a video recorder as a single signal, comprising both the Y and the C components. This is known as encoded video, often referred to as composite video. It is then necessary to separate the luminance and chrominance data held on the video tape as part of the recording process. This separation of the Y and the C signals is achieved by feeding the composite video signal through two sets of filters. These filters function by allowing only certain frequency ranges of the signal to pass through. At playback, the Y and C signals are again combined to give a composite video output from the VTR, only to require a further filtering process within the TV monitor to separate once more the Y and C signals which are then fed to the electron guns that generate the display on the monitor screen.

This process of combining, separating and re-combining the Y and C signals impairs the quality of the signal at every stage, with a resultant deterioration of the original signal's bandwidth which defines how much information can be sent over a given time. This adversely affects the resolution and signal-to-noise ratio of the final signal that is displayed to the user.

However, in the high quality Super VHS (S-VHS) video system, the signal damaging process of combining and separating the Y and C signals several times is virtually eliminated by the Y/C connecting system (Fig. 6.2). With this, the S-VHS system can split the Y and C signals and process them separately before recording them on to tape. The same is true for the playback of the tape. This has separate Y and C outputs

which pass through the recorder and out to a TV monitor which accepts separate Y and C signals (i.e. it is fitted with a miniature 4-pin connector known as the “S-connector”); thus filtering for colour separation is not required.

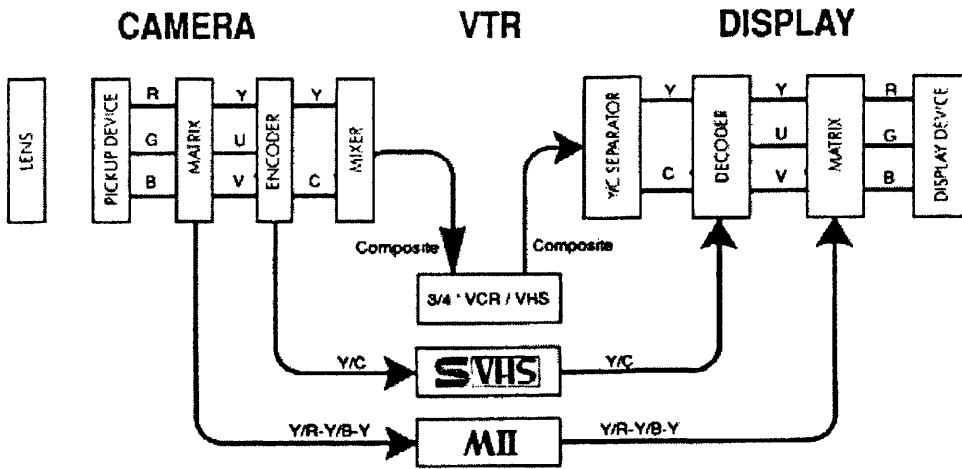


Fig. 6.2. The separation of Y and C signals with the S-Video system (JVC, 1988).

The net result of this separate processing of the chrominance and luminance is the elimination of cross-colour disturbance and dot interference. Cross colour disturbance occurs when the displayed image shows flickering on fine-striped patterns. Dot interference takes place when consecutive dots appear along the boundary between colours.

6.3.4 PC Video Standards

In the Personal Computer (PC) domain, quite different video standards have been developed over time to ensure the compatibility of graphics cards, video display monitors and software. Today, the most important are the VGA (Video Graphic Array) and the Super VGA (SVGA) standards (Transtec, 1997). The resolution of the VGA standard is 640 x 480 pixels, whereby 16 (2^4) out of a palette of 256 (2^8) colours can be displayed at the same time. An additional mode allows for the display of the full 256 colours; however the resolution is then limited to 320 x 240 pixels.

Extended VGA or Super VGA (SVGA) allows for a higher resolution of 1,024 x 768 pixels. In order to display 16 out of 256 colours, a graphics card memory or video memory of 512 kbytes is required. With 1Mbyte of video memory on the card, a possible range of 256 colours out of a palette of 16.7 million ($2^8 \times 2^8 \times 2^8$) colours can be displayed. There are a number of SVGA modes that are possible with 1Mbyte of video RAM. These are given in Table 6.4 below. If a larger video memory is available on the graphics card, then either a higher resolution can be reached on the display monitor or a larger range of colours can be displayed.

Video RAM	Display/Pixels	Colours
1Mbyte	1,280 x 1,024	16 (2^4)
"	1,024 x 768	256 (2^8)
"	800 x 600	65,536 (2^{16})
"	640 x 480	16.7M. (2^{24})

Table 6.4. SVGA modes used with 1Mbyte of Video RAM.

6.3.5 Workstation Video Standards

For workstations, the video standards of the PC domain are of little importance. The graphics cards available in the high-performance Digital, HP, IBM and SGI graphics workstations support resolutions from 1,024 x 768 and 1,280 x 1,024 to a maximum of 1,600 x 1,280 pixels at varying refresh rates which are an indication of how often the picture displayed on the monitor is re-drawn. The higher the rate, the more stable the image on the monitor appears. Optimal refresh rates start at about 72Hz; this is the level where the eye cannot detect flicker, thus limiting eye strain. The graphics cards used with the SPARCstations and their clones usually support a resolution of 1,152 x 900 pixels with a refresh rate of 66 or 76Hz. The Leica digital photogrammetric workstations by Helava use the Connectware Rasterflex graphic card in certain SPARCstation models. Rasterflex uses the default video format of 1,152 x 900 pixels (@66Hz). However, it can support other video formats including 1,024 x 768 (@76Hz), 1,152 x 900 (@76Hz), 1,280 x 1,024 (@60Hz), 1,280 x 1,024 (@67Hz) and 1,280 x 1,024 pixels (@76Hz). Their colour ranges lie between 256 (2^8) and 16.7

million (2^{24}) individual colours. The Intergraph IMD integrated digital photogrammetric workstation which has the InterMAP 6887 Image Station as its base provides stereoscopic viewing on a 24 bit true colour 27 inch diagonal monitor with the 120Hz image rate used by the StereoGraphics CrystalEyes stereo-viewing system.

6.4 Synchronisation and Transmission of Video Signals

The synchronisation and data transmission of analogue (video) signals requires that a certain amount of information must be transmitted so that a receiver can either synchronise or receive the pictorial data. The information required for complete data transmission comprises the following:

- (i) the analogue (video) data;
- (ii) the zero reference and range reference of the analogue video data (black and peak white reference);
- (iii) the sampling times used (pixel clock);
- (iv) the start of a new line (horizontal synchronisation);
- (v) the start of a new field/frame (vertical synchronisation); and
- (vi) if interlaced, an indication of the first and second field.

The specification of the voltage levels, the impedance and the polarity of the signals are also required for the design of the electronic elements. From this information, a receiver can reconstruct the original image through digitisation of the analogue data, irrespective of the number of pixels per line, lines per field, fields per frame and radiometric level and range that it may possess.

6.4.1 The Composite Video Signal

As already discussed above, the timing characteristics and voltage levels of composite video signals are defined in standards such as RS-170 and CCIR. It can be seen from Table 6.2, that, although they differ with respect to timing characteristics such as frames per second, number of lines per field, etc., basically they are based on and

employ the same principle. The following discussion can thus be restricted to the CCIR standard.

In the CCIR video standard, the interlacing is arranged so that the centre-to-centre spacing of adjacent lines in the time domain is two or more times the spacing of adjacent lines in the spatial domain. The basis of 2:1 interlacing is depicted in Fig. 6.3. This shows that a single frame (image) consists of two fields. The even field contains all the even numbered lines and the odd field those with odd line numbers.

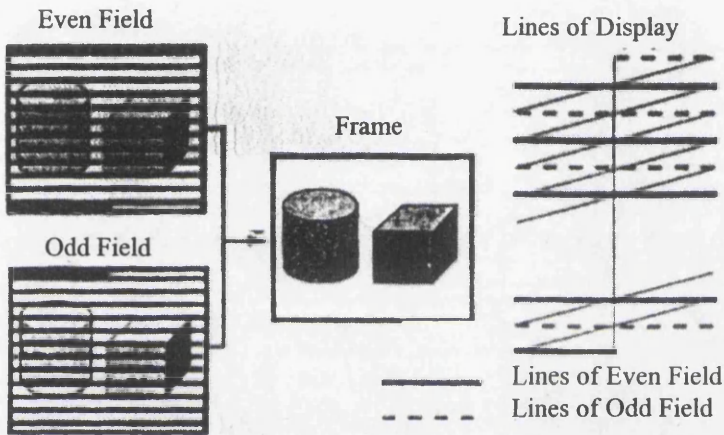


Fig. 6.3. Frame and fields used in interlaced video (Beyer, 1990)

Fig. 6.4 shows the composite video signal with its synchronisation signals and pictorial information. A frame (image) consists of two fields that are transmitted alternately each 25 times per second resulting in 25 full frames being displayed per second. The start of each field is indicated by a vertical synchronisation signal (field sync, vertical sync, vsync). There are 22 hsync periods at the start of fields, called the vertical blanking or field blanking period, during which time, equalisation pulses, broadcast pulses and lines without pictorial information are transmitted. Equalisation and broadcast pulses are used to perform the vertical retrace on video monitors, while the lines without pictorial information contain the vsync signal used by frame grabbers. The period from vsync to vsync is 312.5 hsync periods or 20msec.

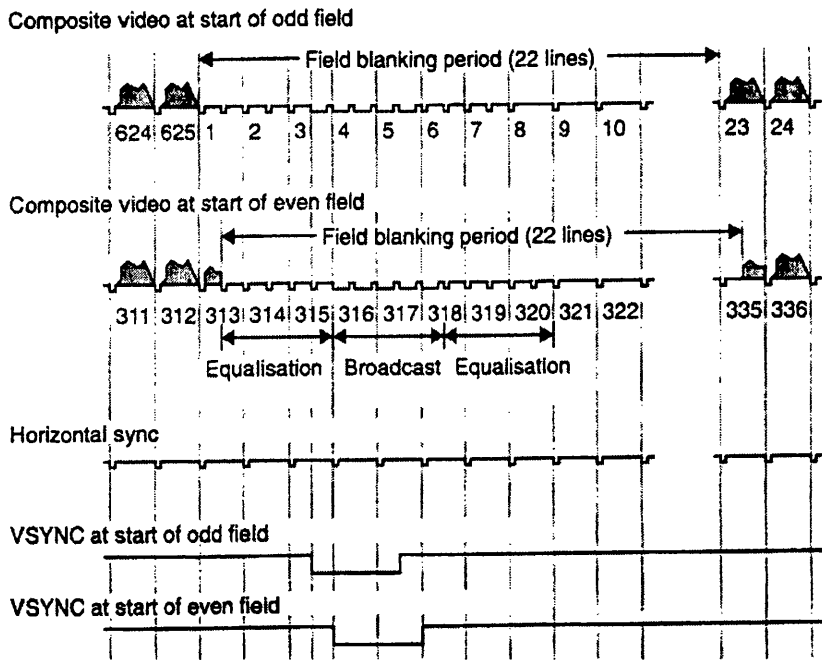


Fig. 6.4. The CCIR video format with synchronisation signals (Beyer, 1992)

Lines of video data are separated by the horizontal blanking period, which consists of a front porch, a line sync pulse and a back porch as shown in Fig. 6.5. The start of a line (or row of an image) is referenced to a level on the falling edge of the line sync pulse, called the line synchronisation signal (line sync) or horizontal synchronisation (hsync), defined by the falling edge of the line sync pulse. This edge is not sharp and requires precise level detection and signal stability for horizontal synchronisation.

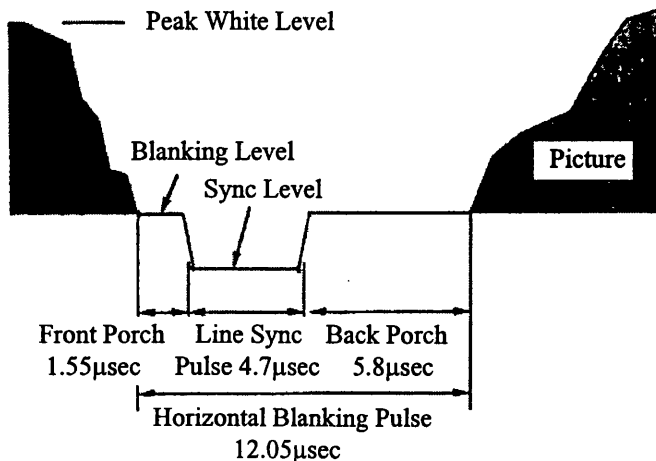


Fig. 6.5. Horizontal synchronisation pulses (Beyer, 1990).

The timing signals incorporated in composite video define the geometric properties of the image transmission (Beyer, 1990). The origin of the y-axis for each field is given by the vsync pulse and the origin of the x-axis is defined by the hsync signal when using an image coordinate system with the x value given in rows and the y value in columns. The spacing (scale) is defined by the steps from line to line. Errors in the detection of the vsync signal have no influence as long as they are smaller than one line time, which is usually the case. Nevertheless, the scale is not explicitly transmitted in x and causes the line jitter effects that will be discussed later.

The radiometric properties of an image are encoded as voltages with respect to the blanking level. Any error in the detection of the blanking level on the backporch shifts the grey level of the following row. The lack of a peak white reference for the definition of the range requires an exact calibration of both the transmitter and the receiver with respect to this range. The lack of this reference gives the possibility to freely select the analogue offset and gain before the A/D conversion takes place, thus transforming the image radiometrically.

6.4.2 Other Synchronisation Signals

Composite sync has identical synchronisation signals to those of composite video (standard video signal), but contains no video data (pictorial information). It is frequently used to synchronise several cameras with one another. The vertical synchronisation signal (vsync) indicates the start of a field and has a period of 20msec. It can be used to synchronise cameras to acquire images at the same time. The horizontal synchronisation signal (hsync) indicates the start of a new line and has a period of 64msec. Both are rectangular periodic signals and have, depending on the implementation, different reference levels, impedances, high/low ratios and polarity. The pixel-clock is a periodic signal with a frequency identical to the sensor element clock. It can have a phase shift with respect to the transmitted data. This must be able to be accommodated by the frame grabber. The pixel-clock provides for a transmission of the scale with each line.

6.5 Conclusions

In this chapter, the various standards for the analogue video signals that are output from infrared video imagers have been dealt with. Thus, the characteristics of those signals that are used to transmit, store, process and display the infrared image have been fully covered. In addition, the main radiometric and geometric properties of video signal transmission and synchronization and their impact on the infrared image that is used for later processing have been discussed. However, for the computer processing of the infrared images that are generated by the analogue video signals, they have to be converted to digital form. This conversion - which has a great importance for the later evaluation of the infrared images - is carried out by a frame grabber that is installed in a PC or other computer. In the next chapter, this analogue-to-digital (A/D) conversion of the infrared images by the frame grabber will be explained in detail.

CHAPTER 7: ANALOGUE VIDEO TO DIGITAL CONVERSION

7.1 Introduction

Analogue-to-digital (A/D) conversion plays an important part in the calibration, processing and measurement of infrared images. In this process, the analogue image acquired by a video-based infrared imager is transformed into digital form which is an ordered matrix of discrete grey values. This conversion is performed using a frame grabber in conjunction with the signals generated by an analogue video imager.

A frame grabber is typically a printed circuit board equipped with processing and memory elements that is designed to reside in a host computer (Fig. 7.1). The purpose of a frame grabber is to sample the output from a VTR which is transmitting over a cable an analogue video signal that is in a broadcast or other television standard. The samples collected by the frame grabber are converted to digital form and loaded into an on-board solid state digital memory which can then be accessed by the host computer. Stored as a contiguous array of intensity values, the fields or frames are assembled into a digital image composed of pixels structured according to the line and pixel organization given by the video standards.

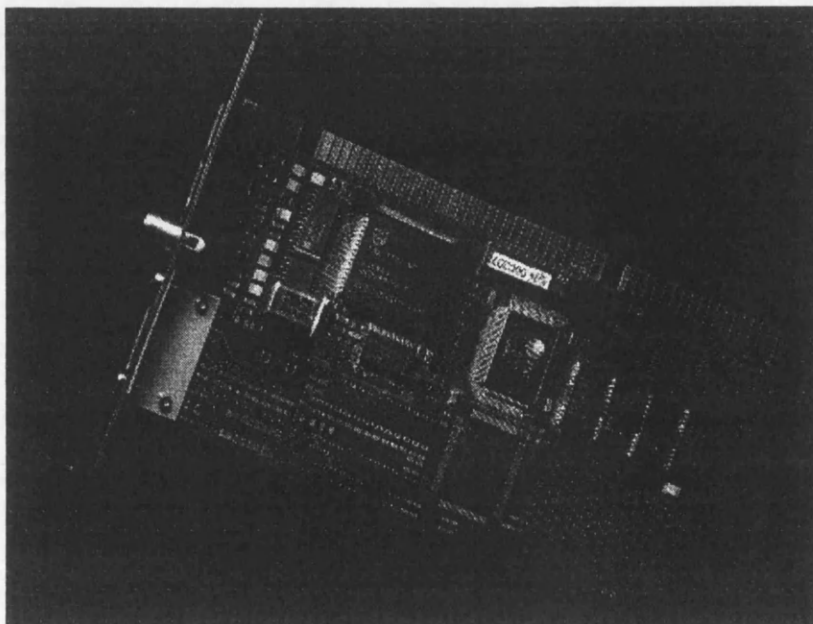


Fig. 7.1. Shark II frame grabber for standard video signals.

A large number of frame grabbers with widely differing characteristics are available on the market. Although they are special purpose devices for image acquisition and conversion, they often incorporate processing capabilities and so they will include image data storage and processing elements. Their input capabilities, synchronisation methods, pre-processing facilities, resolution and speed of A/D conversion, type and amount of on-board memories, processing units, and output capabilities are some of the factors that determine their performance. With respect to their image acquisition capabilities, they can be grouped into slow-scan devices; frame grabbers used in conjunction with cameras that have standard video outputs and extended synchronisation capabilities; and frame grabbers for multimedia applications.

The characteristics of the frame grabber are of great importance to this project for the following three main reasons.

- (i) As was discussed in Chapter 5, the frame grabber is one of the main parts of the system that has been used throughout this research.
- (ii) All analogue video images have to be digitized by a frame grabber before any processing can be done - since all the measurements carried out in this research have been made on images that are in digital form.
- (iii) The A/D conversion of video images can change their radiometric and geometric characteristics - which are the main concern of this project.

In this chapter, the pre-processing of analogue video signals, the synchronisation of the video signals and the conversion of these signals to digital values in the frame grabber will be explained broadly. In addition, the frame grabbers that have been used in this project and their characteristics will be reviewed. Finally the digital-to-analogue (D/A) conversion of digital images to display them on a video monitor and the processing hardware required for this operation will be examined in some detail.

7.2 Monochromatic Frame Grabber

Fig. 7.2 shows the basic components of a monochromatic frame grabber. The analogue front end consists of the input and impedance matching unit and the DC-

restoration and analogue pre-processing section. The analogue front end provides a raw video signal to the sync separator and a pre-processed video signal to the A/D converter. The synchronisation section comprises the sync separator, synchronisation detection, internal sync/address generation, and the generation of synchronisation signals for the output to external devices such as cameras, strobe light, etc. The A/D converter receives the pre-processed video signal, the sampling clock, and reference voltages. It performs the A/D conversion and passes the data on to a data buffer, typically via a latch. The buffer can be memory that is synchronised with the detector clock or FIFO (First In First Out) device. The signal output section contains the output drivers to send signals to those external devices that have to be synchronised.

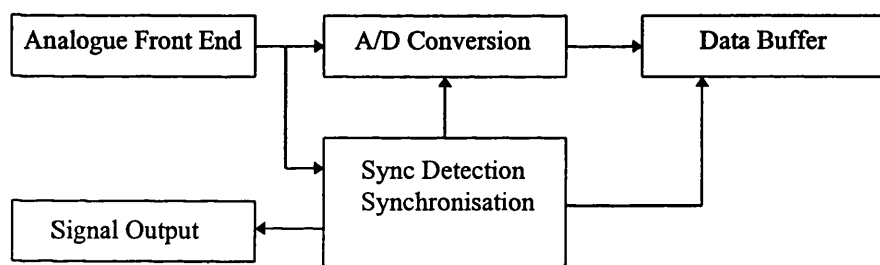


Fig. 7.2. Typical image acquisition components of a frame grabber (Beyer, 1992)

7.2.1 Analogue Front End

The analogue front end, as shown schematically in Fig. 7.3, performs a number of important analogue processing tasks. The input to the frame grabber can be a composite video signal (black-white, colour, S-VHS,.....) or it may consist of video and other synchronisation signals such as hsync, vsync and pixel-clock. The video signal is typically terminated at 75 ohm and is AC-coupled from the camera. The synchronisation signals require considerable flexibility to adjust the input impedance and threshold level for signal detection. This has been found generally to be a problem for the pixel clock. Some cameras can drive a 300 ohm termination with TTL (Transistor-Transistor Logic) levels, but some deliver only a 1Vpp (Volt peak-to-peak). The input must be well-designed to eliminate any imprecision in signal detection at this stage (Raynor and Seitz, 1990). Any improper termination can cause ringing through signal reflections (Beyer, 1992).

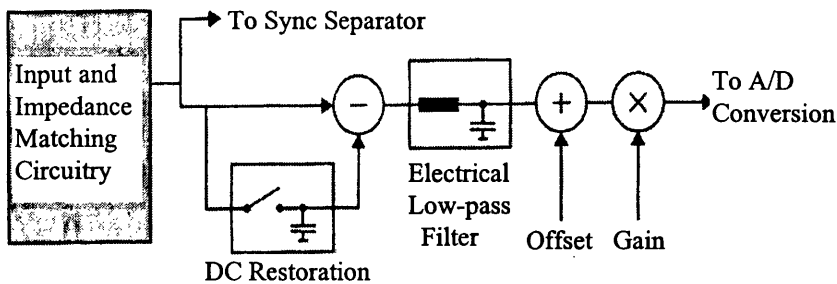


Fig. 7.3. Analogue front end (Beyer, 1994)

After passing through the input and impedance matching circuitry, the signal is split. One path leads to the sync separation, which removes the pictorial information from the signal and passes the resulting composite sync signal to the synchronisation section; the second path leads via analogue pre-processing elements to the A/D converter.

Another part of the processing carried out in the analogue front end is DC-restoration (or black level clamping). This serves to adjust the video signal to a defined voltage level. This part of the analogue front end is very important because all the other parts of the device use the signal that is restored and delivered by it. Thus it carries out basic processing of the infrared video signals that make up the digital infrared images that will be used for later stage of this project. The DC-restoration is achieved by subtracting the voltage found at the back porch - defined to be at a level of 0 volt - from the signal. It is often implemented via a sample switch to discharge the AC coupling capacitor at the back porch. Raynor and Seitz (1990) showed that this can lead to clamping errors. Therefore, they designed another DC restoration circuit with a sample and hold and one using a feedback loop to assure accurate DC restoration. The sample and hold device samples the video signal at the back porch during a time determined by the clamping pulse. The feedback loop uses the video signal after the video amplifier and the black level reference of the A/D converter to derive a precise and stable DC restoration via its feedback loop. Other problems associated with DC-restoration are the timing and precision of the sampling at the back porch as well as the stability of the voltage to be subtracted.

The electrical low-pass filter (LPF) that forms part of the analogue front end serves to suppress high frequency disturbances such as clocking noise as well as other degradations induced during transmission. It is often designed for much lower frequencies than the ones used, inducing a strong asymmetric impulse response and ringing. Some newer frame grabbers provide for a selection of electrical LPFs, such that they can be adapted to the requirements of a particular situation.

The analogue offset and gain controls serve to adapt the analogue video signal to the input range of the A/D converter. The analogue offset and gain should not be changed during an application since they change the radiometric characteristics of the resulting imagery (Beyer, 1992).

7.2.2 Synchronisation

The steps to be performed by the sync detection and synchronisation elements depend on the exact signals used and the synchronisation method employed in the frame grabber. Different methods are used, either employing composite video alone or using it in connection with a pixel-clock signal. The respective methods are called PLL (Phase-Locked-Loop) line-synchronisation (see Fig. 7.4) and pixel synchronous sampling. Both synchronisation modes require the removal of the pictorial information by the sync separator and that of the equalisation and broadcast pulses by the csync (composite sync) conditioning circuitry. Frame grabbers with PLL line-synchronization have been used throughout this project.

7.2.2.1 PLL Line Synchronization

With PLL line-synchronisation, the resulting hsync signal is fed to the phase-locked-loop. This generates the (internal) sampling clock and is controlled through the feedback of an internal hsync, generated by dividing the sampling clock by the desired number of pixels per line (hsync to hsync).

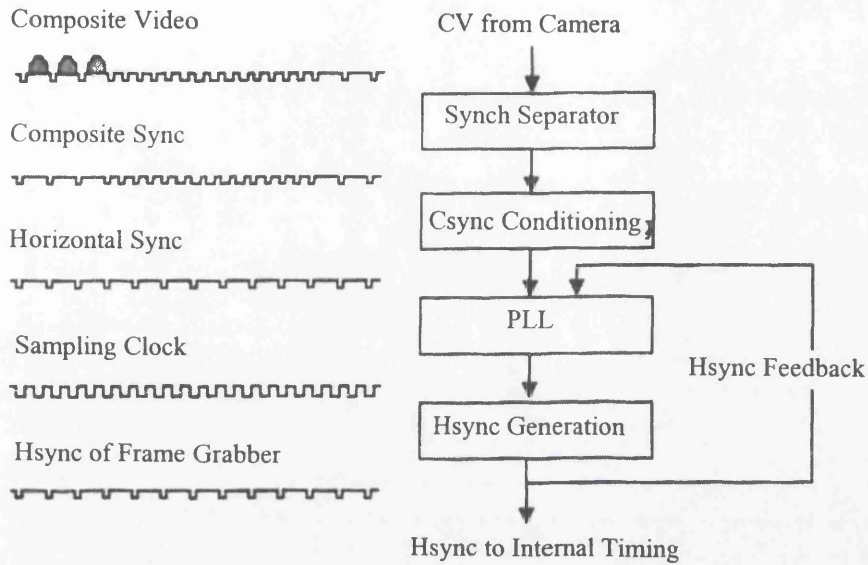


Fig. 7.4. PLL line-synchronization (Beyer, 1992)

Any imprecision in the phase comparison and the PLL control loop will result in a displacement of the sampling position, the result of which is called line jitter (Beyer, 1992). Its occurrence or non-occurrence is a measure of pixel timing consistency. A frame grabber using the PLL design offers at best $\pm 10\text{ns}$ line jitter (Data Translation Ltd., 1995). It is a problem encountered with all standard video sources including cameras and video tape recorders (VTRs). When used with these devices, the frame grabber must generate its own pixel-clock, and lock this clock to the sync signals provided by the input device. Line jitter occurs when the frame grabber fails to make its free-running pixel-clock change instantly to synchronise with the horizontal sync signal that starts the digitisation of a new line. This reduces the line-to-line consistency. Fig. 7.5 shows the line jitter of an image grabbed from a VTR.



Fig. 7.5. Line-jitter shows for an image grabbed from a VTR (Beyer, 1992).

Fig. 7.6 depicts some of the effects resulting from lack of synchronization with a PLL. They are: (i) the shear of the imagery due to disturbance of the PLL during the vertical retrace; (ii) the line jitter of a magnitude typically larger than 0.1 pixel; (iii) changing scale within each line; and (iv) re-sampling of the video signal at a rate different to that of the detector clock, resulting in a re-scaling in the x direction and various aliasing effects.

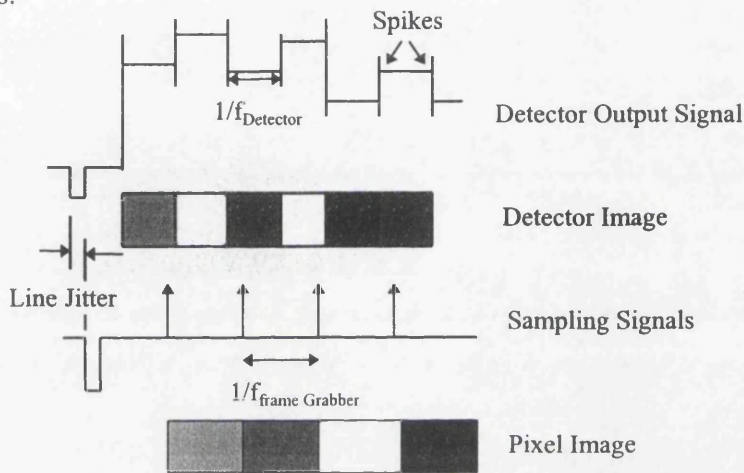


Fig. 7.6. Some effects of frame grabber synchronisation with a PLL (Beyer, 1992).

7.2.2.2 Pixel Synchronous Sampling

To eliminate line jitter and to provide one-to-one mapping of the detector elements to the image pixels, **pixel synchronous sampling** must be used instead of a PLL circuit. Hsync and pixel-clock signals are available from some video cameras and can be accepted as input to some frame grabbers. Fig. 7.7 depicts the main characteristics of pixel-synchronous frame grabbing.

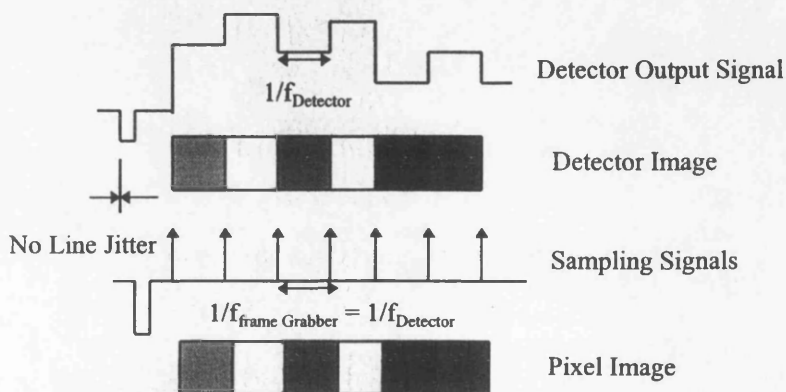


Fig. 7.7. Characteristics of pixel-synchronous sampling (Beyer, 1992).

They are:-

- (i) no line jitter;
- (ii) the sampling clock is identical to the detector clock; and
- (iii) the detector is mapped one-to-one to the image memory.

Table 7.1 compares the three main synchronisation and transmission methods. It shows that a large difference exists between analogue transmission using the PLL synchronization method and the other two techniques - pixel synchronous and digital transmission. The major difference between implementing the pixel-synchronous technique in the video imager with digital transmission versus the execution of pixel-synchronous sampling in the frame grabber is the elimination of noise during transmission in the former case. However, the digital transmission of images is still very expensive and its general availability is limited both by the lack of communication standards for interfacing them to frame grabbers and by the high data transmission rates that are required. Appropriate frame grabbers, or other interfaces with sufficient data rates, are as rare as frame grabbers equipped with a pixel-clock.

Effect	Analogue PLL	Pixel-synchronous	Digital
Line jitter (pixel)	>0.1	none	none
Noise	larger	lower	lowest
Mapping	undefined	one-to-one	one-to-one
Cost	low	low	higher
Standard	yes	plus pixel-clock	partial
Transmission	simple	simple	difficult over long distances for high data rates

Table 7.1. Comparison of signal transmission methods (Beyer, 1992)

7.2.3 Analogue-to-Digital (A/D) Conversion

Both the sampling clock and the pre-processed video signals are passed to the A/D converter for digitisation. There are several methods available for the analogue-to-

digital conversion. The high conversion rate required in video applications makes the parallel or flash analogue-to-digital conversion the most widely used in practice.

As shown schematically in Fig. 7.8, a flash A/D converter consists of a comparator network, an encoding network, and the digital output. Besides the video signal and sampling clock, at least upper and lower reference voltages need to be provided. A flash A/D converter requires a $2^n - 1$ comparators for 2^n quantisation steps, where n is the number of bits or resolution. At the time of sampling, each comparator indicates whether or not the signal is higher than the reference value at the comparator input. The output of the comparator network is the grey code value (Beyer, 1992). It is converted through the use of an encoding network to a binary output.

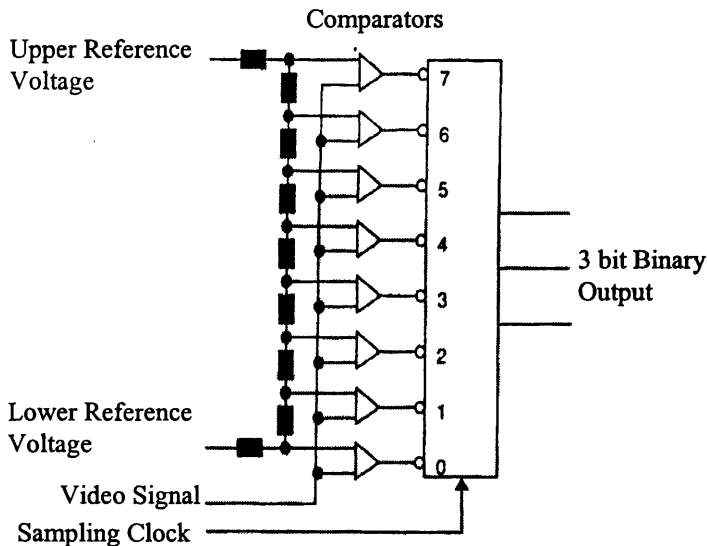


Fig. 7.8. Schematic diagram of a 3-bit flash A/D converter (Beyer, 1994)

The A/D conversion section is the heart of the frame grabbing operation. This process has a decisive influence on the radiometric and geometric characteristics of the infrared images that are delivered to it in analogue form. Hence, it is necessary to describe certain important parameters that are used to characterize the accuracy of the A/D converter which produces the final digital images that will be used for the geometric and radiometric calibration of infrared video imagers.

7.2.3.1 Quantization Error

The quantization error is the basic uncertainty associated with digitizing an analogue signal due to the finite resolution of an A/D converter. It is given by Beyer (1994) as

$$s_{\text{quant}} = \left(\int_{-0.5}^{+0.5} x^2 dx \right)^{-1/2} = (1/12)^{-1/2} = 0.29[Q] \quad (7.1)$$

with Q denoting a quantisation step.

7.2.3.2 Signal-to-Noise Ratio (SNR)

The SNR of a flash A/D converter is computed by

$$\text{SNR} = 20 \log(2^n / (1/12)^{-1/2}) \cong 20 \log 2^n + 11 [\text{dB}] \quad (7.2)$$

However, SNR is also defined by Beyer (1992) as

$$\text{SNR}_{\text{BB}} = 10 \log(\text{sinewave signal power/output noise power}) \quad (7.3)$$

which, for an ideal A/D converter, results in

$$\text{SNR}_{\text{BB}} = 6.02 \times n + 1.76 \quad (7.4)$$

Table 7.2 gives the number of grey level values and the SNR for examples of A/D converters with different resolutions.

Resolution (bit)	Number of grey values	SNR (dB)	SNR _{BB} (dB)
6	64	47	38
8	256	59	50
10	1,024	71	62
12	4,096	83	74

Table 7.2. SNR and resolution of A/D converters (Beyer, 1992)

7.2.3.3 Integral Linearity Error

This particular error value is measured as the deviation of the analogue input values from a line fit and is expressed as a percentage of the full scale range or as a fraction of the LSB (Least Significant Bit). The linearity of a good A/D converter is ± 0.5 of the LSB (see Fig. 7.9).

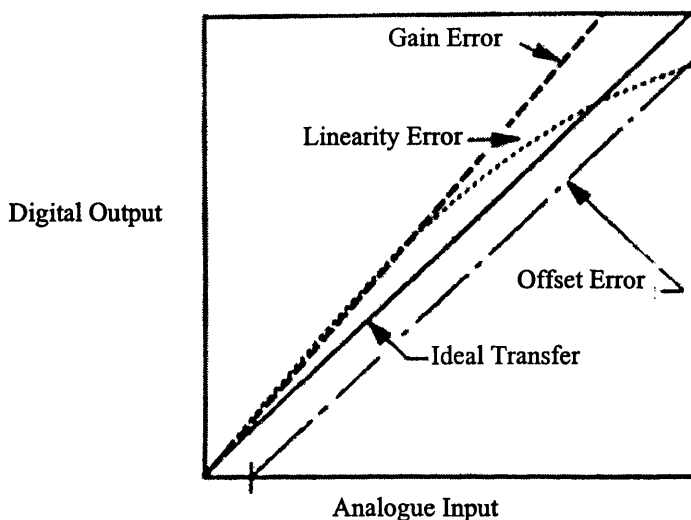


Fig. 7.9. Gain, offset and linearity errors (Gupton, 1986).

7.2.3.4 Differential Linearity Error

This is the deviation of an A/D converter step width from the ideal step width of 1 LSB. A differential linearity error of larger than 1 LSB results in a missing code, which means that one of the 2^n values will not occur.

7.2.3.5 Missing Code

This occurs in an A/D converter when the output code skips a digit. This happens when the differential linearity is greater than 1 LSB.

7.2.3.6 Offset Error

This is the error by which the transfer function fails to pass through the origin, referred to the analogue axis (see Fig. 7.9). This is adjustable to zero in most available A/D converters.

7.2.3.7 Gain Error

This particular error is defined by the difference in slope between the actual transfer function and the ideal function in percent. This is also adjustable to zero in most available A/D converters (see Fig. 7.9).

7.2.3.8 Resolution

The resolution (n) of an A/D converter is the number of bits of the output signal resulting in 2^n digital values to represent the analogue input signal.

7.2.4 Data Buffering

The digitised data and the synchronisation/addressing signals are finally transmitted to the data buffer. The task of data buffering is to provide a means to allow the input of the data from the A/D converter at one rate, to store the data and to read it out at another rate.

Frame grabbers use one of the following three methods for data buffering:-

- (i) Dual ported memory;
- (ii) Double buffered memory; and
- (iii) FIFO (First In / First Out) data buffer.

Dual ported memory provides simultaneous read and write access to the identical data held in the memory. It is more complex than the alternative methods since the hardware must provide for arbitration between the writing into it from the A/D

converter and the external read access. Double buffering has the advantage that no bus contention and arbitration problems can occur. This technique works in an identical fashion to double buffering in computer graphics. One part of the memory is used to write to, while the other can be read. The drawback of double buffering is the reduction in the memory that is available for one of the two tasks if both read and write must be performed concurrently. The simplest data buffer is a FIFO which is a simple intermediate storage buffer. The data is written into the FIFO at the sampling clock frequency and is read out at a specific speed as required by the system. FIFOs are typically used in frame grabbers that are not equipped with image memory.

7.3 Frame Grabbers Used in the Project

Four different frame grabbers have been used in the course of this project. They are:-

- (i) A FOR.A FM60 video frame store;
- (ii) A frame grabber belonging to the Department of Mechanical Engineering in this University;
- (iii) The Shark II frame grabber from the Department of Chemistry in this University; and
- (iv) The VideoMagic frame grabber which is available in this Department.

The FOR.A FM60 monochrome frame store (see Fig. 7.10) accepts analogue video data from the VTR and converts it to digital data which are then stored in its memory. If the image has to be displayed, it is converted back into analogue form using a D/A converter and it is then sent to the display monitor at a refresh rate of 50 fields per second. The size of its digital memory is 512 x 512 pixels with a 6 bit resolution giving 64 (2^6) grey levels of varying intensity. It has been used in the earlier stages of this project to grab the thermal images which had been acquired for the previous project carried out in the Department by Dr. Amin (1986). It was also connected to the video monocomparator used to measure manually the x and y coordinates of the calibration crosses recorded by the thermal infrared images. The aim of doing this was to increase the familiarity of the author with thermal images and to give him a idea

about the distortions inherent in these images. Its main limitation is that it does not give access to the digital data stored in the device and allow its transfer to the computer used for the processing and measurement of the images.

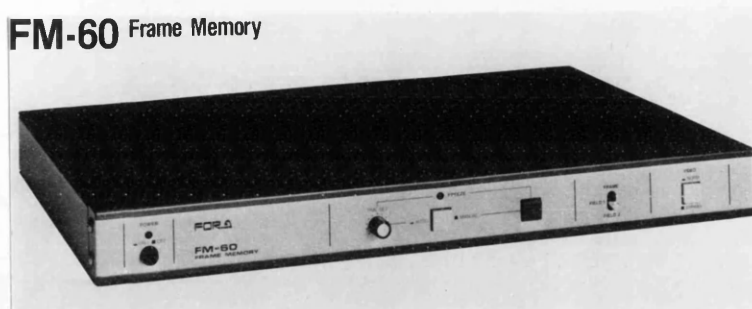


Fig. 7.10. FOR.A FM-60 video frame memory (Amin, 1986).

Later in the project, to validate the main programs that have been developed to carry out the geometric and radiometric calibration of infrared video imagers, a frame grabber that had been constructed in-house by the Department of Mechanical Engineering at this University was used. With this frame grabber, the digitized images were 512 x 512 pixels in format with a grey level range that lies between 0 and 255.

During the main experimental stage of this project, two other frame grabbers have been used. The Shark II frame grabber (see Fig. 7.1) which is available in the Department of Chemistry at this University has mostly been used. This has a 2Mbyte video memory, a 1 Mbyte display memory and compatibility with the all the video standards that were set out in Chapter 5. In addition, its A/D converter has 60dB SNR; $\pm 1/2$ LSB differential linearity error; and ± 1 LSB integral linearity error. It can produce digital infrared images in a 768 x 576 pixel image or format size with a 8 bit resolution giving 256 (2^8) grey levels of varying intensity.

The other one used is the VideoMagic frame grabber which has recently become available in this Department for work being carried out by the author's research colleague, Mr. Yom. It can also produce digital version of video images in a 768 x 576 pixel image size with 256 different grey levels.

7.4 Image Display

Most frame grabbers contain D/A circuitry which converts the digital pixel data back into an RS-170 or CCIR compatible signal for the direct display of the image on a standard video monitor - as was done in the FOR.A device described above. This can be accomplished by the connecting the monitor to the PC computer in which the frame grabber has been installed. Alternatively it can be accomplished by direct attachment of the monitor to the frame grabber so by-passing the computer. Digital-to-analogue conversion for the output of grabbed images provides the means to view the stored or processed image to check the acquisition or processing either on a separate analogue RGB monitor called the image monitor or for display on the PC system monitor.

For monochromatic frame grabbers, the image display hardware consists of an output look-up table (LUT) and a D/A converter. For a colour display of the stored data, three D/A converters are needed. Such an arrangement does not use the LUT since true colour information is inherent in the acquired image; thus the LUT is not needed to enhance the display.

The data from the frame-store memory is sent to an output LUT. The pixel value obtained from the memory becomes an index into the table; the table output values specify the number of grey values that will be displayed. Each location in the output LUT maps to a separate value, the number of bits in the mapped value being a function of the particular board being used.

Image display hardware typically operates in real-time, i.e. a complete frame must be written out in 1/30th second. To accomplish this, special video-signal converters must be used, e.g. in a 512 by 512 pixel frame grabber, D/A converters with a throughput of almost 10Mhz are required (Data Translation Ltd., 1995).

7.5 Processing Hardware

Digital image processing can be implemented either at lower speeds in software or at higher speeds using dedicated processing hardware. Software implementations require the use of the computer system in which the image acquisition hardware board is installed. The host computer takes the pixel values from the frame memory, performs operations on them under instructions from the software program, and returns them to the frame memory. The hardware implementation involves the use of specialized image processing hardware, which is either inserted or mounted on the same board as the image acquisition hardware, or is connected to the acquisition hardware using separate, dedicated data lines. Image processing hardware varies greatly in sophistication, from simple look-up tables to general-purpose floating point processors. Depending on the type of processing hardware provided, all or most of the pixel processing can then be performed without using the CPU (Central Processing Unit) of the host computer.

The simplest processing element is the input look-up table (LUT). The input LUT maps any data value to any other value in real-time, and can be used either for thresholding; for addition, subtraction, multiplication, or division by a constant; or for inverse video. Each input LUT uses the digital data value of the pixel as an input or index into the table. Each index value has a corresponding output value. The output values are determined at the time the output LUT is defined. Note that there is no necessary correspondence between the input or index value and the output value. Increasing index values can map to decreasing output values (as in inverse video); all index values can map to a single value; groups of four index values can map to a single value, which increments (as in grey scale reduction); and so on. The choice is determined by the particular function that the input LUT is intended to serve.

Providing a direct connection between the output of the frame grabber's frame-store memory and the input LUT adds considerable flexibility to the system. Image data can be passed repeatedly through different look-up tables to accomplish multi-step image

processing. Moreover, the addition of an onboard ALU (Arithmetic Logic Unit) or processor permits multi-frame operations to be supported in real-time. The incoming frame data can be combined with a stored frame to add or subtract the two frames. While frame grabber ALU operations typically occur in real-time, they are often restricted to 8-bit resolution because of the frame grabber's memory and data architecture.

Some frame grabbers combine a frame grabber and a frame processor on a single board. For example, the Data Translation DT2867 frame grabber has an onboard 16-bit frame processor. As a result, this frame grabber can perform most processing operations in real-time. The Data Translation Fidelity 200 and Transtech TDM435-436 units both have an onboard TMS34020 graphics system processor to speed up image processing operations as well as implementing the acceleration of graphics images generated by the Microsoft Windows operating system.

7.6 Conclusions

In the previous chapter, the video standards used for the transmission of analogue infrared images have been discussed. In this chapter, the analogue-to-digital (A/D) conversion of these images carried out by a frame grabber has been fully covered. Thus through the discussion in this chapter, one of the main parts of the system that has been used in this project has been described and assessed. In addition, its influence on the calibration of the geometric and radiometric characteristics of digital infrared images that will be used in the later stages of this project have become well understood. In the next two chapters, the actual infrared imaging systems that generate the images and supply the analogue video output will be described. Their main functions that affect the radiometric and geometric characteristics of infrared images will also be discussed.

CHAPTER 8: INFRARED FRAME TYPE (PLANAR) IMAGERS

8.1 Introduction

In the previous chapters, the optical and electronic principles that form the basis of infrared imaging systems; the main characteristics of their output; and its conversion to digital form using frame grabbers have all been outlined and discussed. Through these accounts, the main parts of the systems that affect the radiometric and geometric quality of infrared images have been fully covered also.

A fundamental step in carrying out photogrammetric operations on middle and thermal infrared imagery is the image acquisition process in which images of the object of interest are captured and stored to allow photogrammetric measurements to be made on them. The measurements made on the images are then subjected to one or more photogrammetric transformations to determine the characteristics or dimensions of the objects lying within the object space. In general, photogrammetry relies on optical processes to acquire images. Such images operate typically in the visible or near visible regions of the electro-magnetic spectrum, although other wavelength bands - e.g. these used by microwave radar and radiometers - have been used for specialized applications. However, with all optically-based systems, regardless of the wavelength, a lens system and focal plane are used to record a perspective projection of the object field.

In photography, the image acquired at the focal plane is captured by silver halide based emulsions mounted on a film or glass plate base. Since the science of photography is well established, in general terms, the integrity, stability and longevity of photographic recordings is controllable and predictable. However, for certain applications, the clear disadvantages of conventional photographic emulsions are the time required for photographic processing and the inflexibility of the image record after the process is complete. Of course, there are advantages too, notably the compact storage and the ease of access to and the viewing of the image without need for instrumentation which is important, for example in field work.

The development of the cathode ray tube in 1897 first raised the possibility of non-photographic imaging, but it was not until 1923 that a tube camera was perfected that could acquire images. The arrival of broadcast television in the 1930s paved the way for more widespread use of video imaging. The first attempts at map production using video tube camera systems were made in the 1950s (Rosenberg, 1955). Since those early developments, these systems have been used in a variety of applications such as imaging from space, industrial measurement control, metrology, security systems and model tracking, as well as close range photogrammetry. Video frame scanner systems, based on an optical-mechanical scanning of the field of view for thermal infrared imaging, have found extensive applications in military operations, surveillance and satellite and airborne remote sensing.

Video tube and scanner systems have the disadvantages that, either there are moving parts (as found in scanners) or, in the case of video tube cameras, parts are vulnerable to electromagnetic and environmental influences, especially vibration. In particular, the inherent lack of stability of the imaging tube and the complex optical and scanning components and structure of a video frame scanner may limit the reliability and accuracy of these systems.

Solid-state CCD cameras have recently become available for infrared imaging applications. In these devices, the image is sensed by conversion of the incident photons into an electric charge, rather than the chemical change that takes place in a photographic emulsion or the change in a charge pattern on the target plate of video tube. The substantial advantage of these cameras is that the light or radiation sensitive components are essentially discrete elements and are embedded in a monolithic substrate, leading to higher reliability and the potential for greater geometric accuracy than that obtainable by video tube or scanner systems.

The performance of CCD cameras is continuously improving and they are expected to dominate image acquisition in the future. However, at present, they have poor resolution and have a small dynamic range and a small format size with comparatively

few sensitive elements. In this respect, a solid-state imaging device would have to deliver approximately 20,000 by 20,000 pixels to match the information content of an aerial photographic image and 6,000 by 6,000 pixels to match that of a typical medium format close-range camera (Beyer, 1992). Thus, photography is used to provide very much better recognition of fine details in the visible and near infrared range, but it cannot record images in the middle and thermal infra-red region.

8.1.1 Classification of Infrared Imagers

Based on the discussion above, video imaging devices operating in the middle and thermal infrared region can be classified into three main groups:

- i) Video tube based devices based on the use of the pyroelectric vidicon. These have been used extensively in industrial, medical, surveillance and fire-fighting applications and have similar geometric characteristics to those of the vidicon cameras operating in the visible part of the spectrum.
- ii) Thermal video frame scanners (TVFS) using photon detectors. With these devices, the object space is scanned using optical elements such as oscillating mirrors and rotating polygons, often in combination with a complex optical telescope.
- iii) Infrared CCD cameras employing staring arrays of photon detectors. These devices are equivalent to the video cameras equipped with CCD areal arrays that are available for use in the visible part of the spectrum. Although the difficulties encountered in producing focal plane arrays in the middle infrared region of electromagnetic spectrum are considerable as compared with the situation in the visible part of the spectrum, these devices have recently become available for industrial and scientific applications.

Fig. 8.1(a)(b) shows that all three types of infrared imager produce a discrete frame-type image, as distinct from the continuous strip images (Fig. 8.1(c)(d)) that are

produced from optical-mechanical line scanners or from pushbroom scanners employing linear arrays. These rely on the platform motion, e.g. of an aircraft or spacecraft, to produce a single continuous strip image. However, while the first two types (i.e. the vidicon and CCD-based cameras) produce a planar image (Fig. 8.1(b)), the video frame scanner produces an image on a spherical surface (Fig. 8.1(a)) arising from the scanning action which comprises scans by two optical elements operating at right angles to one another.

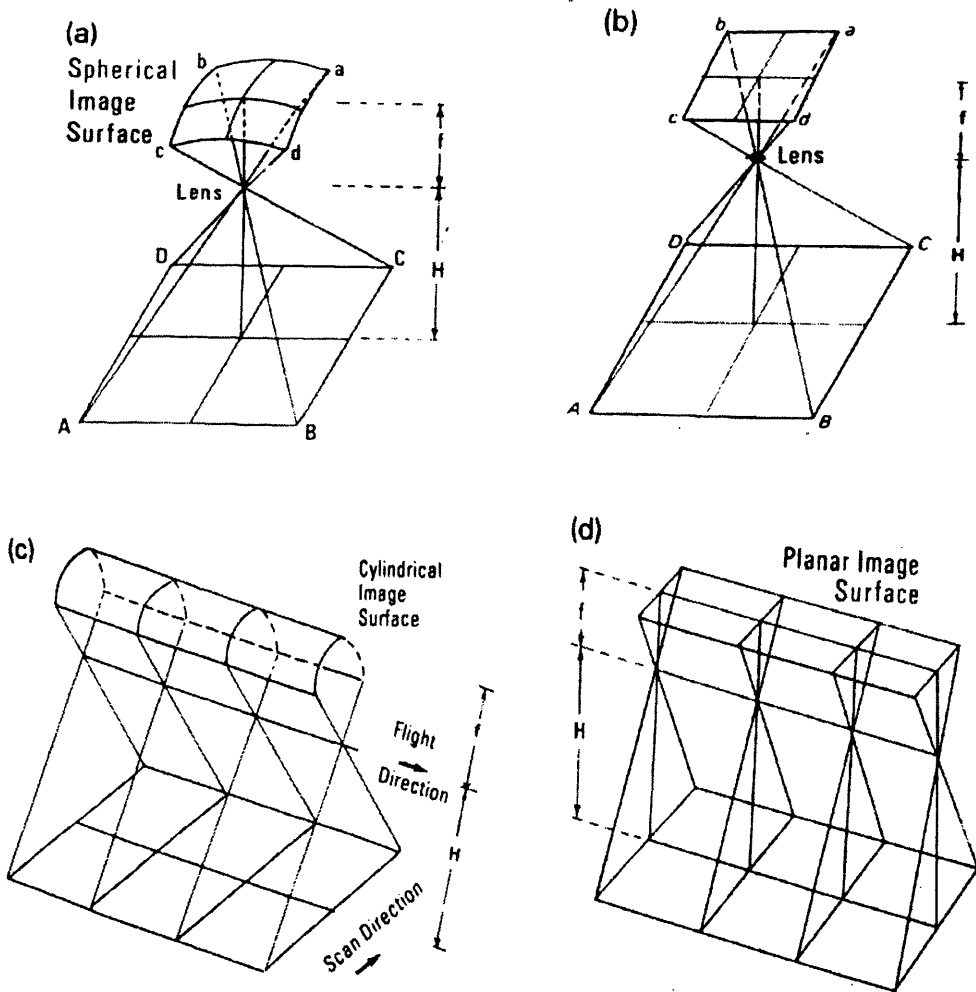


Fig. 8.1. Basic geometry of images from (a) video frame scanner; (b) photographic, video or CCD camera; (c) an optical-mechanical line scanner and (d) a linear array pushbroom scanner (Amin and Petrie, 1994).

Video tube based and CCD areal array imaging systems that operate in the infrared region of the EM spectrum and produce planar images will be described in this

chapter, while infrared scanners will be discussed in the next chapter. Additionally, a summary of recently produced and commercially available imaging systems for each type of imager will be presented in conjunction with tables that summarize the main characteristics of the devices described and discussed in these two chapters.

8.2 Thermal Infrared Pyroelectric Vidicon Cameras

This type of camera is based on the pyroelectric vidicon and forms the basis for a highly successful infrared imager (Fig. 8.2). Thermal radiation from a scene is imaged by a lens on to a thin pyroelectric target after passing through a germanium faceplate. Changes in the temperature of the target due to the thermal scene induce corresponding changes in the surface charges on the reverse side of the target. The state of these charges is then read by a scanning electron beam in much the same way as in a conventional TV camera as explained in Chapter V. The scanning electron beam neutralises the surface charge and so the temperature of the target must be changed once more to produce a new charge distribution before another scene can be imaged.

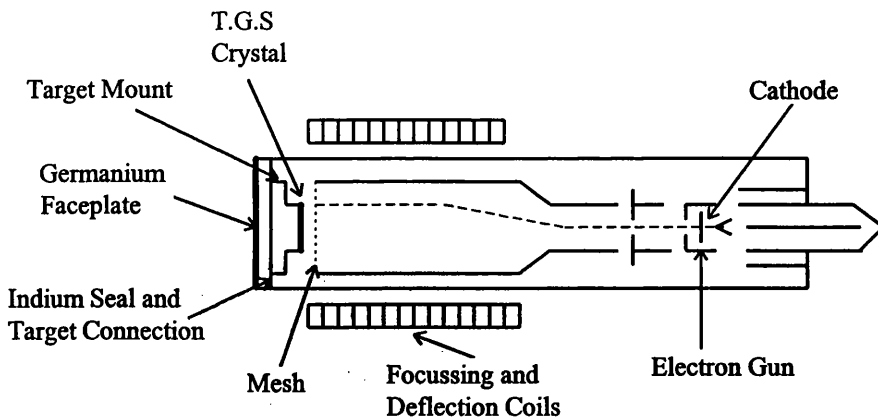


Fig. 8.2. Schematic diagram of a pyroelectric vidicon tube (Burney et.al., 1988).

The vidicon is used either in panned mode or else in conjunction with a chopper running at a TV field rate. In the panned mode, the image on the monitor represents changes in the temperature differences in the field of view, and the picture will disappear if the camera steadily views a constant temperature distribution in the scene.

In this mode, the camera must be oscillated slightly by the user in order to maintain the image. In the chopped mode, a rotating chopper wheel in the camera chops the incoming radiation (Fig. 8.3), and the image effectively represents the scene temperature distribution whenever the viewer is stationary.

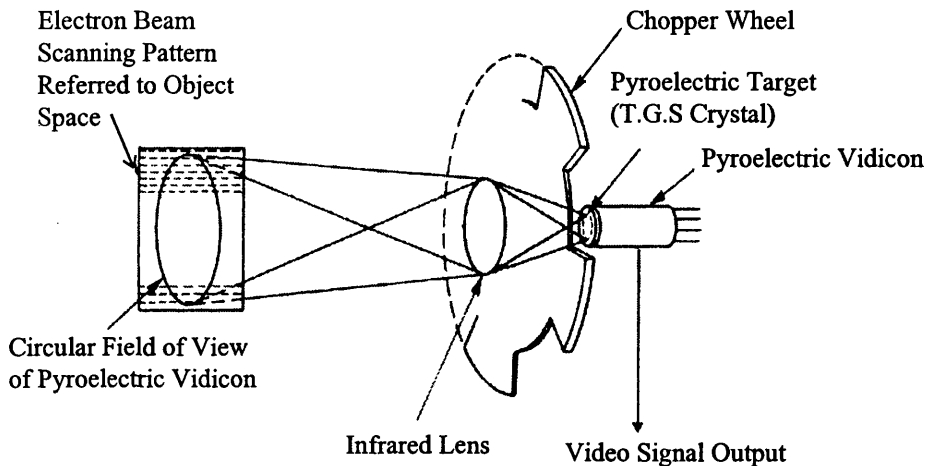


Fig. 8.3. Pyroelectric vidicon with the chopping mode (Wolfe and Zissis, 1978).

The pyroelectric vidicon has resulted in a cheap, lightweight infrared imaging system; in this respect, the fact that it uses an uncooled detector is a considerable advantage. On the other hand, it has a poorer thermal sensitivity and an inferior spatial resolution to that of a conventionally cooled thermal imager such as a TVFS. However it is a suitable infrared imager for use at comparatively short ranges and has proven to be very useful in firefighting operations and to have many industrial uses, especially since it costs much less than the other types of infrared imager.

8.2.1 Image Modulation - Chopping versus Panning Mode

As discussed above, to image a stationary scene, one must modulate the scene radiation pattern reaching the pyroelectric vidicon either with a chopper wheel or by panning the camera. Both methods have advantages. Most reports in the literature say that better minimum resolvable temperature differences result from the use of the panning mode rather than the chopping mode, despite analysis which predicts that a better MTF will result when chopping is used (Wolfe and Zissis, 1978).

8.2.1.1 Lag

Lag is a smear effect that occurs with pyroelectric vidicons when moving objects are viewed in dimly lit scenes. In the chopping mode, the target heats for one frame time, then cools for one frame time. The signal charge does not add up from frame to frame. By contrast, in the panned mode, since there is no chopping of the incoming radiation, the target plate continues to warm up in subsequent frames. So, it steadily increases the signal current that is produced thereby increasing the signal value that is read out. Thus, some of the charges generated by scanning the target in one frame are added to the charge generated in the next frame. By comparison, those pyroelectric vidicons that are used in the chopping mode have a low lag effect.

A second problem relates to the lag effects experienced with a pyroelectric vidicon. If the scene contains, for example, a large object whose temperature is much above the average scene temperature, the corresponding area of the pyroelectric target will reach a high temperature. This area of the pyroelectric target will then take many frame times before it return to an equilibrium temperature, and during the entire recovery time, it will produce a dark area in the displayed image. Thus, in the panning mode, any hot object is followed by a dark or black trail in the image which can and often does mask other scene details.

8.2.1.2 Observer Fatigue

Another drawback to the panning mode is observer fatigue. For many applications, the observer has to move the camera in the panned mode which is a real inconvenience for him. Also, when the image is displayed by the television monitor, the continuous motion over the entire displayed image requires the observer to make a real conscious effort to examine the image and to extract the required information detail, which is also tiring.

8.2.1.3 Compensating Positive Current

In chopped mode, a most serious problem is to provide a compensating positive current to the target surface of the pyroelectric vidicon. As shown in Fig. 8.3, a chopper wheel interrupts the radiation from scene in synchronization with the electron beam scanning pattern so that, in alternate frames, the target views first the scene image framed by infrared lens, then that obscured by the chopper wheel.

If a scene area is hotter than that viewed with the chopper in the open position, the target warms up during the scene exposure, so producing a corresponding positive charge pattern. It then cools during the period when the chopper wheel has closed off the exposure to the incident radiation, so producing a negative charge pattern. This presents a problem in pyroelectric vidicon camera, since normally a low-energy scanning beam reads a charge pattern from the target surface by depositing electrons to charge the surface approximately to the electron gun cathode potential. If a positive charge pattern was read in one frame, the negative charge pattern in the following frame would charge the surface below its cathode potential and no analogue video signal would be produced. For continuing operation, a compensating positive current, which is known as a "pedestal", must flow to the target surface to balance the negative current of signal electrons. It is generally supplied by positive gas ions. A low pressure of hydrogen can be maintained in the tube envelope by electrically heating a hydrogen reservoir. In this case, some of electrons in the scanning beam will collide with gas ions, creating positive ions. The positive ions used for the pedestal current generation are created by the scanning beam in the space between the mesh and the target plate (see Fig. 8.2), and an electron beam scans across the target together with the ion beam generated in this space.

The various characteristics that are discussed above affect the radiometric properties of images taken by the pyroelectric vidicon camera. Therefore, these matters need to be taken into account in the radiometric calibration stage.

8.2.2 Geometric Aspects of the Pyroelectric Vidicon

Vidicon tube camera imagery is generated virtually instantaneously, since the images of the object is first focussed on the camera faceplate and stays there for 1/25sec, during which time, the intra-lens shutter blocks any additional light from falling on the tube while the electron beam of the vidicon tube scans the camera faceplate. Thus basically, the geometry of the imagery produced by a vidicon tube camera corresponds to the geometry of the photographs produced by a photogrammetric frame camera. Difficulties only arise from electronic distortions which must be eliminated by proper calibration. The nature of the electronic distortions inherent in vidicon tube cameras has been given in detail in Chapter V. These electronic distortions were of particular concern in the early investigations carried out by Wong (1969, 1970, 1973, 1975) on the vidicon cameras used from space vehicles. It was found in these investigations that the electronic distortions of vidicon cameras were largely systematic and relatively stable over long periods of time so that corrections were possible, especially if a calibrated reseau was etched on the photoconductive surface of the video tube. It was also noted that a large portion of the electronic distortion was caused by scale differences between the horizontal and vertical axes of the video image. Simple affine scale corrections could remove large amounts of the distortion present in the video image. The remaining, or residual, distortion is then found to be relatively stable with time, even though the scale corrections may themselves vary. Among several approaches for correcting the residual electronic distortion present in the image plane, the use of high order polynomial interpolation was proposed by Wong (1973) and indeed it has been used extensively for this purpose since then.

8.2.3 Commercially Available Pyroelectric Vidicon Cameras

There are many types of pyroelectric vidicon cameras available for users' applications. The technical specifications of some of these cameras are given below in Table 8.1. The main source of information for each camera included in the Table has been the manufacturer's brochure and the patent specification. The main difference in

the design of these various cameras lies in the construction of the vidicon tube and in its resolution.

Model Characteristics	Lentech VideoTherm84	EEV P8092,93,94	Insight 80 Series	Alrad Inst. Ltd. Video Therm300	Lambda Photometrics Ltd. Model 5480
P.E. Tube	Thompson CSF TH-9851 and TH-9855	EEV types 8092 / 93 / 94 or Thompson CSF 9857	2/3" Pyroelectric Vidicon	Pyroelectric vidicon	Pyroelectric vidicon
Wavelength (μm)	8-14 μm	8-14 μm	8-14 μm or 3-5 μm	8-14 μm	8-14 μm
Resolution	238 TV lines	200 TV lines	250 TV lines	-	300 TV lines
Scanning & Video Standard	NTSC standard 2:1 interlaced 525 lines and 60 fields per second	PAL standard 2:1 interlaced 625 lines and 50 frames per second	625/50Hz PAL or 525/60Hz NTSC	625/50Hz PAL or 525/60Hz NTSC	625/50Hz PAL or 525/60Hz NTSC
Lens Focal Length and Aperture	50 mm $f/0.74$	50 or 75 mm $f/0.75$	12.5-75 mm $f/1.8$	-	-
Range of Operating Temperatures	-15 $^{\circ}\text{C}$ to 45 $^{\circ}\text{C}$	-10 $^{\circ}\text{C}$ to 40 $^{\circ}\text{C}$	-15 $^{\circ}\text{C}$ to 30 $^{\circ}\text{C}$	-	0 $^{\circ}\text{C}$ to 40 $^{\circ}\text{C}$
Temperature Sensitivity	0.2 $^{\circ}\text{C}$ (at 25 $^{\circ}\text{C}$)	0.2 $^{\circ}\text{C}$	0.25 $^{\circ}\text{C}$	0.15 $^{\circ}\text{C}$ at 25 $^{\circ}\text{C}$	0.2 $^{\circ}\text{C}$ at 25 $^{\circ}\text{C}$

Table 8.1. Main characteristics of commercially available pyroelectric vidicon cameras.

8.3 Infrared CCD Camera

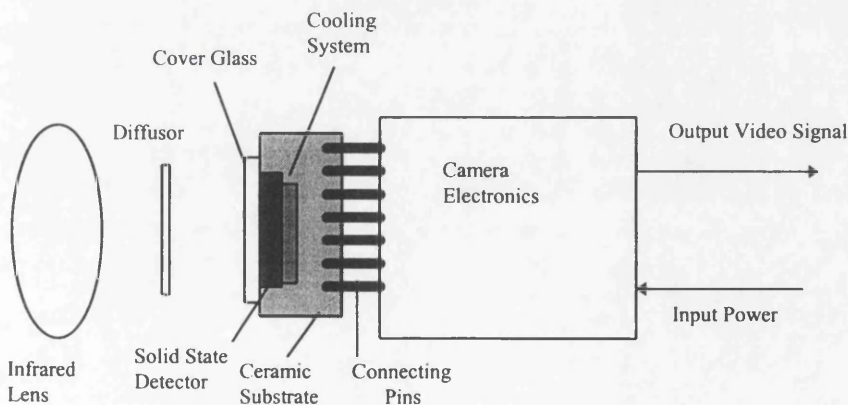
In the Chapters 3 and 4, the fundamental components of infrared CCD cameras (lens, detector system, etc.) have been discussed in some detail. With this account, the overall design and the main structure of infrared CCD cameras, which are one of main concerns in this research project, can be more easily understood. When one compares these with visible solid state systems and cameras, one can, of course, find many differences between them, especially about the materials used in each system. However, much of the electronics and physical structures that are used (including the video output system, charge transfer and read out mechanism, etc.) are almost same in these different systems.

As stated before, CCD-based imagers have become a quite commonly used device for certain photogrammetric applications in the last two decades. They are arranged in linear arrays or in two-dimensional arrays. Linear arrays are used to scan a scene and this introduces time-dependent geometry. Two-dimensional arrays as employed in a infrared CCD camera, provide a complete record of the radiation falling onto a two-

dimensional surface at a particular instant of time. There is a limitation on the size of staring arrays and therefore linear arrays are primarily used for satellite or airborne imagers but two-dimensional arrays are used for these close range applications that can tolerate small format images.

The size of the detector array and the pixel size are the most important characteristics of a CCD camera for photogrammetric use. The size of the array is limited by technology that is currently available. CCD cameras operating in the visible part of the spectrum can have arrays as large as 5,120 x 5,120 pixels and detector sizes as small as 1 μ m can be fabricated (Seitz et al, 1995). However, the size of the arrays that are currently available for infrared CCD cameras is limited to 320 x 240 pixels with a pixel size of 50 μ m. The reasons for this low resolution have been explained in Chapter 4.

Fig. 8.4 shows a schematic of the functional elements of an infrared CCD camera operating in the middle infrared band. As explained in Chapter 3, the lens is a silicon-based glass which is fitted to the camera body by a screw thread. However, this type of lens is not as highly transmittive as the germanium lenses that are used with the thermal video frame scanner.



8.4. Schematic diagram of the infrared CCD camera.

Between the lens and the detector are one or more optical elements. A diffusor, often a birefringent quartz plate, is found in most cameras using interline transfer detectors. It

acts as an optical low-pass filter to suppress aliasing. The detector is located on a ceramic substrate and usually protected by a glass plate. The diffusor and cover glass are not always accounted for in the lens design. If they are ignored, they can decrease the imaging performance of the system. The cooling system that minimizes the detector noise and increases the dynamic range of the detector, is installed in the main body of the camera.

The assembly of the detector and lens is sometimes not too stable - which is a rather serious defect if the camera is to be deployed on photogrammetric operations. In some CCD cameras, it was found that there is no direct connection between the detector and the lens mount (Beyer, 1992). The detector is only kept in place by the pins on the electronics, which are loosely attached to the camera housing. If present, then this defect has to be taken into account in the geometric calibration process of the camera.

CCD cameras that are operated in the visible and infrared bands of the EM spectrum can also be differentiated according to their output signal characteristics. Most of the visible CCD cameras can transmit the images using digital signals which are already in a form suitable for computer processing. However, as the author of this thesis can testify, the transmission of images from commercially available infrared CCD cameras can only be achieved using the analogue video signals that have been fully discussed in Chapter 6. The reason for this is that there is no mechanism (A/D converter) available inside the camera that can convert the analogue signals that are generated by the detector system to the corresponding digital form. So, in the infrared region of EM, invariably images have to be transmitted using the video signals that are characterized by the broadcasting television standards. Detailed information about these standards and analogue video signals have already been given in Chapter 6. As can be seen from the next section, all the available infrared CCD cameras use signals which adhere to the PAL and NTSC television standards to transmit the images. In addition, as explained in Chapter 7, all of these analogue images have to be converted to digital form by an A/D converter to be suitable for computer processing.

8.4 Commercially Available Infrared CCD Cameras

Infrared CCD cameras have passed from the military into the civilian domain where they are now being used routinely by a wide variety of users. These cameras are used especially in close range applications such as medical and certain specific industrial applications. The performance characteristics of the currently available infrared CCD cameras known to the author are given in Table 8.2. These specifications have been obtained from the brochures issued by the companies manufacturing these cameras. The important differences between these cameras lie in the type of CCD detector used and its resolution.

Model	Agema 550	Agema 510	Amber AE-4128	Amber AE-4256
Characteristics				
Detector	FPA	160 element linear array	Photovoltaic staring InSb FPA	Photovoltaic staring InSb FPA
Pixel resolution	320 x 240	160 lines per field	128 * 128	256 * 256
Pixel size(μm)	-	-	43 * 43	38 * 38
Cooling	Stirling engine	Thermoelectric (Peltier effect)	Liquid nitrogen	Liquid nitrogen
Operating temperature	-15 to 50°C	-20 to 55°C	0 to 40°C	0 to 40°C
Spectral response	3.6 to 5 μm	3 to 5 μm	1 to 5.5 μm (3 to 5 μm with filter)	1 to 5.5 μm (3 to 5 μm filter)
Video output	PAL, NTSC S-Video	PAL, NTSC	PAL, NTSC	PAL, NTSC
Lenses	10° x 7.5° / 1.5m 20° x 15° / 0.5m 40° x 30° / 0.3m	18° x 9° / 0.7m	-	-
Temperature sensitivity	0.1°C at 30°C	0.1°C at 30°C	<20mK	10mK

Table 8.2. Characteristics of solid-state cameras operating at middle infrared wavelengths.

Model	Amber Radiance PM	Hadland Photonics PRISM	Mitsubishi IR-300	Mitsubishi IR-M500
Characteristics				
Detector	Photovoltaic InSb FPA	PtSi Schottky Barrier FPA array	PtSi Schottky Barrier FPA array	PtSi Schottky Barrier FPA array
Pixel resolution	256*256	320*244	256*256	512*512
Pixel size(μm)	50	-	-	-
Cooling	Liquid nitrogen	Stirling cooled	Stirling cooled	Stirling cooled
Operating temperature	0 to 50°C	-10 to 55°C	-10 to 50°C	-10 to 50°C
Spectral response	3-5 μm	3-5 μm	3-5 μm	3-5 μm
Video output	PAL, NTSC	PAL, NTSC	PAL, NTSC	PAL, NTSC
Lenses	11° / 1.5m	-	-	-
Temperature sensitivity	0.025°C	0.1°C	0.2°C(27°C)	0.15°C(27°C)

Characteristics of solid-state cameras operating at middle infra-red wavelengths.
(Continued)

As can be seen from Table 8.2, there are quite a number of CCD cameras now available which operate in the middle infrared part of the electromagnetic spectrum. These cameras have been only begun to appear for infrared imaging applications since the end of the 1980s. Thus many are quite new - for example, the Agema Thermovision 550 hand-held infrared cameras were only introduced to the market in 1995. This camera has been used in this project. Another CCD camera that has been used in this research is the Amber Radiance PM. More detailed information about these specific cameras and their geometric and radiometric characteristics derived from the author's calibration work will be given in Chapter 15.

8.5 Conclusions

This chapter has described the essential elements of the frame-type vidicon and CCD based imaging systems (i.e. cameras) that operate in the middle and thermal infrared bands of the electro-magnetic spectrum and will be used in the course of this project. The next chapter (IX) will explain the thermal video frame scanner TVFS that is the other available class of infrared imaging system. As mentioned before, it has a quite different geometry to that of the planar type of infrared imaging systems that have been described in this chapter. In addition to this account, those other devices that operate using optical-mechanical scanner techniques in the thermal infrared region of E.M will be described together with their geometric and radiometric characteristics.

CHAPTER 9: INFRARED SCANNER IMAGERS

9.1 Introduction

In the previous chapter, video tube and CCD based cameras, which produce frame-type planar images, have been discussed in some detail. Thus the essential elements that affect the geometric and radiometric characteristics of these infrared imaging systems have been fully covered.

In this chapter, firstly, infrared optical-mechanical line scanners will be dealt with, with an emphasis on their geometric characteristics. The main features of line scanners that are operated in airborne and spaceborne applications will be described only briefly since they fall outwith the scope of this project. As mentioned in the previous chapter, this type of imager produces continuous strip images which, from a geometrical viewpoint, have either a cylindrical or a planar (but non-frame) imaging surface. In this case, line scanners image the object field in one direction only, while the forward motion of the platform advances the scan pattern to build up the single continuous strip image.

Secondly, the thermal video frame scanners (TVFS), which are extensively used in thermal imaging applications, will be described and their main functions discussed in more detail since they fall very fully within the scope of the author's research project. As explained before, this type of imager generates a frame-type image which has the basic geometry of a spherical surface. By contrast with the line scanners, a TVFS scans the object in two dimensions in the object space using two scanning mirrors or prisms to produce individual video frame images which are not dependent on the motion of the platform. Thus, entire frames of image data are captured from a single exposure station with the TVFS rather than a single line as in the case of the line scanner.

9.2 Optical-Mechanical Line Scanners

The principle of operation and construction of the optical-mechanical line scanner is shown in Fig. 9.1. An oscillating plane mirror is used to scan the ground line-by-line in the direction perpendicular to the flight path, while the forward motion of the platform allows the exposure of successive lines to build up a single strip image of the terrain. The radiation received from the ground is focussed onto the sensitive area of the detector. This detector transforms the received radiation into an electrical signal whose intensity is proportional to the amount of the received radiation. The analogue signal is recorded on video tape, and may be used to modulate a light beam moving across a CRT to produce a "quick look" hard copy image that is generally recorded on a continuous strip of moving film.

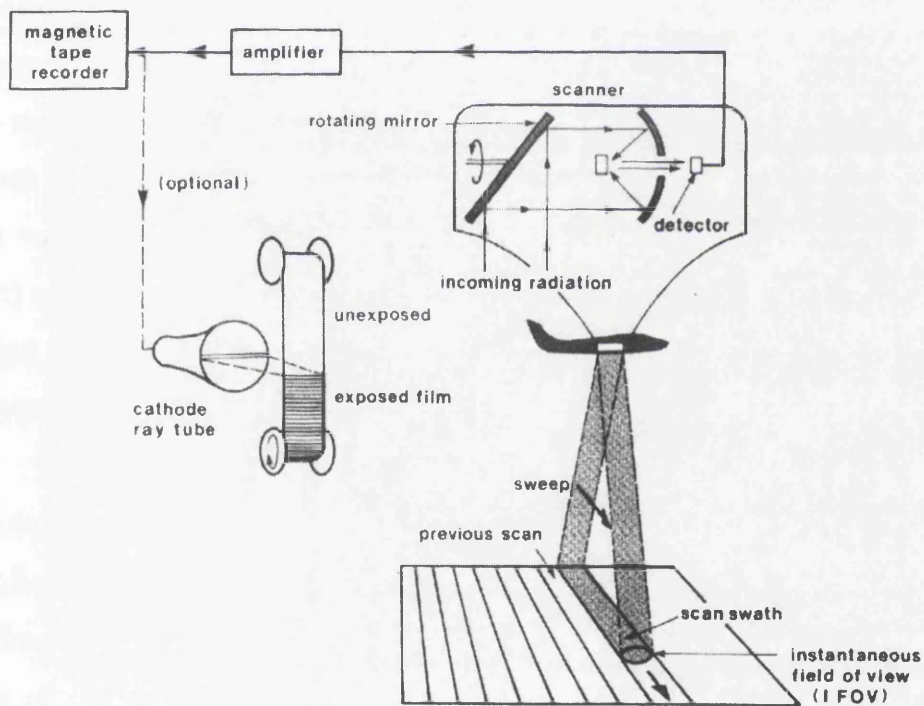


Fig. 9.1. Components of a optical-mechanical line scanner (Kennie, 1985)

9.2.1 Airborne Infrared Line Scanner

Airborne infrared line scanning is that branch of remote sensing concerned with measuring the radiant temperatures of Earth surface features using detectors operated from an aircraft. The equipment used is a thermal infrared linescanner which consists

essentially of an optical system to focus the thermal radiation received from the ground on to suitably sensitive detectors. Those which are most commonly used are mercury cadmium telluride (HgCdTe) in the 8 to 14 μ m band; indium antimonide (InSb) in the 3 to 5 μ m band; and mercury doped germanium (Ge:Hg) in the 3 to 14 μ m wavelength band. The output from this type of imager is recorded on magnetic tape for later playback and production of imagery. Several airborne infrared linescanners are currently in use in the U.K. They include the EMI Airscan; the Hawker-Siddeley 201 / 204 / 214 series; the Daedalus DS-1250 and DS-1230; the Bendix BTM; and Texas Instruments RS-310 scanners.

9.2.2. Geometry of Optical-Mechanical Line Scanner Imagery

The basic geometry of the line scanner imagery produced by a rotating optical system (using rotating lens, mirror or polygon) has been shown in Fig. 8.1(c). The oscillating plane mirror scans in the cross track direction, while the forward motion of the platform allows for the successive scan lines to build up a continuous strip image which will take a cylindrical shape. The imagery produced by a linear array (push broom) scanner will have a quite different geometry (see Fig. 8.1(d)) but will not be discussed here since no infrared imaging devices have as yet been produced using this arrangement.

In the scan direction the instantaneous area scanned by the scanner is a function of the flying height (H), the IFOV (α) and the scan angle (β). This area is represented on the reproduced image by a constant pixel size equal to the value $f.\alpha$, where f is the focal length of the scanner as shown in Fig. 9.2(a). This is done regardless of the scan angle. The result is a gradual decrease in the image scale away from the centre of the strip in the y -direction as shown in Fig. 9.2(b).

In the flight direction (x -direction), the dimension of the instantaneous area imaged in a single scan also increases away from the centre of the strip. If the scanned strips are continuous on the ground along the centre line, successive scanned lines or strips will

overlap away from the centre line (Fig. 9.2(c)) and this will result in a constant scale along the image x- direction (Isong, 1987).

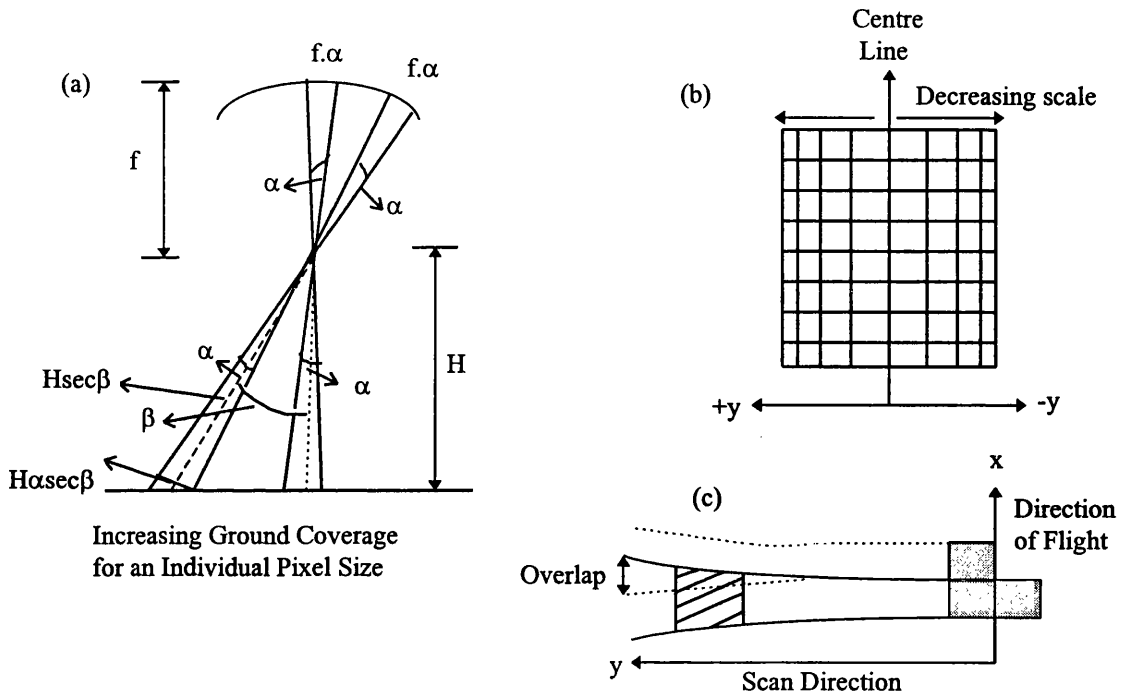


Fig. 9.2(a) Scanning effect; (b) Scale change; and (c) Overlap between the successive scanned lines (Isong, 1987).

9.2.3 Multispectral Line Scanners

The multispectral line scanner (MSS) is similar in principle and operation to the simple optical-mechanical line scanner described above. The main difference lies in the separation of the incoming radiation into several spectral channels by means of a diffraction grating or prism. These direct the radiation from each spectral band to the corresponding detector. Depending on the specific model of MSS being used, one or more of these detectors will often operate in the infrared part of the EM spectrum. The output signal from each detector can be recorded on a magnetic tape or used to generate an image on a CRT in the same manner as with the simple line scanner.

In recent years a considerable amount of interest has been shown in the use of airborne MSS systems. The Environmental Institute of Michigan (ERIM) started work in this field in 1965 and this led to the development of an eleven-channel scanner

covering the wavelength range from 0.38 to 12.25 μ m. Several other organizations also developed airborne scanners, but it was not until relatively recently that airborne MSS data become available. Quite a number are operated in the U.K on a commercial basis.

Some of the specific features likely to be encountered in airborne scanner systems include:

- (i) Inaccurate navigation and atmospheric turbulence can give rise to departures from nominal flying path, the specified constant altitude of the platform and the desired altitude of the scanner with consequent effects on the resulting images; and
- (ii) Aircraft systems give limited areal coverage as compared with satellite systems, but offer much higher spatial resolution and are usually capable of being operated over a greater number of spectral bands than satellite systems. On the other hand, the images that are produced contain significant relief displacement.

9.2.3.1 Satellite Systems

Those satellites which use some type of infrared line scanner are given in Table 9.1 together with their main characteristics. They are:-

- (i) METEOSAT , a European meteorological satellite;
- (ii) TIROS-N AVHRR (Advanced Very High Resolution Radiometer);
- (iii) HCMM (Heat Capacity Mapping Mission);
- (iv) NIMBUS-7 CZCS (Coastal Zone Colour Scanner);
- (v) SEASAT VHRR (Very High Resolution Radiometer);
- (vi) Landsat MSS and TM (Thematic Mapper) series; and
- (vii) ESA ATSR-1.

Amongst these scanners, those which might be regarded as representative are HCMM and the Landsat MSS and TM series.

Satellite	Channel	Wavelength (μm)	Resolution (km)
METEOSAT	Channel 2	10.5 - 12.5	5.0
	Channel 3	5.7 - 7.1	5.0
TIROS-N AVHRR	Channel 3	3.55 - 3.93	1.1
	Channel 4	10.5 - 11.5	1.1
HCMM	Channel 2	10.5 - 12.5	0.6
NIMBUS-7 CZCS	Channel 6	10.5 - 12.5	0.825
SEASAT VHRR	Channel 2	10.5 - 12.5	5.0
Landsat MSS	Channel 5	10.4 - 12.6	0.237
Landsat TM	Channel 6	10.4 - 12.5	0.120
ESA ATSR-1	Channel 1	3.7	1
	Channel 2	10.8	1
	Channel 3	12.0	1

Table 9.1. Features of commonly used optical-mechanical line scanner (from Cracknell and Hayes, 1991).

9.2.3.1.1 HCMM (Heat Capacity Mapping Mission)

The HCMM was a satellite system designed specifically to evaluate the concept that orbital observations of temperature differences at the Earth's surface at different points in the daily heating/cooling cycle might provide a basis for the estimation of thermal inertia and other thermal properties of surface materials. The satellite was placed in a Sun-synchronous orbit, at an altitude of 620km, bringing it over the Equator at 2 P.M local Sun time. At 40°N latitude, the satellite passed overhead at 1.30 P.M, then again at 2:30 A.M. These times provided observations at two points in the diurnal heating/cooling cycle. The HCMM radiometer used two channels; one in the reflective portion of the spectrum ($\lambda = 0.5$ to $1.1\mu\text{m}$), which had a ground pixel size of about 500m x 500m. A second channel was available in the thermal infrared region, from 10.5 to $12.5\mu\text{m}$ wavelength, and had a ground pixel size of 600m x 600m. The image swath was about 716km wide. The HCMM was launched on 26 April 1978 and acquired data until 30 September 1980. The archive of HCMM imagery is maintained by the National Space Science Data Center (located at the

NASA Goddard Space Flight Center) and provides archival coverage for many mid-latitude regions (including North America, Australia, Europe, and Northern Africa).

9.2.3.1.2 Landsat MSS and TM Series

The Landsat 3 MSS, unlike earlier Landsats, included a single channel (MSS Band 5, formerly designated as Band 8) that was sensitive to thermal radiation in the region $\lambda = 10.4$ to $12.6\mu\text{m}$. Due to the decreased sensitivity of the thermal detectors, the ground pixel size of this band was significantly coarser than that of the MSS visible and near infrared channels ($237\text{m} \times 237\text{m}$ compared to $79\text{m} \times 79\text{m}$). Each of the MSS Band 5 pixels therefore corresponded to about nine pixels from any one of the other four bands. This band in Landsat 3 was designed to detect apparent temperature differences of about 15°C . Although initial images were reported to meet this standard, progressive degradation of image quality was observed as the thermal detectors deteriorated over time. In addition, Band 5 was subject to other technical problems. Because of these problems, the MSS Band 5 thermal imaging system was turned off about one year after Landsat 3 was launched. As a result, relatively few images were acquired using the MSS thermal band and relatively little analysis appears to have been attempted using them.

The Landsat TM also includes a thermal band, usually designated as TM Band 6, which again is sensitive in the wavelength region $\lambda = 10.4$ to $12.5\mu\text{m}$. It has lower radiometric sensitivity and coarser ground pixel size (about 120m) relative to the six other TM bands which have a ground pixel size of 30m .

9.3 Thermal Video Frame Scanners (TVFS)

A TVFS uses an optical-mechanical scanning mechanism over the sensitive area of the detector so that it scans the whole object area lying within the field of view of the scanner. Depending on the detector configuration and the scan mechanism speed, the output from the frame scanner can be a standard TV-compatible video signal that can

be displayed directly on a conventional video monitor and recorded on a standard VTR (see Fig. 9.3).

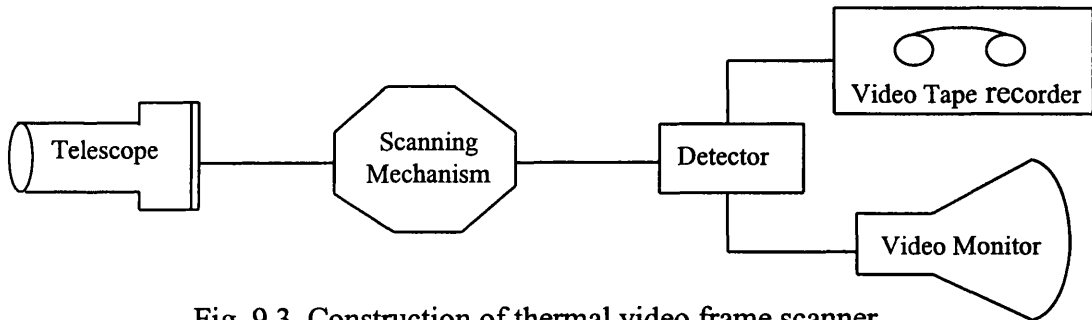


Fig. 9.3. Construction of thermal video frame scanner

Typically, a TVFS can be divided into three main parts:-

- (i) a telescope;
- (ii) a scanning mechanism; and
- (iii) a detector.

The telescope and detector systems have been discussed in Chapters 3 and 4. Thus only the scanning system will be described here.

9.3.1 Scanning Configuration

The scanning configuration employed in thermal video frame scanners may be arranged to utilize a horizontal array of detectors to perform serial scanning; a vertical array of detectors to perform parallel scanning; or a small matrix array to perform serial/parallel scanning.

9.3.1.1 Serial Scanning

In this technique, a serial array or strip of detector elements is scanned over every line in the field in turn as shown in Fig. 9.4. If N elements are used, each pixel will be scanned N times, and the output for the same pixel from each detector will be added and meaned or averaged by a process called time delay and integration (TDI). In this process, the signal from each detector is amplified, delayed by an amount proportional

to the scan speed and inversely proportional to its position in the row and then added together and divided to give an average value for a specific pixel.

The use of the serial scanning technique will yield an improvement in the signal-to-noise ratio (SNR) proportional to the square root of the number of serial detectors (Amin, 1986). However, it still requires an exceptionally high speed scanning mechanism for its implementation.

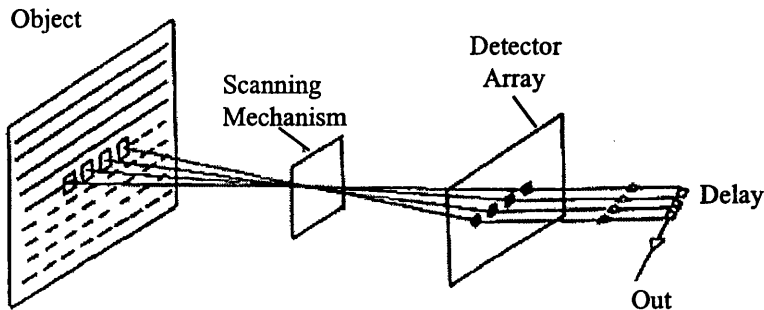


Fig. 9.4. Serial scanning (Amin, 1986)

9.3.1.2 Parallel Scanning

In this method, the image is scanned by a vertical linear array of detector elements as shown in Fig. 9.5. Thus a number of lines in the image plane are scanned simultaneously, i.e. in parallel. Parallel scanning may give a “liney” or “stripey” image if the detectors have varying responses, but it allows a lower scanning speed to be used, thus reducing the electronic bandwidth and facilitating scanner design.

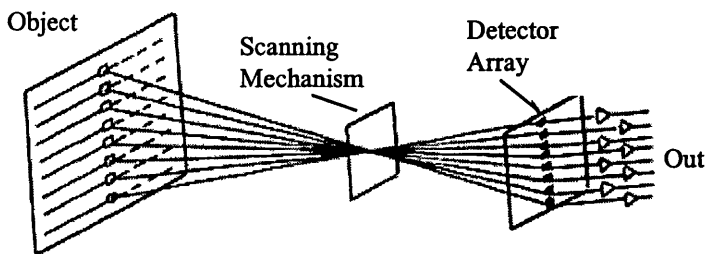


Fig. 9.5. Parallel scanning (Amin, 1986)

9.3.1.3 Serial/Parallel Scanning

In serial/parallel scanning, an areal array or matrix of $N \times M$ detector elements is used as shown in Fig. 9.6 below. This will combine the SNR advantage of serial scanning, together with the practical advantages of the slower scan speed of the parallel scanning technique. However, providing separate connections to all the detector elements requires a very complex electronic circuitry which may be difficult or impractical to implement. This problem was overcome by the use of the SPRITE detector (see Section 4.5.4) devised originally by Dr. C.T. Elliott and developed at the Royal Signal and Radar Establishment (RSRE), Malvern, now forming part of the Defence Evaluation and Research Agency (DERA), Malvern.

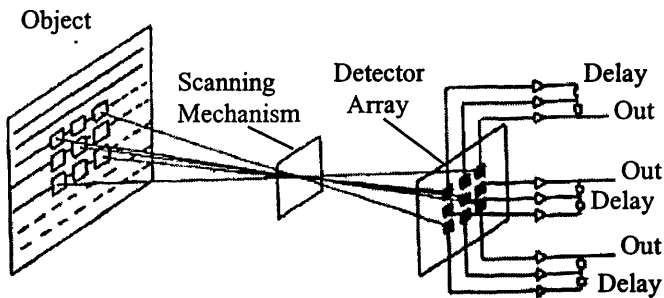


Fig. 9.6. Serial/Parallel scanning (Amin, 1986)

9.3.2 Scanning Mechanism of TVFS

The function of the scanning mechanism is to displace the object image formed by the telescope in such a way that the telescope sequentially scans the object within the field of view. Two scanning elements are required, one to scan the object line by line which is usually termed the frame scanning element, while other scans each line pixel by pixel and is called the line scanning element. The most commonly used scanning elements are:-

- (i) the oscillating plane mirror;
- (ii) the rotating reflective polygon; and
- (iii) the rotating refractive polygon.

A combination of any two of these elements produces a complete scan of the object field in two dimensions.

9.3.2.1 The Oscillating Plane Mirror

As shown in Fig. 9.7, the oscillating plane mirror is a reflective device oscillating periodically in a systematic manner between two stops, so producing a ray angular deviation of twice the mirror scan angle. The oscillating plane mirror is commonly used as the frame scanning element located in front of the telescope.

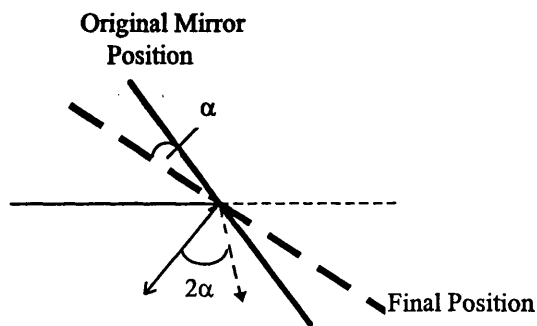


Fig. 9.7. The oscillating plane mirror (Amin, 1986)

9.3.2.2 The Rotating Reflective Polygon

The scanning action of the rotating reflective polygon is similar to that of the oscillating plane mirror except that the polygon sided prism, which has a fixed centre and several facets, moves continuously clockwise. Thus, it produces a continuous scan of the object line by line as shown in Fig. 9.8.

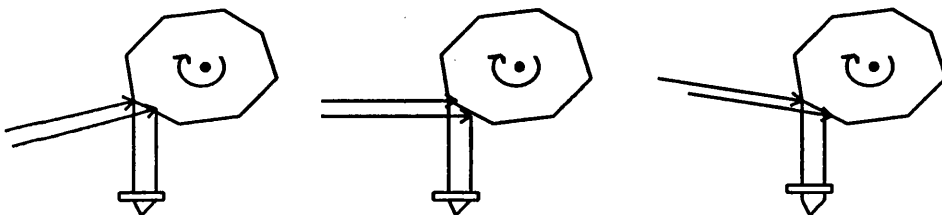


Fig. 9.8. The rotating reflective polygon (Amin, 1986)

9.3.2.3 The Rotating Refractive Polygon

This type of scanning element is made of a material that can transmit infra-red radiation. It produces the scan by laterally displacing the incident ray and sweeping it across the detector or across the second scanning element. If the incident and exitant beams are in the same medium, the angles that both beams make with the horizontal will be the same because the refraction at the first surface is reversed by that at the second surface. The scanning action of the refractive polygon is shown in Fig. 9.9.

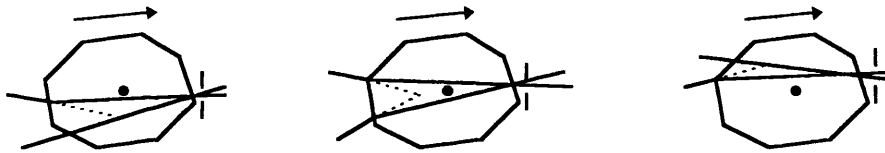


Fig. 9.9. The rotating refractive polygon (Amin, 1986)

Rotating refractive and reflective polygons are commonly used as line scanning elements where they are driven to rotate at very high speed. This speed depends on the number of facets on the prism together with the required frame size (i.e. number of pixels per frame).

9.3.3 Geometric Effects of the Scanning Mechanism

The video image resulting from the action of the scanning mechanism of the TVFS will take the form of a spherical surface with all points equidistant from a single central point, as shown in Fig. 9.10. In this figure, point (a) was recorded in the spherical video image with coordinates x, y . Its corresponding image coordinates in the plane tangential to the video image at its geometric centre are x', y' . The corrected image coordinates of any point (a) can be computed as follows:-

$$\begin{aligned} x'_a &= f \tan \beta_a \\ y'_a &= f \tan \theta_a \sec \beta_a \end{aligned} \quad (9.1)$$

where:-

β, θ are the two scan angles for point a in the frame and line scan directions respectively; and
 f is the equivalent focal length of the scanner.

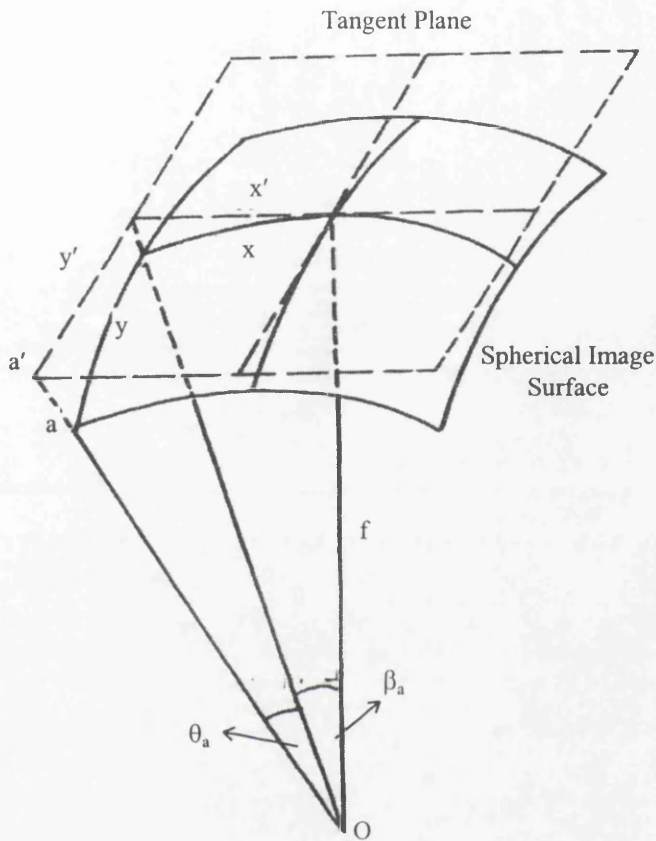


Fig. 9.10. Spherical distortion in a frame scanner image (Amin, 1986)

The effect of the spherical distortion on the image is a gradual change in scale in both the x and y directions from the geometric centre of the image as shown in Fig. 9.11.

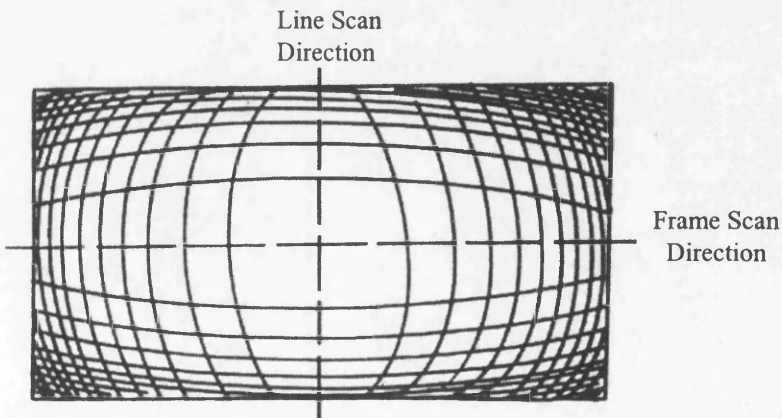


Fig. 9.11. Spherical distortion of frame scanners (Amin, 1986)

In summary, the video image produced by thermal video frame scanners (TVFS) will have the following characteristics:-

- (i) perspective geometry;
- (ii) a spherical imaging surface;
- (iii) low image resolution when compared to the resolution of the photogrammetric frame camera images due to the use of solid-state detectors, but a good resolution when compared with the alternative infrared imagers - based on the use of either the pyroelectric vidicon or the CCD areal array; and
- (iv) electronic distortion caused by the scanner's electronic circuits.

9.3.4 Geometric Potential of TVFS

It is quite labour-intensive to calibrate a TVFS using manual methods since it has a much more complex optical system and there is no focal plane present in a video frame scanner of the type that is present in vidicon or CCD array cameras. Thus there is no possibility of using a method such as an etched reseau as has been done with vidicon cameras. As yet, the study of the geometric characteristics and the calibration of TVFS has only been carried out by Amin (1986) and published by Amin and Petrie (1993 and 1994).

In that study, a special calibration plate, which has a good thermal emissivity to ensure a high contrast between the target images of this plate and its background, was designed and calibrated using a Ferranti monocomparator equipped with high resolution (1 μ m) linear encoders. The four commercially available video frame scanners (see Table 9.2) which were employed in the study included the Barr & Stroud IR-18; the GEC Avionics/Rank Taylor Hobson TICM II; the Rank Pullin Controls RPC and the Agema Thermovision. Images of the target plate on which 130 calibration crosses were etched were taken by each of TVFSs. These were then measured on a video-based monocomparator first described by Petrie (1983).

The set of coordinate values derived from the calibration of the plate using the Ferranti monocomparator were regarded as being error-free. The second set of coordinates from each of the scanner images measured using the video monocomparator contained the various distortions generated by the frame scanner including lens distortion and those generated both by its basic system geometry (i.e. its spherical image plane) and any deviation from its nominal operation, e.g. by its scanning elements. These two sets of coordinate values were analysed using a general 25-term polynomial transformation which was implemented as a FORTRAN program running on an ICL/VME mainframe computer. As a result, two specific transformation polynomials having the form

$$\begin{aligned}x' &= a_0 + a_1x + a_2y + a_3xy^2 + a_4x^3 \\y' &= b_0 + b_1x + b_2y + b_3x^2y + b_4y^3\end{aligned}\tag{9.2}$$

were recommended to compensate for the effects of geometric distortion when measuring video frame scanner imagers.

9.3.5 Commercially Available Thermal Video Frame Scanners

The design characteristics of the off-the-shelf video frame scanners that were discussed and detailed in Amin (1986) have been summarized in Table 9.2. These scanners were representative of the TVFS imagers that were available at that time. Since then, many developments have taken place in the design and construction of thermal video frame scanners. During this period, manufacturers have been endeavouring to ensure better performance for their thermal imagers. The principal developments are as follows:-

- (i) The afocal telescope is now controlled by a microprocessor. This reads the temperature sensors which are incorporated in the objective and eyepiece. Then, using the field of view of the telescope it computes a voltage which is the input to an analogue servo controlling the position of the focussing lens. Thus the telescope remains in focus over the desired range as the ambient temperature changes and as the field of view changes.

Model Characteristics	AGA(Agema)	Inframetrics	Barr&Stroud IR-18	Rank Pullin controls	TICM II
Field of view	20° *20°	28° *21°	38° *25°	40° *30°	60° *40°
Spectral band	8-14μm	8-12μm	8-13μm	8-13μm	8-13μm
IFOV(mrad)	3.4	2.0	1.73	2.1	2.27
MRTD	0.1°C	0.1°C	0.17°C	0.15°C	0.10°C
Detector	1 element InSb	2 element CMT	4 element SPRITE	8 element SPRITE	8 element SPRITE
Scanning	single	paralel	serial/paralel	serial/paralel	serial/paralel
Video format	Non-standard	NTSC	PAL	PAL	PAL
Lines/frame	280	445	500	448	512
Pixels/line	70	400	384	333	384

Table 9.2. Thermal video frame scanners used by Amin (1986).

- (ii) Better scan efficiency has been achieved, thus more pixels per second or pixels per frame can be extracted using the detector once its bandwidth has been determined by the scan rate which should be chosen to maximize the detectability.
- (iii) Considerable reduction in the size of the scan mechanism;
- (iv) An increased number of SPRITE detector elements has been used.
- (v) Integral cooling, such as the incorporation of a tiny Stirling engine is now being employed instead of the use of an external cooling source such as liquid nitrogen.
- (vi) Highly improved electronics have been incorporated which allow comprehensive signal procesing; and
- (vii) Reduced size and weight is a feature of most current TVFS devices.

The main characteristics of those thermal video frame scanners that are currently available on the market are given in Table 9.3. For this table, the main sources have been the manufacturer's catalogues and patent specifications. The main differences in the design of these various scanners lie in the construction and operation of the scanning mechanism in conjunction with the detector configuration.

Between 1980 and 1990, the Agema company introduced the Thermovision 400 and 800 series of thermal video frame scanners especially for condition monitoring. These were mainly low resolution devices when compared to the latest products of Agema. In 1991, the Thermovision 900 came into the market for use in research

establishments. This imager featured higher resolution imaging and more accurate temperature measurement which is vitally important in industrial applications. Agema also entered the security and military surveillance market with the development of the Thermovision 1000 series, offering high resolution imaging over long distances in a manner similar to that of the Barr & Stroud used in Dr. Amin's research work.

Model	Agema 210	Agema 450	Agema 470	Agema 880	Agema 900 SW/TE
Characteristics					
Detector type	Lead Selenide (PbSn)	Single element SPRITE	Single element SPRITE	SPRITE	2 element SPRITE
Cooling	Thermoelectric (Peltier effect)	Thermoelectric (Peltier effect)	Thermoelectric (Peltier effect)	Liquid Nitrogen cooler	Thermoelectric (Peltier effect)
Spectral Response	2-5 μ m	2-5 μ m	2-5 μ m	8-12 μ m	2-5.4 μ m
Frame frequency	15Hz	20Hz	20Hz	25Hz	20-30Hz
Line frequency	-	4kHz	4kHz	2.5kHz	3.5kHz
Lines/frame	48	140	140	280	128
Samples/line	-	-	-	175	204
Temperature range	20 to 800°C	-20 to 500°C (to 2000°C)	-20 to 500°C (to 2000°C)	-	-10 to 500°C (to 2000°C)
Temperature sensitivity	0.1°C(30°C)	0.1°C(30°C)	0.1°C(30°C)	0.07°C(30°C)	0.1°C(30°C)
Operating Temperature	-10 to 55°C	-15 to 55°C	-15 to 55°C	-15 to 55°C	-15 to 55°C
Storage Temperature	-40 to 70°C	-40 to 70°C	-40 to 70°C	-40 to 70°C	-40 to 70°C
Video Output	PAL NTSC	PAL NTSC	PAL NTSC	PAL NTSC	PAL NTSC
Field of view of and focus of the lenses	8° *16°/0.4m	25° *25°/0.4m	7° *7°/1.1m 12° *12°/0.65m 20° *20°/0.38m 40° *40°/0.19m	7° *7°/1.2m 12° *12°/0.8m 20° *20°/0.5m	2.5° *1.55°/20m 10° *6.25°/1.0m 20° *12.5°/0.5m 40° *25°/0.06m

Table 9.3. Specification of thermal video frame scanners

Model	Agema 900SW	Agema 900LW	Agema 1000	Barr&Stroud Ltd. HDTI Variant I	Barr&Stroud Ltd. HPS2000/AB
Characteristics					
Detector type	2 element InSb	SPRITE	5 element SPRITE	8 element SPRITE	8 element SPRITE
Cooling	Cryogenically cooled	Cryogenically cooled	Closed cycle Stirling cooler	Stirling cycle cryogenic engine	Joule-Thompson cooler
Spectral Response	2-5.6 μ m	8-12 μ m	8-12 μ m	8-12 μ m	8-12 μ m
Frame frequency	15-30Hz	15-30Hz	25-30Hz	-	-
Line frequency	2.5kHz	2.5kHz	3kHz	-	-
Lines/frame	136	136	450	422(for 525 line) 525(for 625 line)	-
Samples/line	272	272	565	690	-
Temperature range	-20 to 500°C (to 2000°C)	-30 to 1500°C (to 2000°C)	-	-	-
Temperature sensitivity	0.1°C(30°C)	0.08°C(30°C)	0.16°C(20°C)	0.11K	0.27K
Operating Temperature	-15 to 55°C	-15 to 55°C	-15 to 55°C	-40 to 55°C	-35 to 71°C
Storage Temperature	-40 to 70°C	-40 to 70°C	-40 to 70°C	-57 to 71°C	-57 to 71°C
Video Output	PAL NTSC	PAL NTSC	PAL NTSC	PAL NTSC	PAL NTSC
Field of view of and focus of the lenses	2.5° *1.55°/20m 10° *5°/1.0m 20° *10°/0.5m 40° *20°/0.06m	2.5° *1.55°/20m 10° *5°/1.0m 20° *10°/0.5m 40° *20°/0.06m	5° *3.3° 20° *13.3° 32.4° *21.6°	2.88° *1.88°/80m 9° *6°/80m	1.9° *2.88° 6° *9°

Specification of thermal video frame scanners (Continued)

Model Characteristics	Barr&Stroud Ltd. HPS2000/AFV	Barr&Stroud Ltd. HPS2000/N	Hadland Photonics IQ 812	Metax Varioscan 1010-11 Model	Rank Taylor Hobson Ltd. TALYTERM Thermal camera
Detector type	8 element SPRITE	8 element SPRITE	SPRITE	SPRITE	8 element SPRITE
Cooling	Joule-Thompson cooler	Joule-Thompson cooler	Closed cycle electric	Liquid Nitrogen	Joule-Thompson or liquid nitrogen
Spectral Response	8-12 μ m	8-12 μ m	8-12 μ m	8-12 μ m (1011) 3-5 μ m (1010)	8-12 μ m (standart) 3-5 μ m (special)
Frame frequency	-	-	30Hz	-	25-30Hz
Line frequency	-	-	-	-	-
Lines/frame	-	-	240	-	512
Samples/line	-	-	384	-	-
Temperature range	-	-	-20 to 500 $^{\circ}$ C (to 1500 $^{\circ}$ C)	-10 to 800 $^{\circ}$ C(1010) -40 to 800 $^{\circ}$ C(1011)	0 to 85 $^{\circ}$ C(low) 0 to 1000 $^{\circ}$ C(high)
Temperature sensitivity	0.19K	0.19K	0.06 $^{\circ}$ C	0.1K(30 $^{\circ}$ C)(1010) <0.1K(30 $^{\circ}$ C)(1011)	0.03 $^{\circ}$ C
Operating Temperature	-40 to 71 $^{\circ}$ C	-40 to 71 $^{\circ}$ C	-15 to 55 $^{\circ}$ C	-10 to 40 $^{\circ}$ C	-20 to 50 $^{\circ}$ C
Storage Temperature	-57 to 71 $^{\circ}$ C	-40 to 71 $^{\circ}$ C	-	-	-
Video Output	PAL NTSC	PAL NTSC	PAL, NTSC S-Video (Y/C)	PAL, NTSC S-Video (Y/C)	PAL, NTSC, RGB
Field of view and focus of the lenses	10 $^{\circ}$ *15 $^{\circ}$ 3.3 $^{\circ}$ *5 $^{\circ}$	8 $^{\circ}$ *12 $^{\circ}$ 2 $^{\circ}$ *3 $^{\circ}$	30 $^{\circ}$ *22 $^{\circ}$	-	60 $^{\circ}$ *40 $^{\circ}$ (50Hz) 48 $^{\circ}$ *32 $^{\circ}$ (60Hz)

Specification of thermal video frame scanners (Continued)

In this research project, amongst the lower resolution 400 and 800 series from Agema, both the Thermovision 470 and 880 TVFS have been tested. From the latest series of Agema products, the Thermovision 900 and 1000 imagers has been calibrated as a high resolution TVFS. Although their main characteristics have been set out in the above tables, more detailed information about them, together with the results and analysis from their geometric and radiometric calibration will be given in Chapter 16.

During 1988 and 1989, Barr & Stroud, which is still a leading company in the thermal imaging field, introduced the new the High Definition Thermal Imager (HDTI) to the market. This a TVFS that is targetted at the military surveillance market and has an improved resolution with a better temperature sensitivity when compared with the older IR-18. The author of this thesis has tried to make a experimental tests with the HDTI at the stage of the construction of new target plate which will be described in some detail in Chapter 13. However, due to lack of availability of this imager, he has never been able to take the images of test plate using the HDTI and to calibrate it. However, he has had the oppurtunity to work and test images taken by the older IR-18 which were used for the previous project in this Department. All the work carried out with the IR-18 will be described in Chapter 12.

In addition, Hadland Photonics, Metax and Rank Taylor Hobson have also introduced new high resolution TVFSs which are specifically designed for military applications. Unfortunately access to these imagers was not possible. Nevertheless it is felt that a representative group of TVFS imagers has been tested in this project.

9.3.6 Optical Arrangement of the TVFSs

Despite the differences in design between the various types of video compatible frame scanners, (e.g. in the arrangement and number of detector elements used or the type and speed of the scanning mechanism), they are all based on the same principle in which two mirrors or polygons are used to scan the object field over the sensitive area of the detector in the image space so that the image of the object formed by the telescope is completely scanned. Thus, in this section of the chapter, the optical arrangement of the Barr & Stroud HDTI and Agema Thermovision 1000 TVFSs are presented and discussed as representatives of this class of imagers.

9.3.6.1 Optical Design of the HDTI

The method of forming the images of the objects within the field of view of the HDTI is shown in Fig. 9.12.

- (i) An afocal telescope collects and focusses the emitted radiation from object onto the frame scan mirror which is driven to oscillate at 50 Hz. At any particular moment, the mirror will be directed towards a small area in the object field whose angular size is defined by the scanner's IFOV. The size of the image of this elemental area on the frame scan mirror is known as the frame scan pupil.
- (ii) The image on the frame scan pupil is reflected by the frame scan mirror towards a spherical mirror which in turn focusses the image onto a spherical focal plane.

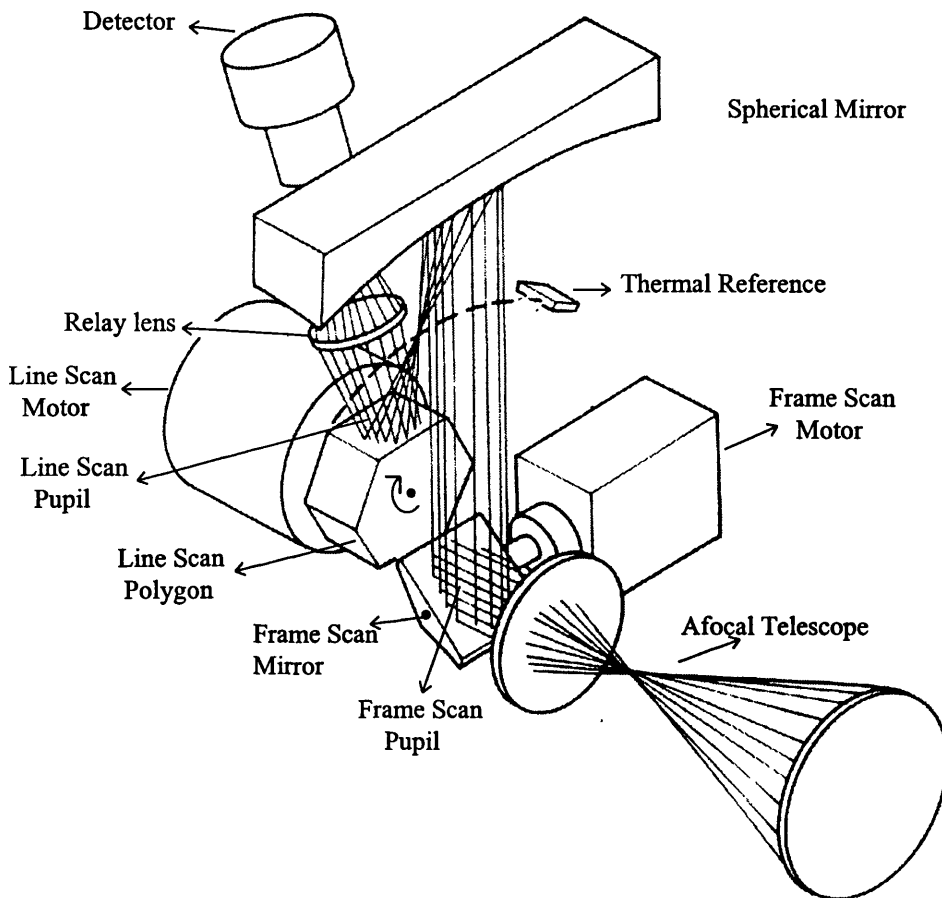


Fig. 9.12. Optical principle of the Barr & Stroud HDTI TVFS

- (iii) The line scan mirror, which is a hexagonal prism, which has 6 facet, is caused to rotate about its axis by line scan motor at a rate of 39,000 rpm, so that it scans the focal plane of the spherical mirror in such a manner that, at any rotational position, the principal axis forming the image defined on the frame scan pupil always passes through the centre of the line scan pupil.
- (iv) The image on the line scan pupil is focussed by the relay lens onto the sensitive area of the detector.
- (v) The HDTI scanner is using an eight-element SPRITE detector to scan the scene from top to bottom and left to right in swathes of eight lines. These swathes overlap by four lines, giving a two-fold overwrite to improve the sensitivity. The scene is scanned from top to bottom and left to right in two interlaced fields at the same rate (see. Fig. 9.13).

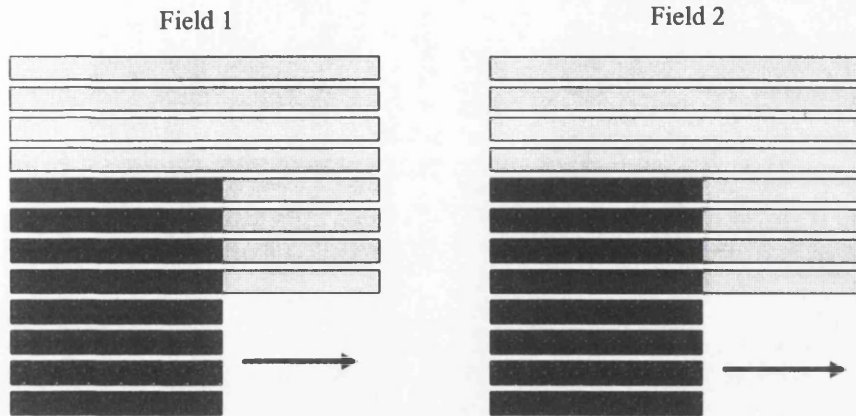


Fig. 9.13. Scan pattern in HDTI

- (vi) The outputs from the eight SPRITE detectors are stored in an analogue storage unit and then read out in a raster form which corresponds to the standard television format.

9.3.6.2 Scanning Arrangement of the Agema Thermovision 1000

Compared with Agema's previous TVFS imagers, the Agema 1000 TVFS uses a redesigned scanner system, - which is called LK-4 (see Fig. 9.14). The first part of this system comprises an oscillating plane mirror (imparting the vertical scan motion), a fixed plane mirror and an aspheric mirror, followed by third plane mirror which projects the radiation on to a rotating polygon that carries out the horizontal scan motion. This reflects the radiant energy on to a second aspheric mirror and then on to a final mirror which reflects the radiation back on to the opposite face of the rotating polygon. From there, the radiation passes through a field-stop into the relay optics of the detector unit which consists of 5 SPRITE detectors and a mini Stirling cooler. These detector elements scan the scene in swathes of 5 lines. The vertical mirror movement provides a 67% overscan that results in the second scan being partially interlaced with the first scan - resulting in improved vertical resolution.

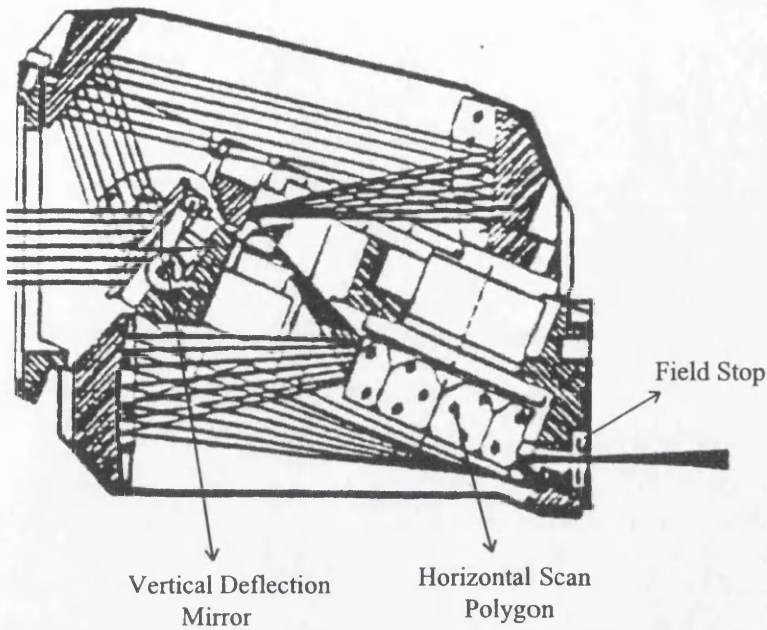


Fig. 9.14. Agema Thermovision Scanning Mechanism

9.4 Conclusions

In the previous chapter, the essential elements of the vidicon and CCD based frame type imagers that operate in the middle and thermal infrared region of the electromagnetic spectrum have been discussed. In this chapter, scanner type infrared imaging systems have been described and their main elements discussed and analyzed. Optical-mechanical line scanners have been covered briefly since they do fall into the category of device that is being investigated in this project. However the basic functions of the TVFS, which has a unique spherical surface geometry and is widely used as a military thermal infrared imager, have been covered in more detail. In the next chapter, the radiometric and geometric characteristics of all infrared imaging systems, which are the main concern of this thesis, will be fully covered in some detail.

CHAPTER 10: GEOMETRIC AND RADIOMETRIC CHARACTERISTICS OF INFRARED IMAGING SYSTEMS

10.1 Introduction

In the previous two chapters, the main types of image acquisition systems that operate in the middle and thermal infrared regions of the EM spectrum have been described. Thus the basic optical and mechanical mechanisms that are used to generate their infrared images have been covered together with the characteristics and effects of their individual elements. In addition, the main characteristics of the CCD and pyroelectric vidicon types of infrared camera and the thermal video frame scanners that are that have been produced recently and are commercially available have been presented in tables. In this chapter, the geometric and radiometric characteristics of these imaging systems, which are the main concern of this thesis and should be established and corrected by geometric and radiometric calibration, will be discussed in some detail.

10.2 Geometric Characteristics

The Field of View (FOV), Instantaneous Field Of View (IFOV), the object resolution element and the lens distortion are some of the more important of the geometric characteristics of an imaging system that need to be considered in photogrammetric operations. In this context, optical resolution and lens distortion have been explained in Chapters 3 and 5; the others will be dealt with here in some more detail.

10.2.1 Instantaneous Field of View of the Infrared Imaging System

Quite different instantaneous fields of view (IFOV) are utilized by scanners and by cameras operating within the infrared part of the EM spectrum.

10.2.1.1 IFOV and FOV of Infrared Scanners

At any instant of time, the detector “sees” the energy within the imager’s instantaneous field of view (IFOV). The IFOV can be expressed as the angular field of

view (α) of the optical system. The projection of this field of view onto the object space defines the area that contributes radiance which will be picked up by the detector.

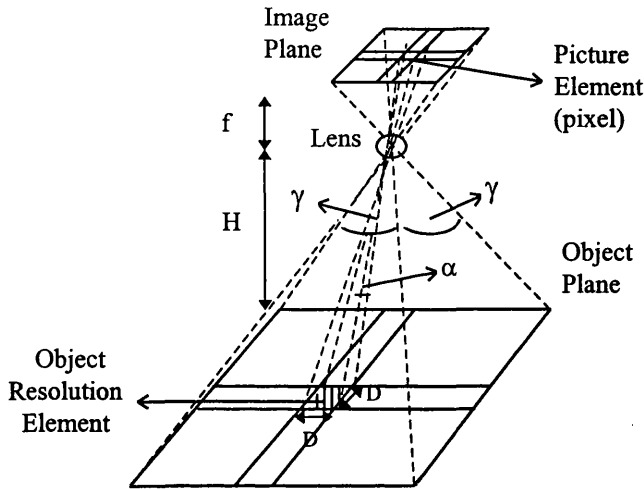


Fig. 10.1. IFOV of an individual detector element used in scanner type imagers.

Fig. 10.1 illustrates the area of the object surface observed when the IFOV of the individual detector element of the infrared scanner imager is oriented directly towards this surface. The width of this surface can be expressed as

$$D = H\alpha \quad (10.1)$$

where:-

D is the width of the object resolution element;

H is the object distance to the imager; and

α is the IFOV of the individual detector element (expressed in milliradians)

Since the infrared scanners scan the object sequentially using a single detector element at one time, the total field of view (FOV) of the scanner is not equal to the IFOV of the individual detector. The FOV - shown as γ in Fig. 10.1 - is the summation of the angular field covered by the detector's IFOV over the period of time of the scan.

However, as shown in Fig. 10.2, the field of view (FOV) of the thermal video frame scanner can be defined by two angles. The angle β subtends the object in the frame scan direction while the angle \varnothing subtends the object in the line scan direction.

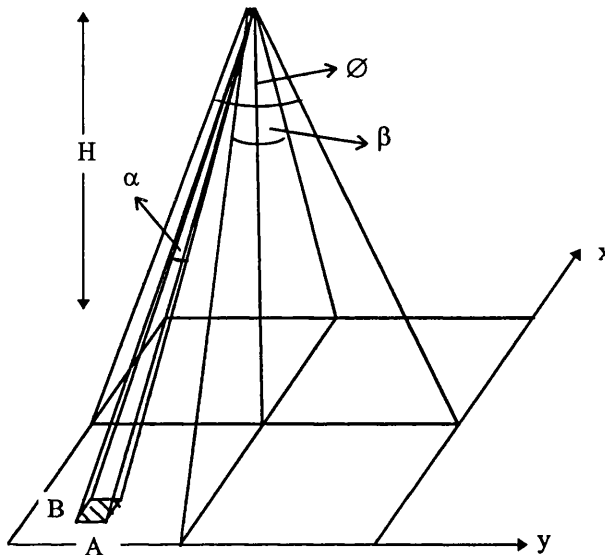


Fig. 10.2. Object resolution element of thermal video frame scanner

The object resolution element at a specific point that is produced by a frame scanner is a function of the distance to the object (H), the two scanning angles (β , \varnothing) and the IFOV (α) (expressed in milliradians). The size of the object resolution element in each direction has been derived by Amin (1986). These were given as follows:

$$A = H \sec \beta \cdot \sec^2 \varnothing \cdot \alpha \quad B = H \sec \varnothing \cdot \sec^2 \beta \cdot \alpha \quad (10.2)$$

As can be seen from Eq. 10.2, the size of the object resolution element changes with the scanning angles when the object distance (H) and IFOV (α) are assumed to be constant. In the centre of the image, where $\beta = \varnothing = 0$, it is equal to the value $H\alpha$ which has been given in Eq. 10.1. Near the centre of the image, the object resolution element is relatively small, near the edge of the image, it is larger. This size variation of the object resolution element has important effects on the interpretability of the image. The output from the frame scanner at any point represents the integrated radiance from all the features lying within the object resolution element. Because the element increases in size near the edge of the image, only larger objects will

completely fill the IFOV and be independently resolved in the image. When an object smaller than the area viewed by the IFOV is imaged, background details will contribute to the strength of the recorded signal. This is particularly important in thermal infrared imaging applications where accurate temperature information is required. For an object to be registered with its proper radiant temperature, its size must be larger than the object resolution element (Lillesand and Kiefer, 1994). However, an advantage of the size of the object resolution element changing towards the edge of the scanned area is that it compensates at least partly for the off-centre radiometric fall-off. If the object resolution element area was constant, then the increased distance between the detector and object would decrease the radiance received by the scanner. But, since the object resolution element area increases with increased distance, the radiance fall-off is partly compensated for and a more consistent radiance is recorded from uniformly radiating surfaces.

10.2.1.2 Trade-off Between the Geometric and Radiometric Resolution of Scanners

As discussed above, a small IFOV is obviously desirable in scanners to achieve good object resolution. This stems from the fact that an object can only be resolved independent of its background when the size of the object is equal to or greater than the size of the object resolution element. Therefore, the smaller the IFOV, the smaller the size of the minimum resolvable scene element. On the other hand, the use of a larger IFOV means that a greater quantity of radiated energy is focused on an individual detector. This permits more sensitive scene radiance measurements due to the higher signal levels. This results in an improvement in the radiometric resolution, or the ability to discriminate very slight energy or temperature differences. Thus there is a trade-off between high spatial resolution and high radiometric resolution in the design of an imager. A large IFOV yields a signal that is much greater than the background noise (unwanted response) associated with any system. Thus, other things being equal, a system with a large IFOV will have a higher signal-to-noise ratio (SNR) than will one with a small IFOV. Again, this results from the fact that a larger IFOV results in a larger dwell time, or residence time of measurement, over any given

object resolution element. For these higher signal levels, spatial resolution is sacrificed at the expense of a better radiometric performance.

10.2.1.3 IFOV and FOV of Infrared Cameras

The resolution of infrared cameras based on the use of a CCD areal array depends on the lens resolution and the number of elements included in the detector array.

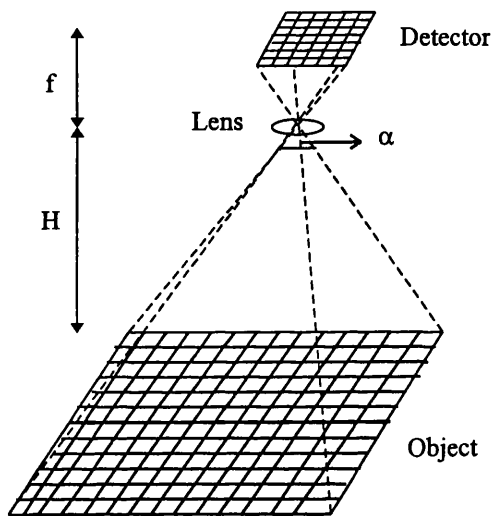


Fig. 10.3. IFOV and FOV of the infrared camera

As can be seen from Fig. 10.3, when the shutter of the lens opens, all the detector elements see the object at the same time. Therefore, by contrast with the scanner, the IFOV is equal to the field of view (FOV). Thus, the two dimensional detector arrays utilized in CCD cameras provide a complete record of the radiation falling on to object at a particular instant of time.

As discussed in detail in Chapter 8, the size of the detector array and the pixel size are the most important characteristics of a infrared CCD camera for photogrammetric use. Other important feature for the cameras is the lens resolution. The on-axis resolution of a photogrammetric camera ranges from approximately 20 to 30 lp/mm and 35 to 55 lp/mm for low and high-contrast targets respectively (Slama et al, 1980). Nowadays this has improved considerably with 60 lp/mm being possible on-axis with the new generation of photogrammetric camera lenses: The off-axis resolution is determined

by the effects of lens aberrations that normally increase with angular distance from the optical axis. For a wide angle camera, resolving power remains high up to approximately 15° of off-axis; however, thereafter the maximum resolutions may be limited to about 25 lp/mm at 30° off the axis and 10 lp/mm in the extreme corners (see Fig. 10.4).

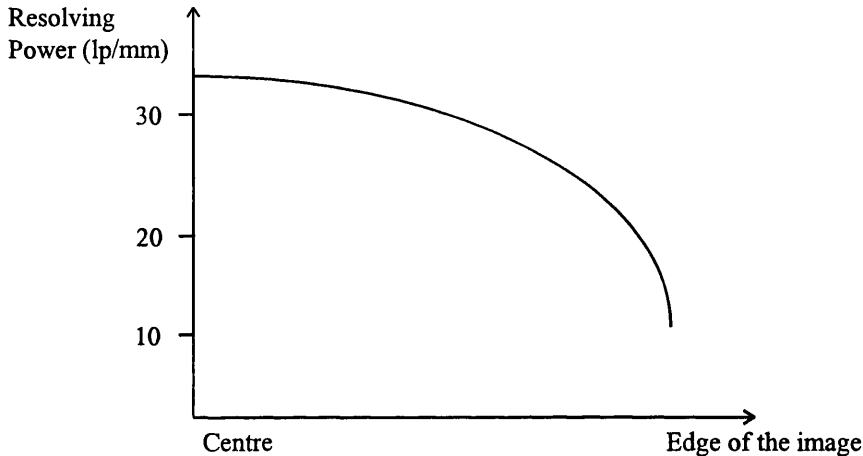
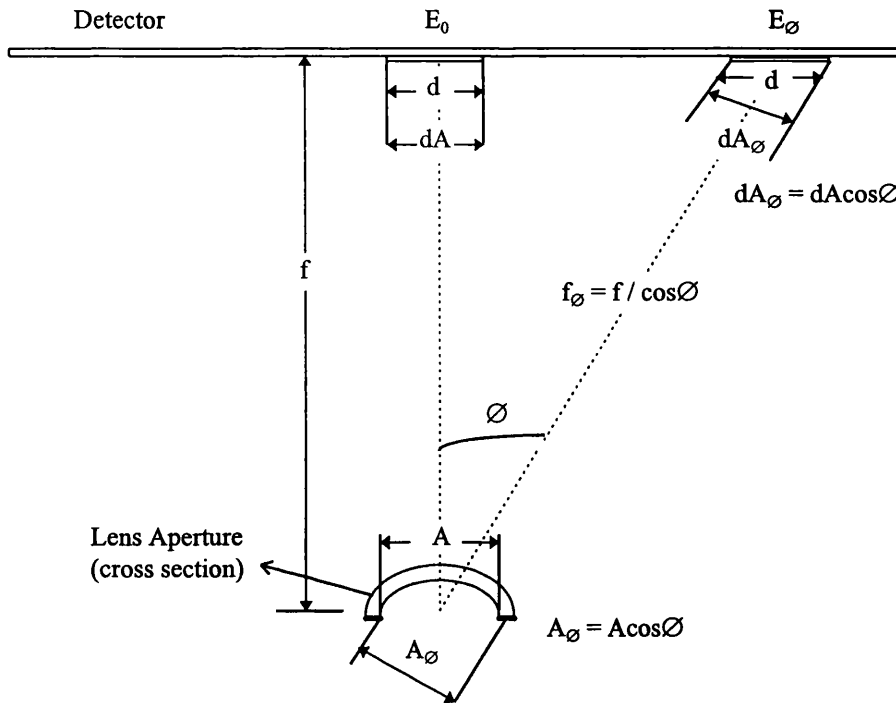


Fig. 10.4. Resolution of the on and off-axis targets

In this account, an important figure is the intensity fall-off - which can be considered as a radiometric parameter. The factors causing fall-off are depicted in Fig. 10.5, which shows that, for an object assumed to be of uniform radiant intensity, less radiance is collected by the lens system of the infrared camera towards the edge of the angular coverage than at the centre.

For radiation coming from a point directly on the optical axis, the intensity E_0 is directly proportional to the area, A , of the lens aperture and inversely proportional to the square of the focal length of the lens, f^2 . However, for a point at an angle \varnothing to the optical axis, the intensity E_\varnothing is reduced from E_0 for three reasons:

- (i) The effective radiation collecting area of the lens aperture A , decreases in proportion to $\cos\varnothing$ when imaging off-axis objects ($A_\varnothing = A \cos\varnothing$).
- (ii) The distance from the camera lens to the focal plane, f_\varnothing , increases as $1/\cos\varnothing$ for off-axis points, $f_\varnothing = f / \cos\varnothing$. Since intensity varies inversely as the square of the distance, there is an intensity reduction of $\cos^2\varnothing$.



10.5. Factors causing a intensity fall-off (Lillesand and Kiefer, 1994)

- (iii) The size of a detector element, d , projected perpendicular to the radiation decreases in proportion to $\cos \phi$ when the element is located off-axis, therefore $dA = d$ and $dA_\phi = dA \cos \phi$.

Combining above effects, the overall theoretical reduction in intensity for an off-axis point is

$$E_\phi = E_0 \cos^4 \phi \quad (10.3)$$

where:-

- ϕ is the angle between the optical axis and the ray to the off-axis point;
- E_ϕ is the intensity at the off-axis point; and
- E_0 is the intensity that would have resulted if the point had been located at the optical axis.

The actual fall-off effect of the illumination can be determined by a radiometric calibration of the camera. Essentially this calibration involves imaging an object of uniform illumination or temperature such as a blackbody target in the case of infrared cameras. Afterwards, measuring the intensity (grey values) at various ϕ locations on

the image and identifying the relationship that best describes the fall-off. For most cameras, this relationship takes on the form

$$E_{\varnothing} = E_0 \cos^n \varnothing \quad (10.4)$$

Because modern cameras are normally constructed in such a way that their fall-off characteristics are much less severe than the theoretical $\cos^4 \varnothing$ fall-off, n in the above equation normally lies in the range 1.5 to 4 (Lillesand and Kiefer, 1994). All the intensity values measured off-axis can then be corrected in accordance with the fall-off characteristics of the camera in use.

In this project, infrared cameras with different lenses have been tested. To show the implications caused by the intensity fall-off, the grey values of pixels within a quadrant of the blackbody images have first been measured. Then later the results have been drawn using SURFER package, which is a grid-based contouring and three-dimensional surface plotting program. This will be explained in more detail in the later part of this thesis when the radiometric calibration of infrared images is discussed.

10.3 Radiometric Characteristics

The radiometric characteristics of video cameras and scanners have a major impact on the performance and achievable accuracy of a camera. Dynamic range, SNR, noise, signal non-uniformities and resolution are important characteristics of all imagers. Noise Equivalent Temperature Difference (NETD) and Minimum Resolvable Temperature Difference (MRTD) can be added to these parameters since they are peculiar to the imaging systems operating in the infrared bands of EM. The overall performance of an infrared imager is governed by these parameters. Although not all of these parameters can be corrected for, if possible, the amount of each parameter has to be determined to verify the capability of the imaging system to carry out photogrammetric measurements. The influence of these parameters can be reduced

only by some special method such as multi-grab digitisation and by the avoidance of measurements during the warm-up stage of the camera operation (Peipe, 1994).

10.3.1 Dynamic Range

To get a good response from its detectors, the infrared video imager should view a given object long enough to accumulate enough photons to generate strong signals. The time interval required for this is defined as the detector's dwel time (or residence time) as discussed above. At the lower end of an imager's sensitivity range is the dark current signal (see Section 4.8.4). At low levels of brightness, a detector can record a small level of brightness from this effect even when there is no radiation present in the scene. At an imager's upper level, bright targets saturate the detector's response - in which case, the imager fails to record any further changes in target brightness. These characteristics of detectors are analogous to the characteristic curve which is described for photographic films. In other words, they define the upper and lower limits of the imager's sensitivity to brightness levels and the range of brightness values over which a imager can record images and generate measurements with consistent relationship to scene brightnesses (Campbell, 1996). The range brightnesses that are accurately recorded are known as the detector's dynamic range (Fig. 10.6).

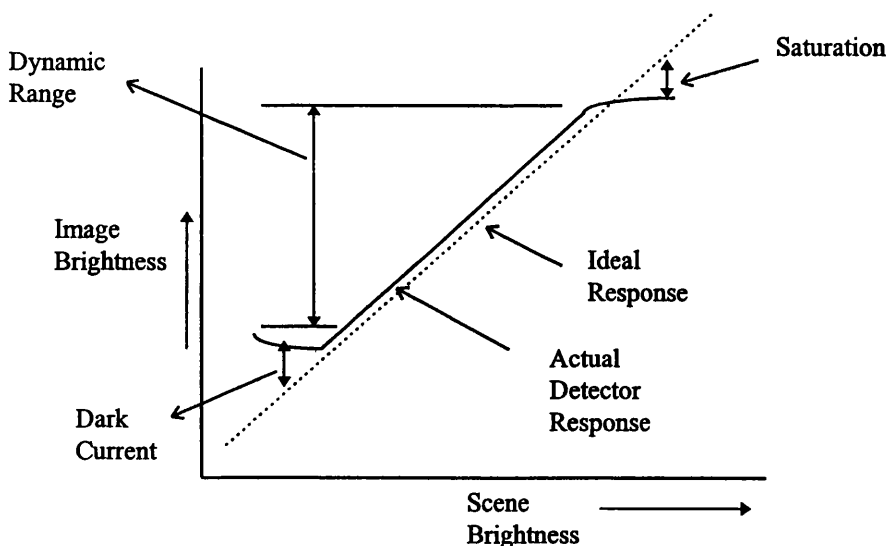


Fig. 10.6. Dark current, saturation, and dynamic range

10.3.2. Noise

Each detector creates responses unrelated to target brightness. This is called noise and it is created by the accumulated errors arising from the various components of the detector and the associated electronics. However, in imaging applications, the overall performance of an imaging system is affected by noise that stems from errors either in the detector or in the digitisation (A/D) operation. This combined noise significantly degrades the radiometric accuracy. For effective (practical) use, the imager must be designed so that the noise levels are small relative to the signal resulting from the brightness of the target. This is measured as the signal-to-noise ratio (SNR), the ratio of the measured intensity or brightness to the noise. Image analysts desire signals to be large relative to the noise, so the SNR should be large enough not only for bright targets but especially with lower levels of sensitivity where the signal is small relative to noise. Therefore, the lowest intensity or brightness that can be reliably measured is an indication of the sensitivity of a detector; this quality is measured as the noise equivalent temperature difference (NETD) when the SNR = 1. A low NETD with the highest minimum resolvable temperature differences indicates a detector with high sensitivity. These matters will be discussed in more detail in the later part of this section.

SNR and dynamic range can be increased by increasing the maximum charge capacity of the detector elements. The charge capacity of detector material is essentially proportional to the sensitive area of each element and, therefore larger detector elements give larger capacity but poorer spatial or geometric resolution.

Three methods can be used to analyze the noise.

Method 1- The standard deviation of the grey values of individual pixels is determined from several frames in a first step. The root mean square error of the grey values of pixels over a region or the complete frame is used to characterize the noise. These values are usually expressed in DN (Digital Number) units. This method is called the single pixel (pixel averaging) method.

Method 2- The standard deviation is determined from the grey values of the pixels of several sub-areas of the frame expressed in DN units. This method is called the patch method. It uses sub-areas of approximately 20 by 20 pixels.

Method 3- The standard deviation of grey values is computed using a large number of frames using statistics gathered from all of the pixels over the whole frame in DN units. This is called frame averaging.

These three methods have been used widely in this project to carry out the analysis of the noise occurring in infrared images. For this analysis, a number of individual frame images should be digitised by the frame grabber.

10.3.3 Signal Non-Uniformities and Radiometric Correction

Signal non-uniformities inherent in the imaging system can be divided into two parts:

- (i) Photo Response Non-Uniformity
- (ii) Dark Signal Non-Uniformity (DSNU)

10.3.3.1 Photo Response Non-Uniformity (PRNU)

In actual imaging tasks, the response of each individual detector element and/or pixel is of interest. Since each detector in an imaging device responds in a different way, i.e. in a non-uniform way, to that of its neighbours, this produces an undesirable “fixed pattern” that is superimposed on the image obtained from the device. The presence of this fixed pattern or non-uniform response in uncompensated infrared imagery obscures low contrast detail and limits the imager’s sensitivity. To achieve state-of-the-art sensitivity, the detector response must be compensated for to correct for this pattern and achieve uniformity. A two-point non-uniformity correction algorithm, which requires two separate calibration temperatures, can be used in association with a uniform blackbody source to remove the spatial noise which is the

dominant factor in the imagery acquired in the high background radiation environments encountered at infra-red wavelengths (3 to 5 μm and 8 to 14 μm) (Hou et al, 1995).

10.3.3.1.1 Non-Uniformity Correction Algorithm

(a) For two given reference temperatures, T_1 and T_2 , ($T_2 > T_1$), the average value of all the pixel responses $s'(T_1)$ and $s'(T_2)$ are calculated from the grey value of each pixel $s(i,j,T_1)$ and $s(i,j,T_2)$. Here, $s(i,j,T_1)$ is called the offset (i,j).

(b) The gain coefficient of each pixel, i.e, the gain (i,j) is calculated by

$$\text{gain } (i,j) = [s'(T_2) - s'(T_1)] / [s(i,j,T_2) - s(i,j,T_1)] \quad (10.5)$$

where $s(i,j,T_2) > s(i,j,T_1)$ for $T_2 > T_1$.

(c) For an image acquired at temperature T , ($T_1 < T < T_2$), then using the values of the offset, gain and the uncorrected signal $s(i,j,T)$, the corrected signal $s_c(i,j,T)$ is calculated as

$$s_c(i,j,T) = \text{gain } (i,j)[s(i,j,T) - \text{offset } (i,j)] + s'(T_1) \quad (10.6)$$

10.3.3.1.2 Pre-processing and Conditions for Radiometric Correction

Instead of using a single frame to calculate $s'(T_1)$ and $s'(T_2)$, the average of several frames acquired at temperatures T_1 and T_2 can be used to reduce the random temporal noise. In practice, temporal noise is reduced by the square root of the number of frames. For example, the use of 16 frames is sufficient to reduce the temporal noise by a factor of 4. The temperature difference ($T_2 - T_1$) which is used should be large enough to keep the grey value difference much higher than the noise level. Furthermore the response variation (i.e. changes in the grey value) between temperatures should be linear.

In Kosonocky et al (1985), images of a test pattern and of a man's face have been acquired by a CCD camera employing a Platinum Silicide (PtSi) Schottky Barrier focal plane array operating in the middle infrared band of the spectrum. This camera was equipped with an $f = 175\text{mm}$, $f/2.35$ lens, and had a 160×244 pixel resolution. It was operated at 30 frames per second and had a standard TV field interlace. The authors noted that the image quality increased with the application of a non-uniformity correction and through the use of an increasing number of averaging frames.

In Hou et al (1995), images of a blackbody source have been taken by a middle infrared CCD camera built at the New Jersey Institute of Technology. This camera used a focal plane array comprising 320×144 Platinum Silicide (PtSi) Schottky Barrier detectors. In this experiment, two offset images have been recorded at blackbody temperatures of 25°C and 55°C . The images for testing the non-uniformity correction procedure have been recorded at blackbody temperatures of 35°C and 45°C . It has been noted that, in both cases, the non-uniformity correction results in at least a six fold improvement in the value of the root mean square error of the non-uniformity.

10.3.3.2 Dark Signal Non-Uniformity (DSNU)

When there is no incident radiation (e.g. with the lens cap on), an infrared imager still provides a signal, known as the dark current, which is a thermally generated signal. The origin and nature of this signal has been explained in Section 7.3.5(a). In this case, the detectors in an array can produce a slightly different dark current. This creates the dark signal non-uniformity over an array which is small when compared to the PRNU.

Usually several images are acquired without any incident radiation in order to assess the DSNU. The average of the grey values for each pixel of these images is computed and the mean and sigma values in forms of their DN values is determined. Beyer

(1992) has indicated that the DSNU is a factor which is present both in the camera and the frame grabber. The analysis of the DSNU correction should therefore be determined for every camera/frame grabber combination.

10.3.4 Modulation Transfer Function (MTF)

In photogrammetry, the image resolution is the minimum distance between close objects that can be distinctly discerned as two objects on the image. This resolution is best represented in terms of the MTF (Naithani, 1990).

The modulation transfer function (MTF) describes the degradation of the contrast in the image of the object as a function of the spatial frequency of the image. Mathematically, the MTF is equal to the normalised Fourier transform of the line spread function which is the distribution of illuminance across the image of a slit of negligible width (Boberg, 1994).

The ratio of the modulation in the image to that of the object will be a measure of how well the image is formed for that particular spatial frequency. This ratio is called the modulation transfer ratio, that is,

Modulation transfer ratio = modulation of image / modulation of object

When this measurement is made over a range of spatial frequencies, one can plot a curve of the modulation transfer ratio as a function of spatial frequency. This is known as the modulation transfer function (MTF).

The MTF has a number of interesting properties, some of these are as follows:-

(a) The MTF covers a range of spatial frequencies and hence gives more information regarding image performance than does the limiting spatial or geometric resolution, which is essentially the endpoint of the MTF. The lower and mid-range spatial frequencies can be particularly important with regard to observed image sharpness.

(b) A single MTF value for the camera system could be obtained by multiplying the responses of the appropriate lens, detector and other relevant variables in the camera system, frequency by frequency. This process of combining individual MTF curves is known as cascading (El-Hassan, 1978).

(c) The MTF is related mathematically, by the Fourier transform, to the image of a line, which is known as the line spread function, or to the image of a perfect point, which is known as the point spread function.

Before the actual MTF values can be determined, it is necessary to determine the modulation values of the test pattern. This is done using a microdensitometer or by CCD scanning. In this way, values of the maximum and minimum density for each of the scanned areas can be obtained. Thus,

$$\text{Modulation} = (10^{\Delta D} - 1) / (10^{\Delta D} + 1) \quad (10.7)$$

where ΔD is the difference between the maximum and minimum density values. Such values must be obtained for all spatial frequencies.

10.3.5 Noise Equivalent Temperature Difference (NETD)

The NETD is a measure of the ability of the system to produce a usable image from low temperature differences across a fairly uniform target. It takes no account of the physical size of the target, makes no allowance for the performance of the eye and brain in discerning the noise or targets and is a summary of some of the basic design parameters of the equipment, arranged to give an indication of the fundamental lowest infrared resolution limit that could be achieved (Lloyd, 1975).

An overall practical assessment of NETD has been given by Lloyd (1975). According to this, the imager is set to observe a large square blackbody target whose size exceeds the imager's angular resolution by one order of magnitude and with a target to

background temperature difference ($T_T - T_B$) that exceeds the estimated NETD by at least an order of magnitude. The video signal is taken from the imager at the point closest to the display. Typically the video signal voltage (V_S) is determined from an oscilloscope trace of the voltage waveform corresponding to the target. The signal-to-noise ratio (SNR) of the target (V_N) is measured electrically by a voltmeter. The NETD is then given by

$$\text{NETD} = (T_T - T_B) / (V_S / V_N) \quad (10.8)$$

In this measurement, the bandwidth of the voltmeter must be compatible with that of the imager. Generally the measurement bandwidth should be from DC (Direct Current - zero level or black level) to F_R , where the latter term is given by

$$F_R = 1 / 2t_d \quad (10.9)$$

and t_d is the detector dwell time which is the time taken for the detector to be scanned across a point source in the scene.

During the measurement, care must be taken to measure only the noise that could be expected to be visible on the display. Timing signals outside the active scan time should be removed. In addition to this, modern systems are now being designed with NETDs in the region of 10mK. This implies stringent requirements regarding the accuracy and uniformity of the target and its background and careful and sensitive measurement.

10.3.6 Minimum Resolvable Temperature Difference (MRTD)

Another important performance parameter for infrared imaging systems is the minimum resolvable temperature difference (MRTD). The NETD parameter just described gives a good measure of the infrared sensitivity of the system, but it takes no account of the size of the target or the ability of the observer to resolve that target in the imager display.

The MRTD parameter is essentially the signal-to-noise (SNR) limited infrared sensitivity of the imager as a function of spatial frequency. This sensitivity includes an allowance for the display and takes some account of the observer's eye performance. In practical measurement, the overall quality of the image is also taken into account. This quality includes the measured parameters of sharpness, displayed contrast, noisiness and spurious image structure.

For the measurement of the MRTD, four-bar targets, representing spatial frequencies across the designed range of the infrared imager, are observed in turn (Lloyd, 1975; Burnay et al, 1988). For each target, the temperature difference of the bar with respect to the background is increased slowly from zero until the bars are judged to be just discernible by the tester. This process is repeated with bars cooler than the background. The MRTD is then half the difference between the positive and negative temperatures. This measurement should be repeated a number of times for each bar target and an average derived.

In practice, the accuracy and repeatability of the measurements will be influenced by a large number of external factors. These typically include the tester's experience, the ambient lighting and the target-bar temperature control. One of the biggest variables can be the tester's interpretation of "just discernible". This has been known to vary with the tester's state of health, mental stress, familiarity with the imager type and even some commercial pressures! (Lloyd, 1975).

Accurate testing does take a considerable time and requires experienced observers. For these reasons, much attention is being paid to producing an automatic test method. Most of these are based on the use of an imaging system, a frame store and image analysis carried out on a computer. The work centers on the definition of appropriate algorithms for modelling the observer's interpretation of the display.

Current generations of infrared imagers normally incorporate an internal temperature reference which takes the form of a blackbody radiation source. The temperature of

this blackbody can be precisely controlled and it provides a continuously updated information about the temperature. It must mentioned here that, infrared imagers do not measure the object's temperature directly, although it can be computed indirectly in terms of the object's emissivity and use of the internal temperature sources. However this quantative approach is outside the scope of the present project.

10.4 Conclusions

Chapters 8 and 9 have described the essential elements of infrared imaging systems that will be used throughout this project. In this chapter, the geometric and radiometric characteristics of those imaging systems have been discussed. Thus, the various matters that have to be taken into account and corrected in the calibration stage have been fully covered. In the next chapter, the image matching method which has been used in the present project to measure the centre of the cross targets in the infrared images will be explained in some detail. In this way, the image coordinates that are the main source of data to establish the geometric distortions that are present in digital infrared images will be obtained at the sub-pixel level that is required for digital photogrammetric applications.





**GEOMETRIC AND RADIOMETRIC CALIBRATION OF
VIDEO INFRARED IMAGERS
FOR
PHOTOGRAMMETRIC APPLICATIONS**

BY

GURCAN BUYUKSALIH

VOLUME II

**A Thesis Submitted for the Degree of Doctor of Philosophy (Ph.D.)
in Photogrammetry and Remote Sensing
in the Faculty of Science at the University of Glasgow**

Topographic Science, November 1997

GLASGOW
UNIVERSITY
LIBRARY

Thms 11043 (copy 1)

GLASGOW UNIVERSITY
LIBRARY

TABLE OF CONTENTS

VOLUME I

ABSTRACT	i
ACKNOWLEDGEMENTS	ii
TABLE OF CONTENTS	v
CHAPTER 1 : INTRODUCTION	
1.1 The Importance of the Infrared Imaging Systems for Photogrammetric Applications	1
1.1.1 The Unique Characteristics of Infrared Imaging Systems	2
1.1.2 The Photogrammetric Processes Required on Infrared Imagery Acquired for Mensuration and Mapping Purposes	5
1.2 The Geometric and Radiometric Characteristics of Different Infrared Imaging Systems	6
1.2.1 Pyroelectric Vidicon Cameras	7
1.2.2 CCD-based Cameras	8
1.2.3 Thermal Video Frame Scanners	10
1.2.4 Radiometric Aspects of Infrared Imagers	12
1.3 Research Objectives	13
1.4 Outline of the Thesis	14

CHAPTER 2 : FUNDAMENTAL THEORY UNDERLYING THE INFRARED IMAGING SYSTEMS

2.1 Introduction	18
2.2 Nature of Electromagnetic Radiation	18
2.3 Characteristics of Electromagnetic Radiation	23
2.4 Electromagnetic Wavebands	25
2.4.1 The Infrared Spectrum	26
2.5 Basic Laws of Infrared Radiation	27
2.5.1 Planck's Blackbody Law	27
2.5.2 Wien's Displacement Law	28
2.5.3 Stefan-Boltzmann Law	29
2.6 Atmospheric Transmission	30
2.7 Total Scene Radiation and Contrast	31
2.8 Conclusions	33

CHAPTER 3: INFRARED OPTICAL MATERIALS AND COMPONENTS

3.1 Introduction	34
3.2 Infrared Optical Materials	35
3.3 Optical Arrangements	37
3.3.1 Refracting Optics	38
3.3.2 Reflecting Optics	42
3.3.3 Catadioptric Optics	45
3.3.4 Relay Lens (Auxiliary Optics)	45
3.4 Anti-Reflection (AR) Coatings	46
3.5 Infrared Telescopes and Lens Systems	47
3.5.1 Examples of Infrared Imager Optical Systems	48
3.6 Infrared Lens Quality	50
3.7 Resolution	54
3.7.1 Aperture and Resolution	55
3.7.2 Wavelength and Resolution	56

3.7.3 Depth of Field and Aperture	57
3.7.4 Depth of Focus	58
3.8 Conclusion	59

CHAPTER 4: INFRARED DETECTORS

4.1 Introduction	60
4.1.1 Detectors	60
4.2 Definition of Relevant Terms	61
4.3 Thermal Detectors	65
4.3.1 Bolometers	65
4.3.1.1 Metal and Semi-conductor (Thermistor)	
Bolometers	66
4.3.2 Pyroelectric Detectors	67
4.4 Physics of Semi-conductors	68
4.4.1 The Periodic Lattice	68
4.4.2 Energy Bands in a Perfect Crystal	69
4.4.3 Imperfections in the Lattice	71
4.5 Photon (Quantum) Detectors	71
4.5.1 Photoconductive Detectors	72
4.5.2 Photovoltaic Detectors	73
4.5.3 Materials Used for Photon Detectors	74
4.5.4 The SPRITE Detector	76
4.6 Noise In Detectors	77
4.7 Detector Cooling	78
4.8 Detector Arrays	79
4.8.1 Read Out Mechanisms of Detector Arrays	80
4.8.2 Organization of Different Detector Types in Areal	
Array CCDs	82
4.8.3 Geometric Properties of Arrays of CCD Detectors	85
4.8.3.1 Geometry of Detector Elements	85
4.8.3.2 Surface Flatness	86

4.8.4 Spurious Signals	87
4.8.5 Infrared CCD (IR-CCD) Areal Arrays	90
4.8.5.1 Monolithic IR-CCDs	90
4.8.5.2 Hybrid IR-CCDs	91
4.8.5.3 Practical Limitations with IR-CCDs	92
4.9 Conclusions	93

CHAPTER 5 : VIDEO TECHNOLOGY

5.1 Introduction	94
5.2 Video System	96
5.2.1 Video Tube Camera	96
5.2.1.1 Electron Beam Scanning	99
5.2.1.2 Colour Video Cameras	100
5.3 Video Imaging Devices in the Infrared Band	102
5.4 Video Image Resolution	102
5.5 Video Image Geometry	106
5.6 Video Recording	106
5.6.1 U-matic VTR	108
5.6.2 VHS, Betamax and Video 2000 VTR systems	108
5.7 Video Displays	109
5.7.1 Monochrome Displays	109
5.7.2 Colour Displays	110
5.7.3 Computer Graphics Display	112
5.8 Distortions in the Video System	113
5.8.1 Distortions in the Video Camera	113
5.8.1.1 Distortions in the Vidicon Tube	113
5.8.1.2 Lens Distortions	115
5.8.1.2.1 Radial Distortion	115
5.8.1.2.2 Decentering (Tangential) Distortion	118
5.8.2 Distortions Stemming From the VTR	119
5.8.3 Distortions in a CRT-based Display Monitor	120

5.9 Conclusion	122
----------------------	-----

CHAPTER 6 : VIDEO STANDARDS

6.1 Introduction	124
6.2 Data Capture and Signal Transmission	125
6.3 Video Inputs	127
6.3.1 Standard Video Formats	128
6.3.2 High Definition Television (HDTV)	131
6.3.3 S-Video	133
6.3.4 PC Video Standards	134
6.3.5 Workstation Video Standards	135
6.4 Synchronisation and Transmission of Video Signals	136
6.4.1 The Composite Video Signal	136
6.4.2 Other Synchronisation Signals	139
6.5 Conclusions	140

CHAPTER 7 : ANALOGUE VIDEO TO DIGITAL CONVERSION

7.1 Introduction	141
7.2 Monochromatic Frame Grabber	142
7.2.1 Analogue Front End	143
7.2.2 Synchronisation	145
7.2.2.1 PLL Line Synchronization	145
7.2.2.2 Pixel Synchronous Sampling	147
7.2.3 Analogue-to-Digital (A/D) Conversion	148
7.2.3.1 Quantization Error	150
7.2.3.2 Signal-to-Noise Ratio (SNR)	150
7.2.3.3 Integral Linearity Error	151
7.2.3.4 Differential Linearity Error	151
7.2.3.5 Missing Code	151
7.2.3.6 Offset Error	152

7.2.3.7 Gain Error	152
7.2.3.8 Resolution	152
7.2.4 Data Buffering	152
7.3 Frame Grabbers Used in the Project	153
7.4 Image Display	155
7.5 Processing Hardware	156
7.6 Conclusions	157

CHAPTER 8: INFRARED FRAME TYPE (PLANAR) IMAGERS

8.1 Introduction	158
8.1.1 Classification of Infrared Imagers	160
8.2 Thermal Infrared Pyroelectric Vidicon Cameras	162
8.2.1 Image Modulation - Chopping versus Panning Mode	163
8.2.1.1 Lag	164
8.2.1.2 Observer Fatigue	164
8.2.1.3 Compensating Positive Current	165
8.2.2 Geometric Aspects of the Pyroelectric Vidicon	166
8.2.3 Commercially Available Pyroelectric Vidicon Cameras	166
8.3 Infrared CCD Camera	167
8.4 Commercially Available Infrared CCD Cameras	170
8.5 Conclusions	171

CHAPTER 9 : INFRARED SCANNER IMAGERS

9.1 Introduction	172
9.2 Optical-Mechanical Line Scanners	173
9.2.1 Airborne Infrared Line Scanner	173
9.2.2 Geometry of Optical-Mechanical Line Scanner Imagery	174
9.2.3 Multispectral Line Scanners	175
9.2.3.1 Satellite Systems	176
9.2.3.1.1 HCMM (Heat Capacity Mapping	

Mission)	177
9.2.3.1.2 Landsat MSS and TM Series	178
9.3 Thermal Video Frame Scanners (TVFS)	178
9.3.1 Scanning Configuration	179
9.3.1.1 Serial Scanning	179
9.3.1.2 Parallel Scanning	180
9.3.1.3 Serial/Parallel Scanning	181
9.3.2 Scanning Mechanism of TVFS	181
9.3.2.1 The Oscillating Plane Mirror	182
9.3.2.2 The Rotating Reflective Polygon	182
9.3.2.3 The Rotating Refractive Polygon	183
9.3.3 Geometric Effects of the Scanning Mechanism	183
9.3.4 Geometric Potential of TVFS	185
9.3.5 Commercially Available Thermal Video Frame Scanners	186
9.3.6 Optical Arrangement of the TVFSs	190
9.3.6.1 Optical Design of the HDTI	190
9.3.6.2 Scanning Arrangement of the Agema Thermovision 1000	192
9.4 Conclusions	193

CHAPTER 10: GEOMETRIC AND RADIOMETRIC CHARACTERISTICS OF INFRARED IMAGING SYSTEMS

10.1 Introduction	194
10.2 Geometric Characteristics	194
10.2.1 Instantaneous Field of View of the Infrared Imaging System	194
10.2.1.1 IFOV and FOV of Infrared Scanners	194
10.2.1.2 Trade-off Between the Geometric and Radiometric Resolution of Scanners	197
10.2.1.3 IFOV and FOV of Infrared Cameras	198
10.3 Radiometric Characteristics	201

10.3.1 Dynamic Range	202
10.3.2. Noise	203
10.3.3 Signal Non-Uniformities and Radiometric Correction	204
10.3.3.1 Photo Response Non-Uniformity (PRNU)	204
10.3.3.1.1 Non-Uniformity Correction Algorithm ..	205
10.3.3.1.2 Pre-processing and Conditions for Radiometric Correction	205
10.3.3.2 Dark Signal Non-Uniformity (DSNU)	206
10.3.4 Modulation Transfer Function (MTF)	207
10.3.5 Noise Equivalent Temperature Difference (NETD)	208
10.3.6 Minimum Resolvable Temperature Difference (MRTD)	209
10.4 Conclusions	211

VOLUME II

CHAPTER 11: SUB-PIXEL MEASUREMENTS OF CROSS TARGETS IN THE DIGITAL INFRARED IMAGES

11.1 Introduction	212
11.2 Image Segmentation	213
11.2.1 Thresholding	213
11.2.2 Edge Detection	215
11.2.2.1 Edge Operators	216
11.2.2.2 Edge Locators	217
11.2.3 Image Correlation	219
11.2.3.1 Image Correlation Classification	220
11.2.3.2 Image Matching Fundamentals	221
11.2.3.3 Image Matching Problems	222
11.2.3.4 Least Squares Image Matching Method	222
11.2.3.4.1 Image Pyramids	225
11.3 The Measurement of the Positions of Cross Targets	226
11.3.1 Automatic Detection, Recognition and Location	

of Cross Targets	226
11.3.1.1 Detection of Cross Targets	226
11.3.1.2 Recognition of Cross Targets	227
11.3.1.3 Location of Cross Targets	228
11.3.2 Cross Target Measurement	229
11.3.2.1 Measurement of the Cross Position Using the Gradient Method	230
11.3.2.2 Image Modelling and Least Squares Matching Method for Cross Target Measurement	234
11.3.2.2.1 The General Adjustment Model	235
11.3.2.2.2 Measuring a One-dimensional Edge	238
11.3.2.2.3 Point Spread Function	240
11.3.2.2.4 Edge Pointing With Gaussian Spread Function	241
11.3.2.2.5 Cross-type Targets	241
11.4 Conclusion	243

CHAPTER 12: COMPUTER PROGRAMMING OF THE IMAGE MATCHING PROCEDURE

12.1 Introduction	244
12.2 Development of Program SUBPIX	244
12.2.1 Structure of Program SUBPIX	245
12.2.2 Sub-Program GRAD	249
12.2.3 Sub-Program PTSUB	251
12.2.4 Routines	253
12.3 Test Results	254
12.3.1 Test Results With Thermal Images	255
12.3.2 Test Results With CCD Images	258
12.3.3 Tests with Alternative Method	258
12.3.4 Comments on the Use of the Program and the Accuracy Results	259

12.4 Conclusions	260
------------------------	-----

CHAPTER 13: EXPERIMENTAL PROCEDURES AND SUBSEQUENT DATA PROCESSING

13.1 Introduction	261
13.2 Actual Experimental Procedures	261
13.2.1 Geometric Calibration Procedures	263
13.2.1.1 Difficulties with the Target Plates	265
13.2.1.2 Characteristics of Dr. Amin's Plate	267
13.2.1.3 Design of the New Calibration Target Plate	269
13.2.2 Radiometric Calibration Procedures	272
13.2.3 Problems Experienced During the Experimental Work	274
13.3 Processing of the Data	275
13.3.1 Digital Image Processing by Photoshop	276
13.3.1.1 Grey Level Value Adjustment and Contrast Enhancement	276
13.3.1.2 Photoshop's Filters	281
13.3.1.2.1 Median Noise Filter	281
13.3.1.2.2 Sharpen Filters	282
13.3.2 Data Processing for Geometric Calibration Purposes	283
13.3.3 Data Processing for Radiometric Calibration Purposes	284
13.4 Analysis of the Data Obtained During the Geometric Calibration	285
13.4.1 Linear Conformal Transformation	286
13.4.2 Affine Transformation	287
13.4.3 Polynomial Transformation	288
13.4.4 Plotting of Residual Errors	290
13.4.5 Systematic and Random Components of Geometric Distortion	291
13.5 Analysis of the Data Obtained During the Radiometric Calibration ...	292
13.5.1 Computation of the Mean and Standard Deviation of the Grey Level Values	293

13.5.2 Temporal Average of the Quadrants	293
13.5.3 Spatial Average and Noise	294
13.5.4 Statistical Processing of the Grey Level Values of the Quadrant	295
13.5.5 Graphical Representation of the Grey Level Values of the Pixels by SURFER	297
13.6 Conclusion	298

CHAPTER 14: RESULTS AND ANALYSIS OF THE GEOMETRIC CALIBRATION OF INFRARED CCD CAMERAS

14.1 Introduction	299
14.2 Agema 550 CCD Camera	299
14.2.1 Experimental Procedure with Agema 550	300
14.2.2 Results and Analysis of the Geometric Calibration of the Agema 550	301
14.2.2.1 Results and Analysis with the 20° Lens	301
14.2.2.2 Results and Analysis with the 10° lens	308
14.2.2.3. Results and Analysis with the 40° Lens (Second Occasion)	313
14.3 Amber Radiance PM1 CCD Camera	318
14.3.1 Result and Analysis of the Geometric Calibration of the Radiance PM1	318
14.4 Overall Analysis	322
14.4.1 Analysis of the Effective Terms for Each of the Lenses	323
14.4.2 Analysis of the Residual Errors	325
14.4.3 Systematic and Random Components of Geometric Distortion	328
14.5. Conclusion	329

CHAPTER 15: RESULTS AND ANALYSIS OF THE RADIOMETRIC CALIBRATION OF INFRARED CCD CAMERAS

15.1 Introduction	330
15.2 Radiometric Calibration of the Agema 550 CCD Camera	330
15.2.1 Radiometric Calibration with the 20° lens	330
15.2.1.1 Radiometric Calibration of Whole Frames	331
15.2.1.2 Radiometric Calibration of Quadrants and Patches	337
15.2.1.2.1 Computation of the Means and Standard Deviations of the Grey Level Values	337
15.2.1.2.2 Non-Uniformity Correction	337
15.2.1.2.3 Statistical Processing of the Grey Level Values of Pixels	341
15.2.1.2.4 Graphical Representation of the Grey Level Values of the Pixels	344
15.2.1.2.5 Different Fixed Patterns Present at Different Temperatures	346
15.2.2 Radiometric Calibration with the 10° Lens	347
15.3 Radiometric Calibration of the Amber Radiance PM1 Camera	352
15.3.1 Discussion of the Results from the Radiance PM1 Camera	356
15.4 Overall Analysis	363
15.5 Conclusion	366

CHAPTER 16: RESULTS AND ANALYSIS OF THE CALIBRATION OF THERMAL VIDEO FRAME SCANNERS

16.1 Introduction	367
16.2 Agema 1000	368
16.2.1 Geometric Calibration of the Agema 1000	368
16.3 Agema 900 LW	373

16.3.1 Geometric Calibration of the Agema 900	374
16.4 Agema 880	378
16.4.1 Geometric Calibration of the Agema 880 TVFS	378
16.5 Agema 470	381
16.5.1 Geometric Calibration of the Agema 470	383
16.6 Systematic and Random Components of the Distortion	385
16.7 Radiometric Calibration of the Agema 1000	385
16.8 Radiometric Calibration of the Agema 900	391
16.9 Radiometric Calibration of the Whole Frames	396
16.10 Conclusion	397

CHAPTER 17: CONCLUSIONS AND RECOMMENDATIONS

17.1 Introduction	399
17.2 Conclusions	399
17.2.1 General Conclusions	400
17.2.2 Specific Conclusions	404
17.3 Recommendations for Future Work	410
17.4 Potential Applications	413
17.5 A Final Note	414

REFERENCES	416
-------------------------	------------

APPENDICES

APPENDIX A: PROGRAM SUBPIX	427
APPENDIX B: REFERENCE COORDINATES OF THE CROSS TARGETS	448
APPENDIX C: PROGRAM LINCON	452
APPENDIX D: PROGRAM POLY25	470
APPENDIX E: PROGRAM STMN	489
APPENDIX F: PROGRAM PRNU	493
APPENDIX G: PROGRAM STAT	498

CHAPTER 11: SUB-PIXEL MEASUREMENTS OF CROSS TARGETS IN THE DIGITAL INFRARED IMAGES

11.1 Introduction

In the previous Chapter, the geometric and radiometric characteristics of middle and thermal infrared imaging systems, which have to be taken account during the calibration stage, have been discussed in some detail. In this chapter, the main methods of measurement that have been used to calibrate infrared video imagers geometrically in this project, will be dealt with broadly. As explained before, it is quite labour-intensive to carry out the measurements required to calibrate these devices using manual (non-automatic) methods. Therefore, an automatic method of carrying out the required measurements has been developed using digital image matching techniques.

For years, image matching techniques have been applied to pattern recognition, stereo-correlation and the classification of remotely sensed images. During the 1980s, some work was also carried out in connection with the accurate measurement of targets appearing on images using these techniques (Tabatabai and Mitchell, 1984). However, in recent years, there has been a trend towards carrying out the high accuracy mensuration of target positions on digital images as a routine operation. This often concerns the measurement of the positions or dimensions of well defined features such as edges, lines, crosses, and the like.

In this project, the automatic measurement of cross targets on the calibration plates that are needed to calibrate middle and thermal infrared imagers is the main interest. For this purpose, two different approaches have been used to determine the location of the centre of the cross targets. The first approach uses a gradient edge detection method to obtain the initial coordinates of the cross centre. The second approach utilises an Image Modelling technique based on the Least Squares method (IMLS) which minimizes the grey value differences between the real image target and an artificially produced target that is formed according to the point-spread function of the

imaging system. Thus it provides an improvement in the measured coordinates of the cross centre derived by the first approach. Thurgood and Mikhail (1982) first investigated the location of a cross using the IMLS approach. They reported having obtained positional accuracies in the order of ± 0.05 pixel in both the row and column directions. In real-time photogrammetry, since the speed of computation is a critical factor, less sophisticated methods are used. Direct interpolation techniques for the location of the target centre have achieved accuracies ranging from ± 0.1 to 0.4 pixel (El-Hakim, 1986; Haggren, 1986; Wong and Ho, 1986). However, real time operations are not needed in the calibration work being reported in this thesis, so the IMLS approach has been preferred since it promised greater accuracy.

A detailed explanation of the gradient edge detection and IMLS image matching technique will be presented in this chapter.

11.2 Image Segmentation

In the conventional photogrammetric measurement task, two major steps may be considered. The first is to detect, locate and identify a point of interest, and the second to carry out the precise pointing to that target. In digital photogrammetry, the measurement of the point position within a particular digital image coordinate system can be determined using the same steps. In order to carry out the first step, an automated feature extraction needs to be implemented in which the specific features of interest must be isolated from their background by using some prior knowledge about the target. Thus, in the specific context of the target crosses used in this calibration work, the image is segmented into two areas: the target, and the background.

11.2.1 Thresholding

The most common way to extract objects from this type of image is to threshold the image. The grey level histogram shown in Fig. 11.1(a) corresponds to an image, $f(x,y)$, comprising light objects against a dark background, such that the object and the

background pixels have grey levels that are grouped into two dominant modes. In this case, one obvious way to extract the objects from the background is to select a threshold T that separates these two modes. Thus, any point (x,y) for which $f(x,y) > T$ is called an object point; otherwise, it is a background point. A slightly more general case of this approach is shown in Fig. 11.1(b). In this case, the image histogram is characterized by three dominant modes (for example, two types of light objects on a dark background). A point (x,y) is classified as belonging to one object class if $T_1 < f(x,y) \leq T_2$, or to the other object class if $f(x,y) > T_2$, and to the background if $f(x,y) \leq T_1$. This type of thresholding is called multi-level thresholding. It is generally less reliable than its single-thresholding counterpart because of the difficulty in establishing multiple thresholds that effectively isolate regions of interest (Gonzales and Wintz, 1987).

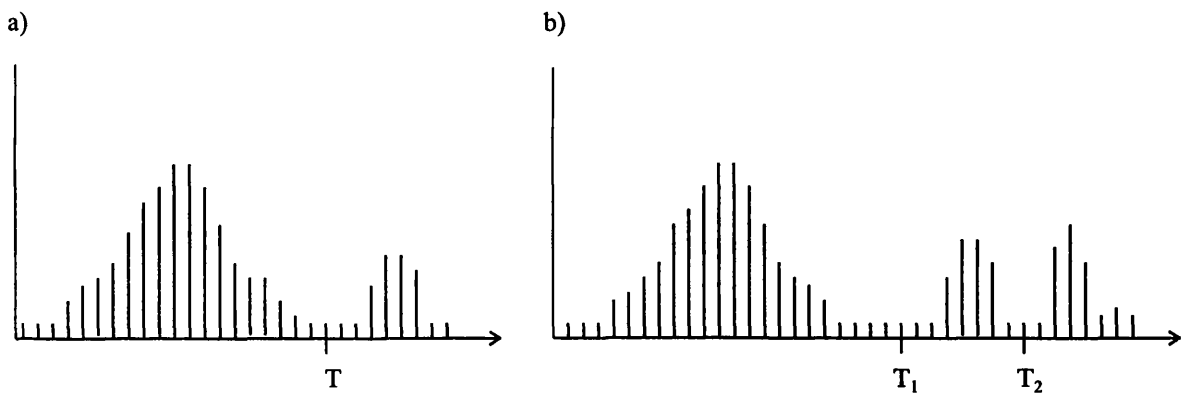


Fig. 11.1(a) and (b). Single and multi-level thresholding (Gonzales and Wintz, 1987)

Thresholding may be viewed as an operation that involves tests against a function T of the form (Schalkoff, 1989),

$$T = T[x,y,p(x,y),f(x,y)] \quad (11.1)$$

where $f(x,y)$ is the grey level of point (x,y) and $p(x,y)$ denotes some local properties of this point.

In which case,

$$g(x,y) = \begin{cases} A & \text{if } f(x,y) \leq T; \\ B & \text{if } f(x,y) > T \end{cases} \quad (11.2)$$

where $f(x,y)$ and $g(x,y)$ are the respective input and output image functions. A and B are the bi-level output image intensity values that have been chosen on the basis of prior knowledge, or by analysing the grey level frequency distribution. When T depends only on $f(x,y)$, the threshold is called global. If T depends on both $f(x,y)$ and $p(x,y)$, then the threshold is called local. In addition, if T depends on the spatial coordinates x and y , it is called a dynamic threshold.

A useful variation on thresholding is what might be called semi-thresholding. Here certain grey levels, e.g. those below a threshold, become 0, but the remaining grey levels remain unchanged, rather than becoming 1. Applied to an image that consists of objects appearing against a background, this technique can be used to "zero out" the background while preserving the grey levels within the objects (Rosenfeld and Kak, 1976).

11.2.2 Edge Detection

The thresholding techniques described above are designed primarily to extract objects that have characteristic grey level ranges or textures; in other words, they yield objects that have some type of uniformity. Edge detection is the most common approach for detecting meaningful discontinuities in grey level values. The reason for this is that isolated points and thin lines are not frequent occurrences in most applications of practical interest (Gonzales and Wintz, 1987). Edges are important because they provide the basis for many of the visual cues for the observer (Kornfeld and Lawson, 1971) but also in photogrammetric applications because frequently they form the actual features of interest in the images being measured.

Basically, the idea underlying most edge-detection techniques is the computation of a local derivative operator. Derivative operators give high values at points where the grey level of the picture is changing rapidly. Evidently, any such operator can be used

as an edge detector; its value at a point represents the "edge string" at that point. Thus a set of edge points can be extracted from image by thresholding these values. Several different operators can be distinguished - these are discussed below.

11.2.2.1 Edge Operators

(a) Edge detection techniques are often based on gradient or discrete differencing operators (Rosenfeld and Kak, 1976; Thurgood and Mikhail, 1982). Hence if $g(i,j)$ denotes the output of an operator, and $f(i,j)$ is the original image;

$$g(i,j) = | f(i + 1,j) - f(i,j) | \quad (11.3)$$

This represents a simple, direction-dependent edge operator since the values of this equation can be either positive or negative, depending on whether the grey level goes upward or downward as one moves in the positive x or y direction. Examples of such direction-independent operators are

$$g(i,j) = \max \{ | f(i,j) - f(i + 1,j + 1) |, | f(i + 1,j) - f(i,j + 1) | \} \quad (11.4)$$

or

$$g(i,j) = \{ [f(i + 1,j) - f(i,j)]^2 + [f(i,j + 1) - f(i,j)]^2 \}^{1/2}$$

(b) Another example, a smoothed gradient operator, which is less sensitive to noise is

$$g(i,j) = [\Delta x f(i,j)^2 + \Delta y f(i,j)^2]^{1/2} \quad (11.5)$$

where

$$\Delta x f(i,j) = 1/2 \{ [f(i,j + 1) + f(i,j + 2)] - [f(i,j - 1) + f(i,j - 2)] \}$$

$$\Delta y f(i,j) = 1/2 \{ [f(i + 1,j) + f(i + 2,j)] - [f(i - 1,j) + f(i - 2,j)] \}$$

The edge operators that are represented by Eqs 11.4 and 11.5, are those which have been implemented in the present project to find the value of the gradient magnitude.

(c) Many edge operators may be expressed as the output from a convolution of the image with a 3 by 3 or 5 by 5 mask. Then an example of a Laplacian operator, which approximates a second-order derivative, is expressed as a convolution with the 3 by 3 mask as follows:-

$$g(i,j) = 4f(i,j) - f(i - 1,j) - f(i,j - 1) - f(i + 1,j) - f(i,j + 1) \quad (11.6)$$

(d) Another edge operator is the Sobel edge enhancement technique which is defined by

$$g(i,j) = (x^2 + y^2)^{1/2} \quad (11.7)$$

where

$$x = [f(i + 1,j - 1) + 2f(i + 1,j) + f(i + 1,j + 1)] - [f(i - 1,j - 1) + 2f(i - 1,j) + f(i - 1,j + 1)]$$

$$y = [f(i - 1,j - 1) + 2f(i,j - 1) + f(i + 1,j - 1)] - [f(i - 1,j + 1) + 2f(i,j + 1) + f(i + 1,j + 1)]$$

11.2.2.2 Edge Locators

The approaches considered so far have been primarily edge detectors, rather than estimators of precise edge location. Edge fitting algorithms provide estimates of edge location and orientation through the use of an ideal model of the edge to which the image data is fitted.

Hueckel (1971, 1973) has developed a procedure for the fitting of two-dimensional straight edges and lines, which expands the modelled feature as a set of basic functions using Fourier series in polar coordinates. Minimization of the mean-square difference between the model and the data is performed using the coefficients of these basic functions to yield estimates for the position and orientation of the edge and for the grey shade values lying on each side of that edge. The algorithm has been shown to perform well even in the presence of high levels of noise (Mikhail et. al., 1984).

Frei and Chen (1977) have developed an algorithm where an "ideal edge element" is defined as a straight boundary line passing through the centre of a 3x3 window, thus separating two regions of constant, but different intensities h_1 , h_2 . They have

characterized the ideal "edge element" by its magnitude $|h_1-h_2|$ and orientation. One disadvantage of this approach is the constraint imposed on the line by forcing it to pass through the centre of the window. Another possible disadvantage of the algorithm is its sensitivity (Tabatabai and Mitchell, 1984).

Machuca and Gilbert (1981) have proposed an algorithm where the location is not based on derivatives but uses integrals to reduce the effect of noise. Their approach uses moments to locate the edges.

Jacobus and Chien (1981) have presented two edge location techniques that are based on the application of edge locators, each sensitive to a different group of edge types.

Tabatabai and Mitchell (1984) applied the concept of moment-preserving to develop a sub-pixel edge locator. Considering the one-dimensional case, their algorithm provides estimates for the three parameters defining a perfect step edge: As shown in Fig. 11.2, h_1 is the signal value below the edge; h_2 is the signal value above the edge; and x is the location of the edge. Moment preserving is used as the criterion of best fit of a set of l measurements of n data points to the ideal edge $f(s)$. Rather than solve directly for x , the edge location is defined as $k+1/2$, where k is the unknown number of samples below the edge. Since there are three unknowns in all, the first three sample moments are set equally to those associated with an ideal edge, that is:

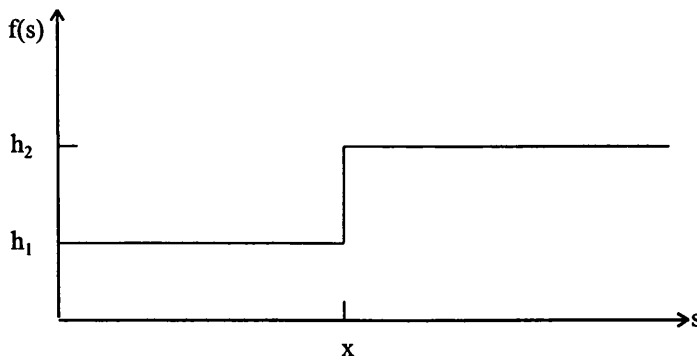


Fig. 11.2. Ideal step function (Mikhail et. al., 1984)

$$m_j = (k/n)h_1^j + n - (k/n)h_2^j \quad (11.8)$$

where

$$m_j = (1/n) \sum_{i=1}^n 1_i^j$$

is the j -th sample moment.

The set of equations may be solved directly in a closed form. In particular, the solution for k is given by

$$k = (n/2) \{ (1 - c) / (4 + c^2)^{1/2} \} \quad (11.9)$$

where

$$c = \{ 3m_1m_2 - m_3 - 2(m_1)^3 \} / \sigma^3$$

is the skewness of the data, and $\sigma^2 = m_2 - m_1^2$.

This method of edge location assumes that the data consists of monotonically increasing values. This will not be the case if noise is present, and processing of the data to smooth out oscillations due to noise has been shown to improve results by a significant amount. Moment preserving is very simple to apply, and yields unbiased estimates if the edge lies near the centre of the area being considered. Biased results may be overcome by re-centering the area to be modelled after an initial solution (Mikhail et al, 1984).

11.2.3 Image Correlation

One of the most fundamental tasks to be undertaken by a photogrammetric stereo-plotter operator is stereo-viewing in which he matches corresponding images in overlapping photographs with a view to carrying out measurements of plan position and elevation. An alternative to this is automatic image matching which is a technique that recognizes conjugate image elements from multiple images of the same object using either analogue (instrumental) or analytical (computational) approaches. Image matching techniques may also be extended to cover the techniques by which targets (e.g. points, lines or signalized targets) are detected and measured using a single image and a simulated target. Such techniques have been used widely in different

fields such as computer vision, microwave radar and communication, computer aided design (CAD), computer aided manufacturing (CAM), quality control, robot guidance, etc. In photogrammetry, image matching has been devised with the main purpose of producing orthophotos or of extracting the three-dimensional information (x-parallaxes) from the object or objects (mainly the Earth's surface) that have been photographed with a view to forming a digital surface model or a digital terrain model (DTM). It has also been used for the automatic measurement of point targets, e.g. automatic measurement of fiducial marks, signalized points and certain other kinds of image points.

A great variety of image matching techniques have been developed over the last few decades. These have been developed within various disciplines and thus they have been influenced by the theory and methods used in each one of them. Unfortunately, there is no unifying theoretical background for what is often a very specific and limited task. Differences in input data, experiment configurations, ways of processing, theoretical assumptions and problems to be solved, have all contributed to a vast number of techniques that are partly or completely different to one another. This situation has also been caused partly by the fact that matching is a very difficult and complicated process and thus no universal algorithm could be developed. In this section, the classification and basic steps of the matching techniques used in photogrammetry will be outlined. The problems related to the matching operation will be explained. To restrict the topic, the analogue (optical and electronic) techniques will be left out. Also the special techniques that are used with active sensors (laser, radar, etc.) as well as those techniques concerned with shape, texture, motion, contours, focussing and photometric stereo will also not be mentioned. The least squares matching method which is the basic technique used during this research will be dealt with in detail.

11.2.3.1 Image Correlation Classification

To try to classify image matching techniques is a difficult task by itself. Makarovic, (1980) classified correlation techniques according to the basic ingredients of,

- (i) the input image data (analogue, digital, hybrid);
- (ii) the processing equipment that is available (electronic and optical correlators, digital computers, etc.); and
- (iii) the kind of operation (on-line, off-line) being implemented.

In general, however, image matching may be classified conveniently into the two broad approaches of analogue and digital correlation techniques. In this project, since digital image matching technique has been implemented to match the cross targets, it will be dealt with in the next sections.

11.2.3.2 Image Matching Fundamentals

In general terms, the procedures involved in digital image correlation may be outlined as follows:

A two dimensional matrix of a certain row and column dimension (called a window array) is selected on the left photo of a stereo-pair. Then a larger corresponding matrix (search array) is selected on the right photo so that it will encompass the corresponding image of the window array. The window array is then systematically shifted within the search array and, in each position, the target is compared with that of equal-sized "sub-search" areas within the search array. The sub-search array having the best similarity is the area which best corresponds to the window array. For the next window on the left image, a corresponding search array is again found using the position of the previously matched point. These procedures are repeated until the desired area is covered.

From what has been mentioned above, it can be seen that image correlation requires two distinct operations:

- (i) An algorithm or algorithms to assess the similarities between two functions.
- (ii) A method or strategy for moving from one matched point to the other.

11.2.3.3 Image Matching Problems

The problems which are nearly always present during the image matching operation:

- (i) Sub-pixel measurement. Due to fact that each pixel has a finite size, sub-pixel matching accuracy is required in most cases.
- (ii) Geometric complexities. These may be caused by slopes or discontinuities in surfaces such as those produced by cliffs, breaklines, trees and buildings, causing occlusions to occur in the image. There are also geometric displacements and affinities on the left and right images due to the camera axes' deviations from the vertical and various image distortions respectively.
- (iii) Radiometric variations. These may include factors such as ground reflection variation with viewing angles; atmospheric refraction; radiometric response variation in different parts of the image; and noise imposed by the detector system and A/D converter; etc. - which may appear in the image in the form of isolated pixels with a very contrasting grey level compared with the surrounding ones.
- (iv) Image texture. Those areas with a low signal content or a highly periodic texture and shadows may cause ambiguous matching.

11.2.3.4 Least Squares Image Matching Method

Image matching based on a least squares approach derives a parallax function and/or a shaping function for homologous image points by minimizing the grey value differences between the matching windows using the least squares technique. This requires the solution of a single set of equations to give the position of best fit rather than the computation of a similarity assessment algorithm at each point and the selection of the best value. The idea of the least squares matching technique was developed and evaluated at the Institute of Photogrammetry of the University of Stuttgart (see Forstner, 1982; Ackermann, 1984; Pertl, 1985). The basic idea of this method may be explained as follows.

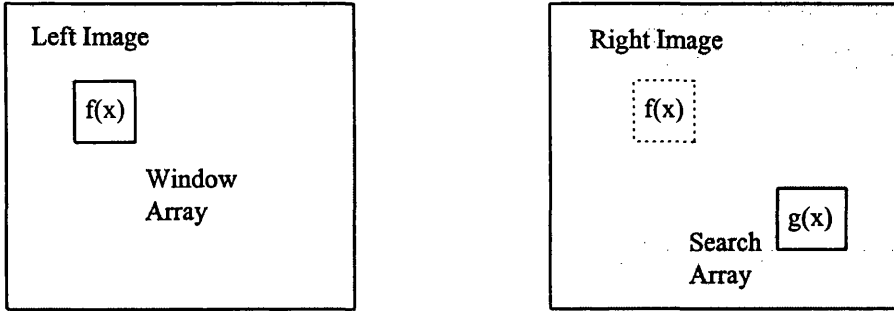


Fig. 11.3. Window and search arrays

Suppose that two homologous image windows $f(x)$ and $g(x)$ of a pair of overlapping photographs (see Fig. 11.3) represent the same object. The assumption that only a linear geometric transformation needs to be carried out between the two windows results in the following equation:-

$$g(x) = f(x + x_p) + n(x) \tag{11.10}$$

where x_p is an unknown shift and $n(x)$ is the additive noise. Eq. 11.10 is non-linear with respect to the unknown shift x_p (see Fig. 11.4). A first order approximation of Eq. 11.10 yields:

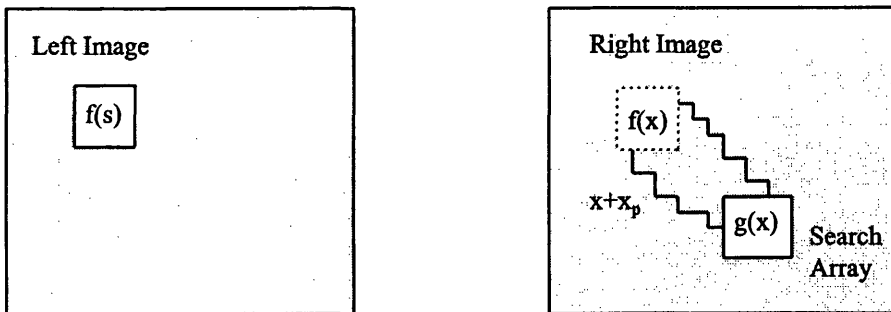


Fig. 11.4. Search array is moved to match the right image.

$$g(x) + v(x) = f(x) + f'(x)dx_p \tag{11.11}$$

where $f'(x) = df(x) / dx$ is the gradient function of $f(x)$; and $v(x) = -n(x)$. By rearranging Eq. 11.11,

$$\Delta g(x) + v(x) = f(x)dx_p \quad (11.12)$$

where $\Delta g(x) = g(x) - f(x)$. Eq. 11.12 may be written for all the pixels of a window array. With N pixels in the window array, the normal equation will be

$$Bdx_p = C \quad (11.13)$$

where

$$B = \sum_{i=1}^N f^2(x_i) \text{ and } C = \sum_{i=1}^N f(x_i)\Delta g(x_i)$$

From Eq. 11.13, the unknown value of dx_p can be found by the solution of the normal equation.

Eq. 11.12 may be extended to include the modelling of the geometric differences (scale variations and shearing) and the radiometric differences between the two images. The final formulation which covers these additional parameters can be given as,

$$\Delta g(x_i) + v(x_i) = f(x_i)dx_p + x_i f'(x_i)da + dh_0 + f(x_i)dh_1 \quad (11.14)$$

where dx_p and da represent a geometric shift and a geometric scale factor; and dh_0 and dh_1 denote a radiometric shift and scale factor respectively.

Since Eq. 11.14 is linearized, the solution has to be iterated. Therefore, two main problems arise - those concerning the initial values for the unknowns and the number of iterations to be employed in the computation. The problem of the initial value is a serious bottleneck for all least squares based correlation techniques (see Thurgood and Mikhail, 1982; Ackermann, 1984; Gruen and Baltsavias, 1986; Day and Muller, 1988). It has been reported in Ackermann (1984), that the pull-in range (convergence radius) of the least squares matching method is very small. Therefore, a very close initial approximation is needed for convergency. The second problem, which is related to the first one, is the number of iterations. There are three possible solutions

for this problem. One is the pre-process the image. Pre-processing functions are performed on the pixels to transform the image so that it has less noise and fewer distortions and to enhance some features and suppress others for easier processing and to speed up the convergency. The second solution is to use a feature-based method, to calculate the initial value for the unknown parameters. The third possibility is to use image pyramids.

11.2.3.4.1 Image Pyramids

This method provides the possibility to work with small sized images which will speed up the computational process. Thus, instead of having to process an image of 512×512 (262,144) pixels, one can use more easily use a reduced size 64×64 (4,096) pixels version of the left and right images for the matching procedure in the first instance (see Fig. 11.5). After matching the same feature of interest in these two images, its coarse position has been determined. Then, the size of each image is extended to 256×256 pixels. In this case, since the coarse position of the feature of interest is already known, the procedure can more easily carry out the required match. Afterwards, the size of the respective images is increased to the real size of 512×512 pixels. The same procedure that has been used in previous stages, is again applied and eventually the fine position of the feature of interest is measured to a sub-pixel level.

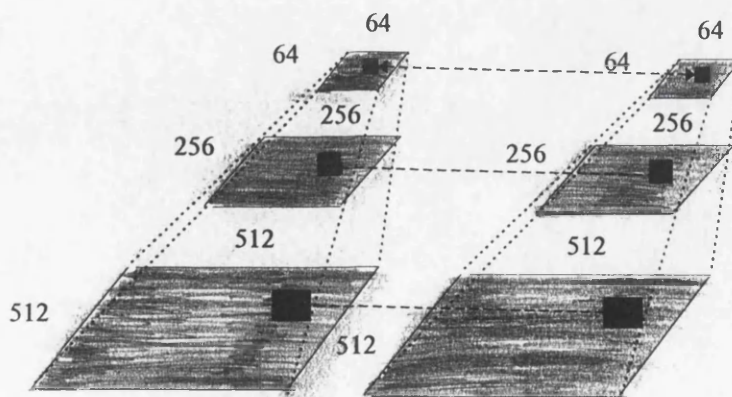


Fig. 11.5. Image pyramids

11.3 The Measurement of the Positions of Cross Targets

To determine the position of the centre of a cross target to a sub-pixel level requires two distinct steps:-

- (i) The detection and approximate location of the target, based upon conventional pattern recognition and feature extraction techniques; and
- (ii) The measurement of the exact position of the target within the image coordinate system using the least squares matching technique.

Each of these steps will be discussed separately.

11.3.1 Automatic Detection, Recognition and Location of Cross Targets

Automatic target measurement normally comprises three different stages - detection, recognition and location.

11.3.1.1 Detection of Cross Targets

This may be accomplished by different methods, such as measuring the local grey level maxima that corresponds to a possible cross target. Detection of the local grey level maxima is a relatively fast and simple procedure when working with digital images. Since the grey level of each cross is greater than that of the cross's surrounding background, the cross target can be viewed as a local maximum.

Implementation of local maxima detection has been carried out by Mikhail et al (1984). According to this study, two processes are needed to detect ground cross targets in digital aerial imagery. Firstly, in order to ensure that true maxima are detected and not those maxima that are attributable to system noise, atmospheric effects, etc., a circular convolutional low-pass filter is applied to the data. Thus, the grey level structure of the low-pass filtered cross can be viewed as a local maximum in two dimensions. Secondly, a process must be developed to find the peaks of these maxima. To implement this feature, each point in the image is considered. At each

point (called a hub point), the image is observed in each of eight directions extending radially away from the hub point (see Fig. 11.6). For each direction, the grey level of each data point in that direction is compared to that of the hub point. If each grey level is lower than the hub point and if one grey level is lower by a specified amount, and the distance from this point to the hub point is less than a given distance, then the hub point is a local maximum in this direction. All eight directions must be satisfied in this way for a hub point to be considered as a two-dimensional local maximum.

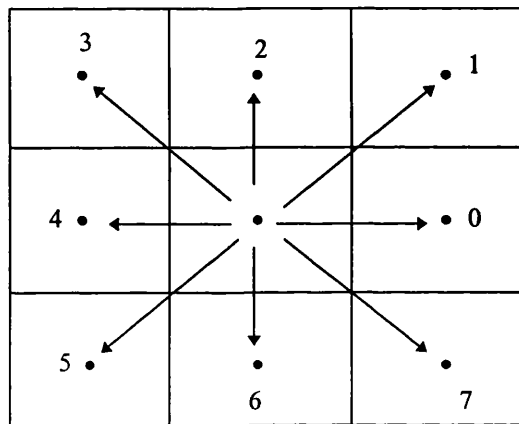


Fig. 11.6. Hub points of the image in the eight directions

11.3.1.2 Recognition of Cross Targets

The recognition process accomplishes two tasks. Firstly, the process needs to discriminate buildings, road intersections, and other physical objects from crosses since all these objects may be two-dimensional local maxima. Secondly, given that the object is a cross, the process must recognize its approximate two-dimensional orientation, size and location. A method based on the calculation and assesment of the descriptors of cross targets has been described by Mikhail et. al. (1984). In this method, the first stage involves the grey value thresholding of the image to yield a binary image. If the threshold is chosen correctly, the object will be segmented from the background data. A Fourier transform is applied to the contour or boundary of the segmented object to produce the object's Fourier coefficients. The coefficients (descriptors) are normalized for comparison with the descriptors of a "true" cross. If the descriptors match those of a cross within a specified accuracy, the object is

classified as a cross. If the descriptors do not match, another grey level threshold is selected for segmentation until the descriptors match.

11.3.1.3 Location of Cross Targets

The existing methods for accurately determining the location of a cross target may be classified into two broad approaches:

(a) Matching Methods

These were considered in detail in Section 11.2.3 where the techniques of image correlation were discussed. Here, template matching and the image modelling approach are discussed since they are the techniques that are most commonly employed for cross location. Template matching could be used either to match a given pattern with part of an image or to match two individual parts of two images together. Given a template $f(x,y)$, consisting of a number of grey level pixels, and an image $g(x,y)$, the centre of the template is placed on each image pixel and the degree of match is computed using the normalized cross-correlation function ρ_{fg} which is given in Eq. 11.15. This is repeated over all possible positions of the image until the best match is found, within a given tolerance, otherwise no match is detected.

$$\rho_{fg} = \frac{\sum_{i=1}^m \sum_{j=1}^n f(i,j) g(i+t, j+h)}{\sqrt{\sum_{i=1}^m \sum_{j=1}^n f(i,j)^2} \sqrt{\sum_{i=1}^m \sum_{j=1}^n g(i+t, j+h)^2}} \quad (11.15)$$

The difficulty that may arise when using this method is that, when searching for cross targets that may have been affected by scale change and orientation differences, a large number of different templates are needed.

The second possibility is to use an image modelling approach which minimizes the differences between the ideal and actual cross target by applying a least squares solution to a series of observation equations which express the measured densities of a digitized target as a function of the densities of an ideal target convolved with certain

types of point spread functions. Thus, the least squares solution yields values for the unknown parameters defining the cross target. The method has been implemented by Thurgood and Mikhail (1982). However, due to the high degree of non-linearity in the functional model, convergence does not occur in all cases. To eliminate this problem, least squares matching has been combined with the gradient edge detection method; a procedure that was devised and evaluated by Azizi (1990). This approach will be used in this project and will be discussed in more detail in later sections.

(b) Edge Detection Method

In this method, different kinds of digital edge operators are used to detect the target position. In Zhou (1986), the centre of a cross target with two bars obliquely intersected in the digital image has been located by using a boundary tracing edge detection method. The centre of a cross is defined as the intersection of two lines which fit two medial axis transformations (MAT) of the cross respectively. A MAT is a set of midpoints in a pair of legs that have the same orientation. The solution to the problem of determining the centre of the cross target is made easier by making some assumptions, e.g. regarding the thickness of the cross - which is assumed to be at least four pixels wide except for those locations lying at the ends of the legs. Also it was assumed that there will be no hole in the cross (Zhou, 1986). In another study reported by Azizi (1990), automatic target measurement has been carried out specifically for each individual fiducial cross of a digitized aerial photograph using the gradient method. As stated above, this approach will be implemented in this present project with the combination of image modelling and least squares method and will be explained fully in the following section.

11.3.2 Cross Target Measurement

For the automatic measurement of the cross target position in digital thermal images, a specific approach which is a combination of two methods - the edge detection method and matching method has been adopted. As explained by Azizi (1990), adopting this approach leads to the elimination of the small pull-in range of

convergency of the least squares method. This method comprises two stages which have been combined in a single computer program that was developed by Azizi (1990). This program with some modifications will be implemented in the present project to carry out automatic measurement of cross targets.

1 - The first stage involves the measurement of the cross position using an edge detection method based on the gradient operator approach. Azizi found that this method has provided satisfactory sub-pixel accuracy for the measured coordinates of the cross centres. In addition to the image coordinates of the cross centres, the program also measures the following parameters of the cross which are shown graphically as Fig. 11.7:-

- the cross mean grey level, i.e. the mean value of the pixel forming the cross;
- the cross mean background grey level, i.e. the mean value of the pixels surrounding the cross; and
- the cross orientation angle with respect to the scan lines.

2 - The second stage employs an image matching technique based on the image modelling and least squares approach. This method requires close initial values of the cross position which are supplied by the first stage, together with the information on the various cross parameters mentioned above. This method was used by Azizi to achieve a further improvement and greater sensitivity in the measurements of the coordinates of the cross centre.

11.3.2.1 Measurement of the Cross Position Using the Gradient Method

To find the cross parameters mentioned above, the following steps are implemented (see Fig. 11.7):

(i) Calculation of the mean grey level (MGL) of the cross and its mean background grey level (MBGL);

The mean grey level (MGL) of the cross and the mean grey level (MBGL) of its background, each comprise a single valued estimation of the overall density of the

cross and its background respectively. These values are computed to serve two different purposes. Firstly, they will be used for the calculation of a threshold value that serves as a criterion for the identification of the cross edges. Secondly, they will be fed, together with the other calculated cross parameters, as initial approximations to the cross measurement program, which is based on the image correlation and image modelling approach.

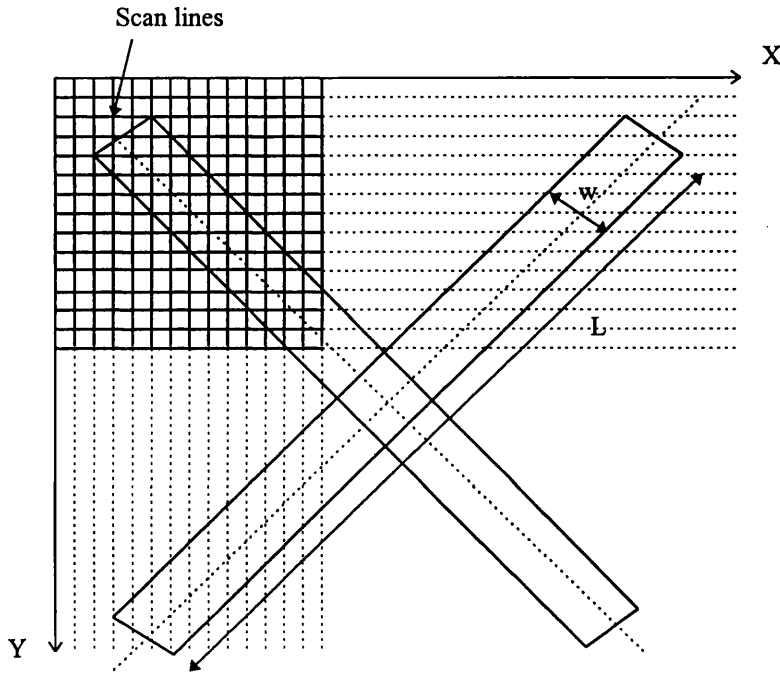


Fig. 11.7. Details of the cross and density values (Azizi, 1990)

To calculate the values of the MGL and MBGL, the cross target needs to be extracted roughly from its background. Each of the crosses exhibits an abrupt change in grey levels as compared with its background. Therefore, to segment the cross, an initial threshold value T is calculated as follows:

$$T = (MXL - MNL) / 2 \quad (11.16)$$

where MXL and MNL denote the maximum and minimum grey levels of the image patch containing the cross target. The MGL and MBGL values are calculated using the so-called area function (AF) and integrated optical density (IOD). The area

function of an image is the number of points having grey levels greater than or equal to a specific value. Thus,

$$AF = \int_T^{\infty} H(p) dp \quad (11.17)$$

where $H(p)$ represents the image histogram; T is the initial threshold value calculated at a previous stage; and dp defines the sum of the number of pixels that have the grey values greater than or equal to the initial threshold value T . For a discrete function (digital image), Eq. 11.17 may be written as

$$AF = \sum_{P=T}^{\max} H(p) dp \quad (11.18)$$

where \max is the maximum range of grey values present in the image.

The integrated optical density (IOD) is defined as the sum of all the grey values of pixels of any specific image feature (e.g. a cross target). For an image $g(x,y)$, the IOD is given by:

$$IOD = \int_a^b \int g(x,y) dx dy \quad (11.19)$$

where the values a and b delimit the region of the object of interest lying within the image; dx and dy define the sum of the all the grey values of pixels in the x and y directions respectively in the region of interest that is delimited by a and b . For a discrete function, Eq. 11.19 can be rewritten as:

$$IOD = \sum_{i=1}^b \sum_{j=1}^a g(i,j) \quad (11.20)$$

where $g(i,j)$ is the density value of pixel at row i , column j . For a cross target, the area limited by a and b can be considered as being equal to the AF calculated by Eq. 11.18. The MGL and MBGL values can now be calculated as,

$$\text{MGL} = \text{IOD}_c / \text{AF}_c \quad (11.21)$$

$$\text{MBGL} = \text{IOD}_b / \text{AF}_b$$

where subscripts c and b denote the cross and its background respectively.

(ii) Calculation of a threshold value using the MGL and MBGL values to differentiate the cross edges from the noise present in the image;

The threshold value is calculated based on the previously determined values for MGL and MBGL using the following relationship:

$$\text{THR} = (\text{MGL}^2 + \text{MBGL}^2)^{1/2} \quad (11.22)$$

(iii) Detection of the positions of the left and right edges of the cross legs using the gradient operator;

The gradient operator is used to enhance the discontinuities of grey levels of cross target on the digital image. The value of the gradient magnitude, given by Eqs 11.4 or 11.5, above the threshold value THR in a given scan line indicates the presence of the cross edge.

(iv) Calculation of the positions of the midpoints of the cross legs for each scan line using the detected positions of the edges;

The calculated value of $\text{grad}(i,j)$ (obtained from Eqs 11.4 or 11.5) for a given cross leg in a scan line, will have positive and negative signs (+grad and -grad) which indicate

the start and end positions of a cross leg respectively. From these values, the cross leg's midpoints for each scan line can be calculated as (see Fig. 11.7),

$$\begin{aligned} W &= j_{+\text{grad}} - j'_{-\text{grad}} \\ \text{xmid} &= j_{+\text{grad}} + W / 2 \\ \text{ymid} &= n \end{aligned} \quad (11.23)$$

where W , xmid and ymid denote the width of the cross leg and the x and y coordinates of the midpoints respectively; $j_{+\text{grad}}$, $j'_{-\text{grad}}$ represent the pixel number in the column direction for which the value of $\text{grad}(i,j)$ has positive and negative signs respectively; and n is the current number of the scan lines.

(v) Fitting a line to each set of midpoints of the legs having the same orientation, and intersecting these lines to give the coordinates of the cross centre and its orientation;

The midpoints of the legs with the same orientation are determined using the following relation:

$$\text{sign}(\text{xmid}_n) = \text{xmid}_n - \text{xmid}_{n-1} \quad (11.24)$$

where xmid_n and xmid_{n-1} are two successive detected midpoints in the left or right cross legs; and $\text{sign}(\text{xmid}_n)$ is a value corresponding to the midpoint xmid_n , which may be positive or negative. The midpoints having negative or positive signs are arranged into separate arrays so that each array comprises only those midpoints with the same sign.

11.3.2.2 Image Modelling and Least Squares (IMLS) Matching Method for Cross Target Measurement

This method offers a solution to various estimation problems involving digital images and digital image processing. It has been developed in response to a need for high-precision measurements of target position for metric applications, especially to

achieve an accurate inner orientation using highly accurate measurements of the positions of the fiducial marks. This results cannot be obtained when any method based on the feature detection approach is employed (Day and Muller, 1988). In this instance, the parameters of most interest are the image coordinates which are related to the column and row positions within the array of picture elements. However, the method has also potential for application to more general problems involving both radiometric and geometric parameters. In fact, for a given image target, the measured density values corresponding to each picture element are related by a functional model written in terms of both types of parameters. This technique requires some a priori knowledge of the imaging system point-spread function. Using approximate values for all unknown parameters obtained using simple or at least conventional methods, a series of iterative computations generate corrections to the parameter estimates to provide a set of values which best fit the ideal model of the image feature.

The detailed treatment of the IMLS method has been presented in Thurgood and Mikhail (1982). Therefore, all the mathematical derivations required to explain this method will not be given here. This section only presents their derivation for the general form of the least squares adjustment model for a two-dimensional image and the case of pointing to an edge within a one-dimensional image - since they provide the basis for the adjustment model of the cross-shaped targets which is the main concern of this project.

11.3.2.2.1 The General Adjustment Model

The basic model has been established by Thurgood and Mikhail (1982). Let $f(s,t)$ represent the output of a perfect imaging system, that is, the ideal picture function. Consider next a linear, spatially invariant imaging system with a normalized point spread function $p(s,t)$ (known also as the impulse response) that is assumed to be known. Then let $l(s,t)$ denote a random variable representing the measurement at the sampling position (s,t) . Then to model the measured quantity using the convolution operation gives the following expression:-

$$l(s,t) = \int_{-\infty}^{\infty} \int_{-\infty}^{\infty} f(\xi,\eta) p(s - \xi, t - \eta) d\xi d\eta$$

$$l(s,t) = f(s,t) * p(s,t) \tag{11.25}$$

where * denotes the convolution operation.

If a set of parameters \underline{x} that completely characterize $f(s,t)$ over the region of interest is then considered, then Eq. 11.25 may be re-written as,

$$l(s,t) - f(s,t;\underline{x}) * p(s,t) = 0 \tag{11.26}$$

Dropping s,t for simplicity, this equation becomes

$$l + F(\underline{x}) = 0 \tag{11.27}$$

where $F(\underline{x}) = -f(s,t;\underline{x}) * p(s,t)$

For the ij -th image element - which is a sample of $l(s,t)$ at $s = s_i, t = t_j$ - the linearized form of 11.27 is

$$l_{ij}^o + \underline{v}_{ij} + \underline{B}_{ij} \underline{\Delta} = -\underline{F}_{ij}(\underline{x}^o) \tag{11.28}$$

- where l_{ij}^o is the initial estimate for the observation,
- \underline{v}_{ij} is the measurement discrepancy,
- \underline{B}_{ij} is the set of partial derivatives of $F_{ij}(\underline{x})$ with respect to parameters, evaluated at $\underline{x} = \underline{x}_o$,
- \underline{x}_o is the set of initial parameter approximations,
- $\underline{\Delta}$ is the set of corrections to the parameter approximations, and
- u is the number of unknown parameters.

Eq. 11.28 represents a single condition equation for the model known as Adjustment by Indirect Observations. If the region of interest contains n pixels, the total set of condition equations may be written using matrix notation as

$$l^o + v + B \Delta = -F(x^o) \quad (11.29)$$

The stochastic information associated with the measurements is characterized by the covariance matrix Σ . The corresponding cofactor matrix Q is often used for convenience and is obtained through the use of a scaling of the covariance matrix, that is,

$$Q = (1/\sigma_o^2)\Sigma$$

where σ_o^2 is known as the reference variance. Furthermore, the weight matrix W is equal to Q^{-1} . The corrections Δ to the parameter approximations may then be calculated by solving the normal equations:

$$B^t W B \Delta = B^t W f^o \quad (11.30)$$

where $f^o = -[l^o + F(x^o)]$.

This may be also be written as

$$N \Delta = t \quad (11.30a)$$

where $N = B^t W B$

$$\Delta = N^{-1} t$$

The non-linearity of the condition equations requires an iterative adjustment procedure, involving re-linearizing the updated parameter values and continuing until the solution converges.

The elements of B may be calculated as follows. Considering a single condition equation, from 11.26, the partial derivative for the k-th parameter:

$$\begin{aligned}
 \partial F_{ij} / \partial x_k &= -\partial / \partial x_k \iint_{-\infty}^{\infty} f(\xi, \eta) p(s_i - \xi, t_j - \eta) d\xi d\eta \\
 &= -\iint_{-\infty}^{\infty} \partial / \partial x_k f(\xi, \eta) p(s_i - \xi, t_j - \eta) d\xi d\eta \\
 &= -\iint_{-\infty}^{\infty} f'(\xi, \eta) p(s_i - \xi, t_j - \eta) d\xi d\eta \\
 &= -f'(s_i, t_j) * p(s_i, t_j)
 \end{aligned} \tag{11.31}$$

where $f'(s_i, t_j) = \partial f(s, t) / \partial x_k$

$$\partial F_{ij} / \partial x_k = -(\partial f_{ij} / \partial x_k) * p_{ij}$$

The notation for $\partial F_{ij} / \partial x = B_{ij}$ as follows:

$$[-(\partial f_{ij} / \partial x_1) * p_{ij} - (\partial f_{ij} / \partial x_2) * p_{ij} \dots \dots \dots - (\partial f_{ij} / \partial x_k) * p_{ij}] \tag{11.32}.$$

11.3.2.2.2 Measuring a One-dimensional Edge

Again the theoretical basis of this model has been established by Thurgood and Mikhail (1982). Consider the ideal model of an edge or discontinuity present in a one-dimensional signal $f(s)$. This model may be completely and uniquely defined in its simplest form by the use of three distinct variables or parameters, as shown in Fig. 11.2, where h_1 is the signal value preceding the edge; h_2 is the signal value following the edge; and x is the location of the edge. This may be expressed as

$$f(s) = h_1 + (h_2 - h_1) U(s - x) \tag{11.33}$$

where U is the unit step function,

$$U(s) = 1 \text{ for } s \geq 0$$

$$0 \text{ for } s < 0$$

Modelling the observable signal as the one-dimensional form of Eq. 11.25 as follows:

$$l(s) = f(s) * p(s) \tag{11.34}$$

This equation can be written as

$$l(s) = \int_{-\infty}^{\infty} f(\xi)p(s - \xi)d\xi$$

$$= \int_{-\infty}^{\infty} h_1 p(s - \xi)d\xi + \int_x^{\infty} (h_2 - h_1)p(s - \xi)d\xi$$

$$= h_1 + (h_2 - h_1) \int_x^{\infty} p(s - \xi)d\xi \tag{11.35}$$

since $\int_{-\infty}^{\infty} p(\xi)d\xi = 1$ and making the change of variable $\eta = s - \xi$

$$l(s) = h_1 + (h_2 - h_1) \int_{s-x}^{-\infty} p(\eta)(\partial\xi / \partial\eta)d\eta$$

$$= h_1 + (h_2 - h_1) \int_{-\infty}^{s-x} p(\eta)d\eta$$

since $\partial\xi/\partial\eta = -1$ and letting $P(s) = \int_{-\infty}^s p(\eta)d\eta$, then

$$l(s) = h_1 + (h_2 - h_1) P(s - x) \tag{11.36}$$

which may be written directly in the form of Eq. 11.27:

$$l(s) + F(x) = 0$$

The partial derivatives with respect to the unknowns are as follows:

$$\begin{aligned}\partial F / \partial h_1 &= -1 + P(s - X) \\ \partial F / \partial h_2 &= -P(s - x) \\ \partial F / \partial X &= -(h_2 - h_1) \partial / \partial x (P(s - x)) \\ &= (h_2 - h_1) p(s - x)\end{aligned}\tag{11.37}$$

At this stage, the type of point-spread function must be known.

11.3.2.2.3 Point Spread Function

The effects of the physical system during the imaging process, such as optical diffraction from the sampling spot, technical imperfections such as aberrations of the camera lens and lack of perfect focusing etc. produce jointly and separately what is called a point spread function (psf). In other words, the psf is the image of a "perfect point" or "point source". If any arbitrary picture $f(x,y)$ could be considered to be a sum of point sources, then the knowledge about the output of an input point source could be used to determine the output for the function $f(x,y)$. For example, if an imaging system with a Gaussian sampling spot is used, the image of a point source will appear as a finite sized circle exhibiting Gaussian intensity variation. This finite circle has the same size and grey level characteristics as the sampling spot itself. For this reason, the psf is also called an impulse response (see also Section 11.3.2.2.1). A knowledge of the mathematical function representing the characteristics of the sampling spot may be used as the psf of the imaging system. It can be used to determine the output for any particular input. Alternatively, a knowledge of the input and output may be used to determine the psf. Therefore, the psf represents the behaviour of the system in mathematical terms. There are two types of psf:

- (i) Rectangular psf and
- (ii) Gaussian psf.

It has been found that the Gaussian psf closely models the impulse response of commonly used photographic materials (Thurgood and Mikhail, 1982). In Mikhail et

al, (1984), two types of psf have been tested using a least squares solution. The result was that the least squares model using a Gaussian psf performed well in the presence of noise, while the Rectangular psf did not. So, the Gaussian psf has been used in this project.

11.3.2.2.4 Edge Pointing With Gaussian Spread Function

A Gaussian spread function may be expressed as

$$p(s) = (1/(0.5d(2\pi)^{-1/2}))\exp(-s^2/(0.5d^2)) \quad (11.38)$$

where d is the width of the function, as shown in Fig. 11.8. The quantity d is the distance between the two inflection points in the curve defining $p(s)$. In this project, different values for the width of the Gaussian spread function were input to the program. The value that provides the best fit between the artificially generated template and the real cross target has been used as the width of the spread function.

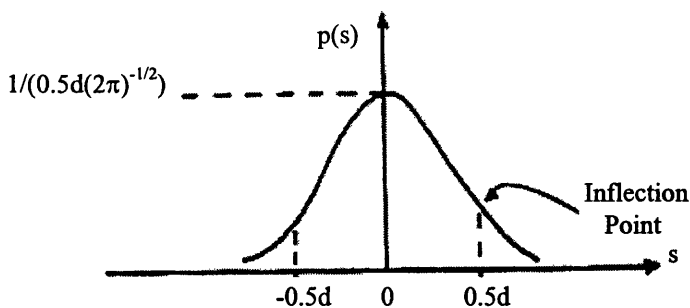


Fig .11.8. Gaussian spread-function (Thurgood and Mikhail, 1982)

11.3.2.2.5 Cross-type Targets

The adjustment model derived for the one-dimensional edge (see Section 11.3.2.2.2) can be applied to the cross-type calibration target which has been used in this project. Considering Fig. 11.9, the following parameters that define a cross need to be specified:-

- (i) the cross density and the background density levels (h_2, h_1);
- (ii) the width and the length of the cross legs (w, l);
- (iii) the angle of the orientation of the cross with respect to the scan lines Q ; and
- (iv) the coordinates of the centre of the cross (x, y).

Eg. 11.35 which was derived for a one-dimensional edge, can be written for cross target by considering each of the cross legs as one segment. This will lead to,

$$l(s,t) = h_1 + (h_2 - h_1) \sum_{i=1}^4 P_{ti} P_{si} \tag{11.39}$$

and correspondingly,

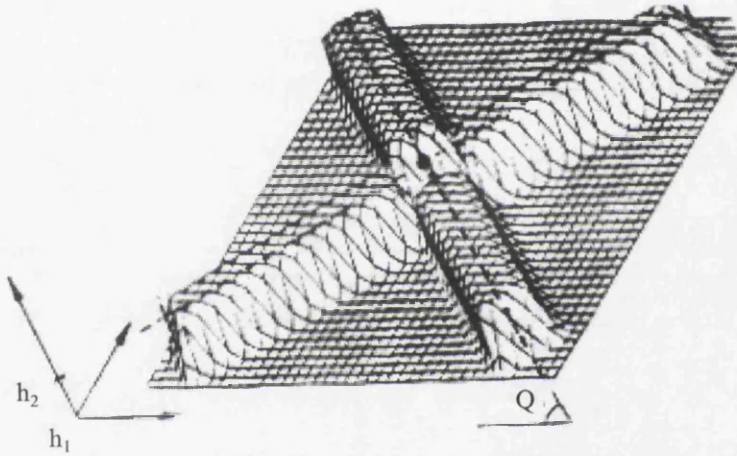


Fig. 11.9. Cross target (Azizi, 1990).

$$F(\mathbf{x}) = -h_1 - (h_2 - h_1) \sum_{i=1}^4 P_{ti} P_{si} \tag{11.40}$$

Hence, the partial derivatives for the unknown parameters of the cross target can be obtained as follows:

$$\frac{\partial F}{\partial h_1} = -1 + \sum_{i=1}^4 P_{ti} P_{si}$$

$$\frac{\partial F}{\partial h_2} = - \sum_{i=1}^4 P_{ti} P_{si}$$

and for the parameters x, y and Q denoted by x_k :

$$\partial F / \partial x_k = -(h_2 - h_1) \sum_{i=1}^4 \partial / \partial x_k (P_{ti} P_{si}).$$

These partial derivatives for unknown cross parameters are input to the normal equations which have been given in Eq. 11.30. Then, these equations are solved to determine the correction to the unknowns. However, as discussed before, the non-linearity of these equations requires an iterative solution that re-linearizes the updated parameter values of cross parameters until they converge.

11.4 Conclusion

In this Chapter, a detailed treatment of the image matching procedure that has been used to determine the centres of the cross targets on the infrared images of the calibration plate has been fully covered. In the next chapter, the computer programming of this procedure using the FORTRAN 77 language will be explained. In addition, the results of testing this program with the thermal images obtained using TVFSs for the previous research project in this Department will be given. The results obtained in actual accuracy tests using these images will be reported in association with the comments on the use of computer program.

CHAPTER 12: COMPUTER PROGRAMMING OF THE IMAGE MATCHING PROCEDURE

12.1 Introduction

In the previous Chapter, a detailed explanation of the image matching technique that has been used in this project, has been given. In this chapter, the programming of this procedure in the FORTRAN 77 language to produce the program "SUBPIX" will be described. The results of testing this program with the cross targets of the calibration plate used with various infrared imagers will be given.

12.2 Development of Program SUBPIX

The program SUBPIX has been developed by the present author to detect and locate the position of the centre of the cross targets on the plates used to calibrate middle and thermal infrared imagers, using the methods described in the preceding Chapter. The program uses as its core the computer program that was developed by Azizi (1990) for use with the fiducial marks of aerial photographs. However, the program has been modified quite extensively and further developed by the author during this research work with the following changes:

(i) Azizi's program was written to determine the centre of the fiducial marks on the digitized aerial photographs. Therefore, program was designed to be used with only the 4 fiducial marks present in each aerial photo. However, in this project, since the target plate consists of 130 crosses, the program had to be changed to accept all these targets. The program also depends on the operator making a manual measurement or pointing to the first and last target crosses on the monitor screen displaying the images of the target crosses. Thereafter the search for and the determination of the location of each of the 130 target crosses is carried out automatically by the program.

(ii) In Azizi's program, the target width and length were determined manually in a prior operation and this data was then input to the program. However, in the new

program SUBPIX, these cross parameters are computed automatically using the method that was developed originally by Thurgood and Mikhail (1982). According to this method, the cross type (see Fig. 11.7) and the ratio (c) between the cross length (L) and cross width (W) in the object space must be known. Then, neglecting the effects of foreshortening and other displacement associated with image tilts, the ratio c on the object space would be equal to the corresponding ratio in the image. In addition, the effective area of the target in the image, IOD_c , which has been given in Eq. 11.19, could be expressed as a function of W and c . Thus, according to Fig. 11.7,

$$2LW - W^2 = IOD_c; \text{ and}$$

$$2cW^2 - W^2 = IOD_c;$$

$$W^2(2c - 1) = IOD_c;$$

$$W = (IOD_c / (2c - 1))^{1/2} \quad (12.1)$$

In this project, $W = 2\text{mm}$ and $L = 14\text{mm}$. Hence, the ratio c is equal to 7. Once the program computes the width from Eq. 12.1, it automatically determines the length, multiplying it by 7.

12.2.1 Structure of Program SUBPIX

The overall structure of program SUBPIX is given in Fig. 12.1. It includes two sub-programs and seven routine programs. One of the routine programs, CORR, connects directly to the main program SUBPIX. However, two of them, EXCHG and FIT are called only by sub-program GRAD, while the other four, AREA, SLVNRM, ZEROM1 and ZEROM2 are called only by sub-program PTSUB. These routine programs contain the main mathematical functions that the program has to execute. As will be seen later, this structure of program provides the reader with the opportunity to follow the sequences easily.

All of the features of the image matching procedure discussed in the previous Chapter have been implemented in the program through the following sequence:

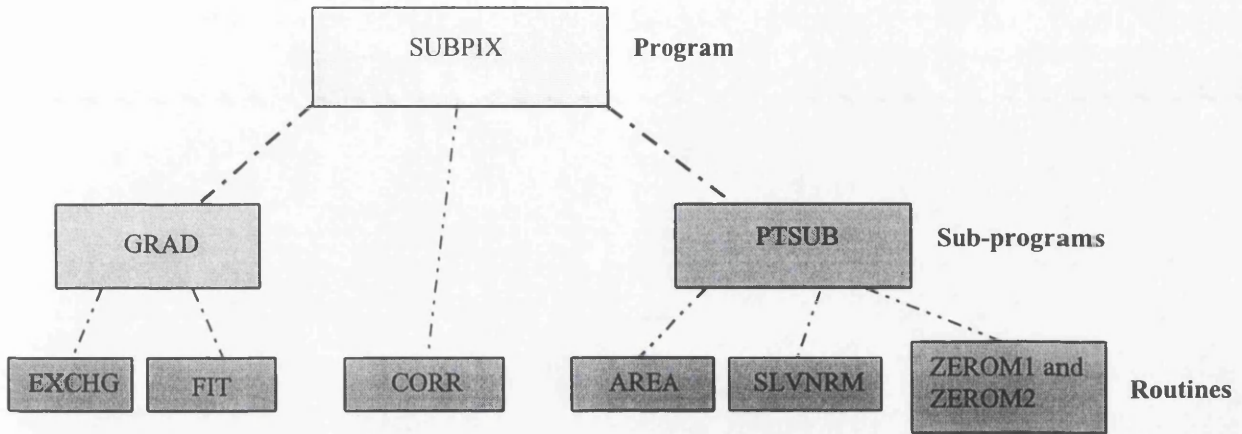


Fig. 12.1. Overall structure of program SUBPIX

- (i) The first step involves loading an image array, which comprises all the images of the cross targets, into the computer RAM (see Block 1 in Appendix A).
- (ii) The program opens the two image windows itself. They contain the first and last targets in the image array which have already been located on the display screen by the operator in a prior operation (see Fig. 12.2).

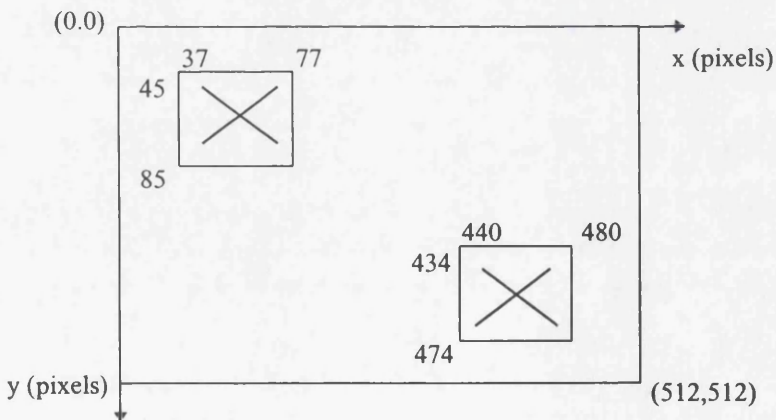


Fig. 12.2. Corner of the image windows

- (iii) The coordinates of the first and last cross targets ($x_f, y_f; x_l, y_l$) are measured automatically by the sub-program GRAD. Then, to check whether they are the same or not, the correlation between these targets is computed using the

normalized cross-correlation coefficient which was given by Eq. 11.15 (for stages (ii) and (iii) see Block 2)

- (iv) Once the number of cross targets in both the x and y directions (n_x ; n_y) have been input to the program, the distances between any two neighbouring targets in both the x and y directions (s_x ; s_y) are computed automatically by the program (see Block 3 in Appendix A). Thus,

$$s_x = (x_i - x_f / (n_x - 1)) \text{ and } s_y = (y_i - y_f / (n_y - 1))$$

- (v) Using the values that are produced by stage (iv) and the coordinates of the first cross target, the approximate coordinates of all the other cross targets in the image array are computed (see Block 4).
- (vi) Using the approximate coordinate values of the cross targets, the program opens a 40x40 pixel search array for each target. Thus it looks for the target in this search array until it finds one with suitable cross parameters (h_1 , h_2 , x , y , Q) (Block 5 in Appendix 5).
- (vii) Once the program measures the coordinates of all the cross targets, they are written to the specific output file (see Block 6).

The program then carries out the various stages which are given below for each cross in the order of row by row. These are contained in Block 7 in Appendix A.

- (vii) The Program calls the sub-program GRAD and computes the parameters of the cross target with the following stages:-
- (a) Based on the MGL and MBGL values (Eq. 11.21), a threshold value is calculated using Eq. 11.22.
- (b) Based on Eq. 12.1, the width (W) and the length (L) of the cross are computed.
- (c) The image is scanned systematically in both the row and column directions and a two-dimensional gradient magnitude (Eqs. 11.4 or 11.5) is calculated for each pixel.
- (d) The location of the midpoints of the cross legs in each scan line are determined using Eq. 11.24. If the calculated value of the cross width (Eq. 11.24) is outside a specified range, it will be rejected. Therefore the contribution of the pixels located at the extreme corners of the legs, which affect the accuracy of the coordinates of the cross centre can be eliminated.

(e) The calculated midpoints on those legs with the same orientation are identified and arranged into different arrays using the approach described in Section 11.3.2.1(v).

(f) If fewer than two midpoints are determined on the two cross legs with the same orientation, then the threshold value is reduced by a certain factor and procedures (c) to (e) are repeated until either more than one midpoint is determined, or the threshold reaches its minimum specified level - which means that no cross is detectable.

(g) A line is then fitted to each series of midpoints and the intersection of the lines and their slopes gives the position of the centre of the cross and its orientation respectively.

```

XL  YL  XR  YR
55.00 62.00 61.00 62.00
63.00 69.00 52.50 69.00
64.00 70.00 51.50 70.00
CL 0.88356 13.39727
////////////////////////////////////
APPROXIMATE VALUES FOR UNKNOWNNS
X      Y      THETA1  THETA2
57.91 64.57   -41.98   39.88
H1     H2
88.    188.
////////////////////////////////////

```

Table 12.1. Output from program GRAD

(viii) The calculated parameters from sub-program GRAD (see Table 12.1) are input to the sub-program PTSUB which carries out the following steps:-

(a) First of all, the conditions for terminating the iterations are input to the program.

(b) The width of the Gaussian spread function and the increment for calculating the area under the Gaussian curve are input to the program.

(c) Weights for the unknown cross parameters are also input to the program.

(d) The geometry of the simulated cross is established.

(e) The coefficients of the observation equations are calculated using the area under a Gaussian curve and the values of the spread function.

(f) The modelled cross is formed and the discrepancies between the modelled image and the original image are computed.

(g) The normal equations are formed and solved using a unified least squares approach. If the conditions for terminating the iterations are fulfilled, the program is ended and the results are output (see Table 12.2).

CROSS POINTING WITH W=3.00 L=21.00 AND SPREAD WIDTH D=1.00						
PARAMETER APPROXIMATION:						
H1	H2	X	Y	THETA		
0.27	1.60	57.915	-64.567	0.7997		
ITERATION CORRECTIONS:						
1		-87.89	-186.74	0.001	0.000	0.00000
VARIANCE		VAR.CH.				
1.015		99.995				

PARAMETER APPROXIMATION:						
H1	H2	X	Y	THETA		
0.27	1.60	58.006	-64.534	0.79995		
ITERATION CORRECTIONS:						
2		-0.00	0.00	0.091	0.033	0.00024
VARIANCE		VAR.CH.				
1.029		-1.360				

////////////////////						
TOTAL CORRECTIONS						
		-87.99	-186.74	0.092	0.034	0.0024
FINAL ESTIMATES						
		0.27	1.60	58.006	-64.534	0.79995 1.0291

Table 12.2. Output from program PTSUB

The sequences of program SUBPIX that have been given above, are also presented as a flow diagram in Fig. 12.3. As was discussed above and illustrated in Fig. 12.1, the program SUBPIX consists of the two main sub-programs: GRAD and PTSUB. These are described below.

12.2.2 Sub-Program GRAD

This was developed originally by Azizi, (1990) and has provided satisfactory sub-pixel accuracy for the measured coordinates of the cross centre. The flow diagram of this program is given in Fig. 12.4. As stated above, this sub-program measures the following parameters of the cross;

- (i) the cross mean grey level, i.e. the mean value of the pixels forming the cross;
- (ii) the cross mean background grey level, i.e. the mean value of the surrounding pixels of the cross;

- (iii) the cross centre coordinates; and
- (iv) the cross orientation angle with respect to the scan lines.

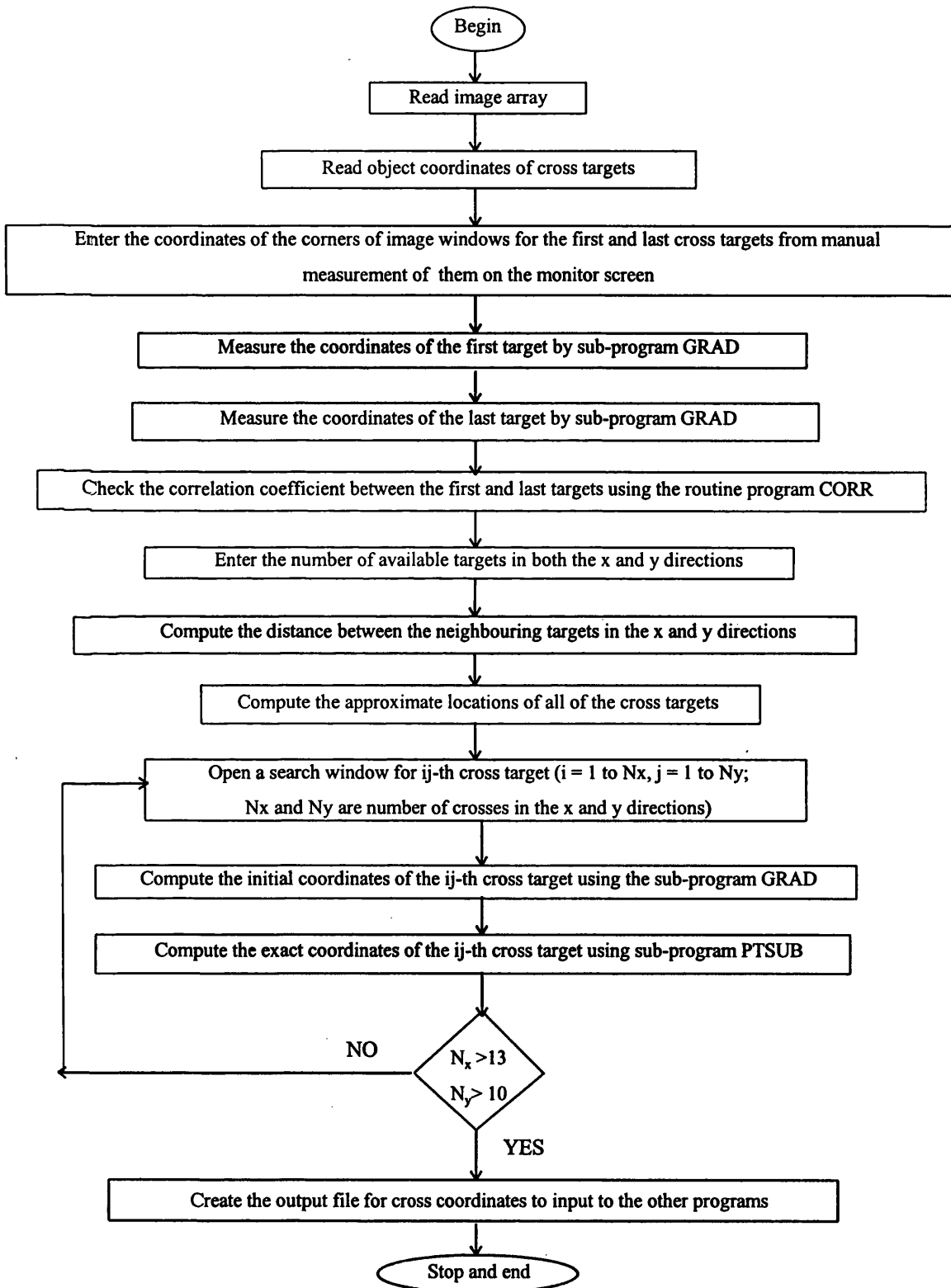


Fig. 12.3. The flow diagram shows an overview of the main program SUBPIX

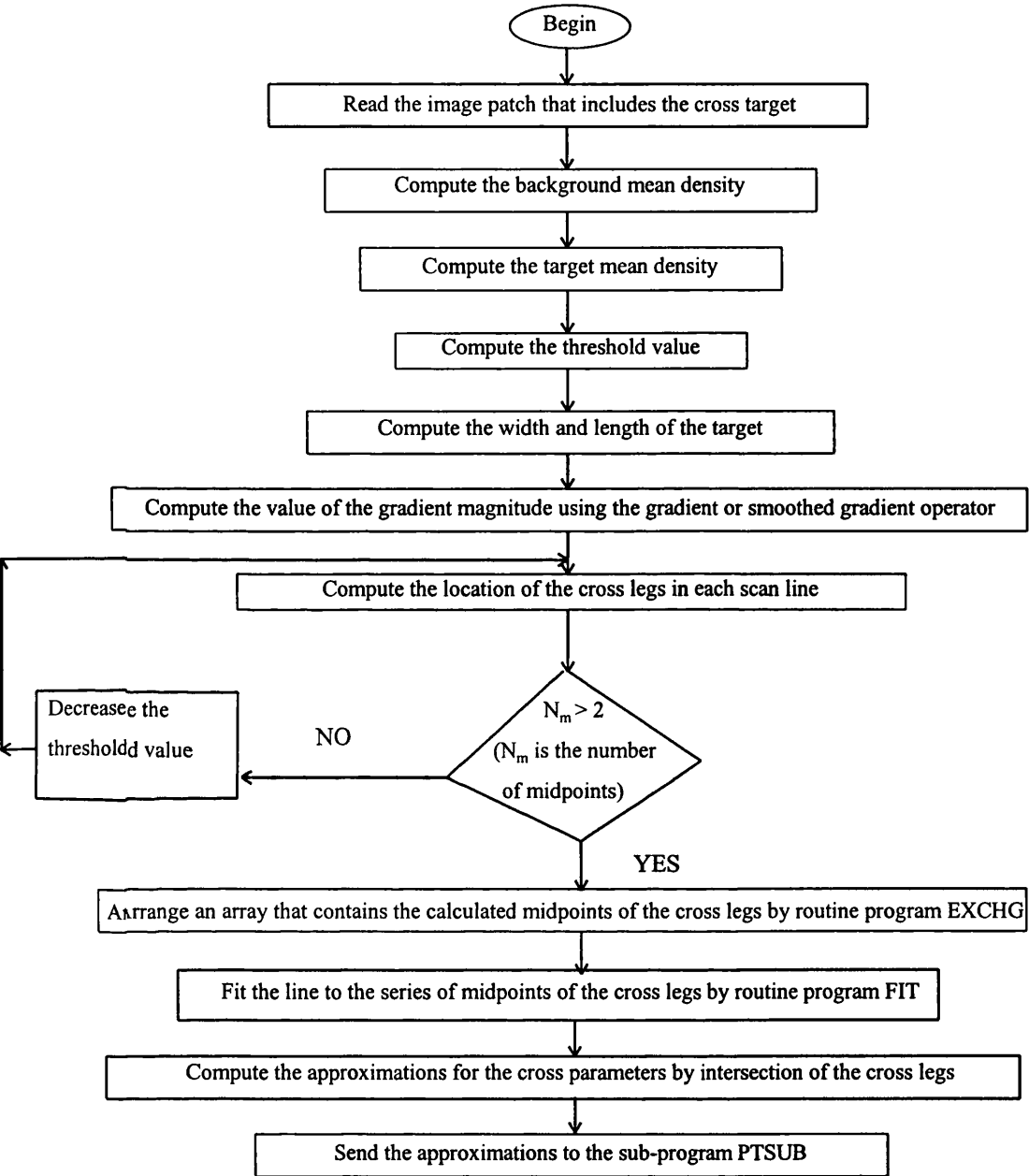
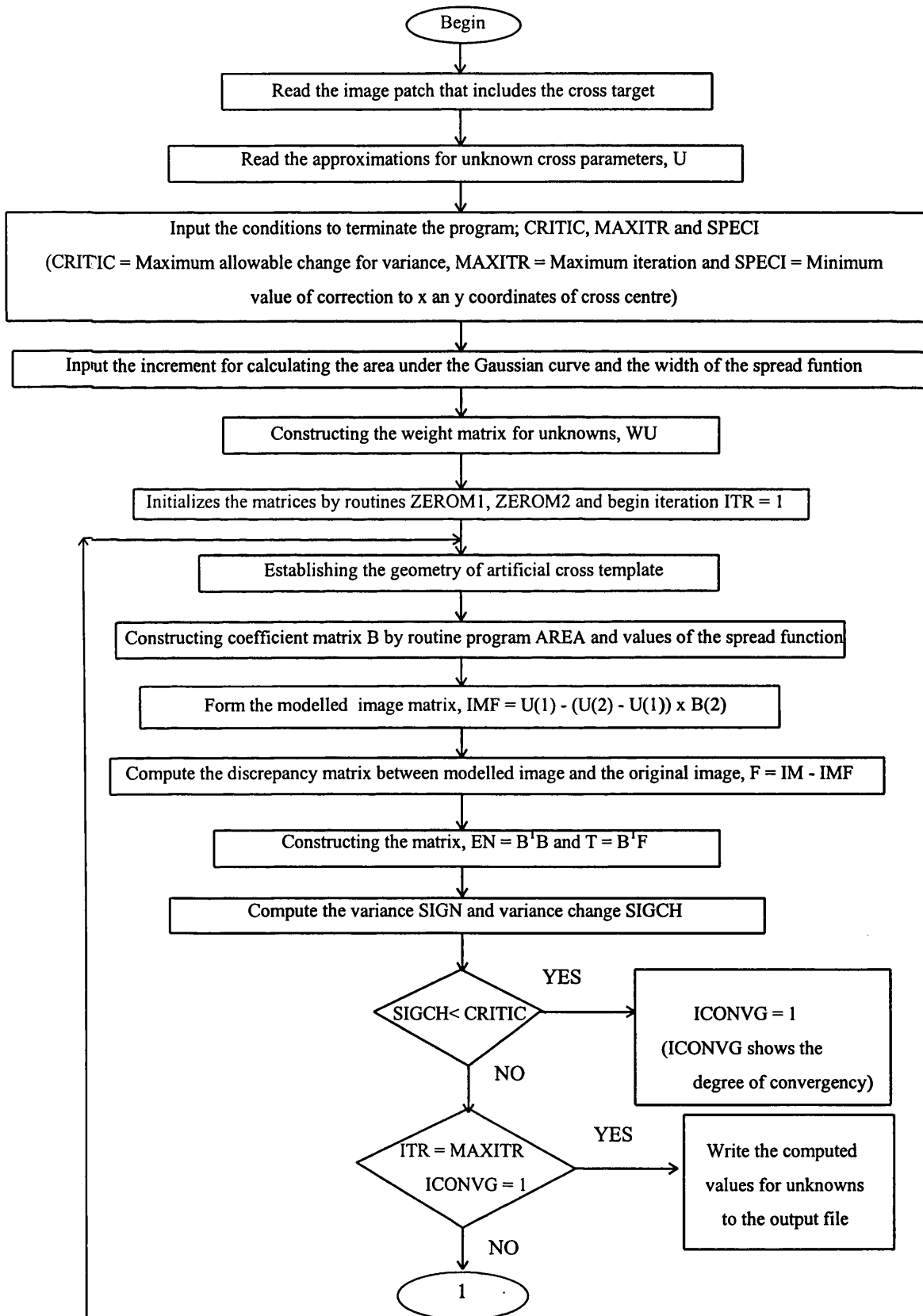


Fig. 12.4. The flow diagram of sub-program GRAD

12.2.3) Sub-Program PTSUB

PTSUB is the second stage of program SUBPIX. It achieves a further improvement in the accuracy of the measured coordinates of each cross through the use of the image correlation technique based on the image modelling and least squares approaches that

have been explained in some detail in the previous chapter. The flow diagram of sub-program PTSUB is given in Fig. 12.5.



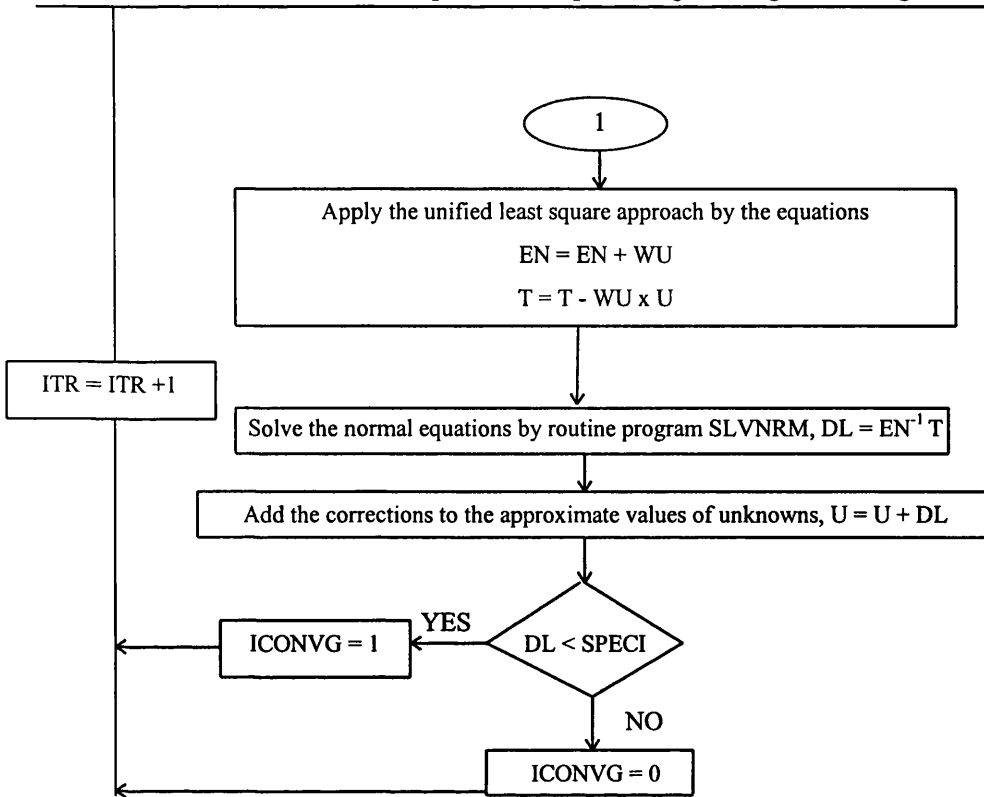


Fig. 12.5. The flow diagram of subprogram PTSUB

12.2.4 Routines

As has been discussed in Section 12.2.1 above, the main program and the subprograms make use of several routine programs to implement various functions. They are:

- (i) **CORR**: this checks the correlation between the first and last cross targets.
- (ii) **EXCHG**: this arranges the detected midpoints of the legs of each cross target with the same orientation into a single array.
- (iii) **FIT**: this fits a line through the detected midpoints of the cross legs with the same orientation.
- (iv) **ZEROM1** and **ZEROM2**: these initialize the one- and two-dimensional matrix arrays respectively.
- (v) **AREA**: this calculates the area lying under the Gaussian curve.
- (vi) **SLVNRM**: this solves the normal equations for the unknown parameters of each cross.

The listing of program SUBPIX is included as Appendix A. Originally, this program has been written in FORTRAN 77 for use on PCs, but many difficulties have been encountered both with the amount of memory available in the PC used for this project and with the program libraries available on the PC version of FORTRAN 77. Therefore, the program had to be transferred to the University's Central Sun Sparc Server machine running under the UNIX operating system which overcome these problems. However, the program runs slowly since many users share the system at the same time.

12.3 Test Results

In order to assess the performance of the program SUBPIX for the measurement of the positions of the cross targets, initially two existing thermal infrared images of a calibration plate, which had been acquired by the Barr & Stroud IR-18 Thermal Video Frame Scanner (TVFS) for the previous research work carried out by Dr. Amin in this Department, have been tested. The thermal images had been recorded on tape cassette in analogue form. Therefore they had to be played back by the Video Tape Recorder (VTR) and digitized to produce a 512 by 512 pixel image size in TIFF image format using the frame grabber which was constructed for use on PCs by the Department of Mechanical Engineering at this University. After conversion, these digital thermal images have then been stored on a 3.5" floppy disk. Testing of these images was followed by another test of the image of the target plate which had been acquired by a CCD camera that belongs to the same Department. To process these digital images using the FORTRAN 77 program, they have been converted to PGM format, which is an ASCII file associated with the X-Windows graphical user interface (GUI) that is running under the UNIX operating system on the Sparc Server. However, this conversion is not one-to-one, which meant that the 512 by 512 size binary file in TIFF format converted to a 15,424 by 17 ASCII data matrix in PGM format. The first four lines of this data matrix include information about the image format type and image size. Other lines contain the image information that is necessary for the running of program SUBPIX. Deleting these four lines and using the CONV1 FORTRAN 77

program which has been written by the author, a one-to-one conversion back to the 512 by 512 data matrix (which consists of the grey values of each pixel over the whole image area) has been carried out.

12.3.1 Test Results With Thermal Images

These thermal images of the target plate, which was designed specifically for the calibration of the TVFSs (Amin, 1986), consist of 150 X-shaped crosses that are arranged in a symmetric pattern of 10 rows and 15 columns (Fig. 12.5). They are distributed over the plate with a 30mm spacing between each pair of adjacent crosses in both the horizontal and the vertical directions. The dimensions of each cross were 14mm (the diagonal length of the arm) by 2mm (the thickness of the arm). Besides these crosses, 24 television targets were etched at intervals across the target plate to test the system resolution in both the horizontal and vertical directions. These had been copied from a test card that was used originally to measure the resolution of vidicon tube cameras. The target plate had been calibrated twice at different temperatures using a Ferranti Monocomparator installed at the National Engineering Laboratories (NEL) in East Kilbride near Glasgow. The 150 crosses were measured twice, forward and backward, in the x and y directions to ensure consistency in the measurements and the mean coordinate value at each point was computed. The precision ($m_x = m_y$) of measuring the crosses was $\pm 20\mu\text{m}$ (Amin and Petrie, 1993). These precisely calibrated x, y coordinates for each of the 150 crosses have also been used as the reference coordinate set in this research and are given in Appendix B.

In Amin (1986), different TVFSs have been calibrated using both these given coordinates and the coordinates of the images of the same crosses measured using a Video Monocomparator which first described by Petrie (1983). These measured video monocomparator coordinates of the crosses contained the various distortion generated by the frame scanner - including lens distortion and those generated both by its basic system geometry (i.e. its spherical image plane) and any deviation from its nominal operation, e.g. by its scanning elements. Since the target plate had been calibrated, the coordinates are considered to be error free. In order to determine the distortion values

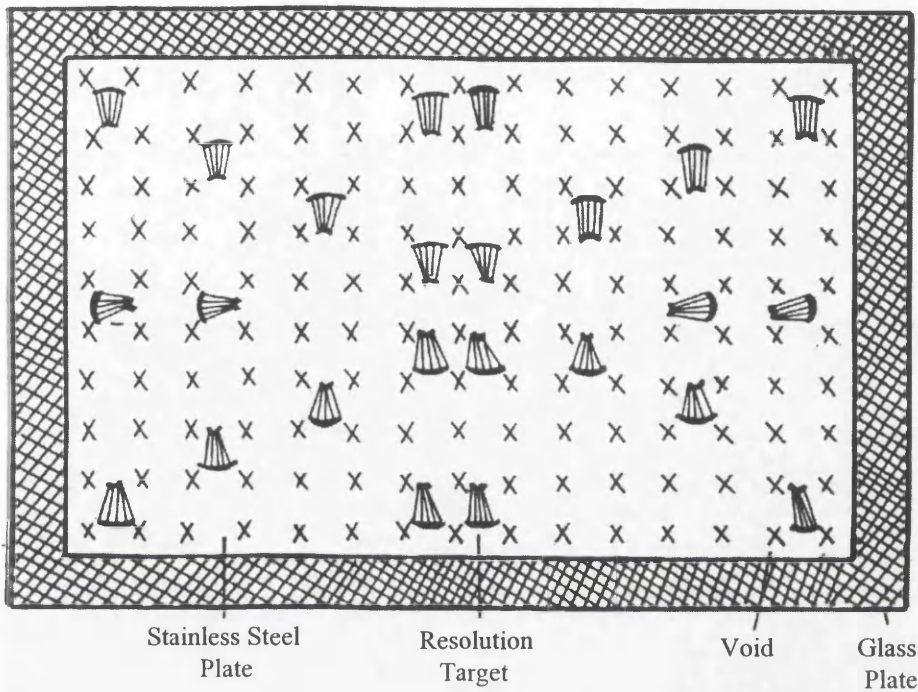


Fig. 12.5. Design of the calibration plate

in both the x and y directions at each of the target crosses in the video image, the POLY25 program was written in FORTRAN 77 to perform the 25-term polynomial transformation. This program was originally implemented on an ICL 2988 mainframe computer of the University of Glasgow running under the standard VME operating system. The present author has modified this program to allow it to run on PCs. This FORTRAN 77 program is arranged so that the user can select any specific set of terms required for any individual run. It is listed and included as Appendix D. It was seen that a drastic change in the magnitude of the distortion was obtained when the affine transformation was used. This showed that the video image contained a large affinity and/or lack of orthogonality between the x and y axes. The accuracy results for the Barr & Stroud IR-18 images were $m_x = 0.67$, $m_y = 0.50$ in pixel (Amin, 1986).

According to Amin and Petrie (1994), the crosses appeared sharp and well defined against an almost black background on the display monitor of the video monocomparator. Thus they had a good contrast against the background. On the other hand, the images of the resolution targets were not resolved. In this preliminary test,

the resolution of the television targets on digitized thermal images also did not exhibit well, which means that these images are poor regarding their absolute resolution. As will be seen later, these resolution targets are resolved quite well in the image generated by the standard (non-thermal imaging) CCD camera.

Since the size of the overall images that have been used in this research is 512 by 512 pixels, as will be seen later, only a part of the target plate has been covered by some of the thermal imagers that have been tested. In these cases, the area covered allows the imaging of only 81 crosses out of the 150 crosses available on the plate. Therefore, to suit these particular cases, a version of the program SUBPIX has been implemented to match 81 crosses only. A final accuracy assessment has been achieved by using an affine transformation (using the first three terms of polynomial transformation) between the image coordinates and the reference coordinates of crosses associated with POLY25 FORTRAN 77 program. The RMSE values in x and y for these images are given Table 12.3.

Thermal Image I		Thermal Image II	
RMSE in X (pixel)	RMSE in Y (pixel)	RMSE in X (pixel)	RMSE in Y (pixel)
±0.86	±0.81	±0.71	±0.61

Table 12.3. Accuracy results of thermal images of the calibration plate using the program SUBPIX.

After carrying out the affine transformation, the residual errors at each of the 81 positions of the calibrated crosses have been plotted out as vectors using the ARC/INFO software package which is used for GIS applications in the Department. The plotting module of this software is called ARCEDIT. This module needs a special data file to be read and plotted. The author has written another FORTRAN 77 program which is called ARCPLOT. The output from this program is loaded into the ARCEDIT module in ARC/INFO; thus the vector plot file is obtained. Various types of Hewlett-Packard plotters have been used to plot out these vectors.

12.3.2 Test Results With CCD Images

For the experiment with the images taken by the CCD camera, the target plate has been moved to a laboratory in the Department of Mechanical Engineering where there is a set-up which allowed the image of the target plate to be taken with the CCD camera. Two images have been taken by this camera. One comes directly from the CCD camera; the other is the same as first one but it was recorded on a VTR to check its effect on the image geometry. The resolution of both these images is very good and the television targets could be resolved very well. The program SUBPIX could detect and measure the coordinates of the centres of the cross targets on the image array using both the direct and indirect CCD images.

The same procedures that had been applied to the thermal images of the calibration plate have also been implemented here and the accuracy results are given in Table 12.4. As can be seen, there is little difference between the results obtained with the direct and indirect images which indicates that there is no additional component arising from the use of the VTR.

CCD Direct Image		CCD Indirect Image (via VTR)	
RMSE in X (pixel)	RMSE in Y (pixel)	RMSE in X (pixel)	RMSE in Y (pixel)
±0.29	±0.26	±0.31	±0.26

Table 12.4. Accuracy results of CCD images of the calibration plate using the program SUBPIX.

12.3.3 Tests with Alternative Method

For comparison, the MSDPW (MOMS SPOT Digital Photogrammetric Workstation) program, which has been developed by my research colleague, Mr. Valadan Zoj for his research work, has also been used to measure the cross coordinates. This program has been written in the C++ programming language and employs the coordinates of

ground control points on the MOMS or SPOT satellite images that have been measured manually. The specific approach utilized in this program is that, when zooming in on the image, the target area is getting larger in size on the screen while the cursor remains the same size. Hence, the centre of the target can be measured more accurately to sub-pixel level. In this project, the cross targets on the thermal and CCD images have been measured using different zoom factors. Using the affine transformation between these coordinates and reference coordinates, the accuracy tests have been carried out and the results given in Table 12.5.

Zoom Factor	Thermal Image I		Thermal Image II		CCD Direct Image	
	RMSE in X (pixels)	RMSE in Y (pixels)	RMSE in X (pixels)	RMSE in Y (pixels)	RMSE in X (pixels)	RMSE in Y (pixels)
1/3	±0.79	±0.80	±0.70	±0.62	±0.34	±0.27
1/7	±0.74	±0.76	±0.69	±0.62	±0.29	±0.28
1/10	±0.75	±0.72	±0.70	±0.62	±0.30	±0.26
1/13	±0.76	±0.71	±0.73	±0.57	±0.29	±0.29
1/17	±0.78	±0.70	±0.67	±0.57	±0.29	±0.27

Table 12.5. Accuracy results from MSDPW

12.3.4 Comments on the Use of the Program and the Accuracy Results

In this section, the performance of the gradient edge detection and IMLS image matching techniques used for automatic target measurement has been reported and discussed. This procedure has several advantages over the non-automatic methods.

They are given as follows:

- (i) It is not a labour-intensive and time-consuming technique.
- (ii) It has the advantage of avoiding the errors that stem from measurements made manually by an operator.
- (iii) It gives a direct output of the cross coordinates to the other programs (POLY25, etc.) which will be used to process them. So there is no need to create another file for the coordinates to input these programs. This decreases the operator's work greatly. He does not have to write the coordinates down

and enter them again with all the possibilities for making mistakes that the use of this procedure would incur.

- (iv) As discussed in Chapter 11, due to the high degree of non-linearity of the mathematical model of the IMLS technique, it shows a rather small pull-in range for convergency. Without having close approximations for the unknown cross parameters, the program could not reach the true results. In particular, it was found that the IMLS technique is very sensitive to the initial value for the orientation angle of the cross target (Azizi, 1990). As mentioned before, this problem has been overcome quite efficiently by using the cross parameter measured by program GRAD as the input approximations for the unknowns. Since the initial values were very close to the actual ones, the program converged in one or, at the most, two iterations to give the final values.

As can be seen above results, program SUBPIX has produced very accurate results for the CCD images when compared those achieved with the thermal images. The reason for this is the trade-off between the resolution and the operating wavelength of the imager. As discussed in detail in Chapter 10, the middle and thermal infrared imaging systems operate in long wavelengths (3 to 5 μm and 8 to 14 μm), so a lower image resolution must be expected and, in turn, this leads to a lower pointing accuracy.

12.4 Conclusions

In this Chapter, the computer programming of the image matching procedure that has been applied to calibrate the thermal video imagers geometrically has been explained. By using this program, the cross targets can be located to sub-pixel level without suffering from the defects of the manual methods which are quite labour-intensive and time consuming. In the next Chapters, this method will be applied to all the thermal images that have been taken by the thermal video scanners and cameras included in the present series of tests. The image coordinates, which will be produced using this method, will be the main source to determine the geometric distortion characteristics of these devices.

CHAPTER 13: EXPERIMENTAL PROCEDURES AND SUBSEQUENT DATA PROCESSING

13.1 Introduction

In the previous two Chapters, detailed descriptions of the image matching technique and the computer programming of this procedure in FORTRAN 77 have been given. In this chapter, the actual experimental procedures for the geometric and radiometric calibration of the infrared imaging systems will be described together with the factors involved in the design of a new target plate. In addition, the computer processing of the image data that have been obtained through the use of these procedures will be explained. Following this section of the chapter, the enhancement of the digital infrared images using the Adobe Photoshop software package will also be outlined. Finally, the methods used in the analysis of the image data obtained during the geometric and radiometric calibration will be explained in some detail.

13.2 Experimental Procedures

For the geometric and radiometric calibration of an infrared imaging system, a suitable environment needs to be provided in which to set up the imager and the other experimental equipment in the required positions and to ensure that these items remain safe and undisturbed. Therefore, in this project, the reprographics laboratory of this Department which is convenient for this kind of test has mostly been used for the purpose since it has no windows and so stray radiation from external sources can be reduced to a minimum. However, when this laboratory was not available, the experiments were carried out in the Department's conference room which has a quite wide dimension in which to set up the equipment and has dark curtains which can be drawn to cut down external sources of radiation that might affect the radiometric measurements.

In this type of experimental work, many additional accessories and equipment have to be used besides the imager and the calibration target plate. With this in mind, the

present author made a check list of all the required items of equipment, such as the video tape recorder, television monitor, measuring tape, level bubbles, etc. In this way, it was very easy to ensure that they were all available when the experimental work had to be carried out; often over quite a short period of time when the imager was available for the purpose.

In Chapters 8 and 9, the author has set out the technical specifications of each of the imagers that has been calibrated in this project. This information has been obtained from the brochures issued by the companies. Hence, before commencing the experimental work with any imager, the author took the opportunity to make a layout plan that showed where the positions of the imager and target plate should be, based on these specifications. Although their final positions will be determined more exactly at the time of the actual experiment; the availability of this plan made the experimental situation easier to envisage and to implement. In particular, the field of view and focal length values of the lens or lenses that would be used on the imager were the most vital pieces of information used for the construction of this plan.

In addition to the plan, the author prepared a recording sheet for each imager that has been tested in this project. The information provided by this sheet includes the name of the imager; which lenses have been employed with the imager; the counter values of the VTR between which each image has been recorded for each test; and the temperatures of the target plate and/or radiation source used in each individual test. Table 13.1 gives an example of a completed record.

Imager	Lens	Counter	Test Type	Temperature
Agema 550	20°	0-50	Geometric	25°C
" "	10°	50-100	" "	25°C
" "	40°	100-150	" "	25°C
" "	20°	150-200	Radiometric	30°C
" "	" "	200-250	" "	40°C
" "	" "	250-300	" "	50°C
" "	10°	300-350	" "	50°C
" "	" "	350-400	" "	40°C
" "	" "	400-450	" "	30°C

Table 13.1. Example of the data recorded during tests of an imager.

Having this record greatly facilitates the data processing that has to be carried out later. In this way, the location of the images of the target plate or radiation source needed for each individual test can be found very easily. For example, in the digitization of the analogue images using a frame grabber, the operation can be done in a very short time using this record; without it, confusion would reign.

Generally speaking, the author only had a limited time to work with each of the imagers that have been tested in this research. In this context, it should be noted that, since most of the higher resolution infrared imagers cost between £30,000 and £100,000 each, it would be quite impossible to buy the range of imagers tested in this project. Instead they have had to be borrowed either from the manufacturer concerned or from other universities that possessed such devices. This meant that they could only be made available for short periods since these imagers have a very busy schedule, being used in many different applications or demonstrations. So, the appointment for using them had to be made a long time ahead in order to have them available for the author's experimental work. The Agema 1000 and 900 TVFS imagers were only available for one day; for the Agema 550 CCD cameras, only half a day was available on each of two occasions in which to carry out the required tests. For the Agema 470, only a short time period was available since the test had to be carried out outside the Department. However, in the case of the Agema 880, the author was able to spend a full week carrying out experiments with it. The availability of this imager for this longer period of time at an early stage of the project increased the author's experience of infrared imaging systems greatly. For the Amber Radiance PM1, two days were available in which to carry out and complete the required tests.

13.2.1 Geometric Calibration Procedures

The experiment for each imager started with the taking of the images of the cross targets of the target plate used for the geometric calibration. Before taking images of the target plate using the imager, these two main components of the experiment have to be set in the correct positions relative to each other so that the calibration plate will

fill the field of view of the imager. The final sharp focussing was carried out by adjusting the lens. In addition, the optical axis of the imager that was to be calibrated had to be adjusted to point directly at the centre of the plate throughout the experiment. This was to help ensure that the plate is set exactly at right angles to the imager so that there was no rotation and no translation in the position of the target plate. Normally, at the time of a calibration, the precise positions of the imager and the target plate would be set using a high-precision optical bench. Once the correct positions of these components have been set, any motion that is needed between them - for example, when an alternative lens is being used - can be carried out accurately. However, in this project, no optical bench of this type was available. So the set-ups were made as carefully as possible on stable tripods and tables by visual observation using a video monitor to ensure accurate motions between the target plate and the imager and using spirit bubbles to provide levelling and alignment.

After taking great care to provide these set-up conditions, the video signals generated by the imager were sent to the VTR and TV monitor using BNC coaxial cables. One set of signals was used for the recording of the analogue image onto the magnetic tape installed in the VTR. The another set of signals was sent to the monitor to allow the user to check on whether the camera and the target plate are in the required position or orientation or not. In addition to this, the displayed image could also be used to control the quality of the images that were being recorded.

For the geometric calibration, the temperature of the target plate was set to 25°C which is high enough to make the crosses appear sharp against their background. After waiting nearly 5 minutes, the target plate reaches this temperature. Normally, the infrared imagers have special functions that measure and display the temperature of the object that is being imaged. When available, the author used these functions of the imagers extensively to check the temperature of the target plate. When these functions were not available, the temperature of the target plate was checked by the built-in thermocouple. After checking the temperature of the target plate and the sharpness of the crosses and the other conditions, the analogue images of the target plate were recorded onto the U-matic magnetic tape mounted in the VTR for a five

minute period. The counter values of the VTR at the beginning and end of the recording period were written down on the record sheet. To check if the recording was successful, it was played back immediately using the VTR and displayed by the TV monitor. Then, a decision could be made as to whether a new set of measurements needed to be carried out and recorded or not. If the imaging system had different lenses, this procedure was repeated for each available lens to determine its effect on the geometric distortions.

13.2.1.1 Difficulties with the Target Plates

In this project, the first attempt was made to calibrate the new Barr & Stroud HTDI imager. The HDTI infrared imager is a modern type of TVFS with a built-in cooler for the detector elements. This integral cooler generates heat. The initial test carried out with it at the Barr & Stroud factory showed that the target plate that had been built originally for the previous project carried out in this Department (Amin, 1986) created a severe reflection. The reason for this phenomenon was the silvered surface of the original target plate. When the radiation emitted from the imager and the surrounding ambient bodies, e.g. fluorescent lighting tubes, strikes this silvered surface, it creates a strong reflection. This could be seen clearly on the image of the target plate that was being obtained using the HDTI imager and displayed on the video monitor. In the old type of infrared imager such as the Barr & Stroud IR-18 used by Dr. Amin, the cooling system used liquid nitrogen which was stored in a vessel located away from the imager and then piped to the imager. In the new generation of infrared imager such as the HDTI, the cooling sources used (such as the Stirling engine) are located inside the imager and generate heat. When this radiation reaches the target plate, it is reflected back from its silvered surface to the imager and shows up clearly on the image. So, it was not possible to obtain good images of the old target plate using the HDTI.

In Amin (1986), this reflection problem mainly occurred through radiation from the surrounding ambient bodies and it was eliminated through the use of a large wooden box that was constructed specifically for the purpose. In this situation, the imager was

mounted at one end of the box with the target plate at the other end, so excluding radiation from outside sources such as ambient lamps. In addition, the interior walls of the wooden box were covered with a black paint to absorb any reflected or emitted radiation occurring inside the box. However, since this box was bulky and could only be used with the IR-18 scanner at the Barr & Stroud factory, it could not be used for any of the other imagers that were tested in that project, since it was impossible to transport this bulky box to places outside the factory. So other methods had to be used by Dr. Amin to screen out unwanted radiation. This problem is increased greatly with the advent of the new generation of infrared imagers in which heat is being generated by their internal cooling engines.

After the initial tests, Mr. Graham Ross of Barr & Stroud suggested that a new target plate should be constructed that would solve this problem permanently. This involved the coating of the target plate using a special paint, Nextel, which absorbed incident infrared radiation. This new target plate should also be designed to eliminate the laborious work which is required to heat the plate and to maintain it at a given temperature. Dr. Amin's plate had to be heated from behind by a hair dryer to get a good contrast between the images of the crosses and their background on the video monitor. This heating process took about 10 minutes for the plate to reach the required temperature and created continuous work for the user to maintain this temperature. The present author also used a hair dryer at the beginning of his experimental work and he can testify feelingly that it is quite time consuming and laborious work. As can be seen later, with the new target plate, this problem was also solved through the incorporation of a special heating plate which also acted as a radiation source. The heating of this plate is provided automatically through the use of adhesive heating pads attached to the back of the plate and equipped with a thermostat or temperature controller. In this case, all that was required was to set the controller to the temperature that was required.

It should also be noted that Dr. Amin's plate was designed and built to carry out only the geometric calibration of the TVFSs. However, in this project, it was intended that the radiometric calibration of the infrared imagers should be carried out in addition to

their geometric calibration. Therefore it was essential that the new target plate should be designed with this in mind. However, since Dr. Amin's plate also formed the base for the new target plate, the manufacturing procedures used in its construction will be explained first.

13.2.1.2 Characteristics of Dr. Amin's Plate

As mentioned above, a special target plate was designed and built for the previous project in which the geometric calibration of TVFS imagers was carried out (Amin, 1986). The reasons for its particular design and construction were as follows:-

- (i) Since TVFSs operate in the thermal infrared region of EM spectrum, the target plate to be used in the calibration must be made of a material of good thermal emissivity to ensure high contrast between the images of the targets and their background.
- (ii) There is no image plane in which a photographic plate, a grid plate or a register glass equipped with reseau can be placed for calibration purposes.

In addition, it was pointed out by Dr. Amin that a target plate needed to be specially designed and constructed for the purpose of calibrating TVFS which took into consideration the resolution limit of these TVFS imagers. So, it was designed specifically for the calibration of the TVFS imagers that were available in the mid-1980s; in particular for use with the Barr & Stroud IR-18 imager which had a field of view of $38^\circ \times 25.5^\circ$. A 1x magnification telescope was not available during the time of the calibration of the IR-18 and focussing without a telescope could not be achieved since the imager is adjusted to view at infinity. Therefore a 1.5x telescope with a $25.5^\circ \times 17^\circ$ field of view and an IFOV of 1.5mrad was used instead. With these characteristics, the field of view at 1.0m distance is 450 x 300mm, and resolution is 1.15mm. Therefore, the calibration target plate was constructed to be 450 x 300 mm in size.

The design of the target plate, the arrangement of the cross targets on the plate and the measurement of their coordinates using a Ferranti monocomparator have been

explained in Section 12.3.1 in some detail. As mentioned in that section, a total of 150 X-shaped crosses were distributed over the whole of the target plate. The reason for choosing an X-shaped mark was that the pointing cursor of the video-based monocomparator that was used for the manual measurement of the image coordinates had a + shape. It was thought that the use of an X-shaped cross would be easier and give more accurate results when using such a measuring mark. In fact, in the present project, this shape of cross was also advantageous for the automatic measurement process since it was easy to describe the cross geometry and to point to the cross targets using FORTRAN program commands. Using the cross type targets also related to photogrammetric applications where this type of target is widely used, e.g. in the form of the fiducial marks used on aerial photographic images.

Prior to the manufacture of this plate, different materials such as aluminium, stainless steel and copper were tested using the Barr & Stroud IR-18 imager to decide which type of metal should be used in the manufacture of the target plate. These tests showed that copper exhibited the best contrast relative to its background, followed by stainless steel. However, stainless steel was chosen since it proved to be a better material to handle during manufacture of the plate than copper. The final design of this target plate is shown in Fig. 12.5. This target plate was manufactured by a chemical milling process by the firm Photofabrication in Huntingdon. The process of manufacturing the target plate has been explained in detail in Amin (1986).

To make the stainless steel target plate very stable, it was bonded on to a glass plate which served not only to make the thin stainless steel plate rigid, but was also suitable as a background radiation source since the glass itself has a very high thermal emissivity factor when compared to any type of metal. Compared to a perfect blackbody (whose emissivity is 1.0) the glass material has an emissivity of 0.95 while that of stainless steel is 0.16. So, if the glass plate was heated from behind, the voids (see Fig. 12.5) being backed on to the glass material would exhibit a high brightness against the dark background represented by the stainless steel material. The glass plate was also painted with a matt-black paint and the target plate was stuck onto the

painted side to ensure good thermal contact between the glass plate and the stainless steel plate.

13.2.1.3 Design of the New Calibration Target Plate:

Mr. Graham Ross of Barr & Stroud contributed his experience and his ideas about the design and construction of the new target plate to those of the present author and Professor Petrie. Additional advice was provided by the senior technical staff of the Departments of Mechanical and Electrical Engineering. Some of the main considerations during the various discussions on this matter were as follows:-

- (i) As mentioned above, in Amin's plate, glass was used behind the stainless steel mask. Mr. Ross proposed that the use of a different material such as a copper or aluminium plate behind the stainless steel mask would be a more appropriate support. In addition, it was decided that a second plate should be provided which could be heated directly to form a background radiation source. This could then be isolated from the target plate using suitable non-conducting nylon spacers.
- (ii) The heated plate the temperature of which could be controlled by a thermostat could be detached completely from the actual target plate and used as a radiation source (instead of a blackbody) when carrying out the radiometric calibration of an imager.
- (iii) It was thought necessary to paint the calibration target plate with matt black paint to cut out the reflections produced by the radiation given off by the integral cooling engine of the imager.

Based on these considerations, the new calibration plate, which has quite different characteristics to that used by Dr. Amin, has been designed and built for this project.

In the new target plate, a 5mm thick aluminium plate was used as the support, mounted behind the stainless steel mask and bonded on to it. Prior to this, 150 holes, each of which has a slightly bigger diameter than the length of the leg of the cross target (14mm), had been drilled into the aluminium plate using a computer-controlled

drilling machine operated by the University's Department of Mechanical Engineering. Afterwards, the stainless steel mask was bonded on to the aluminium plate so that the 150 target crosses on the stainless steel mask were superimposed above the 150 holes on the aluminium plate. Thus, the radiation that is generated by the heating plate will pass to the crosses (which take the form of voids in the mask) via these holes and they will appear sharp against their background. The stainless steel mask of the new target plate, which is used for the geometric calibration of the infrared imagers, was then painted by the author using special ultra low-reflection matt black paint which was supplied by the Agema Company. The use of this paint helped to prevent the reflections which had been produced from the silvered surface of the target plate in the initial tests carried out with the HDTI imager. Fig. 13.1 shows this black painted surface of the target plate and the X-shaped crosses cut on it.

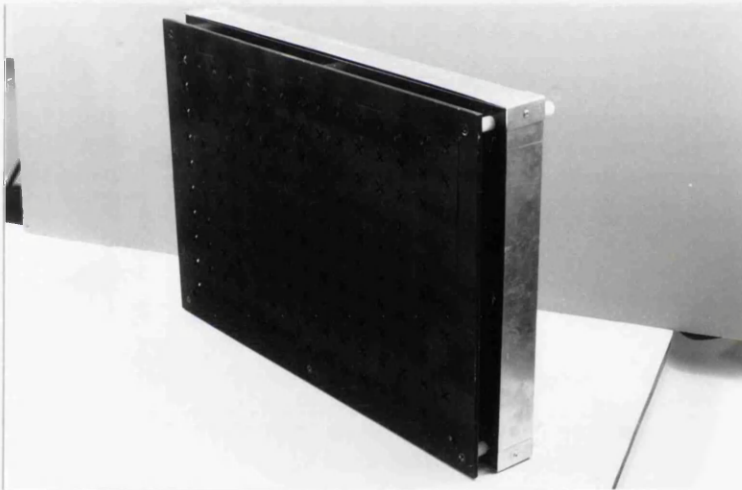


Fig. 13.1. The new target plate which contains the cross targets.

As can be realized from above account, both a stainless steel mask and an aluminium backing plate were needed for the construction of the new target plate. Fortunately, when Dr. Amin's plate was being built, two more copies of the stainless steel mask had been made. One of them remained with the Barr & Stroud company; the other one was stored in this Department. So, this latter copy of the mask was used in the construction of the new target plate. The aluminum backing plate was bought by the Department and the holes drilled by the Department of Mechanical Engineering in this University.

As mentioned above, the heating of Dr. Amin's plate was carried out using a hair dryer. However, for the new plate, a separate radiation source which could be controlled and run without too much human intervention has been aimed at. So, the senior technical staff of the University's Department of Electronics & Electrical Engineering were consulted about its design and construction. The conclusion from the subsequent discussion was that adhesive heating pads (that could be placed on a suitable metal plate) could be employed for the generation of the radiation. If this was done, the Electronics laboratory staff were willing to design and construct the required electronic circuits which would supply and control the electrical energy to these pads. In fact, they built the required radiation source using four heating pads glued on to an aluminium plate. The metal box into which this radiation source was fitted has been made using inexpensive sheet metal material. The radiation source has been enclosed inside this box (see Fig. 13.2) both for safety reasons and to protect the circuitry.

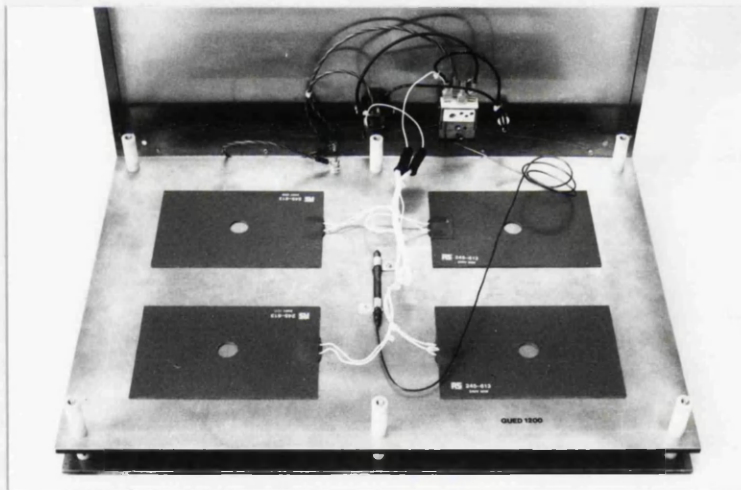


Fig. 13.2. The four heating pads bonded on to the aluminium plate that is used as the radiation source and their attached electrical circuits.

In addition, a thermostat (see Fig. 13.3) was added to the back of the metal box so that the user can set the required temperature for the radiation source. This thermostat operates over the temperature range from 0°C to 120°C . The aluminium plate that acts as the radiation source and which has the same dimensions as that used as the support for the stainless steel mask, has been fitted to the front surface of the metal box. Thus, the heat can pass from the heating pads to the aluminium plate (having an emissivity of 0.55) which then generated the radiation that was given off towards the back of the

target plate. This heated plate, acting as the radiation source, was also painted in matt black so that it will not create any unwanted reflections. Afterwards, the box containing the radiation source and heating system was attached to the target plate using 6 nylon pillars, each of which is 25mm in length. These pillars transmit heat very poorly, thus acting as insulators between the radiation source and the target plate. When the thermostat is set to a specific temperature, the heating pads stuck to the back of the radiation source heat it up until it reaches the desired temperature. After that, the radiation emitted from the source is passed through the cross targets via the drilled circular voids located behind them. This makes them appear sharp and bright against their black background.

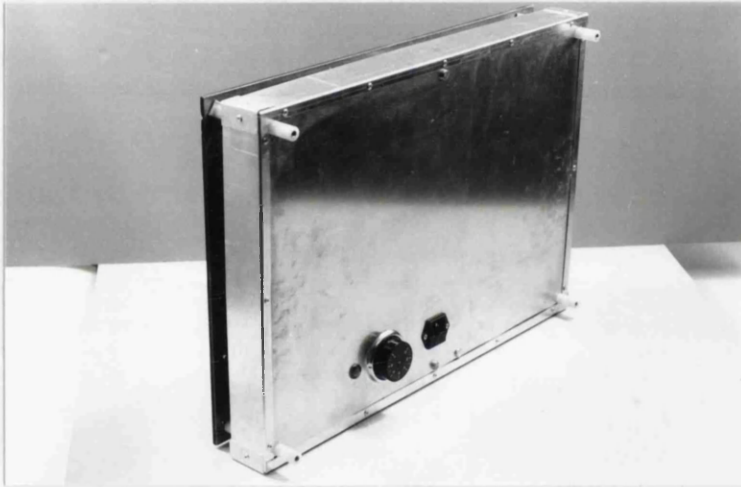


Fig. 13.3. The thermostat knob used to set the required temperature for the heating pads.

13.2.2 Radiometric Calibration Procedures

As discussed previously, the objective of this project has been to carry out not only the geometric calibration of a representative sample of infrared imagers but also their radiometric calibration. So the new, more sophisticated target plate was required. As discussed in some detail in Chapter 10, for radiometric calibration, ideally a blackbody that can generate a uniform radiation at a specific temperature should be used. However this is a very expensive item to buy and its purchase could not be justified; nor could one be found in the Glasgow area that could be borrowed. So, the radiation source described above was used as a substitute (see Fig. 13.4). The four

heating pads stuck to the back of the heated plate created a fairly uniform temperature on its surface. Unfortunately, there was no opportunity to test the uniformity of this source with any device prior to its use in the radiometric calibration, but it appeared to be uniform when viewed as an image on the monitor.

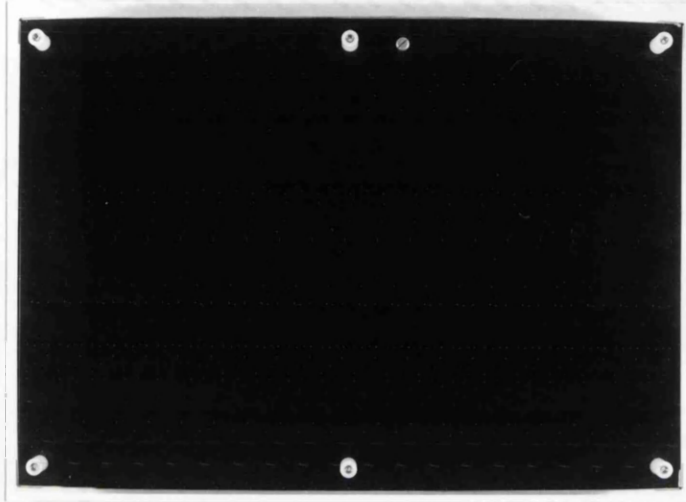


Fig. 13.4. The radiation source used for the radiometric calibration.

For the radiometric calibration of each infrared imager, the front target plate that is used for the geometric calibration was removed carefully using a screw driver without losing the position of the plate or altering its orientation. Thus, only the heating plate acting as a radiation source remained. Afterwards, all the experimental conditions were again checked using the video monitor. As described in Chapter 10, in order to calibrate the imaging system radiometrically, images of the radiation source have to be obtained at three different temperatures. So, the thermostat of the radiation source was set to the first specified temperature. In practice, it takes some time for the radiation source to reach that temperature, more especially with high temperature values. The time taken also depends on the ambient temperature of the environment. After setting the required temperature, first the regions of the heating pads grow hot. However, the heat spreads quickly across the plate and a few minutes later, the temperature becomes fairly uniform all over the heated plate.

Once this situation had been achieved, the images of the radiation source were recorded on magnetic tape using the VTR and the counter reading was also written down on the record sheet. Then the thermostat was set to the second temperature, in

which case, the plate started to heat up again. In the meantime, the author checked the images of the heated plate that had been recorded at the first temperature by playing them back on the VTR and displaying them on the video monitor. If the recording was not good, the process was repeated. When the temperature on the heated plate had become uniform at the second temperature, the analogue images of the plate were again recorded on U-matic tape using the VTR and the corresponding counter readings were noted on the record sheet. Then, the temperature of the plate acting as the radiation source was increased to the third temperature using the same procedure. At the end of the process, all the recorded images were displayed on the video monitor for a last check. If the imager had different lenses, this calibration procedure was repeated to find out the effects of the different lenses on the radiometric characteristics of the resulting images.

13.2.3 Problems Experienced During the Experimental Work

During the experimental stage of geometric and radiometric calibration of the infrared imagers, some general problems came to light.

- (i) As explained before, the stainless steel target plate used in all the previous and present calibration work was designed specifically for the calibration of the Barr & Stroud IR-18 TVFS which has a resolution of 500 x 384 pixels. Therefore, it is only possible to image this target plate fully with an imager which has either the same or a greater resolution. As will be seen later in the chapters covering the results of the calibration work, for lower resolution imagers, only a small part of the target plate could be imaged satisfactorily. For example, the Agema 900 TVFS could only image 13 x 6 (= 78) crosses out of 150 crosses because of its low resolution of 272 x 136 pixels. The problem occurred even more severely with the Agema 470 and 880 imagers. With the decreasing resolution of some of the newer, less expensive imaging systems, it becomes difficult to obtain a sufficient number of cross targets on the image to carry out a really thorough geometric calibration of the imager.

- (ii) As explained above, it has been observed that it takes some time for the radiation source (i.e. the heated plate) to reach the specified temperature. For higher temperatures, such as 50°C and 60°C, after reaching the set temperature, it is difficult to keep the temperature stable since the ambient temperature in the laboratory is much lower. So heat is quickly lost and the heating pads are cooling and re-heating quickly attempting to maintain the specified temperature. So only a short time period is available in which to acquire images at the exact specified temperature. This affected the temperature values on the actually recorded images, and, in turn, it affected the grey level values of the frames that were grabbed (digitised) from them. This matter will be examined in some more detail in later chapters dealing with the radiometric calibration of the various infrared imaging systems.
- (iii) As stated before, the calibration work requires a very precise set up for both the imager and the target plate. Therefore, ideally an optical bench should have been used for this purpose. In this project, accurate level bubbles and stable tripods and tables were used since there was no optical bench available. However, it was realised that all of these matters required great care and attention and indeed this was carried out to the limits of the author's abilities.
- (iv) The imaging process in the infrared part of the spectrum can easily be affected by the emission and reflections caused by other ambient bodies such as lighting elements and heating radiators. As far as was practical, these were shut down prior to the calibration work which was carried out in darkness or very subdued light. The author has observed that especially the CCD cameras that are operated in the middle infrared region of the EM spectrum can suffer a lot from these external radiations and reflections. So, for calibration purposes, they should be operated in a dark environment with a very stable temperature.

13.3 Processing of the Data

After the acquisition of the images of the cross target plate and the radiation source required for the geometric and radiometric calibration, they were processed through a number of stages which can be summarized as follows:-

(a) The analogue images recorded on tape were first played back by the VTR and displayed on the video monitor. Thus, through visual inspection, the best recorded images of the target plate were identified and the appropriate counter values of the VTR were noted with the help of the record sheets.

(b) Using this information, normally three frames were digitized from each set of images using a frame grabber. So, the three frames needed for the geometric calibration and the nine frames required for radiometric calibration (three for each temperature) were obtained.

(c) For the geometric calibration, the three frames were enhanced using the Adobe Photoshop image processing package. So, the next section will be devoted to an explanation of the enhancement of the digital infrared images carried out using Photoshop.

13.3.1 Digital Image Processing by Photoshop

An unprocessed digital image will reflect both the characteristics of the imaging system and the environmental conditions under which the image was acquired. This will not necessarily produce an optimum image for the purpose in hand - in this case, for calibration. Therefore, image enhancement operations may have to be applied to modify the raw image for this particular purpose. Specifically these operations should improve the image both for viewing and for measurement. In this project, they have involved contrast enhancement, edge sharpening, etc., - operations that have been carried out using the Adobe Photoshop 3 image processing package. In the following section, the main functions of the Photoshop package that have been used in this research will be described.

13.3.1.1 Grey Level Value Adjustment and Contrast Enhancement

The Image_ Adjust_ Levels command set of Photoshop allows gradual adjustments to be made to the brightness, gamma and contrast present in an image. Alterations to these parameters can cause a quite dramatic enhancement of an image's quality. Brightness is the degree of intensity that can be perceived as a grey tone on the image

that is formed by the radiation reflected and emitted by an object. The relevant command available in Photoshop can display a histogram of the range of the brightness values that are present in an image. This is a graph that represents the range of brightness that is present in the image measured against the number of pixels corresponding to each grey level value available in the range. This graph or histogram is created on the scale of 0 (no brightness) to 255 (absolute brilliance). In Fig. 13.5, the darkest pixels appear at the left end of the graph (i.e. with the lowest grey level values), while the brightest pixels (with the highest grey level values) appear at the right end. The result of changing an image's original histogram is the redistribution or reassignment of the image's grey level values. To remap a histogram, the user begins by specifying the ideal darkest and lightest shades in the brightness range. The Levels command defines truncating points other than those that were used to create the original histogram of the image. By moving these truncating points within a image, the range of grey level values available for the representation of the image is increased. Thus, for example, instead of the representation of an image being confined to a range of 60 grey level values, it could be expanded to use the whole of the available range of 256 grey level values with great benefit to the clarity of the detail contained in the image.

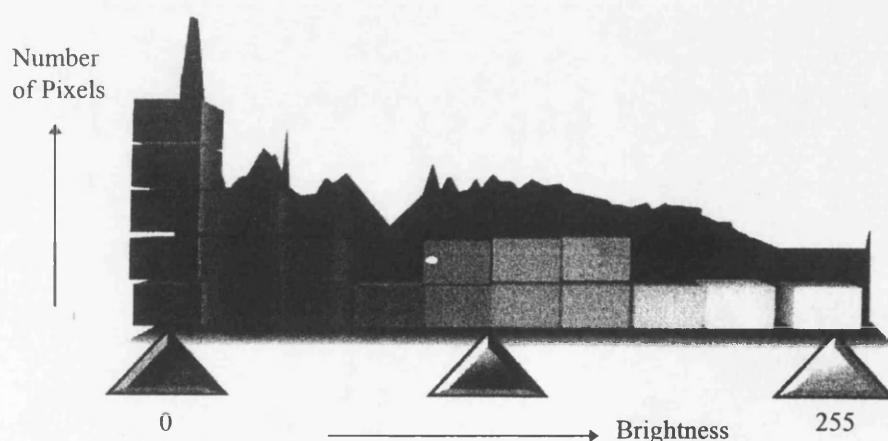


Fig. 13.5. A Photoshop histogram of the range of brightness values present in an image.

The relationship between the exposure time and the resulting density value on the image can be expressed using the characteristic curve which is a familiar concept to

those photogrammetrists using photographic films to record images taken by a camera. This plots the resulting density values as a function of the log exposure (LogE) (see Fig. 13.6). There are three general divisions to the curve. First, as the exposure time (E) increases from that of point A to that of point B, the density increases from a minimum D_{\min} , at an increasing rate. This portion of the curve is called the toe. As the exposure time increases from point B to point C, the resulting changes in the density of the resulting image are nearly linearly proportional to the changes in log exposure (LogE). This region forms the straight-line portion of the curve. Finally, as the exposure time increases from point C to point D, the density is increasing only slowly at an ever decreasing rate. This portion is known as the shoulder of the curve. The shoulder terminates at a maximum density, D_{\max} , beyond which there is no increase in the density with exposure time.

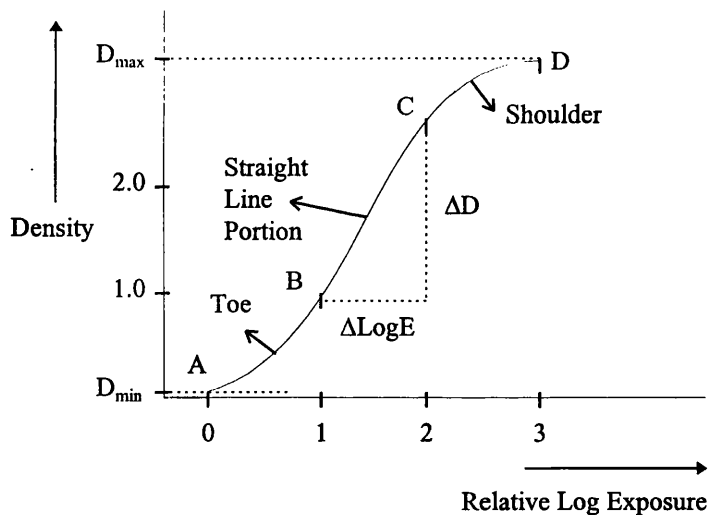


Fig. 13.6. Components of a characteristics curve.

An important characteristics of this D v. LogE curve is the slope that the linear portion of the curve makes with the horizontal coordinates axis. The tangent of this slope is called the gamma (γ) value and is expressed as

$$\gamma = \Delta D / \Delta \text{LogE} \quad (13.1)$$

Gamma is a determinant of the image contrast that indicates the range of density values obtained by the imager. The higher the gamma value, the steeper the straight line portion of the characteristic curve and the higher the contrast of the image, i.e. the

greater the range of density values that are present. With a high contrast image, the exposure range for a given scene is distributed over a large density range; the reverse is true of a low contrast image. For example, consider a image taken of a light grey and a dark grey object. On the high contrast image, the two grey level values may lie at the extremes of the density scale, resulting in one being nearly white and the other nearly black. On the low contrast image, both grey level values would lie much closer together on the density scale, showing the two objects in shades of grey that make it more difficult to differentiate between them.

In general, the use of the Auto Levels command that is available in the Levels menu of Photoshop can give good results when a simple contrast enhancement (which is often called a contrast stretch) is applied to an image with an average distribution of pixel values throughout the grey scale. This command sets the truncating points automatically and carries out the redistribution of the grey level values lying between them so that they occupy the whole of the available grey level value range, thus increasing the contrast. However, it is also possible for the user to set the truncating values manually using the interactive dialog boxes under the Levels Adjust Command. Of course, when setting these values, the visual quality of the image, as observed by the user's eye, plays an important role.

Fig. 13.7(a) illustrates a histogram of the brightness levels actually obtained for a scene by the infrared imager. Assuming that the output device (i.e. the computer monitor display) is capable of displaying 256 grey level values, the histogram shows that the range of brightness values (grey level values) recorded for this scene lie within the limited range of 60 to 158. If these image values are used directly in the display device (Fig. 13.7(b)), only a small portion of the full range of possible grey level values would be used. Thus the grey level values 0 to 59 and 159 to 255 would not be utilized. Consequently, the tonal information in the scene is compressed into a small range of grey level values, reducing the interpreter's ability to discriminate radiometric detail. Equally this could influence the capabilities of the image matching procedure employed to measure the positions of the target crosses used in the geometric calibration procedure.

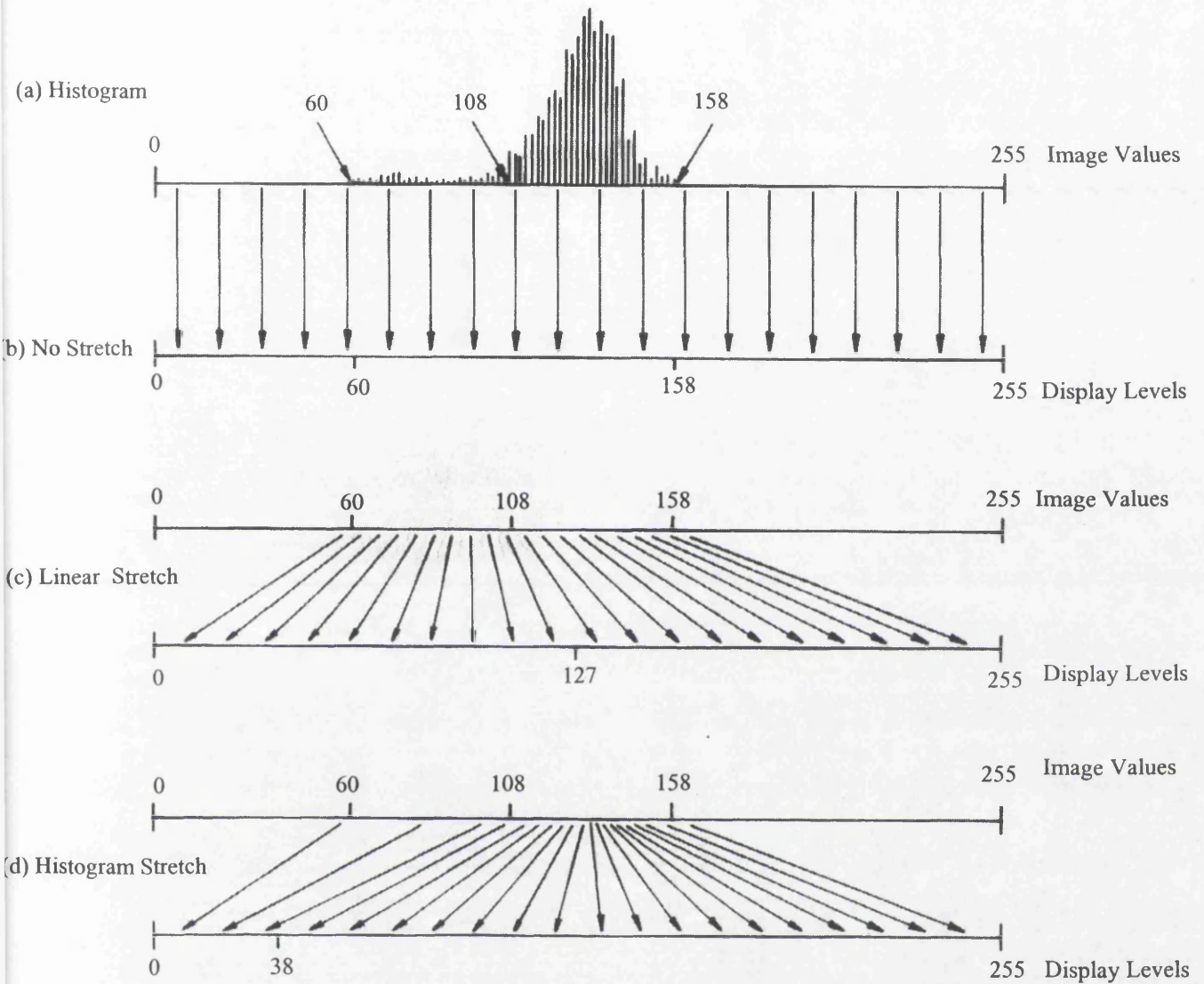


Fig. 13.7. Principle of contrast enhancement.

A more useful image would result if the range of grey level values present in the scene (60 to 158) was expanded to fill the full range of values (0 to 255) that are available. In Fig. 13.7(c), the range of grey level values has been uniformly expanded to fill the total range of the display device. This uniform expansion is called a linear stretch. Subtle variations in input image data values would now be displayed in output tones that would more readily distinguished by the interpreter or photogrammetrist. Light tonal areas would appear lighter and dark areas would appear darker.

One drawback of the linear stretch is that it assigns as many display levels to the rarely occurring image values as it does to the frequently occurring values. For

example, as shown in Fig. 13.7(c), half of the dynamic range of the output device (levels 0 to 127) would be reserved for the small number of pixels having image values lying in the range 60 to 108. The bulk of the image data (values 109 to 158) would then be confined to half of the range of output display levels (128 to 255). Although this might improve the image to be better than the direct or raw image given in (b), the linear stretch would still not provide the most expressive display of the data or that optimised for use with the image matching program.

To improve on the above situation, a histogram-equalized stretch can be applied. In this approach, the image grey level values are re-assigned to the new levels on the basis of the frequency of their occurrence. As shown in Fig. 13.7(d), more grey level values are assigned to the frequently occurring portion of the histogram, often resulting in greater radiometric detail. The grey level value range of 109 to 158 of the original image is now stretched over a larger portion of the display levels (39 to 255). A smaller portion (0 to 38) is reserved for the infrequently occurring grey level values of 60 to 108 in the original image. The author has made considerable use of these two contrast enhancement routines when pre-processing the target plate images prior to the use of the image matching program to measure the positions of the target crosses - to the benefit of this process.

13.3.1.2 Photoshop's Filters

The filters that are available in the Photoshop package can be applied to produce special effects in digital images. Although there are many filters available in this package, only those that have been used in this project will be described and discussed below.

13.3.1.2.1 Median Noise Filter

The use of this filter helps to reduce the number of random pixels - i.e. which may be produced either by electronic noise or by the presence of dead or blemished detector elements - that are present in a digital image. A random pixel displays a sharp

difference in its brightness or grey level value compared with those of its neighbouring pixels. The Median Noise Filter reduces the number of random pixels by looking at each pixel and replacing that pixel's brightness value with the median brightness value of the pixels occurring within the user defined area around the pixel being examined. In Photoshop, when applying this filter, the user can specify values from 1 to 16 in its dialog box. This value defines the area around the current pixel within which the filter looks at brightness or grey level values.

It should be noted that this filter needs to be used with caution. The elimination of the random pixels using the filter would not be appropriate when the radiometric calibration is being carried out with a view to establishing the location and pattern of the dead or blemished elements in the detector array.

13.3.1.2.2 Sharpen Filters

The pictorial analysis and interpretation of a digital infrared image may also be improved by enhancing the edges of the objects that have been imaged and recorded. In this way, any slight blurring effect produced by the imager can be removed. In the digital images used in the calibration, because of the low-pass characteristics of the imaging systems, the higher spatial frequencies appear to have been weakened more than the lower frequencies. So there was a definite need to apply sharpening techniques to emphasize the higher spatial frequencies. This type of filtering has been used in photogrammetric applications for feature extraction. In this project, since the cross targets represent the edges that are present on the digital infrared image, they needed to be sharpened as much as possible in order to differentiate them from the background. In fact, a feature extraction method based on the gradient operator approach and an edge detection technique has been employed for the detection of the edges (of the cross legs) in the image matching program SUBPIX. These have been described in some detail in Chapter 11.

However, besides employing these techniques, it was still found useful to employ the sharpen filters of the Photoshop package during the pre-processing stage. As the

author can testify, the implementation of such a filter definitely increased the speed of detecting edges (e.g. of the cross legs) and thereby the image matching. The reason for this lies in the use of the sharpened image, since the differences between the grey level values of the edge pixel and the background pixels, (namely the gradient values), are then quite big, so the matching program does not have to carry out so much computation or run the same program cycle as many times. If the sharpen filters are not used, either it takes longer time for the program to find the edge or it cannot detect the edges.

In fact, there are many “sharpen” filters available in Photoshop. They are called sharpen filter, more sharpen filter, sharpen edge filter and the unsharp mask filter. However, amongst them, only the unsharp mask filter has a dialog box that can be used to set the value that determines how far around the current pixel the filter looks at the neighbouring grey level values when implementing the filtering process. The other “sharpen” filters do not have any dialog box to set the specific values to help sharpen the edges. Clicking a particular button implements the operation, but sometimes with unpredictable effects. Unfortunately, the author could not find any information about the mathematical basis of these filters in the Photoshop manuals.

In passing, it should be noted that, although these filtering operations make the edges or features of interest easier to measure or analyze, they may cause the target to shift in the image to some extent, thus reducing the locational accuracy of the point being measured (El-Hakim, 1996; Lee and Faig, 1996). However, this effect was not observed by the author during the calibration operations.

13.3.2 Data Processing for Geometric Calibration Purposes

(a) In order to process those frames that have been captured, digitized and pre-processed, they need to be converted to ASCII format for input to the various FORTRAN 77 programs that have been written by the present author to carry out geometric calibration. The need for this conversion is associated with the use of the X-Windows graphical user interface (GUI) which is running under the UNIX

operating system on the Sun Sparc Server. However, since this conversion is not one-to-one operation, a special FORTRAN 77 program CONV1 has been written by the author to carry out this operation.

(b) The image matching program SUBPIX is then executed for each frame that has been digitized by the frame grabber. In this way, the image coordinates of all the crosses in each frame have been measured to sub-pixel level.

(c) The image coordinates are then input to the FORTRAN programs LINCON and POLY25, (which will be explained below in later sections) in order to carry out a transformation and analysis of the measured data in order to obtain the overall extent and pattern of the geometric distortion that is present in each frame (including its systematic and random components).

(d) The pattern of these distortions is displayed graphically in the form of vectors on the computer screen using the VECTOR program which can also create the plotting file of these distortions in the Hewlett-Packard Graphic Language (HPGL) for use with a Hewlett-Packard Pen (vector) Plotter. However, since it takes much time to execute the plotting of these distortions using this type of vector plotter, the plotting file (which is in HPGL language) can also be input to the COREL DRAW 5 computer graphics package which can read HPGL files. In which case, the data contained in this file can be displayed or printed out rapidly using one of raster-based laser or bubble-jet printers available in this Department.

13.3.3 Data Processing for Radiometric Calibration Purposes

(a) After initial processing of the whole frame, a quadrant within each frame is defined and used for the processing. Within each quadrant, a smaller, homogenous patch is also defined for more detailed analysis.

(b) After determining 9 quadrants and 9 patches for each frame, they are converted to ASCII form using the method given in Section 13.3.2(a).

(c) They are then processed by the FORTRAN program STMN to compute the mean and the standard deviation of the grey level values that are present in each individual quadrant and patch.

(d) For the radiometric correction and determination of the non-uniformity of the imaging system, the quadrant and patch image data for each temperature is input to the FORTRAN program PRNU to compute the gain and offset values for individual pixels and to correct for the non-uniformities in the data that were obtained for the quadrant and patch at the middle temperature. In addition, this program carries out the averaging of the grey level values of these quadrants and patches to remove the temporal noise that was present in each of the quadrants and patches and appears to stem from the frame grabber. The mean and standard deviation values of this averaged data are also calculated by this program.

(e) For further statistical processing, the mean and standard deviation values are input to the FORTRAN program STAT to establish the distribution of grey level values occurring in each quadrant and patch.

(f) To display the fluctuations in the grey level values of the pixels and to determine the location of the dead and/or blemished pixels in each frame, quadrant or patch, these values are plotted using SURFER, which is a grid-based contouring and three-dimensional surface plotting graphics program.

13.4 Analysis of the Data Obtained During the Geometric Calibration

The image coordinates of the cross targets, which have been measured automatically using the gradient and IMLS image matching technique, form one of the two sets of coordinates that will be used to identify and quantify the geometric distortion inherent in each of the infrared imagers that have been tested. The other set of coordinates comprise the calibrated coordinates of the cross targets that have been measured using the Ferranti monocomparator. In this Section, the mathematical models that have been used to relate these two sets of coordinates will be discussed in some detail.

A coordinate transformation procedure is used to transform the calibrated coordinates from the target plate (or object) coordinate system into the image coordinate system (see Fig. 13.8). However, it should be noted that it is equally possible to make the transformation in the reverse direction, i.e. to transform the measured image coordinates of the cross targets into the calibrated coordinate system. Since the target

plate coordinates had been calibrated, they are considered to be error free. After the transformation, the measured image coordinates will be in slightly different positions with respect to the transformed target plate coordinates. In this way, it should be possible to determine the geometric distortion values that are present in both the x and y directions at each of the 130 positions of the crosses that are present in the infrared image. These are the differences between the measured coordinates of any cross on the image and its corresponding transformed target plate coordinates.

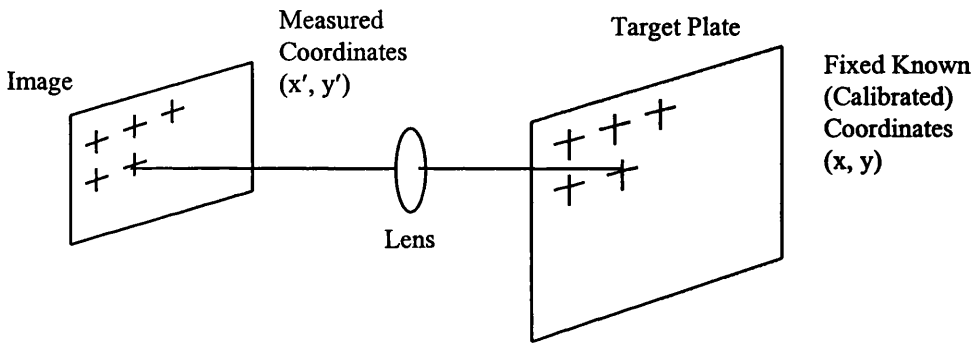


Fig. 13.8. Image and target plate coordinate systems

13.4.1 Linear Conformal Transformation

This well known type of transformation comprises a scale change (λ), a rotation (θ) and two independent translations (a_0, b_0). Let the position of any cross target i on the target plate be defined by its calibrated coordinates x_i, y_i obtained through the measurements of the cross positions on the target plate made using the Ferranti monocomparator. The corresponding position of the same cross in the image acquired by the imager and measured by the image matching program SUBPIX will be expressed by its image coordinates x_i', y_i' . The relationships between the two sets of coordinates can be expressed as follows:-

$$\begin{aligned} x_i' &= a_0 + a_1 x_i - a_2 y_i \\ y_i' &= b_0 + a_2 x_i + a_1 y_i \end{aligned} \quad (13.2)$$

where:-

x_i, y_i are the calibrated coordinates of cross target i ;

x_i', y_i' are the measured image coordinates of cross target i ;

a_0, b_0 are the translation parameters in x and y respectively; and

a_1, a_2 are parameters which are functions of the rotation angle (θ) and the scale factor (λ).

Assuming an error (distortion) value Vx_i, Vy_i at the cross target i , the equations given in Eq. 13.2 can be re-written as:

$$\begin{aligned}x_i' + Vx_i &= a_0 + a_1x_i - a_2y_i \\y_i' + Vy_i &= b_0 + a_2x_i + a_1y_i\end{aligned}\tag{13.3}$$

Every measured cross target gives rise to two such equations. With the use of 130 points, 260 equations will be formed; thus a least squares adjustment procedure will be adopted since there are only four unknown parameters (a_0, b_0, a_1, a_2) to be solved for.

In effect, this transformation does not change the basic relationship between the cross targets on the image; it merely transforms the calibrated coordinates of the target plate into the image coordinate system. If the image coordinates have been measured accurately, the results from this transformation will show the geometric fidelity of the images in their original state as produced by the infrared imaging system.

In this project, the linear conformal transformation between the image coordinate system and the calibrated coordinate system has been implemented using the LINCON program written in FORTRAN 77. It is available in the Department's software library and has been modified slightly by the author for this project. The program LINCON is listed and included as Appendix C of this thesis, which also provides sample output from this program.

13.4.2 Affine Transformation

This transformation has the form:-

$$\begin{aligned}x' &= a_0 + a_1x + a_2y \\y' &= b_0 + b_1x + b_2y\end{aligned}\tag{13.4}$$

Thus it employs only the first three terms from the general polynomial equations, which will be explained in the next section, both in the x- and y-directions. It will be seen that, in addition to the two translations (a_0 and b_0) and the general rotation of the linear conformal transformation, the affine transformation applies two separate and discrete scale factors in the x- and y-directions. Furthermore, one of the coordinate axes may be rotated to account for any lack of orthogonality in the image. This transformation procedure will be solved for the six unknowns (a_0 to a_2 and b_0 to b_2).

13.4.3 Polynomial Transformation

The polynomial transformation used in the analysis carried out on the geometric calibration data was that developed by Wong (1975). It has been used extensively for the planimetric accuracy tests of space images. As will be seen later, 23 transformations of varying degree are available in a continuum and can be applied to the input coordinate values using this polynomial. The whole purpose of using the polynomial transformation is to model and identify the individual geometric distortions that are present in a calibration image. Once this has been done, the effective terms can be included in a correction polynomial.

This general 25-term polynomial transformation equation is having the form:-

$$\begin{aligned}x' &= a_0 + a_1x + a_2y + a_3xy + a_4x^2 + a_5y^2 + a_6x^2y + a_7xy^2 + a_8x^2y^2 + a_9x^3 \\&\quad + a_{10}y^3 + a_{11}x^3y + a_{12}xy^3 + a_{13}x^3y^2 + a_{14}x^2y^3 + a_{15}x^3y^3 + a_{16}x^4 + \\&\quad + a_{17}y^4 + a_{18}x^4y + a_{19}xy^4 + a_{20}x^4y^2 + a_{21}x^2y^4 + a_{22}x^4y^3 + a_{23}x^3y^4 + \\&\quad + a_{24}x^4y^4\end{aligned}\tag{13.5}$$

$$y' = b_0 + b_1x + b_2y + \dots + b_{24}x^4y^4$$

where:-

x' , y' are the measured image coordinates of the cross target;

x, y are the calibrated coordinates of the cross target; and
 a_0 to a_{24} are the transformation parameters.

This particular form is known as a biquartic polynomial - since it includes all possible terms in x and y and of their products up to and including the fourth order terms. The reason for choosing such a high order polynomial was that the nature and extent of the distortions produced by the infrared imaging systems that were being tested were not known prior to the calibration procedure being undertaken.

Once again, if the error values V_x, V_y at each of the 130 crosses are considered, then a least squares adjustment procedure can be used to solve for the 50 unknowns (a_0 to a_{24} and b_0 to b_{24}) included in Eq. 13.5. It is most helpful when deciding which of these terms should actually be used in the transformation of measured image coordinates of cross targets to the reference coordinates to understand the effects of each term on the transformation and the pattern of distortion or displacement that is modelled or corrected by each term. These are shown graphically in Figures 13.9 (a) and (b) (Petrie and Kennie, 1990).

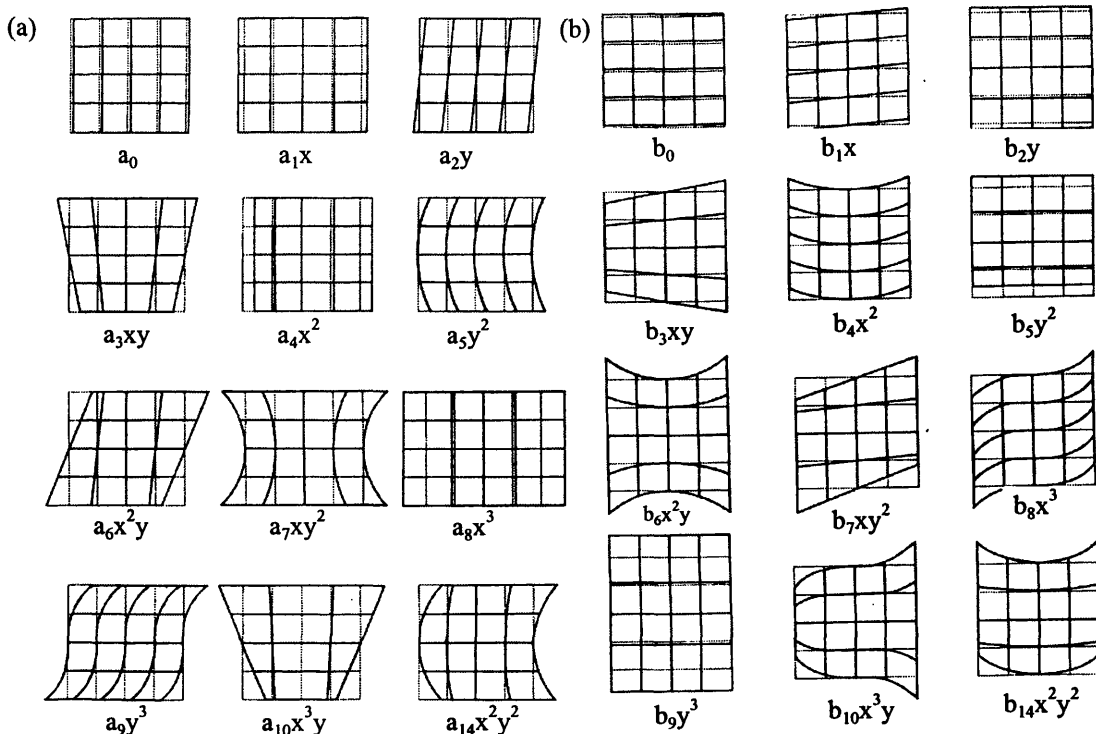


Fig. 13.9 (a) and (b). The effects of the individual polynomial terms in the x - and y -directions.

If Eq. 13.5 can be programmed in such a manner that the user can specify the number of terms to be used in an individual run, then every possible variation in the number of terms used in a specific transformation can be implemented by truncating the unwanted terms from the general purpose polynomial equation.

However, in order to monitor and discover the effective terms of the general polynomial, all possible cases were implemented, starting with the simple 3-term affine transformation, and increasing the overall number of terms by one term each time up to the full 25 terms. Thus for each image that was being calibrated, 23 individual runs of the program were carried out. As explained in Chapter 12, with the computer programming of this procedure, (called POLY25), the operator can specify any number of terms between 3 and 25 for each individual run. A detailed description of this FORTRAN 77 program is given in Appendix D together with sample output.

A first order polynomial or affine transformation will only include the first 3 terms of each equation given in Eq. 13.5; this can accomplish scaling, rotation and shearing. A second order or higher order polynomial can be used to model any more complex distortions that are present in the image (Mather, 1987). The polynomial method is well explained by Wong (1975), El-Niweiri (1988) and Petrie and El-Niweiri (1994). Whatever its defects, it is worth noting that the use of the general polynomial transformation with up to 25 terms has been widespread in remote sensing practice to date.

13.4.4 Plotting of Residual Errors

After carrying out a suitable coordinate transformation, the residual errors at each of the 130 positions of the calibrated crosses were plotted out as vectors using a special program called VECTOR. It has been written in BASIC by Mr. Shearer of this Department. This program allows the immediate graphical display of the pattern of errors either on a computer screen or in hard copy form using a Hewlett-Packard plotter. However, as explained previously, the file is normally transferred to the

COREL DRAW 5 computer graphics package. Afterwards, hardcopy output of the vector file can be obtained using any of the laser or bubble-jet printers that are available in this Department. Through inspection of the plots, any gross error (or blunder) could be detected and put right. After the elimination of all such gross errors, the plot of the errors as vectors gave an immediate view of the error pattern, e.g. whether it is systematic or not.

13.4.5 Systematic and Random Components of Geometric Distortion

The distortion value at each cross target can be divided into its systematic and random components. Systematic distortion remains constant at the same cross on every frame, while random distortion follows a normal distribution with a mean value equal to zero. Thus-

$$\begin{aligned}(Vx_i)_j &= SVx_i + (RVx_i)_j \\ (Vy_i)_j &= SVy_i + (RVy_i)_j\end{aligned}\tag{13.6}$$

where:-

$(Vx_i)_j, (Vy_i)_j$ are the distortion values in x and y at cross i in frame j;
 SVx_i, SVy_i are the corresponding components of systematic distortion at cross i of every frame; and
 $(RVx_i)_j, (RVy_i)_j$ are the corresponding random components of distortion at cross i of frame j.

and

$$\begin{aligned}\frac{1}{n} \sum_{j=1}^n (RVx_i)_j &= 0 \\ \frac{1}{n} \sum_{j=1}^n (RVy_i)_j &= 0\end{aligned}\tag{13.7}$$

where n is the number of frames.

The systematic and random components of distortion may be determined for each imaging system from the measurements made on n frames as follows:-

- (i) using any of the above mentioned transformation methods, the total distortion values V_x , V_y can be determined at each of the crosses for each of the n frames.
- (ii) the systematic component of distortion at each cross can be computed using the formula;

$$SV_{x_i} = 1/n \sum_{j=1}^n (V_{x_i})_j$$

$$SV_{y_i} = 1/n \sum_{j=1}^n (V_{y_i})_j \quad (13.8)$$

- (iii) for any cross i , the measured image coordinates x_i' , y_i' are corrected for the systematic distortion as follows:-

$$Cx_i' = x_i' + SV_{x_i}$$

$$Cy_i' = y_i' + SV_{y_i} \quad (13.9)$$

where:-

Cx_i' , Cy_i' are the image coordinates of cross i corrected for systematic distortion.

- (iv) the same transformation procedure used in (i) above is used again, but this time using the corrected image coordinates Cx' , Cy' . The residuals resulting from this transformation will be the random components RV_{x_i} , RV_{y_i} .

13.5 Analysis of the Data Obtained During the Radiometric Calibration

For this process, first of all, the images of the radiation source have been acquired at three different temperatures (T_1 , T , T_2). From these images, three frames for each temperature were then extracted and digitized using the frame grabber. Afterwards, for the detailed analysis of the grey level data contained in the frames, certain quadrants and patches were extracted from these frames. These binary values have then been converted to the required ASCII file format using the method given in

Section 13.3.2 (a). In this way, the images required for the radiometric calibration of the imager have been obtained.

13.5.1 Computation of the Mean and Standard Deviation of the Grey Level Values

For each frame, quadrant or patch that has been extracted, the mean grey level values and standard deviations are determined by the FORTRAN program STMN. For any area, the average (A) or mean is obtained from

$$A = \frac{\sum_{i=1}^n \sum_{j=1}^m g(i,j)}{n \times m} \quad (13.10)$$

where:-

A is the average or mean of the grey level values present in the frame, quadrant or patch;

n is the number of pixels in the x direction;

m is the number of pixels in y direction; and

g(i,j) is the grey level value of the ij-th pixel.

Thus, the standard deviation

$$\sigma = \sqrt{\frac{\sum_{i=1}^n \sum_{j=1}^m (A - g(i,j))^2}{[(n \times m) - 1]}} \quad (13.11)$$

where σ is the standard deviation of the grey level values of the pixels present in the frame, quadrant or patch.

The program STMN is listed and included as Appendix E, including sample data and output from this program.

13.5.2 Temporal Average of the Quadrants

After computing the mean and the standard deviation values, the temporal average of the grey level values of the pixels is determined. For this purpose, firstly, the sum of

the grey level values of the same pixels in each quadrant at the same temperature is determined. Then, this sum is divided by the number of quadrants available for this temperature determination (see Fig. 13.10). For any temperature,

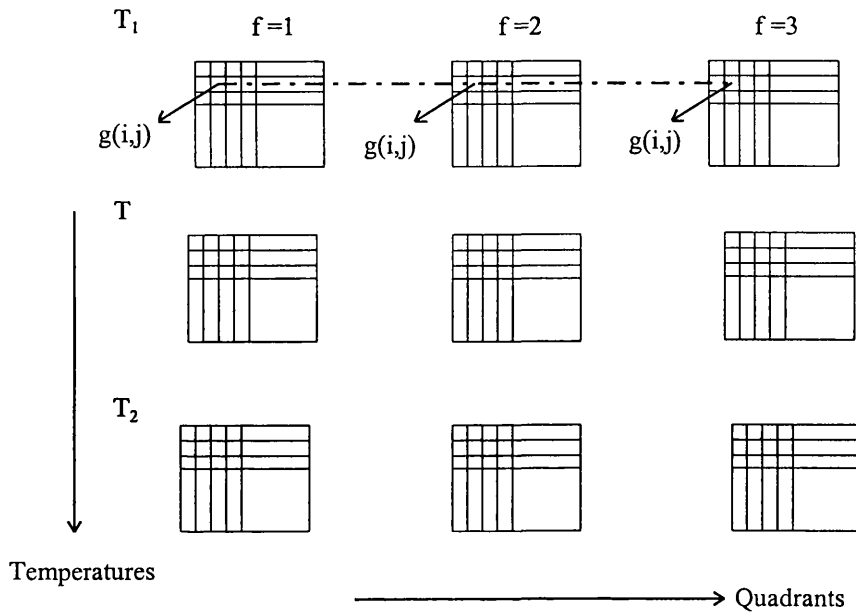


Fig. 13.10. Temporal averaging of the grey level values of the pixels.

$$S(i,j,T_L) = \left[\sum_{k=1}^f g(i,j) \right] / f \quad (13.12)$$

where:-

- f is the number of quadrants available at temperature T_L ;
- $g(i,j)$ is the grey level value of the ij -th pixel; and
- $S(i,j,T_L)$ is the temporal average for the ij -th pixel at temperature T_L .

As explained in more detail in Chapter 10, $S(i,j,T_L)$ is the offset value for the pixels.

13.5.3 Spatial Average and Noise

The spatial average over a quadrant can be computed using the values that have been calculated in the previous section. For any temperature,

$$S'(T_L) = \left[\sum_{i=1}^n \sum_{j=1}^m S(i,j,T_L) \right] / [n \times m] \quad (13.13)$$

where $S'(T_L)$ is the spatial average of the quadrants that have been imaged at the temperature T_L .

Thus, the standard deviation of the spatial average (or spatial noise) can be computed as

$$\sigma_{sp} = \sqrt{\frac{n \ m}{\{ [\sum_{i=1}^n \sum_{j=1}^m (S'(T_L) - S(i,j,T_L))^2] / [(n \times m) - 1] \}} \quad (13.14)$$

After determining the spatial average $S'(T_L)$ and temporal average $S(i,j,T_L)$, they are input to Eq. 10.5. Thus, the gain values for each pixel at temperature T have been computed and the non-uniformity corrected grey level values $S_C(i,j,T)$ have been obtained using Eq. 10.6.

The non-uniformity of the images at temperature T is computed as a percentage,

$$NU = [\sigma_{sp} / S'(T_L)] \times 100 \quad (13.15)$$

where

NU is the non-uniformity;

σ_{sp} is the spatial root mean square error; and

$S'(T_L)$ is the spatial mean.

All the procedures have been given above in Sections 13.5.2 and 13.5.3 have been programmed by the present author using the FORTRAN 77 language. The resulting program PRNU is listed and included as Appendix F. Sample output from this program is also given there.

13.5.4 Statistical Processing of the Grey Level Values of the Quadrant

The distribution of grey level values of pixels in each quadrant (X) should have a normal distribution with a mean value A and a standard deviation σ if it has the following frequency distribution function:

$$f(x) = (1 / \sqrt{2\pi}\sigma) e^{-1/2 [(X - A) / \sigma]^2} \quad (13.16)$$

which is also often referred to as the Gaussian distribution. It describes a bell-shaped curve which is symmetrical about the average or mean value A (Fig. 13.11).

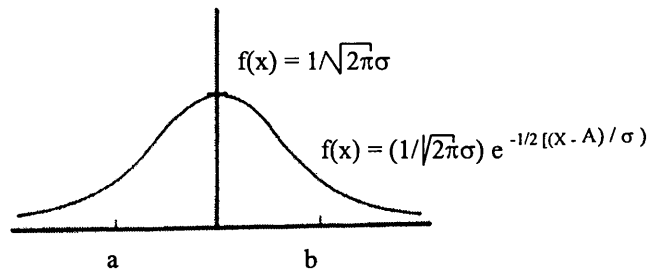


Fig. 13.11. Normal Distribution

Probability tables for this distribution are readily available. The following probabilities are of special interest to photogrammetric applications:

$$P\{-\sigma \leq (X - A) \leq \sigma\} = 0.6827$$

$$P\{-2\sigma \leq (X - A) \leq 2\sigma\} = 0.9545$$

$$P\{-3\sigma \leq (X - A) \leq 3\sigma\} = 0.9973$$

The last probability shows that 99.7% of the grey level values of the pixels lying within the quadrant X should fall within 3σ of the mean value (A). For this reason, the value 3σ is usually taken as a tolerance limit for errors. If the grey level value of a pixel has exceeded 3σ from the mean level of the quadrant, it is assumed to be a blemished or dead pixel, i.e. it is not responding to the incident radiation as it should.

The FORTRAN 77 program STAT has been written by the author to determine the occurrence and distribution of the grey level values of the pixels lying within the quadrant. In this way, the number of blemished pixels is obtained and the distribution of the grey level values and their conformance to the normal distribution or otherwise is determined. This program is listed and included as Appendix G where sample output from the program is also included.

In this matter, the other important point is the significance of the standard deviation σ . It is illustrated in Fig. 13.12. A normal distribution having a large value of σ means that the grey level values of the pixels are spread over a wide range on both sides of the mean (A). A small value of σ means that grey level values of the pixels are concentrated about the mean.

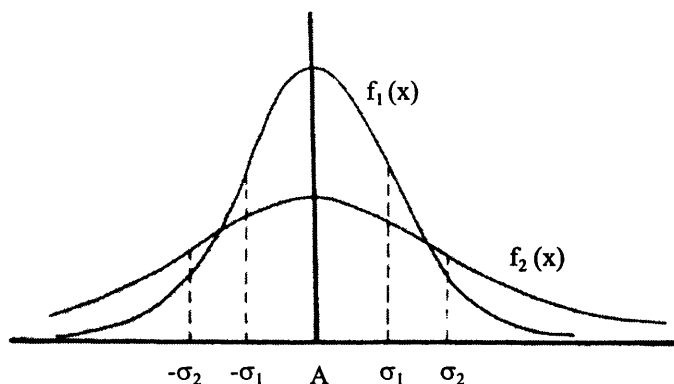


Fig. 13.12. Significance of σ .

13.5.5 Graphical Representation of the Grey Level Values of the Pixels by SURFER

SURFER is a grid-based contouring and three-dimensional surface plotting program that runs under Microsoft Windows. It first interpolates image data on to a regularly spaced grid and then places this interpolated data in a grid [.GRD] file. However, in the present project, since the ASCII image data files (comprising the positions of the pixels (x,y) and their grey level values (z)) are already regularly spaced, there is no need to interpolate the data on to a set of grid nodes. It is possible to produce a grid file that uses the image data directly by use of the option of “creating grid file from a regular array of xyz data” that is offered by SURFER.

The grid files have been used to produce surface plots and contour maps of the image grey level data. In this way, the image data has been represented pixel-by-pixel. Thus, blemished and dead pixels can be located and pointed out immediately. In this project, the program PRNU that supplies the data for SURFER has been written to include many options. It can not only be executed for all the data lying within a frame or

quadrant but it can also divide the quadrant into several sub-areas and can carry out the required computation and analysis for each of these sub-areas (or patches). Thus changes in the means and standard deviations of the grey level values occurring in different parts of the quadrant can be determined in this way. The changes can also be displayed as a surface plot by the SURFER program. Sub-areas with different sizes (5x5, 10x10,.....) have been defined and represented using SURFER, but after several trials, it was realized that the best representation has been obtained by the pixel-by-pixel representation.

This procedure has been applied to each frame, quadrant or patch and a graphical representation of each has been produced by the SURFER program on a pixel-by-pixel basis. The plots resulting from SURFER have been produced using one of raster-based laser or bubble-jet printers available in this Department. The pixel-by-pixel representation of the various quadrants of each infrared imager that has been tested in this project have been included in the various results chapters.

13.6 Conclusion

In this chapter, the experimental procedures that have been followed to calibrate infrared imaging systems geometrically and radiometrically have been discussed in some detail. The design of the target plate that has been constructed specifically for the calibration work carried out in this research project has been described. In addition, the processing and analysis of the digital infrared image data carried out for the geometric and radiometric calibrations have been explained. Furthermore the use of the Adobe Photoshop image processing package that has been employed to enhance the digital infrared images has been described. In the next two chapters, the results of the geometric and radiometric calibration of the infrared CCD cameras that have been tested in this project will be presented, discussed and analyzed.

CHAPTER 14: RESULTS AND ANALYSIS OF THE GEOMETRIC CALIBRATION OF INFRARED CCD CAMERAS

14.1 Introduction

In Chapter 13, the theoretical basis and the actual procedures that have been developed to calibrate infrared imaging systems both geometrically and radiometrically have been explained in some detail. In this chapter, a report will be given on the results achieved using the geometric calibration procedure as applied to a representative group of infrared CCD cameras. The results from this calibration will be presented and analyzed for each individual imager that has been tested. During this work, linear conformal and polynomial transformations have been applied between the image coordinates and the reference coordinates of the cross targets on the calibration plate in order to discover the nature and magnitude of the geometric distortions that are present in each camera. The overall results obtained from the application of each individual term of the polynomial transformation will be presented via tables to find out which are the effective terms with regard to the modelling and correction of the geometric distortions. In addition, the error vectors will be plotted graphically in order to determine the pattern of these distortions and whether the distortions are systematic or not.

14.2 Agema 550 CCD Camera

The Agema 550 CCD camera, shown in Fig. 14.1, is representative of the state-of-the-art in CCD infrared camera technology at the present time. It has been designed for operation in harsh industrial environments and produces a standard PAL TV compatible video signal that can be displayed on a conventional television monitor or recorded on a VTR. It uses a fixed lens having a 20° angular coverage onto which further lenses can be added to give alternative 10° and 40° angular coverages (see Table 8.2). It is operated in the 3.6 to 5.0 μ m wavelength band of the middle infrared region of the EM spectrum and has a detector array of 320 x 240 elements which is cooled by a tiny Stirling engine. The Agema 550 includes a number of special features

which measure the temperature of individual objects falling within the scene. However, since such temperature measurements lie outside the scope of this thesis, this facility has only been used in the radiometric calibration of the imager. In particular, it allowed the author to set the temperature of the radiation source correctly and to check it many times during the experimental work carried out with this imager.



Fig. 14.1. Agema 550 CCD camera.

14.2.1 Experimental Procedure with Agema 550

Images of the calibration target plate have been acquired by the Agema 550 twice during the course of this project. On the first occasion, because of the time limitation during which the imager was available, images of the cross targets were acquired by this camera using both the 10° and 20° lenses for the geometric calibration only. At that time, images of the radiation source needed for the radiometric calibration stage could not be acquired. However, later the Agema engineers who came to the Department to give a seminar about their imagers and to help the author to carry out his experimental work, brought the Agema 550 again to complete the remaining work. The additional images of the radiation source required for the radiometric calibration of this imager were then obtained without any difficulty on this second occasion. In addition, the author took the opportunity to acquire more images of the cross targets using all three available lenses with 10° , 20° and 40° coverage. In this way, all the images of the target plate required for the geometric calibration and of the radiation source for the radiometric calibration have been acquired.

14.2.2 Results and Analysis of the Geometric Calibration of the Agema 550

As explained above, initially images of the target plate had been obtained by the camera using the 10° and 20° coverage lenses. From these images which had been recorded onto magnetic tape using the VTR, only one frame for the 10° lens and two frames for the 20° lens were converted to digital form using the frame grabber. However, on the second occasion, the images of the cross targets have been obtained using the 10°, 20° and 40° lenses. From these images, 3 frames from the image set for each lens have also been digitized. These frames were input to the image matching program SUBPIX to measure the image coordinates of the cross targets automatically. This worked well without any difficulty arising. The resulting coordinates were then entered into the LINCON and POLY25 programs to carry out both the linear conformal and polynomial transformations between the measured image coordinates of the cross targets and the reference coordinates that had already been established. The results and the error diagrams resulting from these operations will be given and discussed in some detail in the following sections.

14.2.2.1 Results and Analysis with the 20° Lens

As stated above, a lens having a 20° angular coverage is built into the imager; it is fixed and cannot be removed. When the imager was used with its 10° and 40° fields of view, special lens elements were added to the basic 20° lens to give the required coverage. Therefore, the results and analysis of the geometric calibration of the Agema 550 CCD camera will start with the 20° lens and will continue on with the 10° and 40° lenses respectively.

As mentioned above, two frames on the first occasion and three frames on the second occasion have been grabbed from the analogue video images of the cross targets which have been taken by the camera using the basic 20° lens and recorded using the VTR. Thus, in total, five frames have been measured and analyzed for the lens with 20° angular coverage. A sample image that has been digitized for this lens is shown in

Fig. 14.2. Each of the five frames have been input to the image matching program SUBPIX to measure the image coordinates of the cross targets. Then, these coordinates have been entered into the LINCON and POLY25 transformation programs to determine the different geometric distortions inherent in these frames. The results from the transformations are given in Table 14.1.

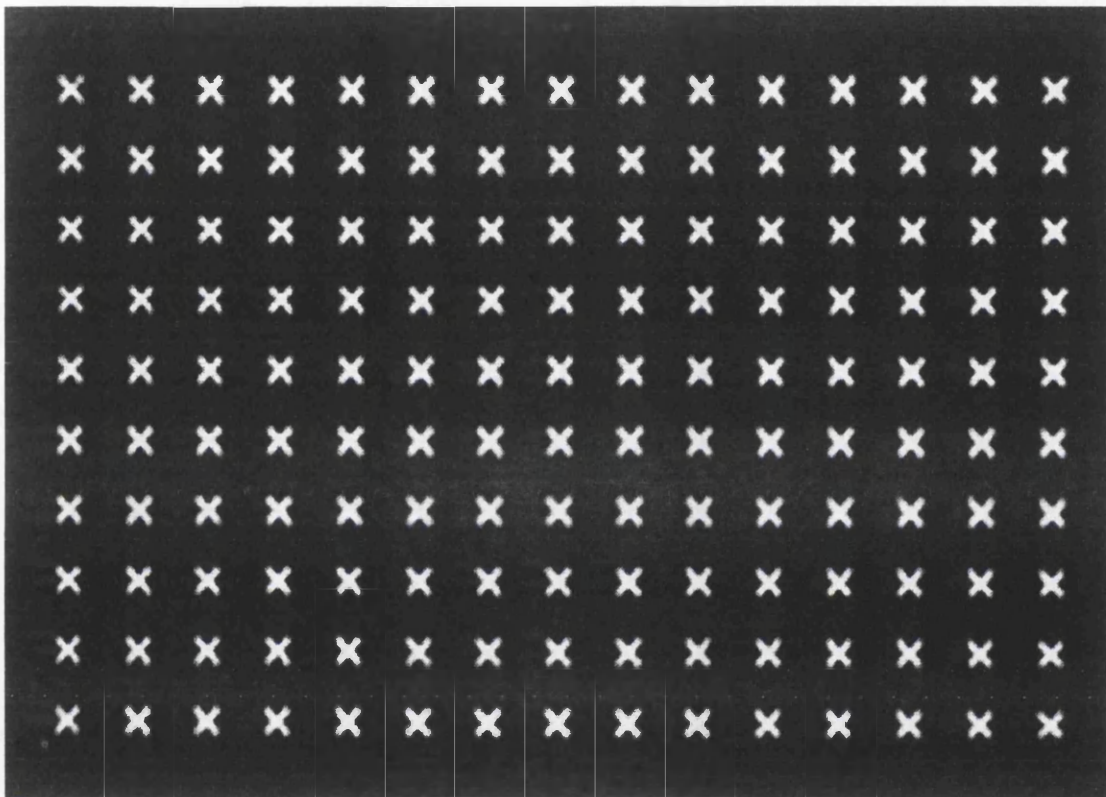


Fig. 14.2. Sample image that was taken using the 20° lens

The linear conformal transformation resulted in rmse values of the residual errors of about ± 0.6 pixel in each direction. The error vectors resulting from this transformation were plotted using the VECTOR program. As can be seen in Fig. 14.3 (a), (b), (c), (d) and (e), quite systematic patterns resulted over all the frames. As can be seen from these figures, the dimension of the geometric errors is increasing towards the corners of the frames.

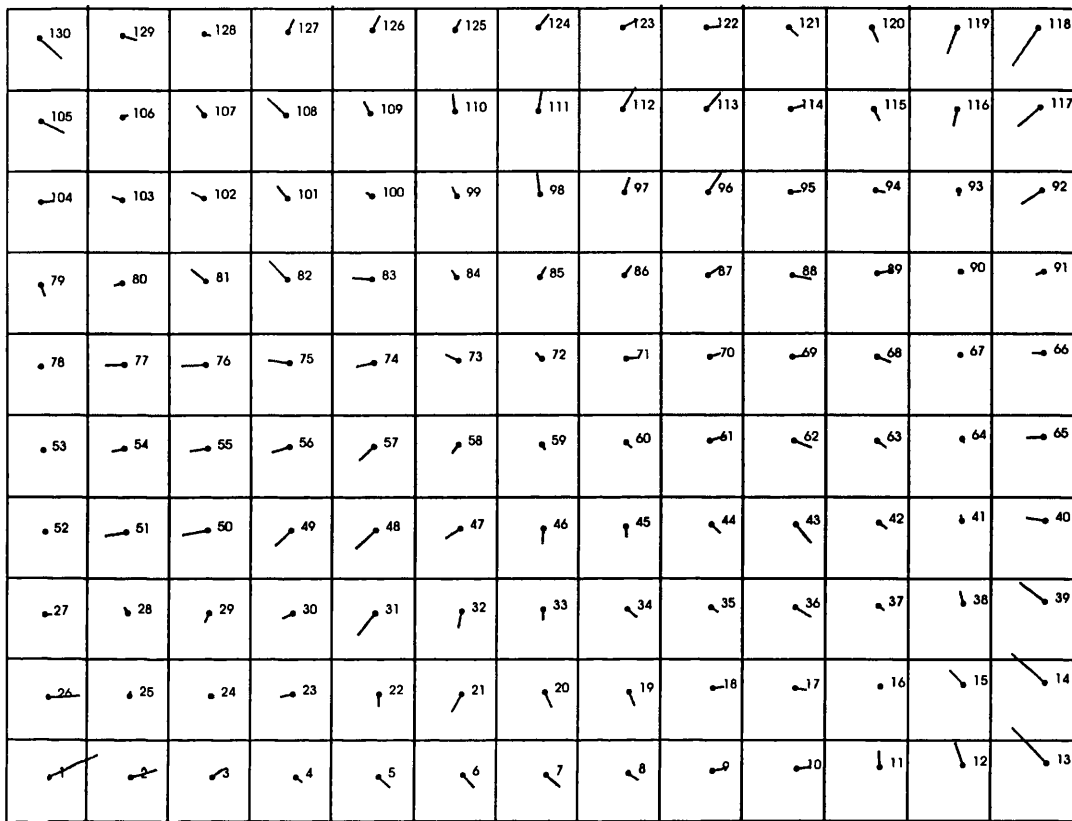
Although the plotting of the residual errors for each frame on the first and second occasions gave almost the same distortion pattern, on the second occasion, a slightly different pattern of vectors resulted compared with that produced from the plotting of

the error vectors for this lens on the first occasion. As can be seen from Fig. 14.3, on the first occasion, the residual errors produced at the edges and the corners of the frames were not as big as those produced on the second occasion.

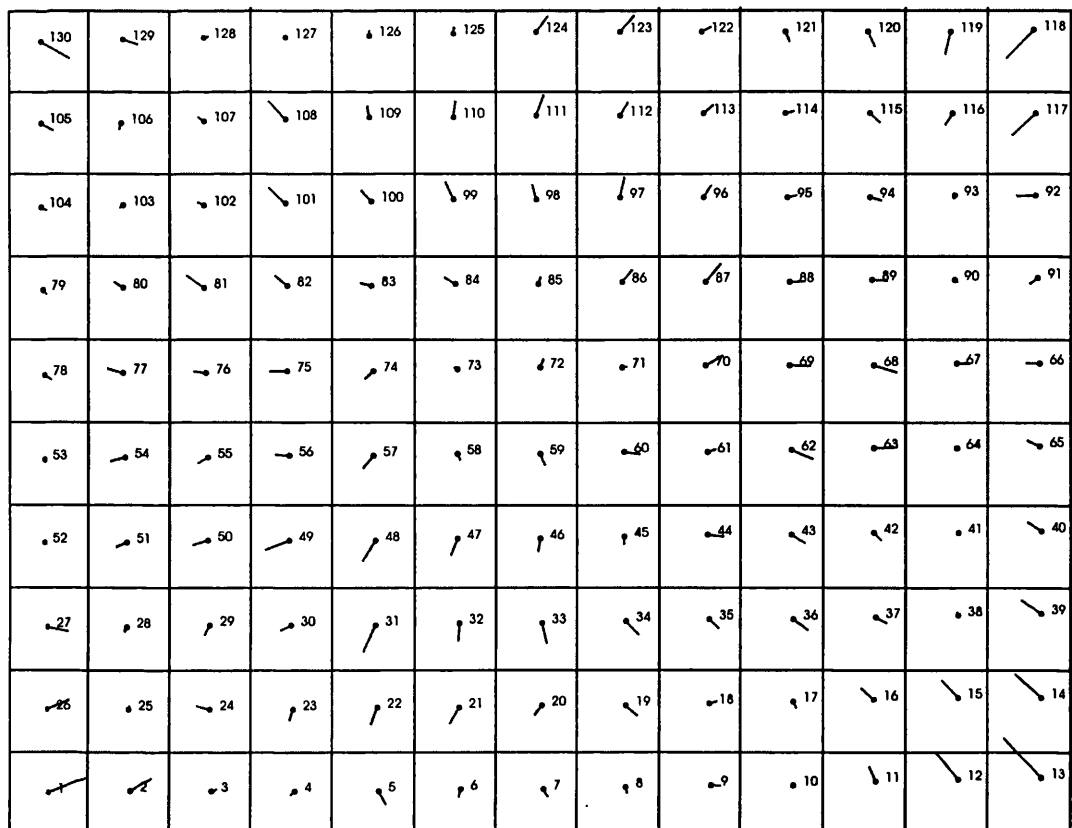
Transformation Procedure	R.M.S.E (Pixels) of Residual Errors									
	First Occasion				Second Occasion					
	Frame I		Frame II		Frame I		Frame II		Frame III	
	m_x	m_y	m_x	m_y	m_x	m_y	m_x	m_y	m_x	m_y
Linear Conformal	±0.60	±0.51	±0.56	±0.50	±0.62	±0.60	±0.68	±0.61	±0.60	±0.61
3-Terms (affine)	±0.60	±0.51	±0.55	±0.50	±0.60	±0.58	±0.64	±0.57	±0.59	±0.59
4-Terms (xy)	±0.59	±0.48	±0.55	±0.47	±0.60	<u>±0.39</u>	±0.64	<u>±0.36</u>	±0.59	<u>±0.37</u>
5-Terms (x^2)	±0.58	±0.48	±0.54	±0.47	<u>±0.40</u>	±0.38	<u>±0.45</u>	±0.36	<u>±0.38</u>	±0.37
6-Terms (y^2)	±0.55	±0.48	±0.54	±0.47	±0.37	±0.38	±0.42	±0.36	±0.37	±0.37
7-Terms (x^2y)	±0.55	<u>±0.27</u>	±0.54	<u>±0.28</u>	±0.37	<u>±0.26</u>	±0.42	<u>±0.26</u>	±0.37	<u>±0.27</u>
8-Terms (xy^2)	±0.47	±0.27	±0.46	±0.28	±0.34	±0.26	±0.37	±0.26	±0.33	±0.27
9-Terms (x^2y^2)	±0.47	±0.27	±0.46	±0.28	±0.34	±0.26	±0.37	±0.26	±0.33	±0.27
10-Terms (x^3)	<u>±0.17</u>	±0.27	<u>±0.19</u>	±0.28	<u>±0.17</u>	±0.26	<u>±0.25</u>	±0.25	<u>±0.18</u>	±0.27
11-Terms (y^3)	±0.16	±0.19	±0.19	±0.19	±0.17	±0.21	±0.17	±0.20	±0.16	±0.25
12-Terms (x^3y)	±0.16	±0.19	±0.19	±0.19	±0.17	±0.21	±0.17	±0.20	±0.16	±0.25
13-Terms (xy^3)	±0.16	±0.19	±0.19	±0.19	±0.17	±0.21	±0.17	±0.20	±0.16	±0.24
14-Terms (x^3y^2)	±0.16	±0.19	±0.19	±0.19	±0.17	±0.21	±0.17	±0.20	±0.16	±0.24
15-Terms (x^2y^3)	±0.16	±0.19	±0.19	±0.19	±0.17	±0.21	±0.17	±0.20	±0.16	±0.24
16-Terms (x^3y^3)	±0.16	±0.19	±0.19	±0.19	±0.16	±0.20	±0.17	±0.20	±0.16	±0.24
17-Terms (x^4)	±0.16	±0.19	±0.19	±0.19	±0.16	±0.20	±0.17	±0.20	±0.16	±0.24
18-Terms (y^4)	±0.15	±0.19	±0.18	±0.19	±0.16	±0.20	±0.16	±0.20	±0.15	±0.24
19-Terms (x^4y)	±0.15	±0.19	±0.18	±0.18	±0.16	±0.20	±0.16	±0.20	±0.15	±0.24
20-Terms (xy^4)	±0.15	±0.18	±0.18	±0.18	±0.16	±0.20	±0.16	±0.20	±0.15	±0.24
21-Terms (x^4y^2)	±0.15	±0.18	±0.18	±0.18	±0.16	±0.20	±0.16	±0.20	±0.15	±0.24
22-Terms (x^2y^4)	±0.15	±0.18	±0.18	±0.18	±0.16	±0.20	±0.16	±0.20	±0.15	±0.24
23-Terms (x^4y^3)	±0.15	±0.18	±0.18	±0.18	±0.16	±0.20	±0.16	±0.20	±0.15	±0.24
24-Terms (x^3y^4)	±0.15	±0.18	±0.18	±0.18	±0.16	±0.20	±0.15	±0.20	±0.15	±0.24
25-Terms (x^4y^4)	±0.15	±0.18	±0.17	±0.18	±0.16	±0.20	±0.15	±0.20	±0.15	±0.24

Table 14.1. Geometric calibration results from the Agema 550 CCD camera equipped with a 20° lens (on the first and second occasions).

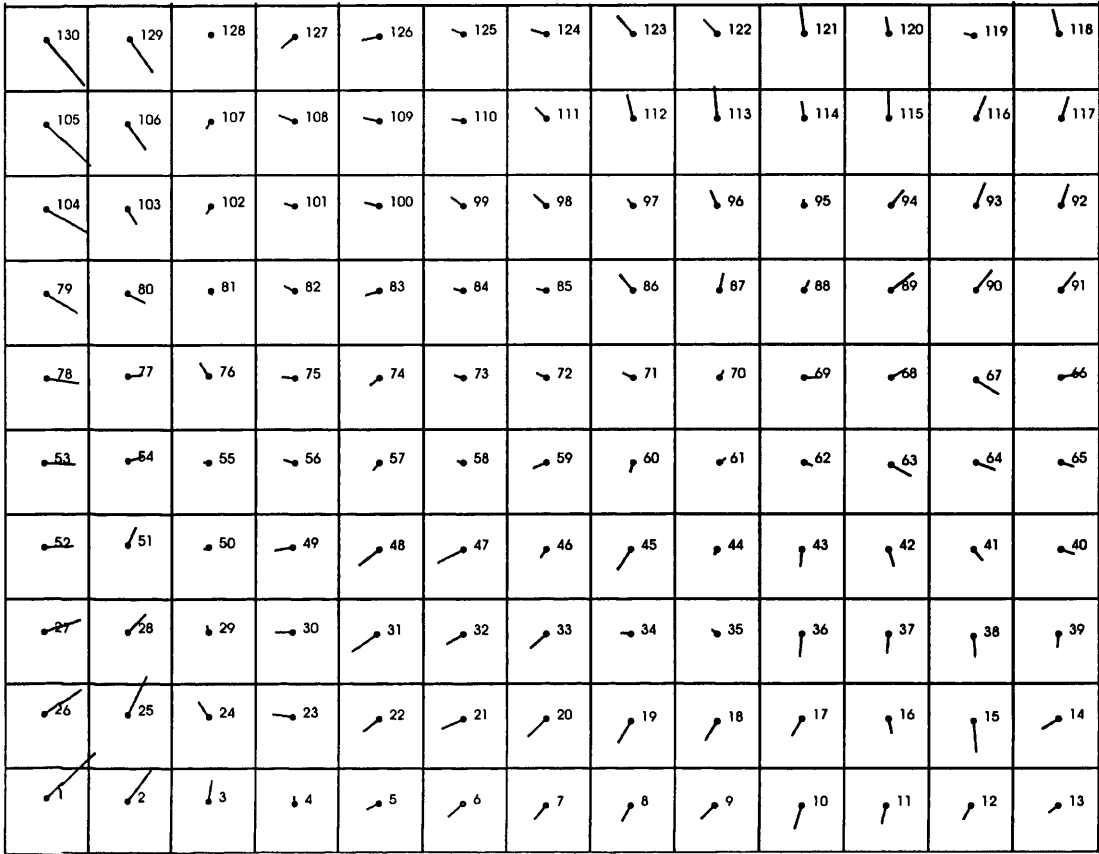
a) Vector plot from Frame I (first occasion)



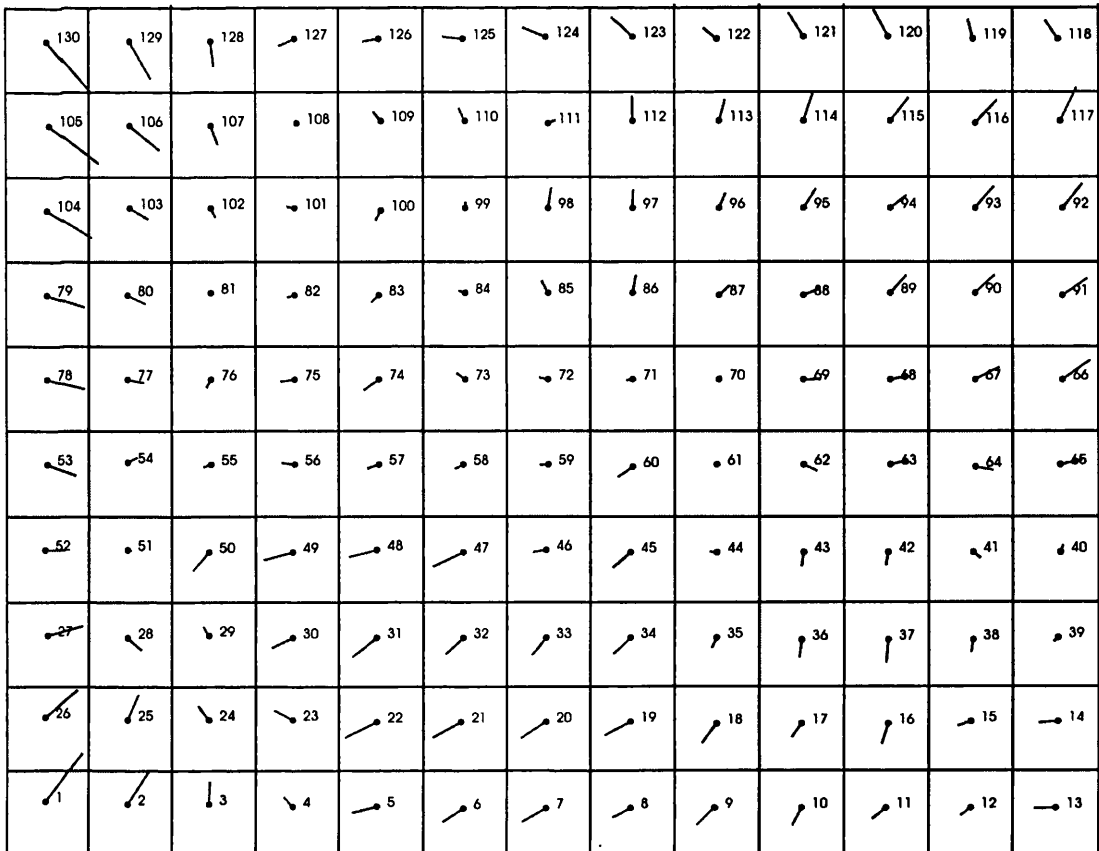
b) Vector plot from Frame II (first occasion)



(c) Vector plot from Frame I (second occasion)



(d) Vector plot from Frame II (second occasion)



(e) Vector plot from Frame III (second occasion)

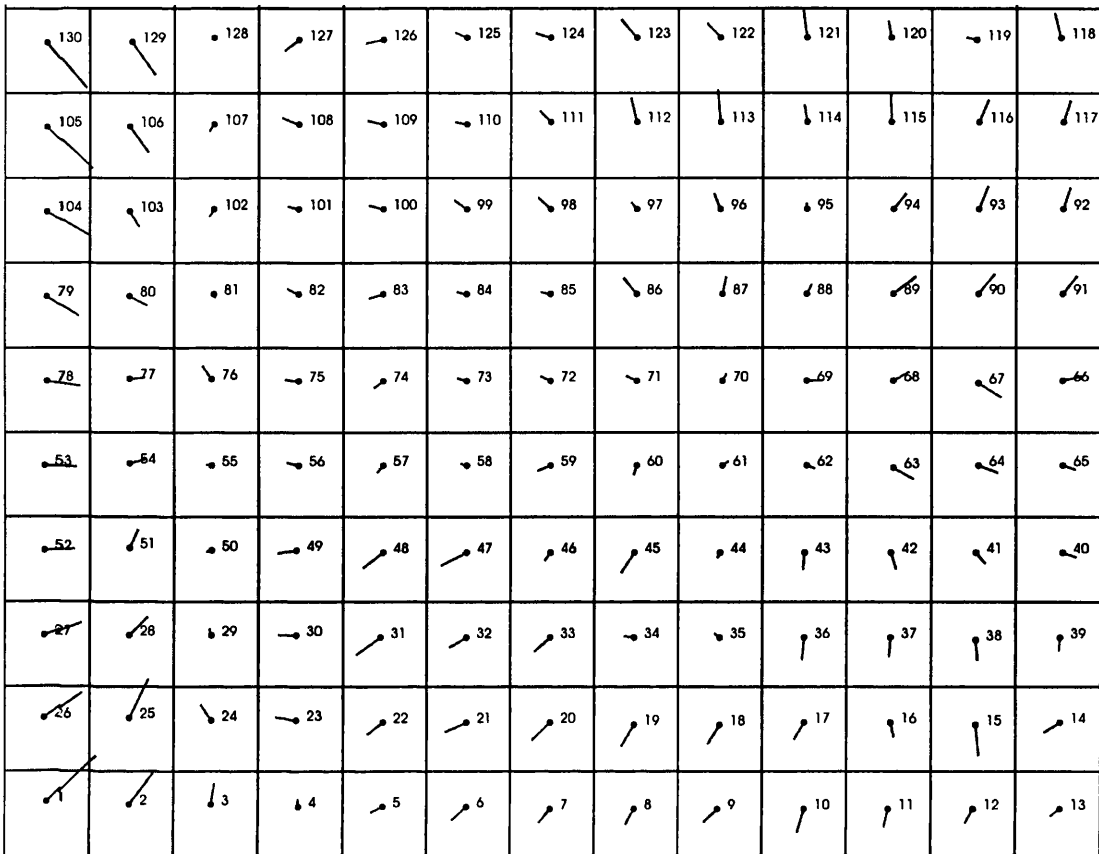


Fig. 14.3(a), (b), (c), (d) and (e). Vector plots of the residual errors resulting from the linear conformal transformation using the Agema 550 CCD camera equipped with a 20° lens (on the first and second occasions) - vectors are 12 times magnified.

In addition, on the first occasion, the amount of the residual errors occurring along the right and left edges of the frames are almost the same. However, on the second occasion, the size of the residual errors that resulted at the left edges of the frames are bigger than those obtained at the right edges.

The application of the affine transformation did not alter the rmse values. They still remained the same in both the x and y-directions. This showed that the image produced by the Agema 550 CCD camera does not contain an affinity and/or lack of orthogonality between the x and y axes. Inspecting next the results from the use of the higher-order terms of the full polynomial transformation, on each occasion, and with all five frames, a common substantial drop in the residual errors occurred in the x-direction with the application of the x^3 term and in the y-direction when the x^2y term

was added to the polynomial. The rmse value dropped to about ± 0.17 pixel in x and ± 0.27 pixel in y . For the frames acquired on the second occasion only, the use of the xy term in the 4-parameter transformation in the y -direction and the addition of the x^2 term in the 5-parameter transformation in the x -direction gave about ± 0.2 pixel reduction in the rmse value.

When the results from this transformation were checked against Fig. 13.9, it could be seen that the overall pattern corresponded to the barrel or pin cushion distortion figure shown there. In this context, it should be noted that when the experiment with the 20° lens was made on both occasions, the camera was connected to the television monitor to check the focussing and image quality of the cross targets. Also, the VTR was connected via daisy chaining to the television monitor. Thus, instead of there being a direct connection from the camera to the VTR, a television monitor was used between them. As explained in Chapter 5, the main distortions that are present in such a monitor are generated by the deflection of the electron scanning beam of CRT tube resulting from the magnetic fields that are present inside the tube. These distortions frequently take the form of a pin cushion or barrel. It could be that this is the source of this particular distortion. Unfortunately the author was unable to obtain the use of the Agema 550 imager for a third time to investigate this particular point by leaving the monitor out of the recording loop. In this experiment, plots of the error vectors that were present at the corners and at the midpoints along the edges of the images were also generated which showed quite clearly the barrel-shaped distortion and suggest that this idea is valid. (see Fig. 14.4).

However, this type of distortion can also be caused by a camera lens that has a wider field of view. In Beyer (1992), it has been reported that barrel distortion is the largest systematic error source occurring when using solid-state CCD cameras. In the present case, it appears that the distortions may have originated from both the camera lens and video monitor, and are superimposed. In addition, as can be seen from the vector plots, the distortion has also an asymmetric pattern. This phenomenon could result from the decentering of the lens elements.

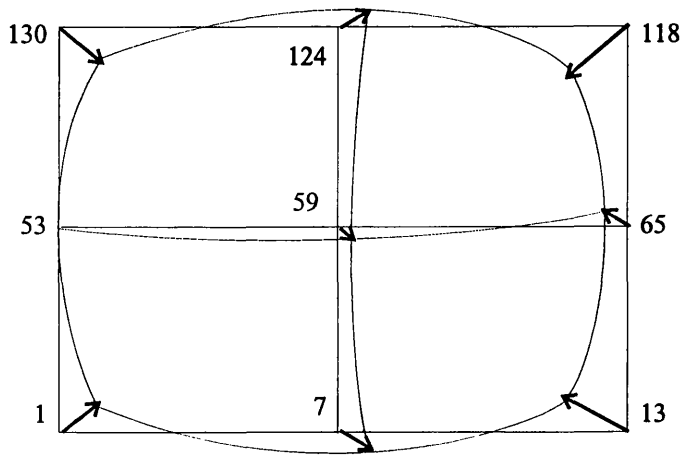


Fig. 14.4. Barrel-shaped distortion pattern from 20° lens.

When the term x^3 was added to the polynomial and the 10-parameter transformation has been used, the error dropped to about ± 0.2 pixel in the x-direction on each occasion. The use of 8 and 11-parameter transformations with the xy^2 and y^3 terms added also drop the overall rmse value (m_y) by about ± 0.08 pixel in the y-direction but it is just smaller than the ± 0.1 pixel that is taken into account as the measuring accuracy of the calibration procedure. The other terms of the transformation had no absolutely effect on the accuracy.

Based on the discussion made above, it can be seen that the x^3 and x^2y terms in the x- and y-directions respectively are the significant terms that are present on each occasion. This consistent result shows the effectiveness of the method that has been applied to calibrate this camera. However, on the second occasion, the x^2 and xy terms in the x- and y-directions respectively are the additional effective terms. The origin of these terms could lie in the experimental setup or the use of a different example of the Agema 550 imager on the second occasion.

14.2.2.2 Results and Analysis with the 10° lens

As stated before, one frame from the first occasion and three frames from the second occasion have been acquired as digital images. In Fig. 14.5, a single sample image that has been digitized for the 10° lens is shown. Thus, in total, four frames have been

input to the image matching program SUBPIX to measure the positions of the array of target crosses automatically. Then, the resulting image coordinates of the crosses have been input to the LINCON and POLY25 programs to carry out the transformations that allow the determination of the different geometric distortions that are present in these frames. The results from these transformations are given in Table 14.2.

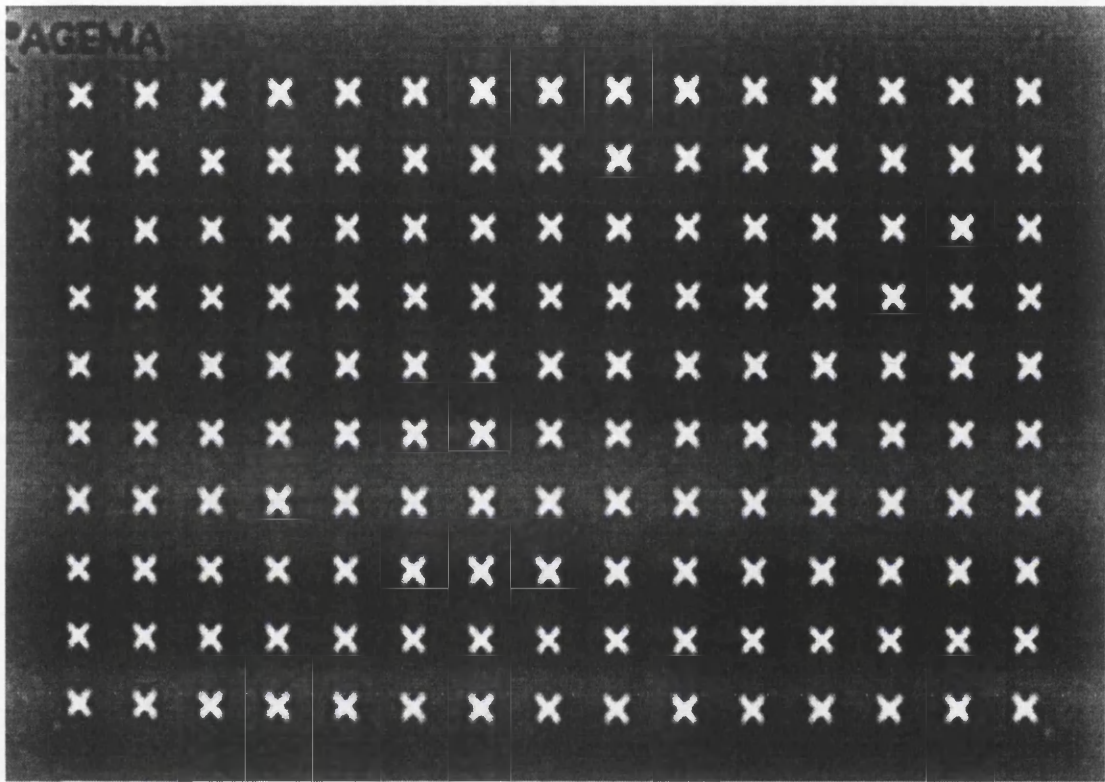


Fig. 14.5. Sample image that was taken using the 10° lens

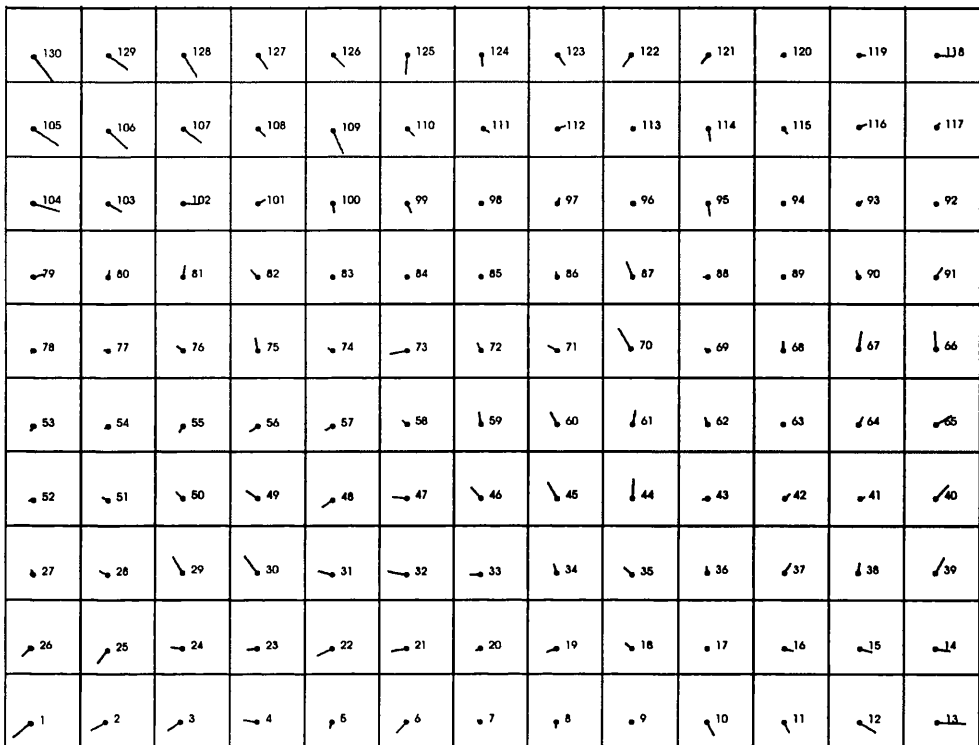
The results from the linear conformal transformation showed that overall only a small geometric distortion is occurring in both the x and y-directions at the cross targets. The rmse value for the residual errors was found to be about ± 0.3 pixel in each direction. The error vectors at 130 crosses for each frame were plotted using the program VECTOR and the resulting plots are shown as Fig. 14.6 (a), (b), (c) and (d). These figures show a fairly consistent and highly systematic pattern of geometric distortion although the overall dimension of this distortion (± 0.3 pixel) is quite small. Again the use of the affine transformation did not result in any significant change in the magnitude of the geometric distortion. For the frame acquired on the first occasion, the 4-parameter and 5-parameter transformations had a small effect on the x

and y-directions, but they were still not large enough to change the magnitude of distortion by the amount of the tenth of a pixel that has been accepted as the precision of the measurements of the image coordinates of the cross targets.

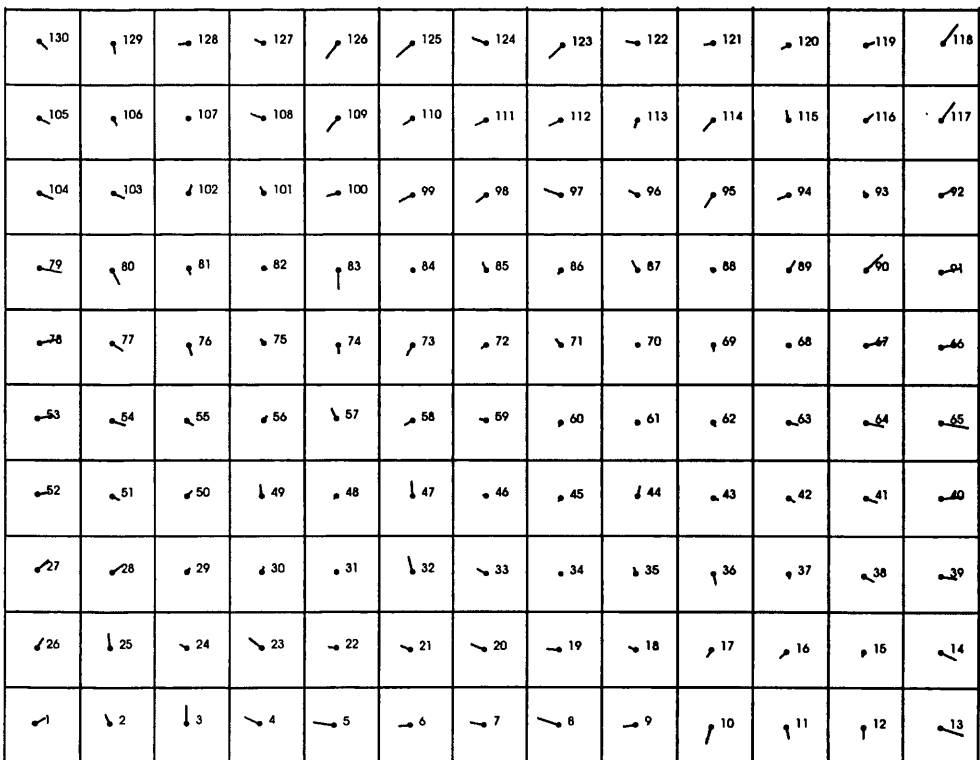
Transformation Procedure	R.M.S.E (Pixels) of Residual Errors							
	First Occasion		Second Occasion					
	Frame I		Frame I		Frame II		Frame III	
	m_x	m_y	m_x	m_y	m_x	m_y	m_x	m_y
Linear Conformal	±0.31	±0.31	±0.32	±0.25	±0.32	±0.30	±0.32	±0.26
3-Terms (Affine)	±0.28	±0.28	±0.32	±0.24	±0.30	±0.29	±0.32	±0.25
4-Terms (xy)	±0.21	±0.28	±0.32	±0.20	±0.30	±0.24	±0.32	±0.19
5-Terms (x^2)	±0.16	±0.28	±0.18	±0.20	±0.18	±0.24	±0.18	±0.19
6-Terms (y^2)	±0.15	±0.20	±0.13	±0.20	±0.16	±0.23	±0.17	±0.19
7-Terms (x^2y)	±0.15	±0.20	±0.13	±0.20	±0.16	±0.22	±0.17	±0.19
8-Terms (xy^2)	±0.14	±0.20	±0.13	±0.19	±0.16	±0.22	±0.17	±0.18
9-Terms (x^2y^2)	±0.14	±0.20	±0.13	±0.19	±0.16	±0.22	±0.16	±0.18
10-Terms (x^3)	±0.14	±0.20	±0.13	±0.19	±0.16	±0.22	±0.16	±0.18
11-Terms (y^3)	±0.14	±0.19	±0.12	±0.19	±0.14	±0.22	±0.16	±0.18
12-Terms (x^3y)	±0.14	±0.19	±0.12	±0.19	±0.14	±0.22	±0.16	±0.18
13-Terms (xy^3)	±0.14	±0.19	±0.12	±0.19	±0.14	±0.21	±0.16	±0.18
14-Terms (x^3y^2)	±0.14	±0.19	±0.12	±0.18	±0.14	±0.21	±0.16	±0.18
15-Terms (x^2y^3)	±0.13	±0.19	±0.12	±0.18	±0.14	±0.21	±0.16	±0.18
16-Terms (x^3y^3)	±0.13	±0.19	±0.12	±0.18	±0.14	±0.21	±0.16	±0.18
17-Terms (x^4)	±0.13	±0.19	±0.12	±0.18	±0.14	±0.21	±0.16	±0.18
18-Terms (y^4)	±0.13	±0.19	±0.12	±0.18	±0.14	±0.21	±0.16	±0.18
19-Terms (x^4y)	±0.13	±0.19	±0.12	±0.18	±0.14	±0.21	±0.16	±0.18
20-Terms (xy^4)	±0.12	±0.19	±0.11	±0.18	±0.14	±0.21	±0.15	±0.17
21-Terms (x^4y^2)	±0.12	±0.19	±0.11	±0.18	±0.14	±0.21	±0.15	±0.17
22-Terms (x^2y^4)	±0.12	±0.19	±0.11	±0.18	±0.14	±0.21	±0.15	±0.17
23-Terms (x^4y^3)	±0.12	±0.19	±0.11	±0.18	±0.14	±0.21	±0.15	±0.17
24-Terms (x^5y^4)	±0.12	±0.19	±0.11	±0.18	±0.14	±0.20	±0.15	±0.17
25-Terms (x^4y^4)	±0.11	±0.19	±0.11	±0.18	±0.14	±0.20	±0.15	±0.17

Table 14.2. Geometric calibration results for the Agema 550 CCD camera equipped with a 10° lens (on the first and second occasions)

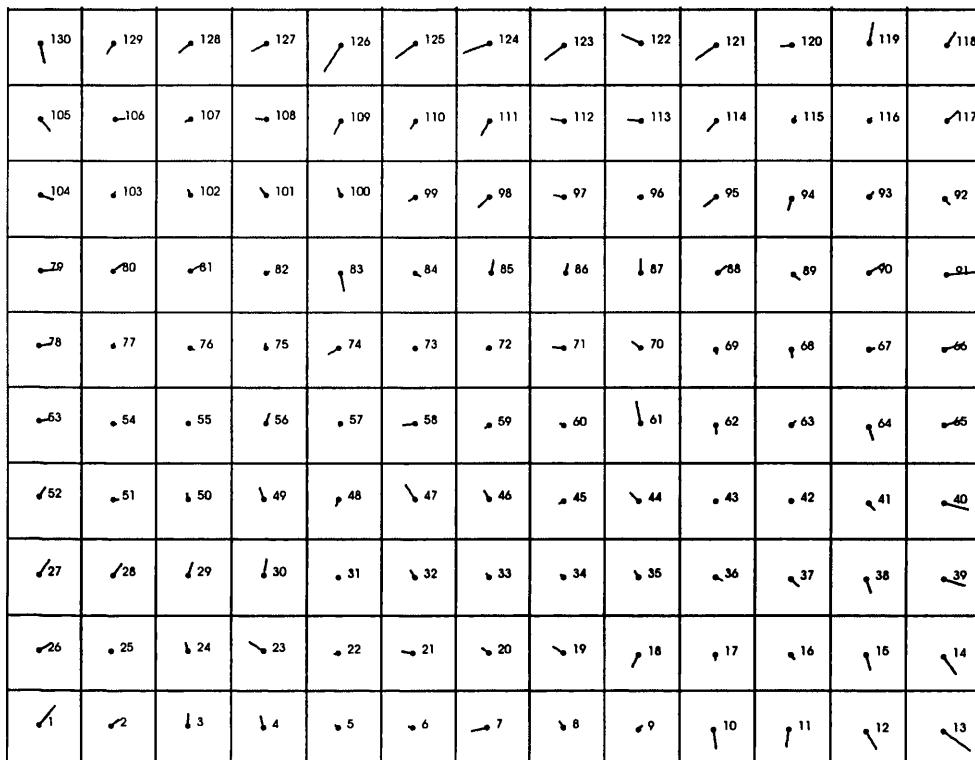
a) Vector plot from Frame I (first occasion)



(b) Vector plot from Frame I (second occasion)



(c) Vector plot from Frame II (second occasion)



(d) Vector plot from Frame III (second occasion)

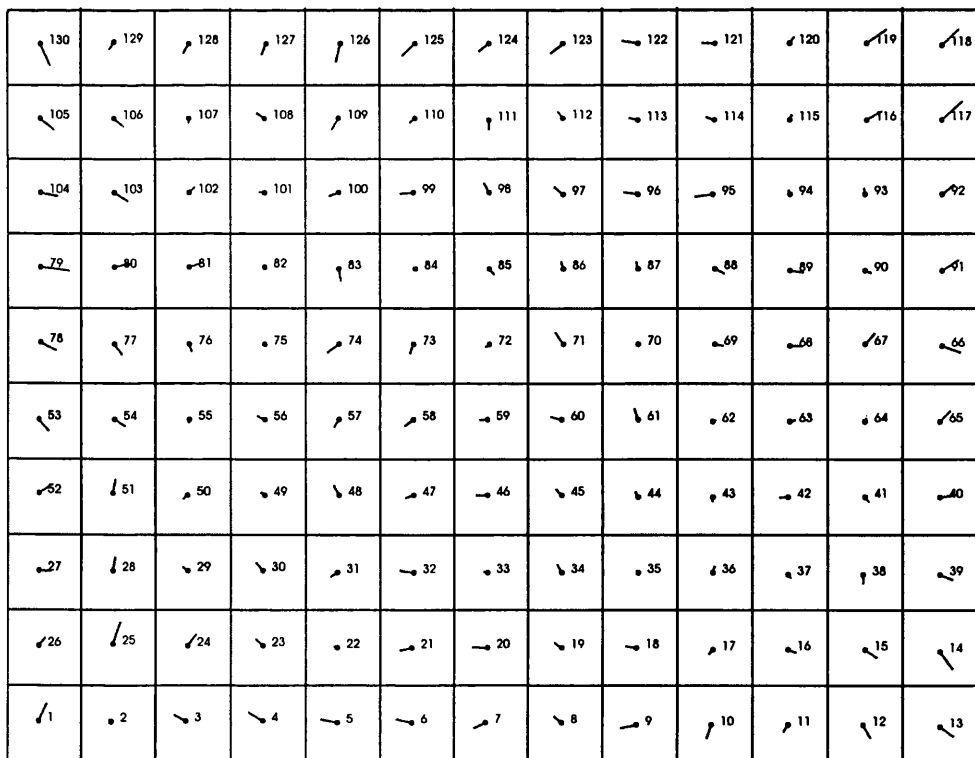


Fig. 14.6(a), (b), (c) and (d). Vector plots of the residual errors resulting from the use of the linear conformal transformation using the Agema 550 CCD camera equipped with a 10° lens (on the first and second occasions) - vectors are 17 times magnified.

However, for the frames acquired on the second occasion, the use of 5-parameter transformation containing the x^2 term had an effect on the rmse value in the x-direction and reduced it to the ± 0.18 pixel level from ± 0.32 pixel before this term had been applied. However, on each occasion, the residual error in the x-direction remained at the same consistent rmse value after the application of this transformation. The other terms had absolutely no effect on the results obtained by the polynomial transformation. In summary, it can be said that the overall geometric errors encountered in the calibration of the Agema 550 equipped with the narrow (10°) angular coverage are relatively small in absolute terms but with a noticeable tendency to increase in dimension towards the edges and corners of the image.

14.2.2.3. Results and Analysis with the 40° Lens (Second Occasion)

On the second occasion of gaining access to the Agema 550 CCD camera, the author had the chance to calibrate it with the 40° lens. Three frames from the recorded analogue images have been digitized and one sample from these is shown in Fig. 14.7. The much larger geometric distortion pattern that is present in the images taken using this lens is immediately apparent, even before the measurements have been carried out.

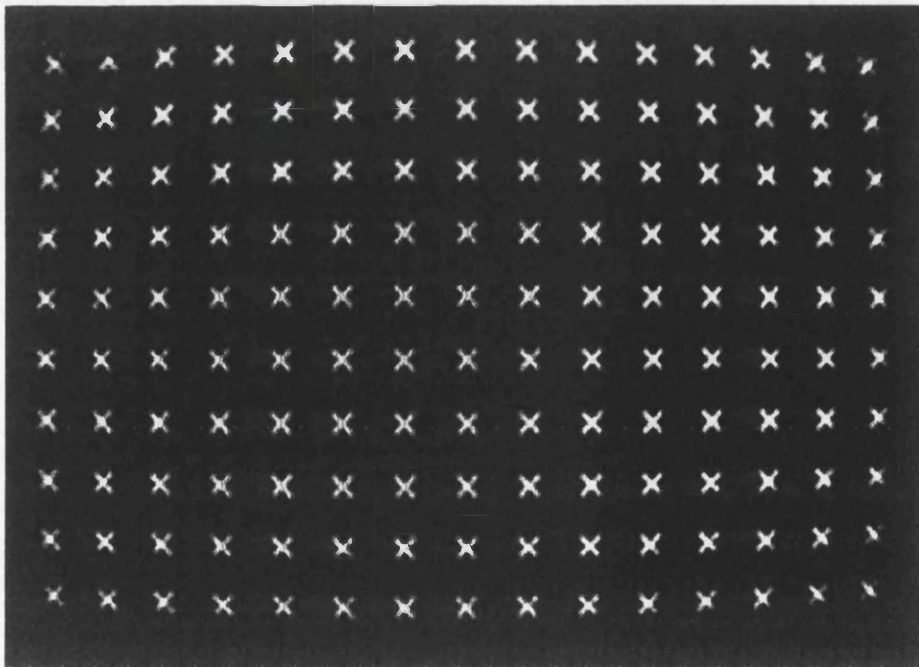


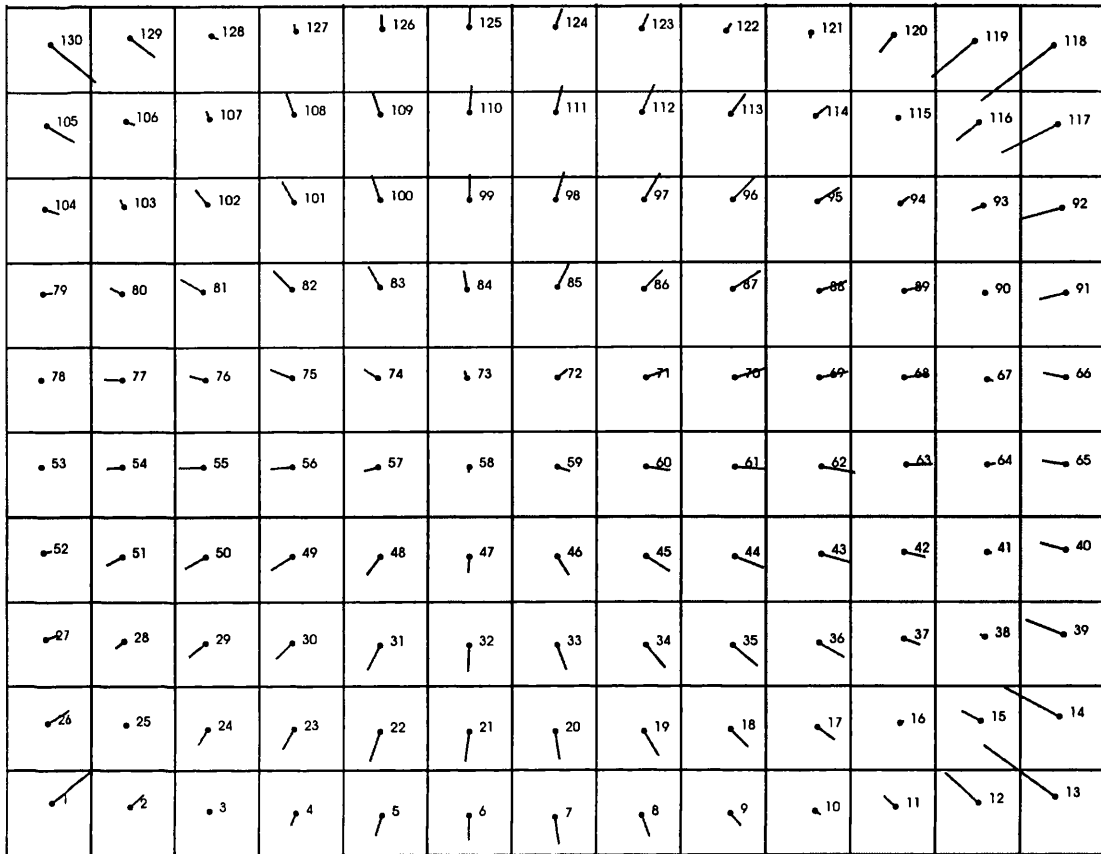
Fig. 14.7. Sample image that is taken by 40° lens

These digitized frames have again been input to the image matching program SUBPIX to measure the positions of the crosses in the image. The resulting image coordinates of the cross targets have then been input to the LINCON and POLY25 transformation programs. The results from these operations are set out in Table 14.3.

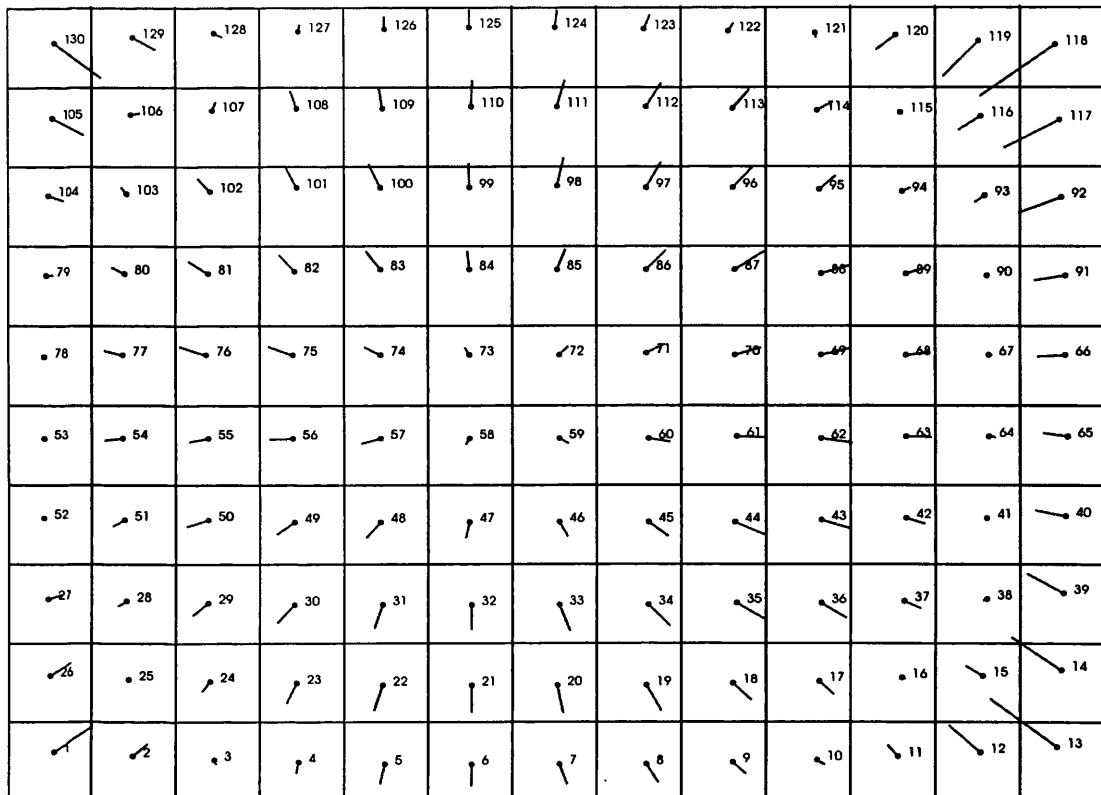
Transformation Procedure	R.M.S.E (Pixels)					
	Frame I		Frame II		Frame III	
	m_x	m_y	m_x	m_y	m_x	m_y
Linear Conformal	±2.55	±2.11	±2.54	±2.14	±2.54	±2.14
3-Terms (Affine)	±2.52	±2.05	±2.50	±2.07	±2.50	±2.07
4-Terms (xy)	±2.51	±1.99	±2.49	±2.01	±2.48	±2.01
5-Terms (x^2)	<u>±2.35</u>	±1.99	<u>±2.33</u>	±2.01	<u>±2.31</u>	±2.01
6-Terms (y^2)	±2.33	±1.98	±2.33	±2.00	±2.31	±2.00
7-Terms (x^2y)	±2.33	<u>±0.93</u>	±2.33	<u>±0.93</u>	±2.31	<u>±0.94</u>
8-Terms (xy^2)	<u>±1.94</u>	±0.93	<u>±1.94</u>	±0.93	<u>±1.94</u>	±0.94
9-Terms (x^2y^2)	±1.94	±0.93	±1.94	±0.93	±1.94	±0.94
10-Terms (x^3)	<u>±0.21</u>	±0.93	<u>±0.24</u>	±0.92	<u>±0.23</u>	±0.94
11-Terms (y^3)	±0.20	<u>±0.20</u>	±0.24	<u>±0.21</u>	±0.21	<u>±0.22</u>
12-Terms (x^3y)	±0.19	±0.20	±0.24	±0.21	±0.21	±0.21
13-Terms (xy^3)	±0.19	±0.19	±0.24	±0.21	±0.21	±0.21
14-Terms (x^3y^2)	±0.19	±0.19	±0.24	±0.21	±0.19	±0.21
15-Terms (x^2y^3)	±0.19	±0.19	±0.24	±0.20	±0.19	±0.21
16-Terms (x^3y^3)	±0.18	±0.19	±0.24	±0.20	±0.19	±0.21
17-Terms (x^4)	±0.18	±0.19	±0.24	±0.20	±0.19	±0.21
18-Terms (y^4)	±0.18	±0.19	±0.23	±0.20	±0.18	±0.21
19-Terms (x^4y)	±0.18	±0.18	±0.23	±0.20	±0.18	±0.20
20-Terms (xy^4)	±0.18	±0.18	±0.23	±0.20	±0.17	±0.20
21-Terms (x^4y^2)	±0.18	±0.18	±0.23	±0.20	±0.17	±0.20
22-Terms (x^2y^4)	±0.18	±0.18	±0.22	±0.20	±0.17	±0.20
23-Terms (x^4y^3)	±0.18	±0.18	±0.22	±0.20	±0.17	±0.20
24-Terms (x^3y^4)	±0.18	±0.18	±0.22	±0.20	±0.17	±0.20
25-Terms (x^4y^4)	±0.17	±0.18	±0.22	±0.20	±0.17	±0.20

Table 14.3. Geometric calibration results for the Agema 550 CCD camera equipped with a 40° lens (on the second occasion).

a) Vector plot from Frame I (second occasion)



b) Vector plot from Frame II (second occasion)



c) Vector plot from Frame III (second occasion)



Fig. 14.8(a), (b) and (c). Vector plots from linear conformal transformation using the Agema 550 CCD camera equipped with a 40° lens (second time) - vectors are 5 times magnified.

All three frames gave more or less the same overall results in terms of accuracy and produced similar error vector figures. The use of the linear conformal transformation resulted in rmse values of the residual errors of ± 2.8 and ± 2.1 pixels in the x and y-directions respectively. The error vectors resulting from this transformation were plotted as usual using the VECTOR program. As can be seen from Fig. 14.8 (a), (b) and (c), a quite systematic pattern resulted from the plotting of the errors which exhibited a marked degree of symmetry all over the plot relative to the centre of the target plate. This larger geometric distortion pattern is associated with the larger angular field of view of this particular lens.

The affine transformation had absolutely no effect in terms of reducing the overall rmse value, as indeed was the case with the other lenses used with the Agema 550 imager. Turning next to the use of the higher order terms in the polynomial

transformation, the 5-parameter transformation with the addition of the x^2 term reduced the rmse value of the residual errors in the x-direction by about ± 0.16 pixel. The use of the 8-parameter transformation with the additional x^2y term showed a further ± 0.4 pixel reduction in the rmse value in the x-direction. The rmse value was reduced very substantially by the 10-parameter transformation with its additional x^3 term in the x-direction by about ± 1.7 pixel. Turning next to the y-direction, the use of the 7-parameter transformation resulted in a significant drop of nearly ± 1 pixel in the rmse value in the y-direction through the application of the x^2y term.

As was done with the 20° lens, the author again took the same 9 representative points that cover the edges of the whole frame and drew the error vectors for these points. After connecting these vectors, a barrel-shaped pattern of distortion appeared (see Fig. 14.9). Once again, the TV monitor had been placed into the recording loop in order to observe the quality of the images of the crosses on the target plate. So, any distortions that are caused by both the camera lens and the video monitor were superimposed. However, as can be seen from this figure, the overall dimension of the geometric distortion is much larger than that found with the 20° lens. This showed that the rmse values were increased substantially through the use of the additional lens elements employed to create the larger angular field of view of the 40° lens. Another significant improvement in the rmse value in the y-direction occurred when the 11-parameter transformation was applied with the addition of the y^3 term. The rmse value was decreased to about ± 0.7 pixel. Other terms had absolutely no effect on the rmse values at all.

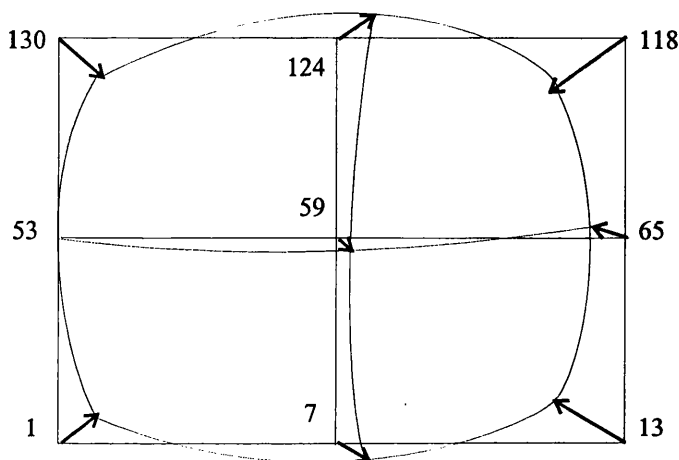


Fig. 14.9. Barrel-shaped distortion arising from the use of the 40° lens.

14.3 Amber Radiance PM1 CCD Camera

The Amber Radiance PM1 is another infrared CCD camera (see Fig. 14.10) that is representative of the current state-of-the-art and has been tested in this project. Like the Agema 550, it produces a PAL analogue video signal which is transmitted to and stored on the VTR. It uses a 256 x 256 (65,536) indium antimonide (InSb) element detector array which is cooled by a tiny internal Stirling engine. This camera is operated in the 3 to 5 μ m wavelength band of the middle infrared region of the EM. It can use any one of three different lenses to collect the radiation from the scene. These have angular coverages of 5.57°, 11.11° and 22.02° respectively. However, in this project, the lens with 11.11° angular coverage has been used because it was the only one available at the time of the experiment.



Fig. 14.10. Amber Radiance PM1 infrared CCD camera.

For the geometric calibration of this camera, three frames of the recorded analogue image have been digitized and input to the various programs developed for the calibration work. One sample frame from this imager is included as Fig. 14.11.

14.3.1 Result and Analysis of the Geometric Calibration of the Radiance PM1

The results from the geometric calibration of the Radiance PM1 camera are shown in Table 14.4. The result from the linear conformal transformation resulted in a small rmse value of ± 0.2 pixel in both the x and y-directions. The error vectors at 130

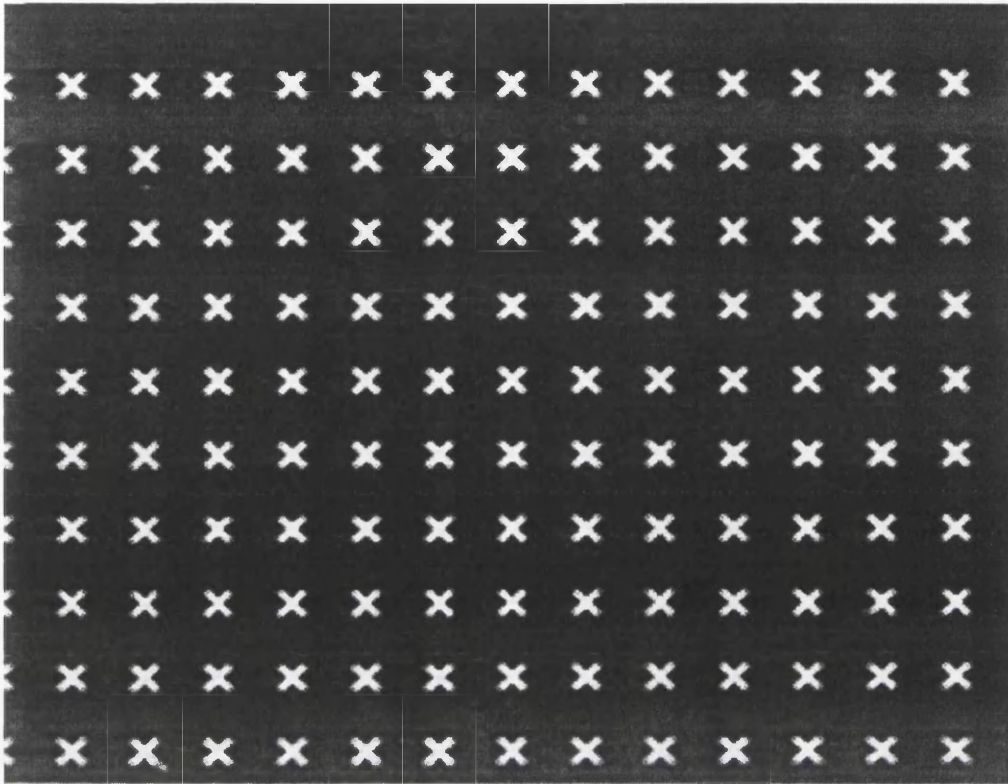


Fig. 14.11. Sample image of the target plate taken by the Radiance PM1 camera.

crosses were plotted using the VECTOR program and the resulting plots are shown in Fig. 14.12 (a), (b) and (c). As can be seen from this figure, although the distortion is quite systematic and is consistent from one frame to another, in some parts of the frame, it is generally random. The affine transformation did not result in any changes in the magnitude of the geometric distortion at all. This showed that the images acquired using the Radiance PM1 do not contain an affinity and/or lack of orthogonality between the x and y axes.

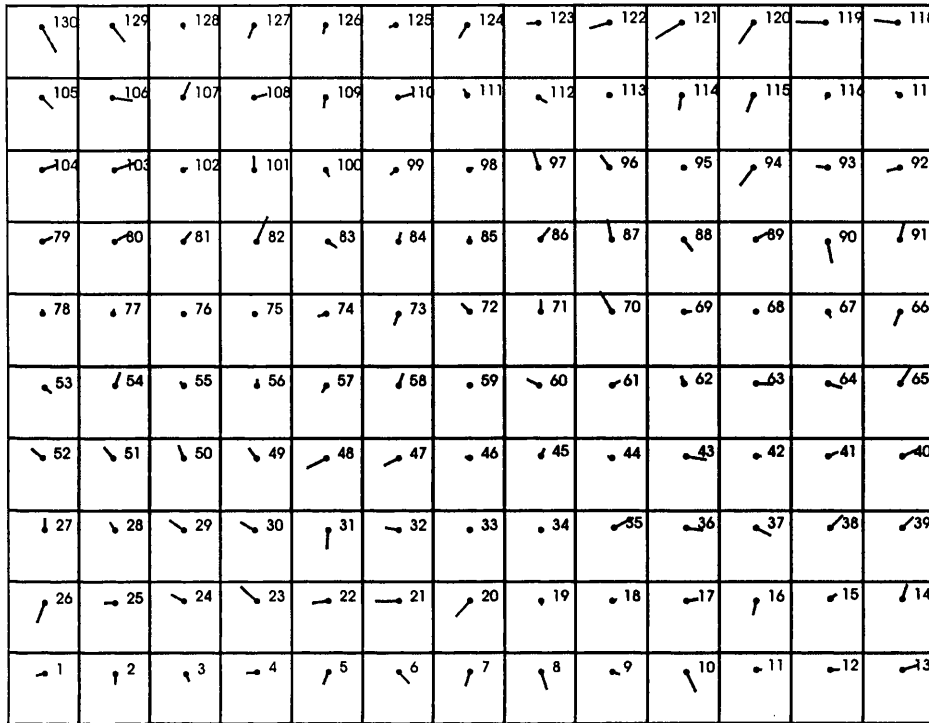
The 4-parameter transformation (with its xy term) had a small effect on the x-direction, but it was not still not enough to change the magnitude of distortion by the amount of the tenth of a pixel that can be accepted as the precision of the measurements of the image coordinates of the cross targets. As can be seen from Table 14.4, the other terms had absolutely no effect on the results obtained using the polynomial transformation procedure. Overall it can be said that the PM1 camera equipped with the 11.11° lens exhibits a very small amount of geometric distortion

that is only just significant in the context of an expected measuring precision of 0.1 pixel.

Transformation Procedure	R.M.S.E (Pixels)					
	Frame I		Frame II		Frame III	
	m_x	m_y	m_x	m_y	m_x	m_y
Linear Conformal	±0.22	±0.21	±0.22	±0.22	±0.23	±0.22
3-Terms (Affine)	±0.22	±0.21	±0.22	±0.22	±0.23	±0.22
4-Terms (xy)	±0.17	±0.21	±0.18	±0.22	±0.18	±0.21
5-Terms (x^2)	±0.16	±0.21	±0.18	±0.22	±0.18	±0.21
6-Terms (y^2)	±0.16	±0.19	±0.17	±0.19	±0.18	±0.19
7-Terms (x^2y)	±0.16	±0.18	±0.17	±0.18	±0.18	±0.19
8-Terms (xy^2)	±0.16	±0.18	±0.16	±0.18	±0.18	±0.18
9-Terms (x^2y^2)	±0.16	±0.18	±0.16	±0.18	±0.18	±0.18
10-Terms (x^3)	±0.15	±0.18	±0.16	±0.18	±0.17	±0.18
11-Terms (y^3)	±0.14	±0.18	±0.14	±0.18	±0.16	±0.18
12-Terms (x^3y)	±0.14	±0.18	±0.14	±0.18	±0.16	±0.17
13-Terms (xy^3)	±0.14	±0.18	±0.14	±0.18	±0.16	±0.17
14-Terms (x^3y^2)	±0.14	±0.18	±0.14	±0.18	±0.16	±0.17
15-Terms (x^2y^3)	±0.14	±0.18	±0.14	±0.18	±0.16	±0.16
16-Terms (x^3y^3)	±0.14	±0.18	±0.14	±0.18	±0.16	±0.16
17-Terms (x^4)	±0.14	±0.18	±0.14	±0.18	±0.16	±0.16
18-Terms (y^4)	±0.14	±0.18	±0.14	±0.18	±0.16	±0.16
19-Terms (x^4y)	±0.13	±0.18	±0.13	±0.18	±0.15	±0.16
20-Terms (xy^4)	±0.13	±0.18	±0.13	±0.18	±0.15	±0.16
21-Terms (x^4y^2)	±0.13	±0.18	±0.13	±0.18	±0.15	±0.16
22-Terms (x^2y^4)	±0.13	±0.18	±0.13	±0.18	±0.15	±0.16
23-Terms (x^4y^3)	±0.13	±0.17	±0.13	±0.17	±0.14	±0.16
24-Terms (x^3y^4)	±0.13	±0.17	±0.13	±0.17	±0.14	±0.16
25-Terms (x^4y^4)	±0.13	±0.17	±0.13	±0.17	±0.14	±0.16

Table 14.4. Geometric calibration results from the Amber Radiance PM1 camera equipped with a 11.11° lens.

a) Vector plot from Frame I



b) Vector plot from Frame II



c) Vector plot from Frame III

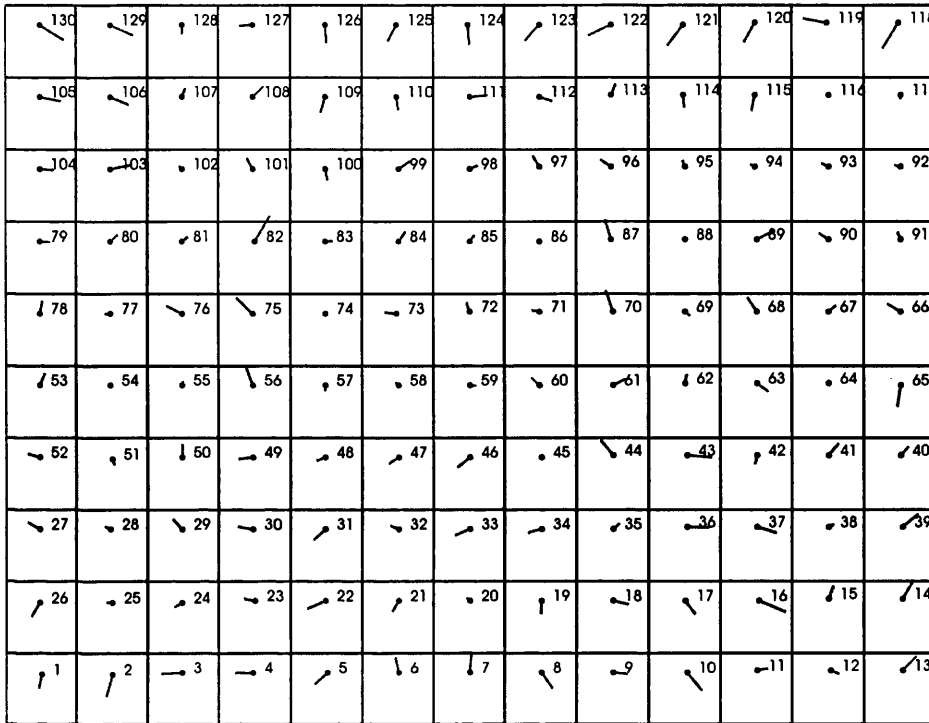


Fig. 14.12(a), (b) and (c). Vector plots from the linear conformal transformation using the Amber Radiance PM1 CCD camera equipped with a 11.11° lens - vectors are 25 times magnified.

14.4 Overall Analysis

In Table 14.5, the average rmse values for each of the lenses used with the Agema 550 imager and the 11.11° lens used with Radiance PM1 CCD camera are shown. On the basis of this table, a further comparative analysis of the results that were obtained using different lenses will be conducted. In addition to this, some further comparisons have been carried out on the basis of the vector plots of the errors which have been produced by each of the lenses used with the two imagers. Thus, differences in the range of the geometric distortion are apparent and the variation of this distortion as shown by the plots will be given. Moreover, the changes in the systematic and random components of the distortion which resulted with different lenses will be examined also.

Transformation Procedure	R.M.S.E (Pixels) of Residual Errors							
	Agema 550 CCD Camera						Radiance PM1 CCD Camera	
	10° Lens		20° Lens		40° Lens		11° Lens	
	m_x	m_y	m_x	m_y	m_x	m_y	m_x	m_y
Linear Conformal	±0.32	±0.28	±0.61	±0.57	±2.54	±2.13	±0.22	±0.22
3-Terms (Affine)	±0.30	±0.26	±0.60	±0.55	±2.51	±2.06	±0.22	±0.22
4-Terms (xy)	±0.29	±0.23	±0.59	±0.41	±2.49	±2.00	±0.18	±0.21
5-Terms (x^2)	±0.18	±0.23	±0.47	±0.41	±2.33	±2.00	±0.17	±0.21
6-Terms (y^2)	±0.15	±0.20	±0.45	±0.41	±2.32	±1.99	±0.17	±0.21
7-Terms (x^2y)	±0.15	±0.20	±0.45	±0.27	±2.32	±0.93	±0.17	±0.19
8-Terms (xy^2)	±0.15	±0.20	±0.39	±0.27	±1.94	±0.93	±0.17	±0.18
9-Terms (x^2y^2)	±0.15	±0.20	±0.39	±0.27	±1.94	±0.93	±0.17	±0.18
10-Terms (x^3)	±0.15	±0.20	±0.19	±0.27	±0.23	±0.93	±0.16	±0.18
11-Terms (y^3)	±0.14	±0.19	±0.17	±0.21	±0.22	±0.21	±0.15	±0.18

Table 14.5. The average rmse values for all three lenses used with the Agema 550 and the one lens employed with the Radiance PM1 CCD camera.

14.4.1 Analysis of the Effective Terms for Each of the Lenses

As can be seen from Table 14.5, for the Agema 550 imager, the use of 5-parameter transformation by adding the x^2 term reduced the rmse value for each of the lenses used. The amount of the reduction in the rmse value in the x-direction after using this transformation is about ±0.12 pixel, ±0.13 pixel and ±0.18 pixel for the 10°, 20° and 40° lenses respectively. This shows that the amount of change is slightly increasing with the angular coverage of the lenses. As mentioned before, in this camera, the 20° lens is fixed and other lenses have to be attached on it. So, this basic distortion appears to be created by the 20° lens and is then encountered in the other lenses. However, with the 10° lens, there is no increase in the size of the rmse value after application of the x^2 term, whereas it is considerably larger in the case of the 40° lens.

However there is a common high-order term that noticeably decreases the residual errors in both the x and y-directions for the 20° and 40° lenses. This term is the x^3

term that is added to the polynomial when the 10-parameter transformation is used. While its effect is ± 0.2 pixel for the 20° lens, it is ± 1.7 pixel for the 40° lens. This shows that the use of the extra lens elements to give the large angular coverage of the 40° lens has a big influence on the geometric distortion. In this context, it will be noted too that, for the 40° lens, the use of the 8-parameter transformation with its xy^2 term created a drop of about ± 0.4 pixel in the rmse in the x-direction. However, this transformation had only a very small effect, ± 0.06 pixel, on the residual error for the 20° lens. This means that it started with the 20° lens and was extended with the large field of view of the 40° lens.

In the y-direction, the use of the 4-parameter transformation resulted in a decrease in the geometric distortion by adding the xy term to the polynomial. Its amount is ± 0.03 pixel, ± 0.14 pixel and ± 0.06 pixel for 10° , 20° and 40° lenses respectively. However this differs from the other terms used in that this transformation only has an appreciable effect on the rmse value for the 20° lens, and the angular coverage of the lenses does not influence the result at all. The another effective term in the y-direction is x^2y . By adding this term to the polynomial, the rmse is reduced to about ± 0.15 pixel and ± 1.00 pixel for the 20° and 40° lenses respectively. The big angular coverage of the 40° lens increases the amount of distortion described by this term.

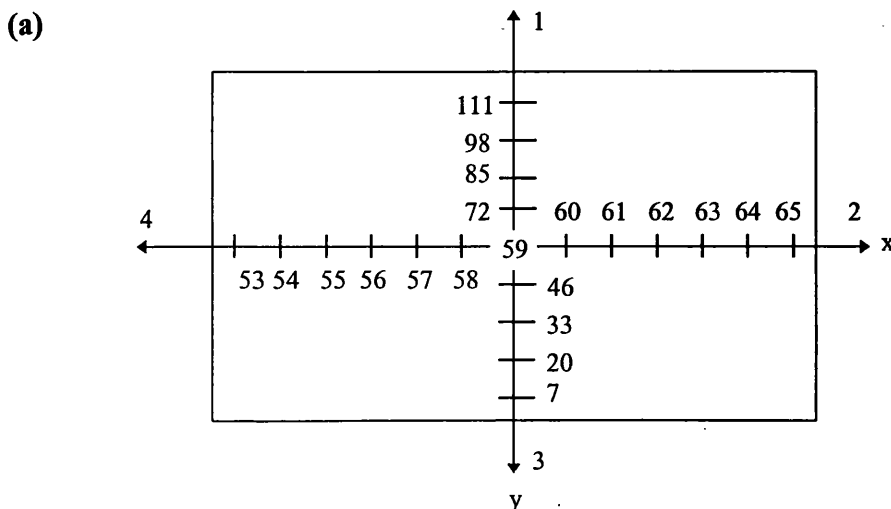
On the basis of the discussion conducted above, it can be said that the angular coverage of the lenses used in the Agema 550 is the major factor on the results. Again as can be seen from Table 14.5, the respective rmse values are about ± 0.3 pixel, ± 0.6 pixel and ± 2.5 pixel for the 10° , 20° and 40° lenses used in the Agema 550 camera. When the 20° lens is employed, the rmse value increases nearly twice compared with that experienced with the 10° lens. However, when the 40° lens is used, the rmse value goes up four times compared with that of the 20° lens. So, these figures show clearly that the geometric distortions obtained using these different lenses increase with the angular coverage of the lens.

For the Radiance PM1 CCD camera, as discussed before, only the 11° lens could be used since the other lenses whose angular coverages are 5° and 22° were not available

at the time of calibration. As can be seen from Table 14.5, rmse values in the x and y-directions obtained from the calibration of this camera using its 11° lens are ± 0.2 pixel. However, for the 10° lens used in the Agema 550, the rmse values are ± 0.3 pixel. Although these two lenses have almost the same angular coverage and same resolution, they do give a slightly different result. The reason for this is that the lens with 10° coverage that is available with the Agema 550 CCD camera is produced by adding additional lens elements onto the 20° lens which is fixed. So, the effect of this built-in lens can be expected to remain in this case. However, for the 11° lens used in the Radiance PM1 camera, the situation is different since the lens is attached directly to the camera and no additional elements have been used.

14.4.2 Analysis of the Residual Errors

The linear conformal transformation of the reference coordinates into the image coordinate system revealed the residual errors in x and y-directions for each of the cross targets which are distributed evenly on the image. These residuals are in the form of tables of numerical values. The author has also taken the 21 points along the 4 radial directions out to the midpoints of each side of the image and 20 points along the 4 diagonal directions (see Fig. 14.13(a) and (b)) and has drawn the error vectors by using the residual errors for each lenses that have been tested in this project. These plots are shown in Fig. 14.14 and Fig. 14.15. The numbers given in these diagrams are the point numbers used to compile them.



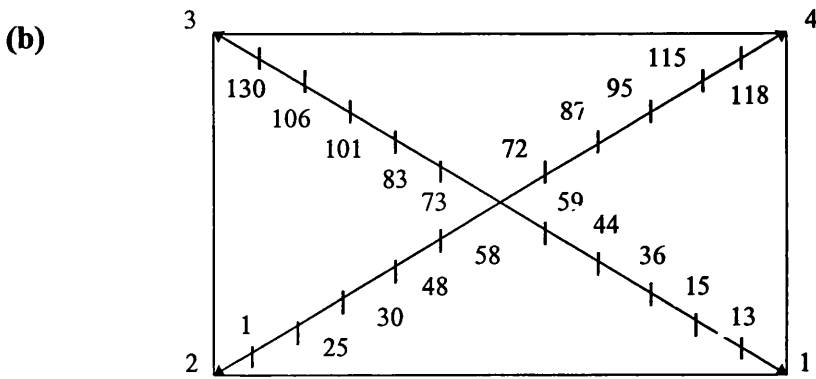


Fig. 14.13(a) and (b). Four radial and four diagonal directions and the points used.

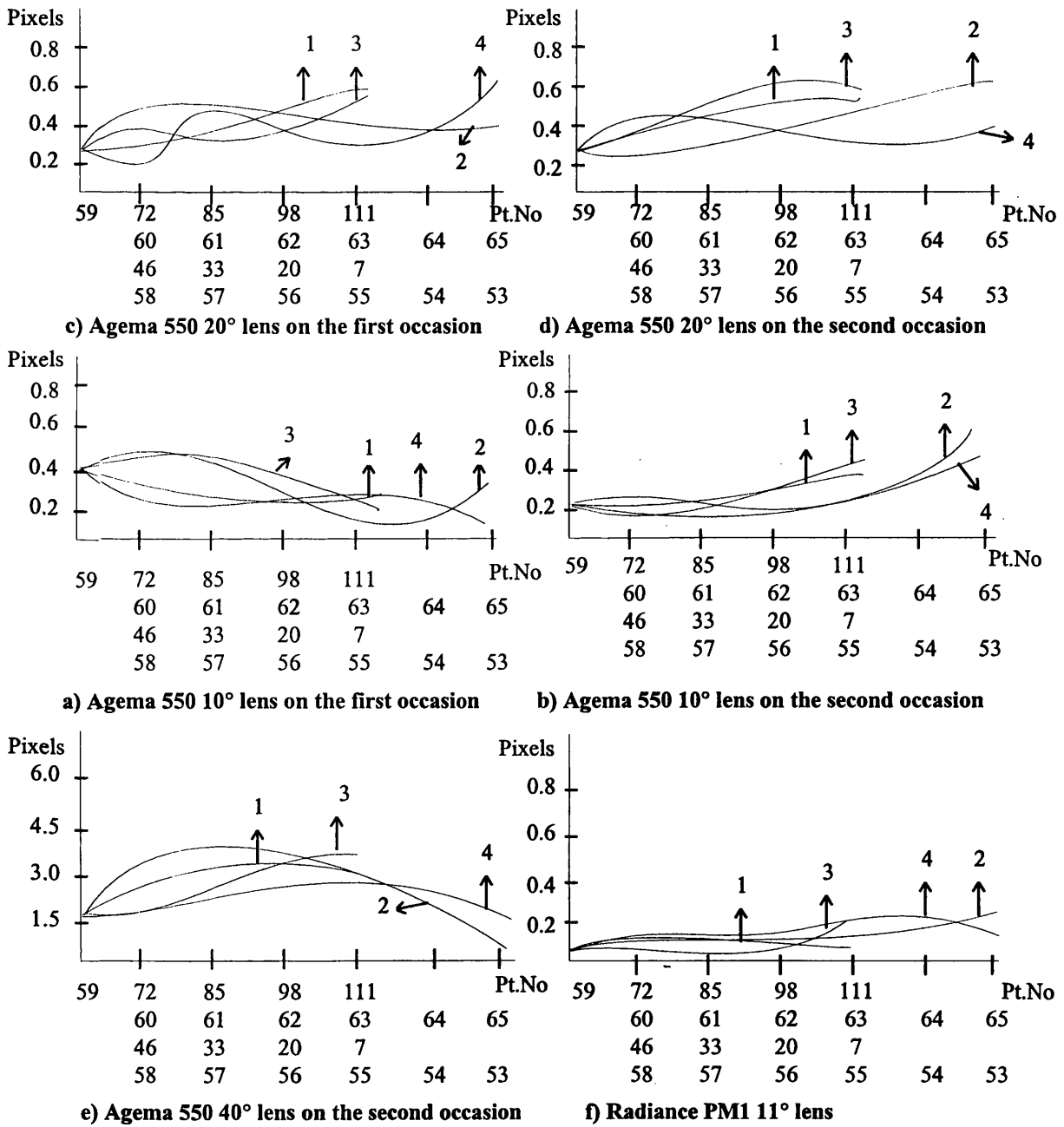
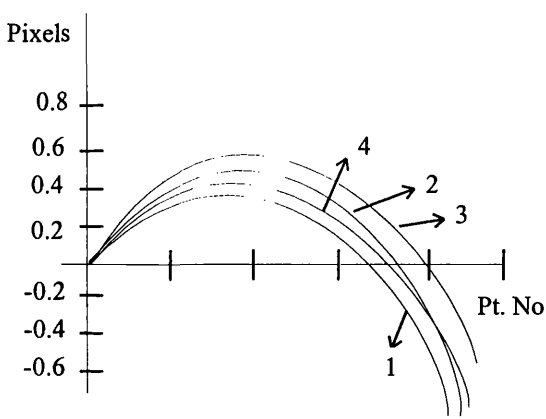
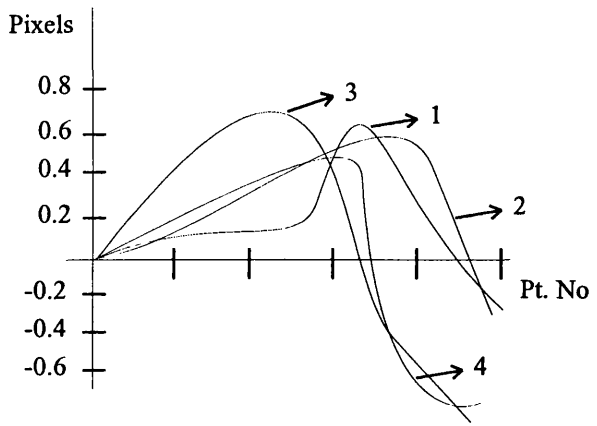


Fig. 14.14. Distortion curves along the 4 radial directions from the image centre to the side midpoints.



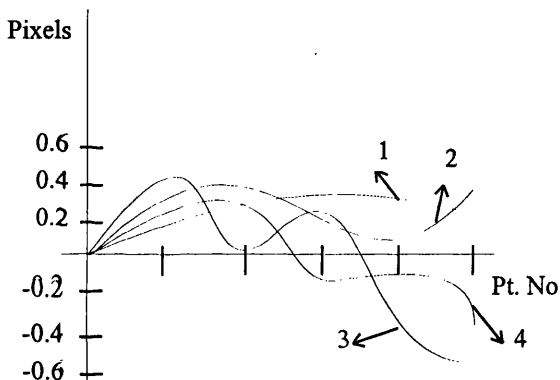
59	44	36	15	13
58	48	30	25	1
73	83	101	106	130
72	87	95	115	118

a) Agema 550 20° lens on the first occasion



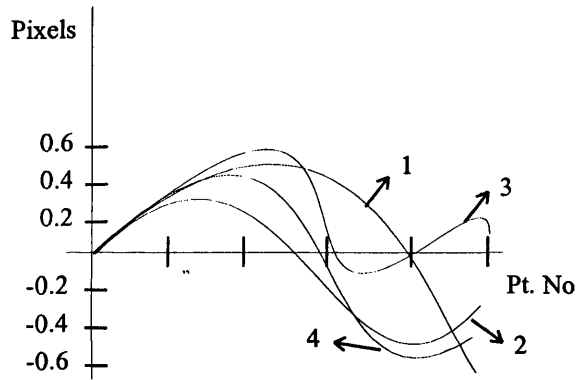
59	44	36	15	13
58	48	30	25	1
73	83	101	106	130
72	87	95	115	118

b) Agema 550 20° lens on the second occasion



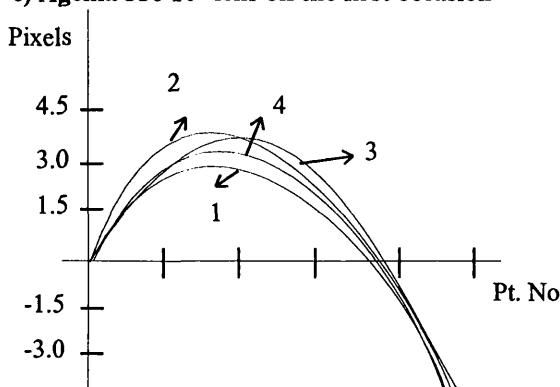
59	44	36	15	13
58	48	30	25	1
73	83	101	106	130
72	87	95	115	118

c) Agema 550 10° lens on the first occasion



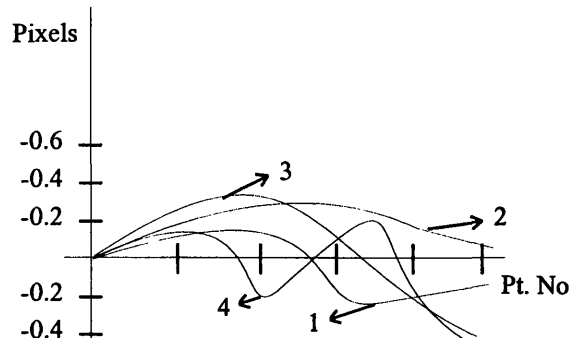
59	44	36	15	13
58	48	30	25	1
73	83	101	106	130
72	87	95	115	118

d) Agema 550 10° lens on the second occasion



59	44	36	15	13
58	48	30	25	1
73	83	101	106	130
72	87	95	115	118

e) Agema 550 40° lens on the second occasion



59	44	36	15	13
58	48	30	25	1
73	83	101	106	130
72	87	95	115	118

f) Radiance PM1 11° lens

Fig. 14.15. Distortion curves along the 4 diagonal directions from the image centre.

As can be seen from Fig. 14.14 (a), (b), (c) and (d), the geometric distortion present with the 10° and 20° lenses used on the Agema 550 camera and the Radiance PM1 11° lens exhibited some variation between any one radial direction and any other and thus showed some degree of asymmetry. For the Agema 40° lens, the plot is somewhat different and shows a symmetry between the different radial directions. However, as can be seen from Fig. 14.15 (a), (b), (c), (d), (e) and (f), only the 20° lens on the first occasion and 40° lens on the second occasion produced the symmetry between the diagonal directions. For the other cases, the distortion curves presented an asymmetry between these directions.

From Figs. 14.14 and 14.15, not only is the symmetrical or asymmetrical nature of the distortion clearly shown but, in the case of the Agema 550, so is the considerable variation in the geometric distortion between any one lens and another. The series of curves shown in the plots in Figs. 14.14 and 14.15 represent an envelope of the geometric distortions that are present in each lens. The range changes with the angular coverage of the lens. As can be seen from these plots, the range of this envelope is changing from ± 0.1 pixel to ± 0.5 pixel for the 10° lens; from ± 0.2 pixel to 1.0 pixel for the 20° lens; and from ± 0.6 pixel to ± 4.0 pixel for the 40° lens. For the Radiance PM1 11° lens, the range of variation lies between ± 0.05 pixel and ± 0.2 pixel.

14.4.3 Systematic and Random Components of Geometric Distortion

The procedures described in Section 13.5.4 for the determination of the systematic and random components of the geometric distortion have been followed and the results are shown in Table 14.6. As can be seen from this table, when the angular coverage of the lenses used in the Agema 550 is increasing, the systematic component of the distortion becomes dominant. This can be easily seen by inspection of the results coming from the 20° and 40° lenses. For these two lenses, while the systematic components were ± 0.6 pixel and ± 2.5 pixel respectively, the random component was only ± 0.14 pixel. However, for the lenses with a small field of view such as the Agema 550 10° and Radiance PM1 11° lenses, although the systematic components

are still present, they are very small in absolute terms compared with those produced by the lenses having an large angular coverage. The random components of distortion of each lens are changing between ± 0.10 pixel and ± 0.15 pixel. This smaller random component of the distortion is in line with the measuring accuracy of the image matching method that has been used in this research.

Imager \ RMSE	m_{xs} (pixel)	m_{ys} (pixel)	m_{xr} (pixel)	m_{yr} (pixel)
Agema 550 with 10° lens	± 0.29	± 0.23	± 0.11	± 0.13
" " 20° lens	± 0.60	± 0.56	± 0.13	± 0.14
" " 40° lens	± 2.55	± 2.12	± 0.16	± 0.14
Amber Radiance PM1	± 0.20	± 0.18	± 0.09	± 0.11

Table 14.6. Systematic and random components of geometric distortion.

14.5. Conclusion

In the previous chapter, the actual experimental procedures that have been carried out for the geometric and radiometric calibration of the infrared imaging systems have been discussed together with the processing and analysis of the obtained digital image data in some detail. In this chapter, only the results and analysis of the geometric calibration of two representative infrared CCD cameras has been given. The next chapter will present and analyze the results of the radiometric calibration of these cameras in some detail.

CHAPTER 15: RESULTS AND ANALYSIS OF THE RADIOMETRIC CALIBRATION OF INFRARED CCD CAMERAS

15.1 Introduction

In the previous chapter, the results of the geometric calibration of representative infrared CCD cameras have been presented and analyzed. In this chapter, the radiometric calibration procedure that has been explained in Chapter 13, will be applied to the same two cameras. For the radiometric calibration of each camera, the images of the radiation source that have been acquired at three different temperatures have been processed using the programs developed by the author and the results will be presented in tabular form. In addition, 3-D graphical representations of the grey level values of the individual pixels will be produced using the SURFER program to visualize the distribution of these values over the whole or part of each frame. Finally, a detailed analysis and discussion of these results will be carried out.

15.2 Radiometric Calibration of the Agema 550 CCD Camera

As discussed in the previous Chapter, the geometric calibration of the Agema 550 camera has been carried out using three different lenses (with 20°, 10° and 40° angular coverages respectively). However, the radiometric calibration of this imager has been carried out using only two of the three lenses (these with 20° and 10° angular coverage). The results from the calibration of the camera when using each of these two lenses will be given in more detail below.

15.2.1 Radiometric Calibration with the 20° lens

For this experiment, images of the radiation source have been taken by the camera at three different temperatures - 30°C, 40°C and 60°C. The resulting analogue video images have been digitized by the frame grabber and three frames for each temperature have been acquired. The size of each frame is 768(H) x 576(V) pixels and the range of grey level values lies between 0 and 255.

15.2.1.1 Radiometric Calibration of Whole Frames

After deleting from the images the badge of the Agema 550 CCD camera and the images of the tops of the screws holding the six nylon pillars, uniform parts of the digitized frames, each covering an area of 600 (H) x 350 (V) pixels, were available for radiometric calibration purposes. These whole frames comprise the raw image data and include those dead or blemished pixels that have not been responding correctly to the incident radiation emitted by the radiation source. The three whole frames that have been acquired for each temperature give a total of nine whole frames that are available for processing and analysis. Each of these whole frame images forms a binary file that has to be converted to ASCII format to allow it to be processed using the FORTRAN 77 programs that have been written by the present author. This has been done using the method given in Section 13.3.2 (a). Afterwards, the STMN program has been used to compute the means and standard deviations of the grey level values of the whole frames acquired at the same temperature. The results are shown in Table 15.1.

Temp.	Quadrant	Mean of the grey level values	Rmse of the grey level values	Mean of the averaged quadrants	Rmse of the averaged quadrants
<i>Agema 550 with 20° lens (image size = 600(H)x350(V) = 210,000 pixels)</i>					
30°C	1	44.35	2.34	44.26	1.32
	2	44.26	2.38		
	3	44.16	2.35		
40°C	1	156.83	6.85	155.42	6.54
	2	156.40	6.98		
	3	153.05	6.84		
50°C	1	237.08	5.37	234.79	6.38
	2	235.42	6.77		
	3	231.87	9.18		

Table 15.1. The means and the standard deviations of the grey level values of the pixels of the whole frames before and after radiometric correction.

As can be seen from this table, the averaged grey level values for the whole frame at the same temperature have been obtained. These grey level values were then sent to

the SURFER program to give graphical representations of the results. The resulting diagrams for each of the temperatures are given in Fig. 15.1(a), (b) and (c).

In the specification of the Agema 550 imager (see Table 8.2), the temperature sensitivity has been given as 0.1°C at 30°C temperature. When the experiment was made, the temperature difference between the right and left edges of the whole frame was measured and it was found to be 1°C . As can be seen from these diagrams, at 30°C temperature, there was a range of 13DN (Digital Numbers) or grey level values available across the whole frame. It is worth noting that approximately 1DN is equal to the 1 grey level value. So, the equivalence for the minimum resolvable temperature difference 0.1°C is 1.3DN which is the dimension of the standard deviation of the grey level values of the pixels of the whole frame at this temperature.

In Table 15.2, the statistical processing of the grey level values of the pixels of the whole frames has been carried out using the STAT program. This program computes how many of the grey level values of the pixels are lying inside certain specified ranges that are given as follows:-

$$A - \sigma \leq g(i,j) \leq A + \sigma$$

$$A - 2\sigma \leq g(i,j) \leq A + 2\sigma$$

$$A - 3\sigma \leq g(i,j) \leq A + 3\sigma$$

where:-

A is the average or mean of the grey level values; and

σ is the standard deviation of the grey level values.

Using the VECTOR program, the author has created a plotting file of the pixels that, on the basis of the $A \pm 3\sigma$ criteria, were not responding correctly and so lie outside this range. These have been displayed and plotted using the COREL DRAW 5 computer graphics package. A copy of this plot is included as Fig. 15.2(a). It shows that there is a tendency for a band of these incorrectly responding pixels to appear across the middle of the frame. However, at the edges of the frame, more of these pixels can be seen also. The locations of those pixels that have grey level values less than $A - 3\sigma$ and greater than $A + 3\sigma$ have also been given in Fig. 15.2 (b) and (c). The

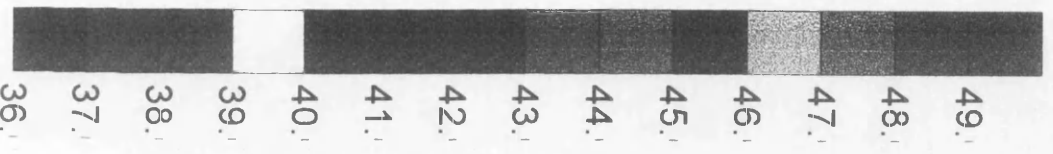
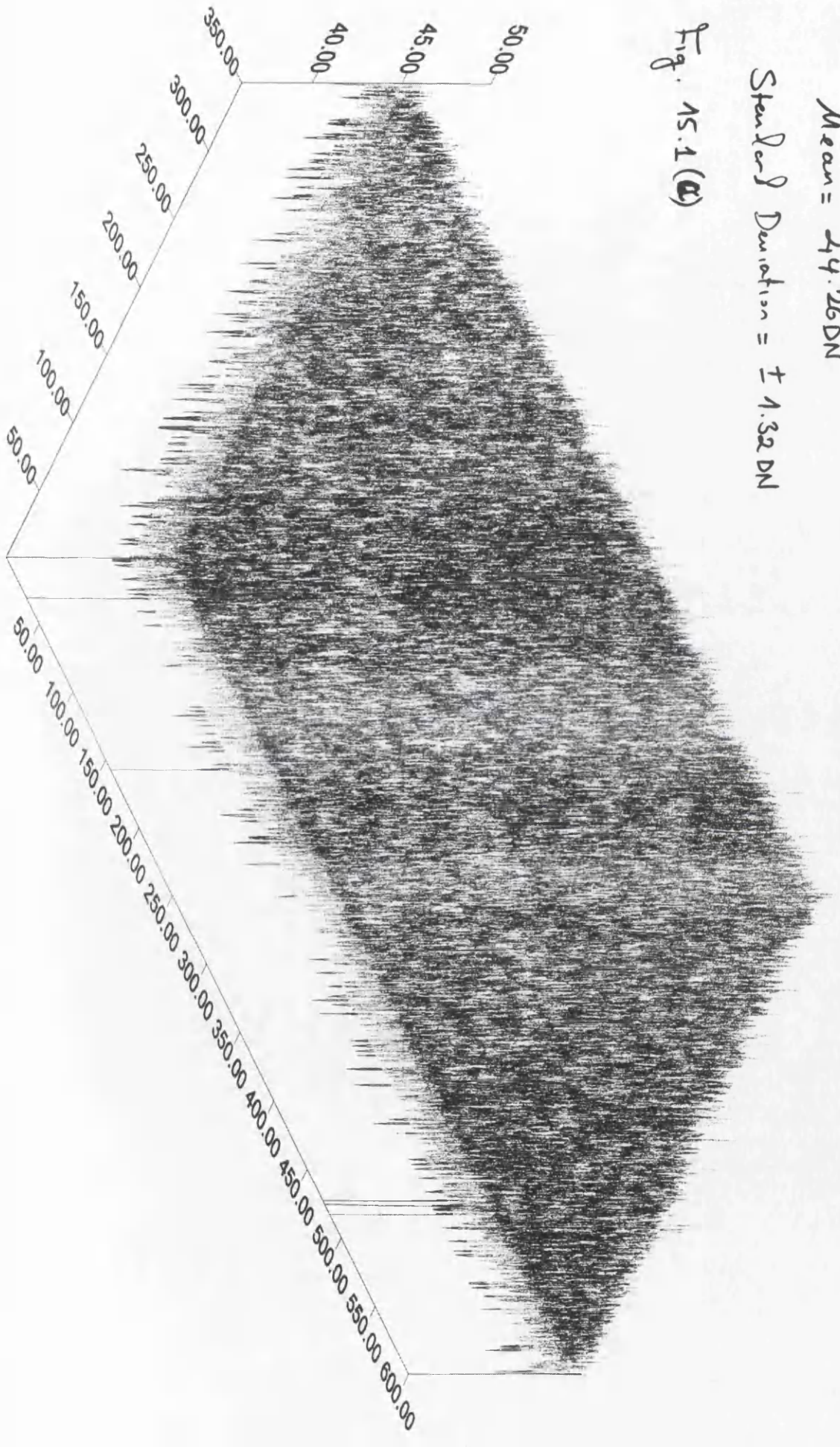
Frame Size = 600 x 350 pixels

Temp = 30°C

Mean = 44.26 DN

Standard Deviation = ± 1.32 DN

Fig. 15.1 (a)



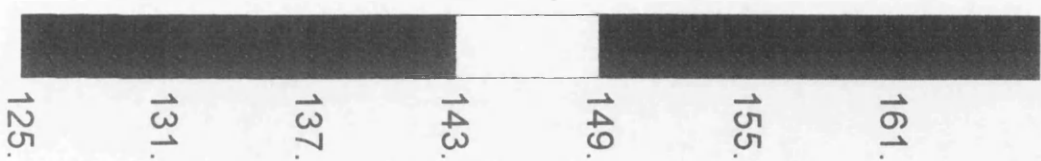
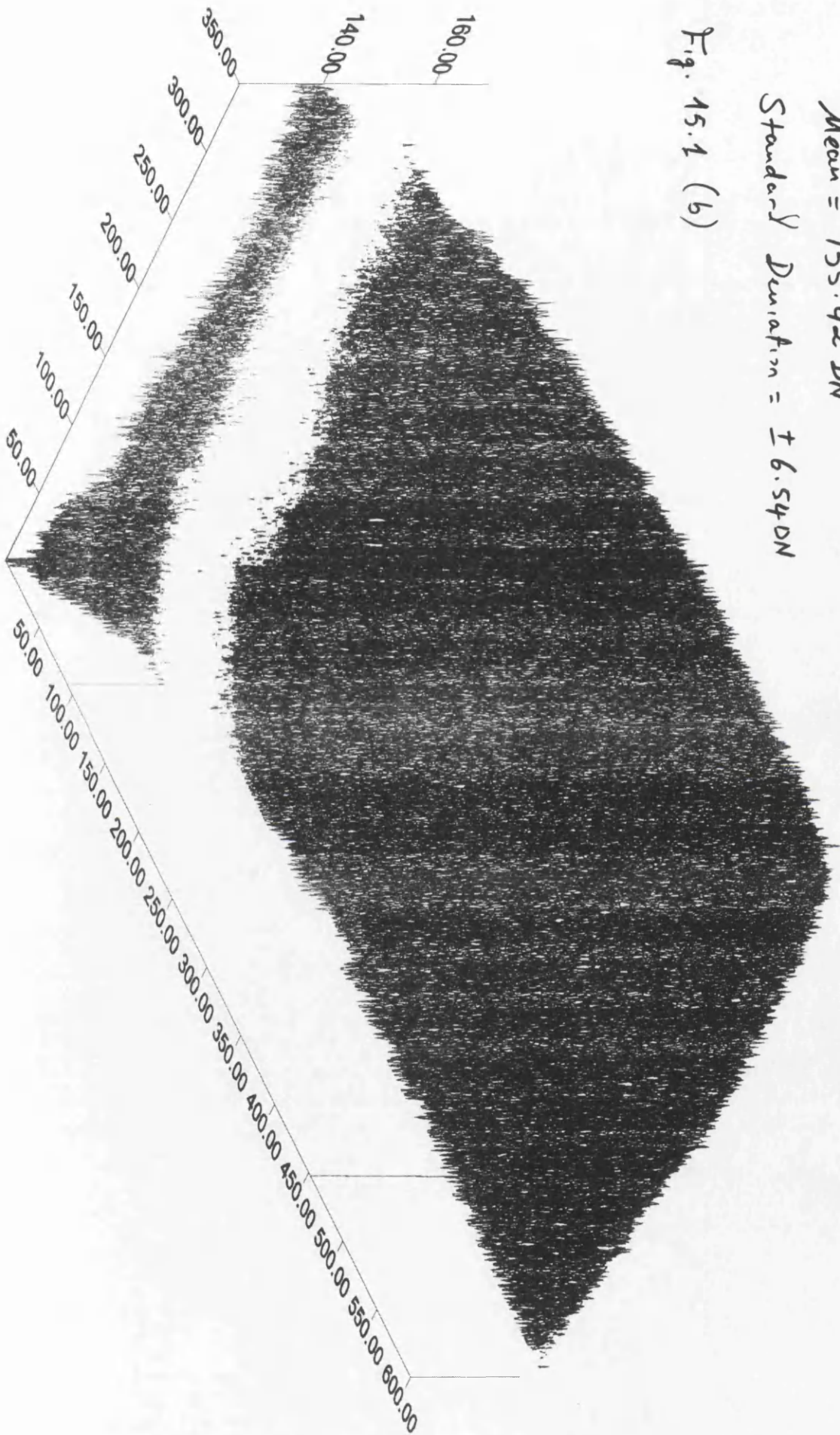
Frame Size = 600 x 350 pixels

$\bar{T}_{temp} = 40^{\circ}C$

Mean = 155.42 DN

Standard Deviation = ± 6.54 DN

Fig. 15.1 (b)



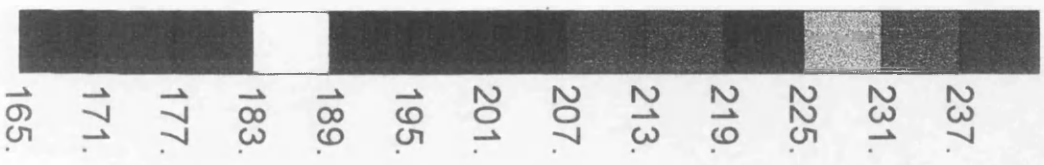
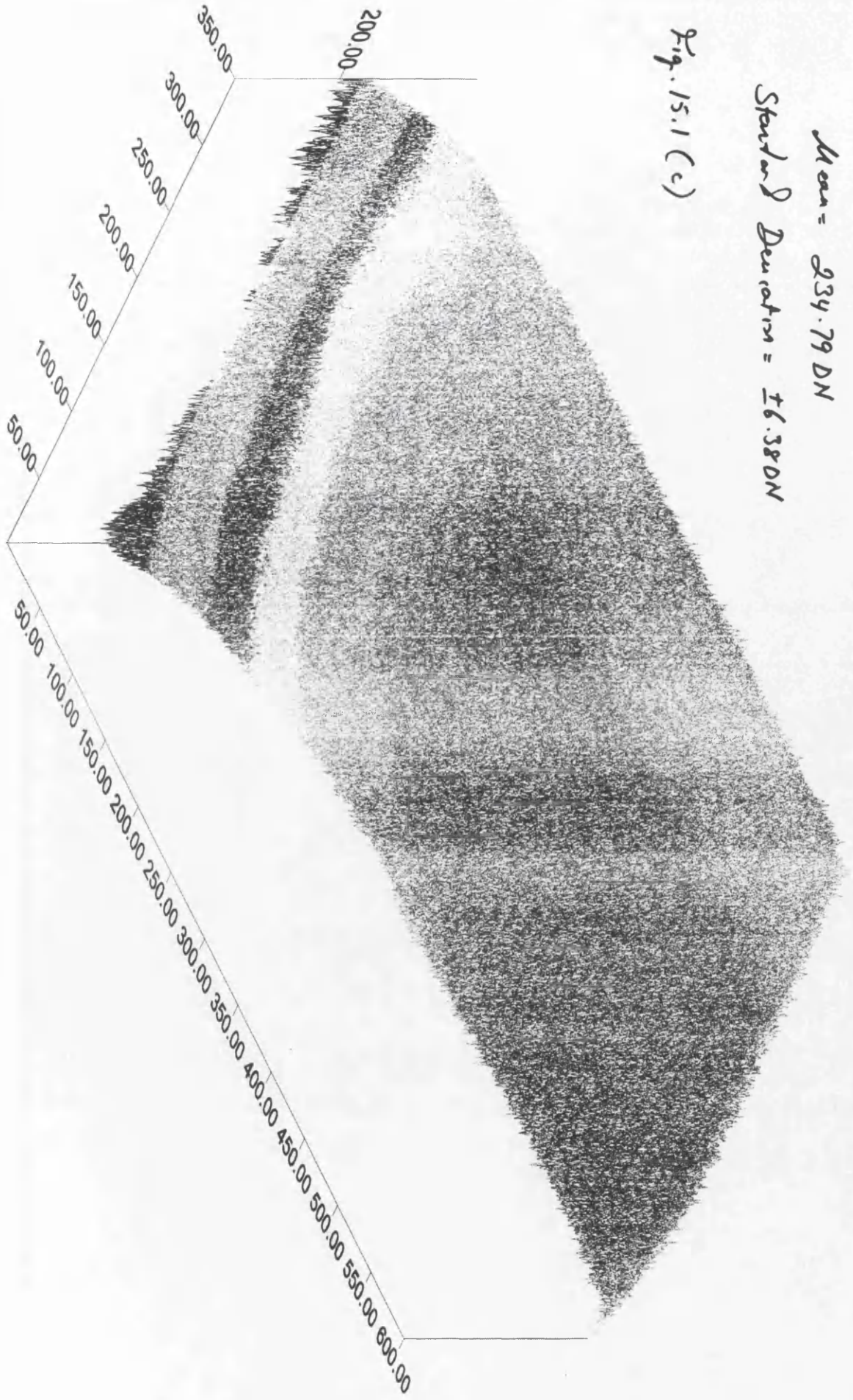
Frame Size = 600 x 350 pixels

Temp. = 50°C

Mean = 234.79 DN

Standard Deviation = ±6.38 DN

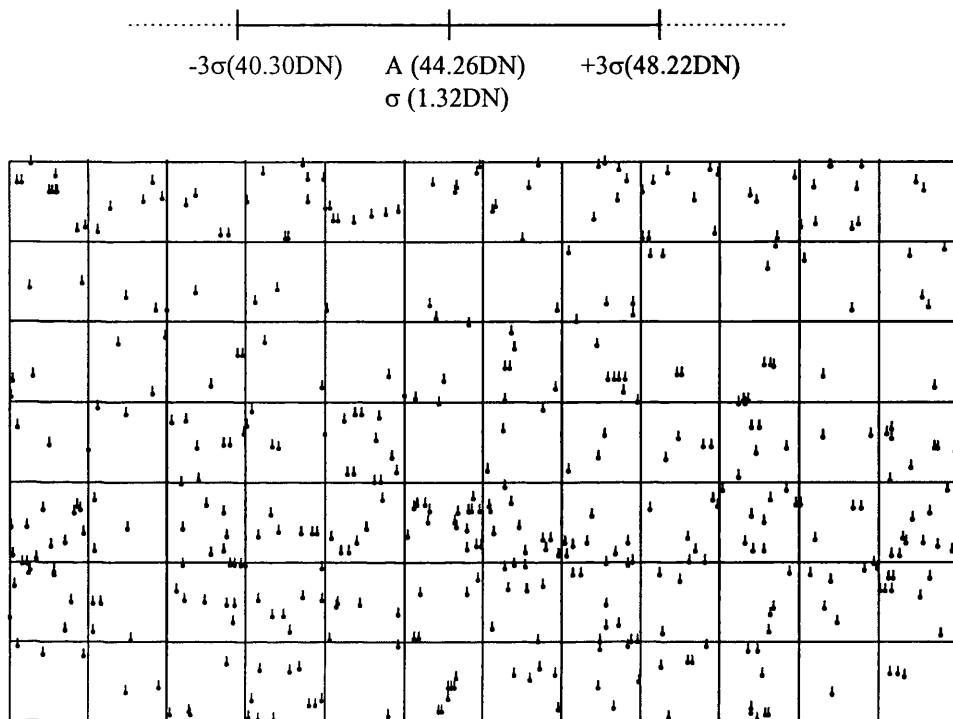
Fig. 15.1 (c)



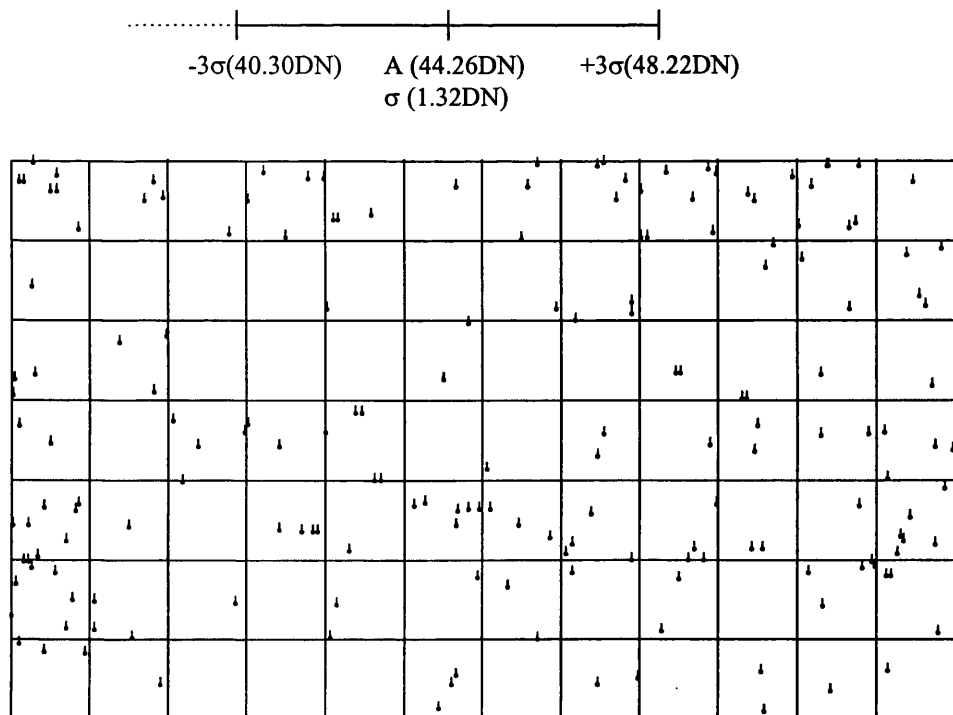
Agema 550 with 20° lens	Total number of pixels in the whole frame: 600(H)×350(V)= 210,000 pixels			
	Number of pixels greater than $\sigma/2\sigma/3\sigma$	Number of pixels less than $\sigma/2\sigma/3\sigma$	Total number of pixels outside the range of $A\pm 3\sigma$	Percentage of the number of pixels lie inside the range of $A\pm 3\sigma$
Temp. = 30°C / Frame No.1				
	36,917	47,498	84,415	≅ 60%
	2,176	3,930	6,106	≅ 97%
	109	193	302	≅ 99.86%
Temp. = 30°C / Frame No.2				
	35,455	27,669	63,124	≅ 70%
	2,276	4,790	7,066	≅ 97%
	105	282	387	≅ 99.82%
Temp. = 30°C / Frame No.3				
	32,058	28,446	60,504	≅ 71%
	6,030	5,128	11,158	≅ 95%
	89	316	405	≅ 99.81%
Temp. = 30°C / Averaged Frame				
	36,649	29,510	66,159	≅ 68%
	5,270	3,755	9,025	≅ 96%
	254	179	433	≅ 99.79%
Temp. = 40°C / Frame No.1				
	31,387	33,097	64,484	≅ 69%
	211	10,846	11,057	≅ 95%
	0	1,695	1,695	≅ 99%
Temp. = 40°C / Frame No.2				
	29,504	36,017	65,521	≅ 69%
	183	9,010	9,193	≅ 96%
	0	1,618	1,618	≅ 99%
Temp. = 40°C / Frame No.3				
	34,160	35,390	69,550	≅ 67%
	225	9,149	9,374	≅ 96%
	1	1,600	1,601	≅ 99%
Temp. = 40°C / Averaged Frame				
	29,467	34,790	64,257	≅ 69%
	10	10,536	10,546	≅ 95%
	0	1,659	1,659	≅ 99%
Temp. = 40°C / Non-Uniformity Corrected Frame				
	39,900	41,292	81,192	≅ 61%
	1,676	1,507	3,183	≅ 98%
	31	10	41	≅ 99.98%
Temp. = 50°C / Frame No.1				
	26,757	19,894	46,651	≅ 78%
	912	9,129	10,041	≅ 95%
	1	4,482	4,483	≅ 98%
Temp. = 50°C / Frame No.2				
	19,606	21,914	41,520	≅ 80%
	281	9,869	10,150	≅ 95%
	0	5,324	5,324	≅ 97%
Temp. = 50°C / Frame No.3				
	15,881	28,219	44,100	≅ 79%
	5	12,695	12,700	≅ 94%
	0	3,171	3,171	≅ 98%
Temp. = 50°C / Averaged Frame				
	11,141	23,903	35,044	≅ 83%
	0	12,085	12,085	≅ 94%
	0	5,743	5,743	≅ 97%

Table 15.2. Statistical processing of the image data of the whole frames acquired by the Agema 550 at different temperatures.

(a) Distortion of pixels that lie outside the range of $A \pm 3\sigma$ (433 pixels out of 210,000 pixels)



(b) Distribution of pixels that have grey level values less than $A - 3\sigma$ (179 pixels out of 210,000 pixels)



(c) Distribution of pixels that have grey level values greater than $A + 3\sigma$ (254 pixels out of 210,000 pixels)

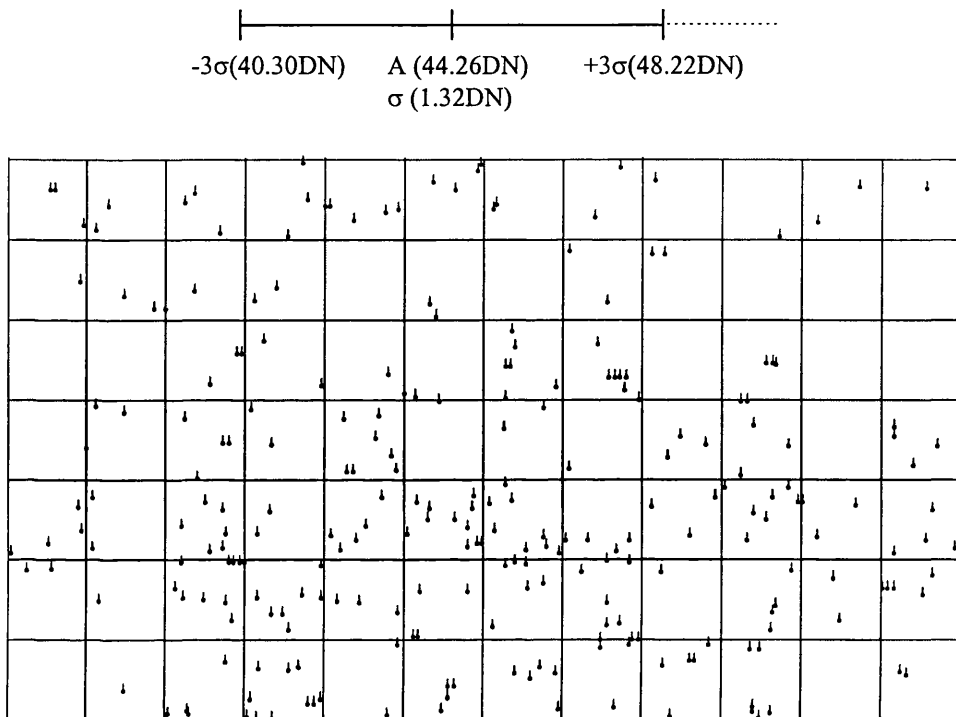


Fig. 15.2 (a), (b) and (c). The vector plot showing the distribution of those pixels that are not responding correctly (i.e. with values outside the range of $A \pm 3\sigma$).

grey level values of these pixels have a range of $\pm 3.96\text{DN}$, in total, amounting to nearly 8 grey level values. However, it is not possible to make any definitive statement on these results using temperature values. It was unfortunate that, apart from the initial check, the equivalence of the grey level values to the temperature was not measured across the frame at the time of the experiment. From the photogrammetrist's point of view, the grey level values are much more important than the corresponding temperature values. Nevertheless, it must be said that many of the other users of this type of imager are often highly concerned with the temperature values since those may be vital for their particular application.

As can be seen from Table 15.1 and Fig. 15.1(b) and (c), at the 40°C and 50°C temperatures, the effect of the radiation source can be clearly seen. The standard deviations (σ) of the grey level values are noticeably increased reaching the value

$\pm 6\text{DN}$. In this case, the graphical plot of these frames by SURFER is invaluable since the high value of the standard deviation tends to hide much detailed information about the radiometric characteristics of the frame. Furthermore the statistical processing of these frames using STAT does not divulge some of the relevant information so that a full analysis can be carried out on the data. However the combination of statistical processing and graphical representation gives a much clearer picture of the situation that existed at the time of the image data acquisition. In this case, at the higher temperatures (40°C and 50°C) the plots show very clearly that the left end of each image has lower grey level values - showing that lower temperatures existed in this area of the heated plate (i.e. the radiation source) at the time when the image data was being acquired. Presumably the environmental conditions existing during the test caused more heat loss at the left end of the plate.

In order to ensure that a fully homogeneous image was being dealt with, and to lessen the effects of this slight cooling around the edges of the radiation source, the top right part of each frame (see Fig. 15.3), 280 (H) x 180 (V) pixels in size has been cut from the whole image. For the purpose of the radiometric calibration, it has been called a quadrant. Furthermore, in order to check the possible effects on the radiometric calibration of the camera caused by the heating pads of the radiation source, a smaller and still more homogenous piece, within the quadrant, which is called a patch, has been used which has a size of 170 (H) x 110 (V) pixels (see Fig. 15.3).

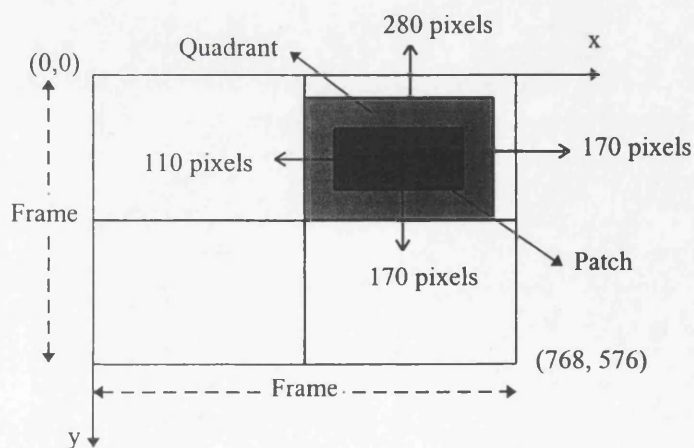


Fig. 15.3. The location of the quadrants and the patches used in the radiometric calibration procedure.

15.2.1.2 Radiometric Calibration of Quadrants and Patches

Three quadrants and three patches for each temperature giving a total of nine quadrants and nine patches in all have been acquired. As was done with the whole frame, these quadrant and patch images have also been converted to ASCII format. Then they have been input to the FORTRAN programs that have been devised and used for the radiometric calibration.

15.2.1.2.1 Computation of the Means and Standard Deviations of the Grey Level Values

For this purpose, the STMN program has been used and the results are shown in Table 15.3. As can be seen from this table, the means and standard deviations of the grey level values of the quadrants at the same temperature are very close to one other. Corresponding values have also been acquired for the patches. There is no big drop in the rmse values when the patches have been processed. This shows that the heating pads did spread the temperature very well and kept the temperature almost uniform all over the surface of the quadrants and patches.

15.2.1.2.2 Non-Uniformity Correction

For the elimination of the non-uniformities that are present, the quadrant data were first input to the PRNU program. This program accepts the data acquired at the lowest and highest temperatures (in this case, 30°C and 50°C) as calibration (reference) data from which to compute the gain and offset values for each individual pixel lying within the quadrants that have been acquired at each of these temperatures. Thus, in this way, it corrects the non-uniform responses of the pixels of the quadrants that have been obtained at the middle temperature (40°C).

However, before applying this correction, the program carries out the averaging of the grey level values of the pixels of each quadrant at the same temperature. Thus, the

Temp.	Image	Mean of the grey level values	Rmse of the grey level values	Mean of the averaged images before corr.	Rmse of the averaged images before corr.	Mean after corr.	Rmse after corr.
Agema 550 with 20° lens (Quadrant image size = 280(H)x180(V) = 50,400 pixels)							
30°C	1	44.26	2.36	44.19	1.28	44.00	0.00
	2	44.19	2.38				
	3	44.12	2.36				
40°C	1	163.04	2.79	161.68	1.81	161.19	2.34
	2	162.92	2.85				
	3	159.08	2.63				
50°C	1	236.26	2.72	236.47	2.00	236.00	0.00
	2	235.54	2.91				
	3	237.62	3.05				
Agema 550 with 20° lens (Patch image size = 170(H)x110(V) = 18,700 pixels)							
30°C	1	44.22	2.36	44.17	1.23	44.00	0.00
	2	44.17	2.33				
	3	44.10	2.37				
40°C	1	163.55	2.56	162.21	1.47	161.72	1.94
	2	163.60	2.33				
	3	159.49	2.56				
50°C	1	235.62	2.51	235.82	1.74	236.00	0.00
	2	234.85	2.68				
	3	236.99	2.89				
Agema 550 with 10° lens (Quadrant image size = 280(H)x180(V) = 50,400 pixels)							
30°C	1	170.29	2.90	165.44	1.76	165.00	0.00
	2	165.19	2.48				
	3	160.86	2.67				
40°C	1	200.09	3.28	194.17	2.61	193.70	2.59
	2	193.97	3.30				
	3	188.45	3.85				
50°C	1	233.30	2.63	233.83	1.96	234.00	0.00
	2	234.11	2.77				
	3	234.07	2.75				
Agema 550 with 10° lens (Patch image size = 170(H)x110(V) = 18,700 pixels)							
30°C	1	171.22	2.55	166.25	1.44	166.00	0.00
	2	165.83	2.34				
	3	161.70	2.51				
40°C	1	201.51	2.92	195.52	1.74	195.02	1.71
	2	194.89	2.90				
	3	190.16	2.81				
50°C	1	232.60	2.39	233.17	1.67	233.00	0.00
	2	233.49	2.56				
	3	233.42	2.54				

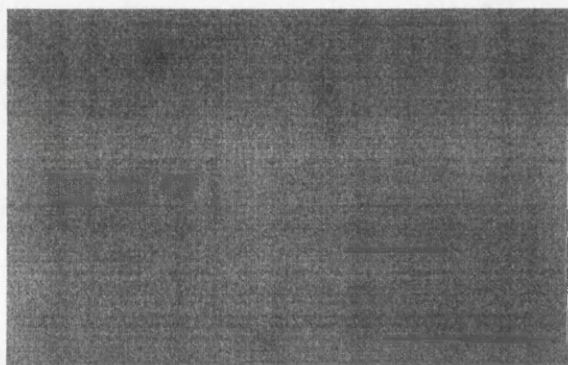
Table 15.3. The means and the standard deviations of the grey level values of the pixels of the quadrant and patch images before and after radiometric correction.

temporal noise that appears to stem from the frame grabber is determined and either eliminated or decreased. The mean and the standard deviation values of the averaged quadrant can be calculated and are also given in Table 15.3. As can be seen from this table, the value of the standard deviation has been decreased and the uniformity increased through the averaging of the grey level values of the quadrants. In Figs. 15.4 and 15.5, the images of the averaged quadrants and patches at each temperature are shown. As discussed in Chapter 10, instead of using a single quadrant for this computation, the averaged quadrant - which consists of the average grey level values of three quadrants at the same temperature - can be used. Thus, three averaged quadrants for the three different temperatures are obtained. As noted above, the averaging of the grey level values reduces the temporal noise. In practice, the amount of this reduction is equal to the square root of the number of quadrants that are employed in this computation (Hou, et al, 1995). For example, employing three quadrants reduces the temporal noise by about $\sqrt{3} = 1.7$ times. As can be seen from Table 15.3, the rmse value at the 30°C temperature level reduced to 1.3DN (Digital number) from 2.4DN; at 40°C, it reduced to 1.8DN from 2.8DN; while for the 50°C, it reduced to 2.0DN from 2.9DN.

Image of the averaged quadrant at 30°C



Image of the averaged quadrant at 40°C



Images of the averaged quadrant at 50°C

Fig. 15.4. Images of the averaged quadrants for the 20° lens.

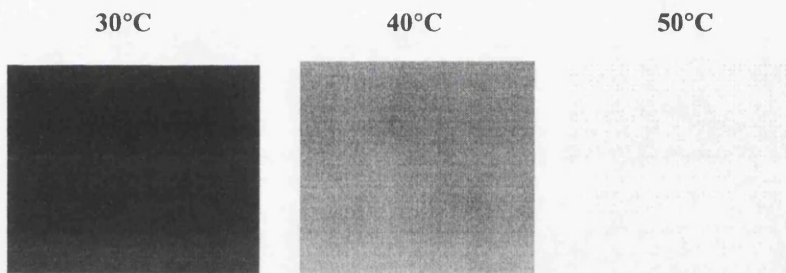


Fig. 15.5. Images of the averaged patches for the 20° lens

As can be seen from Table 15.3, the application of the non-uniformity correction did not give a good result; indeed it increased the standard deviation of the grey level values of the quadrant. The probable reasons for this can be explained as follows:-

- (i) This non-uniformity correction procedure has been evaluated for a linear response variation which presumes that the changes in the grey level values between the different temperatures should be linear. As can be seen from Fig. 15.6, although the grey level values are increasing when the temperatures rise, they do not increase linearly. The mean grey level value for the 30°C temperature was 44; and for the 50°C temperature, it was 236. Interpolating linearly between these, the grey level value for 40°C should be 140, whereas the actual measured grey level value at that temperature was 162. Because of this non-linear variation, it is not possible to get good results using the non-uniformity correction procedure. However, as will be seen later, this method gave good results where there is a linear increment in the grey level values between the temperatures.

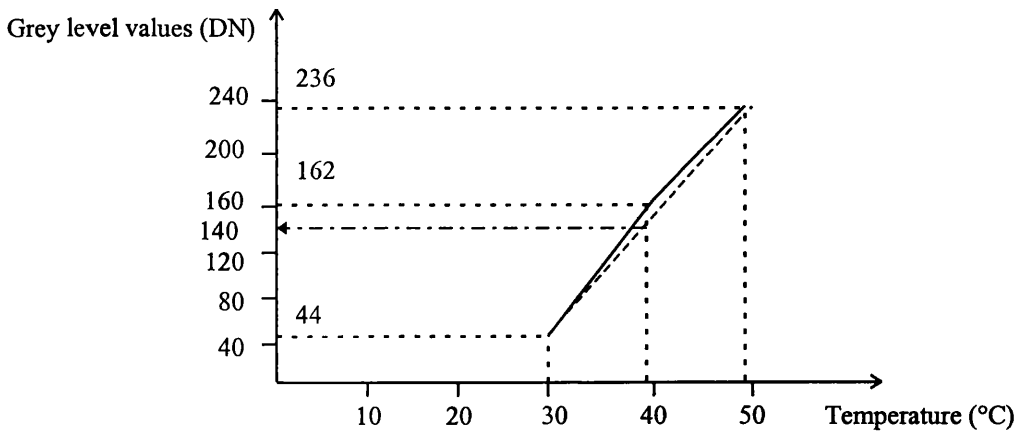


Fig.15.6. Changes in the mean grey level values of the quadrants at different temperatures.

- (ii) For the application of the non-uniformity correction, two temperatures must be taken as reference temperatures which, in this case, are 30°C and 50°C. The important point here is that the standard deviation in the grey level values of the quadrants at these temperatures should be smaller than those obtained at the middle temperature (40°C). However, this is not the case for this experiment. As can be seen from Table 15.3, the quadrants at 50°C have a higher standard deviation than those obtained at the 40°C temperature.

15.2.1.2.3 Statistical Processing of the Grey Level Values of Pixels

For each quadrant, the average or mean (A) and the standard deviation (σ) of the grey level values that have already been determined are input to the program STAT. As described in Chapter 13, if the grey level values of pixels are greater than the $A + 3\sigma$ value and lower than the $A - 3\sigma$ value, these pixels can be regarded as blemished or dead pixels, i.e. they are pixels where the elements of the imaging array did not respond correctly to the incident radiation. In addition, the program computes the percentage of pixels in the quadrant that lie within these ranges. As can be seen from Tables 15.4 and 15.5, only a small number of the grey level values of the pixels lie outside the range $A \pm 3\sigma$.

Agema 550 with 20° lens	Total number of pixels in the quadrant: 280(H)x180(V)= 50,400 pixels			
	Number of pixels greater than $\sigma / 2\sigma / 3\sigma$	Number of pixels less than $\sigma / 2\sigma / 3\sigma$	Total number of pixels outside the range of $\pm 3\sigma$	Percentage of the number of pixels lie inside the range of $\pm 3\sigma$
Temp. = 30°C / Frame No.1				
	8,347	6,567	14,914	$\cong 70\%$
	1,649	1,085	2,734	$\cong 95\%$
	17	67	84	$\cong 99.83\%$
Temp. = 30°C / Frame No.2				
	8,024	6,933	14,957	$\cong 70\%$
	1,585	1,235	2,820	$\cong 94\%$
	25	85	110	$\cong 99.78\%$
Temp. = 30°C / Frame No.3				
	7,490	7,109	14,599	$\cong 71\%$
	1,466	1,297	2,763	$\cong 95\%$
	19	110	102	$\cong 99.80\%$
Temp. = 30°C / Averaged Frame				
	7,648	7,200	14,848	$\cong 71\%$
	946	850	1,796	$\cong 96\%$
	41	122	163	$\cong 99.68\%$
Temp. = 40°C / Frame No.1				
	9,390	9,549	18,939	$\cong 62\%$
	951	1,512	2,463	$\cong 95\%$
	115	165	102	$\cong 99\%$
Temp. = 40°C / Frame No.2				
	9,139	10,161	19,300	$\cong 62\%$
	782	1,961	2,743	$\cong 95\%$
	86	249	335	$\cong 99\%$
Temp. = 40°C / Frame No.3				
	8,662	7,463	16,125	$\cong 68\%$
	1,231	1,098	2,329	$\cong 95\%$
	151	113	264	$\cong 99\%$
Temp. = 40°C / Averaged Frame				
	5,267	7,369	12,636	$\cong 75\%$
	454	3,241	3,695	$\cong 93\%$
	25	462	487	$\cong 99\%$
Temp. = 40°C / Non-Uniformity Corrected Frame				
	7,939	6,371	14,310	$\cong 72\%$
	1,366	1,331	2,697	$\cong 95\%$
	26	196	222	$\cong 99.56\%$
Temp. = 50°C / Frame No.1				
	11,521	7,356	18,877	$\cong 63\%$
	1,639	824	2,463	$\cong 95\%$
	69	85	154	$\cong 99.69\%$
Temp. = 50°C / Frame No.2				
	8,827	7,429	16,256	$\cong 68\%$
	1,198	671	1,869	$\cong 96\%$
	44	37	81	$\cong 99.84\%$
Temp. = 50°C / Frame No.3				
	8,991	7,406	16,397	$\cong 67\%$
	1,084	1,112	2,196	$\cong 96\%$
	67	60	127	$\cong 99.75\%$
Temp. = 50°C / Averaged Frame				
	6,392	10,579	16,971	$\cong 66\%$
	918	1,366	2,284	$\cong 95\%$
	37	55	92	$\cong 99.82\%$

Table 15.4. Statistical processing of the quadrants.

Agema 550 with 20° lens	Total number of pixels in the patch: 170(H)x110(V)= 18.700 pixels			
	Number of pixels greater than $\sigma/2\sigma/3\sigma$	Number of pixels less than $\sigma/2\sigma/3\sigma$	Total number of pixels outside the range of $A \pm 3\sigma$	Percentage of the number of pixels lie inside the range of $A \pm 3\sigma$
Temp. = 30°C / Frame No.1				
	2,983	2,490	5,473	≅ 71%
	426	426	1,049	≅ 94%
	7	30	37	≅ 99.80%
Temp. = 30°C / Frame No.2				
	2,848	2,504	5,352	≅ 71%
	529	425	954	≅ 95%
	8	19	27	≅ 99.86%
Temp. = 30°C / Frame No.3				
	2,759	2,688	5,447	≅ 71%
	546	488	1,034	≅ 94%
	7	14	21	≅ 99.89%
Temp. = 30°C / Averaged Frame				
	2,577	2,638	5,215	≅ 72%
	533	536	1,069	≅ 94%
	29	33	62	≅ 99.67%
Temp. = 40°C / Frame No.1				
	1,956	2,373	4,329	≅ 77%
	457	385	842	≅ 95%
	67	33	100	≅ 99%
Temp. = 40°C / Frame No.2				
	4,040	3,467	7,507	≅ 60%
	309	304	613	≅ 97%
	39	28	67	≅ 99.64%
Temp. = 40°C / Frame No.3				
	1,997	2,076	4,073	≅ 78%
	561	484	1,045	≅ 94%
	25	22	47	≅ 99.75%
Temp. = 40°C / Averaged Frame				
	2,473	3,236	5,709	≅ 69%
	159	989	1,148	≅ 94%
	31	33	64	≅ 99.66%
Temp. = 40°C / Non-Uniformity Corrected Frame				
	3,277	2,266	5,543	≅ 70%
	508	218	726	≅ 96%
	32	11	43	≅ 99.77%
Temp. = 50°C / Frame No.1				
	2,664	3,536	6,200	≅ 67%
	505	412	917	≅ 95%
	21	44	65	≅ 99.65%
Temp. = 50°C / Frame No.2				
	2,456	3,554	6,010	≅ 68%
	308	350	658	≅ 96%
	43	18	61	≅ 99.67%
Temp. = 50°C / Frame No.3				
	3,928	3,492	7,420	≅ 60%
	411	542	953	≅ 95%
	18	26	44	≅ 99.76%
Temp. = 50°C / Averaged Frame				
	2,355	5,375	7,730	≅ 59%
	216	733	949	≅ 95%
	5	32	37	≅ 99.80%

Table 15.5. Statistical processing of the patches.

As can be seen from Table 15.3, the drop in the standard deviation value by making the size of the quadrant smaller and using the patch is not very large. This shows that the heating pads affixed to the back of the radiation source have distributed the heat almost uniformly all over the surface of the plate, and so the frame image is relatively homogenous in appearance. This will also be shown by the plot of the grey values of the pixels using the SURFER program which will be dealt with in the next section.

15.2.1.2.4 Graphical Representation of the Grey Level Values of the Pixels

The grey level values of the pixels of the averaged quadrants at the three temperatures have been plotted by SURFER and are given in Fig. 15.7 (a), (b) and (c). As can be seen from these plots, for the quadrants, the number of blemished pixels is increasing, especially at the edge of the quadrant when the temperature is increasing. At the 30°C temperature, a fairly uniform distribution pattern of the grey level values has been obtained all over the quadrant. By contrast, at the 40°C temperature, pixels with rather different grey level values are starting to appear along the edges of the quadrant; and they become even more evident at the 50°C temperature.

In Fig. 15.8 (a), (b) and (c), the plots of the grey level values of the averaged patches have also been presented. As can be seen from these, the distribution of the grey level values is quite uniform, since they actually consist of the central part of the bigger sized quadrant. The edges of the quadrants, which generally contain the blemished pixels, have been discarded in these patches.

As explained in Chapter 13, for the representation of the grey level values of pixels in the quadrants by SURFER, the ASCII file that contained the positions of the pixels (x,y) and their grey level values (z) was transferred to SURFER. The data contained in this ASCII file was already regularly spaced; so there was no need to grid it again. The options that automatically create the perspective view (fishnet) of the surface or a contour representation of this regularly spaced data were then used for the graphical representation. Afterwards, to display the file in fishnet form, the MAP_SURFACE command of the SURFER was used.

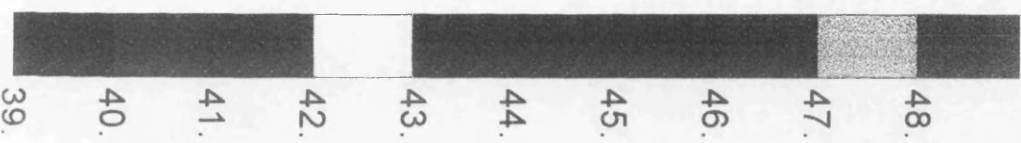
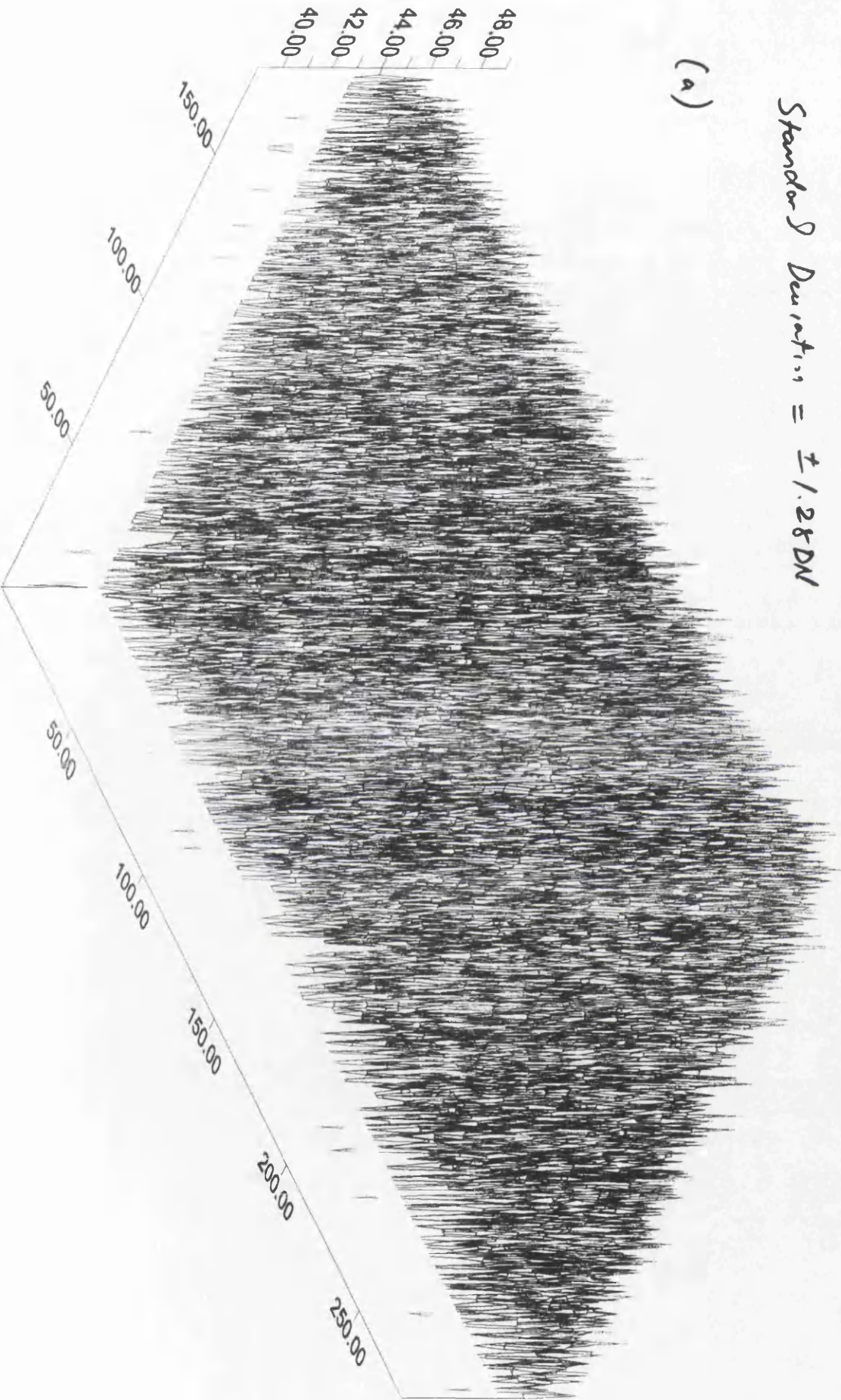
Acemur 550 / 250 / 30°C

Frame Size = 280 x 180 pixels

Mean = 44.19 DN

Standard Deviation = ± 1.28 DN

(a)



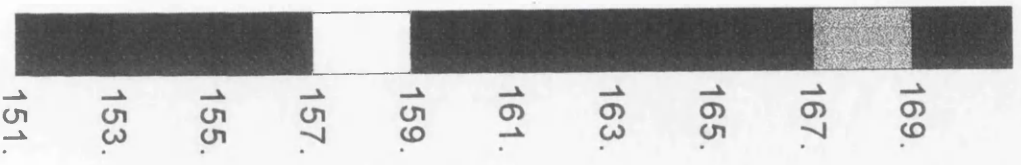
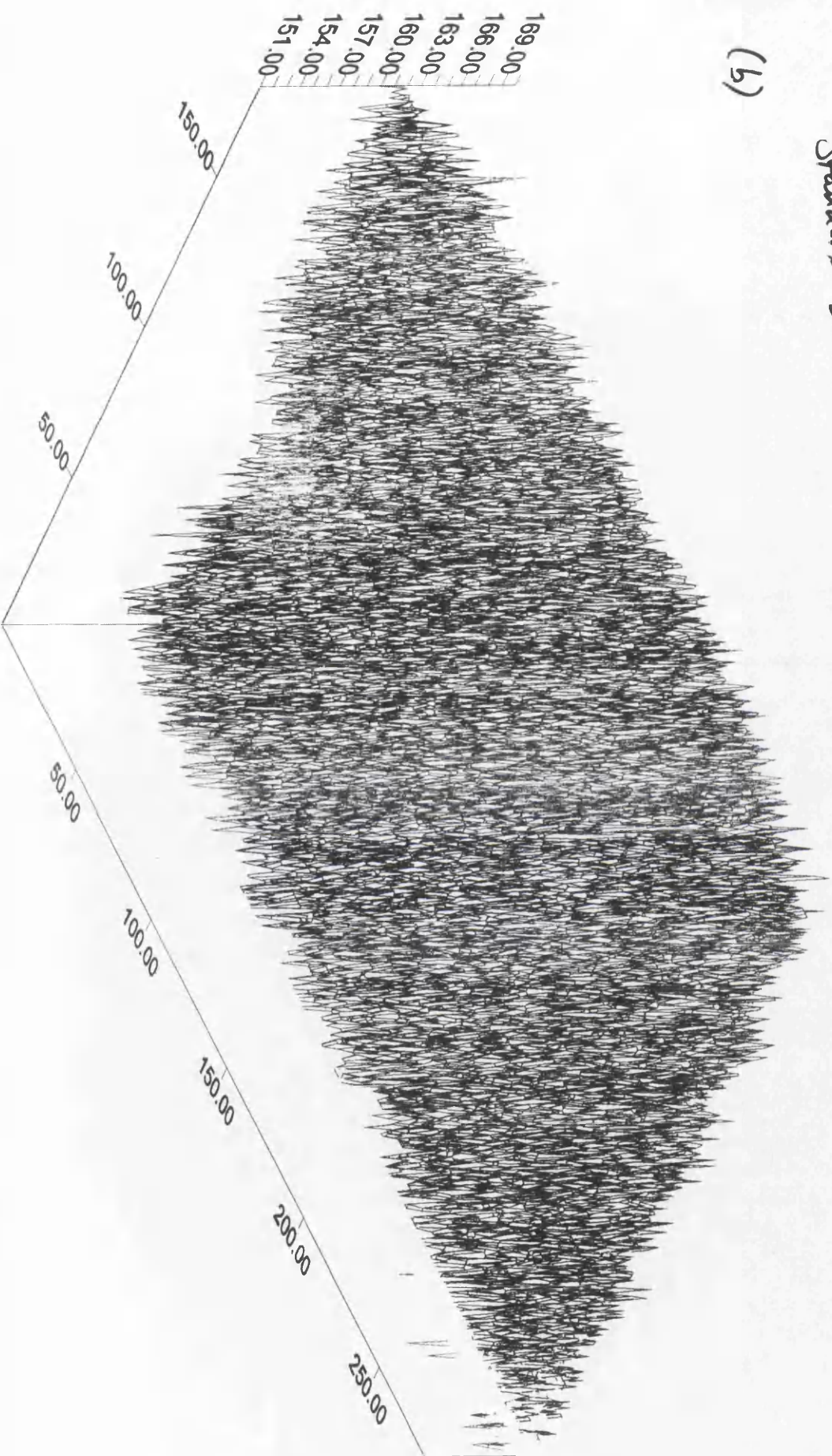
AGEMN 550/20°/40°c

Frame Size = 280x180 pixels

Mean = 161.68 DN

Standard Deviation = ± 1.81 DN

(5)



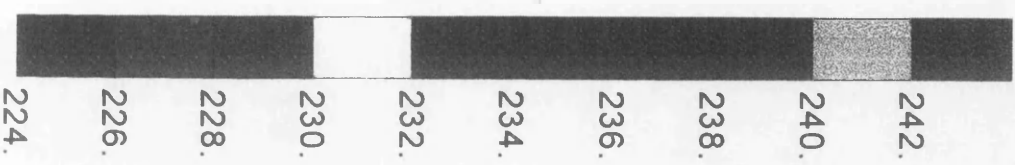
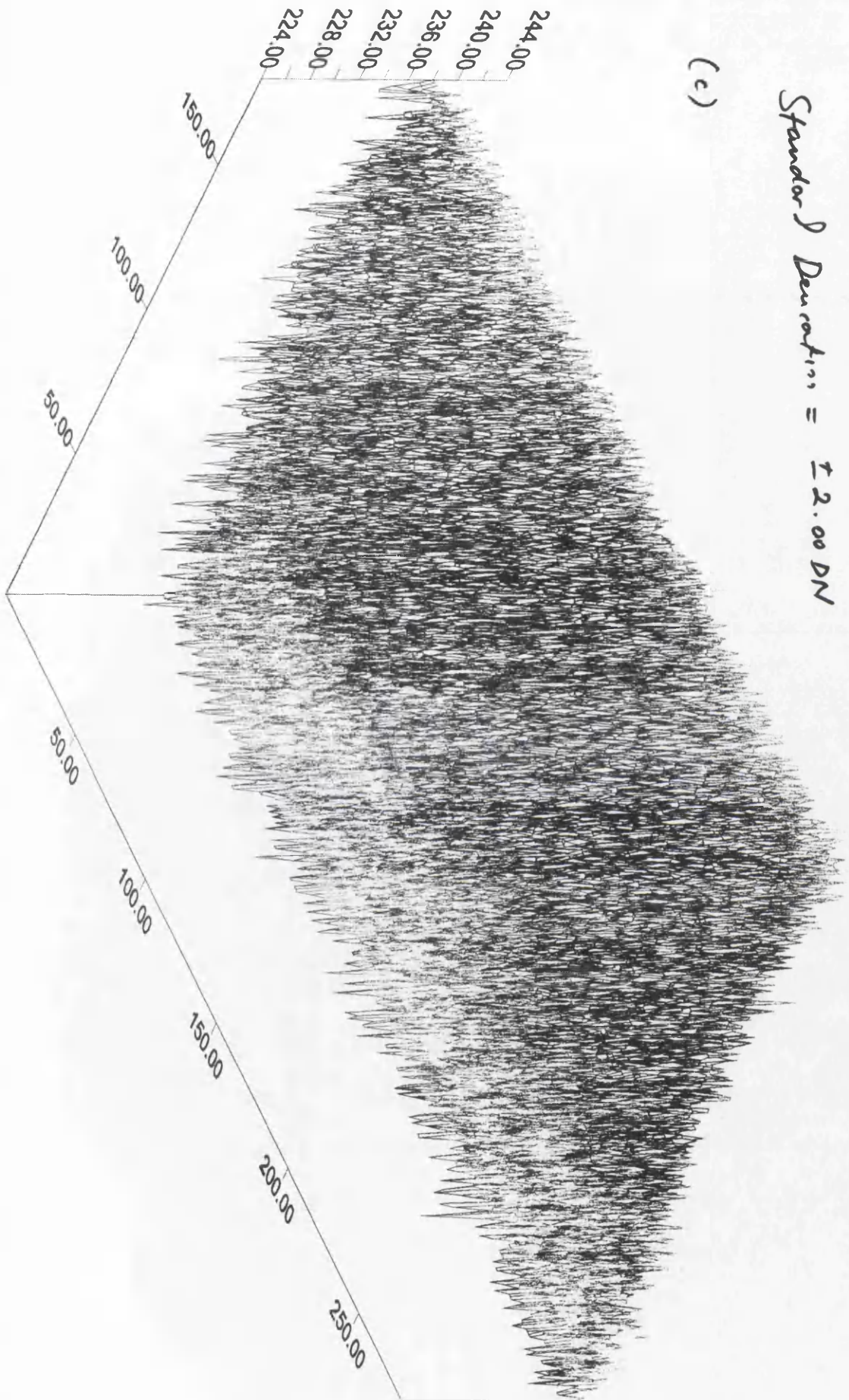
Agema 550 / 2.0° / 500c

Frame Size = 280x180 pixels

Mean = 236.47 DN

Standard Deviation = ± 2.00 DN

(c)



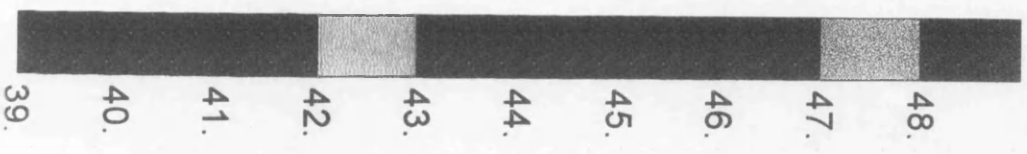
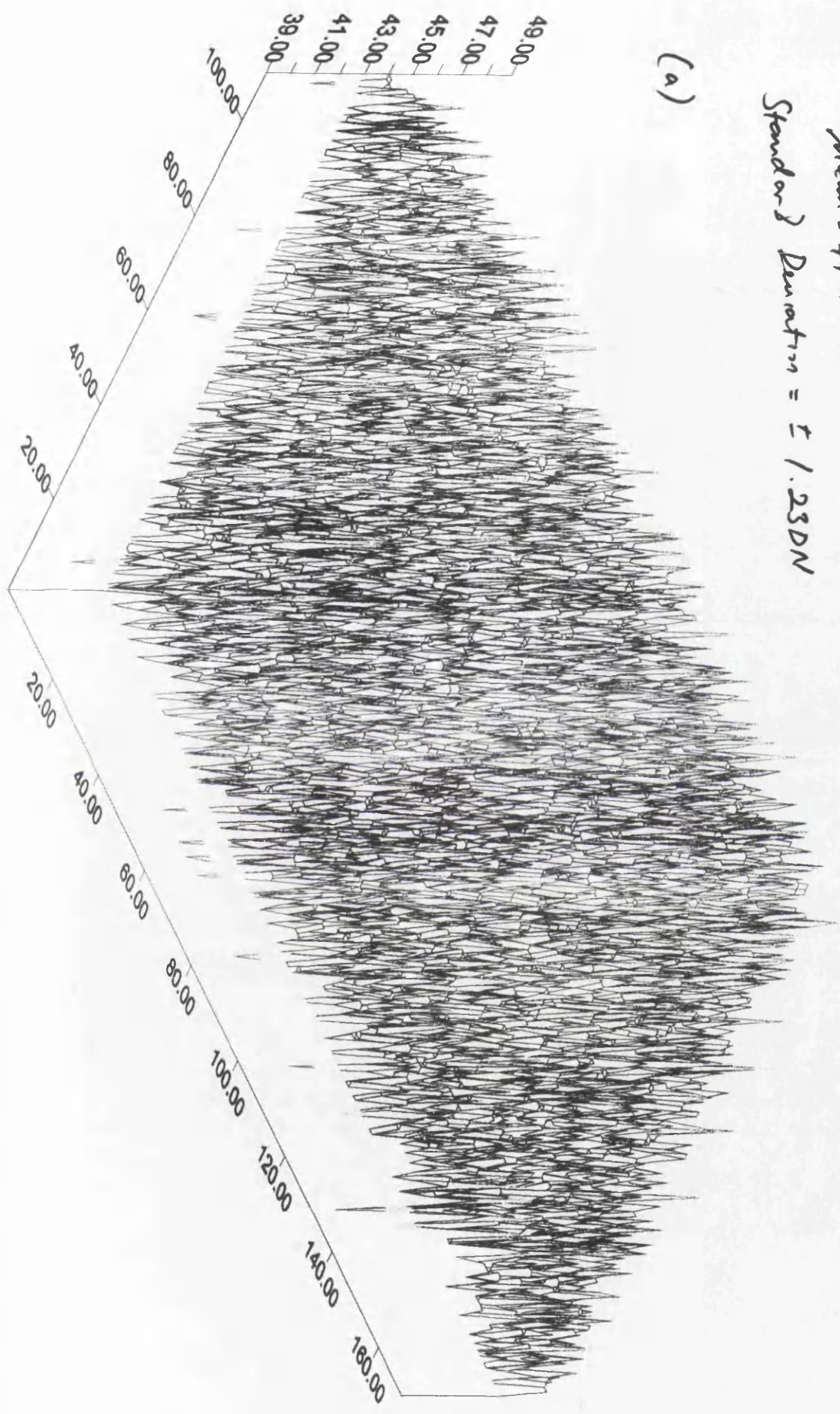
AGEMA 550 / 20° / 30°

Frame Size = 170 x 110 pixels

Mean = 44.17 DN

Standard Deviation = ± 1.23 DN

(a)



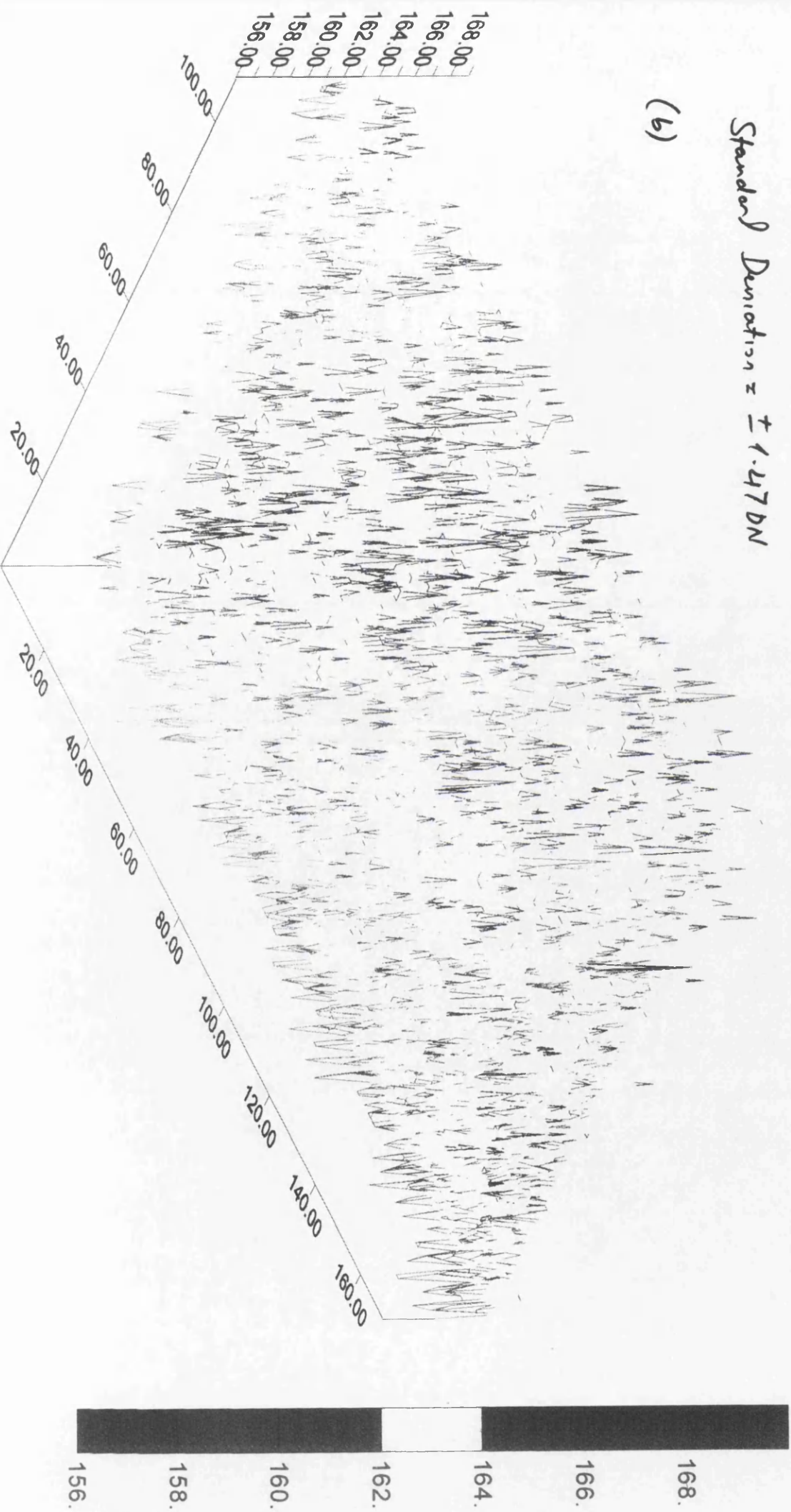
AGEMA 550 / 20° / 40°C

Frame Size = 170x110 pixels

Mean = 162.21 DN

Standard Deviation = ± 1.47 DN

(b)



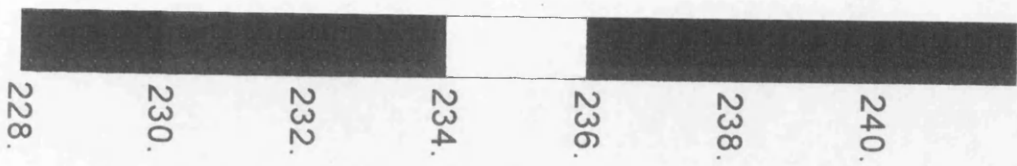
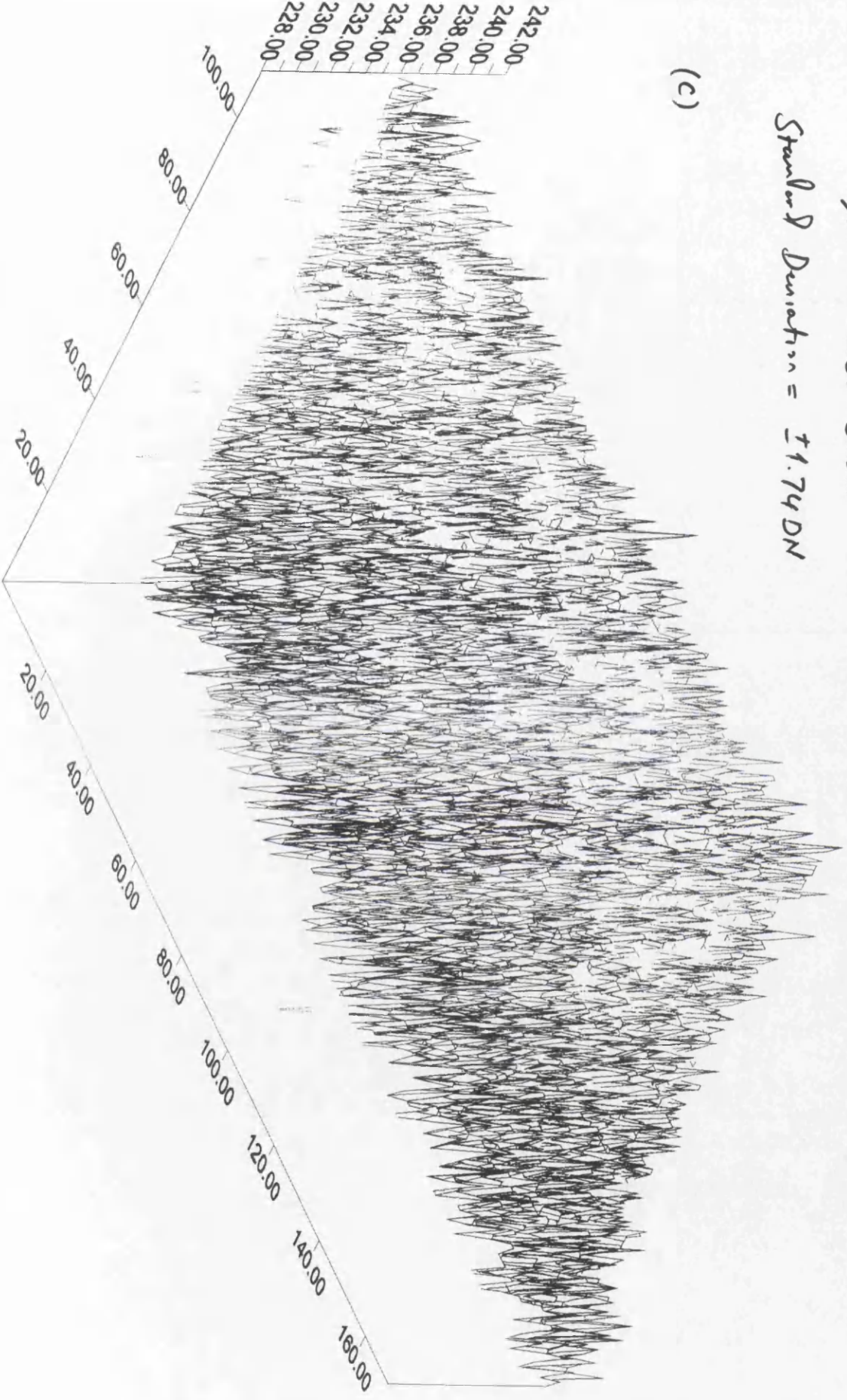
AGEMA 550 / 20° / 50°C

Frame Size = 170 x 110 pixels

Mean = 235.82 DN

Standard Deviation = ±1.74 DN

(c)



However, different colours have been used so that the analyst could see the grey level values changing clearly on the fishnet plot. For this purpose, the total range of grey level values that were present in the image has been divided by the standard deviation of the grey level values. For instance, assuming that the quadrant has grey level values that range from 228DN to 242DN and the standard deviation of the grey level values is ± 2 DN, in this case, seven $[(242-228) / 2]$ different colours could be assigned to the different grey level values on the plot (see Fig. 15.9). In this particular experiment, in order to assign appropriate integer values to the different colours, the standard deviation of the grey level values was taken as ± 1 DN for the quadrant imaged at 30°C ; and ± 2 DN for quadrants at 40°C and 50°C - since their actual standard deviation values were equal to ± 1.28 , 1.81 and 2.00 respectively. This allowed the analyst to see how the grey level values were increasing or decreasing all over the quadrant. Moreover, since SURFER can represent the image data in the form of a perspective 3-D diagram, any dead, blemished or incorrectly responding pixels that occurred within the quadrants could be seen immediately.

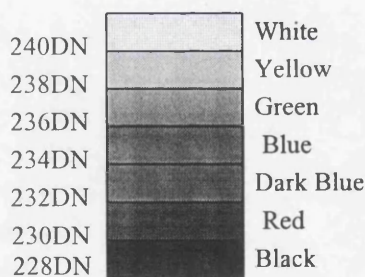


Fig. 15.9. Different colours used for the different grey level values

As was done for the whole frame at 30°C , the author has also plotted the pixels that have grey level values that lie outside the range $A \pm 3\sigma$ (Fig. 15.10(a) and (b)) for both the quadrants and the patches. As can be seen from these figures and Table 15.2, the number of these pixels dropped when the smaller and more uniform data set was used in the programs but the proportion (or percentage) stayed the same. For the quadrant, 163 pixels (0.32%) and for the patch, 62 pixels (0.33%) lie outside this range. For the whole frame, the corresponding figure was 433 pixels (0.21%).

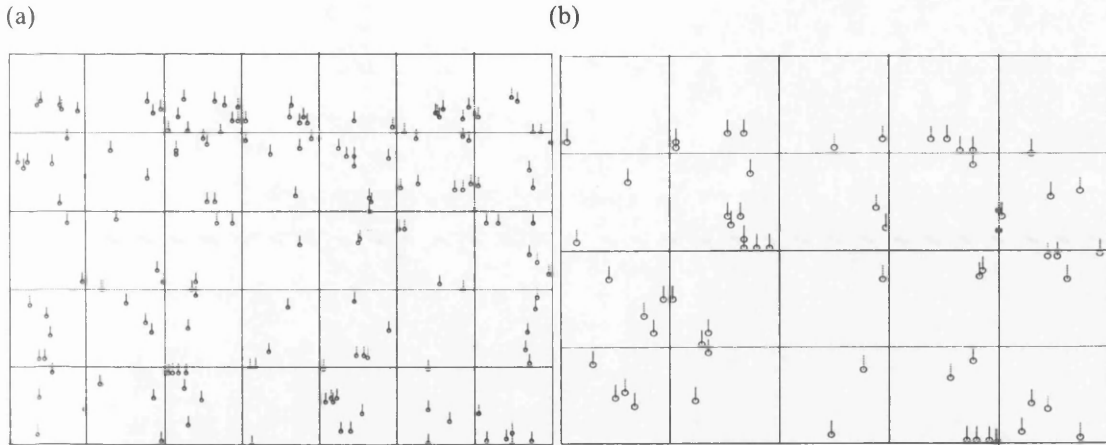
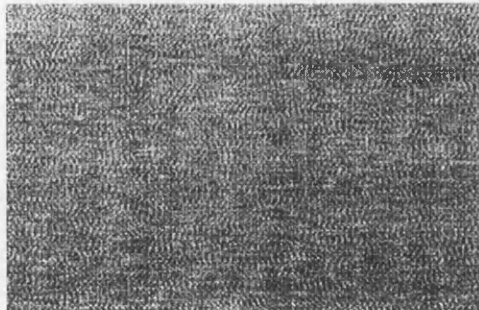


Fig. 15.10(a) and (b). Vector plots of the pixels that are not responding correctly in the quadrant and patch images respectively.

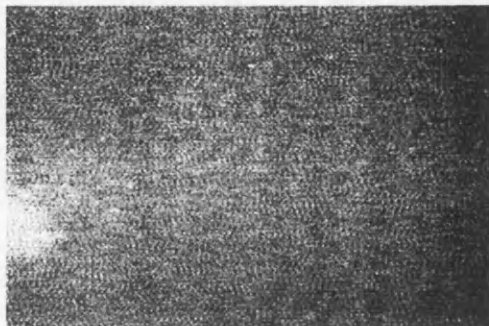
15.2.1.2.5 Different Fixed Patterns Present at Different Temperatures

In this project, the Photoshop Image_Adjust_Level command has been used to enhance the images. Fig. 15.11 shows all the enhanced images of the quadrants for the Agema 550 imager equipped with a lens with 20° angular coverage.

Images of the fixed pattern of the averaged quadrant at 30°C



Images of the fixed pattern of the averaged quadrant at 40°C



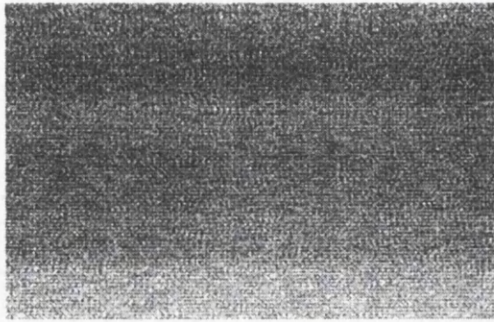
Images of the fixed pattern of the averaged quadrant at 50°C

Fig. 15.11. The fixed patterns of the averaged quadrants for the 20° lens.

As can be seen from this Figure, the images of the quadrants have different fixed patterns of pixels at different temperatures. However, for the same temperature, the quadrants have the same fixed pattern. The present author has spent quite some time investigating the origin of these different fixed patterns. Interestingly, this problem has occurred with every imager that has been tested in this research project. Normally, images of a specific radiation source should have the same fixed pattern at all temperatures. However, this has not happened in the experimental work carried out in this project. The reason for this could be the radiation source used in the work. Essentially it is a kind of hot plate that turns on and off under the control of the thermostat to keep the temperature of the plate at the desired level (see Section 13.2). The solution for this difficulty is to first set the temperature of the plate to a high value and then turn off the power to the plate. Afterwards, the VTR is used to record the natural temperature dropping. However, in this case, it was found that the temperature of the radiation source changed rather quickly at the higher temperatures and there may not have been enough time to record the images of radiation source at the desired temperature before it dropped below this level.

15.2.2 Radiometric Calibration with the 10° Lens

The same calibration procedure has been applied to the images produced by the Agema 550 when equipped with the 10° lens as was done with the 20° lens. Again, three frames for each temperature have been digitized using the frame grabber and so a total of nine quadrants have been obtained from them. These quadrants form the

input to the FORTRAN programs. Thus, the mean value and the standard deviations of the grey level values of each quadrant have been obtained together with their averaged quadrant and non-uniformity corrected quadrant values. The results are shown in Table 15.3. In addition, Fig. 15.12 gives the images of the averaged quadrants and their fixed patterns.

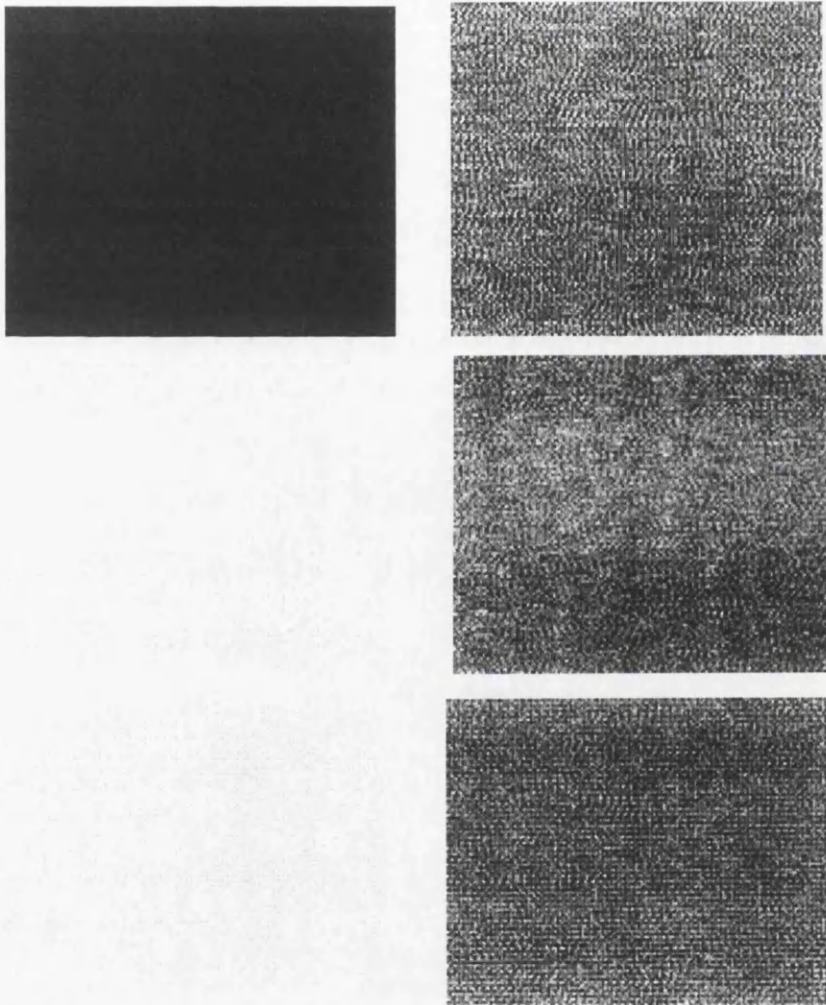


Fig. 15.12. The averaged quadrants and their fixed patterns at the 30°C, 40°C and 50°C levels respectively.

As can be seen from Table 15.3, at the 30°C and 40°C temperatures, the means of the grey level values of the quadrants are different to one other. At the time of the experiment, it was difficult to keep the temperature of the radiation source at the desired level. Although the thermostat controller of the radiation source was set to the desired level, the actual temperature on the radiation source was

changing around this value. This problem had already been encountered in the 20° lens and has been explained in some detail above.

However, in this case, the changes in the grey level values with the temperature changes in the radiation source are almost linear. As can be seen from Fig. 15.13, at the 30°C temperature, the mean grey level value is 165; at 40°C, it is 194; and at the 50°C level, it is 234. Another important point is that the standard deviation of the averaged quadrants at the reference temperatures (30°C and 50°C) is lower than the standard deviation of the averaged quadrant at the 40°C temperature. So, as can be seen from Table 15.3, the non-uniformity correction has provided a small drop in the standard deviation of the averaged grey level values for the quadrant at the 40°C temperature.

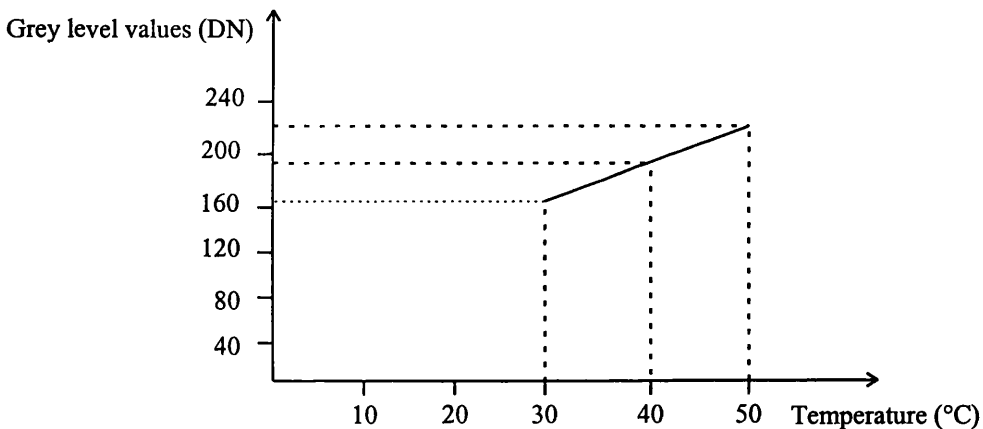


Fig. 15.13. Changes in the mean grey value of the quadrants at different temperatures.

For the statistical processing, the mean (A) and standard deviation (σ) values of each quadrant and patch were input to the STAT program. The results from these operations are given in Tables 15.6 and 15.7. As can be seen from these tables, a small number of pixels lie outside the range of $A - 3\sigma \leq g(i,j) \leq A + 3\sigma$. Only a small number of pixels can be regarded as being blemished and not responding correctly to the emitted radiation and nearly 100% of the pixels of the quadrant lie inside this range. The use of the patches instead of the quadrants provided a drop in the standard deviation values, so they showed still more uniformity than the quadrants.

Agema 550 with 10° lens	Total number of pixels in the quadrant: 280(H)x180(V)= 50,400 pixels			
	Number of pixels greater than $\sigma/2\sigma/3\sigma$	Number of pixels less than $\sigma/2\sigma/3\sigma$	Total number of pixels outside the range of $A \pm 3\sigma$	Percentage of the number of pixels lie inside the range of $A \pm 3\sigma$
Temp. = 30°C / Frame No.1				
	7,027	8,474	15,501	≅ 69%
	445	1,197	1,642	≅ 97%
	50	66	116	≅ 99.77%
Temp. = 30°C / Frame No.2				
	9,141	6,668	15,809	≅ 69%
	676	1,724	2,400	≅ 95%
	99	88	187	≅ 99.63%
Temp. = 30°C / Frame No.3				
	8,947	8,418	17,365	≅ 66%
	670	1,101	1,771	≅ 96%
	81	74	155	≅ 99.69%
Temp. = 30°C / Averaged Frame				
	4,161	9,031	13,192	≅ 74%
	1,013	1,230	2,243	≅ 96%
	78	325	343	≅ 99%
Temp. = 40°C / Frame No.1				
	6,603	6,358	12,961	≅ 74%
	1,333	1,423	2,756	≅ 95%
	84	123	207	≅ 99.59%
Temp. = 40°C / Frame No.2				
	7,461	6,871	14,332	≅ 72%
	819	1,398	2,217	≅ 96%
	71	316	387	≅ 99%
Temp. = 40°C / Frame No.3				
	6,766	8,622	15,388	≅ 69%
	355	1,207	1,562	≅ 97%
	71	77	89	≅ 99.82%
Temp. = 40°C / Averaged Frame				
	6,819	9,299	16,118	≅ 68%
	161	1,850	2,011	≅ 96%
	0	322	322	≅ 99%
Temp. = 40°C / Non-Uniformity Corrected Frame				
	6,983	9,973	16,956	≅ 66%
	1,186	1,302	2,488	≅ 95%
	24	60	84	≅ 99.83%
Temp. = 50°C / Frame No.1				
	10,648	7,265	17,913	≅ 64%
	1,539	1,801	3,340	≅ 93%
	54	56	110	≅ 99.78%
Temp. = 50°C / Frame No.2				
	8,827	8,708	17,535	≅ 65%
	1,754	1,090	2,844	≅ 94%
	65	36	101	≅ 99.80%
Temp. = 50°C / Frame No.3				
	8,646	8,872	17,518	≅ 65%
	1,688	1,074	2,762	≅ 95%
	54	29	83	≅ 99.84%
Temp. = 50°C / Averaged Frame				
	7,815	7,705	15,520	≅ 69%
	1,426	801	2,227	≅ 96%
	78	21	99	≅ 99.80%

Table 15.6. Statistical processing of the quadrants.

Agema 550 with 10° lens	Total number of pixels in the patch: 170(H)x110(V)= 18,700 pixels			
	Number of pixels greater than $\sigma / 2\sigma / 3\sigma$	Number of pixels less than $\sigma / 2\sigma / 3\sigma$	Total number of pixels outside the range of $A \pm 3\sigma$	Percentage of the number of pixels lie inside the range of $A \pm 3\sigma$
Temp. = 30°C / Frame No.1				
	3,569	2,615	6,184	$\cong 67\%$
	206	662	868	$\cong 95\%$
	16	27	43	$\cong 99.77\%$
Temp. = 30°C / Frame No.2				
	1,945	2,872	4,817	$\cong 74\%$
	355	543	898	$\cong 95\%$
	55	42	97	$\cong 99\%$
Temp. = 30°C / Frame No.3				
	2,584	3,434	6,018	$\cong 68\%$
	391	351	742	$\cong 96\%$
	11	40	51	$\cong 99.73\%$
Temp. = 30°C / Averaged Frame				
	2,543	3,008	5,551	$\cong 70\%$
	113	886	999	$\cong 95\%$
	12	30	42	$\cong 99.78\%$
Temp. = 40°C / Frame No.1				
	2,711	2,727	5,438	$\cong 71\%$
	368	363	731	$\cong 96\%$
	26	26	52	$\cong 99.72\%$
Temp. = 40°C / Frame No.2				
	3,696	1,986	5,682	$\cong 70\%$
	432	527	959	$\cong 95\%$
	39	40	79	$\cong 99.58\%$
Temp. = 40°C / Frame No.3				
	3,687	2,830	6,517	$\cong 65\%$
	504	435	939	$\cong 95\%$
	36	23	59	$\cong 99.68\%$
Temp. = 40°C / Averaged Frame				
	1,729	3,130	4,859	$\cong 74\%$
	114	1,137	1,251	$\cong 93\%$
	22	79	101	$\cong 99\%$
Temp. = 40°C / Non-Uniformity Corrected Frame				
	2,190	1,973	4,163	$\cong 78\%$
	300	221	521	$\cong 97\%$
	17	12	29	$\cong 99.84\%$
Temp. = 50°C / Frame No.1				
	3,665	3,503	7,168	$\cong 62\%$
	320	255	575	$\cong 97\%$
	49	31	80	$\cong 99.57\%$
Temp. = 50°C / Frame No.2				
	1,927	2,292	4,219	$\cong 77\%$
	530	557	1,087	$\cong 94\%$
	17	21	38	$\cong 99.80\%$
Temp. = 50°C / Frame No.3				
	2,711	2,727	5,438	$\cong 66\%$
	368	363	731	$\cong 94\%$
	26	26	52	$\cong 99.72\%$
Temp. = 50°C / Averaged Frame				
	2,951	3,922	6,873	$\cong 63\%$
	267	449	716	$\cong 96\%$
	3	97	100	$\cong 99\%$

Table 15.7. Statistical processing of the patches.

3-D representations of the grey level values of the pixels for each averaged quadrant have been made using the SURFER package and have been given in Fig. 15.14 (a), (b) and (c). As can be seen from these plots, the central part of the quadrant has the most uniform grey value distribution, whereas at the edges of the plots, blemished or poorly responding pixels can be seen more frequently. The use of different colours makes the plot more readable and the different grey level values can be seen more easily in this way. When these edges have been discarded using the patches, the effects of the heating pads can be seen to have been eliminated. Thus, only those uniformities that are caused by the differing responses of the detector elements remain. In this way, the plots of the grey level values of the pixels start to become more uniform.

15.3 Radiometric Calibration of the Amber Radiance PM1 Camera

The radiometric calibration of this camera has also been carried out using its 11° lens. Images of the radiation source have been acquired at three different temperatures, 20°C, 40°C and 60°C, and three frames from the recorded images have been digitized using a frame grabber. The digitized frame size was 768(H) x 576(V). However, as was done with the Agema 550, the top right part of each frame, forming a quadrant, 240(H) x 160(V) pixels in size has been cut out from each frame. In addition, a smaller sized section, a patch, 170(H) x 110(V) pixels in size, has also been extracted. As mentioned before, the reason for using this smaller patch was to eliminate as far as possible the effects of the heating pads that are attached behind the radiation source. The data from the quadrants and patches that have been acquired were again input to the STMN and PRNU programs for processing. The results from the application of these programs are shown in Table 15.8. In addition, the images of the averaged quadrants at each temperature have been given together with their fixed patterns in Fig. 15.15.

As can be seen from this table, at the 20°C temperature, the means of the grey level values of the quadrants that are processed were very close to one another. However, for the higher temperatures such as 40°C and 60°C, the means of the grey level values

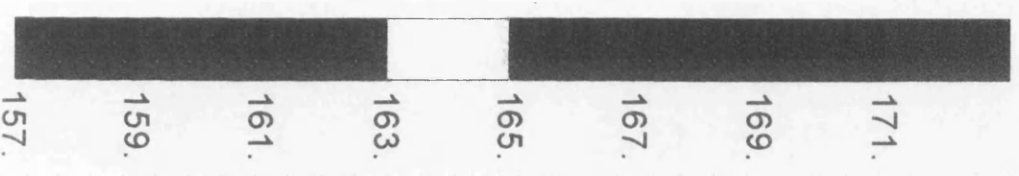
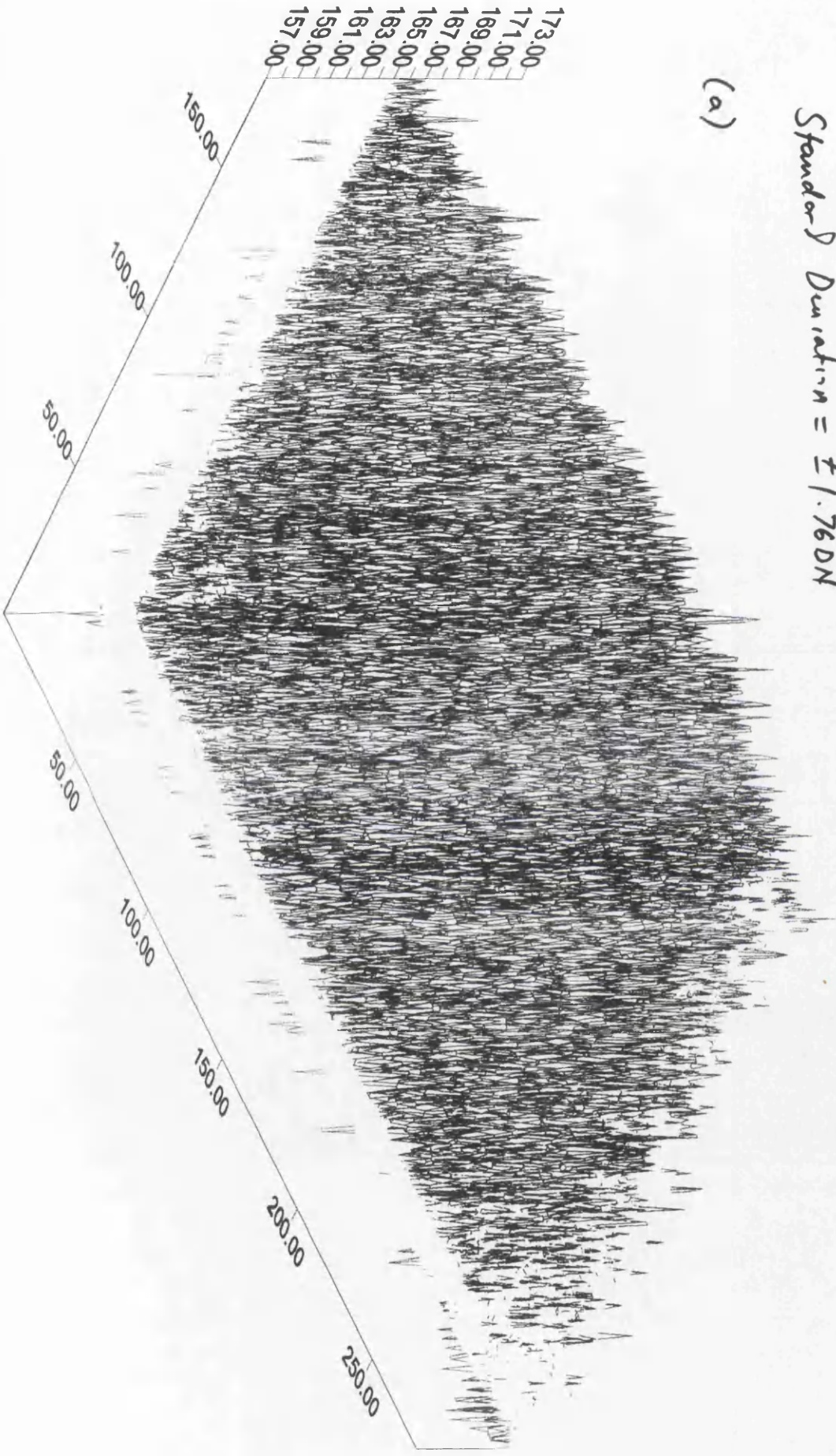
Agemn 550 / 10° / 30°c

Frame Size = 280 x 180 pixels

Mean = 165.44 DN

Standard Deviation = ± 1.76 DN

(a)



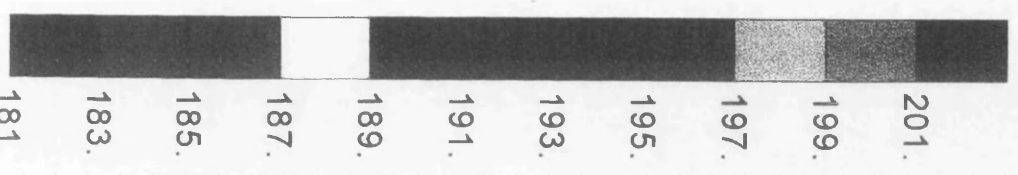
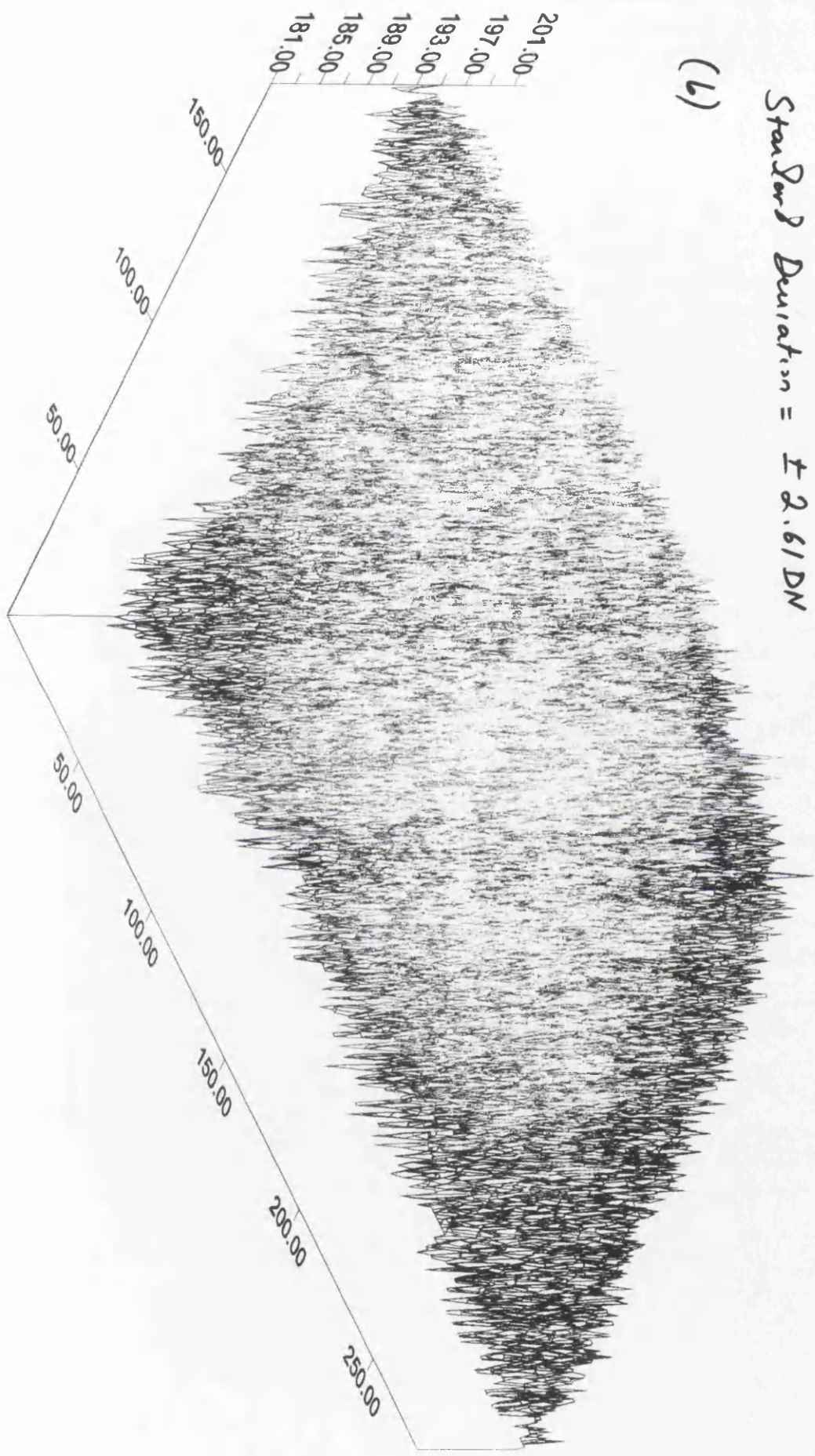
ASWIM 550 / 10° / 40°c

Frame Size = 280 x 180 pixels

Mean = 194.17 DN

Standard Deviation = ± 2.61 DN

(6)



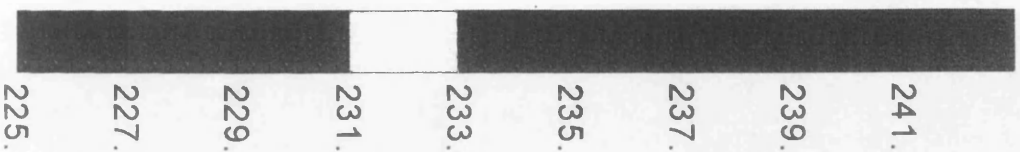
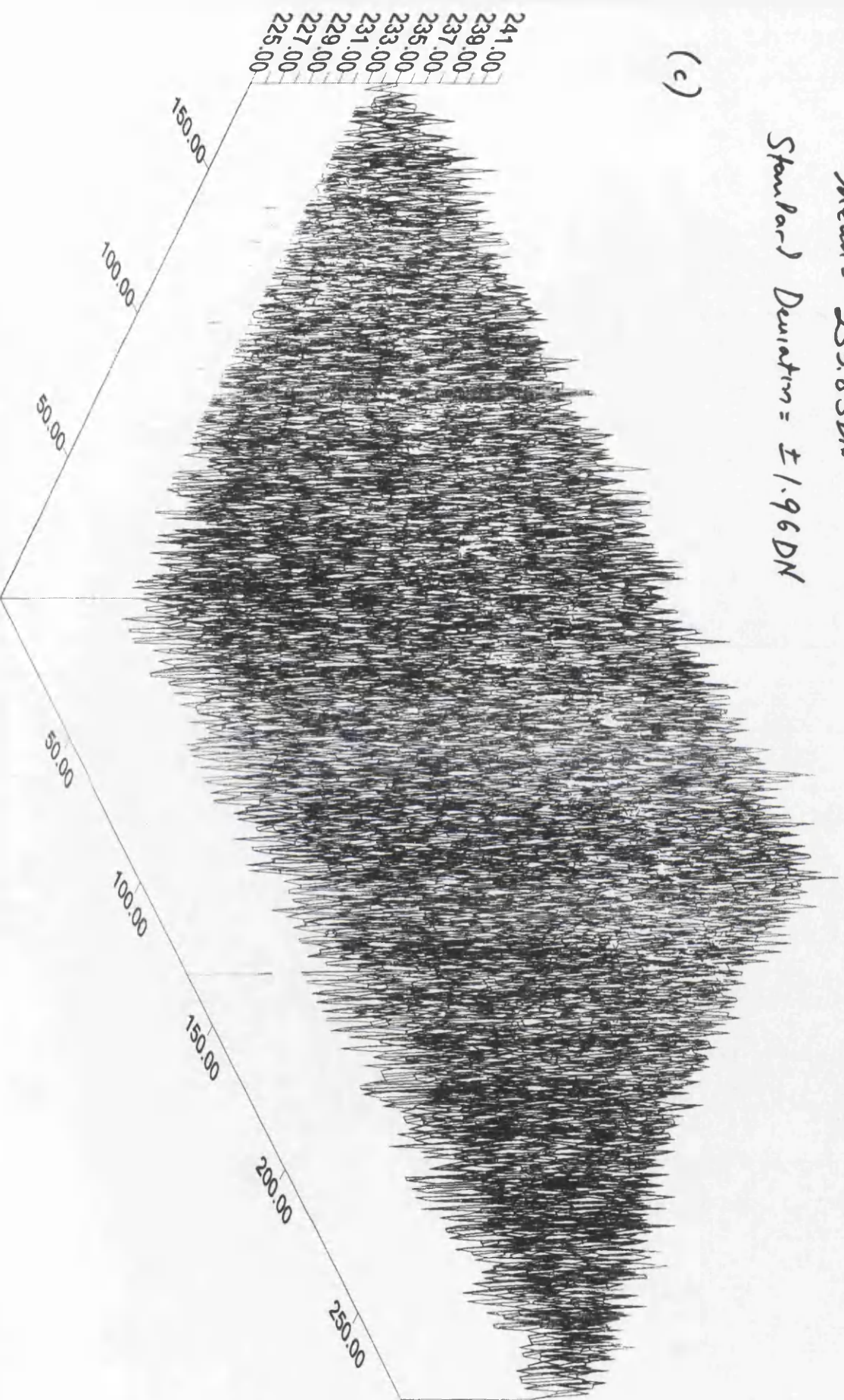
Agema 350 / 10° / 50°C

Frame Size = 280 x 180 pixels

Mean = 233.83 DN

Standard Deviation = ±1.96 DN

(c)



of the quadrants are starting to become slightly different to one another. In addition to this, at these temperatures, the grey level values of the pixels of the quadrants have larger standard deviation values. There are two main reason for this. They are:-

Temp.	Image	Mean of the grey level values	Rmse of the grey level values	Mean of the averaged images before corr.	Rmse of the averaged images before corr.	Mean after corr.	Rmse after corr.
Amber Radiance PM with 11° lens (Quadrant image size = 240(H)x160(V) = 38,400 pixels)							
20°C	1	127.18	2.66	127.65	1.87	128.00	0.00
	2	127.52	2.60				
	3	128.24	2.53				
40°C	1	157.06	6.21	156.73	5.93	156.09	5.16
	2	153.86	5.97				
	3	159.27	7.27				
60°C	1	214.04	16.83	217.14	16.33	217.00	0.00
	2	218.63	16.40				
	3	218.74	16.74				
Amber Radiance PM with 11° lens (Patch image size = 170(H)x110(V) = 18,700 pixels)							
20°C	1	127.05	2.60	127.53	1.75	128.00	0.00
	2	127.40	2.52				
	3	128.15	2.43				
40°C	1	159.19	4.46	159.58	3.77	158.74	2.84
	2	155.76	3.97				
	3	163.81	4.85				
60°C	1	224.51	8.65	226.79	8.25	227.00	0.00
	2	228.10	8.40				
	3	227.77	9.24				

Table 15.8. Average and standard deviation values before and after radiometric correction with the Amber Radiance PM1 camera.

- (i) It is difficult to keep the temperature of the radiation source at the desired level - as already mentioned in the discussion about the Agema 550. As will be seen later, when the grey level values of the pixels are displayed by the SURFER program, the effects of the rapid switching on and off of the heating pads can be seen very clearly. These pads were cooling and re-heating very quickly at the higher (40°C and 60°C) temperatures. So, it was very difficult to keep the temperature stable at those higher levels since the temperature of the radiation source is so substantially different to the ambient temperature of the laboratory in which the test was conducted. This can be seen very clearly from the fixed patterns of the pixels of the quadrants that are averaged at the 40°C and 60°C

temperatures. In Fig. 15.16, only the fixed patterns of the quadrants at 40°C have been given. For each quadrant, there is a different fixed pattern of the pixels. Normally, for the same temperature, the quadrants should exhibit the same fixed pattern of the pixels. In the Agema 550, although the fixed patterns of the pixels of the averaged quadrants for the different temperature were different, the same fixed pattern of the pixels has been obtained for each of the quadrants at the same temperature. With the Radiance PM1, different fixed patterns of the pixels of the quadrant images were obtained at the same temperature.

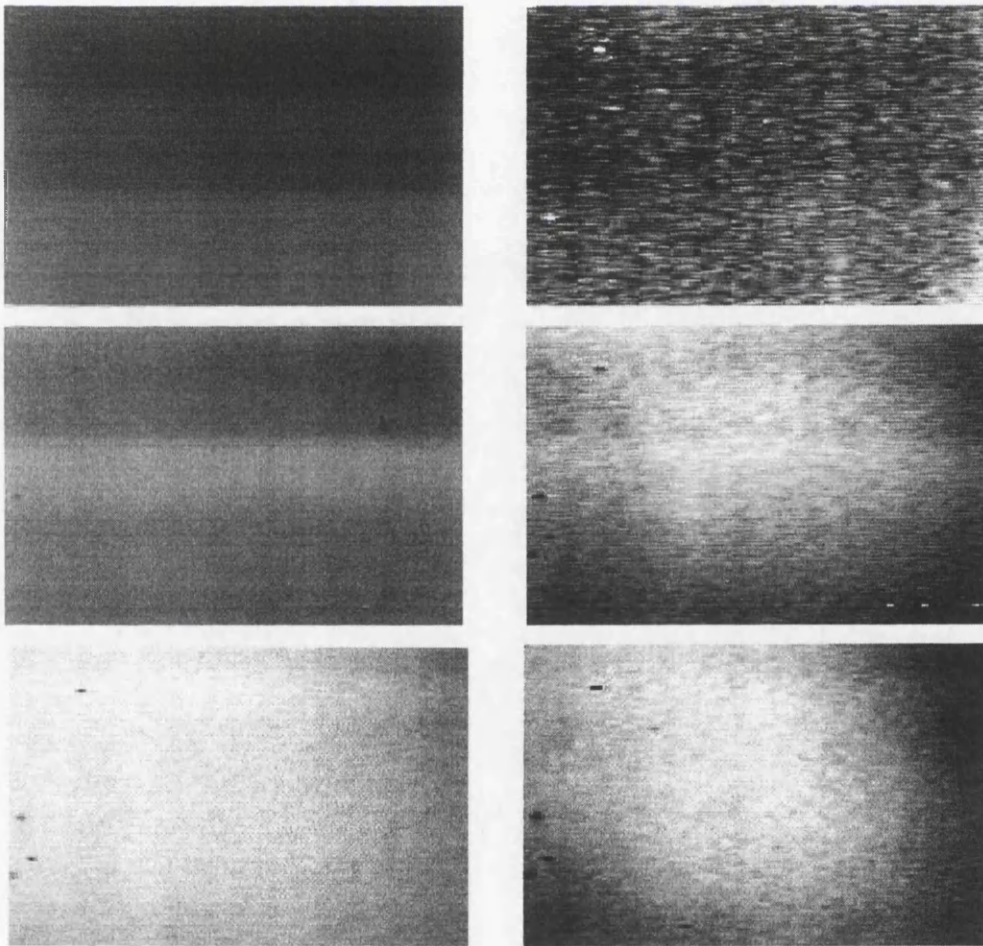


Fig. 15.15. The averaged quadrants and their fixed patterns for the 20°C, 40°C and 60°C temperatures respectively as recorded by the Radiance PM1 camera.

- (ii) The Radiance PM1 itself has an option to set the temperature range that includes the actual temperature of the object that is being imaged. For

example, if the object temperature was set to 40°C, the temperature range that includes this temperature can be set in the imager. However, due to the rapid changes in the temperature of the radiation source at the higher temperatures, this setting of the imager had to be changed also. This caused considerable difficulty at the time of the experiment. The author was trying to obtain images that are uniform and having the same temperature. However, as mentioned above, a very labour intensive effort was involved when attempting to overcome the restrictions that were caused by the heating system of the radiation source and by the large temperature differences between the source and the surrounding environment.

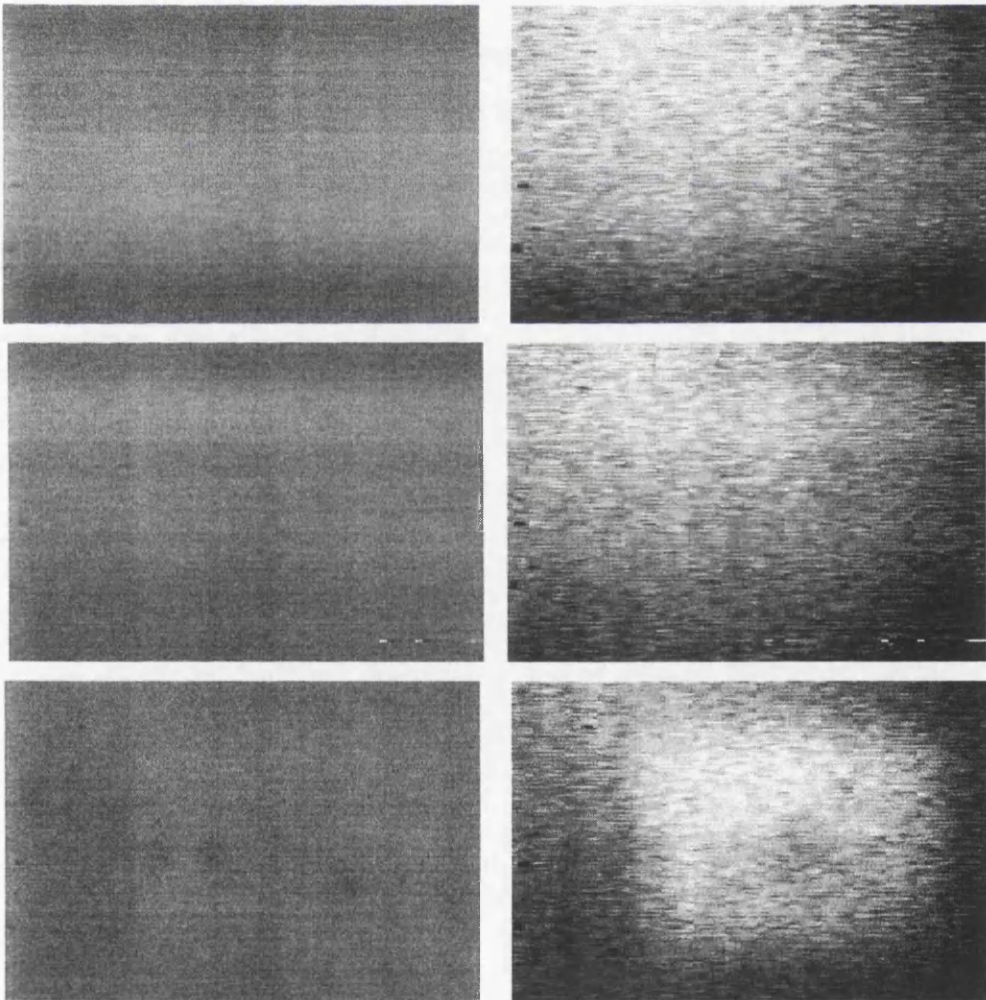


Fig. 15.16. The quadrants at the 40°C temperature and their different fixed patterns.

As can be seen in Fig. 15.17, there is a non-linearity between the mean grey value increment and the temperature increment. The mean grey values are 128, 157 and 217 at the 20°C, 40°C and 60°C temperatures respectively; the mean value at the 40°C level if a linear change occurred would be 173 (instead of the actual 157).

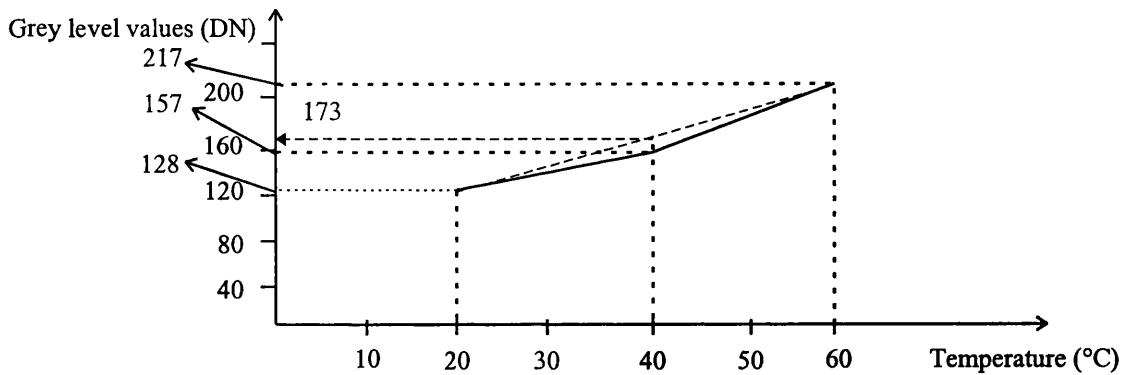


Fig.15.17. Changes in the mean grey level values of the quadrants at different temperatures.

However, the application of the non-uniformity correction gave good results because of the big differences between the temperatures to which the radiation source was set despite the non-linearity and the high standard deviation values of the grey level values in the quadrants at the 40°C and 60°C temperatures. While the percentage of non-uniform pixels in the averaged frames at the 40°C temperature decreased from 3.78% ($5.93 / 156.73$) to the 3.31% ($5.16 / 156.09$) value, the standard deviation of the non-uniformity corrected frame dropped from $\pm 5.93\text{DN}$ to $\pm 5.16\text{DN}$.

15.3.1 Discussion of the Results from the Radiance PM1 Camera

The use of the smaller-sized patches provided a big drop in the rmse value at the higher temperatures such as 40°C and 60°C. At these temperatures, the standard deviations of the averaged quadrants decreased by nearly half. This showed clearly the effect of the rapid temperature loss on the grey levels of the pixels lying inside the quadrants with the PM1 camera.

Tables 15.9 and 15.10 show the results of the statistical processing of the quadrants carried out using the STAT program. The standard deviation values and the means of

Amber Radiance PM with 11° lens	Total number of pixels in the quadrant: 240(H)x160(V)= 38,400 pixels			
	Number of pixels greater than $\sigma/2\sigma/3\sigma$	Number of pixels less than $\sigma/2\sigma/3\sigma$	Total number of pixels outside the range of $A \pm 3\sigma$	Percentage of the number of pixels lie inside the range of $A \pm 3\sigma$
Temp. = 20°C / Frame No.1				
	7,071	6,064	13,135	≅ 66%
	747	654	1,401	≅ 96%
	60	60	120	≅ 99.69%
Temp. = 20°C / Frame No.2				
	4,578	4,773	9,351	≅ 76%
	904	1,103	2,007	≅ 95%
	61	37	98	≅ 99.74%
Temp. = 20°C / Frame No.3				
	6,940	5,101	12,041	≅ 69%
	574	1,344	1,918	≅ 95%
	87	74	161	≅ 99.58%
Temp. = 20°C / Averaged Frame				
	4,472	6,382	10,854	≅ 72%
	407	763	1,170	≅ 97%
	46	151	197	≅ 99%
Temp. = 40°C / Frame No.1				
	6,819	5,699	12,518	≅ 67%
	118	1,191	1,309	≅ 97%
	0	54	54	≅ 99.86%
Temp. = 40°C / Frame No.2				
	7,545	5,240	12,785	≅ 67%
	377	796	1,173	≅ 97%
	16	79	95	≅ 99.75%
Temp. = 40°C / Frame No.3				
	6,596	6,310	12,906	≅ 67%
	178	1,025	1,203	≅ 97%
	0	70	70	≅ 99.82%
Temp. = 40°C / Averaged Frame				
	6,196	6,822	13,018	≅ 66%
	24	1,177	1,201	≅ 97%
	6	91	97	≅ 99.75%
Temp. = 40°C / Non-Uniformity Corrected Frame				
	2,773	2,663	5,436	≅ 86%
	1,018	415	1,433	≅ 96%
	534	86	620	≅ 98%
Temp. = 60°C / Frame No.1				
	5,588	5,985	11,573	≅ 70%
	0	1,839	1,839	≅ 95%
	0	490	490	≅ 99%
Temp. = 60°C / Frame No.2				
	4,320	6,382	10,702	≅ 72%
	0	1,793	1,793	≅ 95%
	0	399	399	≅ 99%
Temp. = 60°C / Frame No.3				
	5,332	6,282	11,614	≅ 70%
	0	1,807	1,807	≅ 95%
	0	254	254	≅ 99%
Temp. = 60°C / Averaged Frame				
	4,460	6,189	10,649	≅ 72%
	0	1,941	1,941	≅ 95%
	0	430	430	≅ 99%

Table 15.9. Statistical processing of the quadrants.

Amber Radiance PM with 11° lens	Total number of pixels in the patch: 170(H)x110(V)= 18,700 pixels			
	Number of pixels greater than $\sigma/2\sigma/3\sigma$	Number of pixels less than $\sigma/2\sigma/3\sigma$	Total number of pixels outside the range of $A \pm 3\sigma$	Percentage of the number of pixels lie inside the range of $A \pm 3\sigma$
Temp. = 20°C / Frame No.1				
	3,132	3,124	6,256	≅ 67%
	288	336	624	≅ 97%
	60	24	84	≅ 99.55%
Temp. = 20°C / Frame No.2				
	3,704	2,402	6,106	≅ 67%
	326	562	888	≅ 95%
	36	12	48	≅ 99.74%
Temp. = 20°C / Frame No.3				
	2,994	2,436	5,430	≅ 71%
	228	614	842	≅ 95%
	14	36	50	≅ 99.73%
Temp. = 20°C / Averaged Frame				
	1,770	3,144	4,914	≅ 74%
	110	1,182	1,292	≅ 93%
	30	76	106	≅ 99%
Temp. = 40°C / Frame No.1				
	3,688	2,060	5,748	≅ 69%
	158	344	502	≅ 97%
	2	12	14	≅ 99.93%
Temp. = 40°C / Frame No.2				
	4,162	2,626	6,788	≅ 64%
	546	302	848	≅ 95%
	10	8	18	≅ 99.90%
Temp. = 40°C / Frame No.3				
	3,014	3,172	6,186	≅ 67%
	174	494	668	≅ 97%
	0	26	26	≅ 99.86%
Temp. = 40°C / Averaged Frame				
	2,686	3,108	5,794	≅ 69%
	76	734	810	≅ 96%
	0	20	20	≅ 99.89%
Temp. = 40°C / Non-Uniformity Corrected Frame				
	3,038	2,330	5,268	≅ 72%
	500	432	932	≅ 95%
	74	16	90	≅ 99.52%
Temp. = 60°C / Frame No.1				
	2,576	2,992	5,568	≅ 70%
	8	816	824	≅ 96%
	0	98	98	≅ 99%
Temp. = 60°C / Frame No.2				
	2,574	3,180	5,754	≅ 69%
	6	918	924	≅ 95%
	0	68	68	≅ 99.64%
Temp. = 60°C / Frame No.3				
	2,492	3,320	5,812	≅ 69%
	16	716	732	≅ 96%
	0	58	58	≅ 99.69%
Temp. = 60°C / Averaged Frame				
	1,868	3,360	5,228	≅ 72%
	0	1,010	1,010	≅ 95%
	0	88	88	≅ 99.53%

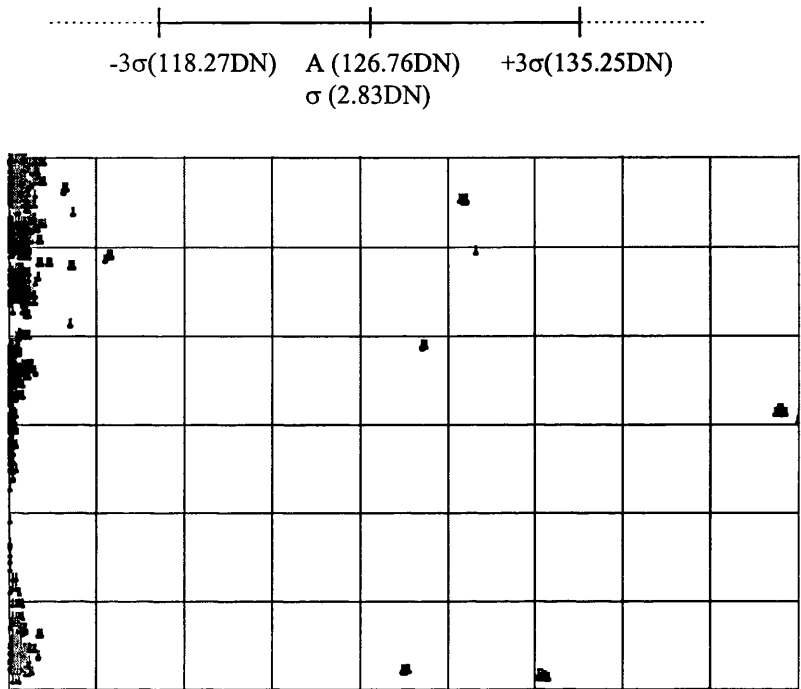
Table 15.10. Statistical processing of the patches.

the quadrants that were obtained from the STMN and PRNU programs were used for this computation. As can be seen from these tables, nearly 100% of the pixels of the quadrants have grey level values that lie inside the range of the $A \pm 3\sigma$. The remaining small number of pixels can be regarded as blemished or poorly responding pixels.

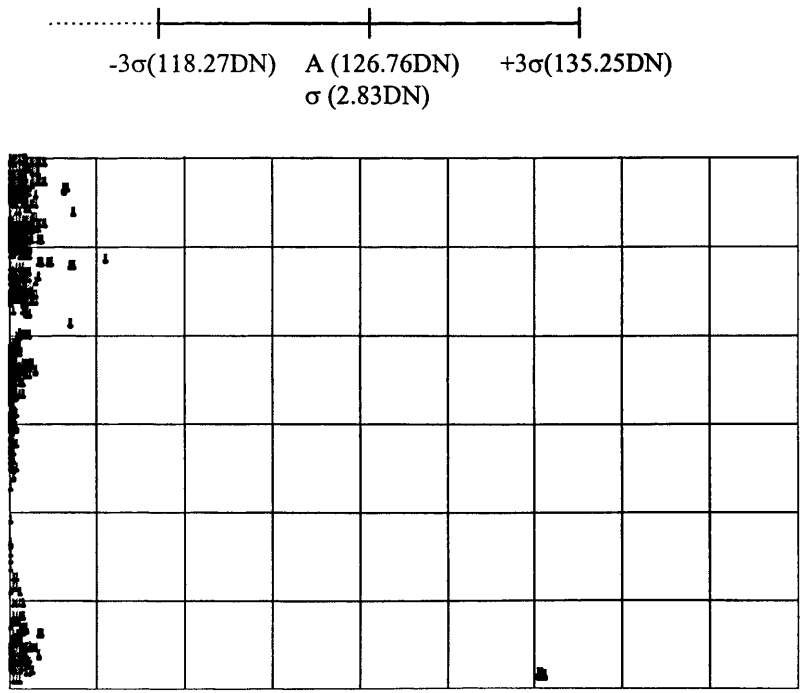
After processing the quadrants and patches, the author has subjected the whole frame from the digitized images at 20°C temperature for Radiance PM1 camera to further processing and analysis. The reason for not using frames at the other higher temperatures for this imager is the somewhat unstable conditions with rapid heating / cooling cycles in the radiation source resulting in large values of their standard deviations. As has been done with the 20° lens of the Agema 550, plotting files have been created for those pixels that are not responding correctly. For this purpose, the mean and standard deviation values of the averaged whole frame at the 20°C temperature have been obtained using the STMN program. The mean value was 126.76DN and the standard deviation was ± 2.83 DN. So, the limits of the $A \pm 3\sigma$ range have been computed to be 118.27DN and 135.25DN. In Fig. 15.18 (a), (b) and (c), the locations of those pixels that lie outside this range are shown. The majority of these pixels are located at the same area (i.e. at the left edge of the frame). The impression being that this is caused by a temperature gradient that is occurring across the face of the radiation source - as occurred in the tests of the Agema 550. A graphical representation of the averaged whole frame given by SURFER at the 20°C temperature has also been included as Fig. 15.19.

In some infrared imagers, there are built-in hardware functions that may hide the occurrence of dead or blemished pixels on the raw image. These functions implement resampling procedures such as nearest neighbour, bilinear or bicubic interpolation - which are well known to the photogrammetry and remote sensing community. If such a function is invoked, then a pixel that has a quite different grey level value to that of its neighbouring pixels is assigned a new grey level value which is simply equal to the mean or some other value interpolated from the grey level values of the neighbouring pixels. So, those pixels that are blemished or dead cannot be discovered on the

(a) Pixels lie outside the range of $A \pm 3\sigma$ (1,411 pixels out of 163,350 pixels)



(b) Pixels that have grey level values less than $A - 3\sigma$ (1,360 pixels out of 163,350 pixels)



(c) Pixels that have grey level values greater than $A + 3\sigma$ (51 pixels out of 163,350 pixels)

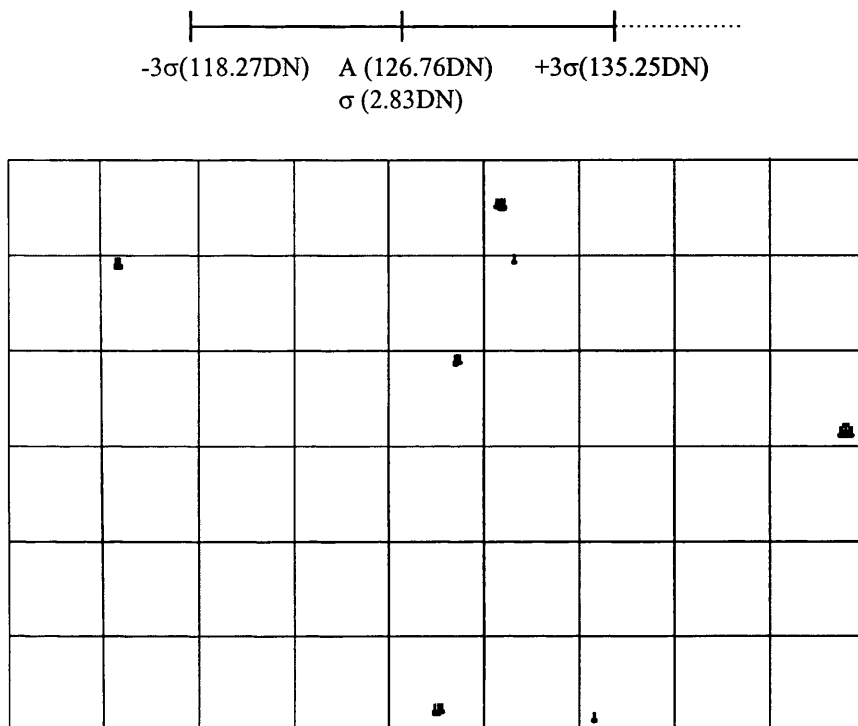


Fig. 15.18. The vector plots showing the distribution of the blemished pixels.

resulting image that is generated by the imager. The Agema 550 CCD camera has these corrective functions built-in and it was not possible to make them ineffective at the time of the experiment. However, it is possible to switch these off on the Radiance PM1 camera and so, in this case, raw image data could be obtained and the presence of blemished or dead pixels could be established for the PM1 camera as can be seen from Figs. 15.15 and 15.16 relating to this camera. It is then possible to see that some elements of the detector array do not give any response at all.

In Fig. 15.20, the 3-D representations of the grey values of the pixels of the averaged quadrants have been given. As can be seen from these plots, at the 20°C temperature, which was also that of the surrounding environment, the grey level values of the pixels show a much more uniform distribution. As noted above, there are also some blemished or poorly responding pixels. However, at the 40°C and 60°C temperatures, where the temperature of the radiation source is so different to that of the ambient temperature, the effects of the temperature gradient experienced all over the face of the quadrant can be seen. In these two plots, the temperature of the radiation source is

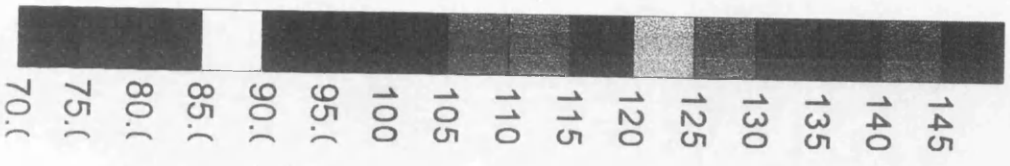
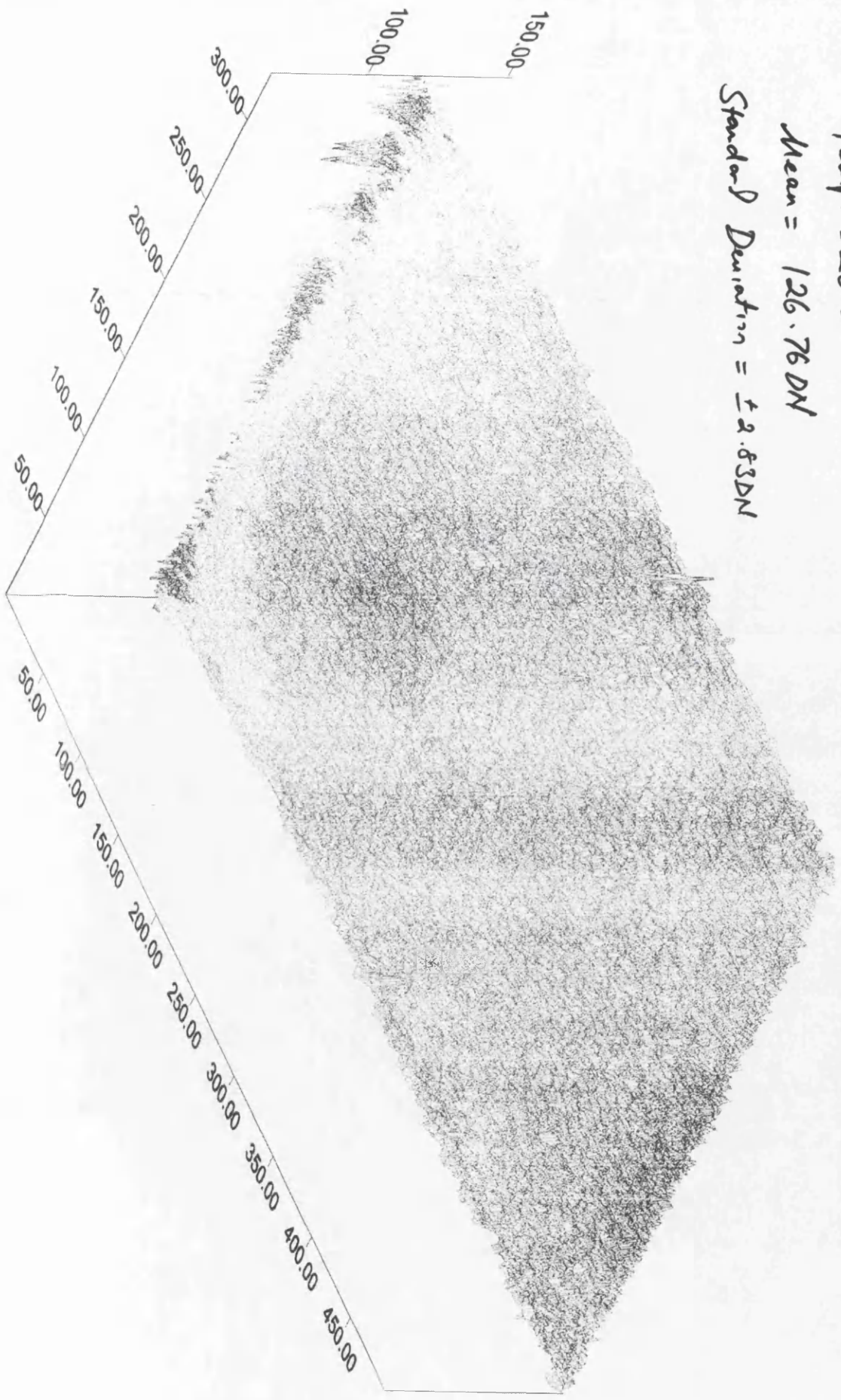
Radiance PMT | 41°

Frame Size = 495 x 380 pixels

Temp. = 20°C

Mean = 126.76 DN

Standard Deviation = ± 2.83 DN



Radarscan Point 110

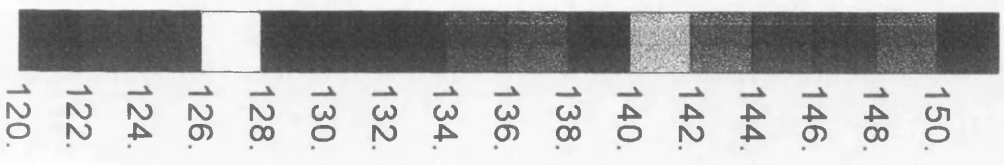
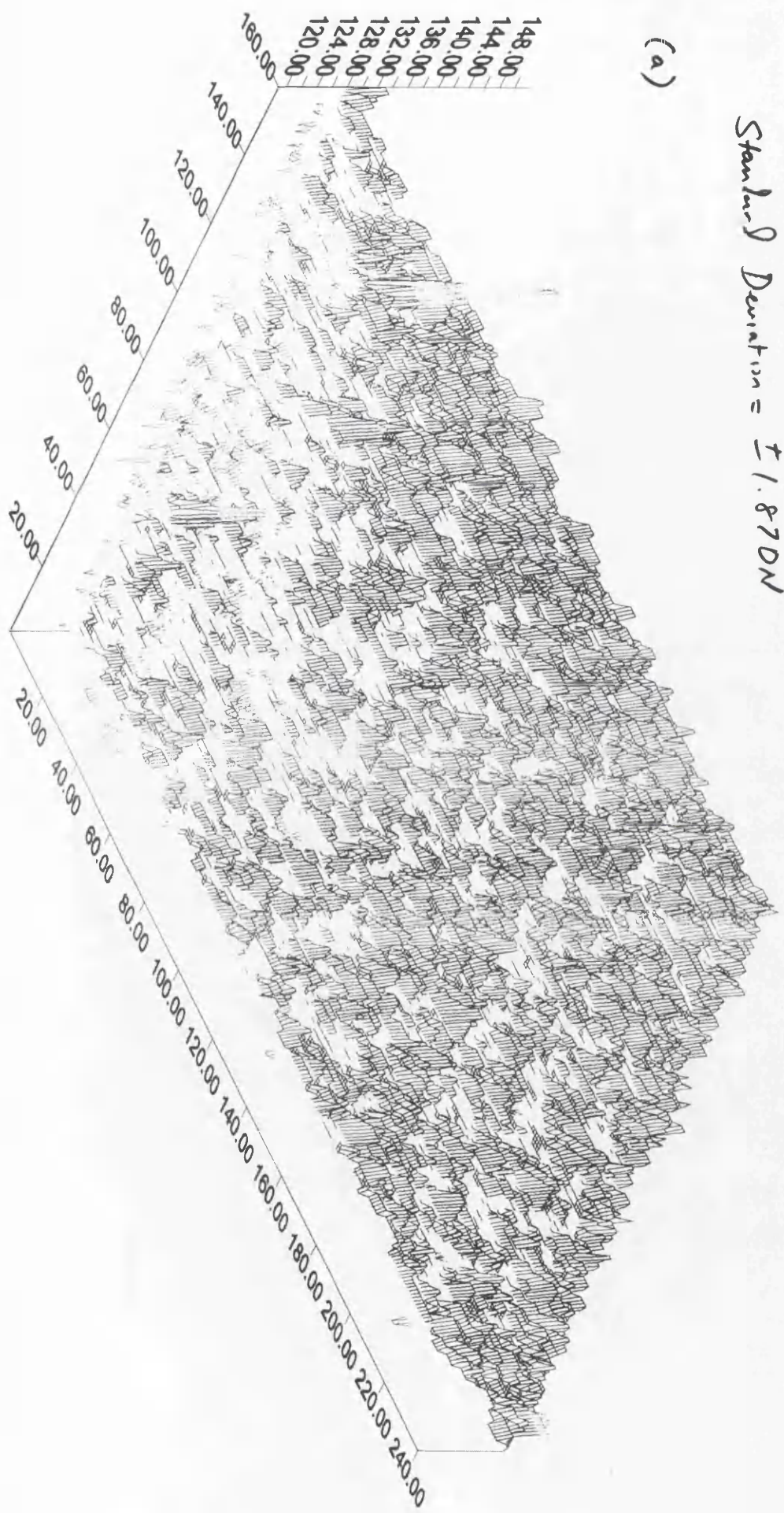
Frame Size = 160 x 240 pixels

Temp. = 20°C

Mean = 122.65DN

Standard Deviation = ± 1.87DN

(a)



Radarance Point 11°

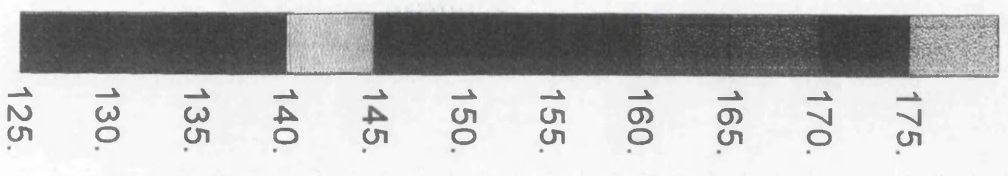
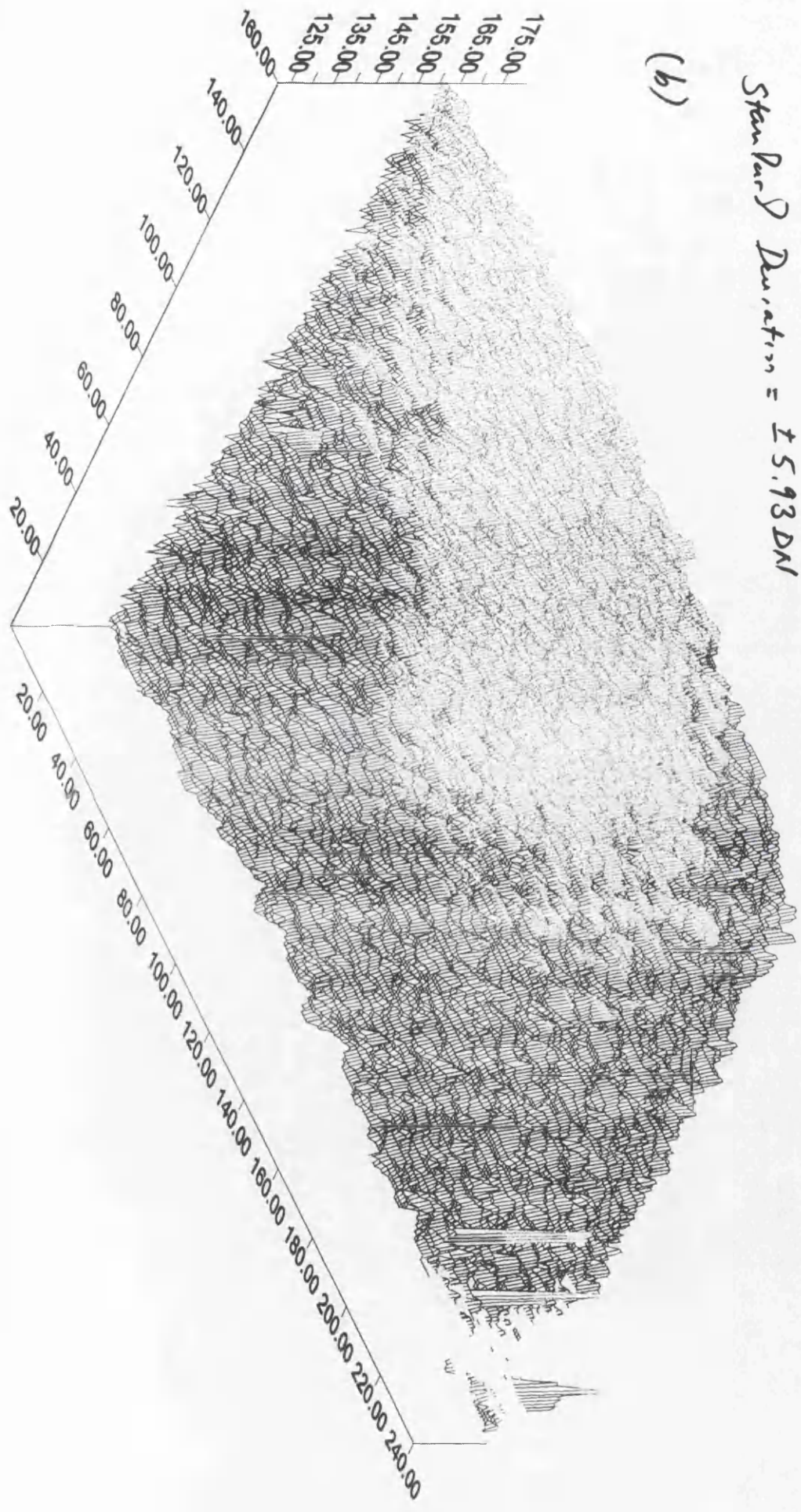
Frame Size = 160 x 240 pixels

Temp = 40°C

Mean = 156.73 DN

Standard Deviation = ± 5.93 DN

(b)



Radiance PM1 / 11°

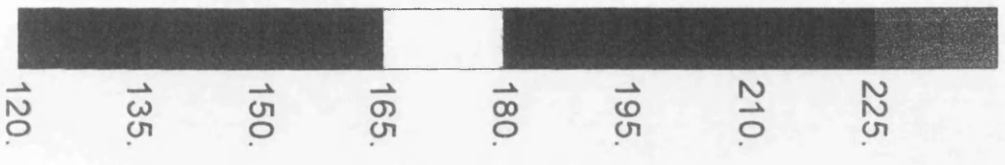
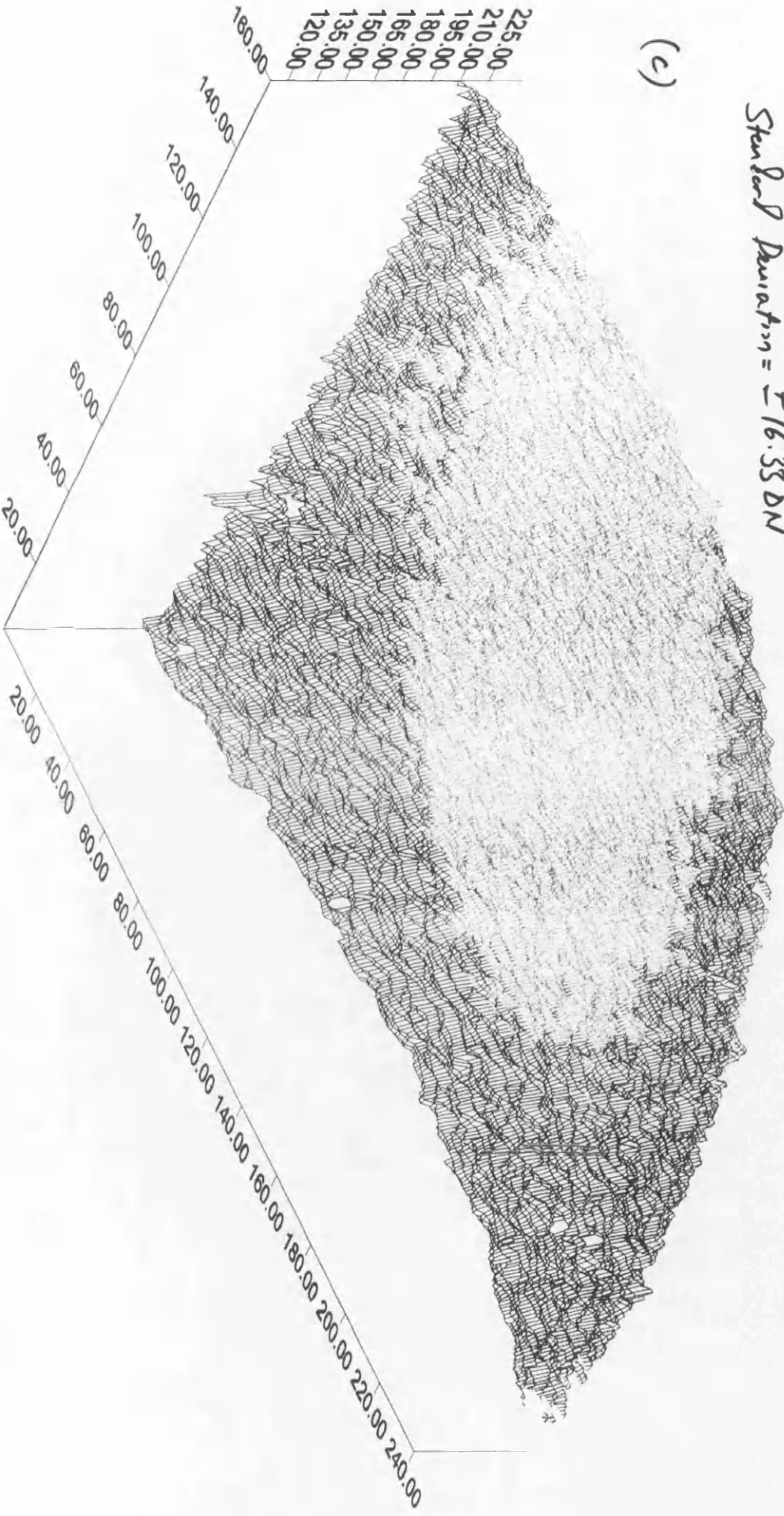
Frame Size = 160 x 240 pixels

$\bar{T}_{emp.} = 60^{\circ}C$

Mean = 217.14 DN

Standard Deviation = ± 16.33 DN

(c)



varying across the face or area of the quadrant. This can be visualized through the colour representation of the different grey level values that were present over the area of the quadrant. In addition, the 3-D perspective representation of the grey level values of the pixels of the patches by the SURFER program have also been given in Fig. 15.21. When the patches are used, effects of the temperature gradient decreases noticeably, thus the uniformity increases all over the patch.

As discussed in Chapter 13, for the higher temperatures such as 50°C and 60°C, after reaching the set temperature it is difficult to keep the temperature of the heating plate stable at the desired level. As mentioned before, almost certainly, the reason for this is the large difference in temperature between the radiation source and the ambient temperature of the environment (i.e. the laboratory) in which the experimental work was carried out. Because of the temperature of this environment is much lower than that of the radiation source, it loses heat quite quickly and the heating pads located on its back are switching on and off many times at short intervals attempting to maintain the specified temperature. In turn, the period of time that is available for taking and recording images of the radiation source at the set temperature is getting very short. The author can testify that, at these higher temperatures, the switching on and off the heated plate is often a few seconds. Whereas the period between this switching at lower temperatures such as 20°C and 25°C can be up to 5 minutes. These large differences between the lower and higher temperatures point to the conclusion that the images of the heated plate for radiometric calibration of the infrared imagers should be confined to lower temperatures. This is obviously a deficiency in the experimental setup which only became apparent towards the very end of the project when there was no time to go back and carry out the same experiments in more suitable conditions.

Closely associated with the behaviour of the radiation source at these too high temperatures is the matter of the temperature gradient that is apparent in the graphical representations given by Fig. 20(b) for 40°C and Fig. 20(c) for 60°C. These show a large gradient in the grey level values rising from the bottom to the top of the plate. This suggests that the strong heat radiation from the vertically mounted plate results in a column of heated air that is rising upwards from the plate surface in the form of a

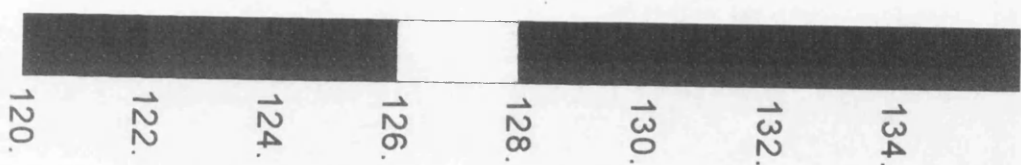
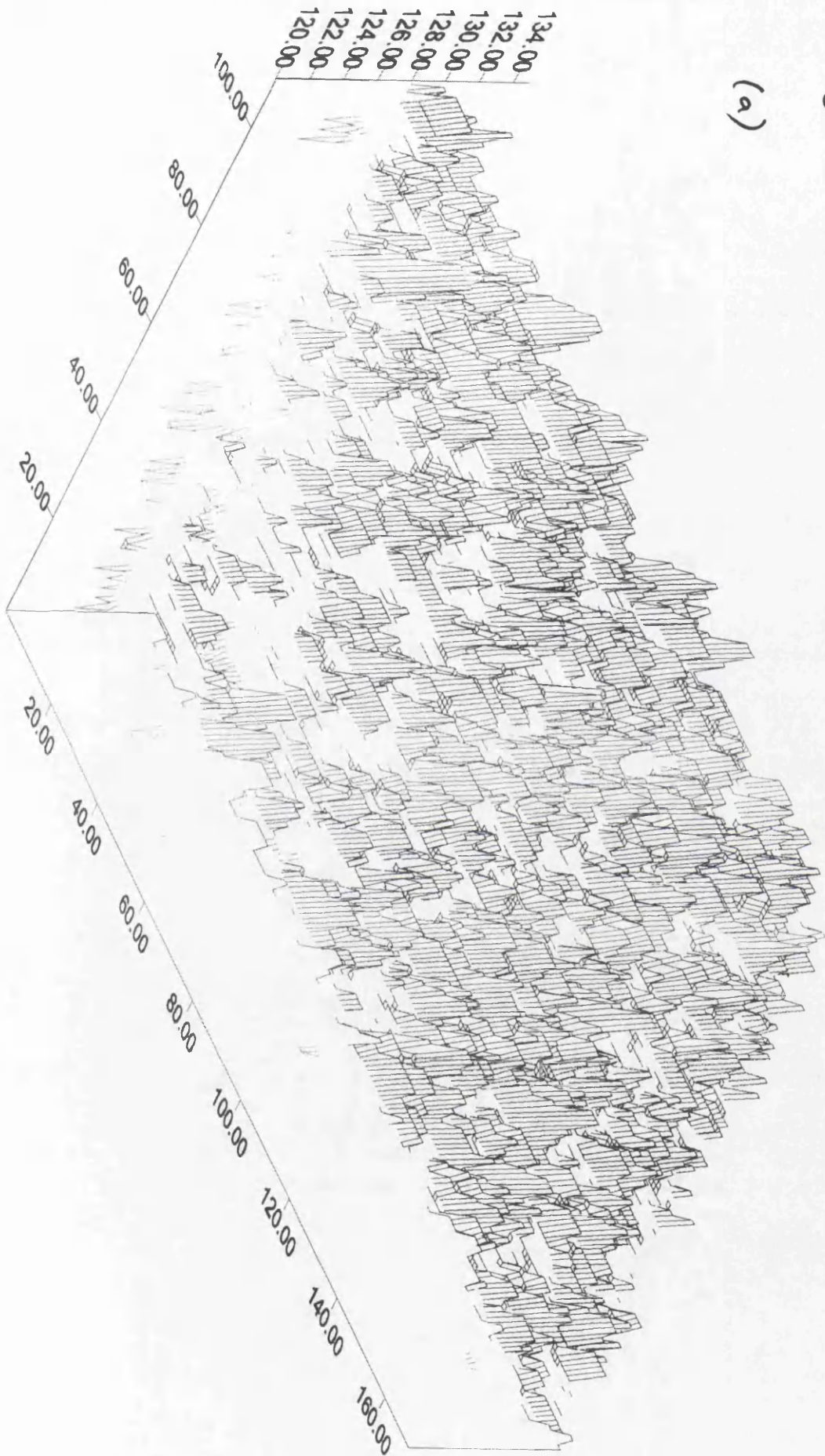
Radiance PMT 11°/20°

Frame Size = 170 X 110 pixels

Mean = 127.53 DN

Standard Deviation = ± 1.75 DN

(a)



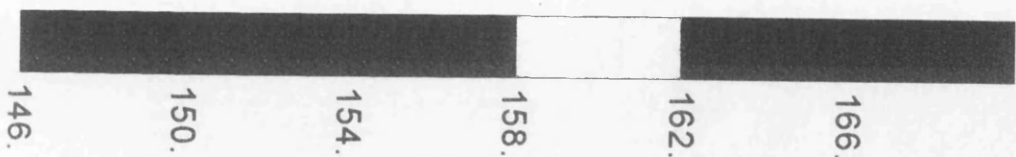
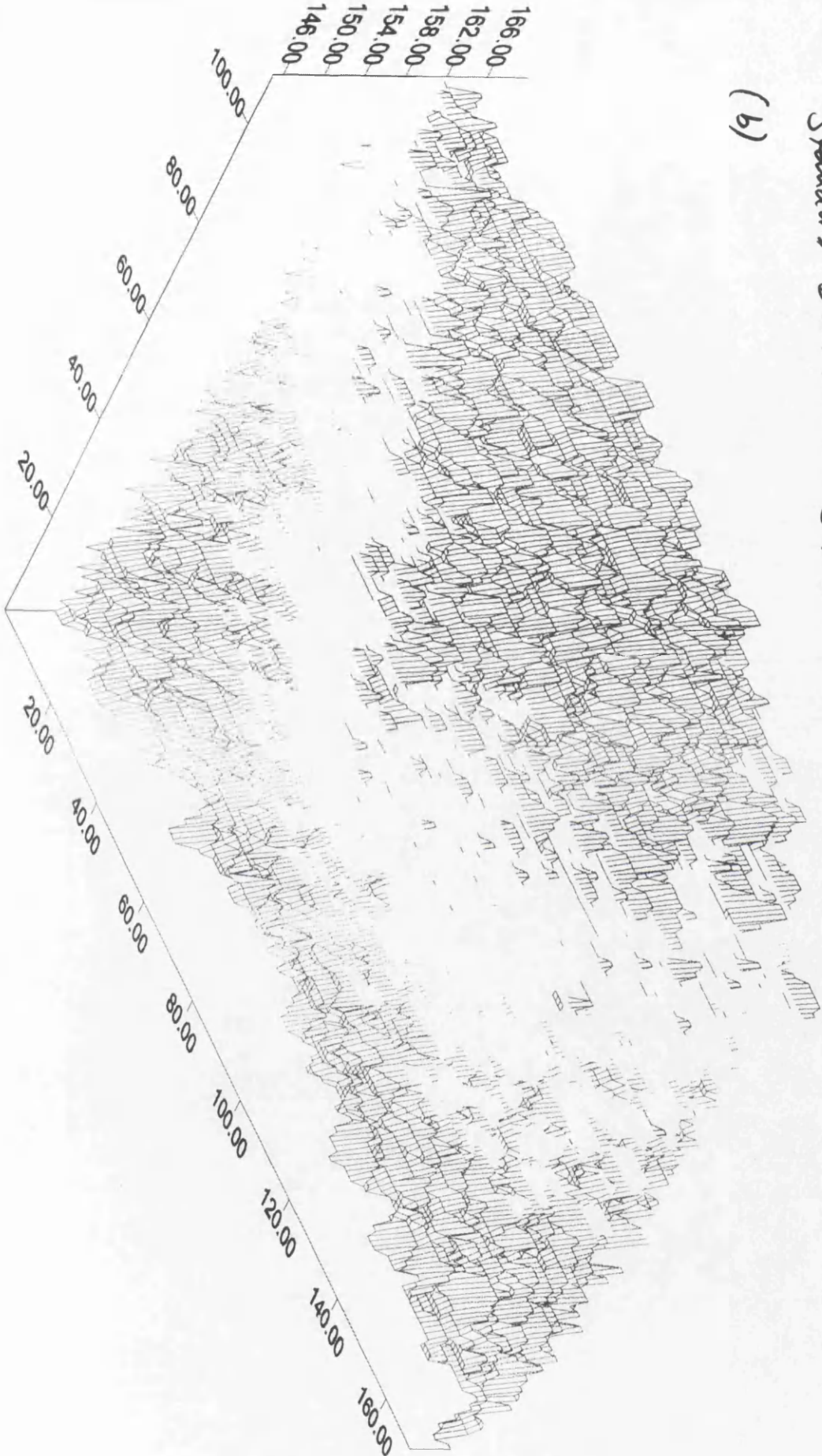
Radiance PM1 11° / 240°c

Frame Size = 170 x 110 pixels

Mean = 159.38 DN

Standard Deviation = ± 3.77 DN

(b)



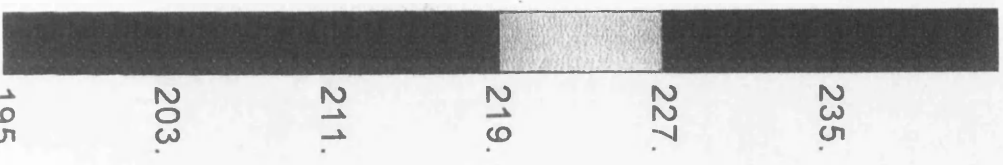
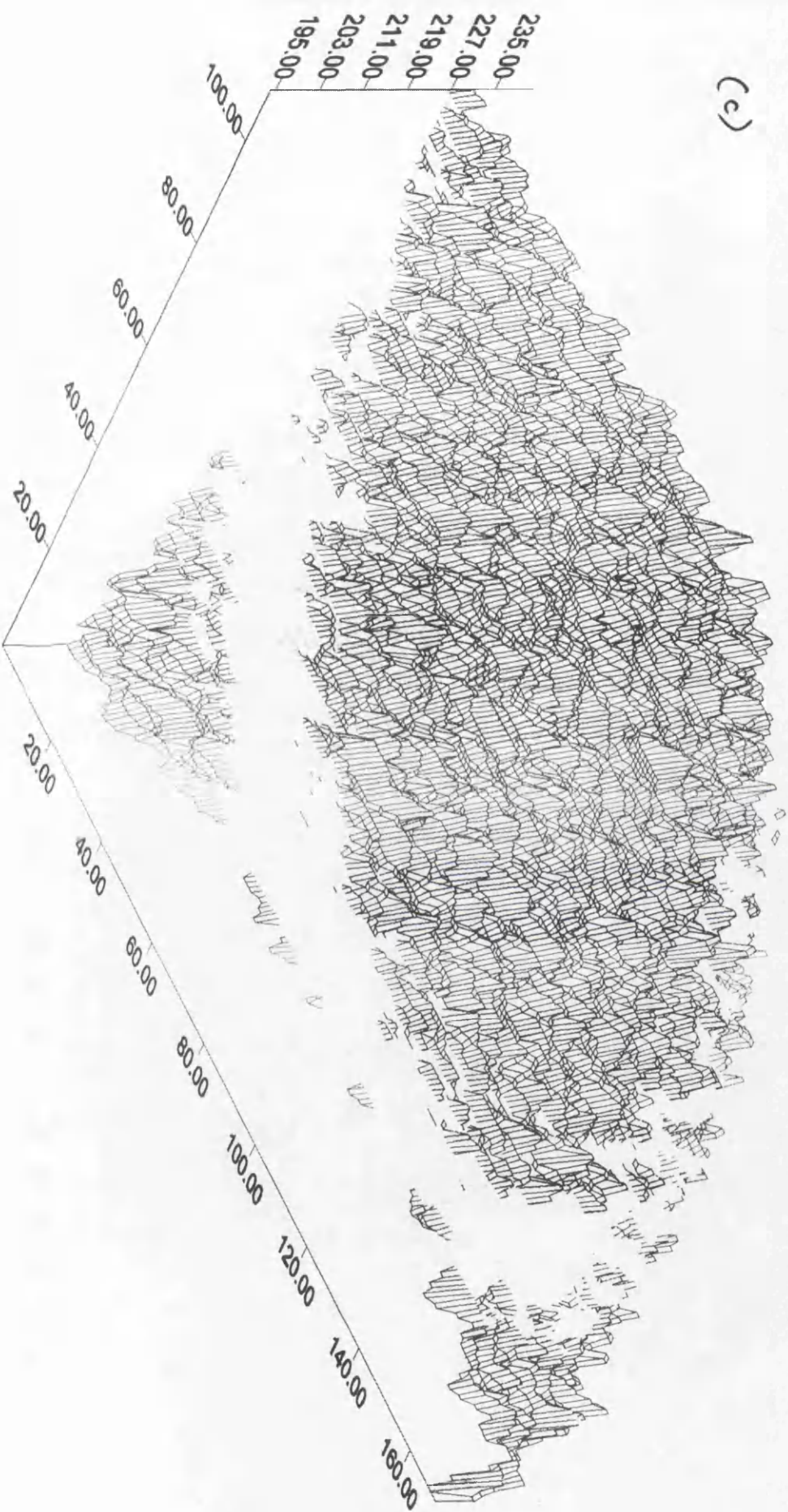
LaRauce PM1 / 11° / 60°

Frame Size = 170 x 110 pixels

Mean = 226.79 DN

Standard Deviation = ± 8.25 DN

(c)



convection current that has its impact on the images that are being acquired by the imager - both of which exhibit this particular characteristic. Again this is a deficiency in the experimental set-up with the PM1 imager which was not realized at the time of the image acquisition. Obviously it can be overcome through the use of lower temperatures with the radiation source.

Although this problem of using too high a temperature arose at least to some extent with almost all the imagers that have tested in this thesis, it affected the result of the radiometric calibration of Radiance PM1 CCD camera most severely since the upper temperature used was 60°C. As can be seen from Figs. 15.21 and 15.22, the standard deviation of the grey level values of the quadrant goes up to $\pm 16\text{DN}$ at higher temperatures, whereas it is less than the $\pm 2\text{DN}$ at the lower temperature. The results and representations obtained from the CCD cameras in this project clearly support this proposition.

15.4 Overall Analysis

On the basis of the results that have been obtained for each of the cameras tested above, some more general conclusions can be drawn. They include the following matters.

(a) For the radiometric calibration of any infrared imaging system, a radiation source on which the temperature can be precisely controlled is required. As can be seen from the experiments with each camera used in this project, the controlling of the temperature of the radiation source with its rapid cooling when the heating source was shut down by the thermostat was something of a problem, more especially at the higher temperatures. Obviously when the temperature of the radiation source was changing quickly, the images of the source had to be recorded in a very short time using the VTR. However, this recording still requires several minutes and, during this period, the temperature of the radiation source may be changing somewhat and does not remain at the desired temperature level. The analogue-to-digital (A/D) conversion of these recorded images of the radiation source was carried out using a one minute

interval with the frame grabber. Although this is quite a short time period, as can be seen from the tables, the means of the grey level values of the digitized images at the same temperature are changing in some cases.

(b) The non-uniformity correction procedure that has been applied to correct the grey level values of the quadrants radiometrically at the middle temperature gave different results for each of the cameras and lenses tested. For the application of this method, the exact reference (calibration) temperatures are required. In addition, the images that have been obtained at these temperatures should have a higher uniformity than those acquired at the temperature which will be corrected. Moreover, a linear relation should also exist between the increment in the grey level values and the corresponding temperature increment. As can be seen from the results, whenever these conditions are provided, the use of this method gave good results and increased the uniformity of the quadrants. However, all the theoretical requirements given above for the successful use of the non-uniformity correction rarely occurs in practical calibration work.

(c) For the radiometric calibration of infrared CCD cameras, quadrants and the patches have been cut from the frames and processed. As mentioned previously, the reason for the use of two different sized and smaller data sets was to try and ensure that an area of uniform radiation is evaluated. The results that have been obtained from the processing of the grey level data of the quadrants and patches showed that the heating pads are quite effective in doing this, since their standard deviation values agree to quite a large extent. However, it is also clear that a smaller rmse value was obtained whenever the smaller patches were used. Of course, by using patches, the pixels with different grey level values that are generally found at the edges of the whole frames have been eliminated and the most uniform part of the quadrant (in radiometric terms) has then been processed.

(d) The statistical processing of the quadrants and patches reveals that most of grey values of the pixels lie inside the range of the $A - 3\sigma \leq g(i,j) \leq A + 3\sigma$. Only the small number of pixels that have grey level values outside this range can be regarded as possibly being dead or blemished pixels that are not responding correctly to the

radiation that is incident upon them. The plotting of the grey level values of the pixels of the quadrants and patches by SURFER helps the user a lot by showing how the grey level values are changing and enabling the blemished pixels to be located visually. As can be seen from the statistical processing tables given above, the number of dead or blemished pixels is really quite small when it is compared to the total number of pixels contained within the quadrant or patch. However, the presence of even a small number of these blemished or incorrectly responding pixels may have a great importance to photogrammetrists as well as being visually unattractive. Moreover, in many more modern infrared imaging systems, the installed image restoration functions such as the analogue gain and offset correction and a resampling function can correct the image radiometrically as soon as the image is taken. In doing so, these hidden control functions can prevent the raw radiometric information from appearing on the image. This has a decided impact on the radiometric calibration of the imager since, in such a situation, the recorded grey level value data have already been restored and enhanced.

(e) As can be seen from the account given above concerning the radiometric calibration of the Agema 550 CCD camera, the calibration of this camera has been carried out using both the 10° and 20° lenses. The same three temperatures have been used for the experiments carried out with these two lenses. However, quite different means of the grey level values have been obtained with the two lenses. For the 20° lens, the mean grey level values were 44, 162 and 236DN for the 30°C, 40°C and 50°C temperatures respectively. For the 10° lens, they were 165, 194 and 233DN respectively for each of these temperatures. As can be seen from these values, the 10° lens has a relatively small range (68DN) of grey level values between the two calibration temperatures. However, with the 20° lens, the corresponding increment was equal to 192DN, which is nearly three times that of the 10° lens. So, the radiometric resolution, which is the ability to discriminate very slight temperature differences, decreases when the 10° lens was employed. This reduced sensitivity could be the result of the extra lens elements which have been placed over the 20° fixed lens to give the 10° angular coverage and could be causing a substantial increase in the absorption and reflection of the object radiation by the lens. This may also be to

do with the temperature settings on the imager when the experiments were carried out. As mentioned before, in the infrared imager, two temperature values that bracket the temperature of the radiation source have to be set. If these settings limit the imager to a small temperature range, it is possible to get more grey level values than that of a bigger range. So, if the temperature settings are different for the two lenses, it is possible to get different ranges of grey level values on the final image.

15.5 Conclusion

In the previous chapter, the results and analysis of the geometric calibration of two representative infrared CCD cameras have been given in some detail. In this chapter, the radiometric calibration of the same two imagers - the Agema 550 and the Amber Radiance PM1 infrared CCD cameras - has been fully discussed. The next chapter will present and analyze the results from the geometric and radiometric calibration of the new generation of thermal video frame scanners that have been produced mainly by the Agema company.

CHAPTER 16: RESULTS AND ANALYSIS OF THE CALIBRATION OF THERMAL VIDEO FRAME SCANNERS

16.1 Introduction

In the previous two chapters, the results obtained during the calibration of infrared CCD cameras have been presented, discussed and analyzed. Thus the geometric and radiometric characteristics of a selection of these commonly used types of imager have been investigated. Following on from this, the results from the geometric and radiometric calibration of some representative examples of the new generation of thermal video frame scanners (TVFS) that have been produced by the Agema company will be given in this chapter. As has been done with the CCD-based imagers, for the geometric calibration of the TVFSs, the linear conformal and the 25-term polynomial transformations have been used to relate the image coordinates of the cross targets of the calibration plate that have been measured by the automatic image matching program SUBPIX to the reference coordinates of these targets which were measured by a Ferranti monocomparator for the previous research project carried out by Dr. Amin. Hence, the effective terms that model the discrepancies (or errors) between the two coordinate sets have been determined. In addition to reporting on this work, the error vectors for all the target crosses recorded by each imager have been plotted to show the pattern of these errors. Furthermore, the systematic and random components of the distortion have been computed and again the results will be reported in this chapter.

For the radiometric calibration of these scanners, the same procedure that has been applied to the other types of imager has also been employed. For this purpose, the FORTRAN programs that have been written by the present author have been used to analyze the images of the radiation source that have been acquired at the three different temperatures by each of the TVFS imagers that have been tested. The results will be presented both in tabular form and in graphical form through the use of the SURFER contouring package to give a 3-D representation of the grey level values of the images of the radiation source. In this way, any dead or blemished pixels that have

grey level values that are outside the acceptable range as shown by the statistical processing of the images will be discovered and their possible sources discussed.

16.2 Agema 1000

The optical configuration and the scanning mechanism of the Agema 1000 imager with its other technical specifications have already been described in some detail in Chapters 3 and 10. The Agema 1000 TVFS (see Fig. 16.1) is a high resolution (565 x 450 pixels) thermal imager which is designed specifically for a wide range of surveillance applications. It uses a 5 element SPRITE detector that is cooled by a small Stirling engine. It is operated in the 8 to 12 μ m wavelength band of the infrared spectrum. As discussed before, it is equipped with dual field optics (5° and 20°) and produces a PAL output signal that can be used for display purposes on a suitable monitor or for the transmission of the image to be recorded on a VTR.

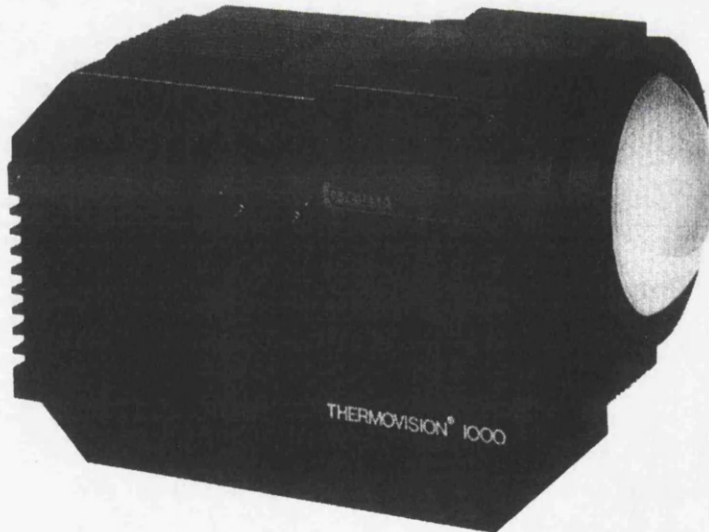


Fig. 16.1. Agema 1000 TVFS.

16.2.1 Geometric Calibration of the Agema 1000

The Agema Engineers brought the Agema Thermovision 1000 to this Department specifically to take images for this project. The images needed for geometric calibration have been acquired using the built-in 20° lens and recorded on magnetic tape by the VTR. Three frames from these analogue images have been digitized using

a frame grabber and pre-processed using the Photoshop image processing package. One of these frames is included as Fig. 16.2. These frames were then input to the image matching program SUBPIX to measure the image coordinates of the cross targets. Afterwards, these coordinates were input to the programs LINCON and POLY25 together with the reference coordinates of the cross targets to carry out the transformation between them and to discover the magnitude and direction of the geometric distortions that were present in the imager. The results from these transformation programs for each frame are given in Table 16.1.

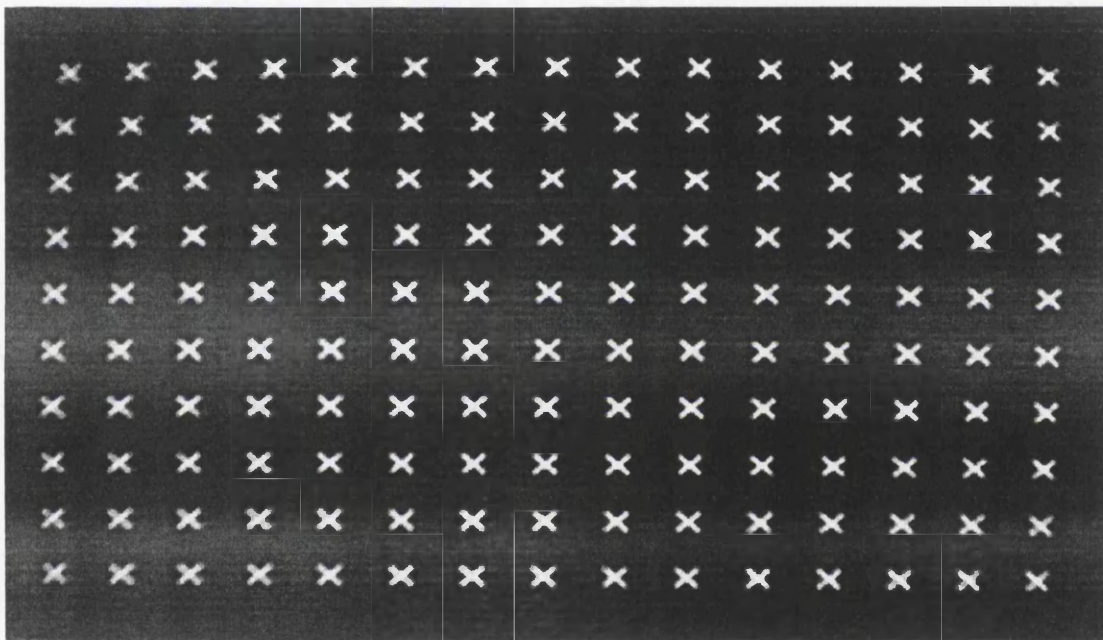


Fig. 16.2. Image of cross targets from the Agema 1000.

The results from the linear conformal transformation showed quite a large distortion occurring in both the x and y-directions at all the image points. The rmse values were found to be ± 11.5 and ± 14.9 pixels in the x and y-directions respectively. The error vectors at the 130 points were produced using the VECTOR program and plotted by a laser printer using the COREL DRAW package. These vector plots of the errors are included as Fig. 16.3. As can be seen from this figure, the geometric distortion is symmetric all over the frame with the highest magnitude errors occurring towards the edges of the frame. This was to be expected due to the spherical surface of the video image that is produced as a result of the scanning geometry. In Fig. 16.3, it can be

seen that the same pattern was obtained from the plots of the error vectors for all three frames obtained using the linear conformal transformation procedure.

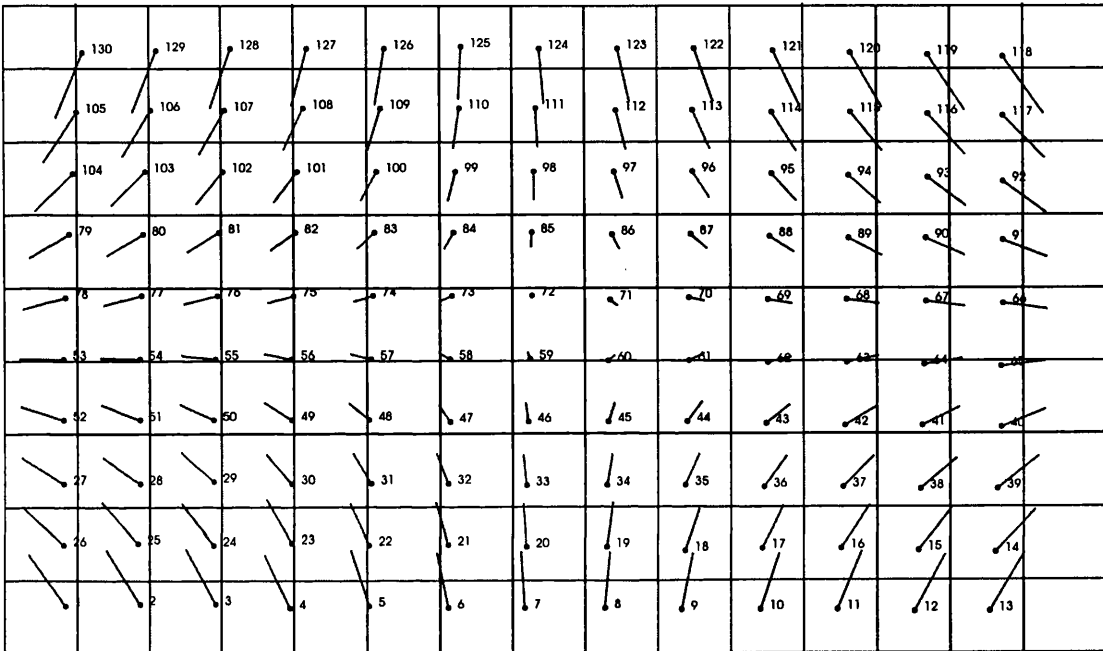
Transformation Procedure	R.M.S.E (Pixels)					
	Frame I		Frame II		Frame III	
	m_x	m_y	m_x	m_y	m_x	m_y
Linear Conformal	± 11.50	± 14.91	± 11.55	± 14.91	± 11.54	± 14.95
3-Terms (Affine)	± 1.22	± 0.92	± 1.33	± 0.87	± 1.34	± 0.86
4-Terms (xy)	± 1.21	± 0.89	± 1.31	± 0.86	± 1.33	± 0.84
5-Terms (x^2)	± 1.15	± 0.61	± 1.25	± 0.58	± 1.26	± 0.61
6-Terms (y^2)	± 1.10	± 0.61	± 1.19	± 0.58	± 1.23	± 0.61
7-Terms (x^2y)	± 1.10	± 0.51	± 1.19	± 0.48	± 1.23	± 0.51
8-Terms (xy^2)	± 0.77	± 0.50	± 0.83	± 0.48	± 0.80	± 0.51
9-Terms (x^2y^2)	± 0.77	± 0.50	± 0.83	± 0.48	± 0.80	± 0.51
10-Terms (x^3)	± 0.19	± 0.49	± 0.24	± 0.48	± 0.22	± 0.51
11-Terms (y^3)	± 0.18	± 0.35	± 0.20	± 0.35	± 0.20	± 0.35
12-Terms (x^3y)	± 0.18	± 0.35	± 0.20	± 0.34	± 0.20	± 0.35
13-Terms (xy^3)	± 0.18	± 0.35	± 0.20	± 0.34	± 0.20	± 0.34
14-Terms (x^3y^2)	± 0.18	± 0.35	± 0.20	± 0.34	± 0.20	± 0.34
15-Terms (x^2y^3)	± 0.18	± 0.35	± 0.20	± 0.34	± 0.20	± 0.34
16-Terms (x^3y^3)	± 0.18	± 0.35	± 0.20	± 0.34	± 0.20	± 0.34
17-Terms (x^4)	± 0.18	± 0.34	± 0.20	± 0.34	± 0.20	± 0.34
18-Terms (y^4)	± 0.18	± 0.34	± 0.20	± 0.33	± 0.20	± 0.34
19-Terms (x^4y)	± 0.18	± 0.34	± 0.20	± 0.33	± 0.20	± 0.34
20-Terms (xy^4)	± 0.18	± 0.34	± 0.20	± 0.33	± 0.20	± 0.34
21-Terms (x^4y^2)	± 0.18	± 0.34	± 0.20	± 0.33	± 0.20	± 0.34
22-Terms (x^2y^4)	± 0.18	± 0.33	± 0.20	± 0.33	± 0.20	± 0.33
23-Terms (x^4y^3)	± 0.18	± 0.32	± 0.20	± 0.33	± 0.20	± 0.33
24-Terms (x^3y^4)	± 0.17	± 0.32	± 0.20	± 0.33	± 0.19	± 0.33
25-Terms (x^4y^4)	± 0.17	± 0.32	± 0.19	± 0.33	± 0.19	± 0.33

Table 16.1. Geometric calibration results for Agema 1000 TVFS with the 20° lens.

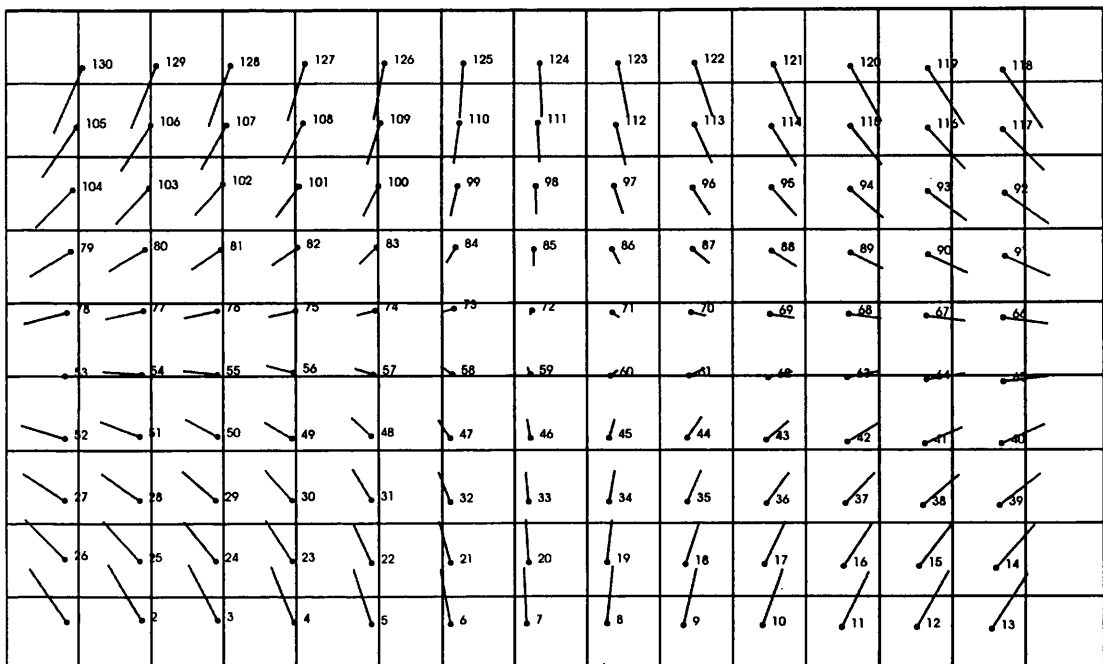
A drastic change in the magnitude of the distortion was obtained when the affine transformation was used. As shown in Table 16.1, the rmse value in pixels was reduced from ± 11.5 (in x) and ± 14.9 (in y) obtained using the linear conformal

transformation, to ± 1.3 (in x) and ± 0.9 (in y) when the affine transformation was used. This showed that the images resulting from this imager contained a big affinity in scale and/or lack of orthogonality between the x and y axes.

a) Plot of the error vectors resulting from the processing of Frame1



b) Plot of the error vectors resulting from the processing of Frame2



c) Plot of the error vectors resulting from the processing of Frame3

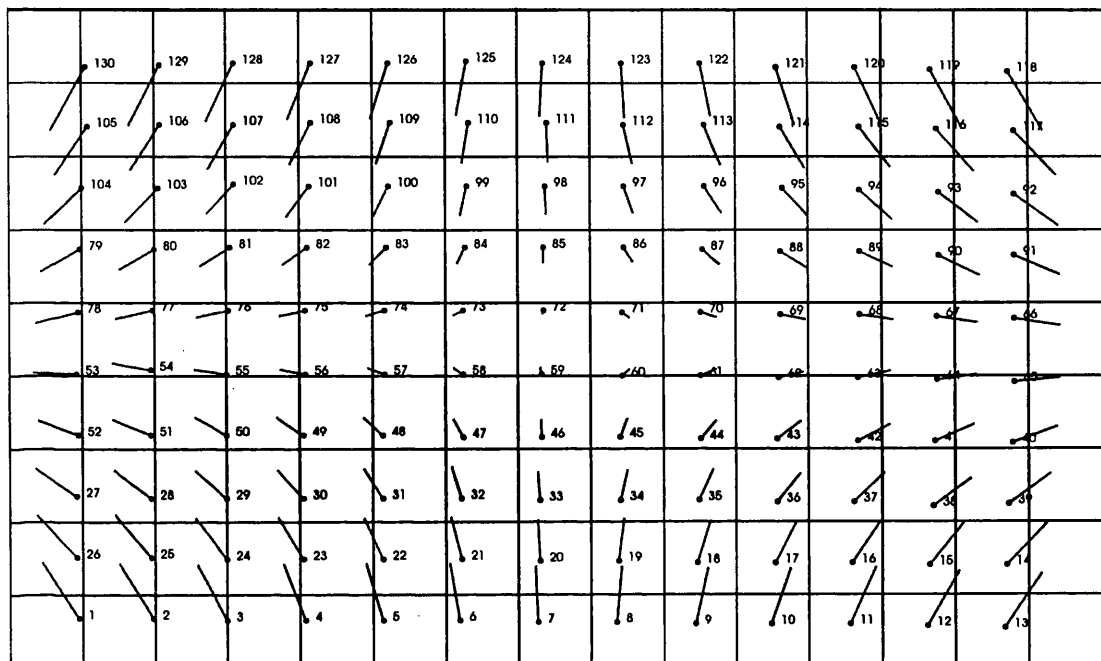


Fig. 16.3(a), (b) and (c). Vector plot from the linear conformal transformation using the Agema 1000 TVFS with 20° lens - vectors are 1.2 times magnified.

Going on to the results obtained from the use of the full POLY25 program, while the four parameter (bilinear) transformation had no effect on the results, the five-parameter transformation reduced the rmse to ± 0.6 pixels in the y-direction by adding the x^2 term.

While the six-parameter transformation showed no improvement in the accuracy, a small drop in the geometric distortion value occurred in the y-direction when the seven-parameter transformation was employed by the adding x^2y term and the rmse value was reduced to ± 0.5 pixel. This term had no effect in the x-direction.

A significant improvement in accuracy resulted in the x-direction when the xy^2 term was added to give the 8-term polynomial. The distortion was reduced from ± 1.3 to ± 0.8 pixels. This term had no effect on the y-direction. In addition, the use of the 9-term transformation showed no drop in the rmse values. Another big improvement

was obtained in the x-direction when the 10-parameter transformation was used by adding the x^3 term. The rmse value was reduced from ± 0.8 to ± 0.2 pixels.

The final significant improvement occurred in the y-direction when the term y^3 was added to the polynomial. The rmse value was reduced from ± 0.50 to ± 0.35 pixels. The use of very high order polynomial transformations containing 4th and 5th order terms had absolutely no effect on the results obtained by the transformation procedure.

In Amin (1986), specific transformation polynomials for use with thermal video frame scanner imagery had been found and have been given in Eq. 9.2. This equation was achieved by eliminating all the terms that showed no significant effect on the accuracy. In the case of the Agema 1000, while the same four terms - xy^2 and x^3 in the x-direction and x^2y and y^3 in the y-direction - are significant in modelling the geometric distortion, the term x^2 in the y-direction was also significant in this respect. While the multi-element objective optics and relay lens (see Chapter 3) may have some influence in this matter, it seems much more probable that the source of this additional geometric disturbance is the redesigned LK4 scanning system of the Agema 1000.

16.3 Agema 900 LW

This is another TVFS from the Agema company that has been tested in this project. The Agema 900 (see Fig. 16.4) uses a single element SPRITE detector which is cryogenically cooled. As can be seen from Table 9.3, three different versions of the Agema 900 are in use. However, in this project, only the Agema 900 LW (Long Wavelength), which is operated in 8 to $12\mu\text{m}$ of the thermal infrared part of the EM spectrum, was tested. As with the Agema 1000, it employs the re-designed LK4 scanning system which also includes two built-in blackbodies for accurate temperature measurements. Although any one of four different and interchangeable lenses (see Table 9.3) can be attached to the Agema 900 LW, only the 20° lens was available for use with the imager. This imager can transmit the analogue thermal image to the VTR employing the PAL video standard.

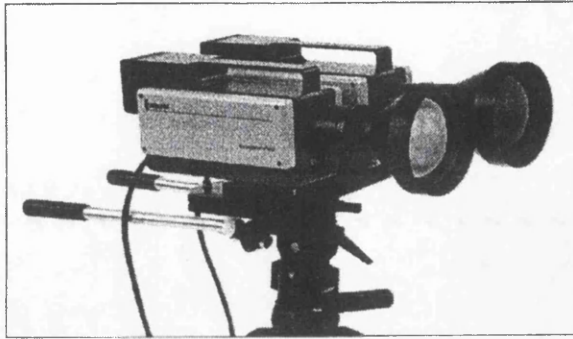


Fig. 16.4. Agema 900 TVFS.

16.3.1 Geometric Calibration of the Agema 900

The Agema 900 TVFS was also brought to the Department by the Agema Engineers specifically for use in the calibration tests. Because of the comparatively low resolution (272(H) x 136(V) pixels) of the Agema 900, only 13 crosses in the x-direction and 6 crosses in the y-direction (making total of 78 crosses) could be covered by the field of view of this imager and still be focussed sharply. Therefore, only 78 cross targets have been used for the geometric calibration of this imager instead of the 130 cross targets used with most of the other imagers. The images of the target crosses were recorded by the VTR and then digitized using the frame grabber. Three frames have again been employed for the geometric calibration. After pre-processing of these frames using Photoshop (see Fig. 16.5), they were input to the program SUBPIX to measure the image coordinates of the crosses of the calibration plate automatically. These measured image coordinates and their reference coordinates were then input to the programs LINCON and POLY25.

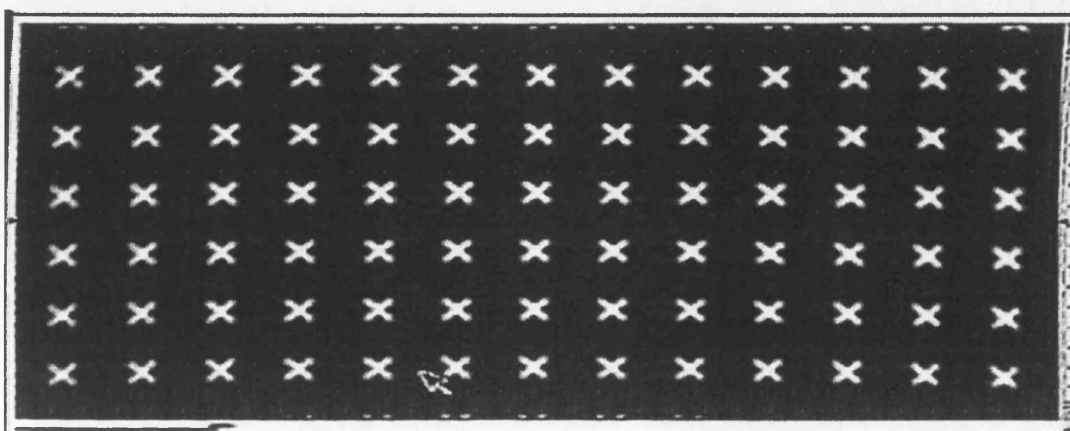


Fig. 16.5. Image of the cross targets taken by the Agema 900 imager.

The results from these transformations for the Agema 900 imager are shown in Table 16.2. The use of the linear conformal transformation resulted in rmse values of ± 5.2 and ± 11.3 pixels in the x and y-directions respectively. The error vectors resulting from this transformation were produced using the VECTOR program and plotted by the printer using COREL DRAW. As can be seen from Fig. 16.6, a quite similar pattern resulted to that produced from the plotting of the error vectors for the Agema 1000 (Fig. 16.3). The only difference here, as explained above, lay in the number of the cross targets that can be covered satisfactorily by this imager. As with the Agema 1000, the geometric distortion is symmetric all over the frame and the highest distortions occur towards the edges of the frame. The spherical surface shape that is typical of this type of imager can also be seen very clearly from Fig. 16.6.

A significant improvement in the accuracy occurred when the affine transformation was used. The rmse values were reduced to ± 0.3 and ± 1.6 pixels in the x and y-directions respectively. This showed that, as with the Agema 1000, the video images produced by the Agema 900 TVFS contain very substantial differences in scale between their x and y-directions. This characteristic appeared in all three frames that were calibrated for this imager.

Turning next to the higher order terms used by the POLY25 program, as can be seen from Table 16.2, a substantial improvement in the geometric accuracy occurred in the y-direction when the x^2 term was added to the polynomial using the 5-term transformation. The geometric distortion in terms of its magnitude was reduced from ± 1.6 to ± 0.6 pixel. Another significant improvement was obtained in the x-direction when the 7-parameter transformation was used by adding the x^2y term to the polynomial. The rmse value was reduced from ± 0.6 to ± 0.3 pixel. Adding the other terms to the polynomials had no absolutely no effect on the results obtained using the polynomial transformation.

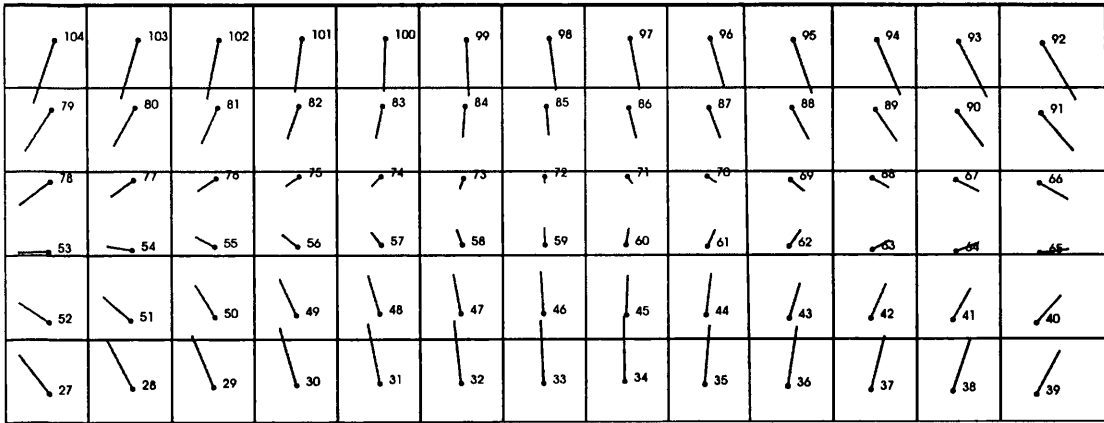
As can be seen from the tables and plots, the results from the geometric calibration of the Agema 900 imager shows that much the same pattern of errors and sequence of

improvements in the accuracy took place to those that occurred with the Agema 1000, except for the last two significant terms.

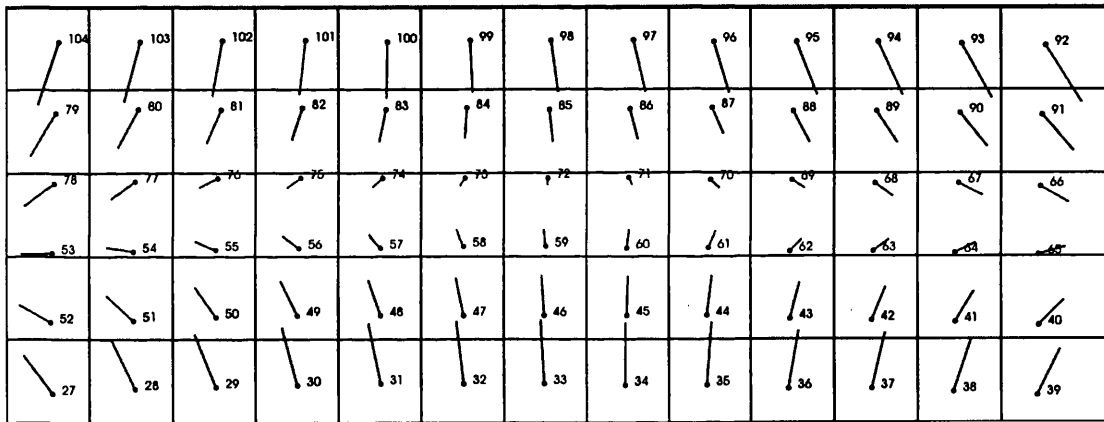
Transformation Procedure	R.M.S.E (Pixels)					
	Frame I		Frame II		Frame III	
	m_x	m_y	m_x	m_y	m_x	m_y
Linear Conformal	± 5.22	± 11.33	± 5.22	± 11.27	± 5.24	± 11.30
3-Terms (Affine)	± 0.34	± 1.56	± 0.32	± 1.56	± 0.30	± 1.53
4-Terms (xy)	± 0.32	± 1.56	± 0.30	± 1.56	± 0.29	± 1.50
5-Terms (x^2)	± 0.32	± 0.62	± 0.30	± 0.56	± 0.29	± 0.60
6-Terms (y^2)	± 0.32	± 0.62	± 0.30	± 0.56	± 0.29	± 0.58
7-Terms (x^2y)	± 0.32	± 0.32	± 0.30	± 0.28	± 0.29	± 0.34
8-Terms (xy^2)	± 0.24	± 0.32	± 0.22	± 0.28	± 0.22	± 0.35
9-Terms (x^2y^2)	± 0.24	± 0.32	± 0.22	± 0.28	± 0.22	± 0.35
10-Terms (x^3)	± 0.21	± 0.32	± 0.20	± 0.28	± 0.19	± 0.33
11-Terms (y^3)	± 0.20	± 0.31	± 0.17	± 0.28	± 0.18	± 0.33
12-Terms (x^3y)	± 0.20	± 0.31	± 0.17	± 0.28	± 0.18	± 0.33
13-Terms (xy^3)	± 0.20	± 0.31	± 0.16	± 0.27	± 0.18	± 0.32
14-Terms (x^3y^2)	± 0.20	± 0.31	± 0.16	± 0.27	± 0.18	± 0.32
15-Terms (x^2y^3)	± 0.20	± 0.31	± 0.16	± 0.27	± 0.18	± 0.32
16-Terms (x^3y^3)	± 0.20	± 0.31	± 0.16	± 0.27	± 0.18	± 0.31
17-Terms (x^4)	± 0.20	± 0.31	± 0.16	± 0.26	± 0.18	± 0.31
18-Terms (y^4)	± 0.20	± 0.30	± 0.15	± 0.26	± 0.18	± 0.31
19-Terms (x^4y)	± 0.20	± 0.30	± 0.15	± 0.26	± 0.18	± 0.30
20-Terms (xy^4)	± 0.20	± 0.29	± 0.15	± 0.26	± 0.17	± 0.30
21-Terms (x^4y^2)	± 0.20	± 0.29	± 0.15	± 0.26	± 0.17	± 0.30
22-Terms (x^2y^4)	± 0.20	± 0.28	± 0.15	± 0.25	± 0.17	± 0.29
23-Terms (x^4y^3)	± 0.20	± 0.28	± 0.15	± 0.25	± 0.17	± 0.29
24-Terms (x^3y^4)	± 0.19	± 0.28	± 0.15	± 0.24	± 0.16	± 0.28
25-Terms (x^4y^4)	± 0.19	± 0.27	± 0.15	± 0.24	± 0.16	± 0.28

Table 16.2. Geometric calibration results for the Agema 900 TVFS equipped with the 20° lens.

a) Plot of the error vectors resulting from the processing of Frame1



b) Plot of the error vectors resulting from the processing of Frame2



c) Plot of the error vectors resulting from the processing of Frame3

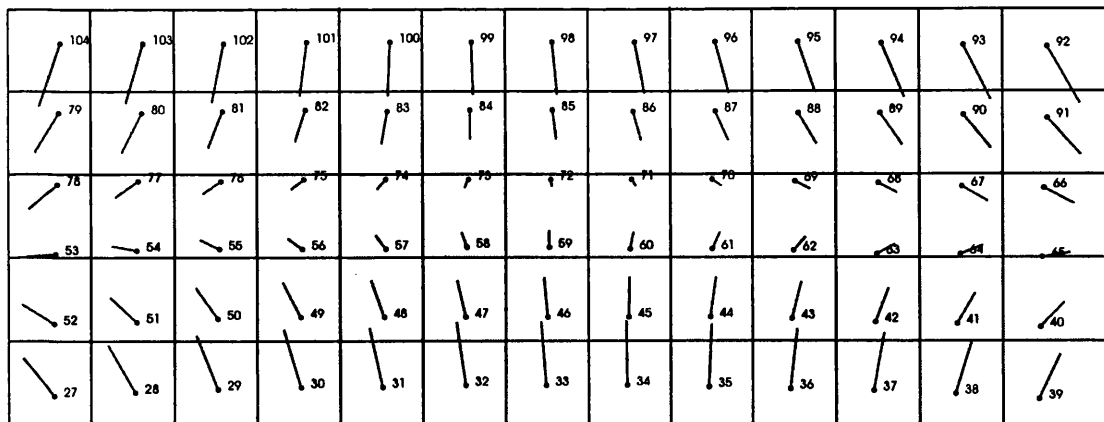


Fig. 16.6. Vector plot from the linear conformal transformation using the Agema 900 TVFS equipped with its 20° lens - the vectors are 2 times magnified.

16.4 Agema 880

The technical specification of this scanner has been given already in Table 9.3. The Agema 880 (see Fig. 16.7) is a thermal imaging system that has been designed primarily for temperature measurement and for the analysis of both dynamic and static heat radiation patterns rather than surveillance or reconnaissance which is the principal role envisaged for the Agema 900 and 1000 imagers. It uses a single element SPRITE detector that converts the incoming radiation emitted from the scene into an electrical signal. The scene is scanned 25 times per second, producing a PAL TV signal for the transmission of the image. The Agema 880 has a spatial resolution of 175 pixels per line and 280 lines per frame. It is operated in the long wavelength region of the infrared part of the spectrum, i.e. in the 8 to 12 μ m wavelength band. It employs a wide range of lenses that makes it possible to adapt the system for use in different operational situations quite easily. The standard range of lenses - with 2.5°, 7°, 12° and 20° fields of view - allow a variety of measurements to be made ranging from small objects over long distances to wide area coverage at close proximity. However, since only the 20° lens was available for the particular unit used for calibration, it has been used with the imager for the purpose of calibration.

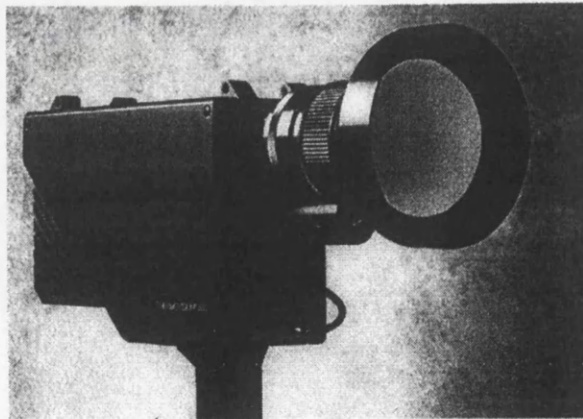


Fig. 16.7. Agema 880 TVFS.

16.4.1 Geometric Calibration of the Agema 880 TVFS

For this project, the Agema 880 TVFS which belongs to the Department of the Biochemistry at the University of Strathclyde has been used. It was borrowed for one

week and brought to the Department for use with a suitable experimental setup - since the laboratory at Strathclyde did not prove to be suitable for calibration purposes. However, during the work with this imager, some problems were encountered. They are:-

- (i) This imager employs liquid nitrogen to cool the detector. This characteristic of the scanner makes it different to the other TVFS imagers that have been tested in this project which have integral cooling engines. Its cooling mechanism is placed at the back of the imager and has to be kept full of the liquid nitrogen. The job of continually topping it up has to be carried out by the user. The Chemistry Department in this University kindly supplied the liquid nitrogen required for the experimental work. It should be noted that this substance can be injurious if spilled on to human skin. Therefore, in the operation of this imager, the present author had to fill the imager cooling mechanism with liquid nitrogen at least once every one hour and often more frequently and wear special protective materials such as special gloves for his hands and glasses for his eyes.
- (ii) The Agema 880 has a special accessory unit provided for direct temperature readout and this has to be used with this equipment in order to acquire images; without using this accessory, it was not possible to obtain images. This unit provides the set of parameters such as the range of temperature and emissivity required for temperature measurement. Thus the imager has to be first connected to this unit and all the parameters required to be set on this unit need to be input correctly. Once this has been done, then the images of the scene can be seen on the television monitor and recorded on the VTR. The setting of these parameters was unfamiliar to the author, so he needed help from the staff who have had experience of using this imager in the University of Strathclyde. They showed him how to set these parameters according to the scene that is being imaged. After setting these parameters correctly, the images of cross targets could be seen on the television monitor.
- (iii) However, another problem was encountered. The image of the cross targets was continually juddering on the monitor. Indeed, with this vibrating motion, it

was not possible to observe the legs of the crosses as straight lines; instead they appeared as a string of small squares! Quite apart from this disconcerting feature, given the low resolution of this imager (280 x 175), the images of the cross targets were not sharp. It was obvious to the author that these matters would definitely create problems for the matching program. Because of the low resolution, the author decided to alter the experimental setup and take the images of only a small number of crosses around the centre of the target plate for test purposes in order to give better conditions for the calibration. Furthermore to prevent the juddering of the cross targets, the image on the monitor screen was frozen to give a single image through the freezing option fitted to the accessory unit.

Eventually and only after much experimentation, it was found that only 9 crosses on the target plate could be covered satisfactorily and only one frame was obtained and used for the test. This image was recorded on magnetic tape using the VTR and digitized using the frame grabber. The image of this frame has been enhanced by Photoshop and is shown in Fig. 16.8. Even after enhancement, the blurred appearance of the crosses is still apparent.

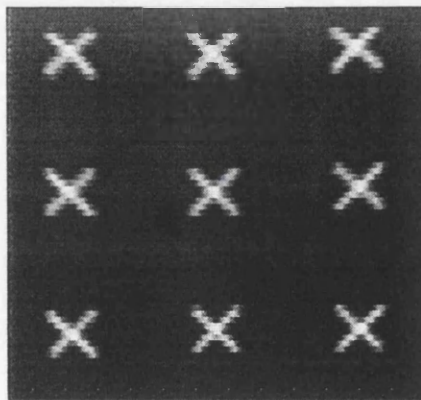


Fig. 16.8. Image acquired by the Agema 880 imager.

This frame was then input to the program SUBPIX to measure the image coordinates of cross targets. In spite of the difficulties that have been explained above, the program was able to measure the positions of all the crosses successfully. Afterwards, these image coordinates of the crosses were input to the transformation programs LINCON and POLY25. The results are given in Table 16.3.

Transformation Procedure	R.M.S.E (Pixels)					
	Frame (Agema 880) No. of Points = 9		Frame (Agema 470) No. of Points = 15		Frame (Agema 470) No. of Points = 12	
	m_x	m_y	m_x	m_y	m_x	m_y
Linear Conformal	± 3.00	± 3.38	± 1.80	± 2.93	± 2.63	± 2.02
3-Terms (Affine)	± 0.64	± 1.68	± 0.73	± 0.82	± 0.68	± 0.71
4-Terms (xy)	± 0.59	± 1.61	± 0.69	± 0.82	± 0.68	± 0.71
5-Terms (x^2)	± 0.51	± 1.16	± 0.56	± 0.81	± 0.65	± 0.71
6-Terms (y^2)	± 0.37	± 1.02	± 0.55	± 0.59	± 0.65	± 0.71
7-Terms (x^2y)	± 0.37	± 0.68	± 0.54	± 0.44	± 0.62	± 0.63
8-Terms (xy^2)	± 0.02	± 0.50	± 0.54	± 0.25	± 0.21	± 0.63

Table 16.3. Geometric calibration results for Agema 470 and 880 TVFSs.

Given the small number of cross coordinates available for measurement and used in this computation, the effective terms that have been shown in this table cannot fully model the geometric distortion inherent in the images. In particular, it is noticeable that the final rmse value in y-direction are considerably larger than that in x. In this respect, because of the lack of redundancy, the results from the polynomial transformation in Table 16.3 are only included up to 8-terms. Beyond this term, the obtained results would give wrong information since the polynomial will simply fit the small number of points correctly to all the available target crosses with no residual errors - since there is no redundancy. However, the plot of the error vectors shown in Fig. 16.9 gives the error vectors for each cross target using the linear conformal transformation. These showed the same general pattern as the Agema 900 and 1000 imagers. It is significant that, once again, an affine distortion is the largest geometric distortion that is present in the image. Also the plot shows the spherical distortion pattern that is typical of a TVFS.

16.5 Agema 470

This imager is the one of the Agema 400 series TVFS. In this project, only the Agema 470 (see Fig. 16.10) from this series was tested; the other imager in this series which



Fig. 16.9. Vector plot from the linear conformal transformation using the image data from the Agema 880 TVFS equipped with the 20° lens - vector are 3 times magnified.

is called the Agema 450 was not available for test. It should be noted that, while all the other TVFS imagers that have been calibrated in this research operate in the 8 to 14 μm thermal infrared region, the Agema 470 is deployed in the 2 to 5 μm middle infrared band of the EM spectrum. It uses a single SPRITE detector which is cooled by an integral thermoelectric cooling system. The Agema 470 generates 100 pixels per line and 280 lines per frame. As can be seen from Table 9.3, a wide variety of lenses can be used with the Agema 470. However, since only the 20° lens was available on the example used in this project, it was used to take the images utilised for calibration purposes. The analogue image which is output from the Agema 470 is in PAL format and was recorded on the magnetic tape by the VTR for later processing.

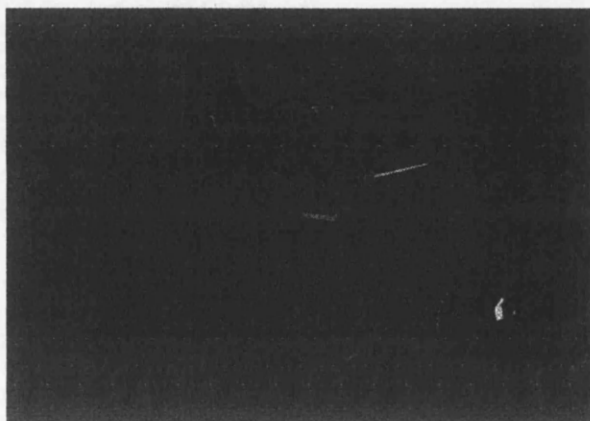


Fig. 16.10. Agema 470 imager.

16.5.1 Geometric Calibration of the Agema 470

The Agema 470 scanner used in this project belongs to the Civil Engineering Department of Glasgow Caledonian University. However, it was not possible to bring the imager to this Department to make the required tests. Therefore, the experiment had to be carried out in that Department at Caledonian University. A large store with no windows provided an adequate environment for the data acquisition. Since this imager has a very low resolution, the cross targets of the calibration plate were of such a small size that they appeared as circular blobs on the monitor when the imager and the target plate were set to the appropriate positions to image all the cross targets. The author and the staff from Caledonian University who are familiar with this imager spent quite some time to get good images of the whole plate with this imager, but without success. So, as with the Agema 880, it was decided to take images of a smaller number of cross targets with the Agema 470 to get better resolution. Thus two different images which have 12 and 15 crosses respectively have been obtained. These images were recorded on the VTR and later digitized by a frame grabber. One frame for each image have been acquired for calibration purposes (see Fig. 16.11(a) and (b)).

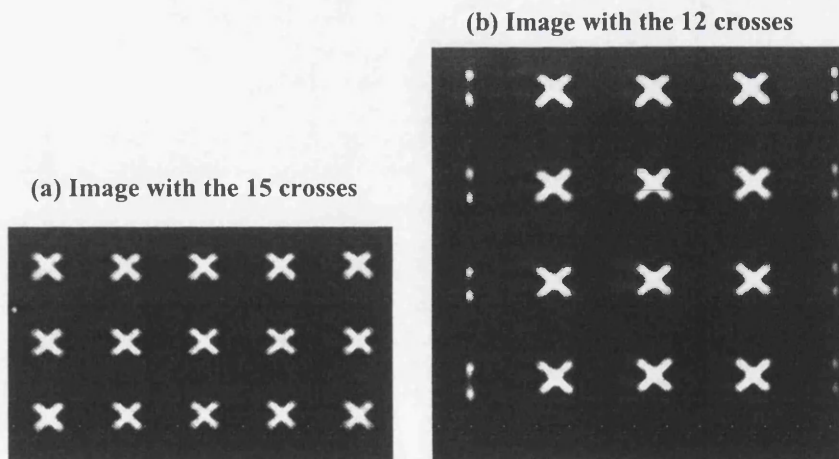
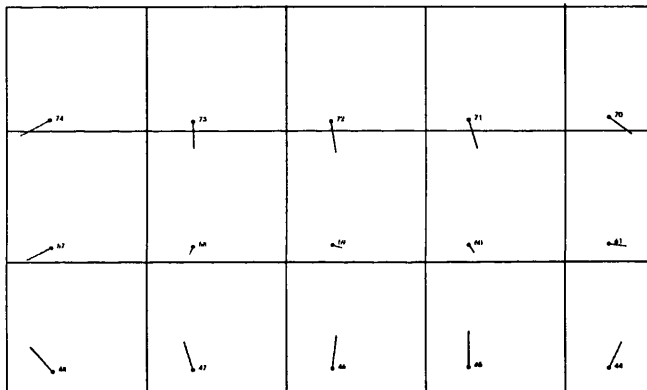


Fig. 16.11(a) and (b). Images from the Agema 470.

These frames were first input to the image matching program SUBPIX. The resulting image coordinates of the cross targets were then input together with their reference coordinates to the transformation programs LINCON and POLY25. The results from each frame are given in Table 16.3. As has been noted above for the Agema 880, after the first few low-order terms, the remaining terms in this table do not model the

distortions inherent in these images since the number of crosses that can be processed for this calibration is too small. However, once again, the vector plots of the residual errors for these images show a similar systematic pattern to those produced by the Agema 1000 and 900. As can be seen from Fig. 16.12, the distortion is symmetric all over the frame with the highest magnitude occurring towards the edges of the frame while the lowest ones are generated by the central targets. This is the typical pattern that is encountered with the video images produced by all TVFS imagers because of their scanning geometry and spherical imaging surface. Once again, the presence of a large affinity between the image scales in the x and y-directions is very obvious in Table 16.3.

(a) Error vector plot for 15 crosses



(b) Error vector plot for 12 crosses

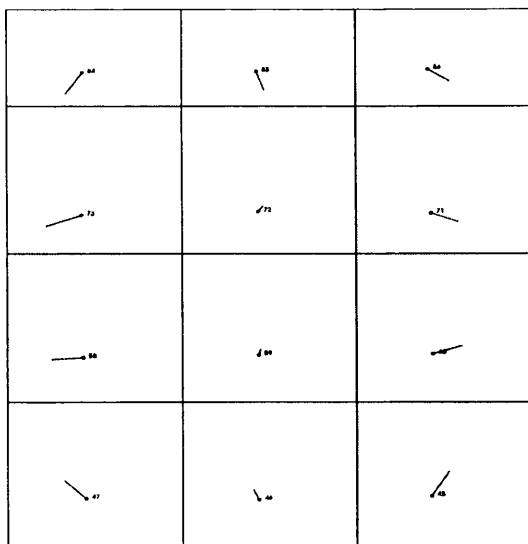


Fig. 16.12(a) and (b). Vector plots from the linear conformal transformation using the image data from the Agema 470 TVFS equipped with the 20° lens - vectors are 6 times magnified.

16.6 Systematic and Random Components of the Distortion

As has been done with the CCD cameras, the procedure described in Section 13.5.4 has also been applied to determine the systematic and random components of distortion that are produced by the Agema 1000 and 900 TVFS since more than one frame is available for them. The results are given in the Table 16.4 below. As can be seen from this table, the distortion is highly systematic, mainly due to the effect of the scanning geometry. Thus the distortion produced by the video frame scanners can be described as being both systematic and symmetric at the same time.

Imager \ RMSE	m_{xs} (pixel)	m_{ys} (pixel)	m_{xr} (pixel)	m_{yr} (pixel)
Agema 1000 with 20° lens	±11.52	±14.93	±0.28	±0.25
Agema 900 with 20° lens	±5.22	±11.30	±0.18	±0.28

Table 16.4. Systematic and random distortions in the Agema 1000 and 900 TVFS.

From the account given up to till now, it will be apparent that the lower resolution video frame scanners could not be tested fully in terms of their geometric calibration because they cannot cover all the cross targets on the calibration plate and still give an adequate or usable image. Although they show the same systematic pattern of geometric distortion as the high resolution Agema 1000 TVFS, the higher-order terms that model the distortion cannot be computed due to the small number of target crosses that are available for measurement. So, for a proper test of these low resolution imagers, a smaller sized calibration plate with a greater density of target crosses will be required. However, because of the time limitation of this project, this alternative type of target plate has been designed but not built. In the next section of this chapter, the radiometric calibration of the Agema 1000 and 900 imagers will be discussed in some detail.

16.7 Radiometric Calibration of the Agema 1000

For this purpose, the images of the radiation source have been taken by the Agema 1000 TVFS at three different temperatures (25°C, 35°C and 45°C). These analogue

images, which were recorded on magnetic tape using VTR, have been digitized by a frame grabber and three frames for each temperature have been processed. Quadrants and patches with two different sizes have been extracted from these frames and input to the FORTRAN programs for further processing. The results from the STMN and PRNU programs are shown in Table 16.5 which gives the means and standard deviations of the individual quadrants and the averaged quadrants for each temperature. In addition, the non-uniformity correction for the averaged quadrant that has been computed for the middle temperature (35°C) is also presented.

As can be seen from this table, the mean grey level values of the quadrants for the same temperature were quite different to one other, especially at the 25°C temperature. As explained in Chapter 15, the reason for this could be that the temperature of the radiation source is changing quite quickly while the thermostat attempts to keep the temperature at the desired level. So, it seems that the temperature was not stable all over the radiation source. Fig. 16.13 shows the images of the quadrants that were obtained at 25°C with their fixed patterns that have been produced using the same method that has been applied to the CCD cameras. As can be seen from these images, they have somewhat different fixed patterns and temperature distributions. The images of the averaged quadrants for each temperature are shown in Fig. 16.14. Their fixed patterns are also given to show how they are changing with the different temperatures.

In addition, as can be seen from Table 16.5, the non-uniformity correction procedure did not give a very good result, which is not too surprising given the big standard deviations of the averaged quadrants at the reference temperatures - 25°C and 45°C for the Agema 1000 and 25°C and 65°C in the case of the Agema 900. However, the comparatively small temperature difference between these reference temperatures also decreases the effects of this correction. In Fig. 16.15, a graph of the response variation versus the different temperatures is shown. The mean grey level values are computed as being 105, 161 and 174 for each of the three temperatures respectively. Obviously the mean grey level value between 105 and 174 is 140, whereas the actual measured value is 161. This shows that the mean grey level increment with respect to the

temperature increment is far from linear, which also has a considerable effect on the non-uniformity correction.

Temp.	Image	Mean of the grey level values	Rmse of the grey level values	Mean of the averaged images before corr.	Rmse of the averaged images before corr.	Mean after corr.	Rmse after corr.
Agema 1000 with 20° lens (Quadrant image size = 280(H) x 160(V) = 44,800 pixels)							
25°C	1	134.21	5.76	104.62	6.37	104.00	0.00
	2	94.75	10.54				
	3	84.90	9.03				
35°C	1	168.52	7.47	161.43	3.82	161.75	5.36
	2	162.06	5.67				
	3	153.71	5.65				
45°C	1	187.06	6.96	173.84	5.54	174.00	0.00
	2	169.43	7.09				
	3	165.05	7.16				
Agema 1000 with 20° lens (Patch image size = 170(H) x 110(V) = 18,700 pixels)							
25°C	1	134.60	5.53	104.58	6.12	104.00	0.00
	2	94.47	10.15				
	3	84.67	8.88				
35°C	1	168.73	7.72	161.85	3.79	161.49	4.69
	2	162.50	5.65				
	3	154.32	5.54				
45°C	1	189.72	6.00	176.49	4.18	176.00	0.00
	2	171.83	6.16				
	3	167.91	6.04				
Agema 900 with 20° lens (Quadrant image size = 280(H) x 140(V) = 39,200 pixels)							
25°C	1	16.17	3.11	16.43	2.47	16.00	0.00
	2	16.90	2.89				
	3	16.22	2.88				
45°C	1	162.46	10.46	131.56	10.40	130.50	6.56
	2	128.74	11.03				
	3	103.47	11.07				
65°C	1	208.27	10.66	208.56	9.82	208.00	0.00
	2	208.85	10.75				
Agema 900 with 20° lens (Patch image size = 170(H) x 110(V) = 18,700 pixels)							
25°C	1	16.86	2.12	17.12	1.37	17.00	0.00
	2	17.69	2.32				
	3	16.82	1.94				
45°C	1	166.10	8.35	135.11	8.31	134.51	5.45
	2	132.57	9.12				
	3	106.64	9.13				
65°C	1	210.82	9.11	211.35	8.10	211.00	0.00
	2	211.88	9.16				

Table 16.5. The means and the standard deviations of the grey level values of the pixels of the quadrants and patches before and after radiometric correction for the Agema 1000 and 900 imagers.

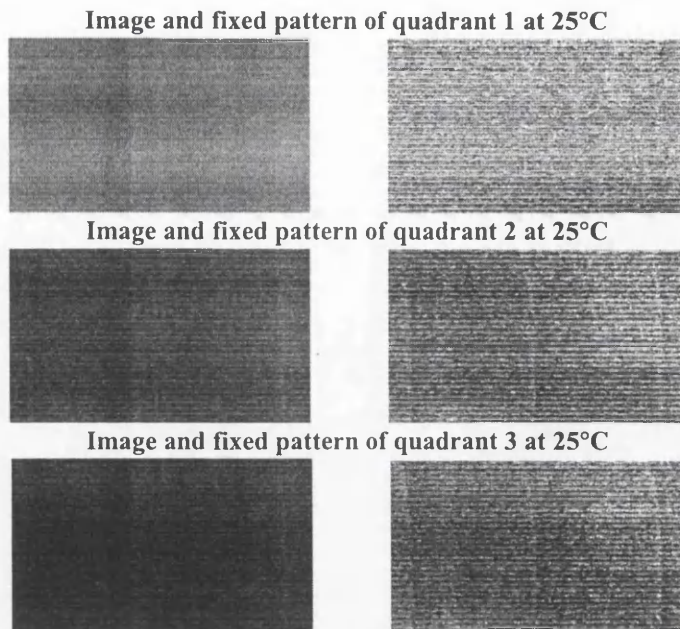


Fig. 16.13. Images and fixed patterns of the quadrants for the 25°C temperature

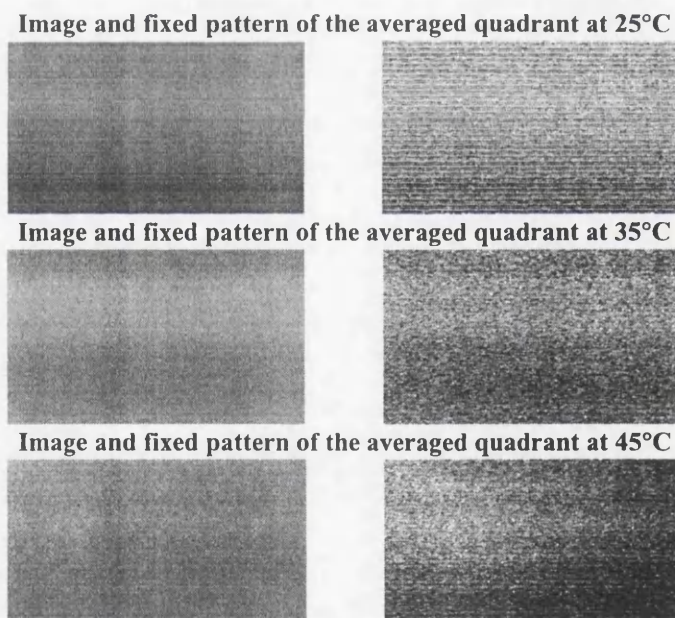


Fig. 16.14. Images and fixed patterns of the averaged quadrants for each temperature.

As was done with the CCD cameras, smaller sized patches were extracted to ensure an area of uniform temperature and emitted radiation and to test the influence of the heating pads on the radiometric calibration of the Agema 1000. As can be seen from Table 16.5, there was little improvement in terms of the rmse value. The heating pad itself appears to generate and distribute the same amount of heat uniformly over the whole of the patch and so this did not affect the results too much.

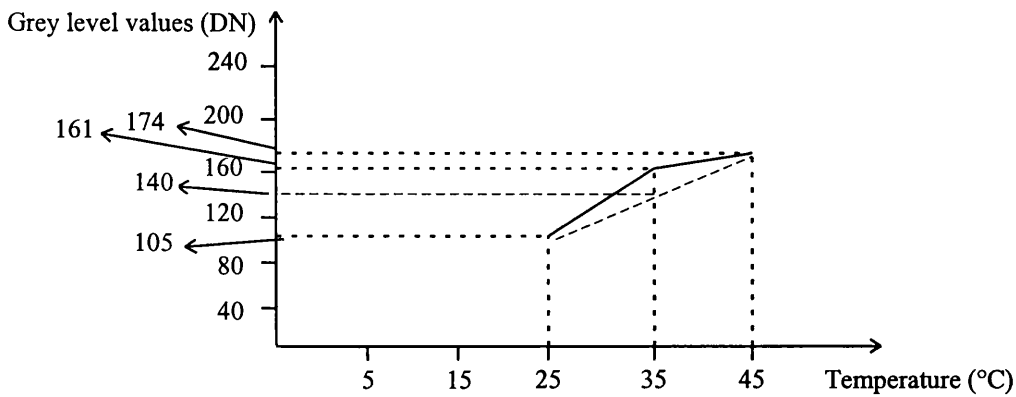


Fig. 16.15. Changes in the mean grey level value of the quadrants at different temperatures

For statistical processing of the averaged quadrants, the appropriate data was input to the program STAT with their mean and standard deviation values. The results are given in Tables 16.6 and 16.7 for both the quadrants and the patches. As can be seen from these tables, only a small number of pixels lie outside the range of $A \pm 3\sigma$. For example, for the averaged quadrants used at each temperature, only 127, 152 and 66 pixels out of 44,800 pixels lie outside this range respectively and they can be regarded as pixels that are blemished and do not respond fully to the radiation that is incident upon them.

Agema 1000 with 20° lens	Total number of pixels in the quadrant: 280(H)x160(V)= 44,800 pixels			
	Number of pixels greater than $\sigma/2\sigma/3\sigma$	Number of pixels less than $\sigma/2\sigma/3\sigma$	Total number of pixels outside the range of $A\pm3\sigma$	Percentage of the number of pixels lie inside the range of $A\pm3\sigma$
Temp.= 25°C / Averaged Frame				
	6,201	8,645	14,846	≅ 67%
	450	1,391	1,841	≅ 96%
	3	124	127	≅ 99.72%
Temp. = 35°C / Averaged Frame				
	5,516	7,686	13,202	≅ 71%
	514	1,156	1,670	≅ 96%
	55	97	152	≅ 99.66%
Temp. = 45°C / Averaged Frame				
	7,772	8,339	16,111	≅ 64%
	1,086	574	1,660	≅ 96%
	60	6	66	≅ 99.85%
Temp. = 35°C / Non-Uniformity Corrected Frame				
	6,299	6,756	13,055	≅ 71%
	1,529	893	2,422	≅ 95%
	191	46	237	≅99%

Table 16.6. The statistical processing of the averaged quadrants for the Agema 1000.

Agema 1000 with 20° lens	Total number of pixels in the patch: 170(H)x110(V)= 18.700 pixels			
	Number of pixels greater than $\sigma/2\sigma/3\sigma$	Number of pixels less than $\sigma/2\sigma/3\sigma$	Total number of pixels outside the range of $A\pm3\sigma$	Percentage of the number of pixels lie inside the range of $A\pm3\sigma$
Temp. = 25°C / Frame No.1				
	2,315	3,374	5,689	≅ 70%
	123	630	753	≅ 96%
	6	113	119	≅ 99%
Temp. = 25°C / Frame No.2				
	3,135	2,942	6,077	≅ 68%
	569	355	924	≅ 95%
	45	10	55	≅ 99.71%
Temp. = 25°C / Frame No.3				
	2,751	2,672	5,423	≅ 71%
	444	350	794	≅ 96%
	50	53	103	≅ 99%
Temp. = 25°C / Averaged Frame				
	3,057	3,291	6,348	≅ 66%
	565	302	867	≅ 96%
	33	4	37	≅ 99.80%
Temp. = 35°C / Frame No.1				
	2,719	3,115	5,834	≅ 69%
	207	664	871	≅ 96%
	15	101	116	≅ 99%
Temp. = 35°C / Frame No.2				
	2,240	2,339	4,579	≅ 76%
	488	609	1,097	≅ 94%
	63	88	151	≅ 99%
Temp. = 35°C / Frame No.3				
	2,976	2,478	5,454	≅ 71%
	461	520	981	≅ 95%
	70	53	123	≅ 99%
Temp. = 35°C / Averaged Frame				
	2,665	3,906	6,571	≅ 65%
	273	642	915	≅ 95%
	10	71	81	≅ 99.57%
Temp. = 35°C / Non-Uniformity Corrected Frame				
	2,566	2,586	5,152	≅ 72%
	529	537	1,066	≅ 94%
	43	45	88	≅ 99.53%
Temp. = 45°C / Frame No.1				
	2,781	2,495	5,276	≅ 72%
	425	476	901	≅ 95%
	51	67	118	≅ 99%
Temp. = 45°C / Frame No.2				
	3,047	2,774	5,821	≅ 69%
	367	418	785	≅ 96%
	49	54	103	≅ 99%
Temp. = 45°C / Frame No.3				
	3,232	2,564	5,796	≅ 69%
	554	376	930	≅ 95%
	55	35	90	≅ 99.52%
Temp. = 45°C / Averaged Frame				
	2,771	3,604	6,375	≅ 66%
	313	734	1,047	≅ 94%
	2	24	26	≅ 99.86%

Table 16.7. The statistical processing of the patches for the Agema 1000.

In Figs. 16.16 and 16.17, the 3-D graphical representations of the grey level values of the pixels of the averaged quadrants and patches by the SURFER have been presented. As was done with CCD cameras, different colours were assigned to the different grey level values so that the interpreter could see immediately the grey level values changing on the plot. For example, in the plot of the averaged quadrant at the 45°C temperature, the pixels that have grey level values between 170DN and 175DN, have been represented in a yellow colour. As can be seen from these plots, at each temperature, the effect of the heating on the distribution of the temperature observed all over the quadrants and patches can be clearly seen. Especially, at the highest temperature, 45°C, this became more evident and it is apparent that the radiation source is cooler at the bottom and hotter at the top of the plate, giving a marked temperature gradient over its surface. Of course, this effect decreases and there is more uniformity in the appearance of the area when the patches are used. However, as can be seen from the Table 16.5, the drop in the standard deviations of the grey level values of the patches was not too great.

16.8 Radiometric Calibration of the Agema 900

The radiometric calibration of this imager has been carried out using the 20° lens. The images of the radiation source have been acquired at three different temperatures - 25°C, 45°C and 65°C respectively. From these analogue images, three frames for the 25°C and 45°C temperatures and two frames for the 65°C temperature have been digitized using a frame grabber. Although the full size of each of these frames was 768(H) x 576(V) pixels, once again homogenous pieces have been extracted from them and used for the processing. Two different sizes have been extracted - the bigger one (quadrant) is 280(H) x 140(V) pixels in size, while the smaller one (patch) is 170(H) x 110(V) pixels. The reason for the use of the smaller patch was to check and compensate for any effect that might come from a lack of a uniform radiation from the radiation source. These quadrants and patches were input to the STMN and PRNU programs respectively. The results from these programs are shown in Table 16.5.

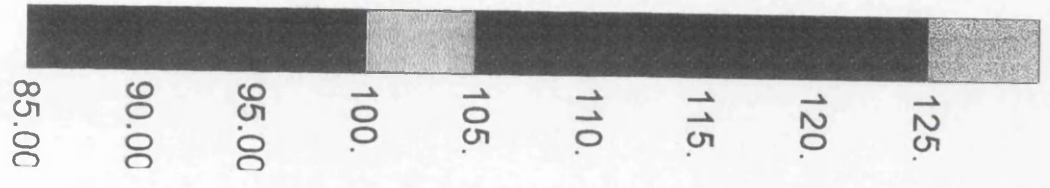
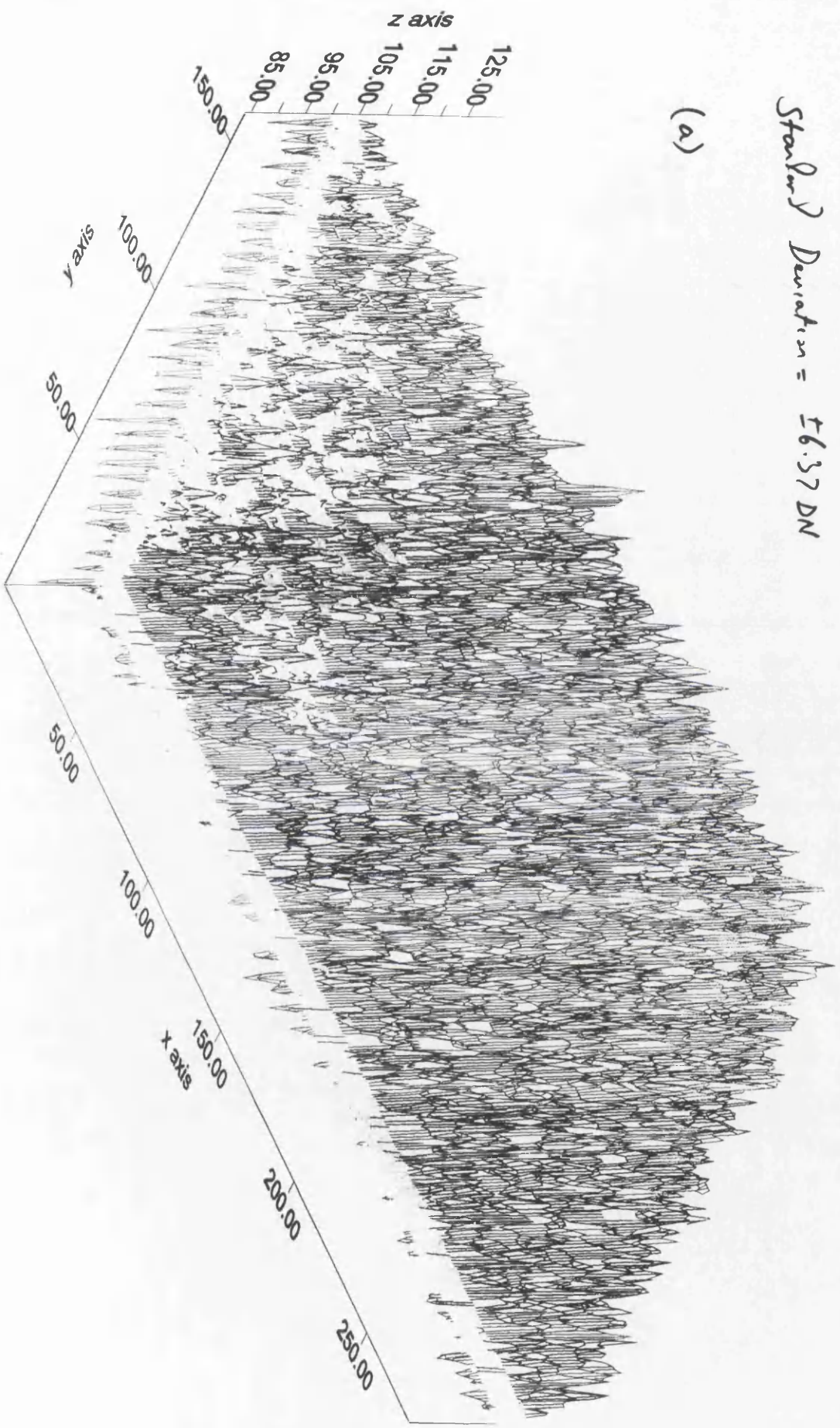
ACEMM 1000 / 25°C

Frame Size = 280 x 160 pixels [Quadrant]

Mean = 104.62 DN

Standard Deviation = ±6.37 DN

(a)



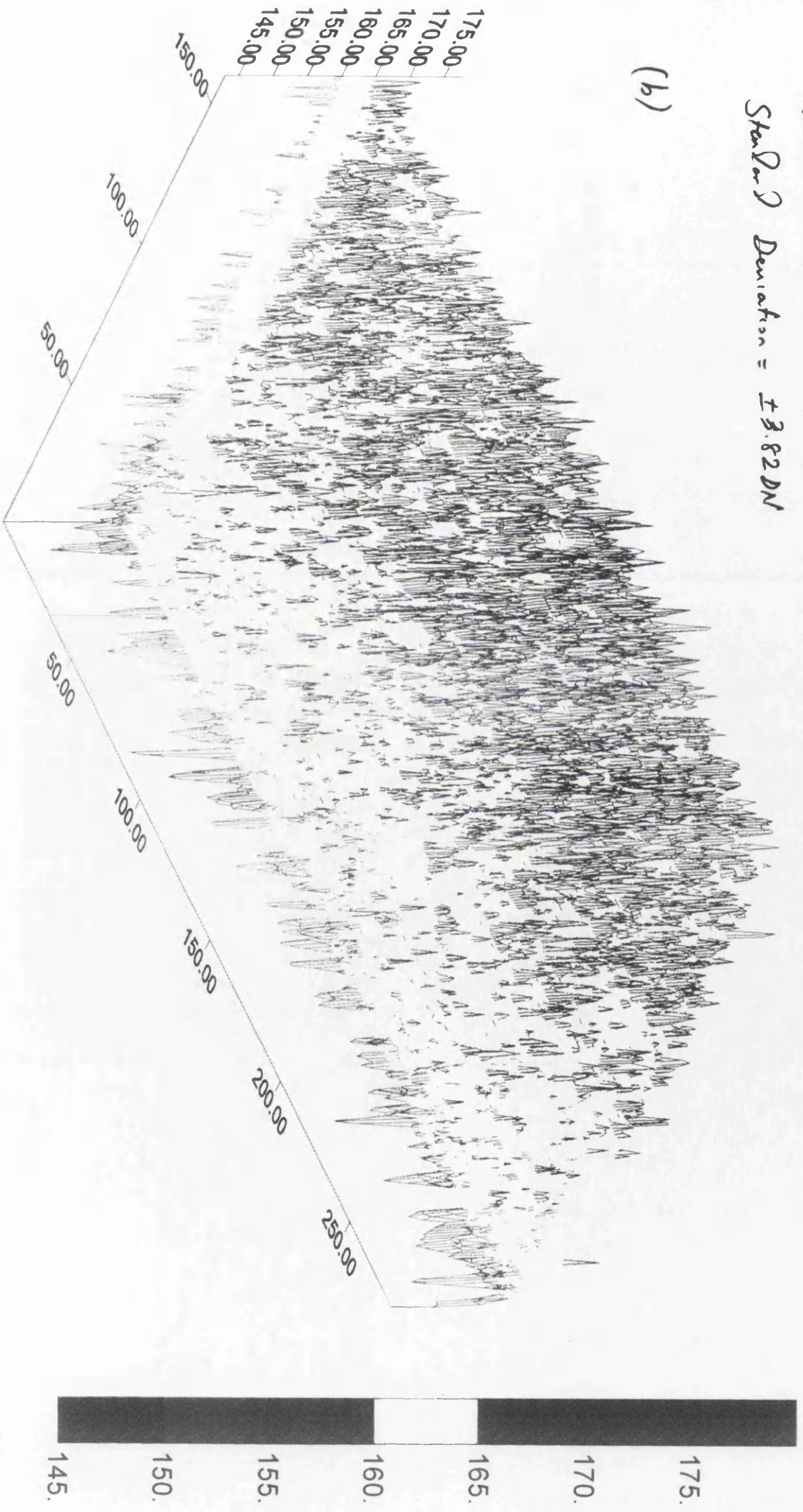
ASGMN 1000 / 352

Frame Size = 280 x 160 pixels [Quadrant 7]

Mean = 161.43 DN

StdDev Deviation = ± 3.82 DN

(b)



AGEMA 1000 / 45°C

Frame Size = 280 x 160 pixels [Quadrant]

Mean = 173.84 DN

Standard Deviation = ± 5.54 DN

(c)

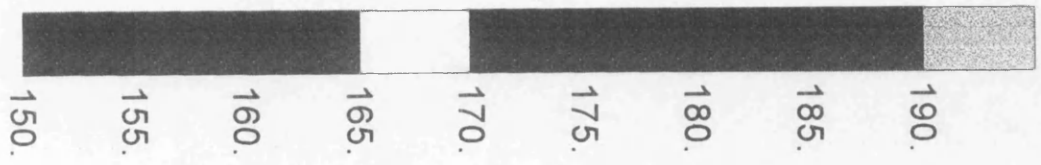
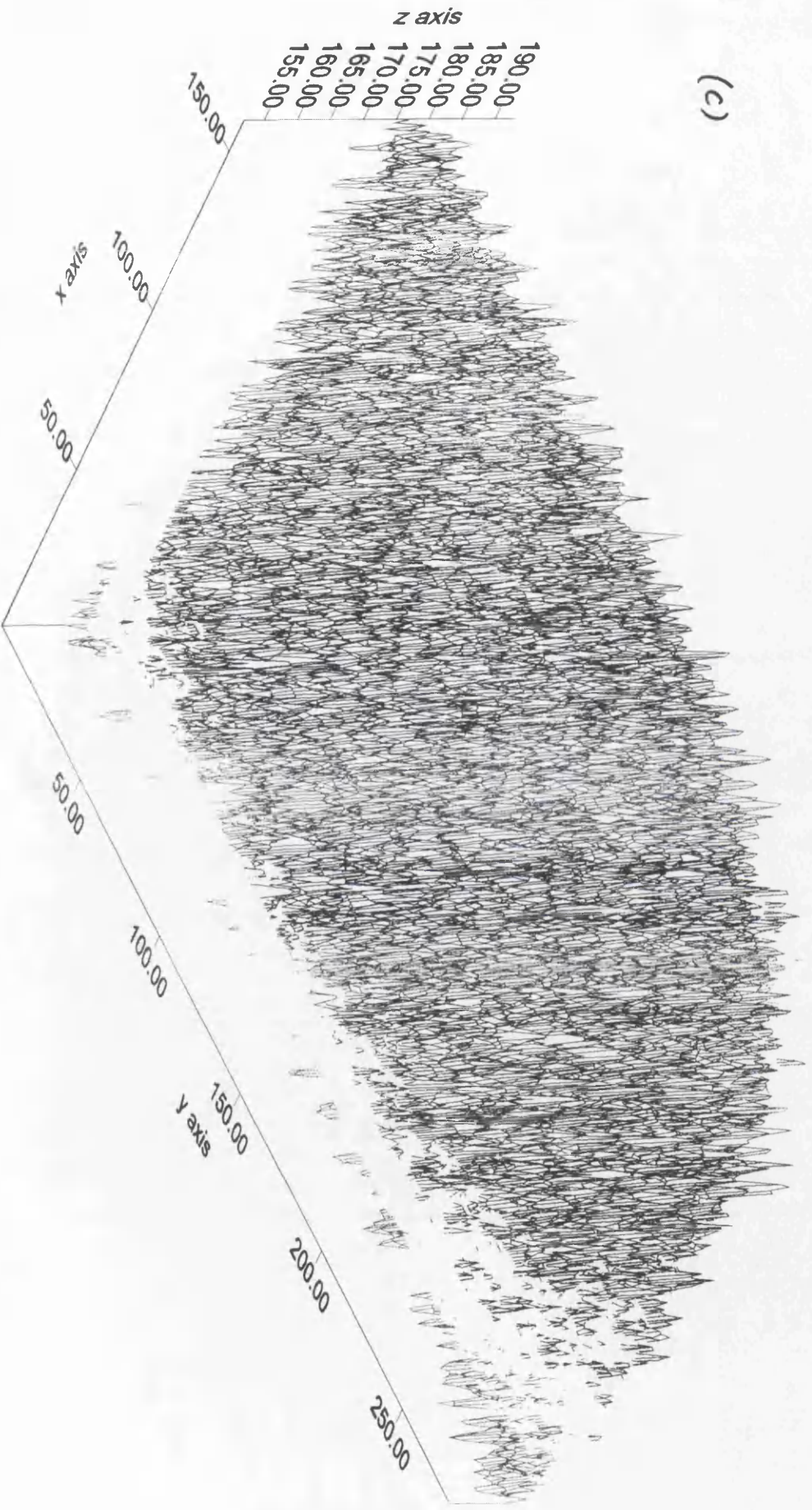


Fig. 16. 16 (a), (b) and (c). The graphical representations of the gray level values

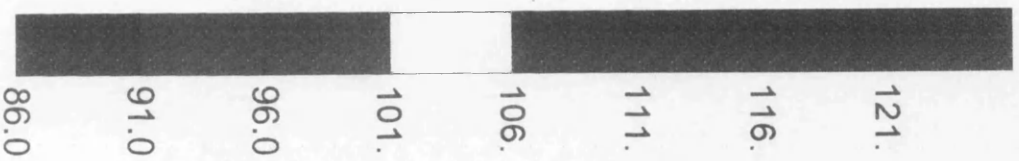
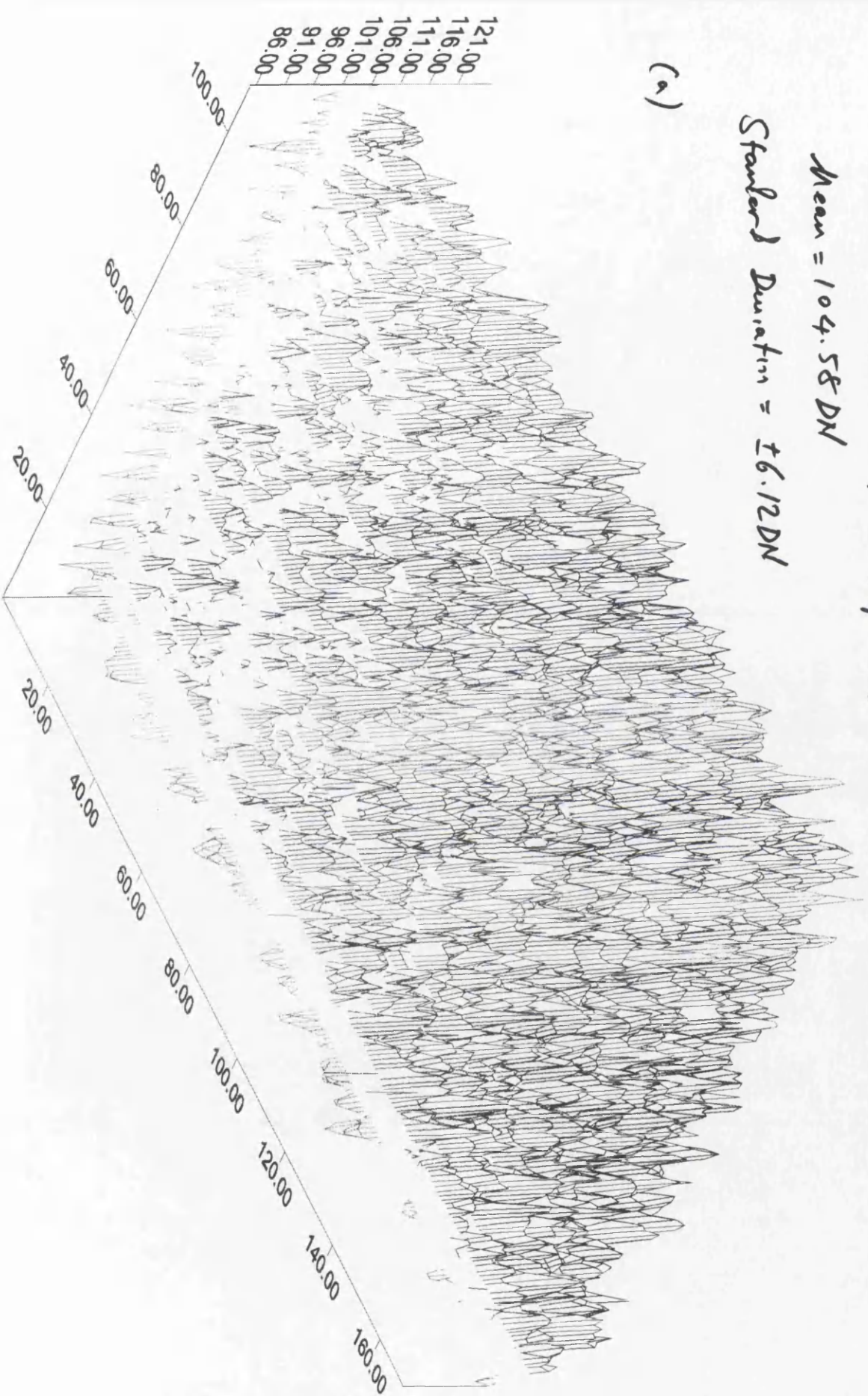
AcEMA 1000 / 25°C

Frame Size = 170 x 110 pixels [patch]

Mean = 104.58 DN

Standard Deviation = ± 6.12 DN

(a)



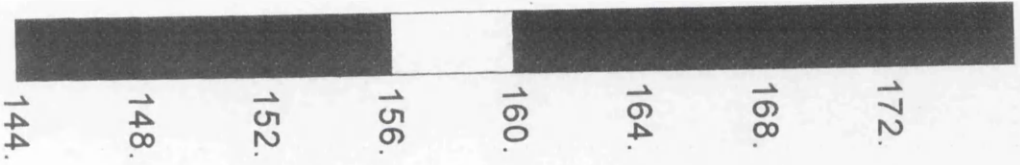
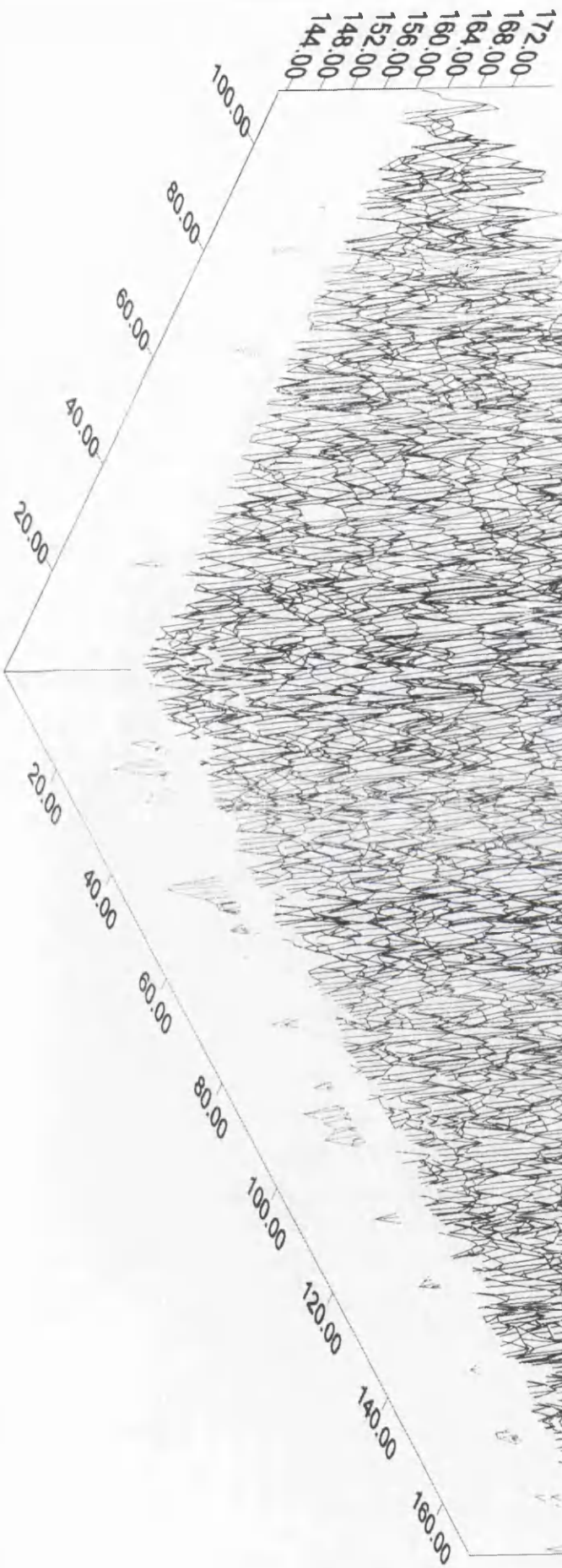
Agema 1000 / 35°C

Frame Size = 170 x 110 pixels [patch]

Mean = 161.85 DN

Standard Deviation = ± 3.79 DN

(6)



Aerum 1000 / 45°C

Frame Size = 170 x 110 pixels [yates]

Mean = 176.49 DN

Standard Deviation = ±4.18 DN

(c)

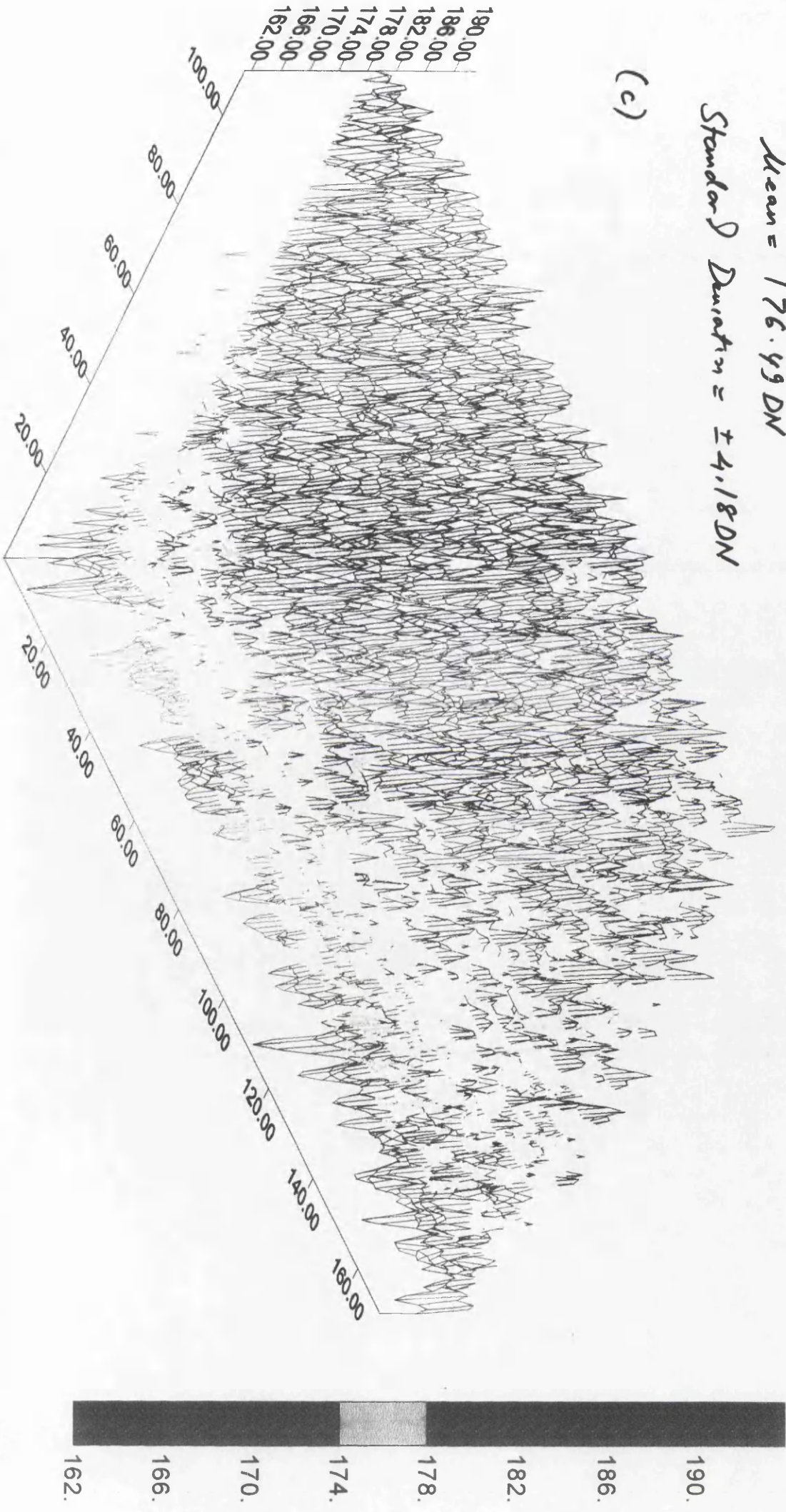


Fig. 16.17 (c) (b) (a) The gray level values

As can be seen from this table, while at the 25°C and 65°C reference temperatures, the means of the quadrants were close to each other, at the 45°C temperature, the means of the quadrants were substantially different to one other. At the 45°C temperature, the heating pads of the radiation source appeared to be cooling and re-heating very quickly to keep the temperature at the desired level; this action of the heating pads was necessary to ensure that the radiation source remained at the specified temperature. However, at the 25°C and 65°C settings, the temperatures of the radiation source were much more stable and the means of the quadrants are very close to one another. As can be seen from Table 16.5, at the 25°C temperature, very uniform values have been obtained with the quadrants. The standard deviations of the quadrants in this temperature are nearly equal to $\pm 3\text{DN}$. However, at the other temperatures, this value is increasing to $\pm 11\text{DN}$. The averaging of the quadrants at each temperature did not change the standard deviation values too much. The images of the averaged quadrants at each temperature are given in Fig. 16.18 together with their fixed patterns.

Image and fixed pattern of the averaged quadrant at 25°C

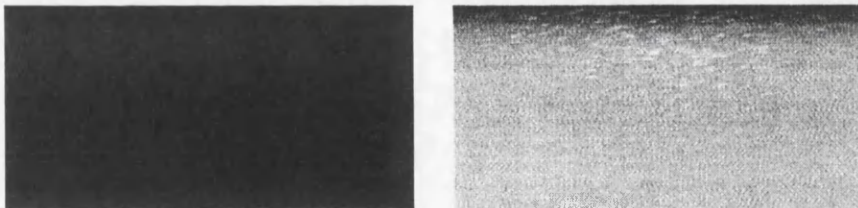


Image and fixed pattern of the averaged quadrant at 45°C

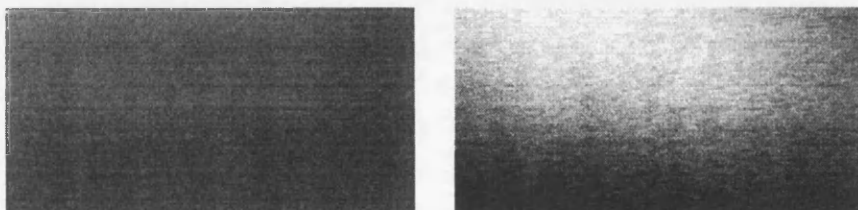


Image and fixed pattern of the averaged quadrant at 65°C

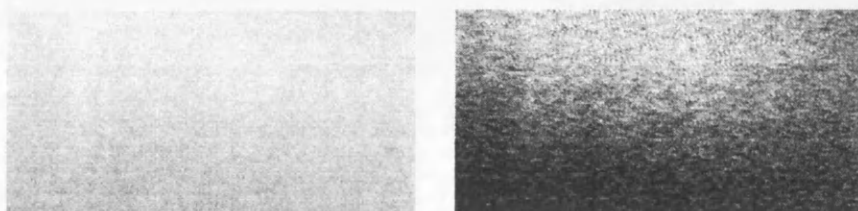


Fig. 16.18. Images and the fixed patterns of the averaged quadrants.

In Fig. 16.19, the relationship between the mean grey level values and the temperatures are given. As this figure shows, there is some non-linearity between them. The mean grey values are 17, 135 and 211 at the 25°C, 45°C and 65°C temperatures respectively, whereas the middle value should be 114 (instead of 135) if a linear relationship existed.

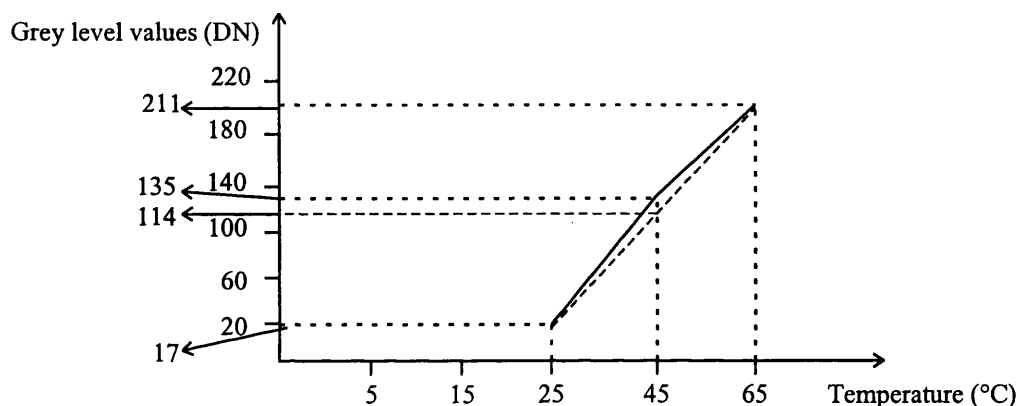


Fig. 16.19. Changes in the mean grey level values of the quadrants at different temperatures.

However, the application of the non-uniformity correction gives a good result since the temperature difference between the reference (calibration) temperatures (25°C and 65°C) was large and the standard deviations of the grey level values of the averaged quadrants at these temperatures were smaller than that of the middle temperature (45°C). With this correction, the standard deviation of the averaged quadrant at the 45°C temperature was reduced from $\pm 10.4\text{DN}$ to $\pm 6.6\text{DN}$. Thus, the non-uniformity of this quadrant was decreased from 7.9% ($10.40 / 131.56$) to 5.0% ($6.56 / 130.50$). For the patches, the standard deviation value of the averaged patch at the 45°C temperature was reduced from $\pm 8.31\text{DN}$ to $\pm 5.45\text{DN}$. Hence, the non-uniformity of the patch dropped from 6.2% to 4.1%.

Tables 16.8 and 16.9 show the results of the statistical processing of the quadrants and patches carried out using the STAT program. The standard deviations and the means of the quadrants that have been obtained from the STMN and PRNU programs were input to this program. As can be seen from Table 16.8, except for the averaged

quadrant at 25°C, nearly 100% of the pixels of the quadrants in the other temperatures have grey level values inside the range of $A \pm 3\sigma$. However, in Table 16.9, by using the smaller sized patches, nearly 100% of the pixels of the quadrants in the 25°C temperature lie within this range. The small number of the pixels in each quadrant that lie outside this range can be viewed as blemished pixels that are not responding correctly to the incident radiation.

Figs. 16.20 and 16.21 give the 3-D graphical representations of the grey level values of the pixels of the averaged quadrants and patches. As can be seen from these plots, at the 25°C temperature, the distribution of the grey level values of the pixels shows a fairly uniform pattern. However, at the 45°C and 65°C temperatures, once again, a marked temperature gradient from the top to the bottom of the plate over the area of the quadrant can be seen. In the plots at these temperatures, it appears that the radiation source is always hotter at the top suggesting that convection currents may be playing an important part in the temperature distribution. This matter can be observed by the colour representation of the different grey levels which makes the plots more readable. The use of the patches did not make too much change in the result. However, as always, they supplied more uniformity than that of the quadrants.

Agema 900 with 20° lens	Total number of pixels in the quadrant: 280(H)x140(V)= 39,200 pixels			
	Number of pixels greater than $\sigma/2\sigma/3\sigma$	Number of pixels less than $\sigma/2\sigma/3\sigma$	Total number of pixels outside the range of $A \pm 3\sigma$	Percentage of the number of pixels lie inside the range of $A \pm 3\sigma$
Temp. = 25°C / Averaged Frame				
	3,207	4,567	7,774	≅ 80%
	13	2,796	2,809	≅ 93%
	0	1,415	1,415	≅ 96%
Temp. = 45°C / Averaged Frame				
	7,697	8,011	15,708	≅ 60%
	2	1,054	1,056	≅ 97%
	0	16	16	≅ 99.96%
Temp. = 65°C / Averaged Frame				
	6,130	6,548	12,678	≅ 68%
	249	1,207	1,456	≅ 96%
	1	64	65	≅ 99.83%
Temp. = 45°C / Non-Uniformity Corrected Frame				
	5,730	6,308	12,038	≅ 69%
	395	1,097	1,492	≅ 96%
	4	18	22	≅ 99.94%

Table 16.8. The statistical processing of the averaged quadrants for the Agema 1000.

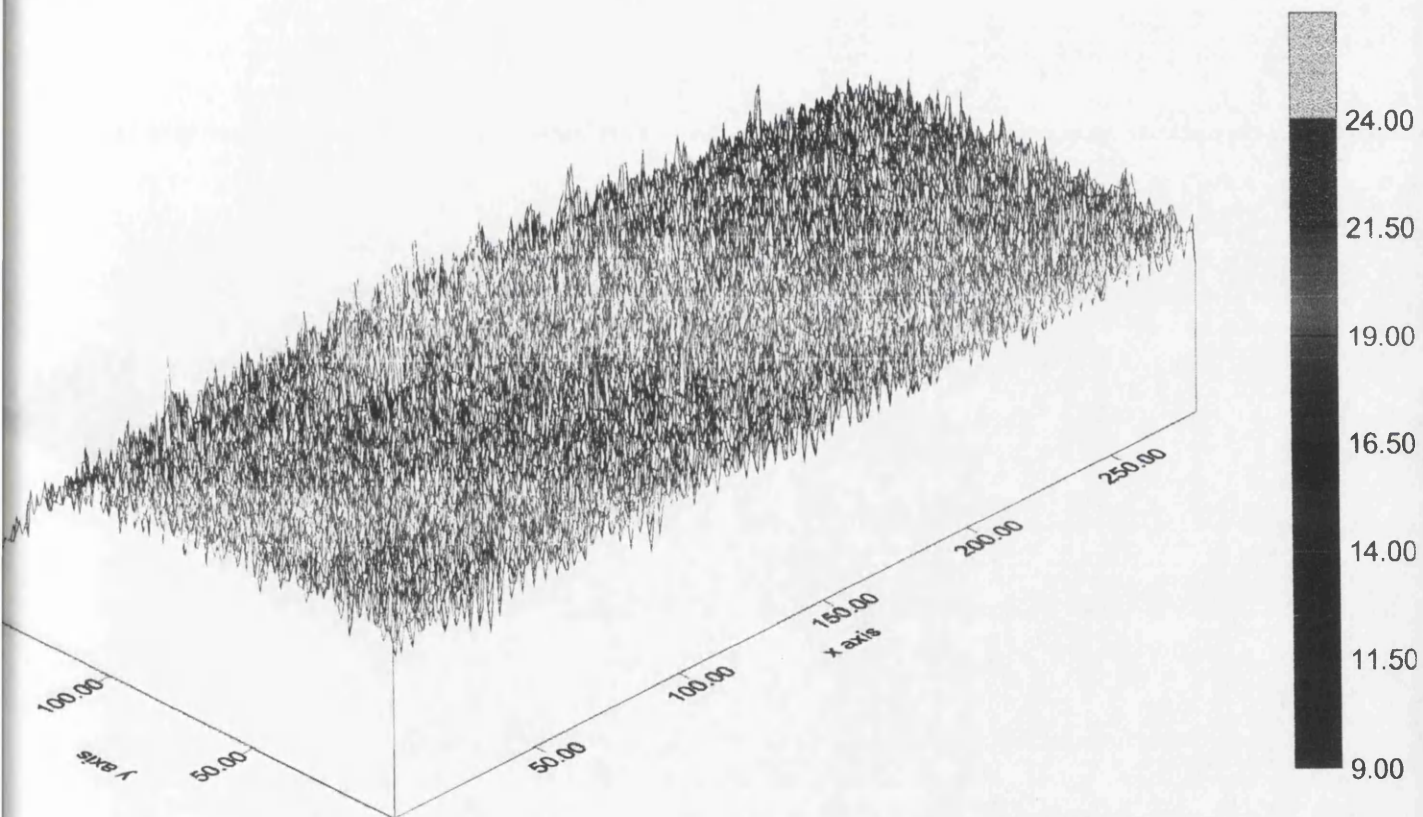
AGEMA 900 / 25°C

Frame Size = 280 x 140 pixels [Quadrant]

Mean = 16.43DN

Standard Deviation = ± 2.47 DN

(a)



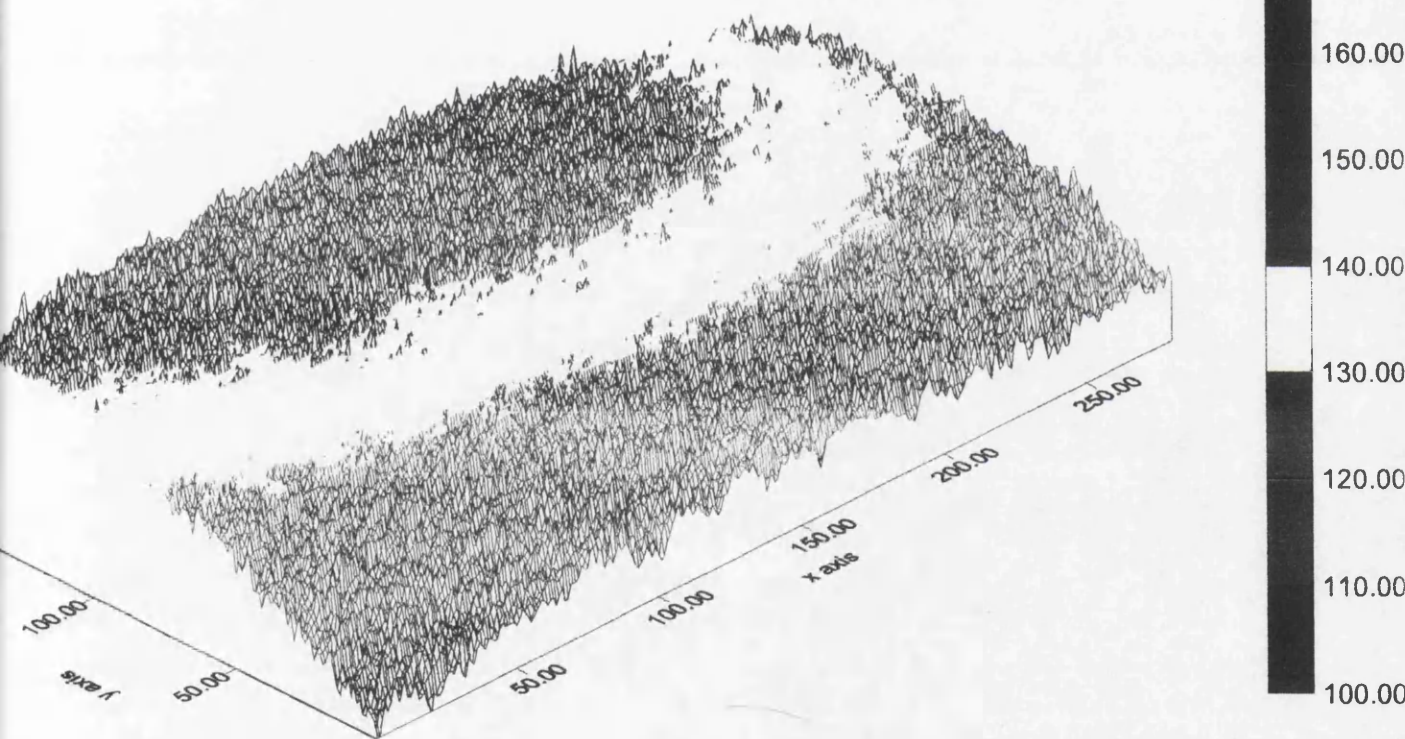
Agema 900 / 45°C

Frame Size = 280 x 140 pixels [Quadrant]

Mean = 131.56 DN

Standard Deviation = ± 10.40 DN

(b)



Agema 900 / 65°C

Frame Size = 280 x 140 pixels [Quadrant]

Mean = 208.56 DN

Standard Deviation = ± 9.82 DN

(c)

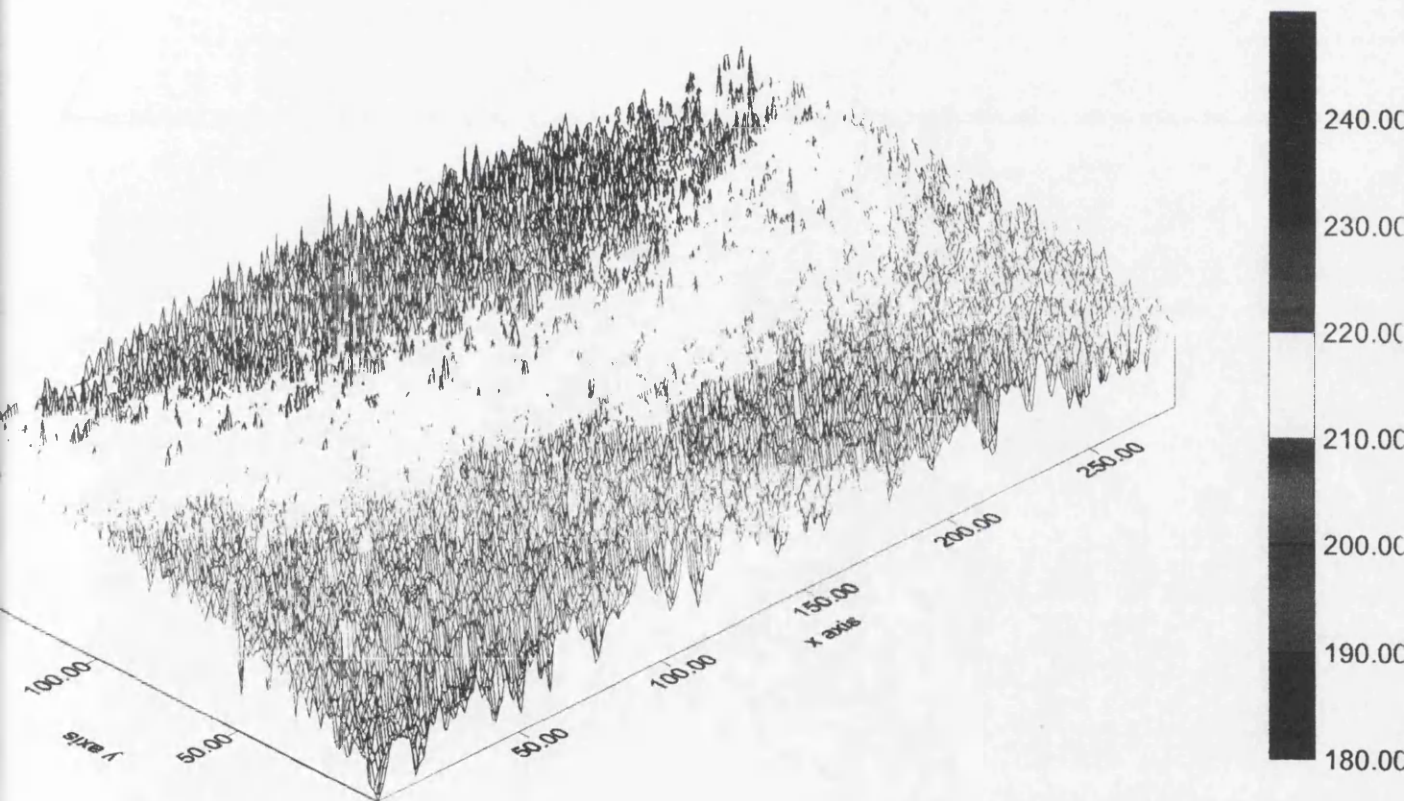


Fig. 16.20 (a), (b) and (c). The graphical representations of the gray level values of the averaged quadrants at each temperature.

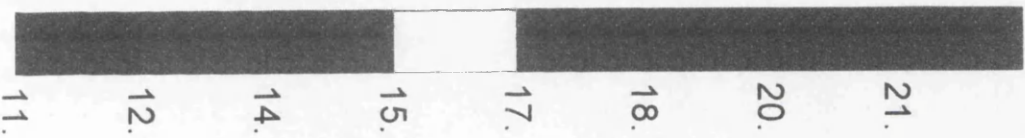
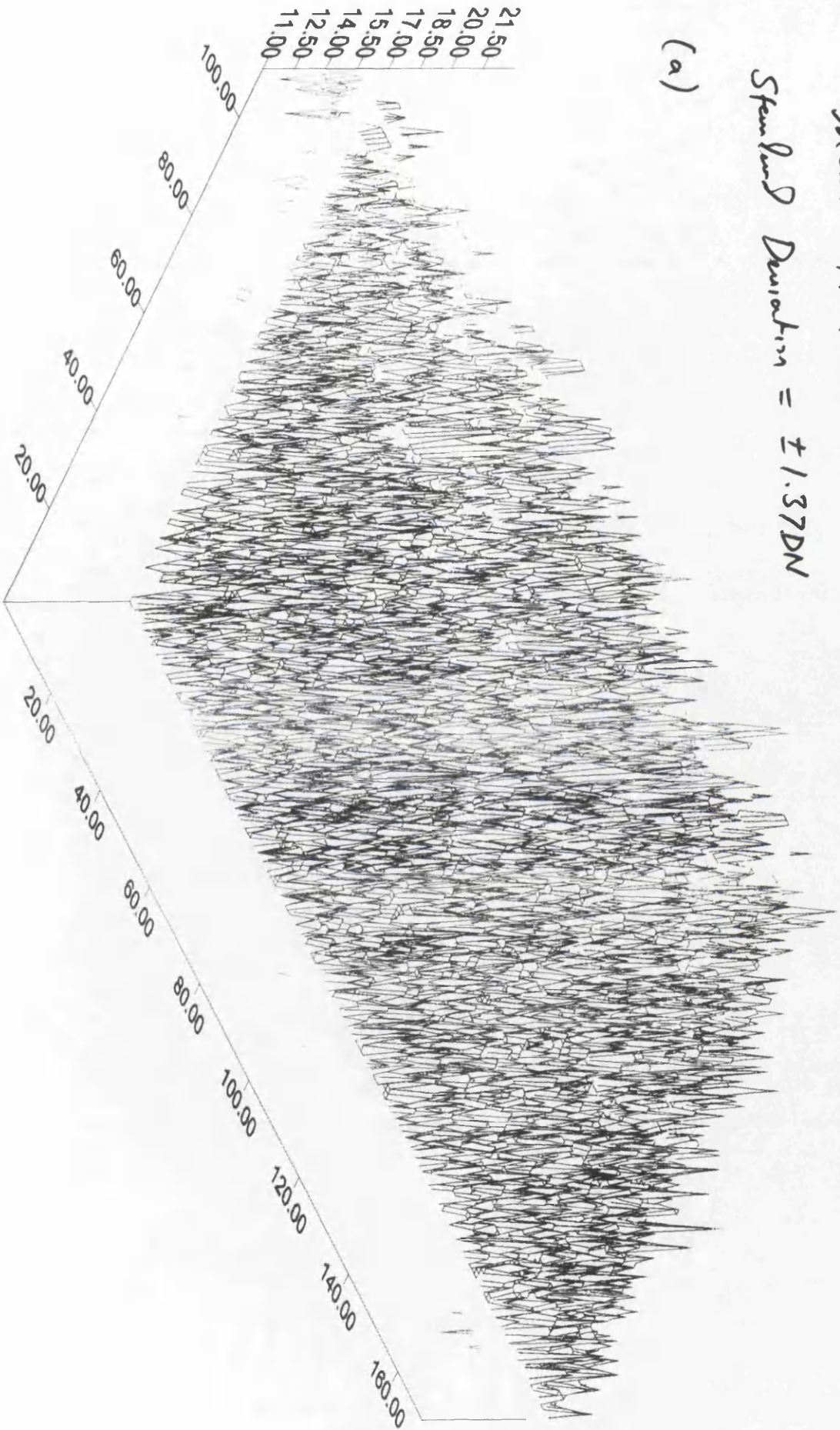
Agemur 900 / 25°C

Frame Size = 170 x 110 pixels [patch]

Mean = 17.12DN

Standard Deviation = ± 1.37 DN

(a)



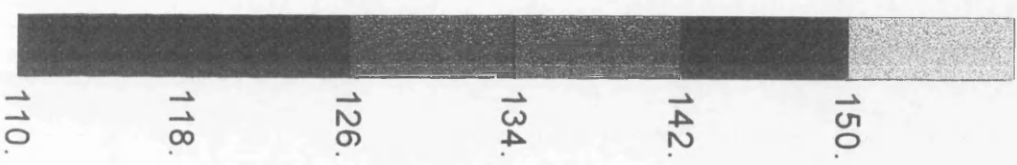
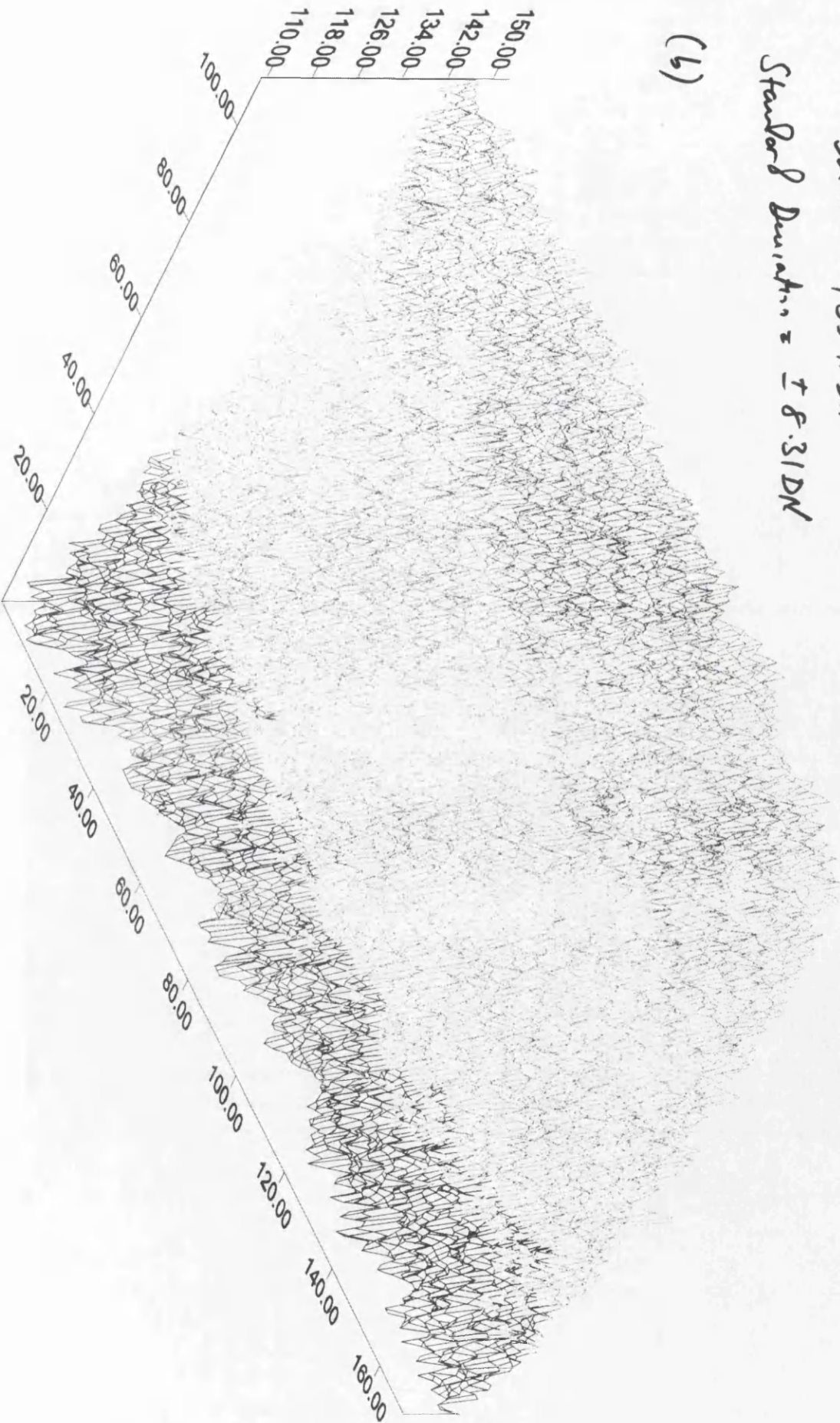
Agema 900 / 45°C

Frame Size = 170 x 110 pixels [patch]

Mean = 135.11 DN

Standard Deviation = ± 8.31 DN

(6)



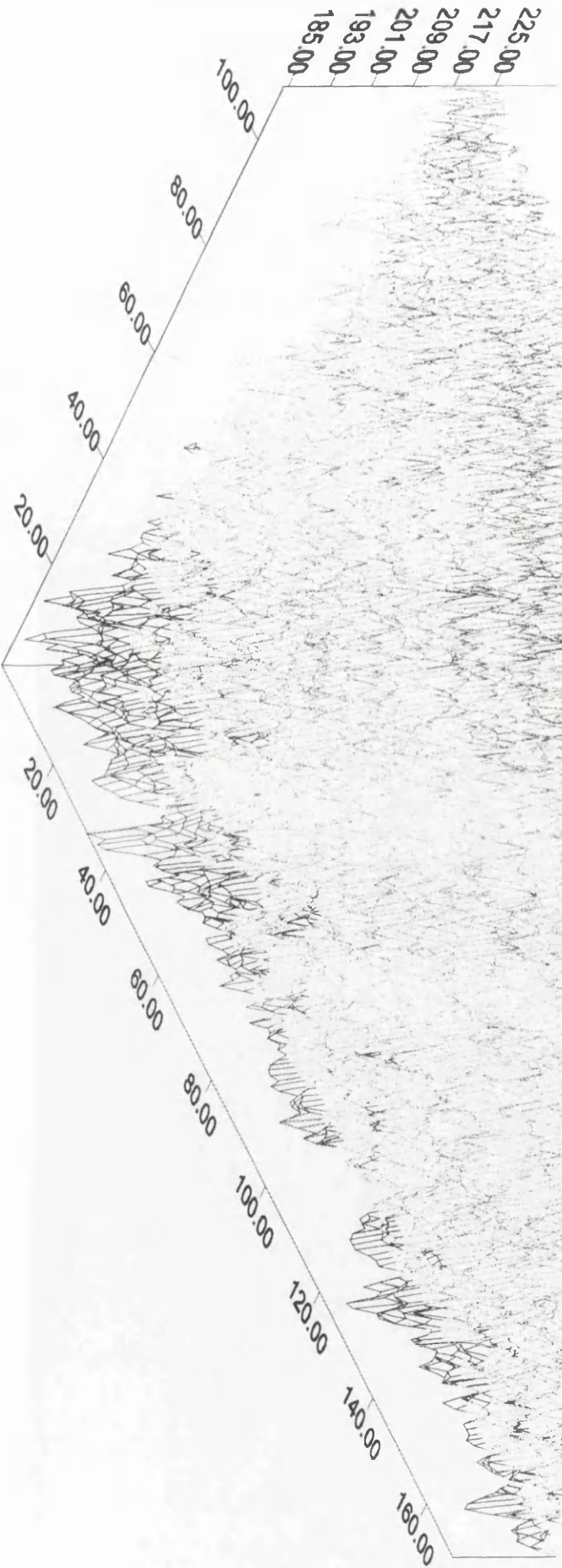
Acema 900 / 65°C

Frame Size = 170 x 110 pixels [Pctd]

Mean = 211.35 DN

Standard Deviation = ± 8.10 DN

(c)



Agema 900 with 20° lens	Total number of pixels in the quadrant: 170(H)x110(V)= 18,700 pixels			
	Number of pixels greater than $\sigma/2\sigma/3\sigma$	Number of pixels less than $\sigma/2\sigma/3\sigma$	Total number of pixels outside the range of $A\pm3\sigma$	Percentage of the number of pixels lie inside the range of $A\pm3\sigma$
Temp. = 25°C / Frame No.1				
	3,653	2,202	5,855	≅ 69%
	368	572	940	≅ 95%
	19	119	138	≅ 99%
Temp. = 25°C / Frame No.2				
	2,020	2,062	4,082	≅ 78%
	696	334	1,030	≅ 94%
	228	25	253	≅ 99%
Temp. = 25°C / Frame No.3				
	3,322	2,009	5,331	≅ 71%
	585	367	952	≅ 95%
	88	61	149	≅ 99%
Temp. = 25°C / Averaged Frame				
	1,701	2,744	4,445	≅ 76%
	379	959	1,338	≅ 93%
	11	343	354	≅ 98%
Temp. = 45°C / Frame No.1				
	3,048	3,251	6,299	≅ 66%
	69	683	752	≅ 96%
	0	20	20	≅ 99.89%
Temp. = 45°C / Frame No.2				
	3,480	3,479	6,959	≅ 63%
	81	406	487	≅ 97%
	0	10	10	≅ 99.95%
Temp. = 45°C / Frame No.3				
	3,315	3,570	6,885	≅ 63%
	54	466	520	≅ 97%
	0	6	6	≅ 99.97%
Temp. = 45°C / Averaged Frame				
	2,755	3,684	6,439	≅ 66%
	3	568	571	≅ 97%
	0	3	3	≅ 99.98%
Temp. = 45°C / Non-Uniformity Corrected Frame				
	3,457	3,535	6,992	≅ 63%
	208	527	735	≅ 96%
	9	22	31	≅ 99.83%
Temp. = 65°C / Frame No.1				
	3,270	2,874	6,144	≅ 67%
	332	414	746	≅ 96%
	17	22	39	≅ 99.79%
Temp. = 65°C / Frame No.2				
	2,845	2,928	5,773	≅ 69%
	331	459	790	≅ 95%
	3	35	38	≅ 99.80%
Temp. = 65°C / Averaged Frame				
	3,056	3,560	6,556	≅ 65%
	212	521	733	≅ 96%
	2	21	23	≅ 99.88%

Table 16.9. The statistical processing of the patches for the Agema 900.

16.9 Radiometric Calibration of the Whole Frames

After processing the quadrants and patches, the author has subjected the whole frames from the digitized images at the 35°C temperature for the Agema 1000 and at the 25°C temperature for the Agema 900 TVFS for further processing and analysis. The reason for not using frames at the other temperatures for these imagers is the large values of their standard deviations and the large temperature gradient shown up by the coloured perspective diagrams. As has been done with the results from the CCD cameras, plotting files have been created for the blemished pixels. For this purpose, the mean and standard deviation of the grey level values of the averaged whole frames have been computed using the STMN program. For the Agema 1000, the mean of the grey level values was 152.09DN and their standard deviation was ± 9.70 DN. In Fig. 16.22, the pixels lying outside the range of $A \pm 3\sigma$ have been plotted. As can be seen from this figure, the pixels that are not responding correctly are concentrated in the lower left corner of the whole frame. The graphical representation of this whole frame using the SURFER program has also been included as Fig. 16.23. As can be seen from these figures, almost certainly, the cause of this concentration of these blemished pixels was the lack of uniformity of the radiation being emitted from radiation source.

Pixels lie outside the range of $A \pm 3\sigma$ (1,281 pixels out of 171,000 pixels - in fact, all of the pixels have the grey value less than $A - 3\sigma$, no pixels have grey values greater than $A + 3\sigma$)

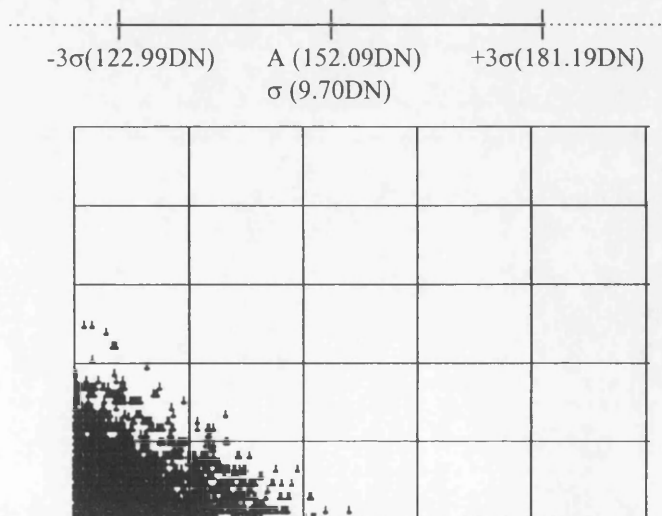


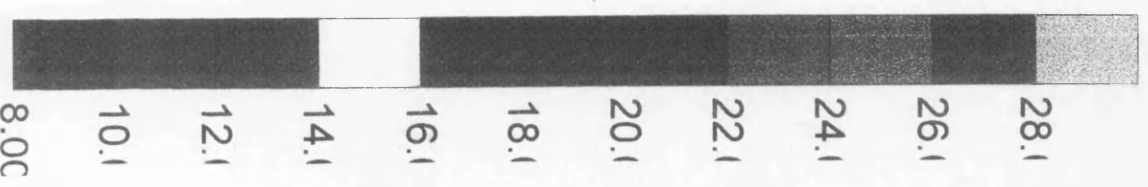
Fig. 16.22. Vector plots of the pixels that are not responding correctly in the whole frame obtained using the Agema 1000 imager.

AGEMA 900 / 25°C

Frame Size = 255 x 590 pixels [Whole Frame]

Mean = 17.41 DN

Standard Deviation = ± 1.57 DN



For the Agema 900, the mean grey level value was 17.41DN and the standard deviation was ± 1.57 DN. In Fig. 16.24, only those pixels that have grey level values less than 10DN have been included. As can be seen from this figure, a line of pixels has not responded correctly. As mentioned before, the Agema 900 has two internal blackbodies which calibrate the individual detector elements radiometrically. These are placed at the beginning and at the end of the line. Most probably, the calibration value that was assigned to these blackbodies was wrong when this line processed. The graphical representation of the grey level values of the pixels for the whole frame also showed up this faulty line quite clearly (see Fig. 16.25).

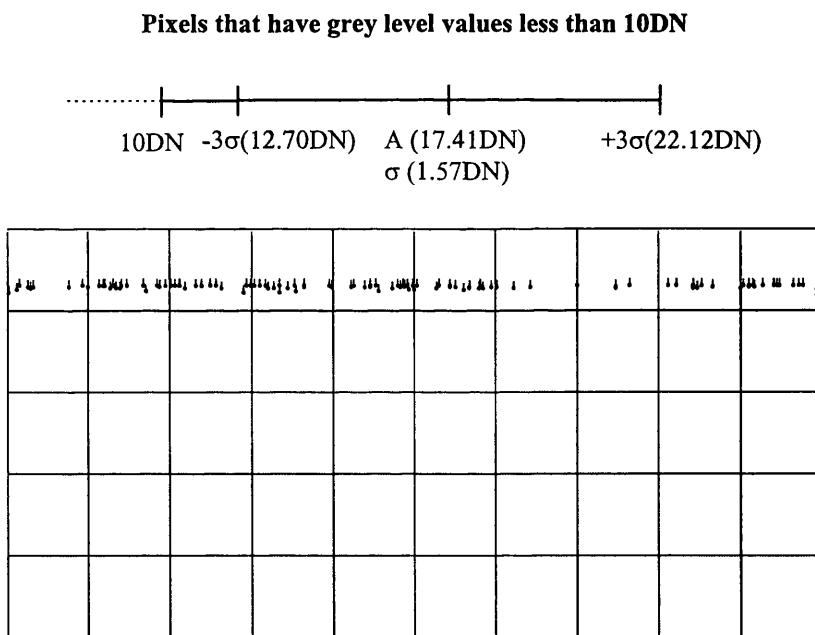


Fig. 16.24. Vector plots of the pixels that are not responding correctly and have grey values less than 10DN over the whole frame obtained using the Agema 900 imager.

16.10 Conclusion

In this and the previous two chapters, the results of the geometric and radiometric calibration of the infrared cameras and scanners have been presented, discussed and analyzed. The next (final) chapter draws some general conclusions from the research work that has been carried out and the results obtained during the present project. In

addition, some recommendations are given for future investigations, which will be undertaken in this area, on the basis of the difficulties and problems encountered in the various stages of this research.

CHAPTER 17: CONCLUSIONS AND RECOMMENDATIONS

17.1 Introduction

As stated in the Introduction (Chapter 1) to this dissertation, infrared imaging systems are being used by an increasing number of users as a source of data for remote sensing applications, for specialised mapping purposes and for close-range industrial and medical applications of photogrammetry. This arises from the various favourable characteristics of this type of imager such as the unique images that can be acquired by them and their comparative ease of use, portability and speed of operation. However, the use of the infrared images that are acquired by these systems involves many considerations and a number of technologies that are unfamiliar to most users and to almost all photogrammetrists. Nevertheless these images contain valuable information for the wide variety of users, some of whom will want to carry out photogrammetric measurements on them. For this purpose, the geometric and radiometric characteristics of these devices should be known in order to assess their suitability for photogrammetric applications and to actually implement such applications.

It must be said that, at the present time, the photogrammetric community only stands on the threshold of making good use of infrared imagery: however much more use of this imagery can be expected in the future. In this context, the geometric and radiometric calibration of infrared cameras and scanners, that has been the main concern of the author's research project, can be regarded as being timely.

17.2 Conclusion

Since the results acquired during the various stages of the present project have been reported and analysed in detail in the relevant chapters, it is not necessary to repeat them in this concluding chapter. However, it is quite appropriate to conduct a more general discussion and attempt to draw some general and specific conclusions

regarding the methodology used, the results obtained and the experience gained during the present project.

17.2.1 General Discussion and Conclusions

The objectives for the author's research project were set out in Chapter 1. In general terms, the project has been successful in terms of reaching or satisfying most of these objectives. However, some objectives could not be achieved because of time and financial limitations. Nevertheless, as can be seen from the relevant chapters, this project has provided much original and accurate geometric information for the two main and commonly used classes of infrared imager - CCD cameras and video frame scanners - that are most likely to be of interest for photogrammetric applications. On the radiometric side, the results obtained are certainly very useful but, as explained in detail in the results chapters, this area needs further work and more development since the images of the radiation source did not give good results for the higher range of temperatures. Still the results obtained at the lower temperatures have provided some valuable radiometric information for these imagers with a view to obtaining and accurately calibrating the grey level value data that is contained in infrared images.

(a) Pyroelectric Vidicon Devices

It will have been noted in Chapter 1 that one of the main research objectives was to calibrate a third group of imagers - the pyroelectric vidicon cameras - both geometrically and radiometrically. However, this was not carried out because of the time limitations of this project. In fact, during the early stages of this research project, the author did attempt to calibrate one of the pyroelectric vidicon cameras that belong to the Strathclyde Fire Brigade. This establishment possesses a number of these imagers for use in firefighting applications. The test was carried out in the Fire Brigade station at Motherwell, but, it soon became obvious from this preliminary work that there were many special problems associated with this type of imager. One is the circular format produced by the imager. But a more serious problem was that it was difficult to get a sharp image of good quality because of the inherently lower

resolution (100 x 100 pixels) of this type of device and the difficulty experienced in getting the image into sharp focus. As the author can testify, it was not even possible to see the crosses on the images of the target plate that were taken by this camera. In the context of firefighting, these shortcomings in resolution and sharp focus do not appear to concern the firefighters themselves. For them, the imager's capability to provide images through smoke is paramount, together with its ability give the location of (a) the source of the fire, and (b) a human body for rescue operations. Accurate position and high resolution of small objects are matters of little concern; the shielding of the camera against high temperatures and smoke are of more importance.

However, throughout this project, the author has been corresponding with manufacturers and following the developments in this type of camera and trying to get information about them from the companies concerned. During the final stages of this project, the VideoTherm VT-300 vidicon cameras from the ISI Group in Albuquerque, USA were introduced, which have a resolution of 270 x 200 pixels. Although an appointment for testing this imager was arranged, it was not implemented because of time limitations. It should be said too that the use of the smaller size of target plate with a higher density of target crosses as suggested for use with lower resolution infrared imagers (see Section 13.2.3) would also be of greater benefit when attempting to calibrate pyroelectric vidicon cameras.

(b) Infrared CCD Cameras

As mentioned before, originally infrared imagers have been developed primarily for military applications. But, nowadays, they have begun to be used by a number of people working in the field of photogrammetry and remote sensing. However, at the present time, their use in photogrammetric applications is somewhat restricted because of their resolution deficiency. Still it is possible to extract a certain amount of metric and topographic information from infrared imagery that can be used by a wide spectrum of users from military personnel through electrical engineers to hospital staff. The main limitation is the low resolution of the imagers when compared to those imagers that operate in visible band of the EM spectrum. As mentioned previously,

the infrared CCD cameras that are currently available have a resolution of 320 x 240 pixels which is quite inappropriate for those types of photogrammetric measurement that require very high resolution. An improvement in the resolution of CCD cameras depends on the largest array size can be produced by the technology. The availability of larger CCD arrays that are sensitive to infrared radiation would improve both the resolution and the geometric accuracy that can be obtained with the images. However, the development of larger arrays may result in larger numbers of dead or blemished pixels being present which might create a problem in calibrating these arrays radiometrically.

At the present time, infrared CCD cameras are probably best used in close range photogrammetric applications in certain specific industrial environments where the unique signatures and images that they generate provide information that cannot be obtained in any other way. Although their performance is continuously increasing, in absolute terms, these cameras still have a poor resolution and a small format size with comparatively few detector elements. This is due to the complexity involved in their manufacture and the high cost incurred in fabricating these devices so that they can operate in the middle infrared region of the EM spectrum. As the technology and fabrication of the CCD arrays develops further to produce larger format sizes, these imagers may be expected to dominate the infrared imaging market, since they dispense with the need for the complex and expensive optical and mechanical scanning elements required in video frame scanners. However there is a need to develop CCD areal arrays that are sensitive to the thermal infrared region, where currently video frame scanners occupy a unique, monopoly position. At the present time, the CCD-type imagers are confined to the middle infrared part of the spectrum.

The infrared CCD cameras are just beginning to be used in certain airborne applications where again geometric resolution is not a major concern. In this context, the prices of these imagers - £60,000 to £100,000 for TVFSs and £15,000 to £30,000 for CCD cameras - are another major drawback to their use in both close-range and airborne applications. In fact, the visible counterparts of these CCD cameras with a resolution of 1,000 x 1,000 pixels cost less than £5,000. This merely shows the big

gap between infrared and visible imagers from the cost and performance points of view at the present time and undoubtedly inhibits their wider use.

(c) *Thermal Video Frame Scanners*

Turning next to consider thermal video frame scanners, originally these devices were developed principally for military applications since the thermal infrared versions allow the continuous production of a video image from an aircraft, helicopter or military vehicle both during daytime and night time conditions. They could also be used for observation and surveillance purposes even in the smoke of a battlefield. They have very complex optical and mechanical scanning systems when compared to the CCD infrared cameras but, by comparison, they produce an image of relatively high quality. However, at present, the size of the image generated by this type of imager is limited since it is associated with the formats of broadcast television technology. However, although the image quality cannot be compared with that of a photogrammetric film camera image, frame scanner images are far better in terms of geometric resolution and image quality compared with those resulting from CCD cameras and pyroelectric vidicon cameras.

While the resolution of these devices is much superior to that of the other two types of imager, nevertheless it is still limited by the adoption of broadcast television standards which lead to the limitation of the geometric resolution to the 576 x 768 pixels available in the PAL format. Notwithstanding the advantages of using inexpensive, well understood and commonly available broadcast television technology in conjunction with video frame scanners, there would be obvious advantages in providing still higher resolutions as would result from the adoption and use of high definition television (HDTV) technology (which has a resolution of 1,080 x 1,920 pixels) in video frame scanners. Indeed this would appear to be an obvious future development with enormous advantages to be gained in terms of the ground or scene resolution and coverage and in terms of the stereo-coverage and viewing which would be useful, especially in airborne applications of this type of imager. Another

possibility would be to use purely digital technology for recording, storage and display purposes, e.g. via the use of non-video LCD displays.

The suitability of thermal video frame scanners for airborne applications has already been tested and proven by Amin (1986). As can be seen from this pioneering work, it is possible to acquire metric, qualitative and quantitative information from the video frame scanner's images. It was found that the processes needed to extract the necessary image data using TVFS are quite similar to those carried out using a photographic / photogrammetric frame camera. Indeed this remark applies to all of the imagers considered in this dissertation - all of which produce frame-type images. This eliminates at a stroke the geometric problems encountered with the line-type infrared scanners that are currently used for remote sensing purposes from airborne and spaceborne platforms - especially those difficulties associated with the modelling and correction of the continuously varying altitude and attitude values that are encountered in the imagery taken with these devices.

However it was noted by Amin that the lack of suitable well-defined signalized points in the test field meant that the precision of measuring the ground coordinates of the control and check points in that project was relatively low which had a significant effect on the accuracy obtained in his geometric test. Obviously, this problem stems from the fact that the signalized points need to be made of a suitable thermal emissive material - which is not too easy to find and maintain.

17.2.2 Specific Conclusions

(a) Geometric Calibration

- (i) The geometric calibration of CCD cameras to determine the magnitude and pattern of the geometric distortion existing in the CCD images has been achieved successfully using a comparatively simple methodology and inexpensive technology. The results of the tests showed that the angular coverages of the lenses that are available for the Agema 550 camera are a

major factor concerning the magnitude of the geometric distortion obtained using these lenses. When the angular coverage of the lenses used with the cameras is increasing, the systematic component of the geometric distortion becomes quite large and certainly needs to be compensated for if photogrammetric work of any quality is being planned. However, for those lenses with a small field of view, although the systematic components still remain, they are small in absolute terms compared with those produced by the lenses having a large angular coverage. The random component of the distortion produced by the CCD cameras was found to be in line with the measuring accuracy of the image matching method used in this project. In spite of the many digitized frames employed in the geometric calibration of these cameras, the magnitude and pattern of the geometric distortion that was obtained remained fairly consistent from one frame to another.

The analysis of the residual errors showed that the lenses exhibited some asymmetry in terms of their geometric distortion between any one cardinal direction and any other. A possibility is that decentering of the individual lens elements may have caused the asymmetric distortion pattern to appear in some lenses. (In this respect, it should be remembered that the cameras were not designed from the outset to be used for photogrammetric work). The graphical plots of the residual errors present an envelope of the geometric distortions that are present in each lens. The range of this envelope is significant and changes with the angular coverage of the lens used with the CCD camera. Moreover, the vector plots of the residual errors showed that the dimension of the geometric errors was increasing towards the corners of the image when the angular coverage of the lens was increasing. When the lens with the largest angular coverage was used, the main distortion that was encountered had a barrel-shaped pattern. However, it appears that this distortion may have originated not only from the camera lens, but also from the video monitor which was inserted between the camera and the VTR. In this case, any barrel distortion originating from the monitor would be superimposed on that of the lens and would cause the overall distortion to be larger.

- (ii) The geometric calibration of the new generation of thermal video frame scanners (TVFS) has been carried out to discover the magnitude and pattern of the geometric distortions that were present in their images. It was found that the distortion is large but quite symmetric and also systematic all over the image with the highest magnitudes occurring towards the edges of the image. This was not unexpected having regard to the spherical surface of the video image that is produced as a result of the scanning geometry. Hence, the patterns and magnitude of the geometric distortion that were obtained in the new tests are in line with the results achieved with the first generation TVFSs tested by Dr. Amin. However, there are some small differences between the effective terms obtained from the use of a polynomial transformation in this project and those found by Dr. Amin. In this project, the Agema 1000 and 900 imagers gave the same effective terms as his, but there was one additional term which appears to stem from the re-designed scanning system used with these imagers. For the other TVFSs (the Agema 470 and 880) tested in this research and which have low resolution, the higher-order terms that may be used to model the geometric distortion cannot be identified due to the small number of target crosses that were available for measurement. However, the overall results from their geometric calibration gave much the same distortion pattern as the TVFSs calibrated by Dr. Amin.
- (iii) The automatic image matching method that was devised and used to measure the image coordinates of the cross targets for geometric calibration purposes worked very successfully. This procedure provided several advantages over manual (non-automatic) methods since it eliminated both the errors originating from the measurements made by a human operator and the labour-intensive and time consuming work that is involved in the manual, operator-controlled measurement of a large number of target crosses. However, another advantage of using this technique was that it gave direct digital output to the other programs that had been developed to ascertain the geometric calibration of infrared imagers. All of the procedures that were employed for the geometric

calibration were computer programmed and were used without any difficulty arising from their application.

- (iv) The linear conformal and polynomial transformations that have been used here had previously been used extensively in the Department in conjunction with the planimetric accuracy tests and rectification of images acquired from space. But they proved to be equally suitable for the geometric calibration process since they supplied a variety of transformations in the form of a continuum that can be applied to the input measured image and reference coordinate values. In addition, these transformations model and identify the individual geometric distortions that are present in an image. Once this has been done, the effective terms can be included in a correction polynomial. Since the nature and extent of the geometric distortions produced by the infrared imaging systems that have been tested were not known prior to the calibration procedure being undertaken, the use of such a high order polynomial was necessary to determine them and proved to be very successful.

(b) Radiometric Calibration

- (i) The radiometric calibration of the various infrared imagers has been carried out using the uniform radiation source devised specifically for the purpose. The results that have been obtained from the processing of the grey level data of the frames, quadrants and patches that were extracted from the digitized images of the radiation source are reasonably useful. However they have their limitations at higher temperatures, their standard deviation values having increased to quite a significant extent, whereas at the lower temperatures, they exhibited a small standard deviation value. The larger figures appear to arise from the effect of the temperature gradient experienced over the face of the radiation source (and therefore of the image) since the temperature of the radiation source was so different to that of the ambient temperature of the surrounding environment. The graphical plots show a large gradient in the grey level values rising fairly consistently from the bottom to the top of the

plate and would appear to result from the heat rising from the plate in the form of a convection current or column of heated air that has its impact on the images. This matter has been visualized through the colour representation of the different grey level values that were present over the image using the SURFER program and is quite striking.

- (ii) To ensure that an area of uniform radiation was evaluated for the radiometric calibration, three different sized data sets - frames, quadrants and patches - have been used with each of the data sets that have been acquired from the imager concerned. The results that have been obtained from the processing of the resulting grey level value data showed that the temperature gradient became more marked when the size of the area was increased. Of course, conversely this effect decreased and there was more uniformity in the appearance of the area when the smaller quadrants and patches were used. Thus the smaller standard deviation values were obtained whenever the smaller sized patches were used for the radiometric calibration of the infrared imagers.

- (iii) The application of the non-uniformity correction procedure to correct the grey level values of the image data radiometrically at the middle temperature gave quite different results for each of the imagers that have been tested in this project. When ideal conditions - such as (a) the requirement that the images that are obtained at the reference temperatures should have lower standard deviation values than those acquired at the middle temperature which will be corrected; and (b) that a linear relationship should exist between the increment in the grey level values and the corresponding temperature increment - were actually realised, then the use of this method produced good results and provided increased uniformity of the image data at the middle temperature. However, it became more evident with the experimental procedure used in this project, that it is very difficult to provide these conditions in practical laboratory situations and a special facility might have to be built to provide an appropriate environment.

- (iv) The statistical processing of the images produced by the CCD cameras equipped with areal arrays of detectors for radiometric purposes showed that most of the grey level values of the pixels lie inside the range of the $A \pm 3\sigma$ criterion adopted by the author. This presumes that only those dead or blemished pixels that are not responding correctly to the radiation that is incident upon them have grey level values lying outside this range. However, the total number of these pixels was really quite small (less than 1%) when compared to the total number of pixels that were contained within the processed image area. The 3-D representation of the grey level values of the pixels of the image data by the SURFER program helped a lot allowing the analyst to see how the grey level values were changing, so enabling the positions of the blemished pixels to be located visually. This is important data for users to have.
- (v) The built-in hardware functions used in some infrared imagers hide the occurrence of dead or blemished pixels on the raw image - which tends to undermine the radiometric calibration procedure. These integral image restoration functions are implemented in these imagers in order to assign a new grey level value to each pixel which is then equal to the mean or some other value interpolated from the grey level values of the neighbouring pixels. In doing so, these built-in processing functions can prevent the raw radiometric information from appearing on the image. This has a decided impact on the radiometric calibration of the image since, in such a situation, the recorded grey level value data have already been restored and enhanced. However, where it is possible to switch these functions off on the infrared imagers, then raw image data could be obtained. It is then possible to identify and locate the pixels that are not responding at all or are not responding correctly to the incident radiation.

17.3 Recommendations for Future Work

Based on the experience gained during the various stages of the present project, the following points may be made regarding work which could be undertaken in the future.

- (i) Basically the target plate used for geometric calibration of the infrared imaging systems in this project, was designed and built specifically for the calibration of the high-resolution type of TVFS. However, for the lower resolution imagers that have been tested, e.g. the CCD cameras and the lower resolution TVFSs, only a comparatively small area located in the central part of the target plate could be imaged satisfactorily. So it then became difficult to obtain a sufficient number of cross targets on the image to carry out a really thorough geometric calibration of the imager - since the small number of effective terms that can be found using the polynomial transformation cannot fully model the geometric distortion that may be present in the images. In addition, because of the lack of redundancy, the use of the polynomial transformation is only applicable to a limited number of lower-order terms. Furthermore, the results obtained may give somewhat misleading information since the polynomial equation will simply fit the small number of points correctly. So, for a proper test of these low resolution imagers, a smaller-sized calibration plate with a greater density of target crosses is needed. In this project, this was designed but not built because of time and financial limitations. For future projects, this modified type of target plate should be constructed to test the low-resolution infrared imagers whose calibration could not be carried out fully in this research project.

- (ii) It is impossible to envisage present day infrared cameras and scanners as operational systems without the supporting video technology. The use of an all-video technology for image acquisition, image recording and display has been successful and has provided adequate data that was suitable for processing and analysis. However, in the near future, it is likely that all types

of infrared imagers will be capable of giving direct digital output which does not require any conversion. If this is the case, then the output from the imagers will be recorded in digital form in the field or in the air and can be processed directly by computer. This means that there may be no need for the intermediate recording stage on video tape using a VTR placed between the imager and computer - as was used in the present project. In this way, the effects arising from the use of this stage will be removed and direct digital infrared images will be obtained that can be used for the geometric and radiometric calibration of these imagers - though it should be noted that it will still have gone through an A/D conversion either within the camera or in the computer. This type of direct digital output from those imagers that operate in the visible part of the EM spectrum is already in use for the calibration of these devices. The same thing should be done for the infrared imagers and the calibration of these devices using direct digital output will be a new step in this area.

- (iii) In purely mechanical and optical terms, the calibration work requires a very precise set up for both the imager and the target plate. In the ideal situation, this should be provided in a specialist laboratory using an optical bench. However, in this project, accurate level bubbles and stable tripods and tables were used instead - since there was no optical bench available. In addition to this, all the adjustment and alignment of the imager with respect to the target plate was carried out visually to the limits of the author's abilities. So, any carelessness will cause a rotation of the imager or the target plate in the experimental setup and this will obviously affect the image resulting from this situation. Then the test measurements that will be carried out on these images will not be as accurate as they should be and the effects of the deficiency will show up in the final results.

Therefore, it is suggested that an optical bench should be used to establish the precise setup for future calibration work which will require great care and attention. On the other hand, it should also be noted that the methodology used

in the present project is low cost and quite practical for most users to implement and, in this respect, it may well appeal to them more, especially after they have investigated the costs of acquiring and installing a high quality optical bench! Indeed, unless a very large number of imagers need to be calibrated (e.g. by a manufacturer) it will be difficult to justify the large expenditure involved.

- (iv) The heated plate that was devised and constructed specifically to act as the radiation source for the radiometric calibration of the infrared imagers worked reasonably well. However, it was found that at higher temperatures, e.g. 50°C and 60°C, after reaching the set temperature, it was difficult to keep the temperature of the source stable since the ambient temperature in the laboratory was so much lower. This created a large gradient in the temperature rising from the bottom to the top of the radiation source which resulted in a heated convection current of air. Furthermore the plate lost heat quite quickly when there were these large differences in its temperature as compared with that of the surrounding air. In which case, the heating pads located on its back were then switching on and off many times within a short time interval attempting to maintain the specified temperature. In turn, the period of time that was available for taking and recording images of the radiation source at the set temperature then got very short. Whereas, at the lower temperatures such as 20°C and 25°C lying close to the ambient temperature, there was more than enough time to acquire a set of images of the plate suitable for calibration. So, this indicates that the images of the radiation source used for radiometric calibration of the infrared imager should perhaps only be obtained at the lower temperatures in future work.

For the benefit of future researchers, it is also worth suggesting that the problems of the temperature gradient that were present in the images used by the author for radiometric calibration may be lessened or even eliminated if a horizontal position of the radiation source was adopted during the set-up instead of the vertical position that was used by the author. The imager could

then be set in a position pointing vertically down towards the plate to obtain the required images. At least, this suggestion should be tried out. The other suggestion to be made is to devise an insulated box with a controlled temperature environment in which the radiation source could be placed with a view to lessening the temperature differences between the source and the surrounding air. However a precisely made (and costly) optical window would then be required through which the imager could view the radiation source.

17.4 Potential Applications

- (i) For airborne applications, the use of a thermal video frame scanner to reconstruct a 3-D model from two overlapping video images and to extract the 3-D information from these models employing analogue and analytical photogrammetric techniques has already been carried out and explained in Amin (1986). However, as far as the author can ascertain, there is no published work on airborne applications of infrared CCD cameras. In this project, both airborne and close-range applications of infrared CCD cameras were envisaged and planned. However, because of time limitations, these were not carried out. For the future, it will be interesting to apply these imagers to these particular fields where their use will provide unique information that cannot be obtained in any other way. For these purposes, using a infrared CCD camera, the same steps that Dr. Amin employed can be followed to create stereo-models and to extract 3-D information from the resulting digital stereo-models using digital photogrammetric techniques. In this way, the results obtained from the geometric and radiometric calibration of infrared imagers carried out in this research will provide vital information to those users who need to remove the geometric distortions and radiometric blemishes that are present in infrared images.
- (ii) As mentioned before, thermal pyroelectric vidicon cameras have been used extensively in certain industrial, medical and firefighting applications because of their low purchase prices (£5,000) when compared to those of the other

infrared imagers. Based on the recent development of their technology and the increasing resolution of these devices, they are now beginning to be used in condition monitoring and predictive / preventative maintenance applications. However, in this project, they could not be tested because of time limitations. Therefore, their main geometric and radiometric characteristics could not be discovered. However, for future researchers working in this area, it will be very interesting for them to define the geometric and radiometric properties of the pyroelectric vidicon cameras that are now finding applications in a number of areas outside firefighting.

17.5 A Final Note

Ending this thesis in a final personal note, the author has greatly benefited from undertaking this research work in various ways. Before commencing this work, he had very limited experience of computing. However, during the project, he has been able to make full use of the extensive facilities available in the Department and in the Computing Service. While much use was made of relevant software in the form of existing packages, the author has also succeeded in writing several computer programs in FORTRAN 77 language during his research work. As a result, the techniques of devising suitable algorithms and of writing the appropriate computer programs to solve such algorithms have been thoroughly grasped.

Furthermore, the author had only limited knowledge of and experience with digital photogrammetry and digital image processing techniques prior to undertaking this project. This knowledge has been greatly enhanced and expanded as a result of the project described in this dissertation. This can only be beneficial since the photogrammetry of the future will be largely digital in nature.

The field of infrared imaging was a completely new area for the author and proved to be interesting and exciting. By the end of his work, he has become very familiar with the geometric and radiometric characteristics of these unusual imaging systems. It goes without saying that the technology of infrared cameras and scanners and the

associated video technology and techniques were also totally unknown to the author before undertaking this research. However, the execution of this research project has greatly expanded and reinforced the knowledge of the author in this field and has taught him how to deal with what was, at first sight, a very strange type of imagery, and to carry out the processing, measurements and the extraction of information and to conduct detailed analyses of the results that come from using infrared images.

Finally, the most important single benefit that the author has gained from carrying out this project is probably his ability to identify the different problems that may arise during research work, to devise and implement solutions to these problems and to analyze the data resulting from these solutions. This will undoubtedly be of great benefit in the author's future career as a University lecturer and researcher.

REFERENCES

- Ackermann, F., 1984. Digital Image Correlation Performance and Potential Application in Photogrammetry. Photogrammetric Record, 11 (64): 429-439.
- Amin, A.M., 1986. Geometrical Analysis and Rectification of Thermal Infrared Video Frame Scanner Imagery and Its Potential Applications to Topographic Mapping, Ph.D Thesis, University of Glasgow, 334 pp.
- Amin, A.M. and Petrie, G., 1993. Geometric Calibration of Thermal Video Frame Scanners. Proceedings of SPIE, Videometrics II, 2067: 44-54.
- Amin, A.M. and Petrie, G., 1994. Design Characteristics and Geometric Calibration of Video Frame Scanners. ISPRS Journal of Photogrammetry and Remote Sensing, 49 (1): 12-24.
- Azizi, A., 1990. The Design and Implementation of A Purely Digital Stereo-Photogrammetric System on the IBM 3090 Multi-User Mainframe Computer, Ph.D Thesis, University of Glasgow, 235 pp.
- Beyer, H., 1990. Linejitter and Geometric Calibration of CCD Cameras. ISPRS Journal of Photogrammetry and Remote Sensing, 45 (3): 17-32.
- Beyer, H., 1992. Geometric and Radiometric Analysis of a CCD Camera Based Photogrammetric Close-Range System. Dissertation, ETH-Zurich, 186 pp.
- Beyer, H., 1994. Determination of Radiometric and Geometric Characteristics of Frame Grabbers. International Archives of Photogrammetry and Remote Sensing, 30 (5): 8-15.

- Boberg, A., 1994. A Synthetic Edge Function for Edge Gradient Analysis of Aerial Images. International Archives of Photogrammetry and Remote Sensing, 30 (1): 30-35.
- Burner, A.W., Snow, W.L., Shortis, M.R. and Goad, W.K., 1990. Laboratory Calibration and Characterization of Video Cameras. Proceedings of SPIE, 1395: 664-671.
- Burnay, S.G., Williams, T.L. and Jones, C.H., 1988. Applications of Thermal Imaging. Adam Hilger, 248 pp.
- Campbell, J.B., 1996. Introduction to Remote Sensing (2nd Edition). The Guilford Press, London, 622 pp.
- Cracknell, A.P. and Hayes, L.W.B., 1991. Introduction to Remote Sensing. Taylor & Francis, London, 293 pp.
- Curry, S., Baumrind, S. and Anderson, J.M., 1986. Calibration of an Array Camera. Photogrammetric Engineering and Remote Sensing, 52 (5): 627-636.
- Data Translation Ltd., 1995. Data Translation 1995 Product Handbook, 288 pp.
- Day, T. and Muller, J.P., 1988. Quality Assesment of Digital Elevation Models Produced by Automatic Stereomatchers from SPOT Image Pairs. Photogrammetric Record, 12 (72): 797-808.
- El-Hakim, S.F., 1986. Real-Time Image Metrology With CCD Cameras. Photogrammetric Engineering and Remote Sensing, 52 (11): 1757-1766.
- El-Hakim, S.F., 1986. A Real-time System for Object Measurement with CCD Cameras. International Archives of Photogrammetry and Remote Sensing, 26(5): 363-373.

El-Hakim, S.F., Burner, A.W. and Real, R.R., 1989. Video Technology and Real-Time Photogrammetry. In: H.M. Karara (ed), Non-Topographic Photogrammetry: 279-304.

El-Hassan, I.M., 1978. Metric Aspects of Reconnaissance Frame Photography, Ph.D Thesis, University of Glasgow, 403 pp.

Everitt, J.H., 1988. Introduction to Videography: Historical Overview, Relation to Remote Sensing, Advantages, Disadvantages. First Workshop on Videography, American Society for Photogrammetry and Remote Sensing: 1-5.

Fan, H. and Yuan, B., 1993. High Performance Camera Calibration Algorithm. Proceedings of SPIE, Videometrics II, 2067: 2-13

Feinberg, G., 1968. Light. Scientific American, 219 (3): 50-60.

Forstner, W., 1982. On the Geometric Precision of Digital Correlation. International Archives of Photogrammetry, 24 (3): 176-189.

Frei, W. and Chen, C.C., 1977. Fast Boundary Detection: A Generalization and a New Algorithm. IEEE Transactions on Computer Analysis, C-26: 188-198.

Fryer, J.G., 1996. Camera Calibration. In: K.B. Atkinson (ed), Close Range Photogrammetry and Machine Vision. Whittles Publishing: 156-179.

Gonzales, R.C. and Wintz, P., 1987. Digital Image Processing (2nd Edition). Addison-Wesley Publishing Company, Massachusetts, 495 pp.

Gruen, A.W., 1986. The Digital Photogrammetric Station (DIPS) at the ETH-Zurich. International Archives of Photogrammetry and Remote Sensing, 26(2): 76-84.

- Gruen, A.W. and Baltsavias, E.P., 1986. High Precision Image Matching for Digital Terrain Model Generation. International Archives of Photogrammetry, 26(3/1): 284-296.
- Gruen, A., 1988. Towards Real-Time Photogrammetry. Photogrammetria, 42(3): 209-244.
- Gulch, E., 1984. Geometric Calibration of Two CCD Cameras Used for Digital Image Correlation on the Planicomp C100. International Archives for Photogrammetry and Remote Sensing, 15(A3): 159-168.
- Gulch, E., 1985. Instrumental Realisation and Calibration of Digital Correlation with Planicomp. Proceedings of the 40th Photogrammetric Week, University of Stuttgart, 91-107.
- Gupton, J.A., 1986. Computer-Controlled Industrial Machines, Processes, and Robots. Prentice-Hall, Englewood Cliffs, New Jersey, 353 pp.
- Hackforth, H.L., 1960. Infrared Radiation. McGraw-Hill Book Company, Inc., New York, 303 pp.
- Haggren, H., 1984. New Vistas for Photogrammetry. International Archives of Photogrammetry and Remote Sensing, 25(A5): 382-391.
- Haggren, H., 1986. Real-Time Photogrammetry As Used for Machine Vision Applications. International Archives of Photogrammetry and Remote Sensing, 26 (5): 374-382.
- Hamamatsu Ltd., 1993. Characteristics and Use of Infrared Detectors. Technical Information, 45 pp.
- Hartwig, R.L., 1995. Basic TV Technology. Focal Press, 172 pp.

Hou, E.S., Li, J. and Kosonocky, W.F., 1995. Real-Time Implementation of the Two-Point Non-Uniformity Correction for IR-CCD Camera. SPIE Proceedings, Videometrics IV, 2598: 1-8.

Hueckel, M.F., 1971. An Operator Which Locates Edges in Digital Pictures. Journal of the Association for Computer Machinery, 18: 113-125.

Hueckel, M.F., 1973. A Local Operator Which Recognizes Edges and Lines. Journal of the Association for Computer Machinery, 20: 634-647.

Isong, M., 1987. An Investigation of the Geometric Fidelity of Spaceborne and Airborne Thematic Mapper Imagery and Its Potential Application to Topographic Mapping. M.App.Sci. Thesis, University of Glasgow, 257 pp.

Jacobsen, K., 1993. Comparative Analysis of the Potential of Satellite Images for Mapping. Proceedings, Workshop and Conference on "International Mapping from Space", ISPRS Working Group IV/2, Hannover: 107-114.

Jacobus, C.J. and Chien, R.T., 1981. Two New Edge Detectors. IEEE Transaction on Pattern Analysis and Machine Intelligence, PAMI-3 (2): 581-591.

Jamieson, J.A., McFee, R.H., Plass, G.N., Grube, R.H. and Richards, R.G., 1963. Infrared Physics and Engineering. McGraw-Hill Book Company, Inc., New York, 673 pp.

JVC Professional Products, 1988. Introduction to the European Version S-VHS Format. London: 2-7.

Kalao, M.A and Petrie, G., 1975. Testing Russar Super-Wide Angle Photography. Photogrammetric Record, 8 (45): 263-286.

- Kennie, T.J.M., 1985. Remote Sensing Scanning Systems. In: T.J.M. Kennie and M.C. Matthews (eds), Remote Sensing In Civil Engineering: 41-85.
- Kern, J., 1987. Hardware Components for Machine Vision System. Proceedings Intercommission on Fast Processing of Photogrammetric Data, Interlaken, Switzerland: 10-34.
- Kornfeld, G.H. and Lawson, W.R., 1971. Visual Perception Models. Journal of Optical Society of America, 61 (6): 47-55.
- Kosonocky, W.F., Shallcross, F.V., Villani, T.S. and Groppe, J.V., 1985. 160x244 Element PtSi Schottky-Barrier IR-CCD Image Sensor. IEEE Transactions on Electron Devices, ED-32 (8): 1564-1573.
- Kruse, P.W., McGlauchlin, L.D., McQuistan, R.B., 1962. Elements of Infrared Technology: Generation, Transmission, and Detection. John Wiley & Sons, Inc., New York, 448 pp.
- Lee, C.K. and Faig, W., 1996. Vibration Monitoring With Video Cameras. International Archives of Photogrammetry and Remote Sensing, 31 (B5): 152-159.
- Lee, T.H., Tredwell, T.J., Burkey, B.C., Kelly, T.M., Khosla, R.P., Losec, D.L., Neilsen, R.L. and McColgin, W.C., 1985. A 360000-Pixel Charge Coupled Color Image Sensor for Imaging Photographic Negative. IEEE Transactions on Electron Devices, ED-32 (8): 1439-1445.
- Lenz, R., 1987. Lens Distortion Corrected CCD Camera Calibration with Co-planar Calibration Points for Real-time 3D Measurements. ISPRS Proceedings Intercommission Conference on Fast Processing of Photogrammetric Data, Interlaken, Switzerland, 60-67.

Lillesand T.M. and Kiefer, R.W., 1994. Remote Sensing and Image Interpretation (3rd Edition). John Wiley & Sons, Inc., New York, 750 pp.

Lintz, J. and Simonett, D.S., 1976. Remote Sensing of Environment. Addison-Wesley Publishing Company, Massachusetts, 694 pp.

Lloyd, J.M., 1975. Thermal Imaging Systems, Plenum Press, 456 pp.

Luhmann, T. and Wester-Ebbinghaus, W., 1987. On Geometric Calibration of Digital Video Images of CCD Arrays. ISPRS Proceedings of the Intercommission Conference on Fast Processing of Photogrammetric Data, Interlaken, Switzerland, 35-47.

Machuca, R. and Gilbert, A.L., 1981. Finding Edges in Noisy Images. IEEE Transactions on Pattern Analysis and Machine Intelligence, PAMI-3 (2): 103-111.

Makarovic, B., 1980. Image Correlation Algorithms. International Archives of Photogrammetry, 23 (B2): 167-175.

Mather, P.M., 1987. Computer Processing of Remotely Sensed Images (An Introduction). John Wiley & Sons, Inc., New York, 352 pp.

Maruyasu, T. and Nishio, M., 1960. On the Study and Application of Infrared Aerial Photography. Report of the Institute of Industrial Science, University of Tokyo, 10 (1): 1-16.

Melen, T. and Balchen, J.G., 1994. Modelling Calibration of Video Cameras. International Archives of Photogrammetry and Remote Sensing, 30(3/1): 569-573.

Mikhail, E.M., Akey, M.L. and Mitchell, O.R., 1984. Detection and Sub-Pixel Location of Photogrammetric Targets in Digital Images. Photogrammetria, 39 (1): 63-83.

- Mooney, J.M., Shepherd, F.D., Ewing, W.S., Murguia, J.E. and Silverman, J., 1989. Responsivity Nonuniformity Limited Performance of Infrared Staring Cameras. Optical Engineering, 28 (11): 1151-1161.
- Murai, S., Otomo, F. and Otani, H., 1986. Automated Three-Dimensional Measurements Using Stereo CCD Camera in the Application to Close-Range Photogrammetry, International Archives of Photogrammetry and Remote Sensing, 26(5): 409-413.
- Murai, S., 1993. Remote Sensing Note. Japan Association on Remote Sensing, 284pp.
- Naithani, K., 1990. 'Can Satellite Images Replace Aerial Photographs' - A Photogrammetrist's View. ITC Journal, 1990-1: 29-31.
- Parr, G., 1941. The Cathode Ray Tube and Its Applications. Chapman & Hall Ltd, London: 146-147.
- Peipe, J., 1994. Photogrammetric Calibration and Performance Test of Still Video Cameras. International Archives of Photogrammetry and Remote Sensing, 30 (1): 108-113.
- Pertl, A., 1985. Digital Image Correlation With Analytical Plotter Planicomp C100. Photogrammetria, 40 (1): 9-19.
- Petrie, G., 1983. The Philosophy of Digital and Analytical Photogrammetric Systems. Proceedings of the 39th Photogrammetric Week, University of Stuttgart: 53-68.
- Petrie, G., 1990. Digital Mapping Technology: Procedures and Applications. In: T.J.M Kennie and G. Petrie (eds), Engineering Surveying Technology, Blackie: 329-389.

- Pol, V., Bennewitz, J.H., Jewell, T.E. and Peters, D.W., 1987. Excimer Laser Based Lithography: A Deep Ultraviolet Waper Stepper for VSLI Processing. Optical Engineering, 26 (4): 311-315.
- Raynor, J.M. and Seitz, P., 1990. The Technology and Practical Problems of Pixel-Synchronous CCD Data Acquisition for Optical Metrology Applications. Proceedings of SPIE, Close-Range Photogrammetry Meets Machine Vision, 1395: 96-103.
- Rosenberg, P., 1955. Information Theory and Electronic Photogrammetry. Photogrammetric Engineering, 21 (4): 543-555.
- Rosenfeld, A. and Kak, A.C., 1976. Digital Picture Processing. Academic Press, New York, 457 pp.
- Sandbank, C.P., 1990. Digital Television. John Wiley & Sons, Inc., Chister, 655 pp.
- Savage, J.A., 1985. Infrared Optical Materials and Their Antireflection Coatings. Adam Hilger, Bristol, 232 pp.
- Schalkoff, R.J., 1989. Digital Image Processing and Computer Vision. John Wiley & Sons, Inc., New York, 300 pp.
- Seitz, P., Vietze, O. and Spirig, T., 1995. From Pixels to Answers - Recent Developments and Trends in Electronic Imaging. International Archives of Photogrammetry and Remote Sensing, 30 (5W1): 2-12.
- Sherr, S., 1979. Electronic Displays. John Wiley & Sons, Inc., New York, 636 pp.
- Shortis, M.R. and Beyer, H.A., 1996. Sensor Technology For Digital Photogrammetry and Machine Vision. In: K.B. Atkinson (ed), Close Range Photogrammetry and Machine Vision. Whittles Publishing: 106-155.

Slama, C.C., Theurer, C. and Henriksen, S.W., 1980. Manual of Photogrammetry (4th Edition). American Society of Photogrammetry, Falls Church, Virginia, 1056 pp.

Tabatabai, A.J., and Mitchell, O.R., 1984. Edge Location to Subpixel Values in Digital Imagery. IEEE Transactions on Pattern Analysis and Machine Intelligence, PAMI-6 (2): 188-200.

Thurgood, J.D. and Mikhail, E.M., 1982. Subpixel Mensuration of Photogrammetric Targets in Digital Images. Technical Report, School of Civil Engineering, Purdue University, CE-PH-82-2: 252 pp.

Transtec, 1997. Catalogue for Unix and Windows NT.

Transtech Parallel Systems, 1995. C4x Product Catalog 1995 and C40 Parallel DSP.

Tsai, R.Y., 1987. A Versatile Camera Calibration Technique for High Accuracy 3D Machine Vision Metrology Using Off-the-Shelf TV Cameras and Lenses. IEEE Journal of Robotics and Automation, RA-3(4): 323-345.

Vlcek, J., 1988. Nature of Video Images. First Workshop on Videography, American Society for Photogrammetry and Remote Sensing: 5-13.

Welch, R., 1971. Modulation Transfer Functions. Photogrammetric Engineering and Remote Sensing, 37 (3): 247-259.

Welch, R., 1972. The Prediction of Resolving Power of Air and Space Photographic Systems. Imaging Technology: 25-32.

Wiebelt, J.A., 1966. Engineering Radiation Heat Transfer. Holt, Rinehart and Winston, New York, 278 pp.

- Wolf, P.R., 1983. Elements of Photogrammetry (2nd Edition). McGraw-Hill Book Company, Inc., Japan, 628 pp.
- Wolfe, W.L., 1965. Handbook of Military Infrared Technology. Office of Naval Research, Department of the Navy, Washington, D.C., 906 pp.
- Wolfe, W.L. and Zissis, G.J., 1978. Infrared Handbook. Environmental Research Institute of Michigan (ERIM), 1653 pp.
- Wong, K.W., 1969. Geometric Distortions in Television Imageries. Photogrammetric Engineering, 35 (5): 493-500.
- Wong, K.W., 1970. Fidelity of Space TV. Photogrammetric Engineering, 36 (5): 491-497.
- Wong, K.W., 1973. Analysis of RBV Television System. Photogrammetric Engineering, 39 (8): 851-861.
- Wong, K.W., 1975. Geometric and Cartographic Accuracy of ERTS-1 Imagery. Photogrammetric Engineering and Remote Sensing, 41 (5): 621-635.
- Wong, K.W. and Ho, W.H., 1986. Close-Range Mapping With a Solid-State Camera. Photogrammetric Engineering and Remote Sensing, 52 (1): 67-74.
- Zhou, G., 1986. Accurate Determination of Ellipse Centers in Digital Imagery. Technical Papers, ACSM-ASPRS Annual Convention, 4: 256-264.

APPENDICES

APPENDIX A: PROGRAM SUBPIX

APPENDIX B: REFERENCE COORDINATES OF THE CROSS TARGETS

APPENDIX C: PROGRAM LINCON

APPENDIX D: PROGRAM POLY25

APPENDIX E: PROGRAM STMN

APPENDIX F: PROGRAM PRNU

APPENDIX G: PROGRAM STAT

APPENDIX A: PROGRAM SUBPIX

A.1 Introduction

This program has been developed to detect and locate the position of the centre of each of the cross targets on the target plate used to calibrate imagers operating in the middle and thermal infrared parts of the EM spectrum. It consists of two main sub-programs - GRAD and PTSUB. The sub-program GRAD was written to generate the cross parameters (i.e. the mean cross and mean background grey level values and cross orientation) and to measure the coordinates of the cross centre automatically using the Gradient method. The sub-program PTSUB was developed to improve the cross parameters calculated by the first method. For this purpose, it employs the Image Modelling and Least Squares (IMLS) image matching approach.

A.2 Definitions of Some of the Variables

NR	number of pixels in the x-direction.
NC	number of pixels in the y-direction.
NJ	number of crosses in the x-direction.
NM	number of crosses in the y-direction.
TMD	the cross mean grey level value.
BMD	mean background grey level value.
TIOD, BIOD	cross and background integrated optical density.
ARET, AREB	cross and background area function.
IHH	initial threshold value.
W, EL	the width and length of a single cross leg.
THETA	cross orientation with respect to the scan line.
C1, C2	the calculated gradient along the row and column directions.
GRAD	calculated gradient value in two dimensions.
JF1, JL1	the column number of the starting and ending positions of the left cross leg.
XLT, YLT	row and column numbers of the midpoint of the left cross leg.

WID1	the calculated width of the left cross leg.
JF2, JL2	the column number of the starting and ending positions of the right cross leg.
XRT, YRT	row and column numbers of the midpoint of the right cross leg.
WID2	the calculated width of the right cross leg.
W	width of the cross target.
D	width of the point spread function.
SIGN	sum of the squared residuals between the grey level values of the modelled and the original crosses.
CRITIC	the minimum allowable change for "SIGN".
MAXITR	maximum allowable iteration.
SPECI	minimum value of correction to x and y coordinates.
H	increment for calculating the area lying under the Gaussian curve.

A.3 Definitions of Some of the Arrays

IM	matrix containing the digital infrared image.
OX, OY	matrix containing the reference coordinates of the cross targets.
HX, HY	matrix containing the approximate coordinates of the crosses.
XX, YY	matrix containing the resulting image coordinates of the crosses.
CL, CR	matrix containing the slope and constant of the lines fitted to the midpoints with the same orientations.
XL, YL	matrices containing the x and y coordinates of the midpoints of the cross legs with the same orientations.
XL1, XR1	working matrices containing the x values of the left and right cross legs respectively.
U	matrix containing the calculated cross parameter, i.e: U(1) - the cross mean grey level value; U(2) - background mean grey level value; U(3) - x coordinate of the cross centre; U(4) - y coordinate of the cross centre; and U(5) - cross orientation angle.

IMF	matrix of modelled image.
F	matrix of discrepancies between the grey level values of the modelled and the original image.
UX	matrix containing the components of the simulated cross.
B	coefficient matrix.
EN	normal matrix.

A.4 Explanation of the Program

The background to and the detailed explanation of the program have been given in Chapter 12, where all the sub-programs and routines that have been included in the program have also been described. Thus they will not be dealt with again here. In this Appendix, the program has been divided further into many blocks, each of which is compatible with the various stages that have been described in that chapter. Thus, the sequence of the program can be easily followed in this way.

A.5 Listing of the Program

```

PROGRAM SUBPIX
PARAMETER(NR=576,NC=768,NM=10,NJ=13)
IMPLICIT DOUBLE PRECISION (A-H,O-Z)
INTEGER*2 IM(NR,NC),NO(NM,NJ)
DOUBLE PRECISION GX(2),GY(2),BMA(2),TMA(2),
1      BP(2),W1(2),HX(NM,NJ),HY(NM,NJ),AX(NM,NJ),
2      AY(NM,NJ),BMB(NM,NJ),TMB(NM,NJ),BTP(NM,NJ),W2(NM,NJ),
3      XX(NM,NJ),YY(NM,NJ),U(10),OX(NM,NJ),OY(NM,NJ)
CHARACTER*32 NAME

```

C

```

100 PRINT*,'PLEASE ENTER THE IMAGE FILE NAME'
    READ(5,990)NAME
    OPEN(3,FILE=NAME,STATUS='OLD',FORM='FORMATTED',ERR=150)
    GOTO 155
150 PRINT*,'CANNOT FIND THE FILE'
    GOTO 100
155 DO 30, I=1,NR

```

```
30 READ(3,1000) (IM(I,J),J=1,NC)
C
  CLOSE(UNIT=3)
C
  PRINT*,'PLEASE ENTER THE OBJECT COOR.FILE'
  READ(5,990)NAME
  OPEN(3,FILE=NAME,STATUS='OLD',FORM='FORMATTED')
  DO 35, I=1,10
  DO 35, J=1,13
35 READ(3,1050) NO(I,J),OX(I,J),OY(I,J)
C -----END OF BLOCK 1.
  R1=45
  R2=85
  T1=37
  T2=77
  R3=434
  R4=474
  T3=440
  T4=480
C
  DO 310, I=1,2
  IF(I.EQ.1) THEN
    JB=R1
    JC=R2
    JD=T1
    JF=T2
  ELSE
    JB=R3
    JC=R4
    JD=T3
    JF=T4
  END IF
  CALL GRAD(IM,JB,JC,JD,JF,GX(I),GY(I),BMA(I),TMA(I),BP(I),W1(I))
310 CONTINUE
C
  PRINT*,GX(1),GY(1)
  CALL CORR(IM,R1,R2,T1,T2,R3,R4,T3,T4,RXY)
  PRINT*,'RXY=',RXY
```

```
C -----END OF BLOCK 2.
PRINT*, 'PLEASE ENTER THE NUMBER OF POINTS IN THE X AND Y DIRECTIONS'
READ*, NX, NY
C
EX=(GX(2)-GX(1))/(NX-1)
EY=(GY(2)-GY(1))/(NY-1)
C -----END OF BLOCK 3.
DO 600, I=1, NY
DO 600, J=1, NX
HX(I, J)=GX(1)+(J-1)*EX
HY(I, J)=GY(1)+(I-1)*EY
600 CONTINUE
C -----END OF BLOCK 4.
NP=20
DO 700, I=1, NY
DO 700, J=1, NX
JB=HY(I, J)-NP
JC=HY(I, J)+NP
JD=HX(I, J)-NP
JF=HX(I, J)+NP
CALL GRAD(IM, JB, JC, JD, JF, AX(I, J), AY(I, J),
1      BMB(I, J), TMB(I, J), BTP(I, J), W2(I, J))
U(1)=BMB(I, J)
U(2)=TMB(I, J)
U(3)=AX(I, J)
U(4)=-AY(I, J)
U(5)=BTP(I, J)
W=W2(I, J)
CALL PTSUB(U, IM, W)
XX(I, J)=U(3)
YY(I, J)=U(4)
700 CONTINUE
C -----END OF BLOCK 5.
PRINT*, 'ENTER THE OUTPUT FILE NAME FOR IMAGE COORDINATES'
READ(5, 990) NAME
OPEN(7, FILE=NAME, STATUS='NEW', FORM='FORMATTED')
DO 820, I=1, NY
DO 820, J=1, NX
```

```

820 WRITE(7,1600) NO(I,J),OX(I,J),OY(I,J),XX(I,J),YY(I,J)
C
990 FORMAT(A32)
1000 FORMAT(768I4)
1050 FORMAT(I8,T12,F10.3,T27,F10.3)
1600 FORMAT(I8,T12,F10.3,T27,F10.3,T42,F10.3,T57,F10.3)
C
2000 STOP
      END
C -----END OF BLOCK 6.
      SUBROUTINE GRAD(IM,JB,JC,JD,JF,FX,FY,BMD,TMD,TP,HP)
      PARAMETER(NR=576,NC=768,NT=40)
      IMPLICIT DOUBLE PRECISION (A-H,O-Z)
      INTEGER*2 IM(NR,NC)
      DOUBLE PRECISION XR(NT),YR(NT),XR1(NT),XL(NT),XL1(NT),
1          YL(NT),CL(2),CR(2)
      IH2=1
      IH1=1000
      DO 25 I=JB,JC
      DO 25 J=JD,JF
      IF(IH2.LT.IM(I,J)) IH2=IM(I,J)
25 IF(IH1.GT.IM(I,J)) IH1=IM(I,J)
      IHH=(IH1+IH2)/2
C
      ARET=0
      AREB=0
      TIOD=0
      BIOD=0
      DO 35 I=JB,JC
      DO 35 J=JD,JF
      IF(IM(I,J).GT.IHH) THEN
      TIOD=TIOD+IM(I,J)
      ARET=ARET+1
      ELSE
      BIOD=BIOD+IM(I,J)
      AREB=AREB+1
      END IF
35 CONTINUE

```

```
TMD=TIOD/ARET
BMD=BIOD/AREB
THRM=SQRT(BMD*BMD+TMD*TMD)
```

C

```
SPCM=SQRT(ARET/13.0)
HP=SPCM
SPC=SPCM
TH=1.0
```

C

```
KK=0
NN1=JB+1
NN2=JD+1
MC=JF-1
MR=JC-1
MX=1
THR=THRM
```

17 SPC=SPCM

```
THR=THR-TH
IF(THR.LT.TH RM/4.5) THEN
PRINT*,'NO CROSS CAN BE DETECTED'
GOTO 1100
END IF
```

11 I=NN1

```
ACC=0
II=0
```

10 J=NN2

```
JF1=0
JL1=0
JF2=0
JL2=0
XLT=0
XRT=0
WID1=0
WID2=0
```

C

20 IF(MX.EQ.1) THEN

```
C1=(IM(I+1,J)+IM(I+2,J))/2-(IM(I-1,J)+IM(I-2,J))/2
C2=(IM(I,J+1)+IM(I,J+2))/2-(IM(I,J-1)+IM(I,J-2))/2
```

```
ELSE
C1=IM(I+1,J)-IM(I-1,J)
C2=IM(I,J+1)-IM(I,J-1)
END IF
GRAD=SQRT(C1*C1+C2*C2)
```

C

```
IF(GRAD.GT.THR.AND.XLT.GT.0) THEN
IF(C2.GT.0) JF2=J
IF(C2.LT.0) JL2=J
IF(JF2.GT.0.AND.JL2.GT.0) WID2=JL2-JF2
END IF
IF(WID2.GE.SPC) THEN
II=II+1
XR(II)=JF2+WID2/2
YR(II)=I
XR1(II)=XR(II)
XRT=XR(II)
WID2=0
END IF
```

C

C

```
IF(GRAD.GT.THR.AND.XLT.EQ.0) THEN
IF(C2.GT.0) JF1=J
IF(C2.LT.0) JL1=J
IF(JF1.GT.0.AND.JL1.GT.0) WID1=JL1-JF1
END IF
IF(WID1.GE.SPC) THEN
XLT=JF1+WID1/2
YLT=I
WID1=0
END IF
```

C

C

```
IF(XRT.GT.0) THEN
XL(II)=XLT
XL1(II)=XL(II)
YL(II)=YLT
GOTO 55
```

END IF

C

J=J+1

IF(J.LT.MC) GOTO 20

55 I=I+1

IF(I.LT.MR) GOTO 10

IF(II.LT.2) THEN

SPC=SPC-1

IF(SPC.LT.1) GOTO 17

GOTO 11

END IF

C

N=1

IF(KK.EQ.2) N=2

16 N=N+1

IF(KK.EQ.3.OR.N.GT.II) THEN

PRINT*,'++'

PRINT*,'NO BETTER RESULT CAN BE OBTAINED'

GOTO 1100

END IF

SL=XL1(N)-XL1(N-1)

IF(SL.LT.0.OR.ACC.GE.1) THEN

ACC=ACC+1

M=N

IF(KK.EQ.1) M=N-1

IF(KK.EQ.2) M=N-2

CALL EXCHG(M,XL,XR,NT)

END IF

IF(N.LT.II) GOTO 16

IF(KK.EQ.1.OR.KK.EQ.2) CALL EXCHG(II,XL,XR,NT)

III=II-1

IF(KK.EQ.2) CALL EXCHG(III,XL,XR,NT)

PRINT*,''

WRITE(*,800)

DO 23, I=1,II

23 WRITE(*,200) XL(I),YL(I),XR(I),YR(I)

PRINT*,''

C

```
CALL FIT(XL,YL,II,CL)
```

```
CALL FIT(XR,YR,II,CR)
```

```
C
```

```
PRINT*,'CL',CL(1),CL(2)
```

```
PRINT*,'CR',CR(1),CR(2)
```

```
IF((CL(1)-CR(1)).EQ.0) THEN
```

```
PRINT*,'THE COEFFICIENT MATRIX IS SINGULAR'
```

```
PRINT*,'THE PROGRAM WILL BE RUN AGAIN BY INTERCHANGING'
```

```
PRINT*,'THE LEFT AND RIGHT CENTRE POINTS'
```

```
KK=KK+1
```

```
GOTO 11
```

```
END IF
```

```
C
```

```
IF(CL(1).EQ.0.AND.CL(2).EQ.0) THEN
```

```
FX=XL(1)
```

```
FY=CR(1)*FX+CR(2)
```

```
T1=1.571
```

```
T2=ATAN(CR(1))
```

```
GOTO 222
```

```
ELSE IF(CR(1).EQ.0.AND.CR(2).EQ.0) THEN
```

```
FX=XR(1)
```

```
FY=CL(1)*FX+CL(2)
```

```
T1=ATAN(CL(1))
```

```
T2=1.571
```

```
GOTO 222
```

```
C
```

```
END IF
```

```
FX=(CR(2)-CL(2))/(CL(1)-CR(1))
```

```
FY=CL(1)*FX+CL(2)
```

```
T1=ATAN(CL(1))
```

```
T2=ATAN(CR(1))
```

```
222 THETA1=-T1*180/3.14
```

```
THETA2=-T2*180/3.14
```

```
PRINT*,'~~~~~'
```

```
WRITE(*,300) FX,FY,THETA1,THETA2
```

```
WRITE(*,400) BMD,TMD
```

```
PRINT*,''
```

```
PRINT*,'~~~~~'
```

C

```
TP=(1.570796327+T1+T2)/2
DEL=180+THETA1-THETA2
IF(DEL.GT.95.00.OR.DEL.LT.85.00) THEN
  KK=KK+1
  GOTO 11
END IF
```

C

C

```
200 FORMAT(4F9.3)
300 FORMAT(/1X,'APPROXIMATE VALUES FOR UNKNOWNNS:',//5X,'X',
  1      9X,'Y',7X,'THETA1',7X,'THETA2',//2F9.3,F11.2,F14.2)
400 FORMAT(/6X,'H1',9X,'H2',//F9.0,F11.0)
800 FORMAT(/5X,'XL',9X,'YL',6X,'XR',9X,'YR')
```

C

```
1100 RETURN
      END
```

C

```
SUBROUTINE EXCHG(M,XL,XR,NT)
IMPLICIT DOUBLE PRECISION (A-H,O-Z)
DOUBLE PRECISION XL(NT),XR(NT)
X1=XL(M)
X2=XR(M)
XL(M)=X2
XR(M)=X1
RETURN
END
```

C

```
SUBROUTINE FIT(X,Y,N,D)
PARAMETER(NR=40)
IMPLICIT DOUBLE PRECISION (A-H,O-Z)
DOUBLE PRECISION GN(2,2),GF(2),D(2),AX(NR,2),
1      AXT(2,NR),X(NR),Y(NR)
CALL ZEROM1(GF,2)
CALL ZEROM2(GN,2,2)
DO 10, I=1,N
  AX(I,1)=X(I)
  AX(I,2)=1
```

```
    AXT(1,I)=X(I)
10  AXT(2,I)=1
    DO 30, II=1,2
    DO 30, JJ=1,2
    DO 30, L=1,N
30  GN(II,JJ)=GN(II,JJ)+AXT(II,L)*AX(L,JJ)
    DO 40, I=1,2
    DO 40, J=1,N
40  GF(I)=GF(I)+AXT(I,J)*Y(J)
C
    DT=GN(1,1)*GN(2,2)-GN(1,2)*GN(2,1)
    IF(DT.EQ.0) DT=0.01
    D(1)=GN(2,2)*GF(1)-GN(1,2)*GF(2)
    D(2)=-GN(2,1)*GF(1)+GN(1,1)*GF(2)
    D(1)=D(1)/DT
    D(2)=D(2)/DT
    RETURN
    END
C
    SUBROUTINE ZEROM1(A,N)
    IMPLICIT DOUBLE PRECISION (A-H,O-Z)
    DOUBLE PRECISION A(N)
    DO 100, I=1,N
100  A(I)=0
    RETURN
    END
C
    SUBROUTINE ZEROM2(Z,N,M)
    IMPLICIT DOUBLE PRECISION (A-H,O-Z)
    DOUBLE PRECISION Z(N,M)
    DO 200, I=1,N
    DO 200, J=1,M
200  Z(I,J)=0
    RETURN
    END
C
    SUBROUTINE PTSUB(U,IM,W)
    PARAMETER(NR=576,NC=768)
```

```
IMPLICIT DOUBLE PRECISION (A-H,O-Z)
DOUBLE PRECISION EN(5,5),SP(4),DL(5),T(5),ARE(4),U(10),
1          WU(5),IMF(NR,NC),F(NR,NC),P(4),UX(4,4),
2          B(5),IM(NR,NC),P1(4)
C
SPREAD(X)=EXP(-X*X/(D*D*0.5))/(1.2533141*D)
C
D0 10, I=1,5
10 WU(I)=0.0
C
EL=7.0*W
CRITIC=20.000
MAXITR=5
SPECI=0.001
H=0.5
ICONVG=0
LN=20
BR=20
D=1.00
ITR=0
C
CALL ZEROM1(U(6),5)
CALL ZEROM1(DL,5)
SIGN=1.0E+15
C
101 ITR=ITR+1
SIGO=SIGN
SIGN=0.0
C
CALL ZEROM2(EN,5,5)
CALL ZEROM1(T,5)
C
C SPECIFY IMAGE GEOMETRY
C
UX(1,1)= +0.5*W
UX(1,2)= -0.5*W
UX(1,3)= -0.5*W
```

```
UX(1,4)= -0.5*EL
C
UX(2,1)= +0.5*EL
UX(2,2)= +0.5*W
UX(2,3)= +0.5*W
UX(2,4)= -0.5*W
C
UX(3,1)= +0.5*W
UX(3,2)= -0.5*W
UX(3,3)= +0.5*EL
UX(3,4)= +0.5*W
C
UX(4,1)= +0.5*W
UX(4,2)= -0.5*EL
UX(4,3)= +0.5*W
UX(4,4)= -0.5*W
C
SN=SIN(U(5))
CS=COS(U(5))
C
LLL=ABS(U(3))-LN
KKK=ABS(U(4))-BR
JJJ=ABS(U(3))+LN
III=ABS(U(4))+BR
DO 106, I=KKK,III
DO 106, J=LLL,JJJ
C
S1=J
T1=-I
C
SS=CS*(S1-U(3))-SN*(T1-U(4))
TT=SN*(S1-U(3))+CS*(T1-U(4))
C
CALL ZEROM1(B,5)
C
DO 103, IL=1,4
C
P(2)=TT
```

```
P(1)=P(2)
P(4)=SS
P(3)=P(4)
C
DO 102, K=1,4
P(K)=P(K)+UX(IL,K)
P1(K)=P(K)
IF(P(K).GT.5.0.OR.P(K).LT.-5.0) P(K)=5.0
SP(K)=SPREAD(P(K))
C
CALL AREA(P1(K),D,ARE(K),H)
C
102 CONTINUE
C
C FORM COEFFICIENT MATRIX
C
B(1)=B(1)+(ARE(1)-ARE(2))*(ARE(3)-ARE(4))
DST=(SP(1)-SP(2))*(ARE(3)-ARE(4))
DSS=(SP(3)-SP(4))*(ARE(1)-ARE(2))
C
B(3)=B(3)-(U(2)-U(1))*(-SN*DST-CS*DSS)
B(4)=B(4)-(U(2)-U(1))*(-CS*DST+SN*DSS)
B(5)=B(5)-(U(2)-U(1))*(+SS*DST-TT*DSS)
C
103 CONTINUE
C
B(1)=-1.0+B(1)
B(2)=-1.0-B(1)
C
C IMF - MODELLED IMAGE I.E.IDEAL FUNCTION CONVOLVED WITH-
C GAUSSIAN SPREAD FUNCTION
C F - DISCREPANCIES BETWEEN MODELLED AND ORIGINAL IMAGE
C SIGN- SUM OF SQUARED RESIDUALS(DISCREPANCIES)
C
IMF(I,J)=U(1)-(U(2)-U(1))*B(2)
F(I,J)=-IM(I,J)+IMF(I,J)
SIGN=SIGN+F(I,J)*F(I,J)
C
```

```
C   FORM NORMAL EQUATIONS
C
C   DO 105, II=1,5
C   DO 104, JJ=1,5
C   EN(II,JJ)=EN(II,JJ)+B(II)*B(JJ)
C
C   104 CONTINUE
C
C   T(II)=T(II)+B(II)*F(I,J)
C
C   105 CONTINUE
C   106 CONTINUE
C
C   SIGN=SIGN/(2*LN*2*BR-5)
C   SIGCH=(SIGO-SIGN)/SIGO*100
C
C   108 IF(ITR.GT.1) THEN
C   WRITE(*,135)
C   WRITE(*,113) W,EL,D,(U(I),I=1,5)
C   WRITE(*,114) (ITR-1),(DL(I),I=1,5)
C   WRITE(*,119) SIGN,SIGCH
C   WRITE(*,135)
C   END IF
C
C   IF(SIGCH.LT.CRITIC) ICONVG=ICONVG+1
C
C   CHECK FOR MAX. ALLOWABLE ITERATION
C
C   IF(ITR.EQ.MAXITR.OR.ICONVG.EQ.1) GOTO 111
C
C   DO 109, I=1,5
C   EN(I,I)=EN(I,I)+WU(I)
C   109 T(I)=T(I)-WU(I)*U(I+5)
C
C   SOLVE NORMAL EQUATIONS
C
C   CALL ZEROM1(DL,5)
C   CALL SLVNRM(EN,T,DL)
```

```

C
C  ADD CORRECTIONS TO THE APPROXIMATE VALUES
C
    DO 110, I=1,5
    U(I)=U(I)+DL(I)
    U(I+5)=U(I+5)+DL(I)
110 CONTINUE
C
    ICONVG=0
    IF(ABS(DL(3)).LT.SPECI.AND.ABS(DL(4)).LT.SPECI) ICONVG=1
C
    GOTO 101
C
C  PRINT THE RESULT
C
111 WRITE(*,136)
    WRITE(*,116) (U(I),I=6,10),(U(J),J=1,5),SIGN
    WRITE(*,135)
C
113 FORMAT(/5X,'CROSS POINTING WITH',1X,'W=',F5.2,1X,'L=',F7.2,
* 4X,'AND SPREAD FUNCTION OF WIDTH=',F5.2,//1X,
* //5X,'PARAMETERS APPROXIMATION:',//9X,'H1',9X,
* 'H2',10X,'X',8X,'Y',7X,'THETA',//4X,2F10.2,2F10.3,F10.5)
114 FORMAT(/1X,'ITERATION',6X,'CORRECTIONS:',//4X,I3,5X,2F10.2,2F10.3,
* F10.5)
119 FORMAT(/1X,'VARIANCE',7X,'VAR.CH.',/,2F10.3)
116 FORMAT(/6X,18HTOTAL CORRECTIONS:./10X,2F10.2,2F10.3,F10.5,
* /6X,16HFINAL ESTIMATES:./10X,2F10.2,2F10.3,F10.5,
* 5X,F14.4)
135 FORMAT(/1X,'-----')
136 FORMAT(/1X,'////////////////////////////////////')
    RETURN
    END
C
    SUBROUTINE AREA(P,D,DD,H)
    IMPLICIT DOUBLE PRECISION (A-H,O-Z)
    DOUBLE PRECISION DD,DH,F,H
    SPREAD(X)=EXP(-X*X/(D*D*0.5))/(1.2533141*D)

```

C

```
DD=P/D+0.5
IF(DD.LT.0.0) GOTO 200
IF(DD.GT.1.0) GOTO 250
```

C

```
DH=0.0
IF(ABS(P).LT.H) GOTO 150
A=H
F=0.0
90 F=F+H
DH=DH+2*SPREAD(ABS(P)-F)
IF(ABS(P)-F.GT.H) GOTO 90
GOTO 100
150 A=ABS(P)
100 DD=0.5*A*(DH+0.7978845/D+SPREAD(P))
IF(P.LT.0.0) DD=0.5-DD
IF(P.GE.0.0) DD=0.5+DD
GOTO 70
200 DD=0.0
GOTO 70
250 DD=1.0
70 CONTINUE
RETURN
END
```

C

```
SUBROUTINE SLVNRM(EN,T,DL)
PARAMETER(NR=5)
IMPLICIT DOUBLE PRECISION (A-H,O-Z)
DOUBLE PRECISION EN(NR,NR),T(NR),DL(NR),ENI(NR,NR)
```

C

```
DO 6, I=1,NR
DO 6, J=1,NR
6 ENI(I,J)=0.0
ENI(1,1)=1.0/EN(1,1)
DO 40, N=2,NR
K=N-1
EK=EN(N,N)
DO 10, I=1,K
```

```
DO 10, J=1,K
10 EK=EK-EN(N,I)*ENI(I,J)*EN(J,N)
   ENI(N,N)=1.0/EK
DO 30, I=1,K
DO 20, J=1,K
20 ENI(I,N)=ENI(I,N)-ENI(I,J)*EN(J,N)/EK
30 ENI(N,I)=ENI(I,N)
   DO 40, I=1,K
   DO 40, J=1,K
40 ENI(I,J)=ENI(I,J)+ENI(I,N)*ENI(N,J)*EK
```

C

```
DO 50, I=1,NR
DO 50, J=1,NR
50 DL(I)=DL(I)+ENI(I,J)*T(J)
   RETURN
   END
```

C

```
SUBROUTINE CORR(IM,R1,R2,C1,C2,R3,R4,C3,C4,RXY)
PARAMETER(NR=576,NC=768)
IMPLICIT DOUBLE PRECISION (A-H,O-Z)
INTEGER*2 IM(NR,NC)
DATA PP1,PP3,PP4,PP6,PP7/5*0.0/
M=R3
N=C3
DO 40, I=R1,R2
DO 30, J=C1,C2
PP1=PP1+IM(I,J)*IM(M,N)
IF(M.EQ.R4.AND.N.EQ.C4) GOTO 1570
IF(N.EQ.C4) THEN
M=M+1
N=C3
ELSE
N=N+1
END IF
30 CONTINUE
40 CONTINUE
```

C

```
1570 DO 50, I=R1,R2
```

```

DO 45, J=C1,C2
PP3=PP3+IM(I,J)
PP4=PP4+IM(I,J)**2
45 CONTINUE
50 CONTINUE
C
PP5=PP3**2
DO 60, I=R3,R4
DO 55, J=C3,C4
PP6=PP6+IM(I,J)
PP7=PP7+IM(I,J)**2
55 CONTINUE
60 CONTINUE
C
PP8=PP6**2
ANUM=(R2-R1)*(C2-C1)*PP1-PP3*PP6
DEN1=(R2-R1)*(C2-C1)*PP4-PP5
DEN2=(R2-R1)*(C2-C1)*PP7-PP8
RXY=ANUM/SQRT(DEN1*DEN2)
C
RETURN
END
C -----END OF BLOCK 7.

```

A.6 Sample Output Data From Program SUBPIX

```

XL  YL  XR  YR
55.00 62.00 61.00 62.00
63.00 69.00 52.50 69.00
64.00 70.00 51.50 70.00
CL 0.88356 13.39727
////////////////////////////////////
APPROXIMATE VALUES FOR UNKNOWNNS
X    Y    THETA1  THETA2
57.91 64.57   -41.98   39.88
H1    H2
88.   188.
////////////////////////////////////
CROSS POINTING WITH W=3.00 L=21.00 AND SPREAD WIDTH D=1.00

```

PARAMETER APPROXIMATION:

H1	H2	X	Y	THETA
0.27	1.60	57.915	-64.567	0.7997

ITERATION CORRECTIONS:

1	-87.89	-186.74	0.001	0.000	0.00000
---	--------	---------	-------	-------	---------

VARIANCE VAR.CH.

1.015	99.995
-------	--------

PARAMETER APPROXIMATION:

H1	H2	X	Y	THETA
0.27	1.60	58.006	-64.534	0.79995

ITERATION CORRECTIONS:

2	-0.00	0.00	0.091	0.033	0.00024
---	-------	------	-------	-------	---------

VARIANCE VAR.CH.

1.029	-1.360
-------	--------

////////////////////////////////////

TOTAL CORRECTIONS

-87.99	-186.74	0.092	0.034	0.0024
--------	---------	-------	-------	--------

FINAL ESTIMATES

0.27	1.60	58.006	-64.534	0.79995	1.0291
------	------	--------	---------	---------	--------

N.B. The sample output from program SUBPIX has also been given in Chapter 12.

APPENDIX B: REFERENCE COORDINATES OF THE CROSS TARGETS

B.1 Introduction

In the project carried out by Dr. Amin (1986), the measurements of the reference (calibrated) coordinates of the 130 cross targets were carried out using a Ferranti Monocomparator located at the National Engineering Laboratories (NEL). This device was equipped with a vidicon tube camera pointing vertically downwards on the target plate and produced a 10X magnified image on a 9" video monitor. A cross-hair cursor allowed the observer to point to the target crosses accurately on the video monitor. The machine was equipped with linear encoders to give the measured plate coordinates (X, Y) of the target crosses to a resolution of 1 μ m with an accuracy of $\pm 7\mu$ m as claimed by the manufacturer. The method of measuring the cross targets using this monocomparator was described in some detail in Chapter 12. The resulting reference coordinates of the target crosses are given below.

No.	X (mm)	Y (mm)
130	-180.374	134.415
129	-150.399	134.484
128	-120.381	134.559
127	-90.407	134.623
126	-60.407	134.824
125	-30.390	134.896
124	-0.414	134.963
123	29.594	135.087
122	59.568	135.103
121	89.606	135.282
120	119.570	135.355
119	149.575	135.395
118	179.555	135.475
105	-180.324	104.434
106	-150.329	104.499
107	-120.333	104.583
108	-90.300	104.600
109	-60.309	104.838

Appendix B: Reference Coordinates of the Cross Targets

110	-30.357	104.905
111	-0.385	104.960
112	29.640	105.058
113	59.639	105.117
114	89.628	105.304
115	119.646	105.379
116	149.618	105.437
117	179.593	105.473
104	-180.201	74.435
103	-150.216	74.507
102	-120.217	74.576
101	-90.226	74.630
100	-60.214	74.845
99	-30.220	74.917
98	-0.221	74.978
97	29.765	75.051
96	59.786	75.124
95	89.793	75.345
94	119.771	75.408
93	149.765	75.399
92	179.734	75.482
79	-180.127	44.481
80	-150.134	44.534
81	-120.169	44.599
82	-90.177	44.659
83	-60.098	44.869
84	-30.145	44.926
85	-0.163	44.990
86	29.833	45.087
87	59.812	45.083
88	89.857	45.348
89	119.825	45.364
90	149.796	45.409
91	179.749	45.503
78	-180.021	14.467
77	-150.010	14.537
76	-120.003	14.603
75	-90.031	14.661

Appendix B: Reference Coordinates of the Cross Targets

74	-60.012	14.890
73	-30.025	14.923
72	-0.017	14.993
71	29.991	15.127
70	59.933	15.197
69	89.964	15.333
68	119.950	15.413
67	149.932	15.467
66	179.911	15.534
53	-179.949	-15.531
54	-149.974	-15.446
55	-119.972	-15.384
56	-89.991	-15.331
57	-59.968	-15.106
58	-29.975	-15.040
59	0.018	-14.993
60	30.004	-14.921
61	60.010	-14.898
62	90.025	-14.650
63	119.968	-14.599
64	149.966	-14.539
65	179.946	-14.496
52	-179.845	-45.519
51	-149.836	-45.462
50	-119.851	-45.381
49	-89.862	-45.335
48	-59.821	-45.097
47	-29.853	-45.041
46	0.133	-44.979
45	30.130	-44.880
44	60.120	-44.895
43	90.156	-44.703
42	120.143	-44.579
41	150.124	-44.528
40	180.074	-44.470
27	-179.837	-75.519
28	-149.798	-75.455
29	-119.803	-75.382

Appendix B: Reference Coordinates of the Cross Targets

30	-89.846	-75.338
31	-59.764	-75.135
32	-29.777	-75.054
33	0.179	-74.988
34	30.180	-74.932
35	60.224	-74.876
36	90.211	-74.672
37	120.187	-74.581
38	150.174	-74.521
39	180.148	-74.491
26	-179.696	-105.534
25	-149.687	-105.459
24	-119.722	-105.374
23	-89.716	-105.298
22	-59.677	-105.115
21	-29.707	-105.060
20	0.288	-104.990
19	30.286	-104.894
18	60.261	-104.858
17	90.295	-104.691
16	120.282	-104.627
15	150.276	-104.548
14	180.252	-104.492
1	-179.687	-135.564
2	-149.690	-135.429
3	-119.690	-135.379
4	-89.698	-135.284
5	-59.647	-135.096
6	-29.669	-135.011
7	0.313	-134.966
8	30.312	-134.896
9	60.302	-134.854
10	90.330	-134.667
11	120.345	-134.599
12	150.326	-134.512
13	180.276	-134.482

APPENDIX C: PROGRAM LINCON

C.1 Program LINCON

This program was developed to carry out a linear conformal transformation in order to establish the magnitude of the systematic and random distortions present in the infrared images. The mathematical basis of the program has been discussed in Section 13.4.1.

C.2 Definitions of Some of the Variables

- N number of points whose calibrated and measured coordinates are known.
- mx rmse value in the x-direction.
- my rmse value in the y-direction.

C.3 Definitions of Some of the Arrays

- A coefficient matrix of transformation parameters.
- AT transpose matrix of A.
- AN inverse matrix of A.
- DX matrix of transformation parameters.
- OB matrix of measured image coordinates of target crosses.
- RE matrix of calibrated target plate coordinates.
- SV matrix of systematic distortions in x and y at each image point.
- V matrix of random distortions in x and y at each image point.

C.4 Explanation of Program LINCON

Once again, the listing of the program below has been divided into a number of blocks to facilitate the explanation of the program.

- Block 1.** In this first block, the program name is defined and the arrays required for input data are dimensioned. The COMMON/BLOCK command has been used in order to reduce the storage space required in the computer during the running of the program.
- Block 2.** In this block, the program asks for the total number of points and the data file name. If a wrong data file name is given, the program will display an error message and gives the operator two alternatives - either to continue and give the correct file name, or to quit.
- Block 3.** This executes the least squares computations to determine the transformation parameters, after which, the residual errors at each image point are computed.
- Block 4.** The transformation parameters for the first image are printed together with the residual errors at each point if required.
- Block 5.** The program asks if this is the last image to be calibrated. If the answer is YES, the residual errors at all the corresponding image points are added to those of the previous images and the mean (systematic) distortion is computed and printed. If the answer is NO, the residuals are added to the appropriate list and the program starts again from Block 2.
- Block 6.** The program asks if it is required to correct any image for systematic distortion and then compute the random distortion. If the answer is YES, the program proceeds to the next block. If the answer is NO, the program ends.
- Block 7.** In this block, the program asks for the data file name, reads the calibrated and measured coordinates, and corrects these measured coordinates for the systematic distortion.

Block 8. The least squares procedure is used again to transform the calibrated coordinates into the image coordinate system. This time, the corrected image coordinates are used for the transformation procedure. After the transformation, the residual errors at each image point are computed and printed.

Block 9. In this block, the random distortion values for the image are printed out. Then the program asks if it is required to correct any other image for systematic distortion. If the answer is YES, the program starts again from Block 7. If the answer is NO, the program ends.

Block 10. Contains the sub-routines used for matrix operations. These are:-

- (1) *FORM* which is used to form the matrix of the coefficients of the unknown parameters;
- (2) *MATINV* to perform matrix inversion;
- (3) *MATVEC* to carry out the multiplication of a matrix array by a vector array;
- (4) *MATMAT* to carry out the multiplication of two matrices;
- (5) *MATSUB* to subtract two matrices from each other;
- (6) *RMSE* to compute the rmse value using the residual errors at each point; and
- (7) *CORR* to correct the measured image coordinates for the systematic distortion.

C.5 Listing of Program LINCON

```
PROGRAM LINCON
PARAMETER(NR=260)
COMMON/BLOCK1/OB(NR,2),RE(NR,2),A(NR,NR),SF(NR)
DIMENSION AT(NR,NR),AN(NR,NR),ANT(NR,NR),F(NR),
1 DX(NR),V(NR),H(NR),NO(NR),SUMV(NR),
```

```

2    SV(NR)
    CHARACTER*32 NAME1,NAME2
    CHARACTER*1 ANS
C
C -----END OF BLOCK 1.
C
    T=0.0
1  PRINT*,'PLEASE ENTER THE NUMBER OF CONTROL POINTS'
    READ*,N
    DO 77, I=1,2*N
77  SUMV(I)=0
145 PRINT*,'PLEASE ENTER THE CONTROL POINTS FILE NAME'
    READ(5,990)NAME1
    OPEN(3,FILE=NAME1,STATUS='OLD',FORM='FORMATTED',ERR=150)
    T=T+1
    GOTO 155
150 PRINT*,'CANNOT FIND THE CONTROL POINTS FILE'
    GOTO 145
155 DO 15, I=1,N
    READ(3,1000) NO(I),RE(I,1),RE(I,2),OB(I,1),OB(I,2)
15  CONTINUE
    CLOSE(UNIT=3)
C
C -----END OF BLOCK 2.
C
    CALL FORM(N)
    CALL MATRAN(A,AT,2*N,4)
    CALL MATMAT(AT,A,AN,4,2*N,4)
    CALL MATINV(AN,4,ANT)
    CALL MATVEC(AT,SF,F,4,2*N)
    CALL MATVEC(ANT,F,DX,4,4)
    CALL MATVEC(A,DX,H,2*N,4)
    CALL MATSUB(H,SF,V,2*N)
C
C -----END OF BLOCK 3.
C
    PRINT*,'*****'
    WRITE(6,700)T

```

```

700 FORMAT(/2X,'TRANSFORMATION PARAMETERS FOR IMAGE NO.',F4.0)
      DO 60, I=1,4
      PRINT*,DX(I)
60 CONTINUE
      PRINT*, '*****'
      PRINT*, 'DO YOU WANT TO PRINT THE SYSTEMATIC DISTORTION?'
      READ(5,255)ANS
      IF(ANS.EQ.'N') GOTO 62
      WRITE(6,710)T
710 FORMAT(/2X,'*RESIDUAL ERRORS FOR IMAGE NO.',F4.0,'**')
      WRITE(6,280)
280 FORMAT(/3X,'PT.NO.',2X,'X',9X,'Y',6X,'DX',7X,'DY')
      DO 70, I=1,2*N,2
      J=I/2+1
70 WRITE(6,274) J,OB(J,1),OB(J,2),V(I),V(I+1)
62 PRINT*, 'DO YOU WANT TO CREATE A PLOTTING FILE FOR THIS IMAGE?'
      READ(5,255)ANS
      IF(ANS.EQ.'Y')THEN
      PRINT*, 'INPUT PLOTTING FILE NAME'
      READ(5,990)NAME1
      OPEN(1,FILE=NAME1, FORM='FORMATTED', STATUS='NEW')
      DO 877, I=1,2*N,2
      J=I/2+1
877 WRITE(1,274)J,OB(J,1),OB(J,2),V(I),V(I+1)
      END IF
      CLOSE(UNIT=1)
      CALL RMSE(V,N, RMSEX, RMSEY, RMSEP)
990 FORMAT(A32)
1000FORMAT(I8,T12,F10.3,T27,F10.3,T42,F10.3,T57,F10.3)
      WRITE(6,357)
      WRITE(6,377) RMSEX, RMSEY, RMSEP
357 FORMAT(//, '   MX   MY   MP')
377 FORMAT(/,3F13.2)
      DO 250, I=1,2*N
250 SUMV(I)=SUMV(I)+V(I)
      WRITE(6,144)
274 FORMAT(I4,2F10.3,2F8.2)

```

C

C -----END OF BLOCK 4.

C

```
144 FORMAT(//,'IS THIS THE LAST IMAGE ?')
      READ(5,255)ANS
      IF(ANS.EQ.'N') GOTO 145
      DO 260, I=1,2*N
260 SV(I)=SUMV(I)/T
      WRITE(6,290)
290 FORMAT(/3X,'**SYSTEMATIC DISTORTION **')
      WRITE(6,280)
      DO 270, I=1,2*N,2
      J=I/2+1
270 WRITE(6,274) J,OB(J,1),OB(J,2),SV(I),SV(I+1)
      81 CALL RMSE(SV,N,RMSEX,RMSEY,RMSEP)
      WRITE(6,357)
      WRITE(6,377) RMSEX,RMSEY,RMSEP
275 FORMAT(3X,I3,3X,F14.8,3X,F14.8)
255 FORMAT(A1)
```

C

C -----END OF BLOCK 5.

C

```
      WRITE(6,156)
156 FORMAT(//,'DO YOU WANT TO COMPUTE THE RANDOM DISTORTION
1     FOR ANY * IMAGE ?')
      READ(5,255)ANS
      IF(ANS.EQ.'N') GOTO 999
```

C

C -----END OF BLOCK 6.

C

```
66 PRINT*,'PLEASE ENTER THE IMAGE FILE NAME'
      READ(5,990)NAME2
      OPEN(9,FILE=NAME2,STATUS='OLD',FORM='FORMATTED',ERR=819)
      GOTO 820
819 PRINT*,'CANNOT FIND THE DATA FILE NAME'
      GOTO 66
820 DO 600, I=1,N
600 READ(9,1000) NO(I),RE(I,1),RE(I,2),OB(I,1),OB(I,2)
      CALL CORR(OB,SV,N)
```

```
C
C -----END OF BLOCK 7.
C
CALL FORM(N)
CALL MATRAN(A,AT,2*N,4)
CALL MATMAT(AT,A,AN,4,2*N,4)
CALL MATINV(AN,4,ANT)
CALL MATVEC(AT,SF,F,4,2*N)
CALL MATVEC(ANT,F,DX,4,4)
CALL MATVEC(A,DX,H,2*N,4)
CALL MATSUB(H,SF,V,2*N)
C
C -----END OF BLOCK 8.
C
WRITE(6,157)
157 FORMAT(//,'DO YOU WANT TO PRINT THE RANDOM DISTORTION ?')
READ(5,255)ANS
IF(ANS.EQ.'N') GOTO 113
PRINT*,' ***** RANDOM DISTORTION *****'
WRITE(6,280)
DO 133, I=1,2*N,2
J=I/2+1
WRITE(6,274) J,OB(J,1),OB(J,2),V(I),V(I+1)
133 CONTINUE
113 PRINT*,'PLEASE INPUT THE PLOTTING FILE NAME'
READ(5,990)NAME1
OPEN(3,FILE=NAME1,STATUS='NEW',FORM='FORMATTED')
DO 456, I=1,2*N,2
J=I/2+1
456 WRITE(3,274) J,OB(J,1),OB(J,2),V(I),V(I+1)
CLOSE(UNIT=3)
CALL RMSE(V,N,RMSEX,RMSEY,RMSEP)
WRITE(6,357)
WRITE(6,377) RMSEX,RMSEY,RMSEP
PRINT*,'DO YOU WANT TO CORRECT ANY OTHER IMAGE?(Y/N)?'
READ(5,255)ANS
IF(ANS.EQ.'Y') GOTO 66
999 END
```

```
C
C -----END OF BLOCK 9.
C
SUBROUTINE CORR(OB,SV,N)
PARAMETER(NR=260)
DIMENSION OB(NR,2),SV(NR)
DO 700, I=1,2*N,2
  J=I/2+1
  OB(J,1)=OB(J,1)-SV(I)
700 OB(J,2)=OB(J,2)-SV(I+1)
RETURN
END
C
SUBROUTINE FORM(N)
PARAMETER(NR=260)
COMMON/BLOCK1/OB(NR,2),RE(NR,2),A(NR,NR),SF(NR)
DO 10, I=1,2*N,2
  J=I/2+1
  A(I,1)=1
  A(I,2)=RE(J,1)
  A(I,3)=-RE(J,2)
  A(I,4)=0
  A((I+1),1)=0
  A((I+1),2)=RE(J,2)
  A((I+1),3)=RE(J,1)
  A((I+1),4)=1.0
10 CONTINUE
DO 20, I=1,2*N,2
  J=I/2+1
  SF(I)=OB(J,1)
  SF(I+1)=OB(J,2)
20 CONTINUE
RETURN
END
C
SUBROUTINE MATINV(A,N,AINV)
PARAMETER(NR=260)
DIMENSION A(NR,NR),AINV(NR,NR),B(NR,NR),X(NR,NR)
```

```
M=2*N
DO 600, I=1,N
DO 605, J=1,N
605 B(I,J)=A(I,J)
DO 600, J=N+1,M
IF((I+N).EQ.J) THEN
B(I,J)=1.
ELSE
B(I,J)=0.0
END IF
600 CONTINUE
DO 610, I=1,N
PIVOT=B(I,I)
DO 615, J=I+1,N
IF(ABS(PIVOT).LT.ABS(B(J,I))) THEN
DO 620, K=1,M
TT=B(I,K)
B(I,K)=B(J,K)
B(J,K)=TT
620 CONTINUE
PIVOT=B(J,I)
END IF
615 CONTINUE
DO 625, K=M,I,-1
625 B(I,K)=B(I,K)/B(I,I)
DO 630, J=I+1,N
DO 630, K=M,I,-1
B(J,K)=B(J,K)-B(I,K)*B(J,I)
630 CONTINUE
610 CONTINUE
DO 640, J=1,N
K=N+J
X(N,J)=B(N,K)
640 CONTINUE
DO 650, I=N-1,1,-1
DO 655, J=1,N
M=N+J
X(I,J)=B(I,M)
```

```
655 CONTINUE
      DO 660, K=N,I+1,-1
      DO 660, J=1,N
      X(I,J)=X(I,J)-B(I,K)*X(K,J)
```

```
660 CONTINUE
650 CONTINUE
      DO 670, I=1,N
      DO 670, J=1,N
670 AINV(I,J)=X(I,J)
```

```
      RETURN
      END
```

C

```
      SUBROUTINE MATVEC(A,X,Z,N,M)
      PARAMETER(NR=260)
      DIMENSION A(NR,NR),X(NR),Z(NR)
      INTEGER M,N
      DO 5, I=1,N
      SUM=0.0
      DO 5, J=1,M
      SUM=SUM+A(I,J)*X(J)
5 Z(I)=SUM
      RETURN
      END
```

C

```
      SUBROUTINE MATMAT(A,U,T,N,M,IP)
      PARAMETER(NR=260)
      DIMENSION A(NR,NR),U(NR,NR),T(NR,NR)
      DO 10, J=1,N
      DO 10, K=1,IP
      T(J,K)=0.0
      DO 10, I=1,M
      T(J,K)=T(J,K)+A(J,I)*U(I,K)
10 CONTINUE
      RETURN
      END
```

C

```
      SUBROUTINE MATRAN(A1,A1T,N,M)
      PARAMETER(NR=260)
```

```

DIMENSION A1(NR,NR),A1T(NR,NR)
DO 11, I=1,N
DO 11, J=1,M
11 A1T(J,I)=A1(I,J)
RETURN
END
C
SUBROUTINE MATSUB(A,B,C,N)
PARAMETER(NR=260)
DIMENSION A(NR),B(NR),C(NR)
DO 95, I=1,N
95 C(I)=B(I)-A(I)
RETURN
END
C
SUBROUTINE RMSE(X,N,RMSEX,RMSEY,RMSEP)
PARAMETER(NR=260)
DIMENSION X(NR)
SUMXX=0.0
SUMYY=0.0
DO 900, I=1,2*N,2
SUMXX=SUMXX+X(I)**2
900 SUMYY=SUMYY+X(I+1)**2
RMSEX=SQRT(SUMXX/(N-1))
RMSEY=SQRT(SUMYY/(N-1))
RMSEP=SQRT(RMSEX**2+RMSEY**2)
RETURN
END
C -----END OF BLOCK 10.

```

C.6 Sample Output Data From Program LINCON

SYSTEMATIC DISTORTION

Pt.No	X	Y	DX	DY
1	68.731	-36.231	-12.13	-27.71
2	106.621	-35.103	-10.85	-26.12
3	144.641	-34.923	-9.49	-25.47
4	183.500	-33.800	-7.23	-23.87

5	222.887	-33.710	-4.48	-23.47
6	262.500	-33.500	-1.52	-22.79
7	301.750	-33.708	1.12	-22.53
8	341.750	-34.000	4.48	-22.42
9	381.380	-34.400	7.50	-22.28
10	420.750	-35.000	10.19	-22.54
11	460.250	-36.000	13.10	-23.08
12	499.000	-37.000	15.21	-23.57
13	537.121	-38.103	16.72	-24.22
14	66.111	-66.333	-14.26	-21.21
15	104.375	-65.000	-12.62	-19.40
16	142.767	-64.800	-10.86	-18.74
17	181.848	-63.848	-8.46	-17.26
18	221.355	-64.090	-5.58	-17.23
19	261.113	-64.290	-2.40	-16.96
20	300.880	-64.400	0.77	-16.58
21	340.900	-65.200	4.12	-16.95
22	380.750	-65.000	7.34	-16.26
23	420.500	-65.800	10.47	-16.74
24	459.900	-65.800	13.21	-16.27
25	499.000	-67.429	15.71	-17.42
26	537.250	-67.750	17.36	-17.23
27	64.397	-97.517	-15.57	-15.75
28	102.545	-97.152	-14.04	-14.92
29	141.438	-95.500	-11.78	-12.80
30	180.250	-95.786	-9.59	-12.60
31	220.000	-95.800	-6.49	-12.32
32	260.206	-96.294	-2.91	-12.34
33	300.000	-96.000	0.25	-11.57
34	340.250	-96.400	3.88	-11.50
35	380.250	-96.600	7.22	-11.24
36	420.250	-97.292	10.57	-11.64
37	460.121	-98.103	13.83	-11.98
38	499.250	-99.000	16.34	-12.31
39	538.000	-100.000	18.49	-12.85
40	62.500	-129.000	-17.00	-10.66
41	100.630	-127.889	-15.50	-9.06
42	140.238	-127.762	-12.48	-8.45

43	178.750	-127.214	-10.60	-7.42
44	218.853	-126.824	-7.23	-6.73
45	258.875	-127.000	-3.78	-6.43
46	299.365	-128.135	0.10	-7.08
47	339.250	-127.600	3.35	-6.11
48	379.631	-128.053	7.12	-6.00
49	419.630	-128.889	10.43	-6.61
50	459.500	-129.571	13.70	-6.75
51	499.000	-131.000	16.60	-7.68
52	537.865	-132.135	18.89	-8.38
53	61.018	-159.786	-18.06	-4.79
54	99.545	-158.848	-16.18	-3.38
55	138.250	-159.000	-14.12	-3.06
56	177.629	-158.903	-11.34	-2.48
57	217.889	-158.500	-7.74	-1.80
58	258.054	-158.351	-4.19	-1.14
59	297.880	-159.400	-1.01	-1.72
60	338.500	-160.111	2.96	-2.03
61	378.500	-160.000	6.40	-1.45
62	419.000	-160.562	10.22	-1.63
63	458.864	-161.273	13.47	-1.88
64	498.379	-161.897	16.37	-2.02
65	537.379	-162.897	18.76	-2.54
66	60.119	-191.619	-18.49	0.01
67	98.687	-191.000	-16.53	1.08
68	137.500	-191.000	-14.35	1.56
69	177.054	-190.351	-11.41	2.70
70	217.500	-191.000	-7.63	2.33
71	257.000	-190.500	-4.75	3.30
72	297.071	-191.493	-1.31	2.81
73	338.054	-192.243	3.06	2.53
74	378.249	-192.247	6.61	3.05
75	418.379	-192.897	10.08	2.65
76	458.362	-193.310	13.50	2.73
77	497.621	-194.103	16.13	2.42
78	536.630	-194.889	18.53	2.14
79	59.816	-222.800	-18.36	5.45
80	98.114	-222.343	-16.71	6.39

81	137.737	-221.789	-13.71	7.40
82	176.500	-222.789	-11.56	6.90
83	216.359	-222.077	-8.39	7.88
84	256.362	-222.690	-4.99	7.75
85	296.629	-222.903	-1.34	8.02
86	337.121	-223.346	2.52	8.01
87	377.359	-223.077	6.14	8.85
88	417.362	-224.310	9.46	7.94
89	457.735	-224.739	13.21	7.91
90	497.000	-226.263	15.87	6.88
91	536.000	-225.500	18.29	8.13
92	60.111	-253.667	-17.52	11.22
93	98.086	-254.138	-16.23	11.22
94	136.714	-253.571	-14.23	12.26
95	176.233	-253.800	-11.30	12.53
96	216.194	-253.500	-8.07	13.14
97	256.000	-254.500	-4.89	12.59
98	296.250	-255.059	-1.22	12.51
99	336.500	-254.945	2.40	13.11
100	376.719	-255.375	5.93	13.17
101	416.879	-255.897	9.47	12.95
102	456.521	-256.292	12.50	13.00
103	495.879	-256.897	15.24	12.88
104	534.500	-257.000	17.26	13.29
105	60.500	-284.500	-16.75	17.04
106	98.380	-284.880	-15.52	17.12
107	137.000	-285.500	-13.49	16.95
108	176.000	-285.500	-11.13	17.41
109	215.865	-286.135	-7.95	17.11
110	255.688	-286.000	-4.73	17.73
111	295.872	-285.860	-1.17	18.34
112	335.750	-286.400	2.07	18.24
113	376.206	-287.294	5.92	17.86
114	415.839	-287.290	8.88	18.22
115	455.518	-287.786	11.94	18.20
116	494.482	-288.214	14.28	18.23
117	533.251	-288.552	16.44	18.38
118	61.000	-315.500	-15.71	22.71

119	99.034	-314.966	-14.30	23.63
120	137.591	-315.364	-12.38	23.73
121	177.000	-316.000	-9.60	23.53
122	215.603	-316.517	-7.70	23.34
123	255.688	-317.000	-4.22	23.31
124	295.379	-316.897	-1.14	23.91
125	335.545	-316.848	2.39	24.43
126	375.138	-317.690	5.36	24.09
127	415.000	-318.200	8.55	23.91
128	454.500	-319.000	11.40	23.58
129	493.121	-319.103	13.41	23.93
130	531.484	-319.719	15.20	23.83

MX	MY	(pixels)
-----	-----	
11.55	14.91	

RANDOM DISTORTION

No	X	Y	DX	DY
-----	-----	-----	-----	-----
1	81.399	-8.922	0.53	-0.41
2	118.133	-9.177	0.66	-0.19
3	154.679	-9.921	0.55	-0.47
4	191.302	-9.968	0.57	-0.04
5	228.147	-10.233	0.78	0.00
6	264.778	-10.924	0.75	-0.22
7	301.113	-11.010	0.48	0.17
8	338.136	-11.371	0.86	0.21
9	374.606	-12.168	0.73	-0.05
10	411.121	-11.907	0.56	0.55
11	447.895	-12.847	0.74	0.07
12	484.452	-13.337	0.66	0.09
13	520.923	-13.664	0.52	0.22
14	80.121	-45.402	-0.25	-0.27
15	116.814	-45.608	-0.19	0.00
16	153.785	-46.142	0.15	-0.09
17	190.331	-46.447	0.03	0.15
18	226.936	-46.766	0.00	0.09
19	263.681	-47.353	0.17	-0.02
20	300.122	-47.859	0.01	-0.04

21	336.847	-48.499	0.07	-0.25
22	373.426	-48.542	0.02	0.19
23	410.055	-48.951	0.02	0.11
24	446.656	-49.291	-0.03	0.24
25	483.212	-50.033	-0.08	-0.02
26	519.694	-49.850	-0.20	0.67
27	80.101	-81.888	0.13	-0.13
28	116.822	-82.584	0.24	-0.35
29	153.064	-82.485	-0.15	0.22
30	189.939	-82.918	0.10	0.27
31	226.491	-83.411	0.00	0.07
32	263.187	-83.974	0.07	-0.02
33	299.685	-84.152	-0.07	0.28
34	336.365	-85.032	-0.01	-0.13
35	372.935	-85.365	-0.10	0.00
36	409.544	-85.656	-0.14	-0.01
37	446.358	-86.019	0.07	0.11
38	482.903	-86.629	-0.01	0.07
39	519.510	-86.832	0.00	0.32
40	79.181	-119.008	-0.32	-0.67
41	116.022	-118.976	-0.11	-0.14
42	153.231	-119.566	0.51	-0.26
43	189.240	-119.797	-0.11	-0.01
44	226.155	-119.969	0.08	0.12
45	262.598	-120.303	-0.06	0.27
46	299.451	-121.494	0.18	-0.44
47	335.793	-121.469	-0.11	0.02
48	372.400	-121.982	-0.11	0.07
49	409.006	-122.212	-0.20	0.07
50	445.603	-122.724	-0.19	0.09
51	482.285	-123.258	-0.11	0.06
52	518.984	-124.215	0.01	-0.46
53	78.917	-155.131	-0.16	-0.14
54	115.749	-155.205	0.03	0.26
55	152.282	-155.898	-0.09	0.04
56	188.766	-156.301	-0.20	0.12
57	225.801	-156.415	0.17	0.28
58	262.367	-156.676	0.12	0.54

59	298.462	-157.892	-0.43	-0.21
60	335.382	-157.864	-0.16	0.21
61	371.845	-158.441	-0.26	0.10
62	408.604	-158.785	-0.17	0.15
63	445.130	-159.363	-0.27	0.03
64	481.744	-159.713	-0.26	0.17
65	518.475	-160.271	-0.14	0.08
66	78.418	-191.876	-0.19	-0.25
67	115.363	-192.534	0.15	-0.46
68	151.829	-192.686	-0.02	-0.13
69	188.331	-192.637	-0.13	0.41
70	225.358	-193.356	0.23	-0.03
71	261.569	-193.372	-0.19	0.43
72	298.077	-194.342	-0.30	-0.04
73	335.026	-194.944	0.03	-0.18
74	371.569	-195.339	-0.07	-0.04
75	408.137	-195.404	-0.16	0.15
76	444.783	-196.200	-0.08	-0.16
77	481.335	-196.491	-0.16	0.03
78	517.864	-196.899	-0.24	0.13
79	77.563	-228.655	-0.62	-0.41
80	114.673	-228.901	-0.15	-0.17
81	151.702	-229.134	0.26	0.06
82	188.019	-230.146	-0.04	-0.46
83	224.739	-229.711	-0.01	0.24
84	260.987	-230.275	-0.36	0.17
85	297.532	-230.826	-0.43	0.09
86	334.383	-231.434	-0.22	-0.08
87	370.869	-231.598	-0.35	0.33
88	407.484	-232.172	-0.42	0.08
89	444.419	-232.465	-0.10	0.19
90	480.919	-233.540	-0.21	-0.39
91	517.445	-233.073	-0.26	0.56
92	77.588	-264.995	-0.05	-0.11
93	114.107	-265.500	-0.21	-0.14
94	150.616	-265.708	-0.33	0.12
95	187.335	-266.151	-0.19	0.18
96	224.123	-266.368	-0.14	0.27

97	260.634	-267.413	-0.25	-0.32
98	297.400	-267.577	-0.07	-0.01
99	333.863	-268.027	-0.24	0.03
100	370.664	-268.555	-0.13	-0.01
101	407.230	-268.664	-0.18	0.18
102	443.744	-269.146	-0.28	0.15
103	480.348	-269.437	-0.29	0.34
104	517.031	-270.331	-0.21	-0.04
105	77.343	-301.521	0.09	0.02
106	113.943	-302.429	0.05	-0.43
107	150.490	-302.928	0.00	-0.48
108	186.855	-303.449	-0.28	-0.53
109	223.850	-303.638	0.03	-0.39
110	260.496	-303.991	0.08	-0.26
111	297.012	-303.982	-0.03	0.22
112	333.385	-304.853	-0.29	-0.21
113	370.305	-305.142	0.02	0.01
114	406.804	-305.455	-0.16	0.05
115	443.492	-305.996	-0.09	-0.01
116	480.061	-306.379	-0.15	0.06
117	516.595	-306.570	-0.22	0.36
118	76.547	-338.402	-0.16	-0.19
119	113.393	-338.360	0.05	0.24
120	150.150	-339.033	0.18	0.06
121	186.828	-339.413	0.23	0.12
122	223.160	-340.295	-0.14	-0.44
123	260.051	-340.731	0.14	-0.42
124	296.628	-340.812	0.11	0.00
125	333.287	-340.935	0.13	0.34
126	369.885	-341.711	0.11	0.07
127	406.714	-342.044	0.27	0.07
128	443.641	-343.200	0.54	-0.62
129	479.842	-342.967	0.13	0.07
130	516.329	-343.719	0.04	-0.17

MX	MY (pixels)
-----	-----
0.28	0.25

APPENDIX D: PROGRAM POLY25

D.1 Introduction

This program can be used to carry out a polynomial transformation for any number of cross targets using a 25-term polynomial equation in such a manner that the user can specify any number of terms between 3 and 25 to be used in each individual run. The mathematical basis of the program has been discussed in Section 13.4.3.

D.2 Definitions of Some of the Variables

NR	number of cross targets.
NC	number of terms to be used in the polynomial equation.
NTRM	input number of terms to be used in an individual run.
X and Y	calibrated target plate coordinates.
VX, VY	image coordinates of the target crosses.
RMSEX and RMSEY	rmse values in the x- and y-directions.

D.3 Definitions of Some of the Arrays

COEFX and COEFY	coefficient matrices on the x and y axes.
VXL and VYL	matrices of measured image coordinates.
VXL1 and VYL1	matrices for the transformed image coordinates.
DVX and DVY	matrices of the residual errors in the x- and y-directions.
A	coefficient matrix of unknown parameters.
INV	matrix inversion.

D.4 Explanation of Program POLY25

The program is listed below. As can be seen in the listing, the program is broken up into a number of blocks to assist the explanation of the sequence of operations carried out by the program.

- Block 1.** In this first block, the program name is defined and the arrays required for input data are dimensioned.
- Block 2.** The name of the file containing the calibrated and measured coordinates of crosses is given. The program opens the file and reads the data contained in this block. In addition, the number of terms to be used in this particular run is defined and is read in this block also.
- Block 3.** In this block, the least squares procedure to compute the transformation parameters is implemented by calling the sequence of sub-routines required for the appropriate matrix operations. It also computes the residual errors in the x and y-directions.
- Block 4.** The systematic distortion values for each point and the rmse values in the x and y-directions are computed and printed. The plotting file for the error vectors is also created and written to the specific output file.
- Block 5.** In this block, the program determines the total systematic distortion for the frame that has been input and asks the user if he requires the computation of the same steps for the other frames. If the answer is YES, the program carries out these steps that have been explained above for that frame as well.
- Block 6.** The program calculates the mean systematic distortion values at each image point. Then, the program asks the user whether he wants to correct any image points for the computed systematic distortion with a view to computing the magnitude of the random distortion that is present at each point in a particular frame. If the answer is YES, the program proceeds to correct the measured image coordinates of the specified frame and uses these corrected coordinates to perform another least squares computational procedure by calling the sub-routines

required for its matrix operations. On the completion of this computation, the random distortion at each image point is printed followed by the rmse values in the x- and y-directions.

Block 7. In this block, there is the option of:-

(i) correcting any other image for systematic distortion and computing the random distortion, in which case, the program starts again from Block 5;

(ii) starting the whole calibration procedure from the beginning, in which case, the program starts from Block 2; or

(iii) ending the program.

Block 8. This block includes the format for writing and reading the input and output files; and of stopping and ending part of the program.

Block 9. Contains the sub-routines used for matrix operations. These are:-

(1) *POLYRI* to compute the rmse value using the computed residuals present at each image point;

(2) *POLYCI* which calls the sub-routines *MATIN* and *PROMAT* to calculate the transformation coefficients: it also used to transpose the matrix;

(3) *PROMAT* to carry out the multiplication of two matrices;

(4) *MATINI* to perform the matrix inversion; and

(5) *CONVTI* which is used to form the matrix of the coefficients of the unknown parameters.

D.5 Listing of Program POLY25

C PROGRAM POLY25

PARAMETER (NR=130,NC=25)

IMPLICIT DOUBLE PRECISION (A-H,O-Z)

DIMENSION LB(NR),SUMVX(NR),SUMVY(NR)

```
DOUBLE PRECISION VYL(NR,1),VYL1(NR,1)
COMMON/BLOCK1/A(NR,NC),VXL(NR,1),VYL,COEFX(NC,1),COEFY(NC,1)
COMMON/BLOCK2/VXL1(NR,1),VYL1,DVX(NR),DVY(NR)
COMMON/BLOCK3/SUMXX,SUMYY,RMSEX,RMSEY
CHARACTER*1 ANS
CHARACTER*32 NAME,NAME1
C
C -----END OF BLOCK 1.
C
5 K=0
  T=0.0
  PRINT *,'ENTER THE IMAGE NAME'
  READ(5,900)NAME
  WRITE(6,1000)NAME
  PRINT *,'NO OF TARGET PLATE CROSSES IN THIS IMAGE='
  READ *,NO
C
  DO 77, I=1,NO
    SUMVX(I)=0
  77 SUMVY(I)=0
C
  PRINT *,'HOW MANY TERMS DO YOU WANT TO USE IN THIS RUN?'
  READ *,NTRM
C
100 PRINT *,'INPUT TARGET PLATE CROSSES DATA FILE NAME'
    READ(5,900)NAME
    OPEN(UNIT=3,FILE=NAME,STATUS='OLD',FORM='FORMATTED',ERR=150)
    GO TO 155
150 PRINT *,'CANNOT FIND THE TARGET PLATE DATA FILE'
    GOTO 100
155 T=T+1
C
  DO 10 I=1,NO
    READ(3,1010)LB(I),X,Y,VX,VY
    CALL CONVT1(I,VX,VY,X,Y,NTRM)
  10 CONTINUE
  CLOSE(UNIT=3)
C
```

```
C -----END OF BLOCK 2.
C
CALL POLYC1(NO,NTRM)
CALL PROMAT(NO,NR,NTRM,NC,1,1,A,COEFX,VXL1)
CALL PROMAT(NO,NR,NTRM,NC,1,1,A,COEFY,VYL1)
C
DO 567 I=1,NO
DVX(I)=VXL1(I,1)-VXL(I,1)
DVY(I)=VYL1(I,1)-VYL(I,1)
567 CONTINUE
C
C -----END OF BLOCK 3.
C
PRINT *,'DO YOU WANT TO PRINT THE SYSTEMATIC DISTORTION?'
PRINT *,'VALUES? (Y OR N)'
READ(5,910)ANS
IF(ANS.EQ.'N') GOTO 310
WRITE(6,1030)T
WRITE(6,1035)
DO 20 I=1,NO
WRITE(6,1040)LB(I),VXL1(I,1),VYL1(I,1),DVX(I),DVY(I)
20 CONTINUE
C
310 CALL POLYR1(NO)
PRINT *,'DO YOU WANT TO PRINT THE ACCURACY (Y/N)?'
READ(5,910)ANS
IF(ANS.EQ.'N') GOTO 62
WRITE(6,1050)RMSEX,RMSEY
C
62 PRINT *,'DO YOU WANT TO CREATE A PLOTTING FILE FOR'
PRINT *,'THIS IMAGE?(Y/N)'
READ(5,910)ANS
IF(ANS.EQ.'N') GOTO 416
PRINT *,'INPUT PLOTTING FILE NAME(MAX 32 CHAR)'
READ(5,900)NAME
OPEN(UNIT=2,FILE=NAME,STATUS='NEW',FORM='FORMATTED')
WRITE(2,1075)NTRM
DO 200 I=1,NO
```

```
WRITE(2,1080)LB(I),VXL1(I,1),VYL1(I,1),DVX(I),DVY(I)
200 CONTINUE
WRITE(2,1050)RMSEX,RMSEY
CLOSE(UNIT=2)
C
C -----END OF BLOCK 4.
C
416 DO 250, I=1,NO
    SUMVX(I)=SUMVX(I)+DVX(I)
250 SUMVY(I)=SUMVY(I)+DVY(I)
C
PRINT *,'IS THIS THE LAST IMAGE?(Y/N)?'
READ(5,910)ANS
IF(ANS.EQ.'N') GOTO 100
C
34 DO 260, I=1,NO
    DVX(I)=SUMVX(I)/T
    DVY(I)=SUMVY(I)/T
260 CONTINUE
    K=K+1
    IF(K.GT.1) GOTO 66
C
C -----END OF BLOCK 5.
C
PRINT *,'DO YOU WANT TO CORRECT ANY IMAGE FOR SYSTEMATIC'
PRINT *,'DISTORTION AND THEN COMPUTE THE RANDOM DISTORTION?(Y/N)?'
READ(5,910)ANS
IF(ANS.EQ.'N') GO TO 8
C
66 PRINT *,'PLEASE ENTER THE IMAGE FILE NAME'
READ(5,900) NAME1
OPEN(UNIT=9,FILE=NAME1,STATUS='OLD',FORM='FORMATTED',ERR=819)
GOTO 820
819 PRINT *,'CANNOT FIND DATA FILE NAME'
GOTO 66
C
820 DO 600, I=1,NO
    READ(9,1010) LB(I),X,Y,VX,VY
```

```
C   WRITE(6,1017) LB(I),X,Y,VX,VY
      VX=VX+DVX(I)
      VY=VY+DVY(I)
      CALL CONVT1(I,X,Y,VX,VY,NTRM)
600 CONTINUE
      CLOSE(UNIT=9)
C
      CALL POLYC1(NO,NTRM)
      CALL PROMAT(NO,NR,NTRM,NC,1,1,A,COEFX,VXL1)
      CALL PROMAT(NO,NR,NTRM,NC,1,1,A,COEFY,VYL1)
C
      DO 896, I=1,NO
      DVX(I)=VXL1(I,1)-VXL(I,1)
      DVY(I)=VYL1(I,1)-VYL(I,1)
896 CONTINUE
      DO 332, I=1,NO
C   WRITE(6,1040)LB(I),VXL1(I,1),VYL1(I,1),DVX(I),DVY(I)
332 CONTINUE
C
      CALL POLYR1(NO)
      WRITE(6,1050)RMSEX,RMSEY
C
      PRINT *, 'DO YOU WANT TO CREATE A PLOTTING FILE FOR'
      PRINT *, 'THIS IMAGE?(Y/N)?'
      READ(5,910)ANS
      IF(ANS.EQ.'N') GOTO 999
      PRINT *, 'INPUT PLOTTING FILE NAME(MAX 32 CHAR)'
      READ(5,900)NAME
      OPEN(UNIT=2,FILE=NAME,STATUS='NEW',FORM='FORMATTED')
      WRITE(2,1075)NTRM
      DO 201 I=1,NO
      WRITE(2,1080)LB(I),VXL1(I,1),VYL1(I,1),DVX(I),DVY(I)
201 CONTINUE
      WRITE(2,1050)RMSEX,RMSEY
      CLOSE(UNIT=2)
C
C -----END OF BLOCK 6.
C
```

```

PRINT *,'DO YOU WANT TO CORRECT ANY OTHER IMAGE?(Y/N)?'
READ(5,910)ANS
IF(ANS.EQ.'Y') GOTO 34
8 PRINT *,'DO YOU WANT TO START AGAIN?(Y/N)?'
READ(5,910)ANS
IF(ANS.EQ.'Y') GOTO 5
GOTO 999
C
C -----END OF BLOCK 7.
C
900 FORMAT(A32)
910 FORMAT(A1)
1000 FORMAT(1H1,2X,'THE IMAGE TRANSFORMED IS:',2X,A32)
1010 FORMAT(I8,T12,F10.3,T27,F10.3,T42,F10.3,T57,F10.3)
1017 FORMAT(1H ,I8,T12,F10.3,T27,F10.3,T42,F10.3,T57,F10.3)
1020 FORMAT(1H ,2X,'THE TRANSFORMATION COEFFICIENTS ARE:',
1/8(2X,I2,' = ',F14.6,',',F14.6/))
1030 FORMAT(///2X,'TRANSFORMED COORDINATES SYSTEMATIC DISTORTION
1VALUES FOR IMAGE NO.',F4.0,")
1035 FORMAT(//,5X,'PT NO',5X,'COMPUTED VX',5X,'COMPUTED VY',
15X,'DVX',5X,'DVY')
1040 FORMAT(1H ,I8,1X,F10.3,1X,F10.3,1X,F10.3,1X,F10.3)
1050 FORMAT(//2X,'RMSE IN x COORDS=',F10.3
*/2X,'RMSE IN y COORDS=',F10.3)
1075 FORMAT(5X,'TERM=',I2)
1080 FORMAT(I4,2F10.3,2F10.3)
1200 FORMAT(2X,I4,10X,F10.3,10X,F10.3)
C
999 STOP
END
C
C -----END OF BLOCK 8.
C
SUBROUTINE POLYR1(M)
PARAMETER (NR=130,NC=25)
IMPLICIT DOUBLE PRECISION (A-H,O-Z)
DOUBLE PRECISION VYL(NR,1),VYL1(NR,1)
COMMON/BLOCK1/A(NR,NC),VXL(NR,1),VYL,COEFX(NC,1),COEFY(NC,1)

```

```

COMMON/BLOCK2/VXL1(NR,1),VYL1,DVX(NR),DVY(NR)
COMMON/BLOCK3/SUMXX,SUMYY,RMSEX,RMSEY
SUMXX=0.0
SUMYY=0.0
DO 687, I=1,M
SUMXX=SUMXX+DVX(I)**2
687 SUMYY=SUMYY+DVY(I)**2
RMSEX=SQRT(SUMXX/(M-1))
RMSEY=SQRT(SUMYY/(M-1))
RETURN
END
C
SUBROUTINE POLYC1(M,NT)
C THIS SUBROUTINE CALLS SUBROUTINES MATIN1 AND PROMAT
C TO CALCULATE TRANSFORMATION COEFFICIENTS
PARAMETER (NR=130,NC=25)
IMPLICIT DOUBLE PRECISION(A-H,O-Z)
DIMENSION AT(NC,NR),P1(NC,NC),P2(NC,1)
DOUBLE PRECISION VYL(NR,1),INV(NC,NC)
COMMON/BLOCK1/A(NR,NC),VXL(NR,1),VYL,COEFX(NC,1),COEFY(NC,1)
C
C TRANSPOSE MATRIX OF A -- AT
DO 10 I=1,NT
DO 10 J=1,M
AT(I,J)=A(J,I)
10 CONTINUE
C
C COMPUTE AT * A
CALL PROMAT(NT,NC,M,NR,NT,NC,AT,A,P1)
C COMPUTE THE INVERSE MATRIX OF [AT * A]
CALL MATIN1(NT,NC,P1,INV)
C COMPUTE AT * VXL
CALL PROMAT(NT,NC,M,NR,1,1,AT,VXL,P2)
C COMPUTE COEFFICIENT MATRIX ON X AXES
CALL PROMAT(NT,NC,NT,NC,1,1,INV,P2,COEFX)
C COMPUTE COEFFICIENT MATRIX ON Y AXES
CALL PROMAT(NT,NC,M,NR,1,1,AT,VYL,P2)
CALL PROMAT(NT,NC,NT,NC,1,1,INV,P2,COEFY)

```

```

C
  RETURN
  END

C
  SUBROUTINE PROMAT(IN, LN, IM, LM, IP, LP, A, B, AB)

C
C  THIS SUBROUTINE WAS WRITTEN TO CARRY OUT MULTIPLICATIONS
C  BETWEEN TWO MATRICES
  IMPLICIT DOUBLE PRECISION(A-H, O-Z)
  DIMENSION A(LN, LM), B(LM, LP), AB(LN, LP)
  DO 10 J=1, IN
  DO 10 K=1, IP
  AB(J, K)=0.
  DO 10 I=1, IM
  AB(J, K)=AB(J, K)+A(J, I)*B(I, K)
10 CONTINUE
  RETURN
  END

C
  SUBROUTINE MATIN1(N, LN, A, X2)

C
C  THIS PROGRAM WAS WRITTEN TO CALCULATE THE INVERSE OF A MATRIX
  IMPLICIT DOUBLE PRECISION(A-H, O-Z)
  DIMENSION A(LN, LN), X2(LN, LN)
  DO 5 I=1, N
  DO 5 J=1, N
5  X2(I, J)=0.
  X2(1, 1)=1./A(1, 1)
  IF(N-1) 500, 501, 500
500 DO 40 M=2, N
  K=M-1
  EK=A(M, M)
  DO 10 I=1, K
  DO 10 J=1, K
10  EK=EK-A(M, I)*X2(I, J)*A(J, M)
  X2(M, M)=1./EK
  DO 30 I=1, K
  DO 20 J=1, K

```

```
20 X2(I,M)=X2(I,M)-X2(I,J)*A(J,M)/EK
30 X2(M,I)=X2(I,M)
   DO 40 I=1,K
   DO 40 J=1,K
40 X2(I,J)=X2(I,J)+X2(I,M)*X2(M,J)*EK
501 RETURN
   END
```

C

```
SUBROUTINE CONVT1(NO,X,Y,VX,VY,NT)
PARAMETER (NR=130,NC=25)
IMPLICIT DOUBLE PRECISION(A-H,O-Z)
DOUBLE PRECISION VYL(NR,1)
COMMON/BLOCK1/A(NR,NC),VXL(NR,1),VYL,COEFX(NC,1),COEFY(NC,1)
A(NO,1)=1.
A(NO,2)=X
A(NO,3)=Y
IF(NT.EQ.3) GO TO 10
A(NO,4)=X*Y
IF(NT.EQ.4) GO TO 10
A(NO,5)=X**2
IF(NT.EQ.5) GO TO 10
A(NO,6)=Y**2
IF(NT.EQ.6) GO TO 10
A(NO,7)=(X**2)*Y
IF(NT.EQ.7) GO TO 10
A(NO,8)=(Y**2)*X
IF(NT.EQ.8) GO TO 10
A(NO,9)=(X**2)*(Y**2)
IF(NT.EQ.9) GO TO 10
A(NO,10)=X**3
IF(NT.EQ.10) GO TO 10
A(NO,11)=Y**3
IF(NT.EQ.11) GO TO 10
A(NO,12)=(X**3)*Y
IF(NT.EQ.12) GO TO 10
A(NO,13)=X*(Y**3)
IF(NT.EQ.13) GO TO 10
A(NO,14)=(X**3)*(Y**2)
```

```

IF(NT.EQ.14) GO TO 10
A(NO,15)=(X**2)*(Y**3)
IF(NT.EQ.15) GO TO 10
A(NO,16)=(X**3)*(Y**3)
IF(NT.EQ.16) GO TO 10
A(NO,17)=X**4
IF(NT.EQ.17) GO TO 10
A(NO,18)=Y**4
IF(NT.EQ.18) GO TO 10
A(NO,19)=(X**4)*Y
IF(NT.EQ.19) GO TO 10
A(NO,20)=X*(Y**4)
IF(NT.EQ.20) GO TO 10
A(NO,21)=(X**4)*(Y**2)
IF(NT.EQ.21) GO TO 10
A(NO,22)=(X**2)*(Y**4)
IF(NT.EQ.22) GO TO 10
A(NO,23)=(X**4)*(Y**3)
IF(NT.EQ.23) GO TO 10
A(NO,24)=(X**3)*(Y**4)
IF(NT.EQ.24) GOTO 10
A(NO,25)=(X**4)*(Y**4)
10 VXL(NO,1)=VX
VYL(NO,1)=VY
RETURN
END

```

C

C -----END OF BLOCK 9.

C

D.6 Sample Output Data From Program POLY25

SYSTEMATIC DISTORTION

TERM= 3

No	VXL1	VYL1	DVX	DVY
-----	-----	-----	-----	-----
130	63.919	-32.724	-4.812	3.507
129	103.559	33.023	-3.062	2.080
128	143.256	-33.316	-1.385	1.607

127	182.895	-33.619	-0.605	0.181
126	222.571	-33.780	-0.316	-0.070
125	262.267	-34.076	-0.233	-0.576
124	301.908	-34.377	0.158	-0.669
123	341.593	-34.618	-0.157	-0.618
122	381.230	-34.972	-0.150	-0.572
121	420.957	-35.156	0.207	-0.156
120	460.582	-35.450	0.332	0.550
119	500.261	-35.780	1.261	1.220
118	539.908	-36.067	2.787	2.036
105	63.138	-64.183	-2.973	2.150
106	102.804	-64.486	-1.571	0.514
107	142.472	-64.769	-0.295	0.031
108	182.187	-65.123	0.339	-1.275
109	221.853	-65.244	0.498	-1.154
110	261.462	-65.545	0.349	-1.255
111	301.098	-65.858	0.218	-1.458
112	340.805	-66.127	-0.095	-0.927
113	380.476	-66.436	-0.274	-1.436
114	420.138	-66.611	-0.362	-0.811
115	459.835	-66.904	-0.065	-1.104
116	499.470	-67.214	0.470	0.215
117	539.109	-67.547	1.859	0.203
104	62.452	-95.661	-1.945	1.856
103	102.105	-95.957	-0.440	1.195
102	141.777	-96.256	0.339	-0.756
101	181.437	-96.570	1.187	-0.784
100	221.130	-96.716	1.130	-0.916
99	260.795	-97.012	0.589	-0.718
98	300.467	-97.319	0.467	-1.319
97	340.121	-97.614	-0.129	-1.214
96	379.822	-97.909	-0.428	-1.309
95	419.509	-98.048	-0.741	-0.756
94	459.153	-98.353	-0.968	-0.250
93	498.815	-98.734	-0.435	0.266
92	538.448	-99.018	0.448	0.982
79	61.703	-127.092	-0.797	1.908
80	101.366	-127.408	0.736	0.481

81	140.992	-127.710	0.754	0.052
82	180.655	-128.019	1.905	-0.805
83	220.436	-128.171	1.583	-1.347
84	260.046	-128.481	1.171	-1.481
85	299.695	-128.785	0.330	-0.650
86	339.364	-129.055	0.114	-1.455
87	379.007	-129.430	-0.624	-1.377
88	418.745	-129.524	-0.885	-0.635
89	458.374	-129.878	-1.126	-0.307
90	498.008	-130.202	-0.992	0.798
91	537.620	-130.474	-0.245	1.661
78	60.994	-158.586	-0.024	1.200
77	100.681	-158.884	1.136	-0.036
76	140.364	-159.186	2.114	-0.186
75	179.999	-159.496	2.370	-0.593
74	219.702	-159.628	1.813	-1.128
73	259.357	-159.964	1.303	-1.613
72	299.040	-160.262	1.160	-0.862
71	338.726	-160.493	0.226	-0.382
70	378.322	-160.790	-0.178	-0.790
69	418.038	-161.019	-0.962	-0.457
68	457.692	-161.306	-1.172	-0.033
67	497.341	-161.621	-1.038	0.276
66	536.986	-161.921	-0.393	0.976
53	60.241	-190.063	0.122	1.556
54	99.881	-190.345	1.194	0.655
55	139.557	-190.651	2.057	0.349
56	179.204	-190.967	2.150	-0.616
57	218.912	-191.102	1.412	-0.102
58	258.575	-191.404	1.575	-0.904
59	298.238	-191.726	1.167	-0.233
60	337.893	-192.021	-0.161	0.222
61	377.573	-192.369	-0.676	-0.122
62	417.270	-192.480	-1.109	0.417
63	456.867	-192.797	-1.495	0.513
64	496.538	-193.105	-1.083	0.998
65	536.183	-193.431	-0.447	1.458
52	59.530	-221.530	-0.286	1.270

51	99.215	-221.841	1.101	0.502
50	138.868	-222.127	1.131	-0.338
49	178.526	-222.450	2.026	0.339
48	218.258	-222.572	1.899	-0.495
47	257.888	-222.885	1.526	-0.195
46	297.542	-223.191	0.913	-0.288
45	337.212	-223.458	0.091	-0.112
44	376.870	-223.845	-0.489	-0.768
43	416.594	-224.015	-0.768	0.295
42	456.251	-224.256	-1.484	0.483
41	495.898	-224.574	-1.102	1.689
40	535.505	-224.884	-0.495	0.616
27	58.692	-253.008	-1.419	0.659
28	98.417	-253.312	0.331	0.826
29	138.083	-253.607	1.369	-0.036
30	177.699	-253.932	1.466	-0.132
31	217.484	-254.091	1.290	-0.591
32	257.140	-254.377	1.140	0.123
33	296.755	-254.679	0.505	0.380
34	336.428	-254.991	-0.072	-0.046
35	376.159	-255.304	-0.560	0.071
36	415.819	-255.461	-1.060	0.436
37	455.461	-255.737	-1.060	0.555
38	495.116	-256.045	-0.763	0.852
39	534.754	-256.385	0.254	0.615
26	58.030	-284.503	-2.470	-0.003
25	97.715	-284.796	-0.665	0.084
24	137.342	-285.078	0.342	0.422
23	177.023	-285.369	1.023	0.131
22	216.751	-285.549	0.886	0.586
21	256.384	-285.862	0.696	0.138
20	296.050	-286.160	0.178	-0.300
19	335.721	-286.431	-0.029	-0.031
18	375.360	-286.764	-0.846	0.530
17	415.081	-286.960	-0.758	0.330
16	454.737	-287.264	-0.781	0.522
15	494.402	-287.553	-0.080	0.661
14	534.043	-287.865	0.792	0.687

1	57.192	-316.013	-3.808	-0.513
2	96.863	-316.243	-2.171	-1.277
3	136.536	-316.561	-1.055	-1.197
4	176.199	-316.833	-0.801	-0.833
5	215.943	-317.008	0.340	-0.491
6	255.587	-317.289	-0.101	-0.289
7	295.235	-317.613	-0.144	-0.716
8	334.907	-317.911	-0.638	-1.063
9	374.566	-318.238	-0.572	-0.548
10	414.279	-318.414	-0.721	-0.214
11	453.972	-318.714	-0.528	0.286
12	493.621	-318.994	0.500	0.109
13	533.226	-319.333	1.742	0.386
RMSE IN x COORDS=				1.224
RMSE IN y COORDS=				0.919

RANDOM DISTORTION

TERM= 3

No	VXL1	VYL1	DVX	DVY
130	63.919	-32.724	-0.319	0.309
129	103.559	-33.023	-0.455	0.117
128	143.256	-33.316	-0.349	0.420
127	182.895	-33.619	-0.375	0.014
126	222.571	-33.780	-0.589	-0.007
125	262.267	-34.076	-0.569	0.240
124	301.908	-34.377	-0.304	-0.124
123	341.593	-34.618	-0.687	-0.143
122	381.230	-34.972	-0.561	0.142
121	420.957	-35.156	-0.398	-0.433
120	460.582	-35.450	-0.587	0.065
119	500.261	-35.780	-0.509	0.072
118	539.908	-36.067	-0.376	-0.034
105	63.138	-64.183	0.425	0.168
106	102.804	-64.486	0.355	-0.079
107	142.472	-64.769	0.009	0.026
108	182.187	-65.123	0.131	-0.181
109	221.853	-65.244	0.147	-0.102
110	261.462	-65.545	-0.027	0.035

111	301.098	-65.858	0.127	0.077
112	340.805	-66.127	0.062	0.304
113	380.476	-66.436	0.111	-0.113
114	420.138	-66.611	0.100	-0.007
115	459.835	-66.904	0.150	-0.107
116	499.470	-67.214	0.189	0.175
117	539.109	-67.547	0.305	-0.495
104	62.452	-95.661	0.000	0.009
103	102.105	-95.957	-0.110	0.261
102	141.777	-96.256	0.276	-0.286
101	181.437	-96.570	0.019	-0.318
100	221.130	-96.716	0.113	-0.095
99	260.795	-97.012	0.039	0.025
98	300.467	-97.319	0.169	-0.255
97	340.121	-97.614	0.101	0.183
96	379.822	-97.909	0.187	0.073
95	419.509	-98.048	0.218	0.102
94	459.153	-98.353	0.006	0.010
93	498.815	-98.734	0.082	0.077
92	538.448	-99.018	0.066	-0.149
79	61.703	-127.092	0.415	0.540
80	101.366	-127.408	0.195	0.041
81	140.992	-127.710	-0.428	0.179
82	180.655	-128.019	0.183	-0.048
83	220.436	-128.171	-0.004	-0.153
84	260.046	-128.481	0.125	-0.281
85	299.695	-128.785	-0.121	0.457
86	339.364	-129.055	0.162	0.019
87	379.007	-129.430	0.157	-0.004
88	418.745	-129.524	0.238	0.016
89	458.374	-129.878	0.230	0.016
90	498.008	-130.202	0.142	0.074
91	537.620	-130.474	0.016	0.615
78	60.994	-158.586	0.214	0.000
77	100.681	-158.884	0.024	-0.372
76	140.364	-159.186	0.129	-0.131
75	179.999	-159.496	0.240	-0.188
74	219.702	-159.628	-0.139	-0.326

73	259.357	-159.964	-0.093	-0.557
72	299.040	-160.262	0.451	0.213
71	338.726	-160.493	0.171	-0.184
70	378.322	-160.790	0.267	-0.052
69	418.038	-161.019	0.176	-0.074
68	457.692	-161.306	0.262	0.070
67	497.341	-161.621	0.255	-0.046
66	536.986	-161.921	0.127	0.062
53	60.241	-190.063	0.206	0.102
54	99.881	-190.345	-0.141	0.333
55	139.557	-190.651	0.025	0.028
56	179.204	-190.967	0.129	-0.487
57	218.912	-191.102	-0.238	-0.026
58	258.575	-191.404	0.172	-0.461
59	298.238	-191.726	0.284	0.035
60	337.893	-192.021	-0.054	0.194
61	377.573	-192.369	0.040	0.085
62	417.270	-192.480	0.123	-0.079
63	456.867	-192.797	0.035	0.248
64	496.538	-193.105	0.111	0.081
65	536.183	-193.431	0.186	0.009
52	59.530	-221.530	0.592	0.250
51	99.215	-221.841	0.122	0.034
50	138.868	-222.127	-0.296	-0.166
49	178.526	-222.450	0.002	0.371
48	218.258	-222.572	-0.035	-0.306
47	257.888	-222.885	0.307	-0.204
46	297.542	-223.191	0.374	-0.109
45	337.212	-223.458	0.150	0.087
44	376.870	-223.845	0.279	-0.298
43	416.594	-224.015	0.339	-0.022
42	456.251	-224.256	0.019	-0.109
41	495.898	-224.574	0.124	0.496
40	535.505	-224.884	0.165	-0.431
27	58.692	-253.008	-0.018	-0.054
28	98.417	-253.312	0.140	-0.003
29	138.083	-253.607	0.254	-0.237
30	177.699	-253.932	0.111	-0.272

31	217.484	-254.091	0.055	-0.341
32	257.140	-254.377	0.157	0.272
33	296.755	-254.679	-0.033	-0.014
34	336.428	-254.991	0.134	-0.028
35	376.159	-255.304	0.015	0.036
36	415.819	-255.461	0.066	-0.137
37	455.461	-255.737	0.152	-0.076
38	495.116	-256.045	0.161	-0.243
39	534.754	-256.385	0.075	0.156
26	58.030	-284.503	-0.196	-0.193
25	97.715	-284.796	-0.157	0.275
24	137.342	-285.078	-0.116	0.347
23	177.023	-285.369	0.156	0.428
22	216.751	-285.549	-0.161	0.309
21	256.384	-285.862	-0.215	0.198
20	296.050	-286.160	-0.107	-0.258
19	335.721	-286.431	0.147	0.199
18	375.360	-286.764	-0.175	0.001
17	415.081	-286.960	-0.002	-0.015
16	454.737	-287.264	-0.077	0.072
15	494.402	-287.553	-0.023	0.021
14	534.043	-287.865	0.042	-0.251
1	57.192	-316.013	0.014	0.008
2	96.863	-316.243	-0.204	-0.401
3	136.536	-316.561	-0.333	-0.199
4	176.199	-316.833	-0.391	-0.235
5	215.943	-317.008	-0.030	0.344
6	255.587	-317.289	-0.317	0.353
7	295.235	-317.613	-0.287	-0.043
8	334.907	-317.911	-0.318	-0.365
9	374.566	-318.238	-0.300	-0.070
10	414.279	-318.414	-0.463	-0.041
11	453.972	-318.714	-0.743	0.666
12	493.621	-318.994	-0.338	0.007
13	533.226	-319.333	-0.257	0.266
RMSE IN x COORDS=			0.255	
RMSE IN y COORDS=			0.235	

APPENDIX E: PROGRAM STMN

E.1 Introduction

This program was written for computing the means and standard deviations of the grey level values of the frame, quadrant or patch image data. In addition, this program averages the grey level values of the individual pixels at each temperature and thus constructs the averaged image data for the frame, quadrant or patch.

E.2 Definitions of Some of the Variables and Arrays

- NR number of pixels in the y-direction.
- NC number of pixels in the x-direction.
- NF number of digitized frames.
- NL number of temperatures.
- IM input array that consists of the grey level values of the pixels.
- TTA output array that contains the grey level values of the pixels of the averaged frame, quadrant or patch image data.
- SP the mean of the grey level values of the averaged image data.
- SSPA the standard deviation of the grey level values of the averaged image data.

E.3 Explanation of Program STMN

This program can be separated into four main blocks. In **Block 1**, the program reads the arrays of grey level values of the frames, quadrants or patches sequentially for each temperature. It also dimensions the arrays for the input and output image data. In **Block 2**, the computation of the mean and standard deviation of the grey level values for the averaged frame, quadrant or patch image data is carried out by calling a sequence of sub-routines for the required matrix operations. In **Block 3**, the output file for the grey level values of the averaged image data is created and written to the specific output file. **Block 4** contains the sub-routines used for the computation of the means and standard deviations of the grey level values. These are:-

- (1) *TEMPAV* to determine the average grey level values for individual pixels and create the averaged image data for frames, quadrants or patches.
- (2) *SPAV* to calculate the average or mean grey level value of the averaged frame, quadrant or patch.
- (3) *SPNO* to compute the standard deviation of the image data for the averaged frame, quadrant or patch.

E.4 Listing of Program STMN

```

PROGRAM STMN
PARAMETER(NR=160,NC=280,NF=3,NL=1)
INTEGER IM(NL,NF,NR,NC)
REAL TTA(NL,NR,NC),STA(NL),SP(NL),SSPA(NL),
CHARACTER*32 NAME
C
DO 10, NT=1,NL
DO 20, K=1,NF
100 PRINT*,'PLEASE ENTER THE IMAGE FILE NAME'
READ(5,990)NAME
OPEN(3,FILE=NAME,STATUS='OLD',FORM='FORMATTED',ERR=150)
GOTO 155
150 PRINT*,'CANNOT FIND THE FILE'
GOTO 100
155 DO 30, I=1,NR
30 READ(3,1000) (IM(NT,K,I,J),J=1,NC)
CLOSE(UNIT=3)
20 CONTINUE
10 CONTINUE
C -----END OF BLOCK 1.
CALL TEMPV(NL,NR,NC,NF,IM,TTA)
CALL SPV(NL,NR,NC,TTA,SP)
CALL SPNO(NL,NR,NC,TTA,SP,SSPA)
C -----END OF BLOCK 2.

```

```

WRITE(6,1050) SP(1), SSPA(1)
DO 910, NT=1,NL
PRINT *, 'INPUT OUTPUT FILE NAME FOR THIS IMAGE (MAX 32 CHAR)'
READ(5,990)NAME
OPEN(UNIT=2,FILE=NAME,STATUS='NEW',FORM='FORMATTED')
DO 920, I=1,NR
920 WRITE(2,1100) (TTA(NT,I,J),J=1,NC)
CLOSE(UNIT=2)
910 CONTINUE
C
990 FORMAT(A32)
1000 FORMAT(280I4)
1050 FORMAT(/2X,'MEAN OF THE GREY LEVEL VALUES=' ,F10.2
      */2X,'STANDARD DEVIATION OF THE GREY LEVEL VALUES=' ,F10.2)
1100 FORMAT(280F6.3)
C
STOP
END
C -----END OF BLOCK 3.
SUBROUTINE TEMP V(NL,NR,NC,NF,IIM,TA)
INTEGER IIM(NL,NF,NR,NC)
REAL TA(NL,NR,NC),SUM1
DO 60, NT=1,NL
DO 60, I=1,NR
DO 60, J=1,NC
DO 70, K=1,NF
70 SUM1=SUM1+IIM(NT,K,I,J)
TA(NT,I,J)=SUM1/NF
SUM1=0.0
60 CONTINUE
RETURN
END
C
SUBROUTINE SPA V(NL,NR,NC,TTA,SPA)
REAL SUM3,TTA(NL,NR,NC),SPA(NL)
DO 310, NT=1,NL
DO 320, I=1,NR
DO 330, J=1,NC

```

```
SUM3=SUM3+TTA(NT,I,J)
330 CONTINUE
320 CONTINUE
    SPA(NT)=SUM3/(NR*NC)
    SUM3=0.0
310 CONTINUE
    RETURN
    END
C
    SUBROUTINE SPNO(NL,NR,NC,TTA,SP,SIGS)
    REAL SUM4,TTA(NL,NR,NC),SP(NL),SIGS(NL)
    DO 420, NT=1,NL
    DO 430, I=1,NR
    DO 440, J=1,NC
        SUM4=SUM4+(TTA(NT,I,J)-SP(NT))**2
440 CONTINUE
430 CONTINUE
        SIGS(NT)=SQRT(SUM4/(NR*NC))
        SUM4=0.0
420 CONTINUE
    RETURN
    END
C -----END OF BLOCK 4.
```

E.5 Sample Output Data From Program STMN

MEAN OF THE GREY LEVEL VALUES = 126.76

STANDARD DEVIATION OF THE GREY LEVEL VALUES = ± 1.57

APPENDIX F: PROGRAM PRNU

F.1 Introduction

This program was developed to carry out the non-uniformity correction of the image data for the averaged frame, quadrant or patch which has been obtained at the middle of the three temperatures used for the radiometric calibration. As with the STMN program, it averages the grey level values of the pixels using several frames at each temperature to generate the averaged image data. However, additionally, this program calculates the gain and offset values for the individual pixels of the average image data and then creates the non-uniformity corrected image at the middle temperature.

F.2 Definitions of Some of the Variables and Arrays

NR	number of pixels in the y-direction.
NC	number of pixels in the x-direction.
NF	number of digitized frames.
NL	number of temperatures used.
IM	input image array that consists of the grey level values of the pixels.
TTA	the array that contains the grey level values of the averaged frame, quadrant or patch.
TTA(1,....)	the averaged grey level value for the reference (calibration) temperature T_1 . It is also defined as the offset value for the non-uniformity correction.
TTA(2,.....)	the averaged grey level value for the reference temperature T_2 .
SP	mean of the averaged image data at each temperature.
SP(1)	the average (A) or mean of the grey level values of the averaged image data at the reference temperature T_1 .
SP(2)	the average (A) or mean of the grey level values of the averaged image data at the reference temperature T_2 .
GAIN	an array that includes the gain values for the radiometric correction.

FMC the output image array that contains the non-uniformity corrected grey level values for the middle temperature T.

F.3 Explanation of Program PRNU

As has been done with the other programs, the listing of this program below has been divided into a number of blocks to explain the sequence of the program more easily.

Block 1. In this block, the program name is defined and the arrays required for input and output data are dimensioned. In addition, the input image data for frames, quadrants or patches are read sequentially at each temperature.

Block 2. This block calls the sub-routines which are exactly the same as those used in the STMN program. So they will not be dealt with again here. This block mainly carries out the operations needed to generate the averaged image data for each temperature and compute the mean and standard deviation values of this averaged image data.

Block 3. The gain and offset values for individual pixels of the averaged image data at the middle temperature are established in this block. Then the resulting grey level values for each pixel of the non-uniformity corrected image are written to the output file.

Block 4. In this block, the program calls the sub-routines SPAV and SPNO again to compute the mean and standard deviation values of the non-uniformity corrected image at the middle temperature. It also calculates the non-uniformity of the image data. Afterwards, the program ends.

Block 5. This contains the sub-routines required for the computation of the mean and standard deviation of the grey level values of the image data. These

particular sub-routines have already been explained in Appendix E.

F.4 Listing of Program

```

PROGRAM PRNU
PARAMETER(NR=160,NC=280,NF=3,NL=3)
INTEGER IM(NL,NF,NR,NC)
REAL FMC(NL,NR,NC),TTA(NL,NR,NC),STA(NL),SP(NL),SSPA(NL),
1     SPF(NL),SSC(NL),GAIN(NR,NC),FMC(NL,NR,NC)
CHARACTER*32 NAME

C
DO 10, NT=1,NL
DO 20, K=1,NF
100 PRINT*,'PLEASE ENTER THE IMAGE FILE NAME'
    READ(5,990)NAME
    OPEN(3,FILE=NAME,STATUS='OLD',FORM='FORMATTED',ERR=150)
    GOTO 155
150 PRINT*,'CANNOT FIND THE FILE'
    GOTO 100
155 DO 30, I=1,NR
    30 READ(3,1000) (IM(NT,K,I,J),J=1,NC)
        CLOSE(UNIT=3)
    20 CONTINUE
    10 CONTINUE

C -----END OF BLOCK 1.
    CALL TEMPAV(NL,NR,NC,NF,IM,TTA)
    CALL SPAV(NL,NR,NC,TTA,SP)
    CALL SPNO(NL,NR,NC,TTA,SP,SSPA)

C -----END OF BLOCK 2.
    DO 570, I=1,NR
    DO 570, J=1,NC
570 GAIN(I,J)=(SP(2)-SP(1))/(TTA(2,I,J)-TTA(1,I,J))

C
DO 700, NT=1,NL
DO 700, I=1,NR
DO 700, J=1,NC
FMC(NT,I,J)=GAIN(I,J)*(TTA(NT,I,J)-TTA(1,I,J))+SP(1)

```

```

700 CONTINUE
C
  DO 910, NT=3,3
  PRINT *, 'INPUT OUTPUT FILE NAME FOR THIS IMAGE (MAX 32 CHAR)'
  READ(5,990)NAME
  OPEN(UNIT=2,FILE=NAME,STATUS='NEW',FORM='FORMATTED')
  DO 920, I=1,NR
920 WRITE(2,1100) (FMC(NT,I,J),J=1,NC)
  CLOSE(UNIT=2)
910 CONTINUE
C -----END OF BLOCK 3.
  CALL SPAV(NL,NR,NC,FMC,SPF)
  CALL SPNO(NL,NR,NC,FMC,SPF,SSC)
C
  WRITE(6,1050) SPF,SSC,UN
990 FORMAT(A32)
1000 FORMAT(280I4)
1050 FORMAT(//2X, 'MEAN OF THE NON-UNIFORMITY CORRECTED IMAGE=', F10.2
  */2X, 'ITS STANDARD DEVIATION VALUE=', F10.2
  */2X, 'ITS NON-UNIFORMITY=', F10.2)
1100 FORMAT(F6.3)
C
  STOP
  END
C -----END OF BLOCK 4.
  SUBROUTINE TEMPAV(NL,NR,NC,NF,IIM,TA)
  INTEGER IIM(NL,NF,NR,NC)
  REAL TA(NL,NR,NC),SUM1
  DO 60, NT=1,NL
  DO 60, I=1,NR
  DO 60, J=1,NC
  DO 70, K=1,NF
70 SUM1=SUM1+IIM(NT,K,I,J)
  TA(NT,I,J)=SUM1/NF
  SUM1=0.0
60 CONTINUE
  RETURN
  END

```

C

```

SUBROUTINE SPAV(NL,NR,NC,TTA,SPA)
REAL SUM3,TTA(NL,NR,NC),SPA(NL)
DO 310, NT=1,NL
DO 320, I=1,NR
DO 330, J=1,NC
SUM3=SUM3+TTA(NT,I,J)
330 CONTINUE
320 CONTINUE
SPA(NT)=SUM3/(NR*NC)
SUM3=0.0
310 CONTINUE
RETURN
END

```

C

```

SUBROUTINE SPNO(NL,NR,NC,TTA,SP,SIGS)
REAL SUM4,TTA(NL,NR,NC),SP(NL),SIGS(NL)
DO 420, NT=1,NL
DO 430, I=1,NR
DO 440, J=1,NC
SUM4=SUM4+(TTA(NT,I,J)-SP(NT))**2
440 CONTINUE
430 CONTINUE
SIGS(NT)=SQRT(SUM4/(NR*NC))
SUM4=0.0
420 CONTINUE
RETURN
END

```

C -----END OF BLOCK 5.

F.5 Sample Output Data From Program PRNU

MEAN OF THE NON-UNIFORMITY CORRECTED IMAGE = 195.02

ITS STANDARD DEVIATION VALUE = ± 1.71

ITS NON-UNIFORMITY = 0.00087

APPENDIX G: PROGRAM STAT

G.1 Introduction

This program was developed to carry out the statistical processing of the frame, quadrant or patch image data. The mean and the standard deviation of the grey level values of the pixels obtained from the STMN program were input to this program.

This program computes:-

- (i) the number of pixels lying outside the range $A \pm 3\sigma$ ($n = 1,2,3$);
- (ii) the number of pixels that have grey level values less than $A - 3\sigma$ ($n = 1,2,3$);
- (iii) the number of pixels that have grey level values greater than $A + 3\sigma$ ($n = 1,2,3$).

G.2 Definition of Some of the Variables and Arrays

MEAN	the mean of the grey level values of the frame, quadrant and patch.
SIGMA	the standard deviation of the grey level values of the frame, quadrant or patch.
IM	an array that consists of the grey level values of the pixels.

G.3 Explanation of Program STAT

As can be seen from the listing of the program, it contains three main blocks. In **Block 1**, the program reads the image data. Then, in **Block 2**, the mean and the standard deviation of the grey level values are input to the program. Finally, in **Block 3**, the program calculates the number of pixels lying outside the specified range that has been given above and it then ends.

G.4 Listing of Program STAT

```
PROGRAM STAT
INTEGER*2 IM(160,280)
```

```

REAL MEAN,SIGMA,S(3),T(3),TOTAL(3)
CHARACTER*32 NAME1
100 PRINT*,'PLEASE ENTER IMAGE FILE NAME'
    READ(5,990)NAME1
    OPEN(3,FILE=NAME1,STATUS='OLD',FORM='FORMATTED',ERR=150)
    GOTO 155
150 PRINT*,'CANNOT FIND THE FILE'
    GOTO 100
155 DO 40, I=1,160
    40 READ(3,1000) (IM(I,J),J=1,280)
    CLOSE(UNIT=3)
C -----END OF BLOCK 1.
    PRINT*,'ENTER THE MEAN AND STD.VALUE'
    READ*,MEAN,SIGMA
C -----END OF BLOCK 2.
    K=1
175 DO 185, I=1,160
    DO 185, J=1,280
    IF(IM(I,J).GT.(MEAN+K*SIGMA)) S(K)=S(K)+1
185 IF(IM(I,J).LT.(MEAN-K*SIGMA)) T(K)=T(K)+1
    TOTAL(K)=S(K)+T(K)
    K=K+1
    IF(K.GT.3) GOTO 195
    GOTO 175
C
195 DO 200, K=1,3
200 PRINT*,S(K),T(K),TOTAL(K)
C
990 FORMAT(A32)
1000 FORMAT(280I4)
C
    STOP
    END
C
C -----END OF BLOCK 3.
C

```

G.5 Sample Output Data From Program STAT

<u>n</u>	<u>$A \pm 3\sigma$</u>	<u>$A \pm 3\sigma$</u>	<u>$A \pm 3\sigma$</u>
1	6,766	8,622	15,388
2	355	1,207	1,562
3	71	77	89

